

Vols. 135, Nos. 1-4 (1995)

REDSEI 135(1-4) 1-412 (1995)
ISSN 1042-0150
ISBN 2-919875-16-7

Radiation Effects — and — Defects in Solids

EDITOR IN CHIEF

Jochen P. Biersack

REGIONAL EDITORS

N. Itoh/H. Kronmüller/M. A. Kumakhov /N. Tolk

DECLASSIFICATION STATEMENT A

Approved for public release
Distribution Unlimited

Proceedings of the
Seventh Europhysical Conference on
Defects in Insulating Materials Eurodim 94
Lyon 1 – University
July 5-8, 1994

Part II

Guest Editors:

M. G. Blanchin, J. Davenas, B. Moine,
C. Pédrini and M. Treilleux

GORDON AND BREACH PUBLISHERS

DO NOT WRITE IN THESE SPACES

19970515 152

Radiation Effects and Defects in Solids

EDITOR IN CHIEF

Jochen P. Biersack Hahn-Meitner-Institut, Glienickerstrabe 100,
14109 Berlin, Germany

REGIONAL EDITORS

N. Itoh Department of Physics, Faculty of Science, Nagoya
University, Furo-cho, Chikusa-ku, Nagoya 464, Japan

H. Kronmüller Max-Planck-Institut für Metallforschung, Institut für
Physik, Heisenbergstrabe 1, 70569 Stuttgart 80, Germany

M. A. Kumakhov Russian Research Center, "I. V. Kurchatov Institute",
Kurachatov Sq, Moscow 123182 Russia

N. Tolk Department of Physics and Astronomy, Vanderbilt University,
P.O. Box 1807-B, Nashville, Tennessee 37325, USA

FOUNDING EDITORS

L. T. Chadderton (Radiation Effects) R. R. Hasiguti (CLDAM)

EDITORIAL BOARD

V. V. Beloshitsky, I. V. Kurchatov Research Center, Russia	J. W. Rabalais, University of Houston, USA
S. Datz, Oak Ridge National Laboratory, USA	S. Radhakrishna, Indian Institute of Technology, India
L. C. Feldman, AT & T Bell Laboratories, USA	E. Rimini, Università di Catania, Italy
A. Gras-Marti, Universitat d'Alacant, Spain	W. A. Sibley, National Science Foundation, USA
E. Kaufmann, Argonne National Laboratory, USA	P. D. Townsend, University of Sussex, UK
M. Kiritani, Nagoya University, Japan	J. C. Tully, AT & T Bell Laboratories, USA
F. F. Komarov, Shevchenko NIIPF, Minsk, Belarus	Z.-L. Wang, Shandong University, China
A. I. Kupchishin, Kirov University, Alma Ata, Kazakhstan	G. Watkins, Lehigh University, USA
G. Margaritondo, Institut de Physique Appliquee, Switzerland	J. Williams, The Australian National University, Australia
W. Möller, Forschungszentrum Rossendorf, Germany	

AIMS AND SCOPE

Radiation Effects and Defects in Solids publishes experimental and theoretical papers of both a fundamental and applied nature that contribute to the understanding of either phenomena induced by the interaction of radiation with condensed matter or defects in solids introduced not only by radiation but also by other processes. Papers are categorised in three groups.

Section A: Radiation Effects — Suitable topics include, but are limited to, atomic collisions, radiation induced atomic and molecular processes in solids, the stopping and range of ions and radiation damage, sputtering and mixing in solids, radiation-induced transport phenomena and the role of defects and impurities introduced by radiation. Papers in ion implantation in metals and semiconductors as well as on radiation effects in insulators and superconductors, in fusion and fission devices and in space research are considered. Studies on fission tracks, isotope dating and ion beam analytic techniques are also welcome.

Section B: Crystal Lattice Defects and Amorphous Materials — Topics covered include atomic and electronic properties of defects, influence of defects on lattice properties and processes, the lattice-defect approach to solid state reactions such as clustering, precipitation, laser annealing and the role of impurities, the defects dynamics in a non-steady state such as under particle or electromagnetic irradiation or during a rapid temperature change and problems associated with the metastable nature of amorphous materials.

Section C: Radiation Effects and Defects in Solids Express — This section is available separately on subscription and presents significant short notes and communications in camera-ready form from the above fields for the fastest possible publication.

Proceedings of the
Seventh Europhysical Conference on
Defects in Insulating Materials Eurodim 94

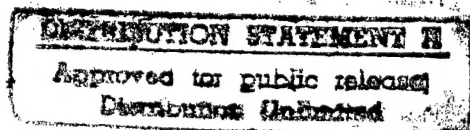
Lyon 1 – University

July 5–8, 1994

Part II

Guest Editors:

M. G. Blanchin, J. Davenas, B. Moine,
C. Pédrini and M. Treilleux



CONTENTS - PART II

Note on Pagination, Author Index and Table of Contents

The Proceedings of the EURODIM 94 Conference is being published in four volumes of Radiation Effects and Defects in Solids (Volume 134, Part I, Volume 135, Part II, Volume 136, Part III and Volume 137, Part IV). To facilitate indexing and referring to this Proceedings, the page numbers of Volume 135, Volume 136 and Volume 137 will run continuously from the end of Volume 134. An author index will appear at the end of Volume 137. A complete table of contents will appear in Volume 134, Part I and Volume 137, Part IV.

4 Spectroscopy luminescence

X-Ray Storage Phosphors J. M. SPAETH, TH. HANGLEITER, F. K. KOSCHNICK and TH. PAWLIK	1/[499]
Fluorescence Line Narrowing in Mn⁴⁺ Doped Gadolinium Gallium Garnet¹ A. SUCHOCKI, M. POTEMSKI, A. BRENIER, C. PEDRINI and G. BOULON	11/[509]
Fine Structure of the Absorption and Emission Spectra of Ni²⁺-Ions in BaLiF₃ E. MARTINS, S. L. BALDOCHI, S. P. MORATO, N. D. VIEIRA JR., A. LUCI, M. CASALBONI, U. M. GRASSANO, G. BALDACCHINI, M. CREMONA, R. M. MONTEREALI, E. KRAUSZ and M. RILEY	15/[513]
Spectroscopic Study of Cr³⁺ in New Elpasolites M. C. MARCO DE LUCAS, J. M. DANCE, F. RODRÍGUEZ, A. TRESSAUD, M. MORENO and J. GRANNEC	19/[517]
Time Resolved Spectroscopy of Ni²⁺ Doped Fluoroclorozirconate Glasses M. A. BUÑUEL, R. ALCALA and R. CASES	23/[521]
Charge Exchange Processes between Impurity Ions and the Host Crystal in Wide Band-Gap Crystals DONALD S. McCLURE, WING C. WONG and SERGEI A. BASUN	27/[525]
The Role of Different Charge States of Impurity Ions in Photoconductivity of Insulators S. A. BASUN	37/[535]
Two-Photon Laser Spectroscopy of Ce³⁺ in LiYF₄ J. C. GÂCON, J. BAUDRY, C. GARAPON and G. W. BURDICK	41/[539]
Optical Spectroscopy of Yb³⁺ Ions in Ca₂Cd_{1-x}F₂ K. ŚWIATEK	45/[543]
ENDOR-Investigations of Rare Earth and Transition Metal Ions in the Cubic Elpasolite Crystal Cs₂NaYF₆ TH. PAWLIK, J.-M. SPAETH, M. OTTE and H. OVERHOF	49/[547]
Optical and EPR Spectroscopy of Impurity Manganese Ions in Disordered Ca₃Ga₂Ge₄O₁₄ Single Crystals A. E. NOSENKO, R. YE. LESHCHUK and B. V. PADLYAK	55/[553]
Interaction of Impurity Centres in Cs₂CdI₄-Mn Crystals I. BOLESTA and Y. FURGALA	61/[559]
Blue Avalanche Upconversion in YAG:Ti S. GUY, M. F. JOUBERT, B. JACQUIER and C. LINARÉS	65/[563]
New Spectroscopic Effects of Ferroelectric Phase Transition in Li₂Ge₇O₁₅ Crystals Doped with 3d³-Ions A. A. KAPLYANSKII, S. A. BASUN and S. P. FEOFILOV	69/[567]
Excited State Absorption in Holmium Doped Gd₃Ga₅O₁₂ Garnet A. BRENIER, C. MADEJ, C. PÉDRINI and G. BOULON	73/[571]

Luminescence of Ytterbium Doped $\text{LiNbO}_3\text{:MgO}$ under UV Excitation A. BRENIER, C. MADEJ, C. PÉDRINI and G. BOULON	77/[575]
Optical Detection of Eu^{3+} Sites in $\text{Gd}_3\text{Ga}_5\text{O}_{12}\text{:Eu}^{3+}$ L. C. COURROL, L. GOMES, A. BRENIER, C. PÉDRINI, C. MADEJ and G. BOULON	81/[579]
Study of Bistable (Shallow-Deep) Defect Systems in $\text{CdF}_2\text{:M}^{3+}$ (M: In, Ga) YANG CAI and K. S. SONG	85/[583]
Polarized Charge Transfer Spectra of Cu^{2+} Doped Perovskite Layers $(\text{RNH}_3)_2\text{Cd}_x\text{Mn}_{1-x}\text{Cl}_4$ ($x = 0-1$) B. BATICLE, F. RODRÍGUEZ and R. VALIENTE	89/[587]
Optical Properties and Local Structure of MnCl_4^{4-} in $\text{ABC}\text{Cl}_3\text{:Mn}^{2+}$ M. C. MARCO DE LUCAS, F. RODRÍGUEZ, C. PRIETO, M. VERDAGUER, M. MORENO and H. U. GÜDEL	95/[593]
Photo-EPR Studies of Electron and Hole Trapping by $[\text{Fe}(\text{CN})_6]^{4-}$ Complexes in Silver Chloride M. T. OLM and R. S. EACHUS	101/[599]
Site Selective Spectroscopy of Eu^{3+} and $\text{Eu}^{3+}\text{-Ho}^{3+}$ Doped Glasses V. D. RODRÍGUEZ, V. LAVÍN, U. R. RODRÍGUEZ-MENDOZA, I. R. MARTÍN and P. NUÑEZ	105/[603]
Thermoluminescence of Brazilian Topaz DIVANÍZIA DO N. SOUZA, JOSÉ F. DE LIMA and MÁRIO ERNESTO G. VALERIO	109/[607]
Point Defects Produced by Grinding of CaS Phosphors: An Electron Spin Resonance Study D. CAURANT, D. GOURIER, N. DEMONCY and M. PHAM-THI	115/[613]
Thermally Stimulated Depolarization Current of Monovalent Copper Ions in Calcium Fluoride L. OLIVEIRA, O. R. NASCIMENTO, M. SIU LI, C. PÉDRINI and H. BILL	121/[619]
Photostimulated Luminescence of KBr-In Crystals I. PLAVINA, A. I. POPOV and A. TALE	125/[623]
Energy Transfer and Up-Conversion in Yb-Tm Codoped Fluorindate Glasses V. D. RODRÍGUEZ, I. R. MARTÍN, R. ALCALÁ and R. CASES	129/[627]
Spectrally Resolved Thermoluminescence of Cu and Eu Doped $\text{Li}_2\text{B}_4\text{O}_7$ M. MARTINI, C. FURETTA, C. SANIPOLI, A. SCACCO and K. SOMAIAH	133/[631]
Reversible Photoionization Process in Luminescent Ce^{3+} Doped Elpasolite-Type Fluoroindates J. P. CHAMINADE, A. GARCIA, T. GAUWANG, M. POUCHARD, J. GRANNEC and B. JACQUIER	137/[635]
Excited Levels of the 2.56 eV Emission in Synthetic Diamond E. PEREIRA, L. PEREIRA, D. M. HOFMANN, W. STADLER and B. K. MEYER	143/[641]
Er^{3+} Ion Concentration and Annealing Temperature Effect on the Fluorescence of $\text{Er}^{3+}\text{:TiO}_2$ Planar Waveguides Prepared by the Sol-Gel Process A. BAHTAT, M. BOUZAOU, M. C. MARCO DE LUCAS, M. BAHTAT, B. JACQUIER and J. MUGNIER	149/[647]
EPR and Photoluminescence of Cr^{3+} Ions in CsCdF_3 and CsCaF_3 B. VILLACAMPA, R. CASES and R. ALCALÁ	157/[655]
Spectroscopic Properties of Mn^{2+} Ions in Mixed Fluoroperovskites F. LAHOZ, P. J. ALONSO, B. VILLACAMPA and R. ALCALÁ	163/[661]
EPR Study of Concentration Dependence in Ce, Ce:La and Ce:Y Doped SrF_2 O. DANKERT, D. VAINSHTEIN, H. C. DATEMA and H. W. DEN HARTOG	169/[667]
Differential Spectroscopic Properties of Nd^{3+} in NdGaO_3 and LaGaO_3 V. M. ORERA, L. E. TRINKLER and R. I. MERINO	173/[671]

CONTENTS

v

EPR of Jahn-Teller Cr^{2+} in CaF_2, BaF_2 and SrCl_2 P. B. OLIVETE, V. M. ORERA and P. J. ALONSO	179/[677]
Nd^{3+} Centres in Highly Neodymium Doped LaBGeO_5 Crystals L. BITAR, J. CAPMANY, L. E. BAUSÁ, J. GARCÍA-SOLÉ, R. MONCORGÉ and A. A. KAMINSKII	183/[681]
Energy Levels of the Eu^{3+} Centers in LiNbO_3 J. E. MUÑOZ SANTIUSTE, I. VERGARA and J. GARCÍA SOLÉ	187/[685]
EPR Study of Nd^{3+} Ions in $\text{Bi}_4\text{Ge}_3\text{O}_{12}$ Single Crystals D. BRAVO, A. MARTÍN, A. A. KAMINSKII and F. J. LÓPEZ	191/[689]
Light-Induced NIR-Absorption in $\text{Sr}_{0.81}\text{Ba}_{0.39}\text{Nb}_2\text{O}_6$: Ce at Low Temperatures G. GRETEN, S. KAPPAN and R. PANKRATH	195/[693]
Sharp R-Lines in Absorption and Emission of Cr^{3+} in Stoichiometric (VTE) LiNbO_3 C. FISCHER, S. KAPPAN, XI-QI FENG and NING CHENG	199/[697]
Clustering Processes in CaF_2 : Gd + Lu and CaF_2 : Gd + Sm N. SUÁREZ	203/[701]
New Symmetry Properties of the Cubic Rare-Earth Centers in Crystals V. LUPEI	207/[705]
Nonradiative Recombination Processes in Wide Band Gap II-VI Phosphor Materials M. SURMA and M. GODLEWSKI	213/[711]
Upconversion Luminescence Properties of Er^{3+} Ions Doped in Lithium Niobate Single Crystals H. J. SEO, T. P. J. HAN, G. D. McCLURE and B. HENDERSON	217/[715]
EPR and Optical Spectroscopy of Cr^{3+} Doped CaYAlO_4 M. YAMAGA, H. TAKEUCHI, K. HOLLIDAY, P. MACFARLANE, B. HENDERSON, Y. INOUE and N. KODAMA	223/[721]
Optical Properties of Cr^{3+}-Ions in $\text{LaSr}_2\text{Ga}_{11}\text{O}_{20}$ A. LUCI, M. CASALBONI, T. CASTRIGNANO, U. M. GRASSANO and A. A. KAMINSKII	227/[725]
Nonlinear Transmission in Cr^{4+}-Doped Silicates V. P. MIKHAILOV, N. I. ZHAVORONKOV, N. V. KULESHOV, A. S. AVTUKH, V. G. SHCHERBITSKY and B. I. MINKOV	231/[729]
Photo-Stimulated X-Ray Luminescence in LiTaO_3 : Tb^{3+} Based Green Emitting Phosphors R. BRACCO, C. MAGRO and R. MORLOTTI	237/[735]
Absorption and Luminescence Spectroscopy of Zinc Borate Glasses Doped with Trivalent Lanthanide Ions LUIGI AMBROSI, MARCO BETTINELLI, GUY CORMIER and MAURIZIO FERRARI	243/[741]
Optical Energy Transfer in Rare Earth Doped Silica Gels A. BOUAJAJ, A. MONTEIL, M. FERRARI and M. MONTAGNA	247/[745]
Samarium Doped Alkaline Earth Halide Thin Films as Spectrally Selective Materials for Hole Burning? A. MONNIER, M. SCHNIEPER, R. JAANISO and H. BILL	253/[751]
5 Excited States	
Upconversion in CsCdBr_3 : Pr^{3+} J. NEUKUM, N. BODENSCHATZ and J. HEBER	257/[755]
Metastable One-Halide Self-Trapped Excitons in Alkali Halides A. LUSHCHIK, CH. LUSHCHIK, F. SAVIKHIN and E. VASIL'CHENKO	263/[761]

Optical Studies of Self-Trapped Holes and Excitons in Beryllium Oxide S. V. GORBUNOV, S. V. KUDYAKOV, B. V. SHULGIN and V. YU. YAKOVLEV	269/[767]
The Experimental Observation of the Potential Barrier for Self-Trapped Exciton Decay into F-H Pair in KCl-Na in Crystals S. A. CHERNOV and V. V. GAVRILOV	275/[773]
Luminescence of ON- And OFF-Center STE in ABX_3 Crystals A. S. VOLOSHINOVSKI, V. B. MIKHAILIK and P. A. RODNYI	281/[779]
Phonon Assisted Excitonic Luminescence in $CsPbCl_3$ I. BALTOG, S. LEFRANT, C. DIMOFTE, and L. MIHUT	285/[783]
Optical Properties Of Pb^{2+}-Based Aggregated Phase In NaCl And CsCl Alkali Halide Hosts M. NIKL, K. POLAK, K. NITSCH, G. P. PAZZI, P. FABENI and M. GURIOLI	289/[787]
Dynamical Processes of Ortho- and Para-Excitons in Alkali Iodides KOICHI TOYODA, TORU TSUJIBAYASHI and TETSUSUKE HAYASHI	295/[793]
Defects and Luminescence in Pure and I-Doped AgBr Crystals L. NAGLI, A. SHMILEVICH, A. KATZIR and N. KRISTIANPOLLER	301/[799]
6 Scintillators	
Scintillation Mechanisms in Rare Earth Orthophosphates A. J. WOJTOWICZ, D. WISNIEWSKI, A. LEMPICKI, and L. A. BOATNER	305/[803]
Scintillation Properties of $Lu_3Al_{5-x}Sc_xO_{12}$ Crystals¹ N. N. RYSKIN, P. DORENBOS, C. W. E. VAN EIJK and S. KH. BATYGOV	311/[809]
Monte-Carlo Simulation of the Creation of Excited Regions in Insulators by a Photon R. A. GLUKHOV and A. N. VASIL'EV	315/[813]
Scintillation Properties of $GdAlO_3:Ce$ Crystals¹ P. DORENBOS, E. BOUGRINE, J. T. M. DE HAAS, C. W. E. VAN EIJK and M. V. KORZHIK	321/[819]
Scintillation Properties of $Y_2SiO_5:Pr$ Crystals¹ P. DORENBOS, M. MARSMAN, C. W. E. VAN EIJK, M. V. KORZHIK and B. I. MINKOV	325/[823]
Scintillation Mechanism in $CsGd_2F_7:Ce^{3+}$ and $CsY_2F_7:Ce^{3+}$ Crystals[†] D. R. SCHAART, P. DORENBOS, C. W. E. VAN EIJK, R. VISSER, C. PEDRINI, B. MOINE and N. M. KHAIDUKOV	329/[827]
Nanosecond UV-Scintillation in Cesium Iodide Crystals S. CHERNOV and V. GAVRILOV	333/[831]
Defects Induced by Irradiation at Room Temperature in Cerium Fluoride E. AUFRAY, I. DAFINEI, P. LECOQ and M. SCHNEEGANS	337/[835]
Local Trap Centres in $PbWO_4$ Crystals E. AUFRAY, I. DAFINEI, P. LECOQ and M. SCHNEEGANS	343/[841]
Temperature Dependence of Crossluminescence Characteristics in CsCl and CsBr in the 20–300 K Range V. MAKHOV, J. BECKER, L. FRANKENSTEIN, I. KUUSMANN, M. RUNNE, A. SCHRÖDER and G. ZIMMERER	349/[847]
Time-Resolved Studies Of Fast Scintillating Crystals Under VUV And X-Ray Synchrotron Radiation Excitation E. G. DEVITSIN, N. M. KHAIDUKOV, N. YU. KIRIKOVA, V. E. KLIMENKO, V. A. KOZLOV, V. N. MAKHOV and T. V. UVAROVA	355/[853]
ODMR of CD Impurity Centers in GG Irradiated BaF_2 Crystals U. ROGULIS, J. TROKŠS, Ā. VEISPĀLS, I. TĀLE, P. KŪLIS and M. SPRINĢIS	361/[859]

Colour Cathodoluminescence from $\text{Bi}_4[\text{GeO}_4]_3$ Crystals	367/[865]
T. A. NAZAROVA, M. V. NAZAROV, G. V. SAPARIN and S. K. OBYDEN	
Further Results on $\text{GdAlO}_3:\text{Ce}$ Scintillator	369/[867]
J. A. MAREŠ, M. NIKL, C. PEDRINI, D. BOUTTET, C. DUJARDIN, B. MOINE, J. W. M. VERWEIJ and J. KVAPIL	
Multiplication of Anion and Cation Electronic Excitations in Alkali Halides	375/[873]
M. KIRM, A. FRORIP, R. KINK, A. LUSHCHIK, CH. LUSHCHIK and I. MARTINSON	
Peculiarities of the Triplet Relaxed Excited State Structure in Thallium-Doped Cesium Halide Crystals	379/[877]
V. NAGIRNYI, A. STOLOVICH, S. ZAZUBOVICH, V. ZEPELIN, M. NIKL, E. MIHOKOVA and G. P. PAZZI	
The Role of Cation Vacancies in Excitation Mechanism of Re-Ions in Alkaline-Earth Sulphides	383/[881]
A. N. BELSKY, V. V. MIKHAILIN and A. N. VASIL'EV	
LSO-Ce Fluorescence Spectra and Kinetics for UV, VUV and X-Ray Excitation	391/[889]
I. A. KAMENSKIKH, V. V. MIKHAILIN, I. H. MUNRO, D. Y. PETROVYKH, D. A. SHAW, P. A. STUDENIKIN, A. N. VASIL'EV, I. A. ZAGUMENNYI and YU. D. ZAVARTSEV	
Luminescence and Scintillation Properties of $\text{In}_2\text{Si}_2\text{O}_7$	397/[895]
A. GARCIA, T. GAUWANG, J. P. CHAMINADE, C. FOUASSIER, B. VARREL, B. JACQUIER, M. MESSOUS, B. CHAMBON and D. DRAIN	
Thermoluminescence of Doped $\text{Gd}_3\text{Ga}_5\text{O}_{12}$ Garnet Ceramics	401/[899]
A. JAHNKE, M. OSTERTAG, M. ILMER and B. C. GRABMAIER	
Luminescence Decay of Rare Earth Ions in an Orthophosphate Matrix	407/[905]
B. FINKE and L. SCHWARZ	

4 SPECTROSCOPY LUMINESCENCE

X-RAY STORAGE PHOSPHORS

J. M. SPAETH, TH. HANGLEITER, F. K. KOSCHNICK and TH. PAWLIK

Universität-GH Paderborn, Fachbereich Physik, 33095 Paderborn, Germany

In X-ray storage phosphors an image is formed and stored by generation of room temperature stable radiation-induced electron and hole trap centres. The image is read-out by recording a photo-stimulated luminescence (PSL) from a doped activator, generally stimulating the electron trap centres. The best-known and hitherto most efficient X-ray storage phosphor is BaFBr:Eu²⁺. However, the exact mechanism of its functioning is not yet understood. The present discussion of the storage and read-out mechanisms is critically reviewed. New results about the role of oxygen contamination of BaFBr:Eu²⁺ are presented: if there is much less oxygen present than Eu²⁺, then the PSL efficiency decreases and the stimulation energy increases. A new efficient X-ray storage phosphor is presented: Cs₂NaYF₆ doped with trivalent rare earth activators. Its properties are described and preliminary results on X-radiation-induced radiation damage centres in undoped Cs₂NaYF₆ are presented.

Key words: Phosphors, X-ray imaging, ODEPR, elpasolites, fluorohalides, radiation damage.

1 INTRODUCTION

X-ray storage phosphors are materials capable of storing images produced by the absorption of X-radiation. Upon X-irradiation of the phosphor, radiation-induced defects are generated, which must be stable at room temperature (at least for a few minutes) for the practical use. It is generally believed that electron and hole trap centres are involved in the image formation. For the read-out process usually the electron trap centres are photo-excited, and the luminescence of a doped activator, in many cases a rare earth ion, is recorded. The X-ray storage phosphors can offer a number of advantages compared to conventional X-ray films which makes the search for a good X-ray storage phosphor a challenge: efficient ones are more sensitive and have a much higher dynamical range (10⁴–10⁵) for the image formation compared to conventional film, and they offer the possibility to obtain immediately digitized X-ray images. One of the main problems is still the poorer spatial resolution due to light scattering effects in the screens from the small phosphor crystallites during the read-out process. Many systems have been proposed (for a concise review see e.g. ¹). The best-known X-ray storage phosphor, and seemingly so far the best one which is commercially used already, is BaFBr:Eu²⁺.² In spite of many efforts to understand the mechanism of the storage and read-out process, no complete understanding has yet been achieved. On the contrary, many controversial ideas have been published in recent years about the nature and role of the electron and hole trap centres and their reactions during read-out. It was shown recently that BaFBr:Eu²⁺ contains a rather high level (typically 100 ppm) of oxygen contamination and that this impurity greatly influences the formation of electron trap centres.^{3,4}

In this article, the present discussion of the mechanisms for storage and read-out is critically reviewed. Then, new experimental results about the role of the oxygen contamination in BaFBr:Eu²⁺ are presented. Finally, we present a new efficient X-ray storage phosphor: Cs₂NaYF₆ doped with trivalent activators, e.g. rare earth ions. Cs₂NaYF₆ is a member of the elpasolite crystal family. Preliminary results on radiation damage centres in undoped Cs₂NaYF₆ are also presented.

2 THE STORAGE PHOSPHOR BaFBr:Eu²⁺

2.1 Imaging Centres and Read-out Process

In a simplistic view, the mechanism might be the following:

X-irradiation produces room temperature stable electron and hole trap centres. Upon photo-stimulation of the electron trap centres, the electron recombines with the hole trap centre, then there is a radiationless transfer of the recombination energy to the activator which is brought to an excited state from which it decays emitting the photo-stimulated luminescence PSL (in case of Eu²⁺ at 390 nm). However, not even in the well studied system BaFBr:Eu²⁺ the mechanism is understood. Three groups have investigated this material very intensely in recent years: a group at Fuji (Takahashi *et al.*), one at Siemens (v. Seggern *et al.*) and our group in collaboration with Eastman Kodak (Eachus *et al.*).

There is general agreement that X-irradiation generates F centres as electron trap centres. In BaFBr, which has the matlockite structure,⁵ two F centres are possible, F(Br⁻) centres and F(F⁻) centres, where electrons are trapped at Br⁻ vacancies or F⁻ vacancies, respectively. Their generation mechanism, however, is controversial. In order to form an F centre after creating an electron-hole pair by the X-irradiation, one either needs to have a halide vacancy present in the crystal or one must generate it during the radiation damage process.

Takahashi *et al.*^{6,7} assumed that Br⁻ vacancies are present in the material. However, he gives no experimental evidence for this assumption. Rüter *et al.*⁸ showed that photostimulable centres can be created by using vacuum UV-light (> 6.7 eV) instead of X-rays and concluded that the decay of self-trapped excitons into F and H centres (Br₂⁻ ions on a halide lattice site, see e.g.⁹), provide the necessary mechanism to create F centres.

However, so far H centres were not detected, neither by EPR, nor by ODEPR which is more sensitive, in spite of a search for them including production of F centres with X-irradiation at low temperature (4 K) where H centres are stable. It was shown recently in KBr that H centres can be detected using the magnetic circular dichroism of the optical absorption (MCDA) and MCDA-detected EPR.¹⁰

In the earlier work on BaFBr it was overlooked that it is extremely difficult to produce BaFBr powders or single crystals which are not contaminated with oxygen. BaFCl and BaFBr scavenge oxygen from their growth environment.^{11,12} Oxygen is incorporated mainly as O²⁻ on F⁻ sites accompanied by a Br⁻ vacancy for charge compensation. Upon X-irradiation at low temperature (< 120 K) V_k(Br₂⁻) centres and F(Br⁻) centres are formed, the latter being near the O_F²⁻ centres. Above 120 K, the V_k(Br₂⁻) centres become mobile. O_F²⁻ centres react with them and an O_F⁻ centre is formed. Above 200 K, the F centre can diffuse away and become isolated.^{3,4} The production of F(Br⁻) centres is strongly influenced by the oxygen contamination. It cannot be excluded that the samples used by Rüter *et al.* [8] did also contain sufficient oxygen contamination to account for the production of F(Br⁻) centres with UV-light.

Interestingly, F(F⁻) centres are not formed by X-irradiation below about 250 K. They are formed by X-irradiation at room temperature, but their concentration does not seem to be influenced by the oxygen contamination directly. F(F⁻) centre formation apparently needs thermal activation.¹³

When measuring the photostimulation as a function of photon energy, two peaks are usually observed; one peaking at 2.15 eV, and one around 2.65 eV. The two peaks are clearly resolved when using single crystals and polarized light (e.g. $\vec{E} \perp \vec{c}$ axis).¹⁴ The spectral shape of the photostimulation curve agrees very well with the optical absorption bands of F(F⁻) centres (peak at 2.65 eV for $\vec{E} \perp \vec{c}$) and F(Br⁻) centres (peak at 2.15 eV for $\vec{E} \perp \vec{c}$). There is only one absorption band for $\vec{E} \perp \vec{c}$ for each F centre which was clearly

identified by magneto-optical techniques.¹⁵ It was argued by Thoms *et al.* [16] that only $F(Br^-)$ centres are photostimulable and the two peaks observed in the photostimulation curve were associated with those centres. We observed, however, that both $F(F^-)$ and $F(Br^-)$ centres are photostimulable. When measuring first the optical density of $F(F^-)$ and $F(Br^-)$ centres and stimulating the PSL by photoexciting e.g. in the $F(Br^-)$ band, then the optical absorption band of $F(Br^-)$ centres is reduced after exhaustion of the PSL, however, that of the $F(F^-)$ centres is not affected. When bleaching into the $F(F^-)$ band, there is also a PSL effect. Thus, both $F(F^-)$ and $F(Br^-)$ centres are photostimulable.

Very little is known about the hole centres. Takahashi *et al.*^{6,7,17} claim that upon electron and hole creation by X-rays holes are trapped at Eu^{2+} and form Eu^{3+} . Upon photostimulation of F centres, the F electrons move through the conduction band and recombine with Eu^{3+} , exciting Eu^{2+} to the $4f^65d$ state, from which the 390 nm luminescence occurs. Thus, in their model the PSL process requires thermal activation since the excited F centres have relaxed excited states below the conduction band. According to Takahashi *et al.*, the thermal activation energy is 37 meV for $F(Br^-)$ and 1.3 meV for $F(F^-)$. Neither v. Seggern *et al.* nor Eachus *et al.* nor our group have been able to identify Eu^{3+} centres after X-irradiation. The EPR signal of Eu^{2+} did not change upon prolonged X-irradiation, nor could the Eu^{3+} luminescence be observed. Furthermore, the observation of an efficient PSL effect by stimulating $F(Br^-)$ centres at 1.5 K contradicts the model that electrons move through the conduction band upon photostimulation of F centres.

No spectroscopic identification has yet been presented for the hole trap centres involved in the PSL process. It has been proposed, though, on the basis of several different experimental findings, that the recombination between electron and holes takes place via tunneling and that a kind of 'aggregates' between F centres, hole centres and the activator Eu^{2+} must be formed during X-irradiation. It was found that the decay of the photostimulated luminescence under continuous stimulation is temperature independent¹⁸ and that the increase in the PSL intensity is proportional to the X-ray dose.¹⁹ This latter result implies that retrapping of electrons after photostimulation does not occur, which makes electron hole recombination via tunneling more likely than via the conduction band. Direct evidence for a spatial correlation between F centres, O_F^- centres and Eu^{2+} was given with cross-relaxation spectroscopy using magneto-optical techniques.^{3,20}

Indirect evidence for the formation of triple aggregate centres was also found in the so-called replenishment effect. When at low temperature (4 K) the phosphor is stimulated and the PSL exhausted, it can be replenished by annealing to temperature above 200 K.²¹ It seems that after exhaustion of the aggregate formed first, new aggregates can be formed by thermally activated motion of either hole trap or electron trap centres or both. The size of the effect depends on the amount of oxygen contamination.

So far, the O_F^- centre (and under certain preparation conditions also O_{Br^-} centres) is the only identified hole centre formed by X-irradiation at temperatures above 120 K.²² Whether or not it is the hole centre searched for, is not yet clear. In order to get further insight, it is important to vary the oxygen contents in the samples. First new results on the role of oxygen are presented in the next section.

2.2 Variation of the Oxygen Contents

A series of single crystals was grown with the Bridgman-Stockbarger method in graphite crucibles varying the oxygen contents. In order to avoid oxygen contamination before crystal growth, the $BaBr_2$ and BaF_2 powders were placed into a vitreous carbon boat in a quartz tube, heated to 1050°C where they were molten. The melt was then treated for 2.5 hours with a mixture of Ar and Br_2 gas. After cooling to room temperature, the powders

thus treated were loaded into the graphite crucibles in a glove box to avoid new oxygen contamination. For back-doping of oxygen, BaO was added.

Doping levels are: 500 ppm Eu^{2+} (added as EuF_2) and 0, 200, 500 and 2000 ppm oxygen added as BaO to the melt. Those doping levels were not measured in the grown crystals, but refer to the melt doping. We are pretty sure that the '0' oxygen level actually does not mean that no residual oxygen contamination could be achieved. However, its level could be reduced by about a factor of 20 compared to crystals grown without the Br_2 treatment before crystal growth. The optical density measured in the series of single crystals ($\vec{E} \perp c$) after 10 minutes exposure to X-irradiation at room temperature (65 kV, 6 mA) showed practically 'no' absorption of $\text{F}(\text{Br}^-)$ centres for the 'oxygen-free' sample, while with increasing oxygen contents more and more optical absorption of $\text{F}(\text{Br}^-)$ centres was measured. A measurement of the MCDA confirms that with increasing oxygen contents more $\text{F}(\text{Br}^-)$ centres are formed after the same time of X-ray exposure. However, for '0' oxygen doping level, a small number of $\text{F}(\text{Br}^-)$ and also O_F^- centres were still detected. An interesting observation was that the ratio between $\text{F}(\text{Br}^-)$ and $\text{F}(\text{F}^-)$ centres is larger at high oxygen level, while at low oxygen contents more $\text{F}(\text{F}^-)$ centres were generated compared to $\text{F}(\text{Br}^-)$ centres. Whether or not the number of $\text{F}(\text{Br}^-)$ centres measured corresponds already to the saturation values for the corresponding oxygen contents was not investigated.

It was found previously¹³ that in BaFBr, contaminated with oxygen, the number of $\text{F}(\text{Br}^-)$ centres saturates when the X-ray dose reaches a certain value, while that of $\text{F}(\text{F}^-)$ centres continues to increase with increasing X-ray dose.

A measurement of the luminescence band of O_F^{2-} centres peaking at 2.4 eV and of the Eu^{2+} luminescence peaking at 3.18 eV at room temperature, both excited at 5.0 eV (247 nm) confirms that the '0' and 200 ppm doping levels contain very little oxygen while the 500 and 2000 ppm samples clearly show the O^{2-} band. According to the luminescence measurements, the oxygen content does not differ much for 0 and 200 ppm and for 500 and 2000 ppm. The results obtained with the MCDA are similar to that. An interesting observation was also that in the samples with high oxygen contents the Eu^{2+} luminescence was much smaller compared to those with low oxygen contents.

In the 2.4 eV luminescence of O_F^{2-} it was possible to measure an EPR spectrum by detecting the microwave-induced change in the luminescence intensity. The EPR spectrum is due to an excited triplet state of O_F^{2-} with a fine structure interaction. The four centre orientations measured point to the presence of a nearby Br^- vacancy confirming the earlier results on the low temperature generation of $\text{F}(\text{Br}^-)$ centres (see above). Details about the ODEPR results will be published elsewhere.²³

The most important result we obtained for the different oxygen contents was the influence on the PSL effect. As seen in Figure 1, the PSL intensity measured at room temperature after the same X-ray exposure is about a factor of 2.5 higher for oxygen-rich BaFBr compared to oxygen-poor material. Also the decay time of the PSL under continuous excitation becomes larger for the oxygen-poor sample. Thus, the stimulation energy needed for the read-out process is higher for oxygen-poor BaFBr. Within experimental error the same observation is made for read-out at 10 K.

It seems that oxygen is involved in various ways into the mechanism:

- i it provides the vacancies for the $\text{F}(\text{Br}^-)$ generation
- ii it seems to positively influence the formation of photostimulable 'aggregate' centres in that less stimulation energy is needed for read-out and a higher PSL intensity results after short stimulation.

We know from cross relaxation spectroscopy that O_F^- centres are spatially correlated to Eu^{2+} , as are the $\text{F}(\text{Br}^-)$ centres. It is conceivable that some O_F^- are near Eu^{2+} together

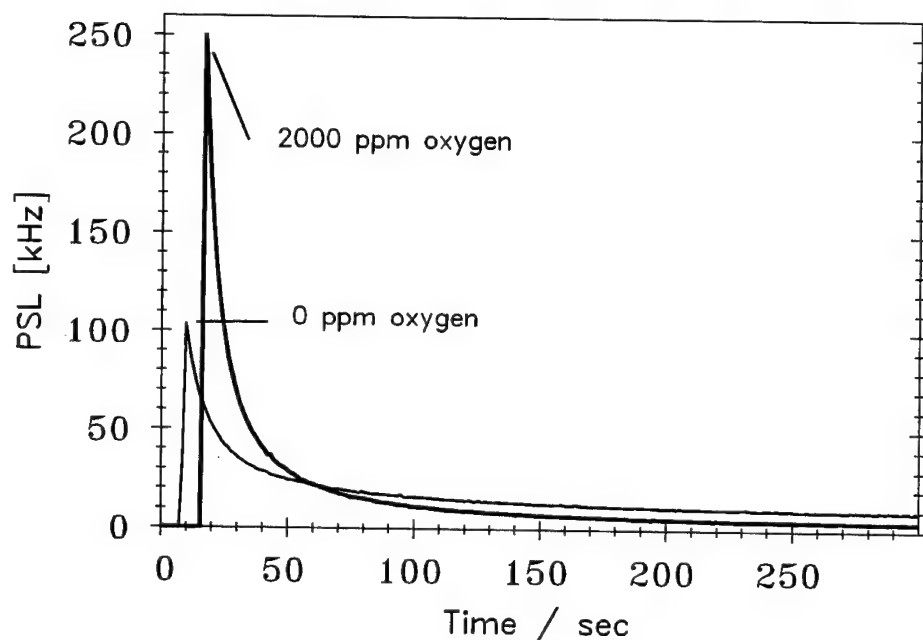


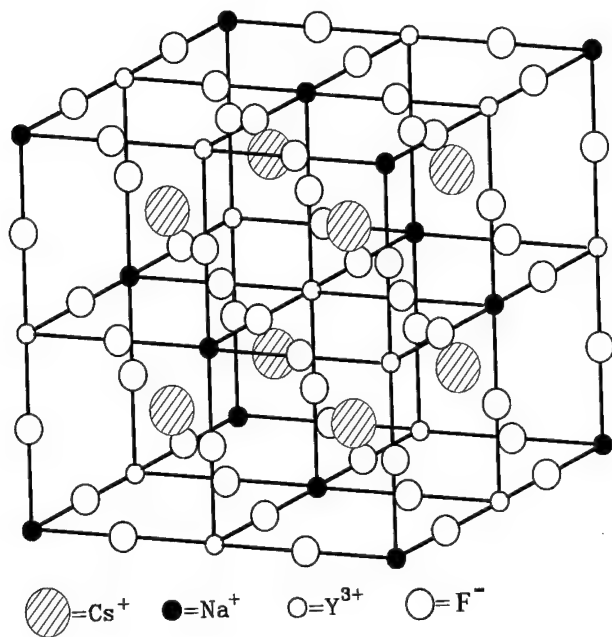
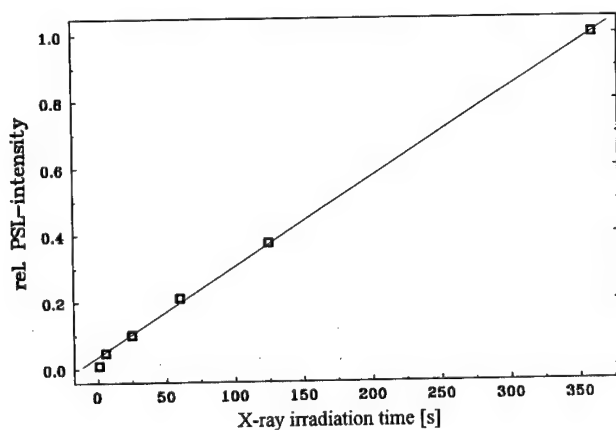
FIGURE 1 PSL of BaFBr:Eu²⁺ under continuous excitation at 575 nm in the F(Br⁻) band at 300 K for nominal oxygen contents of 0 and 2000 ppm oxygen.

with an F centre and then forming such a triple aggregate needed. The improved performance in oxygen-rich material seems to indicate this. One might speculate that there is an optimum oxygen content with respect to the Eu²⁺ doping level.

F(F⁻) centres are also photostimulable. It is not clear how they are generated. Upon prolonged X-irradiation, the number of F(Br⁻) centres decreases after reaching their saturation value in oxygen containing BaFBr and that of F(F⁻) centres more or less starts to increase when F(Br⁻) begins to decrease.¹³ The F(F⁻) production does not seem to be related directly to the oxygen contents. One might therefore think that an intrinsic hole centre is associated with them, unless they are formed by an X-ray-induced conversion of F(Br⁻) centres. To obtain further insight, an aim must be to produce BaFBr:Eu²⁺, in which the residual oxygen contamination is very small and then study the F(F⁻) centre generation.

3 A NEW X-RAY STORAGE PHOSPHOR: Cs₂NaYF₆:A³⁺

Cs₂NaYF₆ is a cubic crystal of the family of the elpasolites.²⁴ It has a site with octahedral symmetry for the trivalent Y³⁺ and thus for any trivalent activator ion A³⁺ (see Figure 2). The heavy Cs⁺ ions provide a good stopping power for X-rays. After X-irradiation at room temperature, a broad absorption band is created peaking at about 2.5 eV (500 nm) and extending to 1.90 eV (650 nm) towards lower energy. This absorption band originates in paramagnetic centres, since several temperature and magnetic field dependent MCDA bands are measured in the spectral range where the optical absorption is found (see below). When the Cs₂NaYF₆ is doped with Ce³⁺, the photoluminescence of Ce³⁺ peaking at

FIGURE 2 Crystal structure of the cubic elpasolite Cs₂NaYF₆.FIGURE 3 PSL intensity of Cs₂NaYF₆:Ce³⁺ as a function of X-irradiation time. $\lambda_{\text{em.}} = 357.9$ nm, $\lambda_{\text{exc.}} = 632.8$ nm, 300 K.

358 nm due to the 5d-4f transitions can be excited in the broad absorption band described above. The Ce³⁺ doped Cs₂NaYF₆ shows a PSL effect. Figure 3 shows that the PSL intensity increases linearly with the X-ray dose. For this measurement, the PSL was excited at 633 nm in the red flank of the broad X-ray induced absorption band.

The PSL emission band is identical with the prompt X-ray induced luminescence of Ce³⁺. A comparison of the decay times of the PSL emission excited at 500 nm with a flash lamp of 5 ns pulse decay time and of the direct excitation of Ce³⁺ at 306 nm shows that the

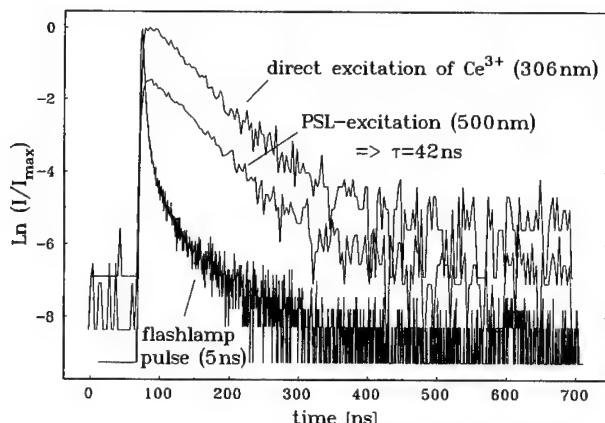


FIGURE 4 PSL after flash light reduced read-out at 500 nm and direct luminescence excited by flash light at 306 nm of $\text{Cs}_2\text{NaYF}_6:\text{Ce}^{3+}$, measured at room temperature.

decay times of both emissions are identical within experimental error, i.e. 42 ns at room temperature (Figure 4). This is qualitatively the same result as found for $\text{BaFBr}:\text{Eu}^{2+}$: the bottleneck for the PSL decay time is the radiative life time of the activator ion. Thus one can assume also for this system that electron-hole recombination occurs via a tunneling process and not via the conduction band.

PSL effects have also been observed for other activators, e.g. Pr^{3+} and Sb^{3+} . For Pr^{3+} , two bands at about 500 nm and 600 nm can be excited which, however, coincide with the broad X-ray induced absorption band while Sb^{3+} emits at about 350 nm. For a practical use, the PSL decay time of Pr^{3+} is too long (4 ms); that of Sb^{3+} is much faster. When crudely comparing the $\text{Cs}_2\text{NaYF}_6:\text{Ce}^{3+}$ phosphor with $\text{BaFBr}:\text{Eu}^{2+}$ with respect to sensitivity and stimulation energy needed for read-out, the performance of the new phosphor is not as good yet, but of the same order of magnitude. However, research on this material is still in its very beginning.

No F centres have yet been reported in Cs_2NaYF_6 , and it is, of course, speculated that the broad absorption band created by X-irradiation is due to F centres. In this crystal, an electron trapped at a F⁻ site would have 4 nearest Cs^+ ions and one nearest Y^{3+} as well as one nearest Na^+ ion (see Figure 2). Figure 5 shows the MCDA spectrum measured in the spectral region between 300 and 800 nm and Figure 6 the MCDA-detected EPR-spectrum measured at 575 nm as a microwave-induced change of the MCDA (see e.g.²⁵) after X-irradiation of the undoped crystal.

An isotropic broad EPR line at $g \approx 2$ with a half width of 67 mT is found superimposed on a narrow EPR line with a half width of 8 mT with opposite sign, i.e. upon inducing microwave transitions the MCDA decreases for the broad line, but increases for the narrow line in contrast to what is usually found when using this method.

The narrow line is slightly angular dependent. Its g -value is higher compared to that of the broad centre by $\Delta g \approx 0.01$. (A precise determination of the absolute g -values has not yet been made). The two EPR lines cannot be measured separately by choosing different wavelengths in the MCDA spectrum. The superimposed ODEPR spectra of Figure 6 are measured always in all portions of the MCDA between 400 and 650 nm. Whether the low MCDA at higher wavelengths does also belong to the two EPR lines is not yet clear. It also grows upon increasing the X-ray dose.

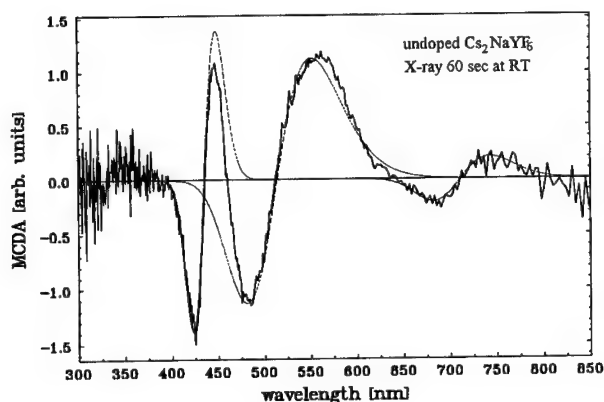


FIGURE 5 MCDA of undoped Cs_2NaYF_6 after irradiation with X-rays at room temperature. The dashed curve is a decomposition into two derivative like MCDA bands. $T = 1.5$ K.

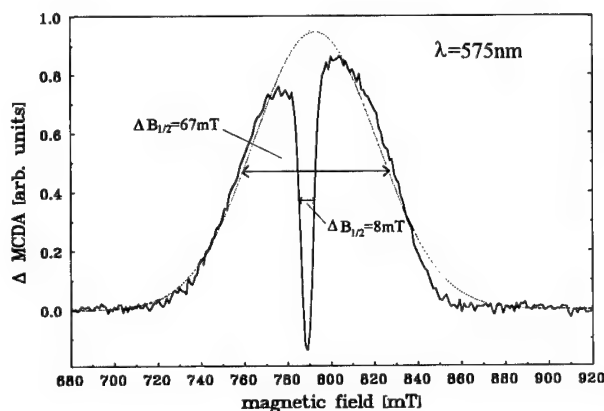


FIGURE 6 ODEPR spectra recorded as MCDA-detected EPR in the MCDA at $\lambda = 575$ nm, $T = 1.5$ K after irradiation of undoped Cs_2NaYF_6 at room temperature with X-rays.

The ODEPR spectrum cannot be due to one centre only. When studying the dynamical behaviour of the MCDA in the middle of the narrow EPR line and in the flank of the broad EPR line, one can see that two different spin lattice relaxation times are involved.

We tentatively assign the broad EPR line to F centres. The F centre EPR line width in CsCl and CsBr is $\Delta B_{1/2} = 82.5$ mT^{26,27} and $g = 1.97$ for CsCl, $g = 1.96$ for CsBr. Considering that in CsBr and CsCl there are 8 nearest Cs^+ neighbours and here only 4 (the Cs^+ interactions ($I = 7/2$) will dominate the line width), it seems reasonable to assign the broad EPR spectrum to F centres. The narrower line is probably due to an impurity, possibly O_F^- . The slight positive g -shift, compared to that of the F centre and the line width $\Delta B_{1/2}$ of 8 mT which is found to be 6 mT for O_F^- measured with ODEPR in BaFBr, suggests this as a plausible idea. The ODEPR spectra must come from an impurity with a nucleus without a nuclear moment. All lattice nuclei have nuclear moments with a 100% abundance and are therefore unlikely to be at the centre of the paramagnetic defect.

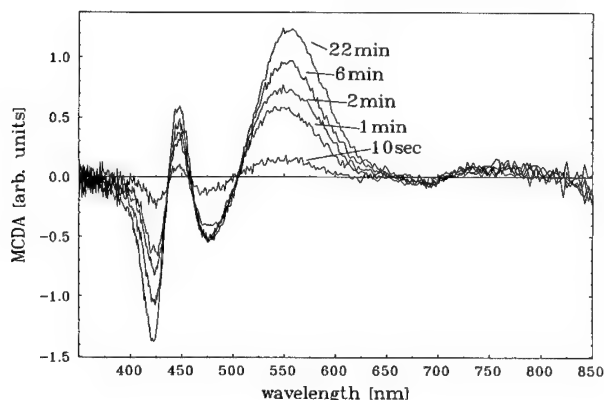


FIGURE 7 MCDA spectra measured as a function of increasing room temperature X-irradiation time.

Fluorides are also known to be easily contaminated with oxygen. There is probably a spatial correlation between the F centre and the paramagnetic impurity resulting in strong cross-relaxation effects. This may be the reason why both EPR spectra, that of the F centre and that of the impurity, are measured in all MCDA bands. Depending on the spin lattice relaxation processes, this can lead to a reversal of sign for the ODEPR effect, as was recently observed for spatially correlated F-H centre pairs in KBr.²⁸ The MCDA is probably the superposition of two derivative like MCDA-bands, one having the zero-transition at 435 nm, one at 515 nm (see dashed lines in Figure 5 for the decomposition). We assign the first one to the paramagnetic impurity (O_F^-), the other one to the F centre. A derivative like structure is expected for an s-p like transition in the F centre and was also observed for O_F^- in BaFBr.^{3,4} The MCDA bands grow as a function of increasing time of room temperature X-irradiation.

Interestingly, the bands between 400 and 650 nm grow in the same way and it seems that a saturation value can be reached (see Figure 7). This observation further supports the assumption that an impurity provides the necessary vacancy to create the F centre and that the impurity also captures the hole. The observed increases of the MCDA bands with X-irradiation could be explained if the MCDA at 435 nm is due to O_F^- , that at 515 nm due to F centres and if both have a strong spatial correlation.

Further studies are needed to establish safely the nature of the electron and hole trap centres and to find out whether impurities play a dominant role as it seems to be in BaFBr:Eu²⁺ also.

4 CONCLUSION

The mechanism in BaFBr:Eu²⁺ is still not fully understood. It seems that the oxygen contamination does play an important role for the functioning of this X-ray storage phosphor, probably a beneficial one. A new efficient X-ray storage phosphor was found in Cs₂NaYF₆, and it seems plausible to assume that also other members of the Elpasolite family are interesting for this application.

REFERENCES

1. G. Blasse, *J. Alloys and Compounds* **192**, 17 (1993).
2. M. Sonoda, M. Takano, J. Miyahara and H. Kato, *Radiology* **148**, 833 (1983).
3. F. K. Koschnick, J. M. Spaeth, R. S. Eachus, W. G. Mc Dugle and R. H. D. Nuttal, *Phys. Rev. Letters* **67**, 3571 (1991).
4. R. S. Eachus, W. G. Mc Dugle, R. H. D. Nuttal, M. T. Olm, F. K. Koschnick, Th. Hangleiter and J. M. Spaeth, *J. Physics Condensed Matter* **3**, 9327 and 9339 (1991).
5. H. P. Beck, *Z. Anorg. Allg. Chemie* **451**, 73 (1979).
6. K. Takahashi, K. Kohda, J. Miyahara, Y. Kanemitsu, K. Amitani, S. Shionoya, *J. Luminescence* **31 & 32**, 266 (1984).
7. K. Takahashi, J. Miyahara and Y. Shibahara, *J. Electrochem. Soc.* **132**, 1492 (1985).
8. H. H. Rüter, H. V. Seggern, R. Reiniger and V. Saile, *Phys. Rev. Letters* **65**, 2438 (1990).
9. K. S. Song and R. T. Williams, Self Trapped Excitons (Springer Series of Solid State Sciences **105**) (1993).
10. J. M. Spaeth, W. Meise and K. S. Song, *J. Phys. Condensed Matter* **6**, 1801 (1994).
11. R. S. Eachus, F. K. Koschnick, J. M. Spaeth, R. H. D. Nuttal and W. G. Mc Dugle, *Proceedings Intern. Conf. on Defects in Insulating Materials*, Nordkirchen, Germany, ed. O. Kanert and J. M. Spaeth, World Scientific (Singapore), p. 267.
12. R. S. Eachus, R. H. D. Nuttal, W. G. Mc Dugle, F. K. Koschnick, J. M. Spaeth, *Proceedings Intern. Conf. on Defects in Insulating Materials*, Nordkirchen, Germany, ed. O. Kanert and J. M. Spaeth, World Scientific (Singapore) p. 1172.
13. F. K. Koschnick, Doctoral Thesis, Paderborn 1991.
14. Th. Hangleiter, F. K. Koschnick, J. M. Spaeth, R. S. Eachus, *Radiation Effects and Defects in Solids*, **119-121**, 615 (1991).
15. F. K. Koschnick, Th. Hangleiter, J. M. Spaeth and R. S. Eachus, *J. Phys. Condensed Matter* **4**, 3001 (1992).
16. M. Thoms, H. V. Seggern, A. Winnacker, *Phys. Rev. B* **44**, 9240 (1991).
17. Y. C. Iwabuchi, K. Umemoto, K. Takahashi, S. Shionoya, *J. Luminescence* **48 & 49**, 481 (1991).
18. D. M. De Leeuw, T. Kovats and S. P. Herko, *J. Electrochem. Soc.* **134**, 491 (1987).
19. H. V. Seggern, T. Voigt, W. Knüpper and G. Lange, *J. Appl. Phys.* **66**, 1405 (1988).
20. F. K. Koschnick, J. M. Spaeth, R. S. Eachus, *J. Phys. Condensed Matter* **4**, 8919 (1992).
21. Th. Hangleiter, F. K. Koschnick, J. M. Spaeth, R. H. D. Nuttal, R. S. Eachus, *J. Phys. Condensed Matter* **2**, 6837 (1990).
22. R. S. Eachus, F. K. Koschnick and J. M. Spaeth, to be published.
23. F. K. Koschnick, J. M. Spaeth, to be published.
24. D. Babel, R. Haegle, G. Pausewang and F. Wall, *Mat. Res. Bull.* **8**, 1371 (1973).
25. J. M. Spaeth, J. R. Niklas and R. H. Bartram, *Structural Analysis of Point Defects in Solids* (Springer Series of Solid State Sciences **43**) (1992).
26. D. Schmid, Ph.D. Thesis, Stuttgart 1966.
27. F. Hughes and J. G. Allard, *Phys. Rev.* **125**, 173 (1962).
28. W. Meise, U. Rogulis, F. K. Koschnick, K. S. Song and J. M. Spaeth, *J. Phys. Condensed Matter* **6**, 1815 (1994).

FLUORESCENCE LINE NARROWING IN Mn^{4+} DOPED GADOLINIUM GALLIUM GARNET¹

A. SUCHOCKI,^a M. POTEMSKI,^b A. BRENIER,^c C. PEDRINI,^c AND G. BOULON^c

^a*Institute of Physics, Polish Academy of Sciences, Al. Lotnikow 32/46, 02-668 Warszawa, Poland;* ^b*High Magnetic Field Laboratory, MPIKF&CNRS BP 166; 38042 Grenoble Cedex 9, France;* ^c*Laboratoire de Physico-Chimie des Matériaux Luminescents, Université Claude Bernard Lyon 1; 43, Bd. du 11 Novembre 1918 69622 Villeurbanne, France*

The laser excitation and luminescence spectra of the R-lines of the Mn^{4+} in gadolinium gallium garnet show that the large broadening which they exhibit is partially related to presence of charge-compensating Ca^{2+} ions, even for the case of manganese center without close compensation. Remaining part of the broadening is due to antiferromagnetic exchange interaction between Mn^{4+} and surrounding them six Gd^{3+} ions. The spectra remain broadened in magnetic fields below 6 T and the higher magnetic fields up to 20 T removes the broadening related to the spin-spin interaction. Luminescence and excitation spectra at 2.2 K show that the transitions occur between levels which magnetic numbers differ by 0 or ± 1 . The estimated value of the spin-spin exchange constant for the ground state of Mn^{4+} is approximately equal to $J \approx 1.9 \text{ cm}^{-1}$.

Key words: spin-spin exchange interaction, inhomogeneous broadening, solid-state laser materials.

The Mn^{4+} ion, which has the same electronic structure as Cr^{3+} ion, exhibits quite different character of the luminescence spectra in Gadolinium Gallium Garnet (GGG) than the latter one. The spectra of usually sharp $^4\text{A}_2 \leftrightarrow ^2\text{E}$ transitions for various Mn^{4+} sites are much broader than for chromium ions and they are located at different energy than in the case of Cr^{3+} . There are several reasons for such behavior. Since manganese ion is smaller than the chromium one the crystal field strength for Mn^{4+} is much larger than for Cr^{3+} . Additionally, codoping by divalent Ca^{2+} or Mg^{2+} ions is required in order to obtain the manganese ions in the 4+ state. Codoping effects in large disorder of crystal structure and inhomogeneous broadening of the electronic transitions. We were able to identify the various Mn^{4+} centers in the GGG crystal¹ using luminescence polarization techniques and codoping by various dopants, which occupy different sites in the GGG host. The Mn^{4+} centers with compensating Ca^{2+} ion located closely to the manganese ion (most probably as nearest neighbor) and the centers without such compensation have been found in the crystal. Nevertheless it remained unclear why the width of the $^4\text{A}_2 \leftrightarrow ^2\text{E}$ transition was in the order of a few tens of wave numbers, in contradiction to the case of the chromium dopant where the width of the same transitions is in the order of a few wave numbers. Additionally the spectral shape of this transitions is not Gaussian and exhibits rather complicated structure.

In order to obtain better insight into the nature of the observed broadening we use photoluminescence (PL) and photoluminescence excitation (PLE) techniques with relatively high resolution in presence of strong magnetic fields up to 20 T at temperature

¹A. Suchocki has been supported by the grant CIPA3510PL921612 of the Commission of the European Communities. The work has been partially supported by the grant 02 0493 91 01 of the Polish State Committee for Scientific Research.

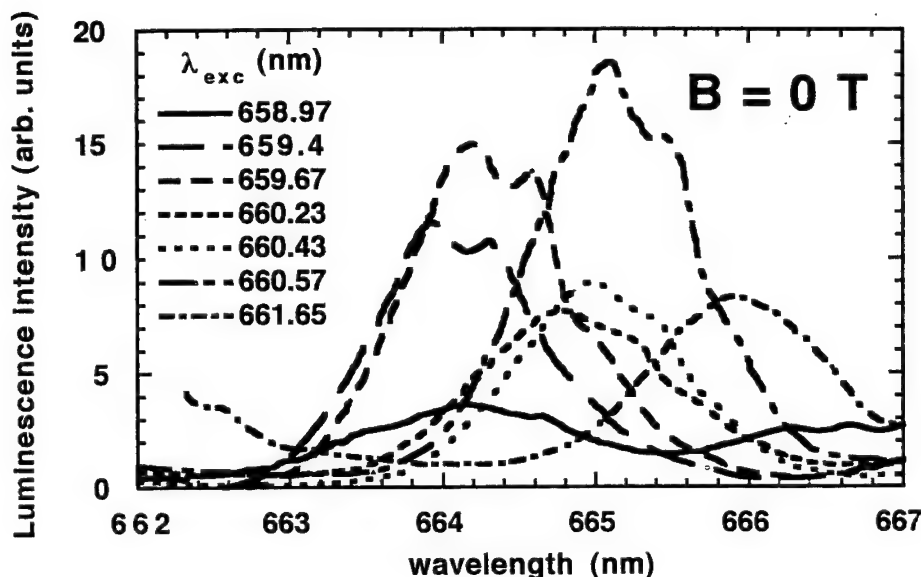


FIGURE 1 Luminescence spectra of GGG:Mn⁴⁺ in the region of R-lines, excited by the various wavelengths of the dye laser at temperature $T = 2.2$ K (without magnetic field).

$T = 2.2$ K. The PL and PLE spectra were obtained with use of a cw dye laser with DCM dye, pumped by argon-ion laser. We studied luminescence associated with Mn⁴⁺ centers without close compensation.¹

Figure 1 shows luminescence spectra of ${}^2E \rightarrow {}^4A_2$ transition, excited by various wavelength of dye laser. The excitation spectra, observed at different wavelength in the region of the R-lines luminescence are presented in Figure 2. Both, PL and PLE spectra depend on the wavelength of excitation or observation, respectively. This is a proof that the broadening is partially related to the crystal inhomogeneity, most probably related to more distant than nearest neighbor charge compensation by Ca²⁺ ions. Although the laser excitation removes part of the observed broadening, the PL spectra remain still broadened.

The remaining part of the broadening cannot be related to crystal disorder and it is associated with antiferromagnetic exchange interaction between the Mn⁴⁺ ions and their six cation nearest-neighbors which are the Gd³⁺ ions. The theory, originated from Murphy and Ohlmann,² describes the interaction in presence of magnetic field by the following Hamiltonian:

$$H_t = -JS_{Mn} \cdot S + g_{Mn}\mu_B S_{Mn} B + g_{Gd}\mu_B S B \approx -JS_{Mn} \cdot S + g_0\mu_B S B \quad (1)$$

where J is the exchange integral, S_{Mn} , S and S are the spin of Mn⁴⁺ ion, total spin of six Gd³⁺ ions and total spin of the interacting system, respectively, $g_{Mn} \approx g_{Gd} \approx g_0 \approx 2$ and μ_B is Bohr magneton. The expectation values of the Hamiltonian without magnetic field are equal to:

$$E_{exp} = -(J/2) \cdot [S(S+1) - S(S+1) - S_{Mn}(S_{Mn} + 1)] \quad (2)$$

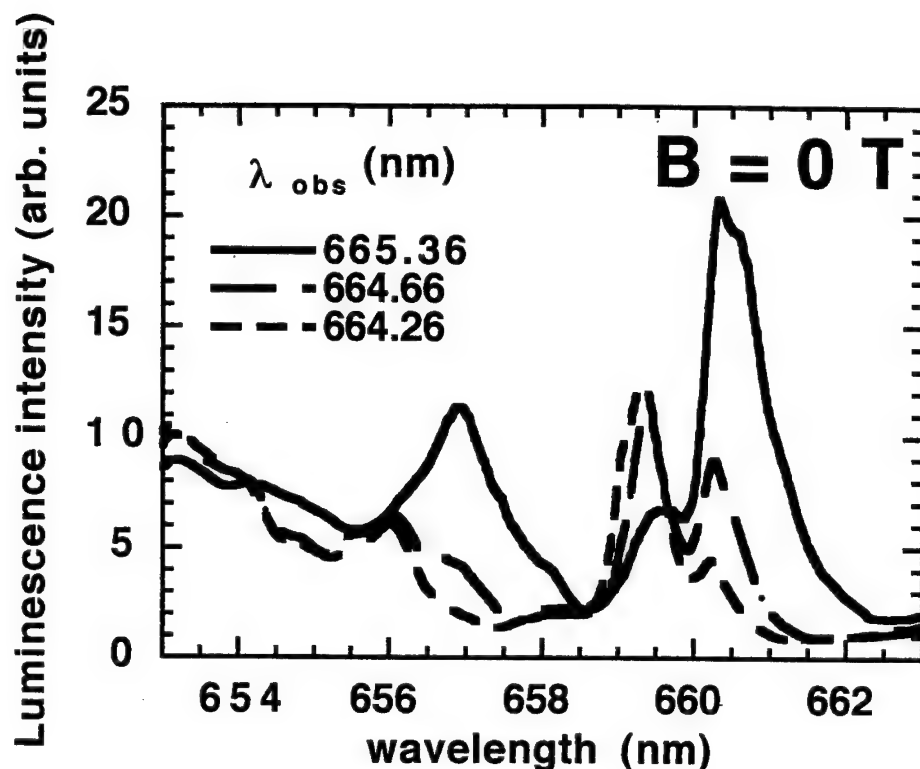


FIGURE 2 Examples of the excitation spectra of $GdG:Mn^{4+}$ luminescence for various wavelengths of recording at temperature $T = 2.2$ K (without magnetic field).

The ground state and excited states of the system are split into a quasi-continuum band of exchange coupled sublevels having different total spin quantum number S . These levels are additionally split by the Zeeman interaction if external magnetic field is applied. At 2.2 K fluorescence occurs only between first excited Zeeman sub-level and certain Zeeman sub-levels of the ground state with magnetic number which differs by 0, ± 1 . Additionally, the total spin of gadolinium ions is conserved.

Strong magnetic field (above 6 T) applied to the sample (in Faraday configuration, along [111] axis of the crystal) removes the remaining part of the broadening and originally broad PL bands split into several lines, associated with transitions to Zeeman sub-levels of the ground state. Figure 3 shows the luminescence spectra at magnetic field $B = 14$ T, excited by 659.28 nm. Similar spectra were obtained by excitation with different wavelengths. The separation between different peaks in the PL spectrum are dependent on the magnetic field, which allows to associate the observed lines in the spectra with particular transitions between the Zeeman sublevels. The value of the exchange integral J for the ground state of the Mn^{4+} ions, estimated from the Figure 3 is equal to 1.9 cm^{-1} . This value is relatively large, similar to that obtained by Murphy and Ohlmann for $GdAlO_3:Cr^{3+}$.² Yamaga *et al.* obtained value of $J \approx 0.25\text{--}0.33 \text{ cm}^{-1}$ for $GSAG:Cr^{3+}$.³

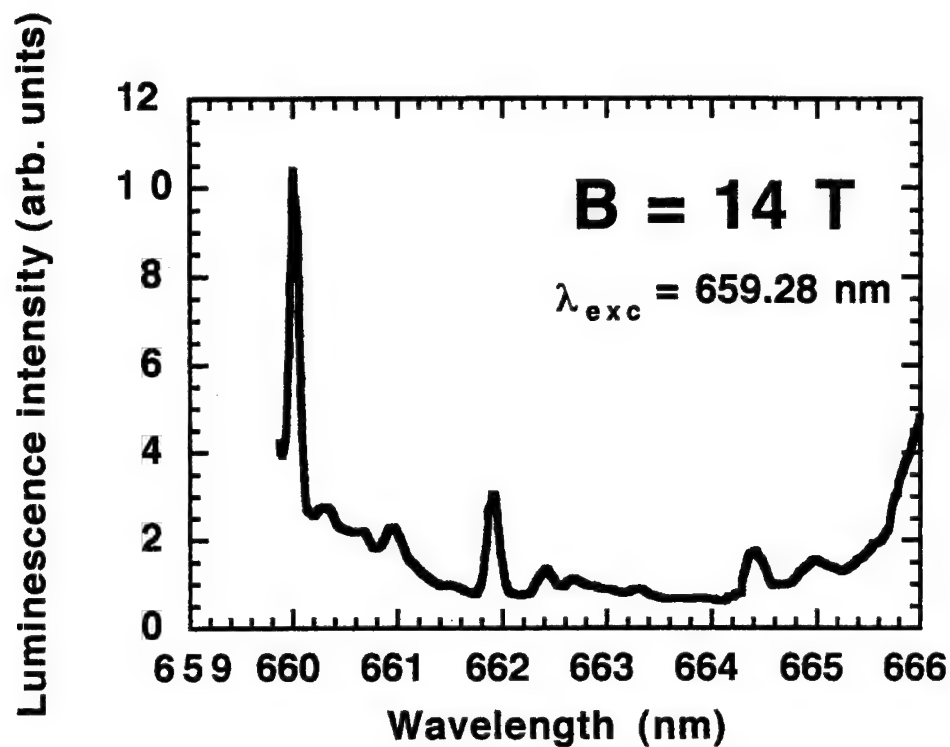


FIGURE 3 Luminescence spectrum of GGG:Mn⁴⁺ excited by the 659.28 nm dye laser line at temperature $T = 2.2 \text{ K}$ and with magnetic field $B = 14 \text{ T}$.

REFERENCES

1. A. Brenier, A. Suchocki, C. Pedrini, C. Madej and G. Boulon, *Phys. Rev. B*, **46**, 3219 (1992).
2. J. Murphy and R. C. Ohlmann, in *Optical Properties of Ions in Crystals*, ed. H. M. Crosswhite and H. W. Moos (New York, Wiley 1967), p. 239.
3. Y. Gao, M. Yamaga, C. Ogihara, K. P. O'Donnell and B. Henderson, *J. Phys.: Condens Matter* **4**, 7307 (1992); M. Yamaga, Y. Gao, K. P. O'Donnell and B. Henderson, *J. Phys.: Condens. Matters* **5**, 915 (1993).

FINE STRUCTURE OF THE ABSORPTION AND EMISSION SPECTRA OF Ni^{2+} -IONS IN BaLiF_3

E. MARTINS,^a S. L. BALDOCHI,^a S. P. MORATO,^a N. D. VIEIRA JR.,^a A. LUCI,^b
M. CASALBONI,^{b†} U. M. GRASSANO,^b G. BALDACCHINI,^c M. CREMONA,^c
R. M. MONTEREALI,^c E. KRAUSZ,^d and M. RILEY^d

^aIPEN/CNEN, Sao Paulo—Brazil; ^bDipartimento di Fisica—Università di Roma Tor Vergata Via della Ricerca Scientifica 1, 00133 Roma—Italy; ^cENEA, Dipartimento Innovazione, Settore di Fisica Applicata, 00044 Frascati (Roma)—Italy; ^dResearch School of Chemistry—Australian National University, Canberra 0200—Australia

The optical properties of Ni^{2+} -ion impurities in a new crystal, the inverted fluoroperovskite BaLiF_3 , have been studied. In particular we have investigated the fine structure of the transition by means of absorption and emission spectra. By analogy to previous results we have assigned the structured absorption band around 1200 nm to the $^3\text{A}_2 \rightarrow ^3\text{T}_1$ transition. Four zero-phonon lines are clearly visible in the absorption spectrum. The emission in the region 1250–1600 nm, due to the same $^3\text{A}_2 \rightarrow ^3\text{T}_1$ transition, consists of two sharp lines with their vibrational sidebands.

Key words: Spectroscopy, Ni^{2+} , Perovskite.

1 INTRODUCTION

The development of tunable solid-state lasers has renewed the interest in the study of impurity ions in solids whose electronic transitions are broadened by strong electron-phonon coupling.

In order to have different laser systems available to cover the interesting near infrared spectral region it is important to study the spectroscopic properties of specific impurity ions in several materials.¹ In particular, host crystals doped with Ni^{2+} (d^8 configuration) show broad vibronically allowed absorption and emission bands.^{2–5}

Although the laser emission of the Ni^{2+} ion has been investigated since 1963,⁶ c.w. laser operation at room temperature has not yet been achieved.^{7,8} However the chemical stability of the Ni^{2+} ion and the presence of several pump bands stimulated the interest in the search for new crystals as hosts for Ni^{2+} . In this work, the basic spectroscopic properties of Ni^{2+} in BaLiF_3 perovskite will be described.

The fluoroperovskite type materials, described by the general formula AMF_3 (A and M mono and divalent cation, respectively), crystallize in the cubic system; they belong to the space group O_h^1 or P_{m3m} .⁹ The coordination number of the monovalent ion is 12 while that of the divalent ion is 6. BaLiF_3 is an *inverted* perovskite compared to the normal perovskite (KMgF_3) with the Ba and Li in exchanged position and therefore with the monovalent Li^+ surrounded by a octahedron of 6 F^- ions and the divalent Ba^{2+} surrounded by 12 F^- ions at the corner of a cube-octahedron (see Figure 1a and 1b). The symmetry of both metal sites is O_h and the Ni^{2+} ion could occupy either of them. However the crystal

[†] Permanent address: Dip. Matematica e Fisica—Università di Camerino, Via Madonna delle Carceri, 62032 Camerino—Italy.

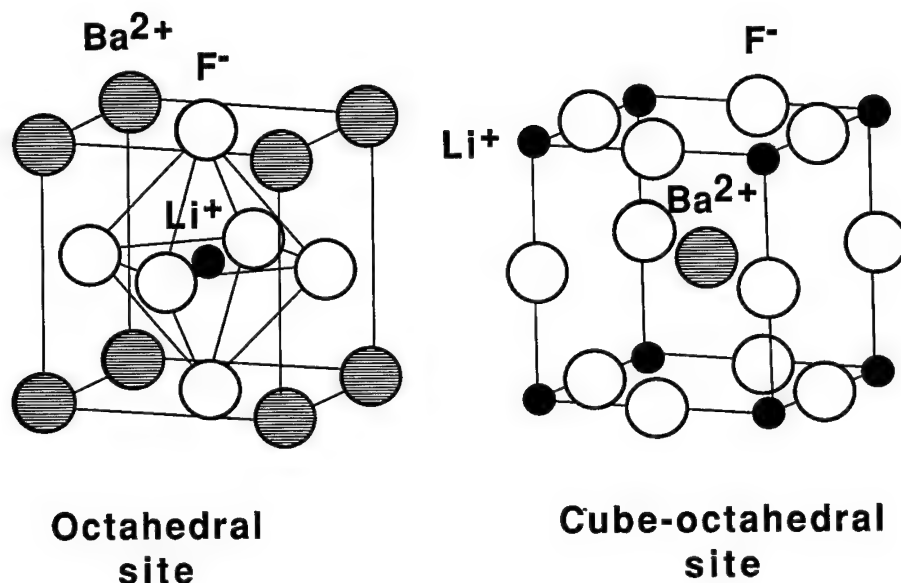


FIGURE 1 Crystal structure of BaLiF₃ fluoroperovskite showing the octahedral (Li⁺) site (left) and cubo-octahedral (Ba²⁺) site (right).

field that Ni²⁺ ion would experience in the two lattice sites should be very different: the field splitting between the e_g and t_{2g} d-orbitals in the two cases would be

$$\Delta_{\text{cube-oct}} = -\frac{1}{2}\Delta_{\text{oct}}.$$

2 RESULTS AND DISCUSSION

The absorption spectrum of BaLiF₃:Ni²⁺ for the sample 0.3 mol% Ni concentration and 5.3 mm thick is shown in Figure 2. The general structure of the spectrum is quite similar to those of KMgF₃:Ni²⁺ and KNiF₃, and three main, broad, absorption bands peaking at 1180 nm, 700 nm and 390 nm are displayed. Moreover there is a narrow structure at about 650 nm, that overlaps the 700 nm band and a weaker absorption band peaking at 500 nm.

The similarity of this spectrum of BaLiF₃:Ni²⁺ with that of KMgF₃:Ni²⁺ where the Ni²⁺ is known to replace the Mg²⁺ in octahedral site³, suggests the same Ni²⁺ coordination in both systems. At first sight one could suppose that Ni²⁺ should replace the equally charged Ba²⁺. However the preference of Ni²⁺ for the Li⁺ rather than the Ba²⁺ site could be attributed to the similar ionic radii of Ni²⁺ (0.69 Å) and Li⁺ (0.68 Å) while that of Ba²⁺ is very different (1.34 Å). The Ni²⁺ ion in the Li⁺ site requires charge compensation which may be provided by either a Li⁺ vacancy or by a Ba²⁺ vacancy, charge compensating for two Ni²⁺ ions.

The main absorption bands were thus attributed to transitions to levels originating from crystal field splitting of the d orbitals and from the electron-electron interaction of Ni²⁺ ion in an octahedral environment, according to the classical Tanabe—Sugano diagram. These

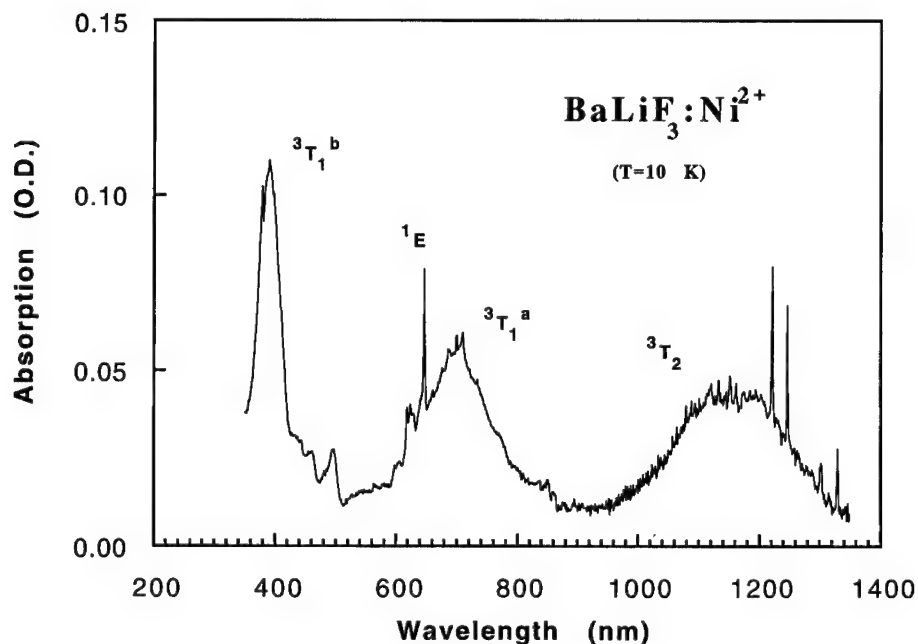


FIGURE 2 Absorption spectrum at 10 K of $\text{BaLiF}_3:\text{Ni}^{2+}$ 0.3 mol%.

bands correspond to electronic transitions between the ground state, $^3\text{A}_{2g}$, and four excited states of symmetries $^3\text{T}_{2g}$, $^3\text{T}_{1g}^a$, $^1\text{E}_g$ and $^3\text{T}_{1g}^b$ respectively.

Figure 3 shows part of the absorption spectrum on an expanded scale. Following the same arguments given in reference³ we attribute the 1150 nm band ($^3\text{A}_{2g} \rightarrow ^3\text{T}_{2g}$) to a magnetic dipole transition containing superposition of zero-phonon lines and broader phonon side bands. In the octahedral symmetry, the first excited level ($^3\text{T}_{2g}$) splits in four spin-orbit components while the ground state remains degenerate. The lines at 1222 nm (8183.3 cm^{-1}), 1247 nm (8019.3 cm^{-1}), 1302 nm (7680.5 cm^{-1}) and 1330 nm (7518.8 cm^{-1}) can be interpreted as the no-phonon transitions to the Γ_2 , Γ_5 , Γ_4 , Γ_3 spin-orbit components of the state $^3\text{T}_{2g}$, respectively.

The spin-orbit splitting between the 1222 nm and the 1247 lines is 164 cm^{-1} and between the 1302 nm and the 1330 lines is 161.7 cm^{-1} . The related lines in $\text{KMgF}_3:\text{Ni}^{2+}$ and $\text{KZnF}_3:\text{Ni}^{2+}$ systems have a spin-orbit splitting very close to the above values.³

The above interpretation for the four zero-phonon lines is also supported to some extent by the calculated magnetic dipole oscillator strengths of the four spin-orbit lines.¹⁰ However experimental assignment of the observed $^3\text{A}_{2g} \rightarrow ^3\text{T}_{2g}$ transition of Ni^{2+} in octahedral sites^{3,4,10} point to much larger intensities for transitions into the Γ_3 and Γ_4 states, while those into the Γ_5 and Γ_2 states are almost completely obscured by the overlapping phonon sidebands.

A different interpretation can thus be the assignments of the more intense 1222 nm and 1247 nm lines to the Γ_4 and Γ_3 no-phonon lines of the Ni^{2+} in octahedral site while the two less intense lines (with the same energy separation) could be due to Ni^{2+} in a different lattice site or with different neighbours producing a lower crystal field.

Figure 3 shows also the infrared emission spectra at 10 K. It is evident the coincidence of the zero-phonon emission lines at 1247 nm and 1330 nm, with two of the

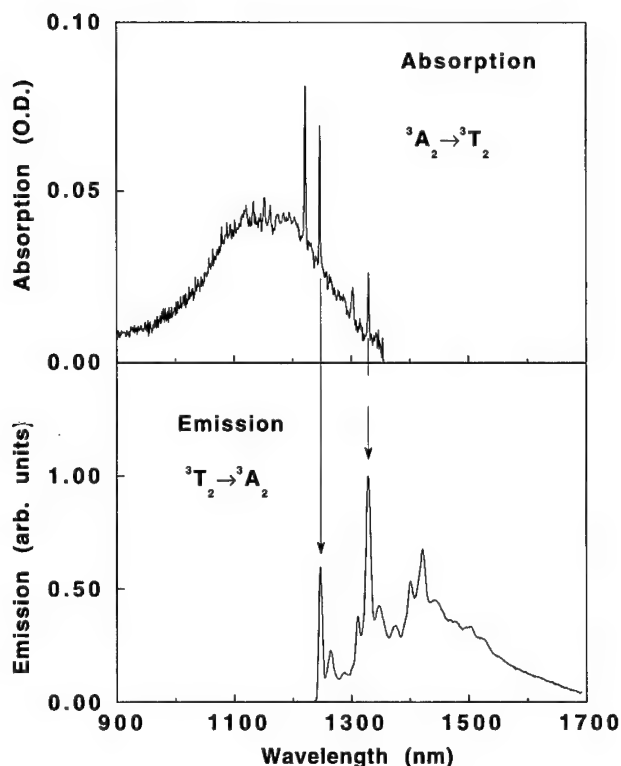


FIGURE 3 Infrared absorption and emission spectra of $\text{BaLiF}_3:\text{Ni}^{2+}$ at 10 K.

absorption lines. This observation could be explained by assuming the presence of two emitting sites, with transitions from the lowest level of the $^3\text{T}_{2g}$ multiplet at 1247 nm and 1330 nm respectively.

The same emission bands are excited by pumping either in the $^3\text{A}_{2g} \rightarrow ^3\text{T}_{2g}$ absorption (Nd-YAG laser) or in the $^3\text{A}_{2g} \rightarrow ^3\text{T}_{1g}$ absorption (He-Ne laser): we could not determine if the relaxation $^3\text{T}_{1g} \rightarrow ^3\text{T}_{2g}$ is radiative or nonradiative.

Magnetic circular dichroism and excited state absorption experiments are presently in progress to obtain a more complete description of Ni^{2+} in this system.

REFERENCES

1. See for example *Tunable Solid State Lasers II* eds. A. B. Budgor, L. Esterowitz, L. G. De Shazer (Springer, Heidelberg, 1986).
2. J. Ferguson, H. J. Guggenheim, L. F. Johnsons and H. Kamimura, *J. Chem. Phys.* **38**, 2579 (1963).
3. J. Ferguson, H. J. Guggenheim and D. L. Wood, *J. Chem. Phys.* **40**, 822 (1964).
4. W. E. Vehse, K. H. Lee, S. I. Yun and W. A. Sibley, *J. Luminescence* **10**, 149 (1975).
5. S. Payne, *Phys. Rev.* **B41**, 6109 (1990).
6. L. F. Johnson, R. E. Dietz, and H. J. Guggenheim, *Phys. Rev. Lett.* **11**, 318 (1963).
7. P. F. Moulton, A. Mooradian, T. B. Reed, *Opt. Lett.* **3**, 164 (1978).
8. P. F. Moulton, A. Mooradian, *Appl. Phys. Lett.* **35**, 838 (1979).
9. S. L. Baldochi and J. Y. Gesland, *Mat. Res. Bull.* **27**, 891 (1992).
10. J. E. Ralph and M. G. Townsend, *J. Phys. C: Solid State* **3**, 8 (1970).

SPECTROSCOPIC STUDY OF Cr^{3+} IN NEW ELPASOLITES

*M. C. MARCO DE LUCAS, **J. M. DANCE, *F. RODRÍGUEZ, **A. TRESSAUD,
*M. MORENO and **J. GRANNEC

**DCITYM. Facultad de Ciencias. Universidad de Cantabria. 39005 Santander, Spain;*

***Laboratoire de Chimie du Solide du C.N.R.S., Université de Bordeaux I, 33405 Talence,
France*

New elpasolites like A_2KMF_6 doped with Cr^{3+} have been investigated by means of optical and EPR techniques. It is shown that though the structural phase transition undergone by Rb_2KGaF_6 at $T = 129$ K is much stronger than that corresponding to Rb_2KInF_6 , the emission band at 10 K of the latter is much broader than that for the former. This inhomogeneous broadening is correlated with the increase experienced by the EPR bandwidth below 150 K reflecting only local changes around Cr^{3+} . An analysis of zero phonon lines through the fluoroelpasolite series reveals that they are very sensitive to changes of the $\text{Cr}^{3+}\text{-F}^-$ distance, R . It is shown that changes ΔR_0 in the perfect lattice induce changes on R given by $\Delta R = fR_0$ where f is only 0.15. At variance with the findings for MnF_6^{4-} , the present results indicate that an increase of R tends to decrease the Stokes shift. The origin of this fact is discussed. Finally, the present results indicate that R increases (about 0.2 pm) in the phase transition of Rb_2KGaF_6 although the lattice volume decreases.

Key words: fluoroelpasolites doped with Cr^{3+} ; luminescence of Cr^{3+} ; EPR of Cr^{3+} ; Phase transitions; Influence of the Cr-F distance.

1 INTRODUCTION

Currently a great deal of work is focused on Cr^{3+} doped fluoride crystals and glasses. Among fluoride lattices, elpasolites have received a particular attention and so the spectroscopic properties of systems like $\text{K}_2\text{NaGaF}_6\text{:Cr}^{3+}$ have been investigated at different temperatures and pressures.^{1,2}

In the present work we report optical and EPR results on some new elpasolites (like A_2KMF_6 ; $\text{A} = \text{Rb}, \text{Ti}$; $\text{M} = \text{Ga}, \text{In}, \text{Cr}$) doped with Cr^{3+} . Apart from studying the optical properties of these new systems and the structural phase transitions undergone by the lattice, a particular attention is paid to the variation of optical properties through the fluoroelpasolite series. In particular, the use of the experimental zero-phonon line (ZPL) for detecting variations of the $\text{Cr}^{3+}\text{-F}^-$ distance along the series is explored. In this line, the local changes around the Cr^{3+} impurity induced by the first order phase transition in Rb_2KGaF_6 are also studied by means of the jumps experienced by optical and EPR parameters.

2 EXPERIMENTAL

Single crystal of Rb_2KGaF_6 , Rb_2KInF_6 , and K_2NaGaF_6 doped with 1 mol% of CrF_3 were grown using the same procedure of Ref. 4. Powder samples of Ti_2KCrF_6 were employed in these experiments.

The excitation and emission spectra at different temperatures were obtained with a Jobin-Yvon JY-3D fluorimeter and a Scientific Instruments 202 closed circuit cryostat equipped with an APD-K controller.

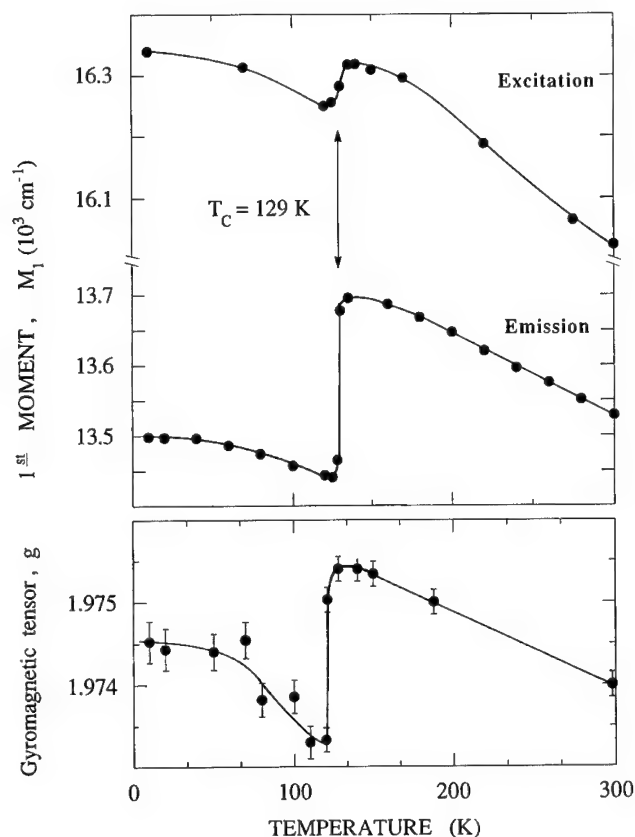


FIGURE 1 Variation of the excitation and emission first moments as well as the gyromagnetic factor, g , with the temperature for $\text{Rb}_2\text{KGaF}_6:\text{Cr}^{3+}$. The abrupt jumps are associated with the structural phase transition temperature at $T_c = 129$ K.

The time resolved low temperature emission spectra were performed on a Jobin-Yvon HR-320 monochromator and photon counting techniques. Crystals were excited with the chopped light of a Coherent Innova 302 krypton Laser operating at 647 nm. For lifetime measurements, the luminescence signal was digitized with a Tektronix 2340 A scope.

3 RESULTS

Figure 2 depicts the ${}^4\text{T}_2 \rightarrow {}^4\text{A}_2$ luminescence band of Cr^{3+} doped K_2NaGaF_6 , Rb_2KGaF_6 , and Rb_2KInF_6 , recorded at 10 K. In the first two cases a rich vibrational structure (mainly due to *progressions* involving the even a_{1g} and e_g modes of the CrF_6^{3-} complex as well as false origins associated to the *odd* t_{1u} and t_{2u} modes) is observed. The assignment of peaks was discussed in previous works.^{3,4} Figure 1 depicts the temperature dependence of the first moment associated with the emission as well as to the ${}^4\text{T}_2 \rightarrow {}^4\text{A}_2$ excitation band. The temperature dependence of the g factor for a powder sample is also included. The three parameters clearly reveal the existence of the phase transition at $T_c = 129$ K upon cooling. In spite of this fact the vibrational structure seen in Figure 2 for $\text{Rb}_2\text{KGaF}_6:\text{Cr}^{3+}$ can be well understood² assuming a *local cubic* CrF_6^{3-} complex in the ground state. By contrast,

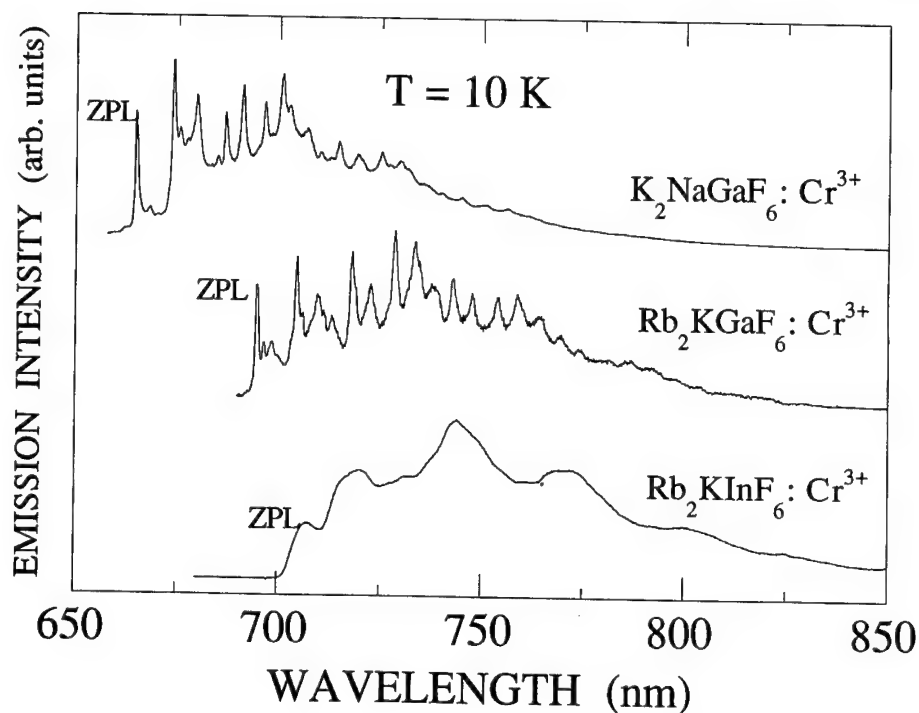


FIGURE 2 Emission spectra at $T = 10$ K of the K_2NaGaF_6 , Rb_2KGaF_6 and Rb_2KInF_6 crystals doped with Cr^{3+} . The Zero-phonon line is indicated by ZPL. Note that the inhomogeneous broadening of the ZPL for $\text{Rb}_2\text{KInF}_6:\text{Cr}^{3+}$ ($\Delta H = 100 \text{ cm}^{-1}$) is one order of magnitude higher than for $\text{K}_2\text{NaGaF}_6:\text{Cr}^{3+}$ and $\text{Rb}_2\text{KGaF}_6:\text{Cr}^{3+}$.

the structural phase transitions observed at 280 K and 260 K in $\text{Rb}_2\text{KInF}_6:\text{Cr}^{3+}$ are very weak and have no important influence upon excitation and emission peaks of Cr^{3+} .

EPR spectra on $\text{Rb}_2\text{KInF}_6:\text{Cr}^{3+}$ show however that below 150 K the bandwidth increases progressively from $\Delta H_{pp} = 30 \text{ G}$ to $\Delta H_{pp} \cong 45 \text{ G}$. This fact would be associated with local changes around Cr^{3+} and can be correlated with the significant broadening displayed by the luminescence band of $\text{Rb}_2\text{KInF}_6:\text{Cr}^{3+}$ when compared to that of $\text{Rb}_2\text{KGaF}_6:\text{Cr}^{3+}$ and $\text{K}_2\text{NaGaF}_6:\text{Cr}^{3+}$. Further investigation about this inhomogeneous broadening in $\text{Rb}_2\text{KInF}_6:\text{Cr}^{3+}$ is under way.

As it has been found for Mn^{2+} doped fluoroperovskites, Figure 2 indicates that the position of the ZPL energy is very sensitive to the host lattice where the CrF_6^{3-} is embedded and thus reflects very well the changes in the $\text{Cr}^{3+}-\text{F}^-$ distance induced by the chemical pressure of the rest of the lattice. The values of the ZPL (measured at 10 K) together with the values of absorption and emission peaks and the lifetime value τ_0 measured at 10 K are given in Table I. Because of Fano resonances, there is an uncertainty on the peak energy associated with the $^4\text{A}_2 \rightarrow ^4\text{T}_2$ transition. The value of E_{abs} given in Table I has always been taken in the second resonance. Table I sees that when the M—F distance, R_0 , of the perfect lattice increases, the ZPL energy decreases. This situation is thus similar to that found for other systems assuming that ZPL mainly reflects $10Dq$, this quantity being proportional to R^{-n} with n being close to five.

Nevertheless if we compare the ZPL of $\text{Rb}_2\text{KInF}_6:\text{Cr}^{3+}$ and $\text{K}_2\text{NaGaF}_6:\text{Cr}^{3+}$ given in Table I this analysis would lead to a difference, ΔR , between the corresponding R values

Table I

Structural and spectroscopic parameters of fluoroperovskites doped with Cr^{3+} . The peak energies, E_{abs} and E_{em} , and the Stokes shift, ΔE_s , are measured at room temperature. Units are given in cm^{-1} and errors are $\pm 100 \text{ cm}^{-1}$. The accuracy of the ZPL energy is given in parenthesis. #: Present work.

Compound	M-F (\AA)	E_{abs}	E_{em}	ΔE_s	ZPL	$\tau_0 (\mu\text{s})$	Ref.
K_2NaAlF_6	1.80	16 200	13 500	2700	15 142 (2)	—	3
K_2NaGaF_6	1.87	16 000	13 520	2480	15 045 (2)	545	1,2,#
Rb_2KGaF_6	1.89	15 950	13 600	2350	14 383 (2)	500	4,#
K_2NaScF_6	1.98	15 850	13 200	2650	14 280 (5)	600	2
Rb_2KInF_6	2.02	15 770	13 200	2570	14 230 (10)	600	#
Ti_2KCrF_6	—	15 650	13 370	2280	14 190 (10)	440	#

equal to about 2.3 pm and thus much smaller than $\Delta R_0 = 15 \text{ pm}$. The ratio $\Delta R/R_0 = 0.15$ is about one half that observed for Mn^{2+} in fluoroperovskites and reflects the smaller compressibility of CrF_6^{3-} when compared to that of MnF_6^{4-} .

In spite of the uncertainties upon E_{abs} , Table I points out that the Stokes shift, ΔE_s , does not increase when R increase as it has been found for Mn^{2+} in fluoroperovskites.⁵ By contrast, it seems that for Cr^{3+} doped fluoroperovskites, ΔE_s tends to exhibit an opposite behaviour. It has been pointed⁶ out that $\Delta E_s \propto R^{6\gamma-2(n+1)}$ where γ is the Gruneisen constant for stretching modes of the complex and the exponent n reflects the R dependence of $10Dq$ through the relation $10Dq \propto R^{-n}$. Thus the present situation is compatible with $\gamma < 2$ (as obtained in Refs 2 and 7) while values of γ lying between 2 and 3 lead to an opposite behaviour.

As a final point, the results reported in Figure 1 allow us to explore the *local changes* around Cr^{3+} induced by the structural phase transition at $T_c = 129 \text{ K}$. The decrement experienced by the excitation and emission first moment together with the increase experienced by $g_o - g$ are all compatible with an increase of the average $\text{Cr}^{3+}\text{-F}^-$ distance. This result is surprising as the volume of the perfect lattice experiences a decrement but the increase experienced by the $\text{Cr}^{3+}\text{-F}^-$ distance below the phase transition temperature would be $\delta R \cong 0.2 \text{ pm}$. Moreover, the absolute value of the jump experienced by the emission first moment (260 cm^{-1}) is certainly higher than that corresponding to the excitation one. This asymmetry can be explained assuming that there is also a small splitting of the 4T_2 state (of about 500 cm^{-1}) in the tetragonal phase, leading to a slightly elongated octahedron. The emission at $T = 100 \text{ K}$ comes essentially from the lowest sublevel which is an orbital doublet and thus experiences a *supplementary* shift to that undergone by the excitation band.

ACKNOWLEDGEMENTS

The support by the CICYT under Project No. PB92-0505 is acknowledged.

REFERENCES

1. J. Ferguson, H. J. Guggenheim and D. L. Wood, *J. Chem. Phys.* **54**, 504, (1971).
2. J. Dolan, A. Rinzler, L. Kappers and R. Bartram, *J. Phys. Chem. Solids* **53**, 905 (1992).
3. P. Greenough and A. G. Paulusz, *J. Chem. Phys.*, **70** 1967 (1979).
4. C. Marco de Lucas, F. Rodríguez, J. M. Dance, M. Moreno and A. Tressaud, *J. Lumin.* **48 & 49**, 553 (1991).
5. C. Marco de Lucas, F. Rodríguez and M. Moreno, *Phys. Rev.* **B50**, 2760 (1994).
6. M. Moreno, M. T. Barriuso and J. A. Aramburu, *J. Phys.: Condens. matter* **4**, 9481 (1992).
7. L. Seijo, Z. Barandiaran and L. M. Pettersson, *J. Chem. Phys.* **98**, 4041 (1993).

TIME RESOLVED SPECTROSCOPY OF Ni^{2+} DOPED FLUOROCOLOROZIRCONATE GLASSES

M. A. BUÑUEL, R. ALCALA and R. CASES¹

Instituto de Ciencia de Materiales de Aragón (Univ. Zaragoza-C.S.I.C) Facultad de Ciencias, 50009 Zaragoza, Spain

Optical absorption, time resolved luminescence and fluorescence decay measurements of Ni^{2+} -doped fluoroclorozirconate glasses are reported. Time resolved luminescence measurements were taken exciting the samples at different wavelengths. The position of the orange emission band (${}^1\text{T}_{2g}(\text{D}) \rightarrow {}^3\text{A}_{2g}(\text{F})$) moves to the blue when the excitation is changed to higher energies. For a fixed excitation wavelength, the emission moves also to the blue when the time of measurement after the laser pulse increases. The fluorescence decays are non-exponential and depend of the detection wavelength. They are slower for the shorter detection wavelengths. The results show a distribution of Ni^{2+} sites with different 'crystal field' environments.

Key words: Glasses, Spectroscopy, 3d ions.

1 INTRODUCTION

In the last years a considerable effort has been devoted to the characterization of the optical properties of ZrF_4 glasses doped with 3d ions (in particular with Ni^{2+} ions^{1–2}). Recently, Ni^{2+} doped fluorozirconate glasses have been studied by time resolved spectroscopy techniques.³ Ni^{2+} sites disorder was indicated by inhomogeneous broadening of emissions and by non-exponential fluorescence decays. The purpose of this work is to give a detailed description of the optical properties of Ni^{2+} ions in fluoroclorozirconate glasses using this kind of spectroscopy.

2 EXPERIMENTAL DETAILS

The starting composition (in mol%) of the glasses was 53ZrF_4 , 14BaF_2 , 6BaCl_2 , 4LaF_3 , 3AlF_3 and 20NaCl . This composition was modified in order to get samples with 1 mol% of NiF_2 .

Emission spectra were obtained with a pulsed tunable dye laser. Fluorescence was detected with a Hamamatsu R-928 photomultiplier tube for the visible and a C30817 RCA silicon avalanche photodiode for the near infrared. Measurements were taken at 10K in a CTI Cryogenics cooler.

3 RESULTS

Figure 1 shows the absorption spectrum of Ni^{2+} ions in ZBLANaCl glass. The observed transition energies were 6800 cm^{-1} , 11140 cm^{-1} , 12760 cm^{-1} , and 21140 cm^{-1} . The emission of Ni^{2+} ions excited at 21000 cm^{-1} and taken $1\text{ }\mu\text{s}$ after the laser pulse is also presented in Figure 1. The energies of the observed emission bands are 11070 cm^{-1} , 12270 cm^{-1} , and 16180 cm^{-1} . No measurements were taken at energies lower than 8500 cm^{-1} .

¹ To whom correspondence should be addressed.

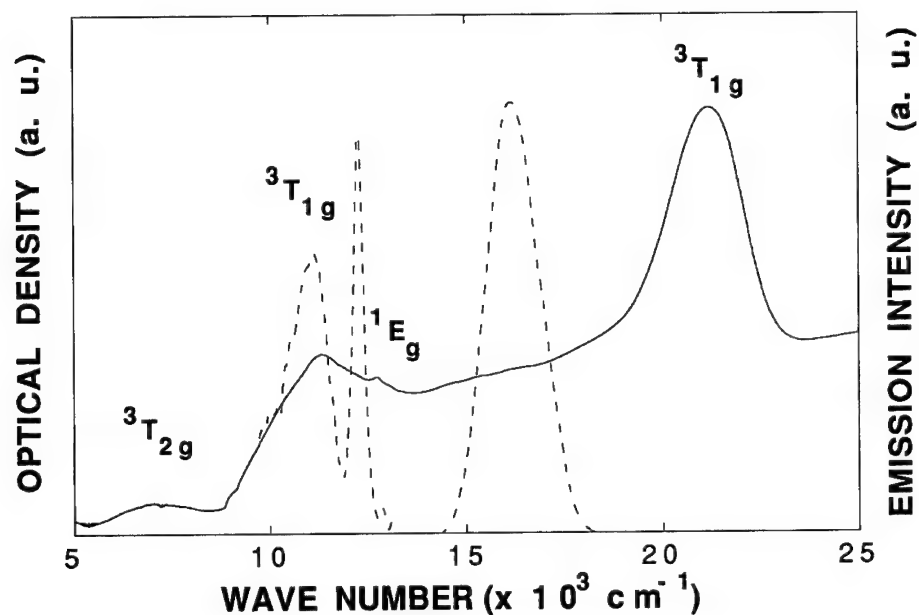


FIGURE 1 Absorption (solid line) and time resolved emission excited at 21000 cm^{-1} (dash line) spectra of Ni^{2+} ions in ZBLANaCl. The energy labels are for absorption.

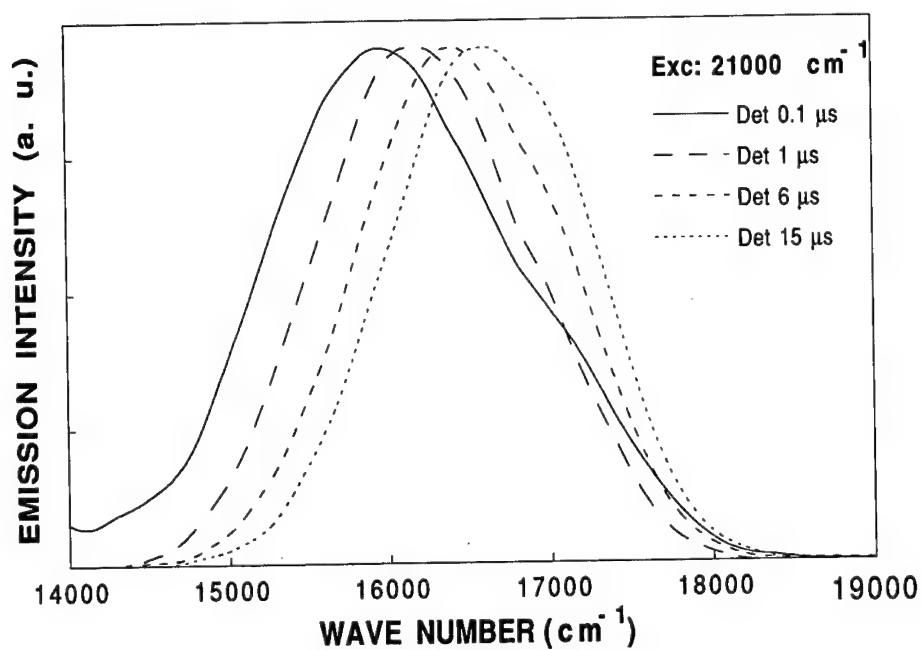


FIGURE 2 Time resolved emission spectra of orange emission of Ni^{2+} ions in ZBLANaCl. The curves are normalized to same intensity.

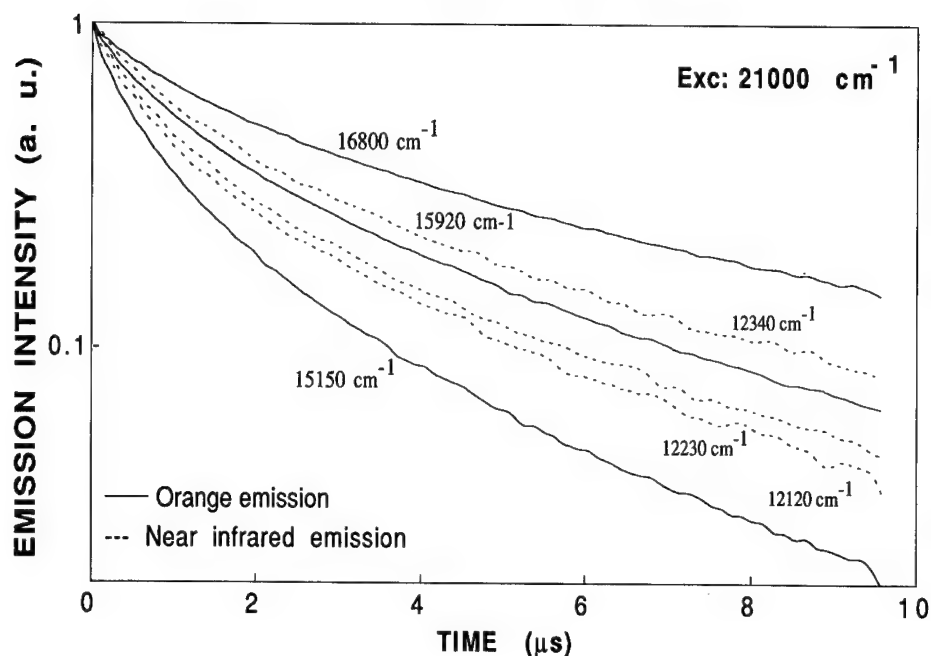


FIGURE 3 Fluorescence decays for orange and near infrared emissions of Ni^{2+} ions in ZBLANaCl detected at the energies given in the figure.

Figure 2 shows the time resolved emission spectra for the orange emission excited at 21000 cm^{-1} and measured at $0.1\text{ }\mu\text{s}$, $1\text{ }\mu\text{s}$, $6\text{ }\mu\text{s}$, and $15\text{ }\mu\text{s}$ after the laser pulse. A shift to higher energies of about 600 cm^{-1} is observed. Similar spectra are obtained when the excitation is at 22730 cm^{-1} or 19800 cm^{-1} , with a shift to the red of about 700 cm^{-1} when we go to lower excitation energies. Time resolved emission spectra for the near infrared emission taken with the same conditions as for the orange one, show that there is a shift of 100 cm^{-1} of the emission spectra with time.

Fluorescence decay measurements (excited at 21000 cm^{-1}) have been carried out for the orange, and the near infrared emissions at several detection wavelengths. They are plotted in Figure 3. The decay for the orange emission has been detected at 15150 cm^{-1} , 15920 cm^{-1} , and 16800 cm^{-1} . It is faster for the lower detection energies. The decay for the near infrared emission has been detected at 12120 cm^{-1} , 12230 cm^{-1} , and 12345 cm^{-1} . It is similar for the three detection wavelengths.

4 DISCUSSION

The absorption and emission bands given in Figure 1 for ZBLANaCl, are very similar to those found in fluorozirconate glasses³ but with an energy shift to lower energies which depends on the studied transition. The correspondence of absorption and emission band energies for ZBLANaCl and fluorozirconate glasses,³ suggests that the same assignments are valid. These energy level assignments from low to high energy in Figure 1 are ${}^3\text{A}_{2g}(\text{F}) \rightarrow {}^3\text{T}_{2g}(\text{F})$, ${}^3\text{T}_{1g}(\text{F})$, ${}^1\text{E}_g(\text{D})$ and ${}^3\text{T}_{1g}(\text{P})$ transitions for absorption and ${}^1\text{T}_{2g}(\text{D}) \rightarrow {}^3\text{T}_{2g}(\text{F})$, and ${}^3\text{A}_{2g}(\text{F})$ transitions for emission.

The results given in Figure 2 can be explained assuming a distribution of ions with different energy levels and transition probabilities. At very short times all the excited ions begin to decay and the emission is broad. At longer times those ions with highest transition probabilities have already disappeared and the emission is narrower. Because ions with higher transition probabilities are those with the ${}^1T_{2g}(D)$ level energy closer to the ${}^1E_g(D)$ level and hence lower ${}^1T_{2g}(D) \rightarrow {}^3A_{2g}(F)$ transition energies, the emission band moves to higher energies as long as the delay increases. For the near infrared emission (${}^1T_{2g}(D) \rightarrow {}^3T_{2g}(F)$), the crystal field energy curves of these levels are almost parallel so that a change of the crystal field does not result in a change of the transition energy between these levels, although it does exist a distribution in transition probabilities. So the near infrared emission does not shift.

The results presented in Figure 3 are complementary to those in Figures 2. The ions with higher ${}^1T_{2g}(D) \rightarrow {}^3A_{2g}(F)$ transition energies have lower transition probabilities, so that the decay is longer for shorter detection wavelengths. For the near infrared emission the decay is almost independent of the detection because all the ions emit in almost the same wavelength and the value obtained is a kind of average of those for the orange emission.

5 CONCLUSIONS

It has been shown that the optical properties of Ni^{2+} ions in ZBLANaCl glasses are characterized by inhomogeneous broadening of the absorption and emission bands and by non-exponential fluorescence decays. The ${}^1T_{2g}(D) \rightarrow {}^3A_{2g}(F)$ emission moves 600 cm^{-1} to higher energies when the delay of measurement after the laser pulse changes from $0.1\text{ }\mu\text{s}$ to $15\text{ }\mu\text{s}$, whilst the ${}^1T_{2g}(D) \rightarrow {}^3T_{2g}(F)$ emission moves 100 cm^{-1} . The orange decay is slower for shorter emission wavelengths. These results indicate a distribution of Ni^{2+} sites with different 'crystal field' environments.

This research was sponsored by Spanish DGICYT. Contract #PB90-0918. M. A. Buñuel thanks D.G.A. for financial support.

REFERENCES

1. P. W. France, S. F. Carter, J. M. Parker, *Phys. Chem. Glasses* **27**, 32 (1986).
2. Y. Suzuki, W. A. Sibley, O. H. El Bayoumi, T. M. Roberts and B. Bendow, *Phys. Rev. B* **35**, 4472 (1987).
3. M. A. Buñuel, R. Alcalá and R. Cases, *J. Non-Crystalline Solids* **161**, 137 (1993).

CHARGE EXCHANGE PROCESSES BETWEEN IMPURITY IONS AND THE HOST CRYSTAL IN WIDE BAND-GAP CRYSTALS

DONALD S. McCLURE, WING C. WONG and SERGEI A. BASUN

Department of Chemistry, Princeton University, Princeton, NJ 08544 USA

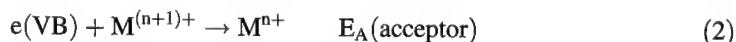
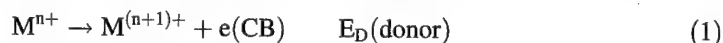
The point of this article is to investigate under what conditions the sum of a donor transition of an impurity ion, $M^{n+} \rightarrow M^{(n+1)+} + e(\text{CB})$, and an acceptor transition $M^{(n+1)+} + e(\text{VB}) \rightarrow M^{n+}$ is equal to the band gap of the host. Our recent work on Ti^{3+} , Ti^{4+} in aluminate host crystals provides the best of the few examples where both a donor and an acceptor transition are known.

Key words: photoconductivity, charge transfer, impurity trapped exciton, transition and rare-earth metal ions, titanium doped aluminates.

1 CHARGE EXCHANGE PROCESSES—PHOTOIONIZATION AND CHARGE TRANSFER

Photoionization and charge transfer of impurity ions in crystals are respectively the electron donor and electron acceptor transitions of the impurity. These exchange processes are the major phenomena observed in semiconductor hosts, while localized transitions are of secondary importance. On the other hand, in wide band gap ionic crystals, charge exchange is of less importance than localized processes. It is becoming clear, however, that one must pay attention to all such transitions in order to understand fully the electronic properties of an impurity-crystal system.¹

If the donor and acceptor processes are written as chemical reactions, we have



then their sum is

$$e(\text{VB}) \rightarrow e(\text{CB}) \quad \Delta E \quad (3)$$

$$\Delta E = E_D + E_A = E_G \quad (4)$$

where E_G is the band gap of the host. Here then is a relation between the photoionization threshold, E_D , and the charge transfer energy, E_A . The first point of this paper is to explore this relationship to see if it is true and useful under whatever restrictions will be necessary.

Eqs. 1 and 2 refer to the relaxed states of the species involved, and in order to have a unique meaning, 1) the electron in Eq. (2) must come from the top of the valence band and the hole must be 'infinitely' distant from the acceptor and 2) the electron in Eq. (1) must go to the bottom of the conduction band and be 'infinitely' distant from the donor. Only under these conditions can Eq. (4) be true. Therefore, the main problem addressed in this paper will be the relationship between spectroscopic data and these idealized E_A and E_D quantities.

There are not many examples in wide band-gap crystals where both a charge transfer and a photoionization threshold are known. Figure 1 shows the charge transfer bands for

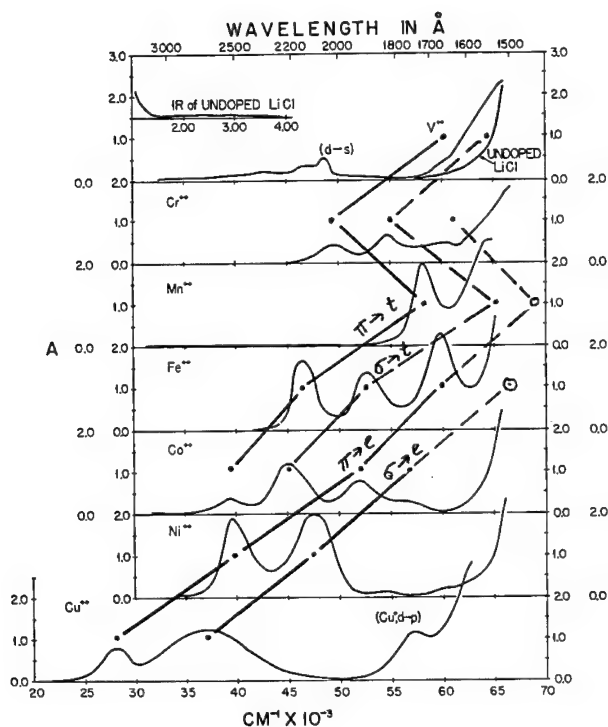


FIGURE 1 Charge transfer spectra of the divalent transition metal ions in LiCl at 10 K. The lines connect equivalent sub bands in each spectrum. The energy ordering is $\pi \rightarrow t$, $\sigma \rightarrow t$, $\pi \rightarrow e$, $\sigma \rightarrow e$ (see Ref. 2), where π , σ are Cl^- orbitals and t , e are 3d metal orbitals.

the series of divalent transition metal ions from V through Cu in LiCl crystal.² Notice that there are up to four peaks in these spectra. The charge transfer multiplet is caused by the interaction of the hole on the $(\text{Cl}^-)_6^{3-}$ with the M^+ d-electrons. The figure illustrates the analysis of these peaks, from which a weighted average charge transfer energy \overline{E}_A is obtained. If a plot of \overline{E}_A versus atomic number is made, it is found that \overline{E}_A is given by a simple formula

$$\overline{E}_A = C - I_2 \quad (5)$$

where $C = 180\,300 \pm 3700 \text{ cm}^{-1}$ and I_2 is the second ionization potential. Adherence to such a relationship as Eq. (5) is the surest way to prove that the transitions are of the charge transfer type. The parameter C should probably depend on the metal ion to a certain extent, since different ions distort the LiCl lattice differently.

To complete the comparison to Eq. (4) we would need to measure the photoionization energy of the monovalent transition metal ions. We know that Cu^+ is a stable species in LiCl and must have an ionization energy of at least several eV. The first charge transfer band for Cu^{2+} has its zero phonon origin at about 3.0 eV and the gap energy of LiCl is 9.3 eV, giving an estimated photoionization energy of 6.3 eV ignoring the refinements discussed above. This energy lies above the $3d \rightarrow 4s$ and below the $3d \rightarrow 4p$ transition of Cu^+ in LiCl. So far, however, no photoconductivity measurement has been made on this crystal.

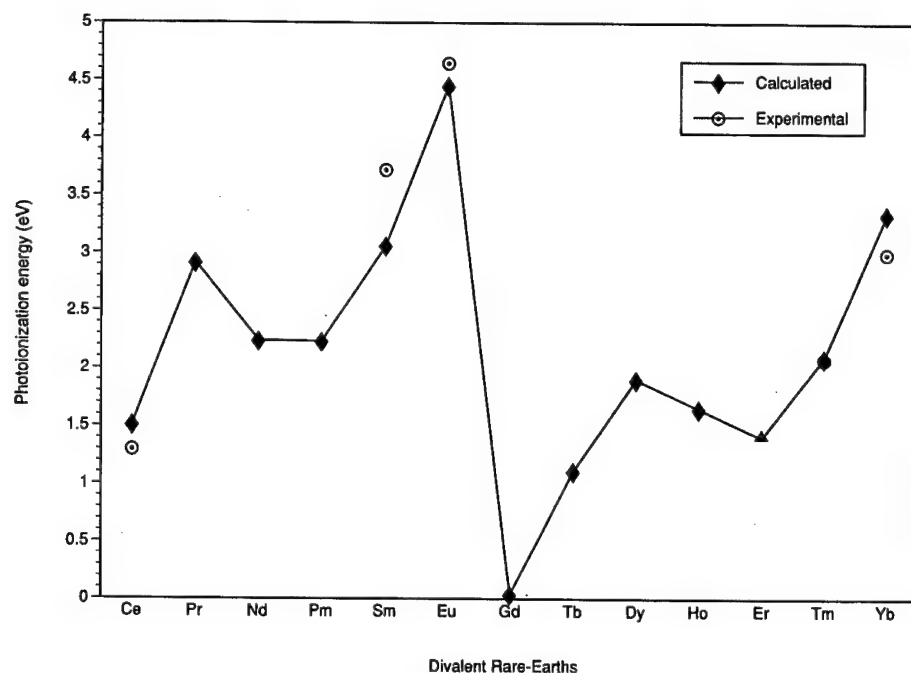


FIGURE 2 Photoionization energies of the divalent rare earths in SrF_2 , showing the calculated values (Eq. 6) and observed values.

The other monovalent transition metal ions must have lower ionization potentials than Cu^+ . Since they are difficult to prepare, there have not been any measurements as yet. Several of them such as Cr^{1+} are ESR active, and by irradiating them in an ESR cavity the ionization energies could be found. Since Cr^{2+} begins its charge transfer absorption at $46\,000\text{ cm}^{-1}$ or 5.8 eV , Cr^{1+} should begin ionizing at 3.5 eV in the near UV.

There has been an extensive series of measurements of the photoionization threshold of the divalent rare earths in CaF_2 , SrF_2 , BaF_2 .³ These results are shown in Figure 2 for SrF_2 and compared to another simple formula

$$E_D \equiv E_{PI} = I_3 - C' = I_3 - [E_M + \Delta E_M + E_{pol} + E_A] \quad (6)$$

Here, C' is shown as the sum of the electrostatic potential at the host metal site, E_M , the change caused by the impurity, ΔE_M , the polarization energy due to removal of an electron and the electron affinity of the host crystal. C' reduces the ionization energy from $I_3 \approx 20\text{ eV}$ to around 5 eV . Although we have good data for the photoionization thresholds, no one to my knowledge has positively identified charge transfer bands of fluoride to trivalent rare earth as was shown for LiCl with transition metal ions. According to Eq. (4), a charge transfer band of Eu^{3+} in SrF_2 should occur at $12 - 5 = 7\text{ eV}$, i.e. in the near vacuum UV region. This is actually close to a band in $\text{KCaF}_3:\text{Eu}^{3+}$ identified by Garcia, *et al.* as a fluoride to Eu^{3+} charge transfer band.⁴

Before spending any more time on these pathological cases where only E_A or only E_D are known, an example will be given where both are known, namely for the case of Ti^{3+} , Ti^{4+} in some aluminate hosts. The data are from work in our laboratory at Princeton.⁵

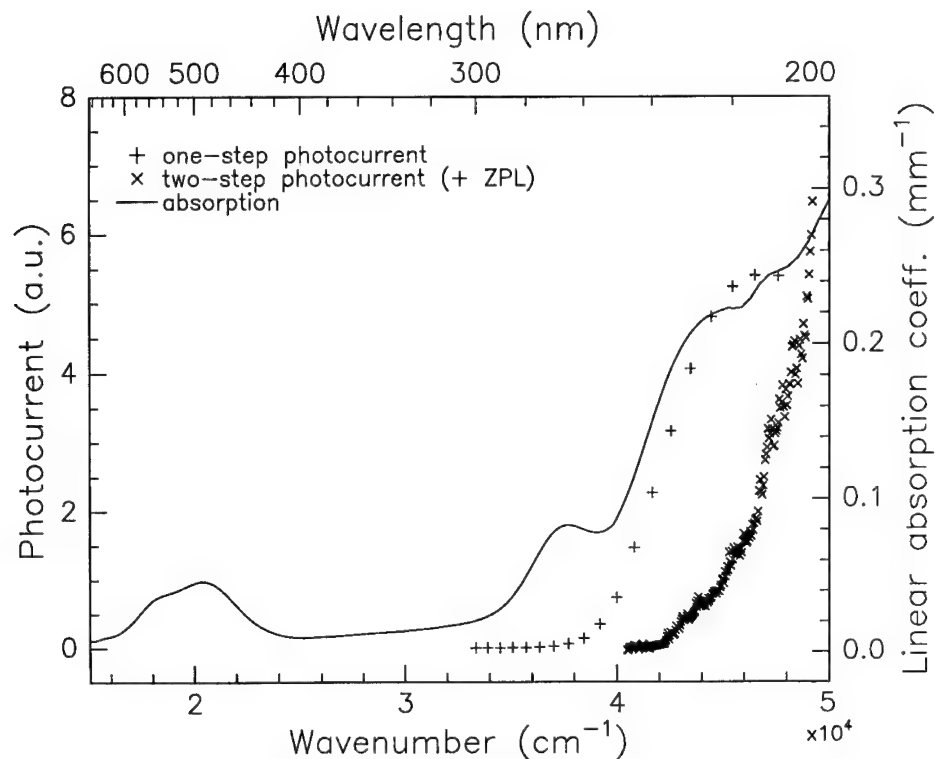


FIGURE 3 Absorption spectrum of $\text{Al}_2\text{O}_3:\text{Ti}^{3+}$, 0.013% Ti^{3+} , 0.00015% Ti^{4+} . The 20 000 and 37000 cm^{-1} bands belong to Ti^{3+} ; the 43000 cm^{-1} band to Ti^{4+} . The one-step and two-step photocurrent spectra are also shown with the ${}^2\text{T}_2 \rightarrow {}^2\text{E}$ zero phonon energy (16000 cm^{-1}) added to the two-step photocurrent. $T = 300$ K.

Figure 3 shows the photoconductivity spectrum of $\text{Al}_2\text{O}_3:\text{Ti}^{3+}$ along with an absorption spectrum. The sample is one having 0.013 mole percent Ti^{3+} and about 0.00016 mole percent Ti^{4+} . The photocurrent corresponds to the ionization of Ti^{3+} and the subsequent trapping of the electrons down-field. The photocurrent is markedly reduced when the sample is changed to one having a high concentration of Ti^{4+} ; the Ti^{4+} acts as a trap and it reduces the free path of the electrons leading to a smaller photocurrent. Figure 3 also shows the two-step photocurrent (similar to the excited state absorption) when the experiment is done with two lasers, one to excite the local ${}^2\text{T}_2 \rightarrow {}^2\text{E}$ transition of Ti^{3+} , and the other to scan the ${}^2\text{E} \rightarrow$ conduction band transition. This experiment positively identifies the Ti^{3+} as the ionizing species. The photocurrent in the two-step experiment occurs at about 0.4 eV higher energy. This is due to the very different configuration of the initial state, ${}^2\text{E}$, compared to the ground state ${}^2\text{T}_2$ in the one-step photoionization. Transitions from ${}^2\text{E}$ are strongly displaced in the e_g coordinate compared to the ${}^2\text{T}_2$ state due to the Jahn-Teller effect. The overlap with the zero phonon level in the conduction band is very small and we cannot determine a zero phonon threshold for photoionization from the two-step data. Similar experiments were done with YAlO_3 , MgAl_2O_4 , $\text{Y}_3\text{Al}_5\text{O}_{12}$, $\text{LaMgAl}_{11}\text{O}_{19}$.

The presence of Ti^{4+} is shown by the strong absorption in the UV and vacuum UV. We have a series of samples of Al_2O_3 having very different $\text{Ti}^{3+}/\text{Ti}^{4+}$ ratios to help distinguish

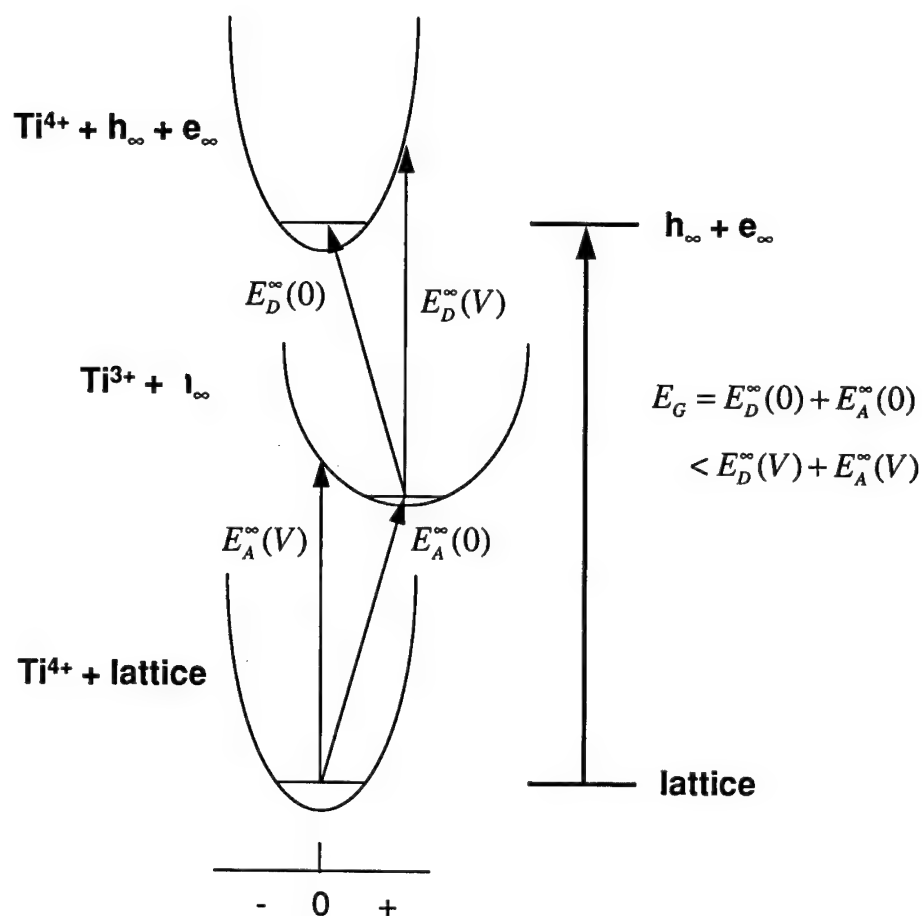


FIGURE 4 Potential curves for the transitions $\text{Ti}^{4+} + e(\text{VB}) \rightarrow \text{Ti}^{3+}$, $\text{Ti}^{3+} \rightarrow \text{Ti}^{4+} + e(\text{CB})$ showing zero phonon transitions and vertical transitions.

the absorption bands of the two oxidation states. It is now accepted that the strong band at $45\,000\text{ cm}^{-1}$ is due to charge transfer, oxygen to Ti^{4+} . There is a much stronger vacuum UV band at $56\,000\text{ cm}^{-1}$ which we have shown is also due to the same charge transfer. The two bands are analogous to the charge transfer multiplets of the transition metal ions in LiCl shown in Figure 1.

We can use the data on Ti^{3+} , Ti^{4+} to see if Eq. (4) is obeyed. Figure 4 will clarify the application of Eq. (4) to the actual data. This diagram (Figure 4) shows how the zero phonon transition energies $E_D^{\infty}(0)$ and $E_A^{\infty}(0)$ (with electron or hole at 'infinite' distance from D or A) add up to the band gap E_G and that the vertical transition sum is greater than E_G . The diagram does not show observable transitions, however, because the hole and electron are supposed to be far enough from the acceptor, or donor so as to have a negligible effect on the total energy of the transition. In a spectroscopically observable transition there must be finite overlap between the initial and final state wavefunctions. Therefore some corrections must be applied to the spectroscopic data.

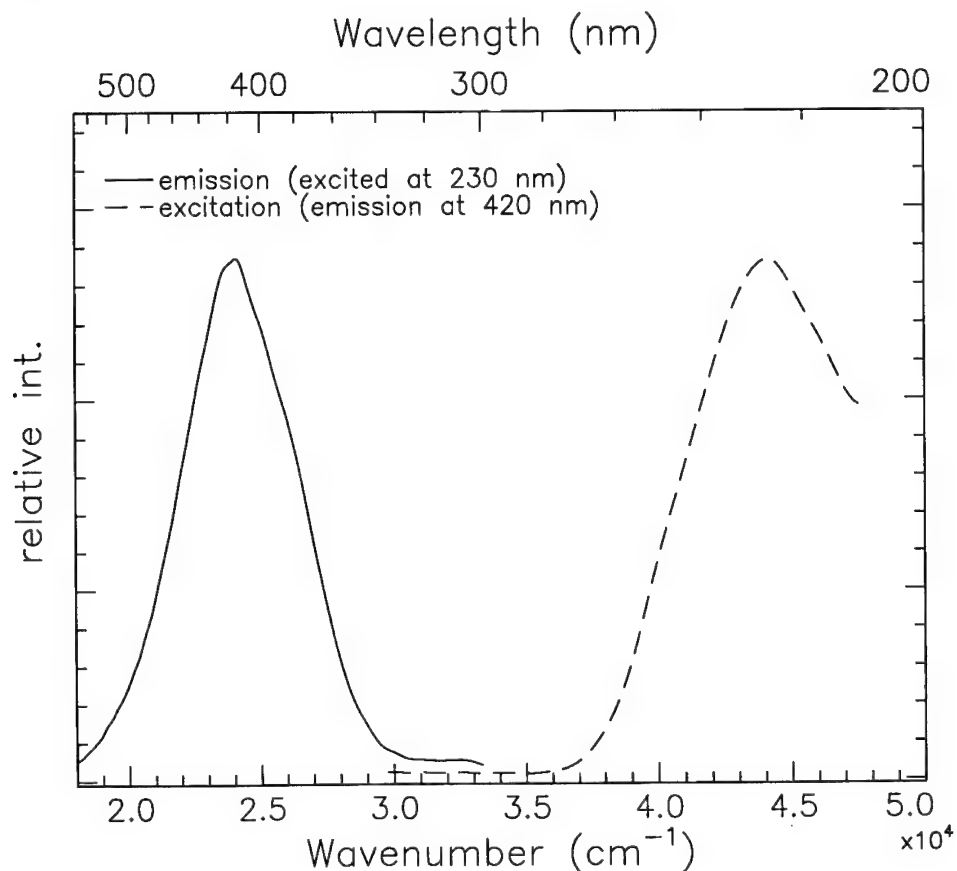


FIGURE 5 Excitation and emission spectra of Ti^{4+} in Al_2O_3 . These spectra correspond to distantly-compensated Ti^{4+} . $T = 300 \text{ K}$.

Before considering these corrections in detail and before bringing out some further spectroscopic studies, we can get an approximate idea of the applicability of Eq. (4). The onset of observable photocurrent in $\text{Al}_2\text{O}_3:\text{Ti}^{3+}$ could be taken as the apparent threshold energy, E_D . But its value depends on the noise level and for one-step photoconductivity it also depends on the possible presence of ionizing impurities. So it is not expected to be very accurate. Taking the value from Figure 3 we have a provisional number $E_D = 38\,000 \text{ cm}^{-1}$.

The acceptor zero phonon energy must be somewhere below the onset of the lower energy charge transfer band. Figure 5 shows the excitation and emission spectra of $\text{Al}_2\text{O}_3:\text{Ti}^{4+}$. The blue luminescence peaking at 420 nm is thought to be the reverse process of charge transfer absorption, and if so the zero phonon line is about halfway between the onset of absorption and the onset of emission. This choice gives a provisional value $E_A = 34\,000 \text{ cm}^{-1}$. The sum $E_D + E_A = 72\,000 \text{ cm}^{-1}$. The band gap of Al_2O_3 is about $9.2 \text{ eV} = 74\,200 \text{ cm}^{-1}$ according to recent data.⁶ These numbers are close and show that it might be worthwhile to get better values of E_D and E_A .

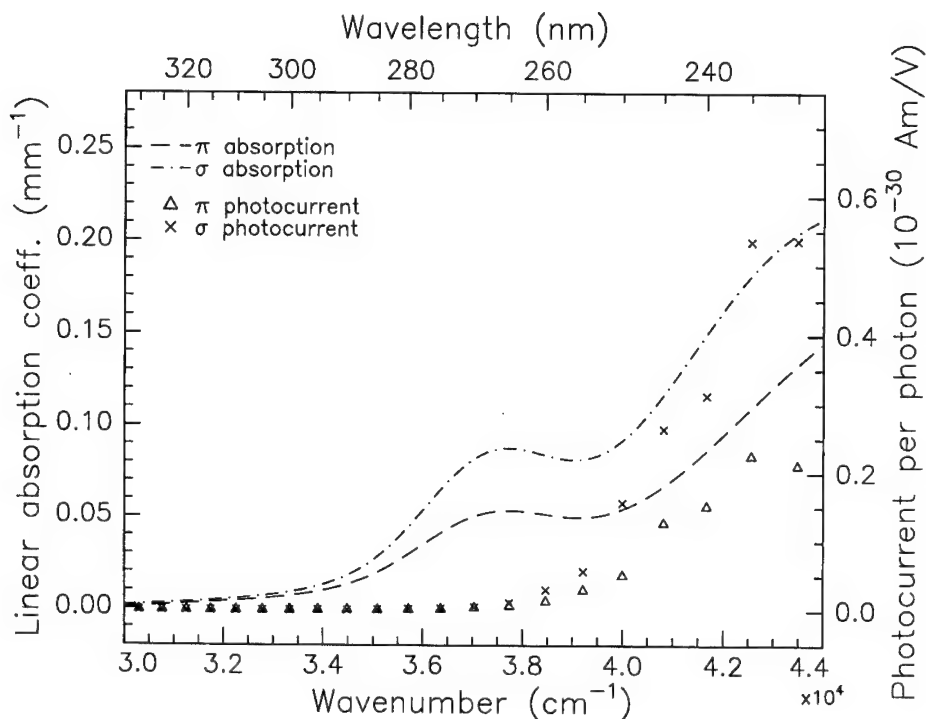


FIGURE 6 Polarized absorption spectra of the 2700 Å band of Ti^{3+} and the polarized photocurrent spectra. $T = 300 \text{ K}$.

2 SPECTROSCOPY OF IONIZATION AND CHARGE TRANSFER PROCESSES

With more careful spectroscopy and analysis of the data, somewhat more reliable values of E_D and E_A can be found.

Since Ti^{3+} has no localized excited states in the vicinity of the ionization threshold, we should see distinct transitions to the conduction band or at slightly lower energies an impurity-trapped exciton. The exciton at lower temperature does not give charge carriers and it therefore gives a lower limit of the ionization threshold.

Figure 6 shows the polarized absorption spectrum of the 2700 Å band of $\text{Al}_2\text{O}_3:\text{Ti}^{3+}$. This band has been given several assignments by others, including Fe^{3+} impurity and $3d \rightarrow 4s$ transition in Ti^{3+} . However, it must be a Ti^{3+} band because its ratio to the ${}^2T_2 \rightarrow {}^2E$ band is constant for different samples if the comparison is made for a single polarization. We don't believe it is a local $d \rightarrow s$ transition because this should occur at a higher energy (10 eV in free Ti^{3+}). Figure 6 also shows the photocurrent in σ and π polarizations. Notice that the photocurrent polarization ratio is the same as the absorption polarization ratio, and also notice that the current begins to be noticeable only at the high energy side of the 2700 Å band. If this band represents an exciton, it would not generate charge carriers except by thermal excitation, in agreement with the above facts. Furthermore if it is an exciton it should decay non-radiatively into the Ti^{3+} manifold of states at temperatures where the thermal ionization rate is small compared to the decay

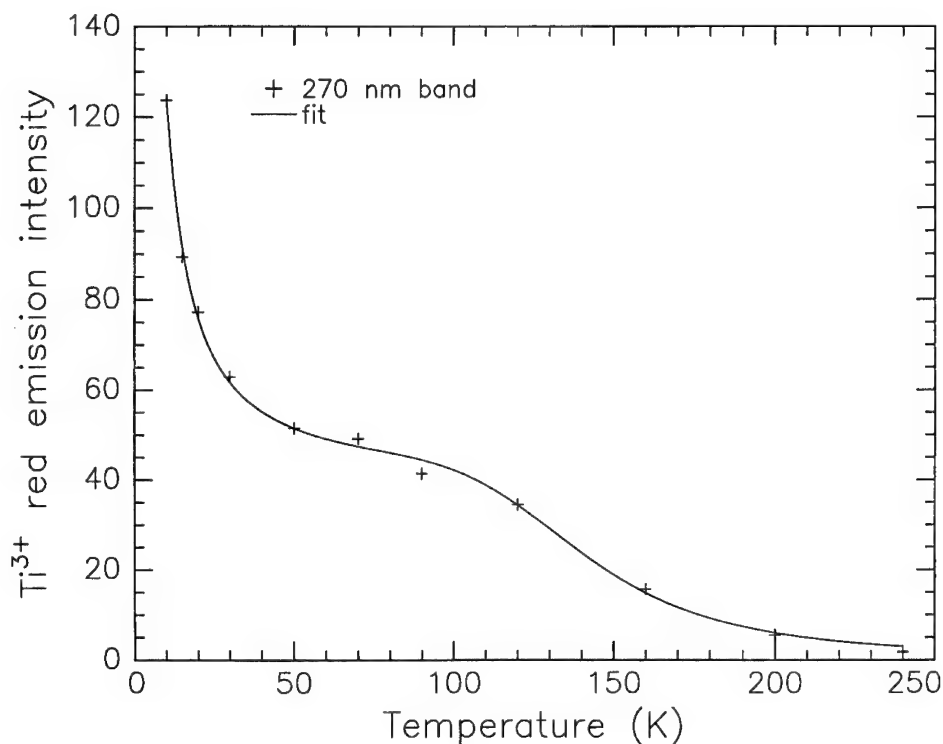


FIGURE 7 Exciton band excitation efficiency of the $\text{Ti}^{3+} {}^2\text{E} \rightarrow {}^2\text{T}_2$ luminescence as a function of temperature from 10 to 250 K.

rate. The decay into the Ti^{3+} manifold generates the red luminescence, ${}^2\text{E} \rightarrow {}^2\text{T}_2$. Figure 7 shows the excitation efficiency of the red luminescence as a function of temperature. There is a sharp rise below 30 K which we take to mean that the radiationless decay into the Ti^{3+} states is competing favorably with the ionization rate. The detailed kinetics of this process will be presented in another publication. Quantitatively, the 2700 Å band has all of the properties expected for an impurity-trapped exciton, and we can use it to give an accurate value for the photoionization threshold. Although we have yet to do a series of absorption and photoconductivity measurements at liquid helium temperature we can say that the zero phonon photoionization threshold for $\text{Al}_2\text{O}_3:\text{Ti}^{3+}$ is $38\,000 \pm 500 \text{ cm}^{-1}$.

An accurate value for the charge transfer zero phonon energy is more difficult to get. We used the halfway point between the onset of the blue emission and the fluorescence excitation in the estimate made above. But the lifetime of the blue emission peaking at 420 nm is 30 μs at 300 K while the oscillator strength of the 230 nm absorption band is close to 0.1. These are not compatible and the emission cannot arise from the same upper state giving rise to the 230 nm band. Our hypothesis is that the emission is due to a lower triplet state of the charge transfer manifold.

When the hole on the O^- lattice is well separated from the Ti^{3+} ion, the single-triplet splitting goes to zero. Therefore a weighted average of the singlet and triplet levels should represent the E_A value we seek.

We can fit the lifetime, intensity and band shift of this luminescence from the paper by Bruce Evans⁷ as a function of temperature to a model having a triplet state about

$1700 \pm 200 \text{ cm}^{-1}$ below a singlet. Furthermore, it is straightforward to fit the data to a perturbation theory of the singlet-triplet mixing in this system, using the measured multiplet splitting of the 2T_2 state of Ti^{3+} to get a value for the spin-orbit parameter. The origin of the charge transfer transition corrected as above for the singlet-triplet splitting is supposed to represent the transition coming from the top of the valence band to the Ti^{4+} . This value is $33\,000 \pm 500 \text{ cm}^{-1}$.

Finally, using these more refined values of E_D and E_A we have $E_D + E_A = 38\,000 \pm 500 + 33\,000 \pm 500 = 71\,000 \pm 700$ while $E_G = 74\,200$. This is about as close as we are going to get without doing a series of low temperature experiments. The difference $E_G - (E_D + E_A) = 3200 \text{ cm}^{-1}$ is quite possibly the energy difference due to the attraction of the hole for the electron trapped on Ti^{3+} . The singlet-triplet weighted average is not the only correction for separating hole and electron. There may well be a significant energy of attraction in view of the fact that the charge transfer multiplet is about $10\,000 \text{ cm}^{-1}$ wide. This attractive energy is the most difficult component of E_A to estimate reliably and there does not seem to be a simple experimental measurement to get it. Except for this it has been possible to find E_D and E_A from spectroscopic data for Ti^{3+} , Ti^{4+} in Al_2O_3 .

The case if Ti^{3+} , Ti^{4+} is a fortunate one for our purpose because we could both locate an impurity centered exciton level and could observe the charge transfer emission band. Neither of these features is to be expected for most of the other transition metal ions.

An exciton band is only observable when the localized transitions do not interfere. Ti^{3+} has only one localized transition which is too low in energy to interfere with the ionization level. In most of the divalent rare earths in CaF_2 , etc, the $4f \rightarrow 5d$ bands cover up the exciton level, but in a few cases such as $BaF_2:Tm^{2+}$, an exciton level should be exposed.

Charge transfer emission bands are also relatively rare. If there is a ladder of localized states lower than the charge transfer energy, the excitation would decay into them and no charge transfer luminescence would be observed.

3 CONCLUSION

Our one good example shows the weak point in trying to get spectroscopic values for E_D and E_A . If we had more such examples we might see a systematic behavior of the discrepancy $E_G - (E_A + E_D)$ and then could try to rationalize it with a model of the hole-electron attraction. There are other chemical systems where one could look for an exciton band and a charge transfer multiplet, systems for which enough accuracy would be available for an evaluation of $E_G - (E_A + E_D)$. Another caution in the use of Eq. (4) is that true band gaps are often not known accurately, and compilations exist showing grossly incorrect values. At least, Eq. (4) can give useful estimates if for any two of the three quantities a reasonable zero phonon energy can be found.

REFERENCES

1. A. Zunger, *Solid State Physics* **39**, 175-464 (1986).
2. J. Simonetti and D. S. McClure, *J. Chem. Phys.* **71**, 793-801 (1979).
3. C. Pedrini, F. Rogemond and D. S. McClure, *J. Appl. Phys.* **59**, 1196-1201 (1986).
4. J. Garcia, W. A. Sibley, C. A. Hunt and J. M. Spaeth, *J. Lumin.* **42**, 35-42 (1988).
5. W. C. Wong, D. S. McClure and S. A. Basun, *J. Lumin.* **60 & 61**, 183-187 (1994).
6. F. G. Will, H. G. deLorenzi and K. H. Janora, *J. Am. Ceram. Soc.* **75**, 2790-2794 (1992).
7. B. D. Evans, *J. Lumin.* **60 & 61**, 620-626 (1994).

THE ROLE OF DIFFERENT CHARGE STATES OF IMPURITY IONS IN PHOTOCONDUCTIVITY OF INSULATORS

S. A. BASUN

A. F. Ioffe Physico-Technical Institute, 194021 St. Petersburg, Russia

The results of experimental studies of stationary photoconductivity of single-crystal $\text{Al}_2\text{O}_3:\text{Ti}^{3+}$, $\text{Y}_3\text{Al}_5\text{O}_{12}:\text{Ti}^{3+}$, $\text{YAlO}_3:\text{Ti}^{3+}$, and $\text{Li}_2\text{Ge}_7\text{O}_{15}:\text{Cr}^{3+}$ where the photocurrent is induced by two-step photoionization of 3d-ions via intermediate metastable state, are presented. The dependence of stationary two-step excited photocurrent j on optical pumping density P ($j \sim P^n$, $n = 2, 3/2$ for different cases) appears to be very informative for studies of all steps of photoelectric processes including photoionization of 3d-ions, capture by traps and release of photocarriers and their recombination.

Key words: doped insulators, $\text{Li}_2\text{Ge}_7\text{O}_{15}:\text{Cr}^{3+}$, photoconductivity, two step photoionization, trapped carriers.

1 INTRODUCTION

The processes of photoionization of impurity ions in insulating crystals are basic for several applications (holographic storage in photorefractive and photochromic media, hole burning, X-ray luminescent screens etc.). The spectral dependencies of photoelectric response give fundamental information on photoionization thresholds and relative positions of impurity and host lattice energies.^{1,2} Of special interest is photoelectric behaviour of some oxide crystals doped with transition metal 3d-ions like Ti^{3+} and Cr^{3+} which have metastable states and can be excited in visible region.³⁻⁷ The photoionization of these ions with visible light takes place as a result of two-step optical process involving intermediate excited state. Such two-quantum photoionization is responsible for important features in hologram recording and reading,^{8,9} in photon-gated hole burning¹⁰ and is closely connected to the excited state absorption (ESA) phenomenon which is important for lasing.¹¹

2 STATIONARY PHOTOCURRENT IN DOPED CRYSTALS

The measurements of DC photocurrent were used in studies of photoelectric properties of oxides doped with 3d-ions. The advantage of two-step photoionization of ions is usually sure knowledge of the first step nature as the excitation of dominating charge state of ion M (Ti^{3+} or Cr^{3+}) into metastable state. Photoelectrons in conduction band (CB) are assumed to appear as a result of second step. The basic expression for stationary photocurrent is

$$j = e \cdot \Gamma \cdot L \sim \Gamma \cdot E \cdot S \sim \Gamma \cdot E / n_+ \quad (1)$$

where e is electron charge, Γ – the photoionization rate, L – the mean displacement of an electron in electric field E . $L \sim \mu \cdot E \cdot T \sim E \cdot S$, where μ is free electron mobility, T is total lifetime of free electron in CB, and $S \sim T$ – mean free path of an electron passed from generation until recombination: $S^{-1} = \sigma_r \cdot n_+$ where σ_r is the recombination cross-section and n_+ – the concentration of ionized 3d-ions M^+ which serve as recombination centers.

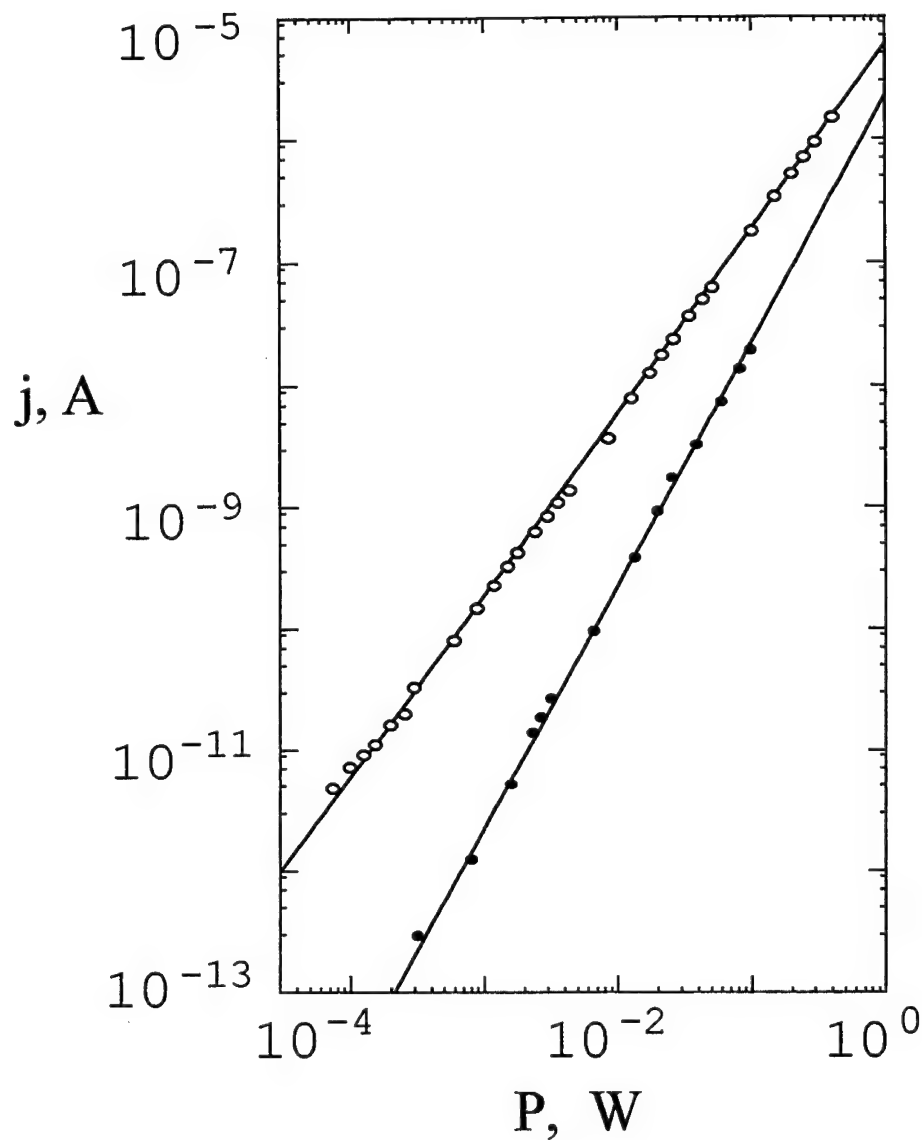


FIGURE 1 Pumping power dependence of stationary photocurrent in LGO:Cr (full circles) and LGO:Cr,Mg (open circles). $T = 77$ K, $E = 100$ kV/cm, $\lambda_{exc} = 514.5$ nm. Laser beam diameter 0.2 mm (LGO:Cr) and 0.5 mm (LGO:Cr, Mg). Straight lines $j \sim P^2$ (LGO:Cr) and $j \sim P^{3/2}$ (LGO:Cr, Mg).

The concentration $n_+ = n_+^0 + n_+^*$ where n_+^0 is the initial concentration of M^+ in sample and n_+^* – the concentration additionally created by photoionization of dominant M ions. As it can be seen, j strongly depends on valence state content of 3d-ions (on n_+^0) which can be changed in sample by changing of crystal growth conditions and by codoping.

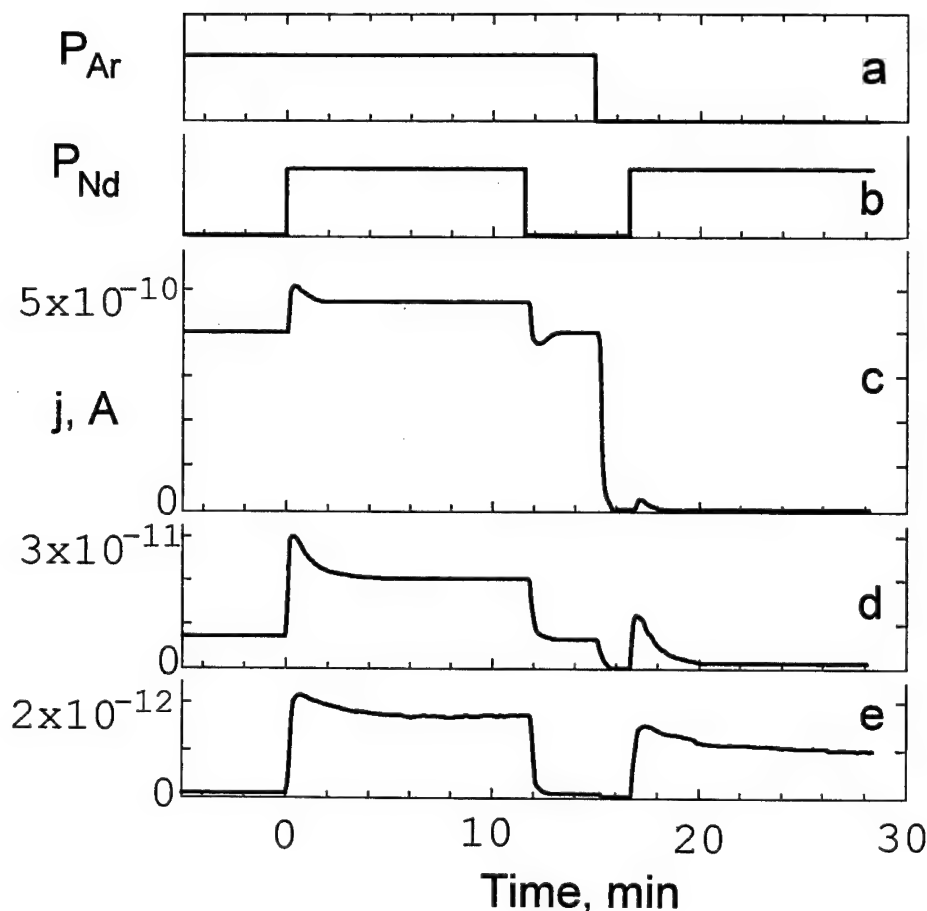


FIGURE 2 Photocurrent kinetics for LGO:Cr, Mg sample excited with Ar laser (514.5 nm) and overlapped cw YAG:Nd laser (1060 nm, 2W). Beam diameters 1 mm, $T = 77$ K, $E = 100$ kV/cm. Switch on/off sequence: Ar laser pumping P_{Ar} (a), YAG:Nd laser pumping P_{Nd} (b), photocurrent j (c-d). $P_{Ar} = 10^{-2}$ W (c), 10^{-3} W (d), 10^{-4} W (e).

In the case A ($n_+^0 \gg n_+^*$) the photocurrent quadratically depends on pumping intensity P for two-step photoionization ($\Gamma \sim P^2$): $j \sim \Gamma/n_+^0 \sim P^2/n_+^0$. This was confirmed experimentally for Ti^{3+} in Al_2O_3 , 3YAG ,⁴ and $YAlO_3$ ⁵ and for Cr^{3+} in $Li_2Ge_7O_{15}$ (LGO)⁶ (see Figure 1). The study of $YAlO_3:Ti$ crystals with different Ti^{4+} content (different n_+^0) shows the strong decrease of photocurrent with increase of n_+^0 .

In the opposite case B ($n_+^0 \ll n_+^*$) the dependence $j \sim P^{3/2}$ can be derived from (1),⁷ taking into account that exciting light plays two different roles – i) producing (in the two-step process) M^+ ions and free electrons which rapidly become trapped but still remain excited (potential) charge carriers, and ii) releasing the trapped electrons (in one-photon process), thus giving them a possibility 'to find' M^+ ions and recombine disappearing as

excited carriers. The dependence $j \sim P^{3/2}$ was observed in LGO:Cr, Mg crystals where codoping by Mg^{2+} (substituting Li^+) reduces strongly the content of intrinsic recombination centers (Cr^{4+}) in the sample.⁷

The different role of trapping and optical release of electrons in cases A and B was directly proved in experiments with IR irradiation (cw YAG:Nd laser) of Cr^{3+} doped LGO crystals. After visible excitation switch off, photocurrent drops to zero value with current amplifier response time (~ 20 s). Switch on of IR light results in steep rise of photocurrent with subsequent slow decay (no *stationary* conductivity is observed under 1.06μ irradiation only). This behaviour is observed for both kinds of samples – LGO:Cr and LGO:Cr, Mg. Repeated IR irradiation switch on gives no current. This shows that i) 1.06μ irradiation is able only to release trapped electrons, and ii) visible irradiation is necessary to produce trapped electrons (it seems reasonable to think that it is also suitable for trapped electron release).

When visible irradiation of LGO:Cr, Mg samples is on during long period of time, a stationary level of n_+^* is achieved causing a stationary photocurrent magnitude determined by (1). Switch on of additional IR irradiation (see Figure 2) results in steep rise of photocurrent due to accelerated escape of trapped electrons. Then n_+^* drops to a new stationary value which is lower than the previous one because of more effective recombination in the conditions of fast one-photon optical release of electrons from traps. Therefore – in accordance with (1) – the new stationary value of photocurrent increases. This effect is the stronger, the weaker is visible irradiation relative to IR light (Figure 2), and it is observed only for LGO:Cr, Mg samples (case B). For the case of LGO:Cr samples, practically no effect of additional IR irradiation on photocurrent magnitude is observed. Indeed, in this case (A) n_+^0 is initially large and cannot be changed markedly by irradiation, hence the current also remains unchanged.

REFERENCES

1. C. Pedrini, D. S. McClure, and C. H. Anderson, *J. Chem. Phys.* **70**, 4959 (1979).
2. C. Pedrini, F. Rogemond, and D. S. McClure, *J. Appl. Phys.* **59**, 1196 (1986).
3. S. A. Basun, A. A. Kaplyanskii, B. K. Sevastyanov, L. S. Starostina, S. P. Feofilov, and A. A. Chernyshov, *Fizika Tverdogo Tela* **32**, 1898 (1990).
4. S. A. Basun, S. P. Feofilov, A. A. Kaplyanskii, B. K. Sevastyanov, M. Yu. Sharonov, and L. S. Starostina, *J. Lumin.* **53**, 28 (1992).
5. S. A. Basun, S. P. Feofilov, A. A. Kaplyanskii, T. Danger, G. Huber, and K. Petermann, *OSA Proc. of the ASSL, New Orleans, USA* (1993), v.15, p. 339.
6. S. A. Basun, S. P. Feofilov, A. A. Kaplyanskii, A. B. Bykov, B. K. Sevastyanov, and M. Yu. Sharonov, *J. Lumin.* **53**, 24 (1992).
7. S.A.Basun, A.A.Kaplyanskii, and S. P. Feofilov, *Fizika Tverdogo Tela* (in press).
8. E. Krätzig, *Ferroelectrics* **21**, 635 (1978).
9. R. Sommerfeldt, L. Holtman, and E. Krätzig, *Ferroelectrics* **92**, 219 (1989).
10. R. Macfarlane, *J. Lumin.* **38**, 20 (1987).
11. K. Petermann, *Optical and Quantum Electronics* **22**, 199 (1990).

TWO-PHOTON LASER SPECTROSCOPY OF Ce^{3+} IN LiYF_4

J. C. GÂCON, J. BAUDRY, C. GARAPON and G. W. BURDICK*

*Laboratoire de Physico-Chimie des Matériaux Luminescents; URA No 442 du CNRS et Université Lyon-I, 69622 Villeurbanne Cedex, France; *Department of Chemistry, University of Virginia, Charlottesville, VA 22901, USA*

One-color two-photon excitation spectra of the $4f^1 \rightarrow 5d^1$ transitions of Ce^{3+} in LiYF_4 have been investigated at 5 K from 33 400 to 44 000 cm^{-1} . A sharp lorentzian line peaking at 33 439.4 cm^{-1} with a width of 2.6 cm^{-1} is observed on the low energy side of a band extending up to 35 200 cm^{-1} . The line and the band are observed to exhibit different polarization dependences. A second band with a maximum peaking around 41 977 cm^{-1} is observed to extend from 40 000 up to 44 000 cm^{-1} . No sharp line associated to this band is seen.

Key words: Ce^{3+} , LiYF_4 , two-photon absorption.

1 INTRODUCTION

The advantages of two-photon absorption (TPA) spectroscopy are well known. Using this technique, energy levels lying in the ultraviolet domain may be reached using visible sources. In the limit of the electric-dipole approximation, TPA transitions between states belonging to configurations of opposite parities are forbidden. However, for ions at noncentrosymmetric sites, odd components of the static crystal-field will mix states belonging to opposite-parity configurations. Moreover, interactions with odd-parity phonons will result in a similar configuration mixing. These mixings make $4f^n \rightarrow 4f^{n-1}5d$ TPA transitions allowed, just as they are responsible for the intensity of intraconfigurational $4f^n \rightarrow 4f^n$ one-photon forced-electric-dipole transitions.

Indeed, $4f^1 \rightarrow 5d^1$ TPA transitions of Ce^{3+} have already been observed in crystals in which cerium ions occupy noncentrosymmetric sites,^{1–5} but never in LiYF_4 , up to now. Usually, these transitions give rise to broad vibronic bands. Associated sharp zero-phonon lines are also observed.^{1,3,5} The $\text{Ce}:\text{LiYF}_4$ system is well known to be an ultraviolet solid state laser material.⁶ The Ce^{3+} ion enters the Y^{3+} sublattice without requiring any charge compensation. Moreover the substitution produces little lattice distortion since both ions have very close ionic radii.⁷ Under these conditions, the crystal-field experienced by the cerium ions has the S_4 symmetry of the Y^{3+} site.⁷ At room temperature, the one-photon absorption spectrum exhibits four bands peaking at 295, 245, 208 and 198 nm.^{6,7} The 300 K one-photon emission spectrum is composed of a broad band in the region of 300–350 nm with two resolved peaks at 310 and 325 nm arising from electric dipole transitions from the lowest $5d^1$ state to the $^2F_{5/2}$ and $^2F_{7/2}$ manifolds of the $4f^1$ configuration.^{6,7} The fluorescence lifetime for $\text{Ce}^{3+}:\text{LiYF}_4$ was found to be on the order of 40 ns at 5 K.⁷

2 EXPERIMENTAL DETAILS

The $\text{Ce}:\text{LiYF}_4$ crystal used in this study was grown at M.I.T. with an estimated cerium concentration of 1 mol%. The suitable laser beam for two-photon excitation of Ce^{3+} ions was delivered by a pulsed XeCl excimer pumped-dye laser from Lumonics (Excimer-500

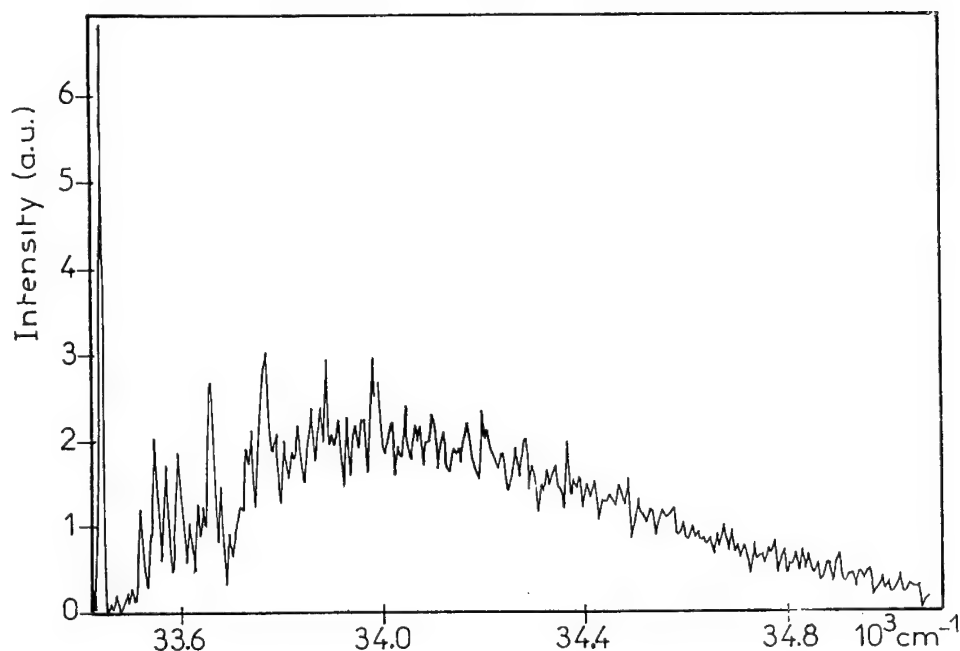


FIGURE 1 TPE spectrum of $\text{Ce}^{3+}:\text{LiYF}_4$ at 5 K: zero-phonon line and lowest energy band (transitions to the lowest $5d^1$ Stark level).

and Hyperdye-300 models), using Rhodamine 590, Rhodamine 610, Coumarine 460 and Courmarine 480 dyes to cover the spectral range from 33 400 to 44 000 cm^{-1} . The linear polarization of the beam could be varied thanks to a Soleil-Babinet compensator adjusted so as to play the role of a half-wave plate in the selected spectral range. The beam was focused onto the sample mounted in a liquid-helium bath cryostat thanks to a $f = 150$ mm lens. The ultraviolet fluorescence induced by two-photon excitation of Ce^{3+} ions was collected with the aid of a set of two quartz lenses forming the image of the sample onto the entrance slit of a Jarrell-Ash monochromator (dispersion: 6 nm with a 1 mm slitwidth). To block any visible scattered radiation from the laser, a MTO H325 filter with a 100 nm passing band centered at 325 nm was introduced at the entrance of this monochromator. The signal at the output of the 6256 S EMI phototube was integrated and averaged in a SRS 250 boxcar. Due to the weakness of the two-photon signals, the input impedance of the boxcar was set at 1 $\text{M}\Omega$, preventing taking full advantage of time-resolved spectroscopy techniques. A 3 ns delay and a 5 μs width were used for the boxcar gate. Since the TPA transitions investigated in this work give rise to broad bands, the spectra should be corrected for the variations of the dye efficiency over the corresponding spectral range. The energy of the impinging laser beam was measured thanks to a Molectron J3-05 joulemeter, the output signal being processed in a second SRS 250 boxcar. Both signals at the output of the boxcars were then processed in an analog-digital converter coupled with a computer monitoring the scanning of the dye-laser and monochromator gratings as well.

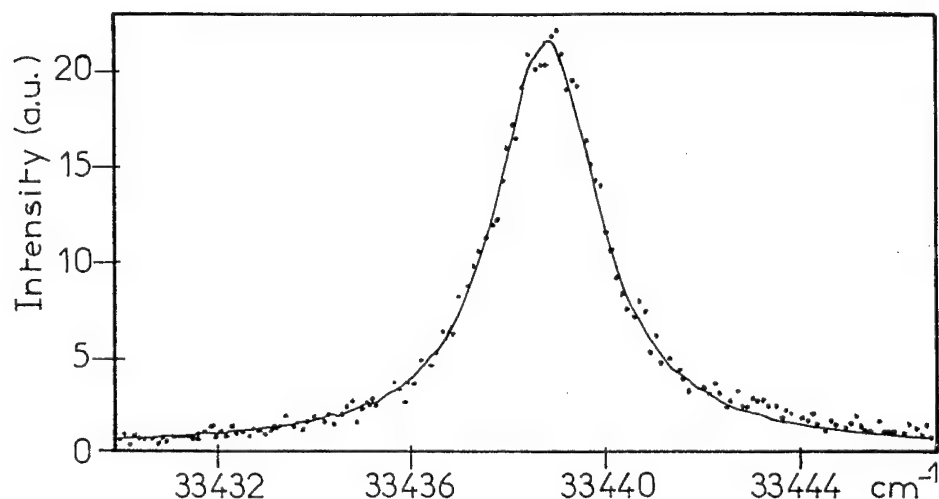


FIGURE 2 TPE spectrum of $\text{Ce}^{3+}:\text{LiYF}_4$ at 5 K: lorentzian fit (continuous line) of the zero-phonon line.

3 RESULTS

The 5 K two-photon excitation (TPE) spectrum shown in Figure. 1 exhibits a sharp line on the low energy side of a broad band. The line has a lorentzian shape with a peak at $33\,439.4\text{ cm}^{-1}$ and a 2.6 cm^{-1} width (Figure. 2). The band extends up to $35\,200\text{ cm}^{-1}$ with a maximum at about $33\,980\text{ cm}^{-1}$ ($\approx 294\text{ nm}$). It corresponds to the lowest energy band observed in the one-photon absorption spectrum.^{6,7} The line could be a zero-phonon line associated to this vibronic band. It is to be noted that such a zero-phonon line was not observed in the room temperature one-photon absorption spectra.^{6,7} Since absorption at 5 K occurs from the lowest Stark component of the $^2F_{5/2}$ multiplet, both line and band are to be attributed to TPA transitions to the lowest $5d^1$ Stark level. Both line and band were observed to be anisotropic. However, they do not exhibit the same polarization dependence, showing the role of the symmetry of the phonons involved in the TPA vibronic transitions. Measurements of the band polarization were achieved at different wavelengths corresponding to small, intermediate, and large frequency shifts from the zero-phonon line. They do not show significant differences, contrasting with the observation that the phonon sideband for $\text{Ce}^{3+}:\text{CaF}_2$ is anisotropic at small frequency shifts from the zero-phonon line and independent of the polarization at larger shifts.^{1,8}

A second band extending from $40\,000$ to $44\,000\text{ cm}^{-1}$ was also observed (Figure 3). It has a gaussian shape with a peak around $41\,977\text{ cm}^{-1}$ ($\approx 238\text{ nm}$). It corresponds to the band appearing at 245 nm in the room temperature one-photon absorption spectrum.^{6,7} No zero-phonon line associated to this band was observed. This band is to be attributed to TPA vibronic transitions to the first excited $5d^1$ Stark level. It also exhibits an anisotropic polarization dependence.

The spectra of the ultraviolet emission following two-photon excitation in the zero-phonon line and the two bands have been recorded at 5 K. The three spectra are similar. They exhibit two resolved bands with maxima at 304 and 324 nm (respectively $32\,895$

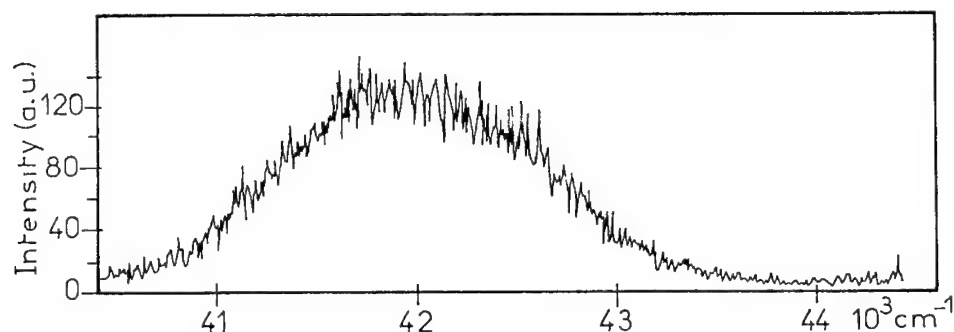


FIGURE 3 TPE spectrum of $\text{Ce}^{3+}:\text{LiYF}_4$ at 5 K: transitions to the first excited $5d^1$ Stark level.

and $30\,864\text{ cm}^{-1}$). No zero-phonon line was observed when the excitation was achieved in the bands. A shift of about 544 cm^{-1} is found between the position of the zero-phonon line observed in the TPE spectrum and the maximum of the high energy band appearing in the emission spectra. This shift is about half the energy gap between the two-photon absorption and one-photon emission peaks associated with the $^2F_{5/2}$ level ($\approx 1085\text{ cm}^{-1}$). This last result is inconsistent with the 2000 cm^{-1} Stokes shift reported in Refs. 6. However, correcting the one-photon emission spectrum shown in this reference for the self-absorption around 300 nm may result in a reduced value of the Stokes shift.

ACKNOWLEDGMENTS

We acknowledge a partial support by NATO under contract N^o.CRG 910902.

REFERENCES

1. S. K. Gayen and D. S. Hamilton, *Phys. Rev.* **B28**, 3706 (1983).
2. S. K. Gayen, G. J. Pogatsnik and D. S. Hamilton, *J. Lum.* **31 & 32**, 260 (1984).
3. D. Piehler, Ph. D thesis, University of California, Berkeley CA, U.S.A. (1990).
4. C. Pedrini, B. Moine, J. C. Gacon and B. Jacquier, *J. Phys: Condens. Matter* **4**, 5461 (1992).
5. J. Sytsma, D. Piehler, and N. M. Edelstein, *Phys. Rev.* **B47**, 14786 (1993).
6. D. J. Ehrlich, P. F. Moulton and R. M. Osgood, *Optics letters* **4** (1979).
7. Li-Ji Lyu, Ph. D thesis, University of Connecticut, Storrs CO, U.S.A. (1990).
8. S. K. Gayen and D. S. Hamilton, and R. H. Bartram, *Phys. Rev.* **B34**, 7517 (1986).

OPTICAL SPECTROSCOPY OF Yb^{3+} IONS IN $\text{Ca}_x\text{Cd}_{1-x}\text{F}_2$

K. ŚWIATEK

Institute of Physics, Polish Academy of Sciences, Al. Lotnikow 32/46, PL-02-668 Warsaw, Poland

Optical properties of Yb^{3+} ions in $\text{Ca}_x\text{Cd}_{1-x}\text{F}_2$ ($x = 0.30$) crystals are investigated. Photoluminescence and absorption spectra of the intra-ion transitions were measured in a wide temperature range (4 - 300 K). It was found that position and shape of the Yb^{3+} zero-phonon emission lines exhibit a noticeable temperature dependence, particularly at temperatures $T < 50$ K. In the same temperature limits, the position and the shape of the Yb^{3+} zero-phonon absorption lines do not change significantly. It was found that the measured shift between energy of the emission and absorption zero-phonon lines is due to the efficient energy migration among the Yb^{3+} ions.

Key words: $\text{Ca}_x\text{Cd}_{1-x}\text{F}_2$ ionic crystals, Yb impurity, optical properties.

The rare earth ions have been extensively studied in various crystal hosts because of the potential applications for phosphors or lasers. For example, many ionic crystals doped with Yb^{3+} and Er^{3+} ions reveal the property of efficient infrared to visible light up-conversion. One of the causes of high efficiency of such process is the fast energy migration among ytterbium ions. In this paper we present results of optical studies of the Yb^{3+} ions in $\text{Ca}_{0.30}\text{Cd}_{0.70}\text{F}_2$ crystal.

The $\text{Ca}_x\text{Cd}_{1-x}\text{F}_2:\text{Yb}$ crystals studied in this paper were grown by the modified Bridgman-Stockbarger method (see, e.g.,¹). Such procedure allows to introduce rare earth (RE) impurities with concentration varying from 0.01 mol% up to several mol%.² The $\text{Ca}_x\text{Cd}_{1-x}\text{F}_2$ mixed crystals possess a fluorite structure³ which consists of a regular cubic fluorine F^- sublattice with every second cube centered by Ca^{2+} or Cd^{2+} . The cation is at a site of cubic point symmetry and is coordinated to eight F^- ions. The Yb^{3+} ion tends to replace the cation in the host lattice. In the cubic crystal field the $J = 7/2$ manifold of the free Yb^{3+} ion is split into a Γ_8 quartet and Γ_6 and Γ_7 doublets, and the $J = 5/2$ manifold is split into Γ_7' and Γ_8' (Figure 1). It is worth mentioning that the extra positive charge of the Yb^{3+} ion replacing cation in the host lattice may be compensated in a variety of ways, each of which gives rise to a site of different symmetry, and thus a different optical spectrum. For example, tetragonal site is caused by the presence of a charge compensating F^- ion occupying the empty body center site adjacent to the RE^{3+} ion along a [100] direction.⁵

Low temperature photoluminescence (PL) spectra of the Yb^{3+} in heavily doped $\text{Ca}_{0.30}\text{Cd}_{0.70}\text{F}_2:\text{Yb}$ (2 mol%) crystals consist of sharp lines at 10 201 cm^{-1} , 10 241 cm^{-1} , 10 334 cm^{-1} , 10 394 cm^{-1} and broad phonon replica band 10 181-9500 cm^{-1} (Figure 2). Detailed PL measurements have shown that the shape and position of all these sharp lines are temperature dependent, especially at 4 K-50 K. It is worth mentioning that in the same temperature range we have not observed any change of the shape and energy position of the absorption lines. A careful analysis of the shape of these emission and absorption lines shows that they are inhomogeneously broadened and are related to the same electronic transition between one ground and one excited states of the Yb^{3+} ions in different cation sites of the mixed $\text{Ca}_x\text{Cd}_{1-x}\text{F}_2$ crystal. Following the ideas proposed by Stapor and Langer⁶ for $\text{CdF}_2:\text{Yb}$, we have analyzed, as an example, the temperature evolution of shape of the 10 201 cm^{-1} emission line. If we assume that energy migration among Yb^{3+} ions is much faster than their intrinsic relaxation, it is possible to use the Fermi-Dirac

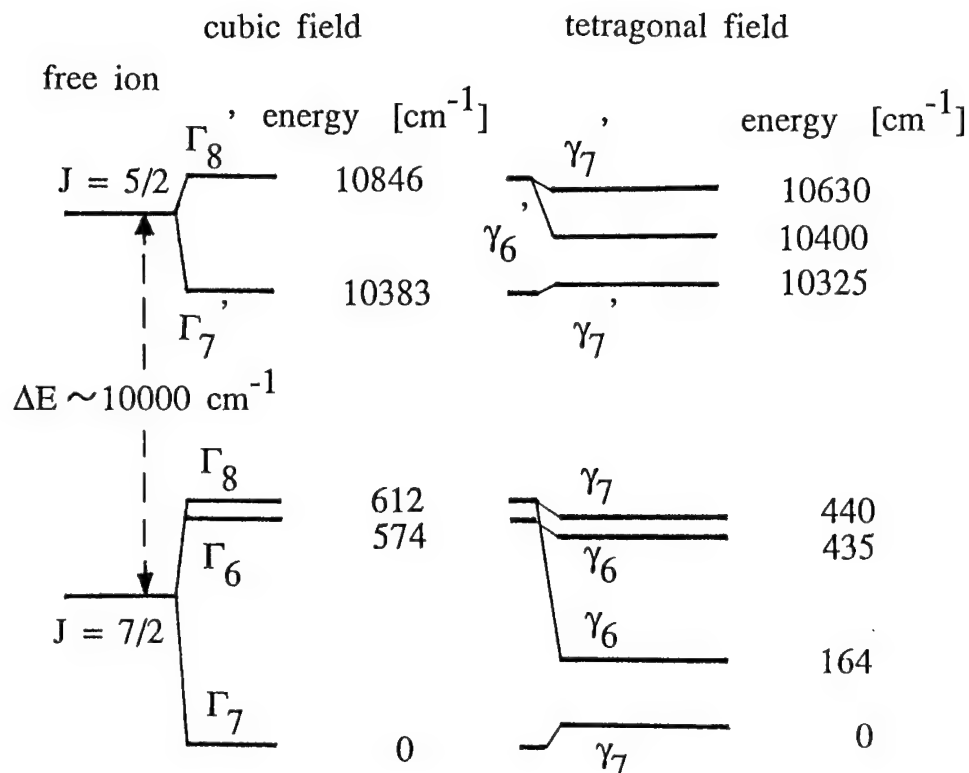


FIGURE 1 The energy levels of Yb^{3+} in CaF_2 in sites of cubic and tetragonal symmetry (after Voronko *et al.*⁴).

statistics to describe population of the Yb^{3+} excited states:

$$n^*(E) = \frac{n(E)}{1 + \exp[(E - \zeta)/kT]} \quad (1)$$

$n(E)$ is the distribution function of the Yb^{3+} ions concentration. E is the transition energy of the Yb^{3+} ions. Dispersion of $n(E)$ comes from changes of the local environment of the impurity ions in the host crystal and can be approximated by the absorption spectrum of the Yb^{3+} zero-phonon line measured at 4 K. Due to the fact that the distribution function $n(E)$ considerably changes its value, the energy ζ of the Fermi quasi-level should be calculated separately for each temperature by use of the following formula:

$$\int n^*(E, T) dE = \int \frac{n(E)}{1 + \exp[(E - \zeta)/kT]} dE \quad (2)$$

The only parameter which should be found from the experimental data is the total population of the excited Yb^{3+} ions. The above simple model gives a good description of the temperature dependence of the position and the shape of the Yb^{3+} zero-phonon emission lines measured at $T \geq 10 \text{ K}$.

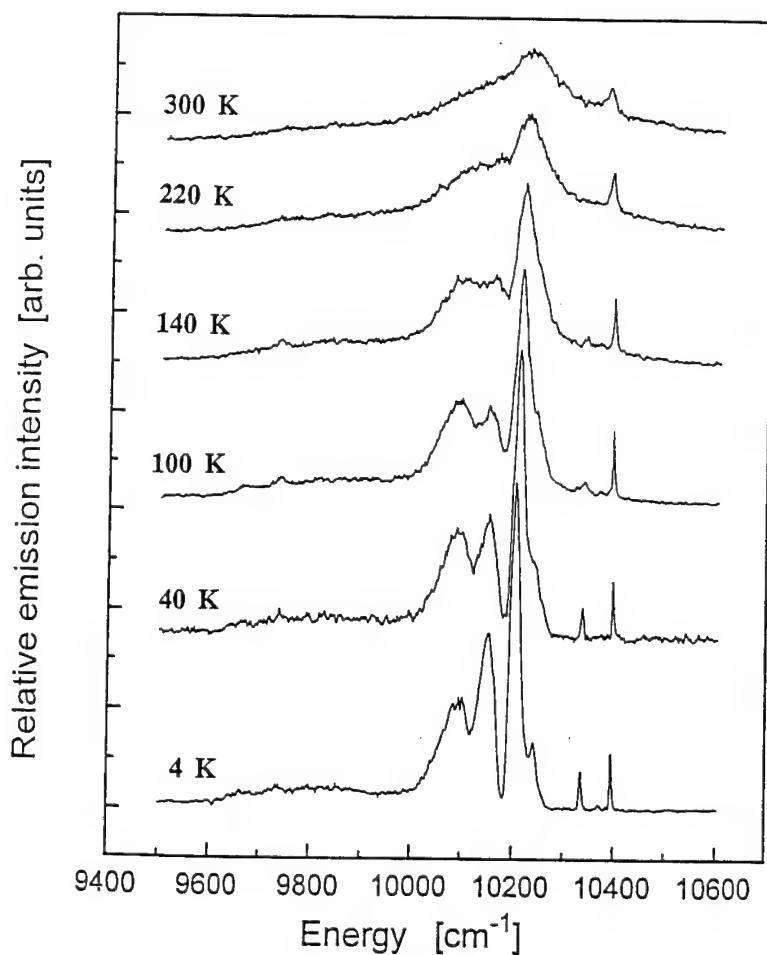


FIGURE 2 The emission spectra of the Yb^{3+} ion in $\text{Ca}_{0.30}\text{Cd}_{0.70}\text{F}_2:\text{Yb}$ (2 mol%) excited by 920 nm line of Ti-sapphire laser, measured at few temperatures.

ACKNOWLEDGEMENTS

The author thanks Dr. Z. Kalinski for growing the crystals. This work was supported in part by research grant of KBN no. 2 0463 91 01.

REFERENCES

1. B. Krukowska-Fulde, T. Niemyski, *J. Cryst. Growth*, **1** (1967) 183.
2. for review, see e.g., J. W. Hodby, in *Crystals in the Fluorite Structure*, ed. W. Hayes, Clarendon Press, Oxford 1974.
3. A. de Kozak, M. Samouël, A. Chretien, *Rev. Chim. Minerale* **8** (1971) 805.

4. Yu. Voronko, V. V. Osiko, I. A. Shcherbakov, *Zh. Eksp. Teor. Fiz.*, **56** (1069) 151 [JETP Sov. Phys., 29 (1969) 86].
5. J. M. Baker, W. Hayes, M. C. M. O'Brien, *Proc. Roy. Soc.* **A254** (1960) 273.
6. A. Stapor, PhD thesis, Warsaw 1984; A. Stapor, J. M. Langer, *Phys. Rev.* **B25** (1982) 3407.

ENDOR-INVESTIGATIONS OF RARE EARTH AND TRANSITION METAL IONS IN THE CUBIC ELPASOLITE CRYSTAL Cs_2NaYF_6

TH. PAWLIK, J.-M. SPAETH, M. OTTE and H. OVERHOF

University of Paderborn, FB Physik, Postfach 1621, D-33098 Paderborn

The paramagnetic rare earth ions Yb^{3+} , Ce^{3+} and Gd^{3+} and the transition metal ion Cr^{3+} were investigated in the cubic elpasolite crystal Cs_2NaYF_6 with ENDOR. The superhyperfine (shf) interaction parameters of the first ^{19}F , ^{23}Na and ^{133}Cs shells were determined. In the case of Gd^{3+} they were analyzed in an overlap model of the transferred hyperfine interaction including exchange polarisation.

Key words: Elpasolites, rare earth ions, EPR, ENDOR, Exchange polarisation.

1 INTRODUCTION

Cs_2NaYF_6 has gained interest recently for various applications (laser crystals, X-ray scintillators, and X-ray storage phosphors) because of the fact that trivalent and monovalent cations can be incorporated as dopants. They are situated in a natural cubic crystalline environment without the need for charge compensation.

We report on ENDOR-investigations of the trivalent Rare Earth ions Ce^{3+} , Yb^{3+} and Gd^{3+} and of the transition metal ion Cr^{3+} in the cubic elpasolite crystal Cs_2NaYF_6 . The analysis of the ENDOR-spectra shows that the Rare Earth ions are incorporated substitutionally on the cubic Y^{3+} site with an octahedron of fluorines in the first shell. The parameters of the superhyperfine interaction with the nearest F^- , Na^+ and Cs^+ neighbours were measured. In the case of Gd^{3+} they are analyzed using the overlap model of the transferred hyperfine (THF) interaction including exchange polarisation.

2 EXPERIMENTAL RESULTS

2.1 EPR Measurements

Ce^{3+}

The investigation of Ce^{3+} in Cs_2NaYF_6 is interesting because of its properties as a luminescent activator with a fast decay time in X-ray scintillators and storage phosphors.[1] The ground state of the Ce^{3+} ion ($4f_1^2, ^2F_{5/2}$) is a Γ_7 doublet. The electron g-factor calculated for the Γ_7 ground state is $g = (-)10/7 = (-)1.429$. In Cs_2NaYF_6 the EPR line of Ce^{3+} is observed below 20 K at 713 mT in the X-band ($f = 9.38$ GHz). This corresponds to an electronic g-factor of $(-)0.942$. $\Delta B_{1/2}$ is about 3.5 mT. The difference of the observed and the calculated g-factor for a pure Γ_7 state is due to the admixture of the excited state doublet $J = 7/2$ into the ground state doublet $J = 5/2$. It is larger in the case of Cs_2NaYF_6 than in the case of $\text{Cs}_2\text{NaYCl}_6$ ($g = (-)1.266$) [2]. If the magnetic field is in a $\langle 100 \rangle$ direction a splitting of the EPR-line is observed that can be attributed to shf interactions with the six neighbouring fluorines. Ce has no nuclear spin.

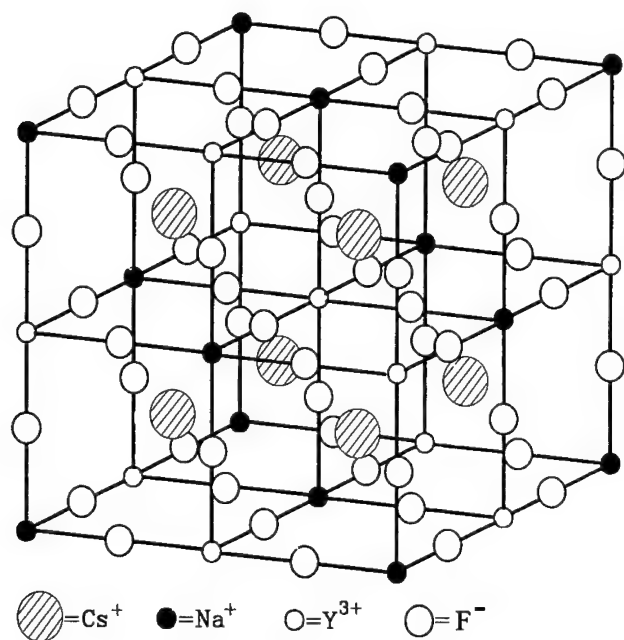
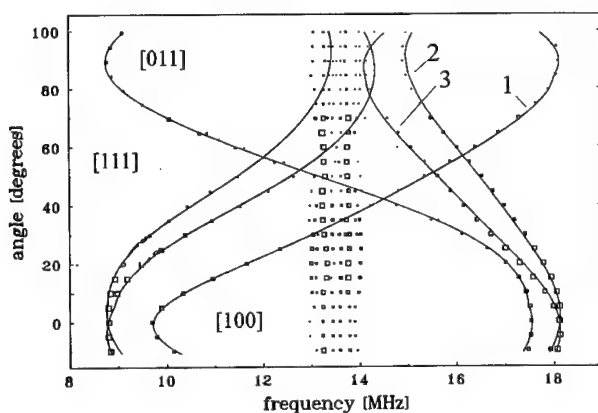
FIGURE 1 crystal structure of Cs₂NaYF₆.

FIGURE 2 ENDOR angular dependence of Gd³⁺ measured on the central fine-structure line ($m_s = -1/2 \leftrightarrow 1/2$), $B = 336.7$ mT, 10 K. the magnetic field is varied in a {110} plane. Squares: experimental line positions; lines: calculated line positions using the parameters in Table III. The ENDOR lines around 13.5 MHz come from the second fluorine shell.

Yb³⁺

The EPR line of Yb³⁺ ($4f_{13}, {}^2F_{7/2}$) is observed below 20 K at 260.2 mT in the X-band corresponding to a g -factor of (-2.581) close to the calculated value for the Γ_6 ground state (-2.667) . The spectrum is split due to hyperfine interaction with the two isotopes of

Yb with nuclear spin (^{171}Yb $I = 1/2$, 14.4%, ^{173}Yb $I = 5/2$, 16.2%). ENDOR spectra were measured at 10 K only on the EPR line of the even isotope with no nuclear spin.

Gd^{3+}

In cubic Cs_2NaYF_6 the EPR lines of Gd^{3+} ($4f_7$ $^8S_{7/2}$) are observed around $g = 2$. The EPR spectrum is anisotropic and split into 7 lines due to the cubic fine structure terms b_4 and b_6 . We obtained the following Spin Hamiltonian parameters:

$$g = 1.987; b_4 = -0.99 \text{ mT}; b_6 = 0.115 \text{ mT (at } T = 20 \text{ K)}$$

The EPR of Gd^{3+} can be observed at room temperature.

Cr^{3+}

The EPR line due to Cr^{3+} ($3d_5$, $^6S_{5/2}$) in Cs_2NaYF_6 is isotropic with $g = 1.972$.

It is superimposed on the Gd^{3+} resonance in all crystals because Gd^{3+} was present as an accidental impurity.

2.2 ENDOR Measurements

2.2.1. ENDOR measurements of Gd^{3+} Good ENDOR signals were obtained at temperatures around 10 K. The crystal Cs_2NaYF_6 has no cleavage planes. It had to be oriented with the Laue method. The ENDOR angular dependencies show that the crystal was still misaligned by about 5° . This results for example in a splitting of the lines 2 and 3 of the ENDOR spectra of Gd^{3+} (Figure 2) which should be superimposed if the axis of rotation were a $\langle 110 \rangle$ axis. Figure 2 shows the ENDOR-angular dependence of Gd^{3+} in Cs_2NaYF_6 measured at 10 K on the central ms ($1/2 \leftrightarrow -1/2$) transition which is almost isotropic in EPR. The magnetic field is rotated in a $\{110\}$ -plane. The solid lines are the calculated line positions of the 19F shf-interactions of the first shell using the parameters in Table III and a numerical diagonalisation of the usual spin Hamiltonian including the influence of the cubic fine structure terms on the electron spin in an effective spin model. The anisotropic part b of the shf-interaction with the second shell (^{133}Cs) and the third shell (^{23}Na) can be explained by a classical point-dipole-dipole interaction assuming a point dipole for the unpaired electron and the nuclei (b_{dd} in Table III). However, for the first shell (^{19}F) the anisotropic constant b is much smaller than expected from this approximation. Furthermore the analysis of the ENDOR spectra of the first shell F neighbours yields that the isotropic shf constant a and the anisotropic shf constant b have opposite signs. This suggests a negative transferred hyperfine contribution to both a and b resulting from a spin polarisation of the Gd^{3+} 5s and 5p shells due to the inner unpaired $4f_7$ electrons. In a simple model this polarisation is transferred by ion overlap as was shown to explain a similar observation in CsCaF_3 . [3]

2.2.2. Overlap model for the transferred hyperfine interaction (THF) We calculated the wave functions for a Gd^{3+} ion in the Local Spin Density Approximation of the Density Functional Theory and the overlap matrix elements with the nearest neighbour ^{19}F ligands (see e.g. [4]).

The calculation of the transferred hyperfine interaction can be expressed as:

$$\Delta E = \frac{\langle \psi | H_{THF} | \psi \rangle}{\langle \psi | \psi \rangle} \quad (1)$$

with

$$H_{\text{THF}} = \frac{\mu_B g_I \mu_K \mu_0}{2\pi I} \left\{ \frac{8\pi}{3} \sum_i s_i \cdot I \delta(0) - \sum_i \left[\frac{s_i \cdot I}{r_i^3} - \frac{3(s_i \cdot r_i)(I \cdot r_i)}{r_i^5} \right] \right\} \quad (2)$$

s_i is the spin of electron i , I the spin of the ^{19}F nucleus and $\delta(0)$ refers to the ^{19}F nucleus.

The wavefunction is the determinant:

$$|\varphi_1 \varphi_2 \dots \varphi_N \phi_1 \phi_2 \dots \phi_M| \quad (3)$$

$\varphi_1 \varphi_2 \dots \varphi_N$ are the Gd^{3+} orbitals 4f, 5s, $\phi_1 \phi_2 \dots \phi_M$ the F-orbitals 1s, 2s, 2p. ($\varphi_i \uparrow \neq \varphi_i \downarrow$)

If we consider only σ -overlap (π -overlap is negligible) the result for the isotropic part of the shf-interaction is:

$$\Delta E = \frac{7}{2} a I = \frac{4}{3} \mu_B g_I \mu_K \mu_0 \sum_i |\langle \varphi_i | 2s \rangle \phi_{2s}(0) + \langle \varphi_i | 1s \rangle \phi_{1s}(0)|^2 s_i \quad (4)$$

where i runs over 4f, 5s and 5p of Gd^{3+} . For the anisotropic part we get:

$$\Delta E = 7bI = \frac{7\mu_B g_I \mu_K \mu_0}{4\pi} \left(\frac{2}{d^3} + \frac{8}{35} r_{2p}^{-3} \sum_i |\langle \varphi_i | 2p \rangle|^2 s_i \right) \quad (5)$$

$$\phi_{1s}(0) = 14.67; \phi_{2s}(0) = -3.43; r_{2p}^{-3} = 6.705 \text{ (all in atomic units)}$$

The shf constants can be calculated according to equation (4) and (5) by taking into account that the φ_i (Gd^{3+} 5s, 5p) are different for spin up and spin down. This leads in the summations to non-vanishing terms from the 5s and 5p Gd^{3+} orbitals and to a negative spin transfer to the nearest F^- neighbours. In Table I and II the various contributions are listed. As can be seen from the last row in both tables, there is agreement with the experimental values within a factor of about 2–3, which seems satisfactory in view of the simple model used. For example, no lattice relaxation effects were taken into account. The inwards relaxation of F^- would improve the theoretical results since the overlap terms increase.

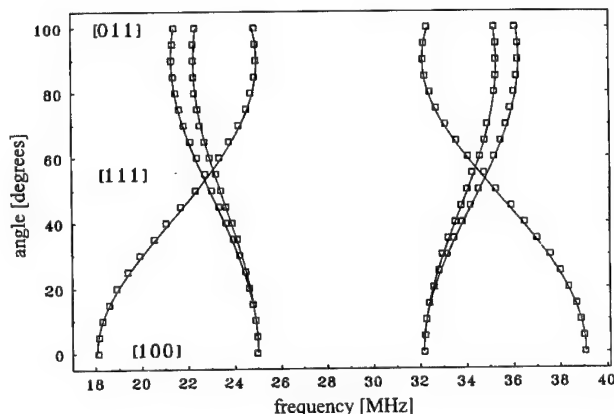


FIGURE 3 ENDOR angular dependence of Ce^{3+} . The magnetic field is varied in a {110} plane. $B = 713$ mT, $T = 8$ K. Squares: experimental line positions; lines: calculated line positions using the parameters in Table III.

Table I
 Overlap contributions to the anisotropic THF constant b ($d = 4.295$ a.u.)

Type	Overlap (10^{-2})	b/h (MHz)	Type	Overlap (10^{-2})	b/h (MHz)
$\langle 5s \uparrow 2p \rangle$	11.17	} -0.145	$\langle 5p \uparrow 2p \rangle$	11.73	} -0.243
$\langle 5s \downarrow 2p \rangle$	11.50		$\langle 5p \downarrow 2p \rangle$	12.25	
$\langle 4f \uparrow 2p \rangle$	2.057				
total $b_{ov}/h = -0.31$ $b_{ov}/h(\text{exp}) = -0.72$					

 Table II
 Overlap contributions to the isotropic THF constant a of Gd^{3+} -centres in Cs_2NaYF_6

Type	Overlap (10^{-2})	a/h (MHz)	Type	Overlap (10^{-2})	a/h (MHz)
$\langle 5s \uparrow 1s \rangle$	0.0319	} <u>-0.411</u>	$\langle 5p \uparrow 1s \rangle$	0.189	} <u>-2.02</u>
$\langle 5s \downarrow 1s \rangle$	0.0327		$\langle 5p \downarrow 1s \rangle$	0.217	
$\langle 5s \uparrow 2s \rangle$	2.569		$\langle 5p \uparrow 2s \rangle$	5.609	
$\langle 5s \downarrow 2s \rangle$	2.709	$\langle 5p \downarrow 2s \rangle$	6.021		
$\langle 4f \uparrow 1s \rangle$	0.137	} <u>+1.000</u>			
$\langle 4f \uparrow 2s \rangle$	1.782				
total $a_{ov}/h = -1.43$			$(a_{exp}/h = -3.66)$		

2.2.3 ENDOR measurements of Ce^{3+} , Yb^{3+} and Cr^{3+} ENDOR measurements were performed in X-band for Ce^{3+} , Yb^{3+} and Cr^{3+} at around 10 K. The ENDOR angular dependence of the first shell of Ce^{3+} is shown in Figure 3.

The shf interaction parameters for both Yb^{3+} and Ce^{3+} are listed in Table III. A comparison of the shf interaction parameters of Yb^{3+} and Ce^{3+} is interesting because of their different electronic structure: Ce^{3+} has one electron in the 4f shell and Yb^{3+} has one hole in the filled 4f shell.

A comparison of the parameters (Table III) shows that the shf constant a and b of Yb^{3+} have opposite sign indicating a negative transferred hyperfine effect on the isotropic and anisotropic shf interaction whereas in the case of Ce^{3+} they have the same sign. The latter indicates a positive contribution to a and b (of approximately the same magnitude if the different electron g factors are taken into account). This leads to larger value of b than is expected from the point dipole-dipole interaction. Additionally the isotropic shf constant of the second shell (Cs) of Yb^{3+} is almost zero whereas in the case of Ce^{3+} the main part of the interaction is isotropic with the anisotropic part being almost zero. This can be explained by a 4f wavefunction which is directed toward 8 Cs^+ neighbours in the case of Ce^{3+} . In Yb^{3+} the opposite occurs with the wavefunction of the hole avoiding the Cs^+ neighbours.

The unpaired spin density of Cr^{3+} is located almost entirely within the first F shell, the nearest cations show only the anisotropic shf constant of the classical point dipole dipole approximation.

3 CONCLUSIONS

We find that in our simple overlap model both sign and size of the isotropic shf-interaction of Gd^{3+} can be accounted for. The anisotropic part of the shf-interaction is mainly of point

dipole nature. An improvement of the overlap model should include the modification of the outer orbitals by crystalline potentials and a relaxation of the F neighbours toward Gd^{3+} .

Table III

Superhyperfine interaction parameters of Ce^{3+} , Yb^{3+} and Cr^{3+} in Cs_2NaYF_6 a is the isotropic shf constant, b is the anisotropic shf constant (see e.g. [5]), b_{dd} is the classical point dipole-dipole interaction, q is the quadrupole interaction parameter. Only relative signs can be determined, b/h was chosen to be positive (see text).

centre	shell	a/h [MHz]	b/h [MHz]	q/h [MHz]	bdd/h [MHz]
Ce^{3+}	F	11.76	4.62		2.99
	Cs	0.555	0.002		0.081
	Na	0.136	0.069	0.074	0.105
Yb^{3+}	F	-22.07	6.198		8.19
	Cs	-0.006	0.239		0.221
	Na	-0.001	0.255	0.016	0.287
Cr^{3+}	F	2.37	12.56		6.26
	Cs	-0.01	0.15		0.170
	Na	-0.081	0.214	0.134	0.220
Gd^{3+}	F	-3.662	5.585		6.30
	Cs	0.076	0.173		0.170
	Na	0.066	0.217	0.028	0.221

REFERENCES

1. J. M. Spaeth, Th. Hangleiter, F. K. Koshnick and Th. Pawlik, *Proc. of EURODIM 94*.
2. R. W. Schwartz, *J. Chem. Soc. Faraday Trans. II*, **70**, 124, (1974).
3. J. Casas Gonzalez, P. Studzinski, J. Andriessen, J. Y. Buzare, J. C. Fayet and J.-M. Spaeth, *J. Phys.* **C19**, 6767, (1986).
4. U. von Barth, L. Hedin, *J. Phys.* **C5**, 1629 (1972).
5. J.-M. Spaeth, J. R. Niklas and R. H. Bartram, *Structural Analysis of Point Defects in Solids* (Springer Series in Solid State Sciences, 1992) **43**.

OPTICAL AND EPR SPECTROSCOPY OF IMPURITY MANGANESE IONS IN DISORDERED $\text{Ca}_3\text{Ga}_2\text{Ge}_4\text{O}_{14}$ SINGLE CRYSTALS

A. E. NOSENKO, R. YE. LESHCHUK and B. V. PADLYAK

Ivan Franko State University, Lviv, Ukraine

The results of optical and EPR spectroscopy of the impurity manganese ions in trigonal $\text{Ca}_3\text{Ga}_2\text{Ge}_4\text{O}_{14}$ single crystals (space group $P321 - D_3^2$) are presented. It is shown that impurity manganese ions are incorporated into the $\text{Ca}_3\text{Ga}_2\text{Ge}_4\text{O}_{14}$ lattice in Mn^{3+} ($3d^4$) valence state, substituting gallium cations in octahedral 1a-sites (local symmetry D_3). The heat treatment of $\text{Ca}_3\text{Ga}_2\text{Ge}_4\text{O}_{14}:\text{Mn}$ crystals in vacuum leads to the reduction of Mn^{3+} ions to divalent state. The influence of structural disordering caused by the statistical filling of the octahedral (1a) and tetrahedral (3f) positions of Ga^{3+} and Ge^{4+} ions on the spectroscopic characteristics of impurity manganese ions is discussed.

Key words: Ca-gallogermanate single crystals, disordered structure, impurity ions, optical absorption and luminescence spectra, electron paramagnetic resonance spectroscopy, heat treatment effect.

1 INTRODUCTION

The change of valence state of the impurity transition metal ions leads to significant variations of spectral properties of crystals. Therefore, determination of all possible valence states of activator ions and their stability have a basic significance in physics of activated crystals. It is well known, that the impurity manganese ions are incorporated into crystals in Mn^{2+} , Mn^{3+} and Mn^{4+} valence states depending on growth conditions, activators and co-activators concentrations and other factors.^{1,2} The problems of impurity manganese ions isomorphism are closely connected with the possibilities of control of their valence states by external influences (ionizing irradiation, heat treatment, etc.).

2 THE STRUCTURE OF Ca-GALLOGERMANATE CRYSTALS AND EXPERIMENTAL PROCEDURE

The crystal structure of $\text{Ca}_3\text{Ga}_2\text{Ge}_4\text{O}_{14}$ type is described in the Ref. ^{3,4} It belongs to the space group symmetry $P321 - D_3^2$ ($Z = 1$) with the unit cell parameters as follows: $a = 8.076 \text{ \AA}$, $c = 4.974 \text{ \AA}$. This structure consists of tetrahedral layers oriented perpendicular to the c-axis separated by the intra-layers formed of distorted oxygen Thomson cubes (3e-positions occupied by large Ca^{2+} ions) and octahedra. The tetrahedral layers consist of the oxygen tetrahedral of two types: the first ones are placed on the three-fold axes (2d-positions) and others are grouped around the octahedra by the three-fold rule (3f-positions). On the basis of X-ray data analysis and spectral characteristics of $\text{Ca}_3\text{Ga}_2\text{Ge}_4\text{O}_{14}$ crystals it was shown that these crystals belong to materials with disordered structure.^{3–6}

The basic crystallographic characteristics of positions and types of active paramagnetic centers in Ca-gallogermanate crystal structure are presented in Table I. Table I shows that in cation positions the substitution centers of trigonal (1a- and 2d-positions) and monocline (3e- and 3f-positions) symmetry only can be formed. The centers of tricline symmetry only can be formed in the anion (oxygen) 1g-positions.

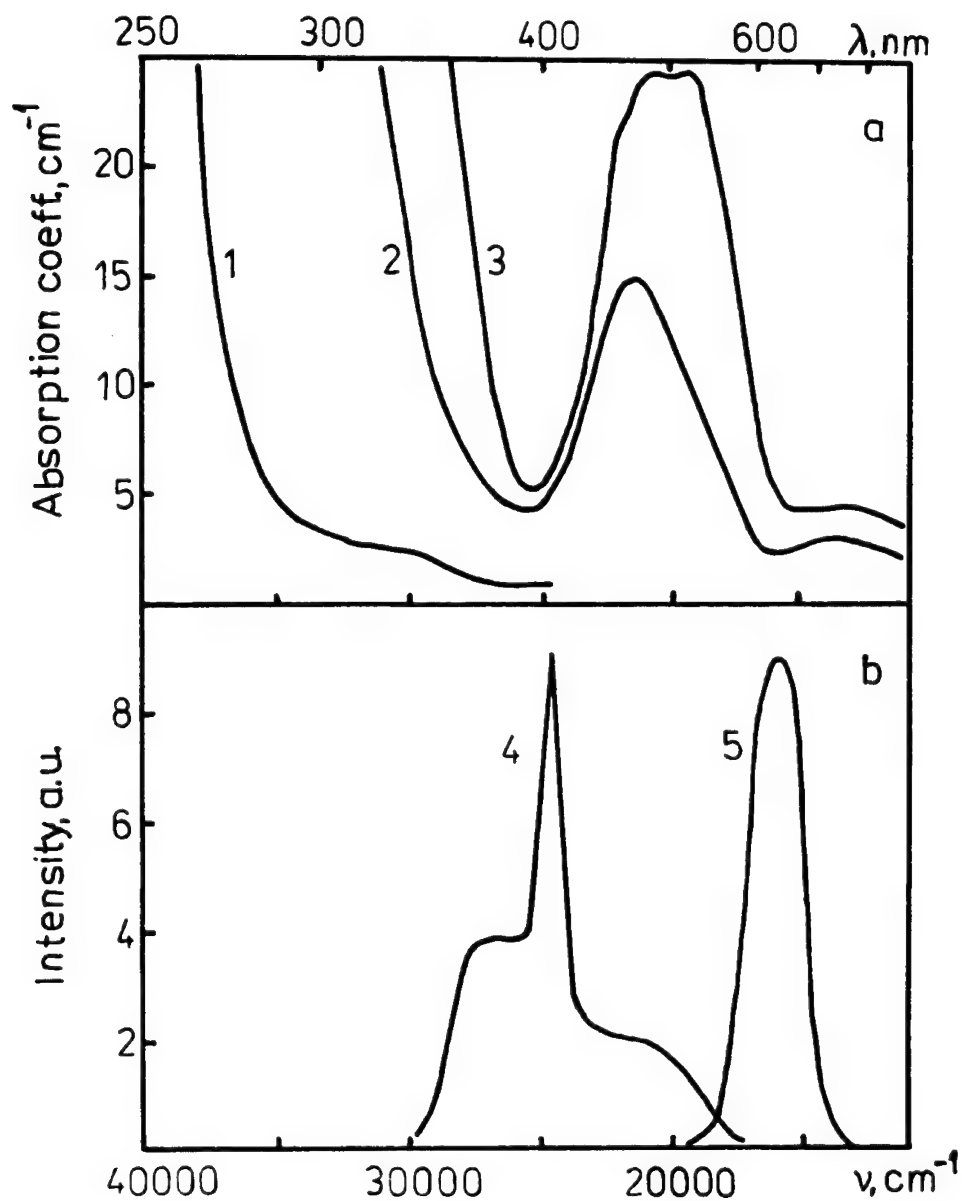


FIGURE 1 Optical spectra of $\text{Ca}_3\text{Ga}_2\text{Ge}_4\text{O}_{14}$ (1) and $\text{Ca}_3\text{Ga}_2\text{Ge}_4\text{O}_{14}:\text{Mn}$ (2–5) single crystals at 300 K: a) polarized absorption σ -spectrum (1, 2) and π -spectrum (3); b) luminescence excitation (4) and luminescence (5) after heat treatment in vacuum.

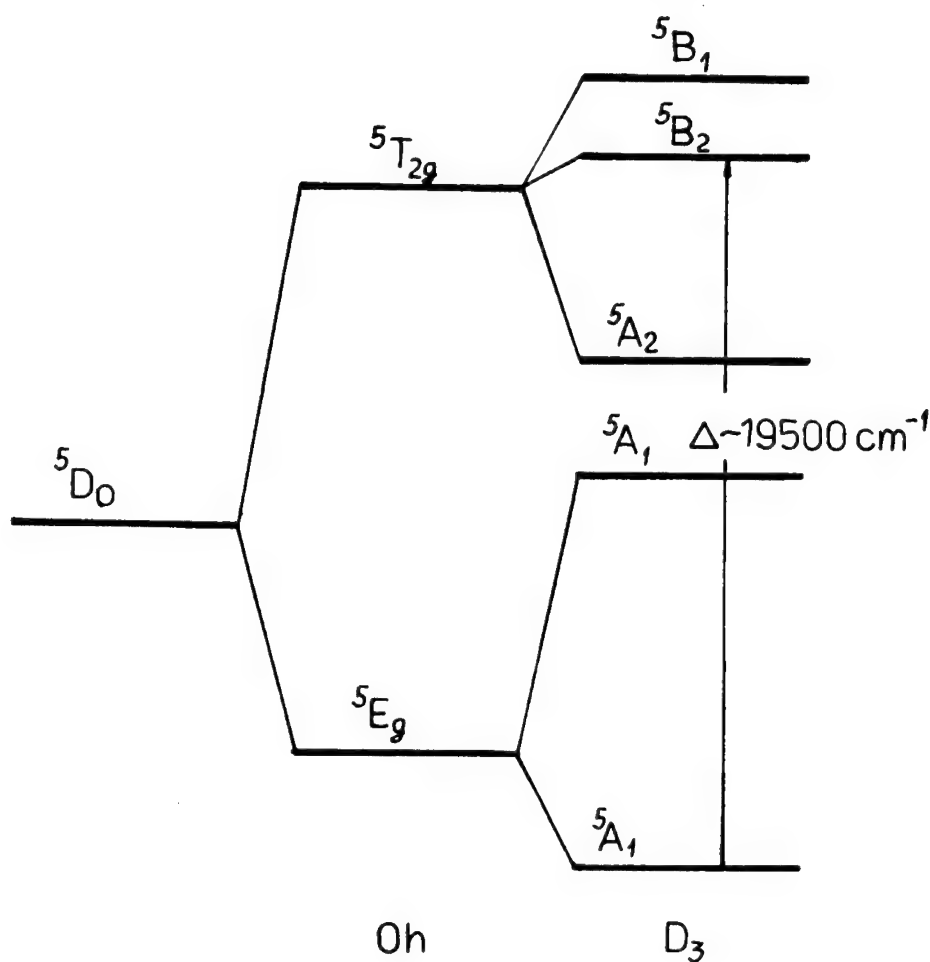


FIGURE 2 The energy level structure of Mn^{3+} ions in the octahedral (1a) positions of $Ca_3Ga_2Ge_4O_{14}$ crystals.

The large (diameter-15, length-100 mm) $Ca_3Ga_2Ge_4O_{14}$ crystals of high optical quality doped with impurity manganese ions at concentrations from 10^{-4} to 10^{-1} at.% were obtained by Czochralski method from platinum crucibles.

The EPR spectra were investigated using an RE-1306 commercial X-band ($\nu = 9.4$ GHz) EPR spectrometer operating in the high-frequency (100 kHz) modulation mode of the magnetic field and in $77 \div 300$ K temperature range. Samples were oriented in accordance with their habit and also by X-ray diffraction method with an accuracy of $\pm 0.5^\circ$. The EPR spectra were investigated in (0001) and (10 $\bar{1}$ 0) crystallographic planes.

Optical absorption spectra were measured by a 'Specord M40' spectrophotometer. The luminescence spectra were investigated using an SDL-2 standard spectrometer at $77 \div 300$ K.

The heat treatment of samples was carried out in vacuum ($p \cong 10^{-3}$ Pa), oxygen and argon atmospheres in $1000 \div 1300$ K temperature range.

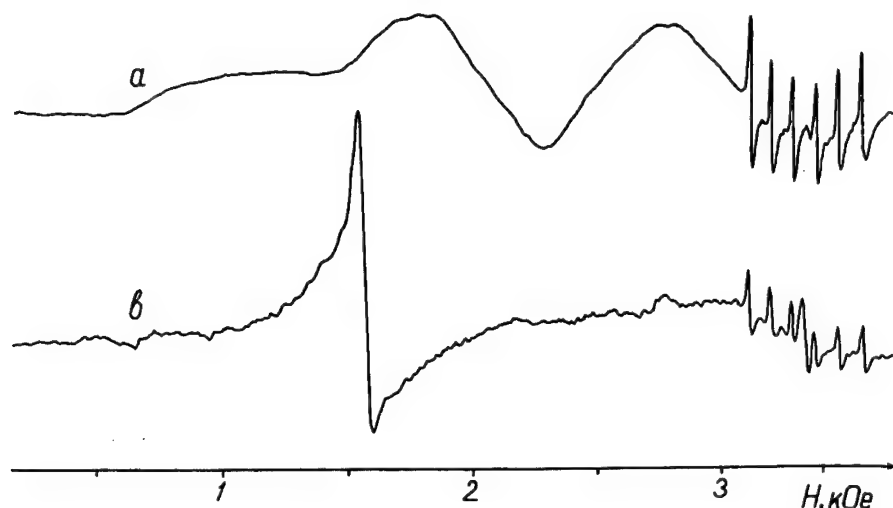


FIGURE 3 EPR spectra of Mn^{2+} ions in $\text{Ca}_3\text{Ga}_2\text{Ge}_4\text{O}_{14}$ crystals for the $H \parallel c$ (a) and $H \perp c$ (b) orientations at 300 K.

3 EXPERIMENTAL RESULTS AND DISCUSSION

The optical absorption spectra of $\text{Ca}_3\text{Ga}_2\text{Ge}_4\text{O}_{14}$ and $\text{Ca}_3\text{Ga}_2\text{Ge}_4\text{O}_{14}:\text{Mn}$ are presented in Figure 1. The nominally pure $\text{Ca}_3\text{Ga}_2\text{Ge}_4\text{O}_{14}$ crystals are transparent in UV-region up to 260 nm (Figure 1, curve 1). The characteristic optical absorption bands of Mn^{3+} (${}^5\text{D}_0$, $3d^4$) ions in octahedral oxygen environment were observed in the spectra of $\text{Ca}_3\text{Ga}_2\text{Ge}_4\text{O}_{14}:\text{Mn}$ crystals. The energy levels scheme of Mn^{3+} ions in octahedral 1a-sites (local symmetry D_3) of Ca-gallogermanate structure is presented in Figure 2. The ground state ${}^5\text{D}_0$ of Mn^{3+} ions is split into lower ${}^5\text{E}_g$ and higher ${}^5\text{T}_{2g}$ levels by the crystal field of octahedral symmetry⁷. The lowering of crystal local symmetry to trigonal one leads to the additional splitting of ${}^5\text{E}_{2g}$ and ${}^5\text{T}_{2g}$ electron levels (Figure 2). Therefore two absorption bands of different polarization in the visible ($25\,000\text{--}16\,000\text{ cm}^{-1}$) region of $\text{Ca}_3\text{Ga}_2\text{Ge}_4\text{O}_{14}:\text{Mn}$ spectrum correspond to optical transitions from ground ${}^5\text{E}_g({}^5\text{A}_1)$ level to ${}^5\text{B}_1, {}^5\text{B}_2$ component of ${}^5\text{T}_{2g}$ level of Mn^{3+} ions. The absorption bands of small intensity in the red region of spectrum are attributed to ${}^5\text{E}_g({}^5\text{A}_1) \Rightarrow {}^5\text{T}_{2g}({}^5\text{A}_1)$ transition. Additional intensive absorption in UV-region of spectrum was identified as the $\text{O}^{2-} \Rightarrow \text{Mn}^{3+}$ charge transfer band transitions.

EPR spectra of manganese ions in $\text{Ca}_3\text{Ga}_2\text{Ge}_4\text{O}_{14}:\text{Mn}$ crystal at 77 and 300 K have not been detected, what also supports the manganese ions are incorporated in a Mn^{3+} valence state only.

Ions with $3d^4$ -configuration are known to be non-stable and readily transferable either to $3d^5$ -configuration that is stable at low field or $3d^3$ -configuration, what is stable at high field.¹ The oxygen heat treatment of $\text{Ca}_3\text{Ga}_2\text{Ge}_4\text{O}_{14}:\text{Mn}$ samples does not change the optical and EPR spectra. The heat treatment in vacuum leads to discolouring of $\text{Ca}_3\text{Ga}_2\text{Ge}_4\text{O}_{14}:\text{Mn}$ crystals. The characteristic for Mn^{2+} ions intensive luminescence in the $20\,000 \div 14\,000\text{ cm}^{-1}$ spectral region excited in $27\,000$, $24\,500$ and $21\,000\text{ cm}^{-1}$

bands was also observed in the thermal chemical coloured crystals (Figure 1b). The ground state of Mn^{2+} ions is a ${}^6\text{S}$ sextet. The ${}^4\text{G}$, ${}^4\text{P}$, ${}^4\text{D}$ and ${}^4\text{F}$ quartet levels are situated above ${}^6\text{S}$ level. The crystal field of trigonal symmetry split the four quartet levels into ten sublevels.^{1,7} The 27 000, 24 500, 21 000 cm^{-1} bands in the excitation spectrum are identified as a transitions from the ground ${}^6\text{A}_{1g}$ level to ${}^4\text{T}_{2g}(\text{D})$, ${}^4\text{A}_{1g}$, ${}^4\text{E}_g({}^4\text{G})$ and ${}^4\text{T}_{2g}(\text{G})$ levels of Mn^{2+} ions, respectively. The luminescence band centered at 16 000 cm^{-1} corresponds to the ${}^4\text{T}_{1g} \Rightarrow {}^6\text{A}_{1g}$ transition of Mn^{2+} ions.

Table I

Crystallographic characteristics of positions and basic types of impurity paramagnetic centers in the crystals with Ca-gallogermanate structure.

Type of positions, α	2(a, b)	2(c, d)	2(e, f)	1g
Local (point) group symmetry of positions, G_α	32 (D_3)	3(C_3)	2(C_2)	1(C_1)
k_α/k_α^M	1/1	2/2	3/3	6/6
The filling position in crystal	1a	2d	3e	3f
Distribution of cations on crystallographic positions	Ga:Ge = 1 : 4	Ge	Ca	Ga:Ge = 3 : 2
Coordination to oxygen	6	4	8	4
Type of oxygen polyhedron	octahedron	tetrahedron	Thomson cube	tetrahedron
Type of impurity paramagnetic centers	trigonal	trigonal	monoclinic	triclinic
Number of magnetonequivalent positions	1	2	3	3
Axes of the paramagnetic centers	+++	--+	+-	+-

Notes: 1. k_α —number (multiplicity) of equivalent points of space lattices in unit cell; k_α^M —magnetic multiplicity of EPR spectrum. 2. The populations of 1a- and 3f-positions both by Ga^{3+} and Ge^{4+} cations are obtained from the analysis of interatomic distances.³

The vacuum heat treatment also clears the EPR spectra response of Mn^{2+} ions with isotropic g-factor ($g = 2.0043 \pm 0.0005$) and well resolved ${}^{55}\text{Mn}$ nuclei (nuclear spin $I = 5/2$, natural contents ~100%) hyperfine structure (HFS) of central ($M_s = -1/2 \Leftrightarrow +3/2$) transition and unresolved HFS of the other four ($M_s = \pm 1/2 \Leftrightarrow \pm 3/2$ and $M_s = \pm 3/2 \Leftrightarrow \pm 5/2$) fine structure transitions (Figure 3). At the same time in the annealed samples at $H \perp [0001]$ orientation the other EPR spectrum with a single unresolved central line ($\Delta H_{1/2} \cong 32$ Oe) and g-factor similar to the g-factor of a free electron ($g_e = 2.0023$) was also observed. Most probably, this spectrum belongs to Fe^{3+} impurity ions (${}^6\text{S}_{5/2}$ -ground state, $3d^5$ -configuration). The heat treatment in oxygen atmosphere leads to disappearance of the EPR spectra and restoration of the initial optical absorption spectra. The thermal chemical colouring of $\text{Ca}_3\text{Ga}_2\text{Ge}_4\text{O}_{14}:\text{Mn}$

crystals results in change of charge state of manganese ions ($\text{Mn}^{3+} \Rightarrow \text{Mn}^{2+}$) at the expense of diffusion and release of oxygen ions from the crystals. Since the Mn^{2+} paramagnetic centers have a trigonal local symmetry D_3 (magnetic multiplicity of EPR spectrum $k_\alpha^m = 1$ and axis $Z \parallel c \parallel [0001]$), one can say, that the change of charge state of Mn ions takes place in the octahedral (1a) sites of Ca-gallogermanate lattice (Table I).

The unusual EPR spectrum of Mn^{2+} ions in octahedral 1a-sites of $\text{Ca}_3\text{Ga}_2\text{Ge}_4\text{O}_{14}$ single crystals can be interpreted as follows. The position of central transition of Mn^{2+} EPR spectrum fine structure for the first approximation does not depend on crystal field variations caused by disordering of Ca-gallogermanate crystal structure. Therefore, the characteristic of ^{55}Mn isotope hyperfine structure ($A_z = (90.9 \pm 0.5) \cdot 10^{-4} \text{ cm}^{-1}$ at 300 K) of central transition was observed. The resolved HFS of $M_s = \pm 1/2 \Leftrightarrow \pm 3/2$ and $M_s = \pm 3/2 \Leftrightarrow \pm 5/2$ transitions was non observable, since their positions depend on crystalline field variations. They consist of $2^N = 64$ ($N = 6$ —oxygen coordination at 1a-sites) hyperfine sextets. These sextets are somewhat shifted about one another because of variations in the local crystal field, which are produced by statistical filling of Ga^{3+} and Ge^{4+} cations, that are second nearest neighbours of Mn^{2+} ions at Ca-gallogermanate lattice 1a-sites, in tetrahedral positions. It should be noted, that the full parameterization of Mn^{2+} and other $3d^n$ -ions EPR spectra in $\text{Ca}_3\text{Ga}_2\text{Ge}_4\text{O}_{14}$ crystals is very difficult because of structural peculiarities in disordered compounds and this is the subject of a separate investigations.

REFERENCES

1. D. T. Sviridov, R. K. Sviridova, Yu. F. Smirk. *Optical Spectra of Transition Metal Ions in Crystals* (Nauka, Moscow, 1976), Chap. 7, pp. 138, 190.
2. B. V. Padlyak, A. E. Nosenko. *Fizika Tverdogo Tela* **30**, 1788 (1988).
3. A. A. Kaminskii, E. L. Beloconeva, B. V. Mill, Yu. V. Pisarevski, S. E. Sarkisov, I. M. Silvestrova, A. V. Butashin and G. G. Khodzhabagyan. *Phys. Stat. Sol. A* **86**, 345 (1984).
4. A. A. Kaminskii, A. V. Butashin, A. A. Demidovich, V. G. Koptev, B. V. Mill and A. P. Shkadarevich. *Phys. Stat. Sol. A* **112**, 197 (1989).
5. A. P. Voitovich, A. E. Nosenko, A. G. Bazylev, V. S. Kalinov, V. V. Kravchishin and R. Ye. Leshchuk. *Zhurn. Prikladnoi Spektroskopii* **51**, 705 (1989).
6. A. E. Nosenko, R. Ye. Leshchuk and V. V. Kravchishin. *J. Phys. (Paris) Suppl.* **4**, C4-445 (1994).
7. Y. Tanabe, S. Sugano. *J. Phys. Soc. Japan.* **9**, 753 (1954).

INTERACTION OF IMPURITY CENTRES IN Cs₂CdI₄-Mn CRYSTALS

I. BOLESTA and Y. FURGALA

*Department of physics, Lviv state university, 50, Dragomanova st., Lviv, UA290005,
Ukraine*

The article deals with the investigation of interaction of impurity centres, formed by Mn²⁺-ions in Cs₂CdI₄ single crystals dependently on the method and intensity of excitation and temperature change rate in different crystallographic phases of crystal.

Key words: Impurity centres, luminescence, phase transitions, energy transfer.

1 INTRODUCTION

Cs₂CdI₄ crystals belong to compounds with β -K₂SO₄ type structure and have the next phase transitions (PT) sequence:¹

$$P_{nma} \Leftrightarrow T_i = 332 \text{ K} \Leftrightarrow IC(q = 0.26) \Leftrightarrow T_C = 260 \text{ K} \Leftrightarrow P_{21/n} \Leftrightarrow T_1 = 184 \text{ K} \Leftrightarrow P1$$

Its lattice is formed by tetrahedral complexes [Cd²⁺I₄]²⁻-bonded with themselves by Cs⁺ ions. Impurity Mn²⁺ ions form in these crystals two types of centres, related to the substitutions of Cd²⁺ and Cs⁺ ions. The substitution of Cd²⁺ ions to Mn²⁺ ions leads to the formation [Mn²⁺I₄]²⁻ centres (G-centres). The Mn_{Cs} together with V_{Cs} vacancies (for balance the excess charge) form [Mn_{Cs}V_{Cs}]⁻ complexes (R-centres). G- and R-centers give rise the luminescence at 2.30 and 1.7 eV respectively.²

2 RESULTS AND DISCUSSION

The previous experimental data show,^{2,3} that Mn_{Cd} and Mn_{Cs} ions occupy neighboring positions in lattice. This results in interaction between them, consisting in excitation energy transfer from G- to R-centers. It results in quenching of G- and sensitization of R-centres, which are observed in temperature region 184...332 K.³ The efficiency of interaction (η) strongly depends on temperature of crystals, as well as the distance and mutual positions of both centres, which vary during the rotation of tetrahedra and shifts of cation in A⁺ sublattice. It was estimated as

$$\eta = 1 - I_G/I_{G0}$$

where I_G and I_{G0} represent the intensity of G-emission with and without energy transfer process respectively. The efficiency of interaction of G- and R-centers depends strongly from the manner of excitation and relative concentration of both centres. Figure 1 shows the temperature dependences of luminescence intensity of G-centres Cs₂CdI₄-Mn crystals at intracentre. ($h\nu = 2.54 \text{ eV}$, $s = 10^{13} \text{ photon}/(\text{cm} \cdot \text{s})$) and N₂-laser excitation ($h\nu = 3.68 \text{ eV}$, $s = 10^{18} \text{ photon}/(\text{cm} \cdot \text{s})$). One can see the quenching of G-emission, which is the largest around $T_C = 260 \text{ K}$. During quenching of G-emission simultaneous sensitization of R-emission is observed in this temperature region, and the highest efficiency of sensitization is observed around T_C as well (Figure 2).

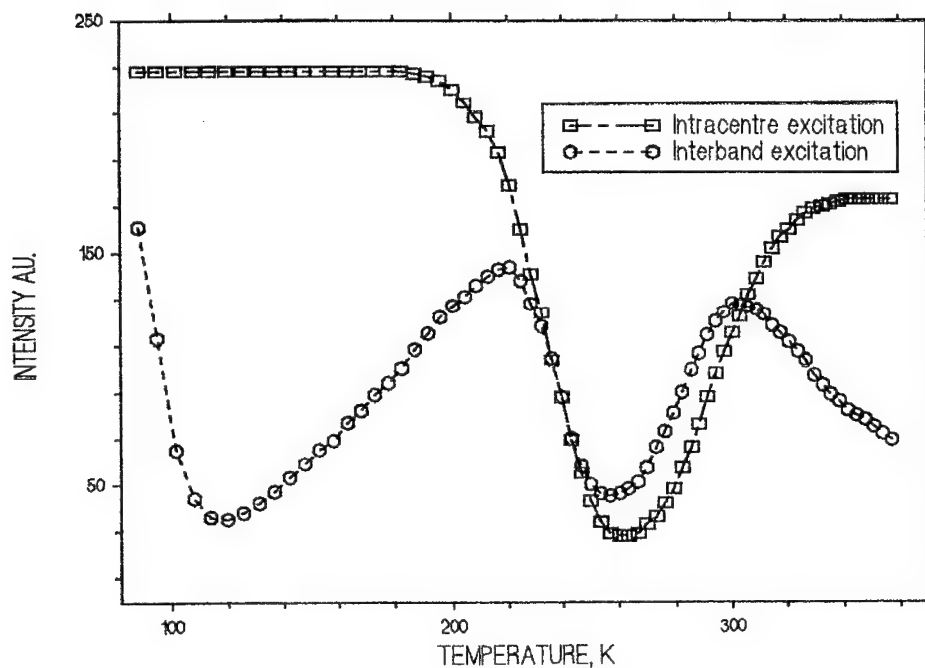


FIGURE 1 The temperature dependencies of G-emission of $\text{Cs}_2\text{CdI}_4\text{-Mn}$ single crystals at intracentre and interband excitation.

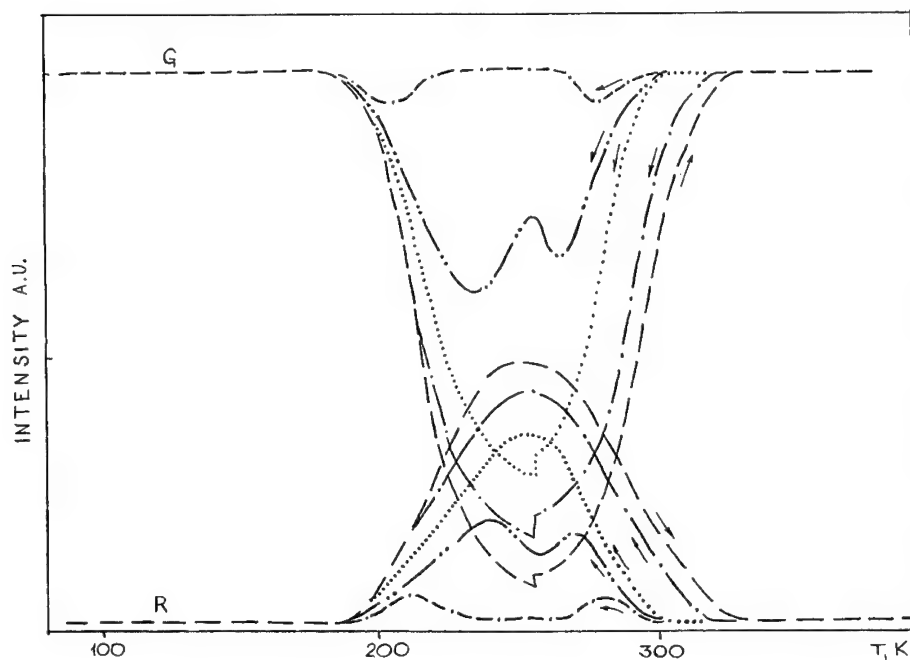


FIGURE 2 Temperature dependencies of G- and R-emission of $\text{Cs}_2\text{CdI}_4\text{-Mn}$ crystals at intracentre excitation at different temperature change rates. Arrows indicate the regime of measurement: cooling or heating.

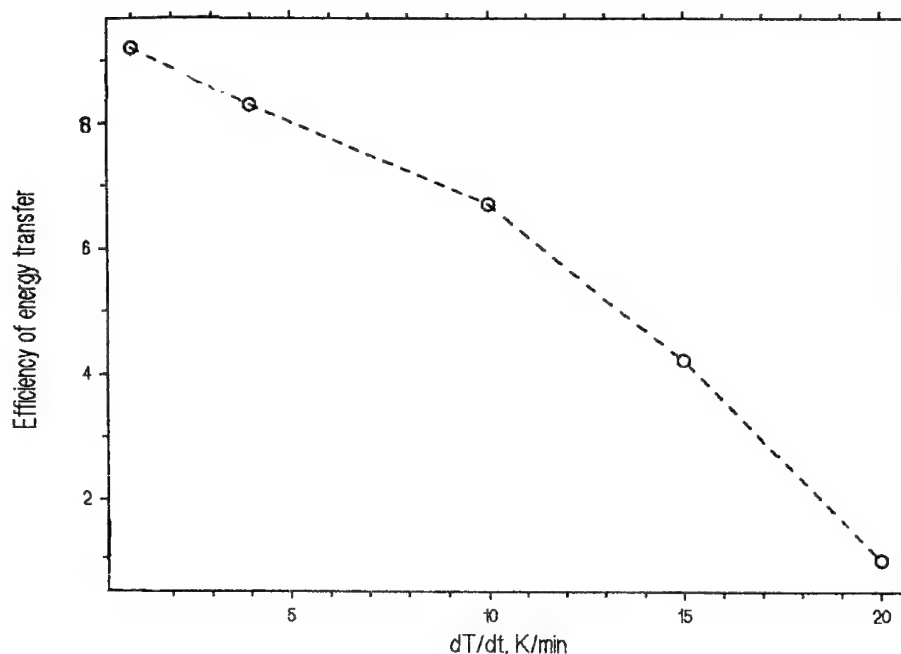


FIGURE 3 Dependence of efficiency energy transfer on temperature change rate.

The quenching of G-emission and sensitization of R-emission strongly depends on temperature change rate dT/dt . The increase of dT/dt leads to reduce of the both processes. (Figure 3). At high values of dT/dt (more than 10 K/min) $I(T)$ dependences for both luminescent bands consist of two extrema at temperatures below and above T_C , and temperature difference between these extremes increase with the dT/dt increasing. The dependence of efficiency of quenching of G-centres on temperature change rate give evidence the important role of the mutual positions of both centres in the crystalline lattice for the energy transfer process. The reduction of energy transfer at higher temperature change rate shows that the reconstruction of the crystalline structure depends on the velocity of temperature change dT/dt . The high value of dT/dt (10 K/min and more) proves the mutual positions of both centres is unchanged, i.e. the temperature reconstruction of lattice is 'frozen'. It is one of the reason for existence of global dynamic hysteresis in A_2BX_4 type crystals.⁵

The Cs_2CdI_4 single crystals with $\beta\text{-K}_2\text{SO}_4$ type structure undergo also the phase transitions into Sr_2GeS_4 ($P2_1/n = C_{2h}$) type structure.⁴ This PT is realized at keeping of crystals on air and last during one week and more. The spectral parameters of luminescence centres are changed during these PT, in particular the relative intensity of R-emission increase in comparison to intensity of G-emission. As a result, after PT at N_2 -laser excitation the R-emission is dominant in spectra, and the $I(T)$ dependences of G-emission changes (Figure 4). These changes are connected with the disappearance the process of quenching in 184...332 K temperature range, and the $I(T)$ dependence have exponential form. Those form of $I(T)$ dependence shows the absence of the tetrahedra rotation and mutual shifts in Cs^+ sublattice in Sr_2GeS_4 crystalline type of Cs_2CdI_4 in agreement with crystallographic data.¹

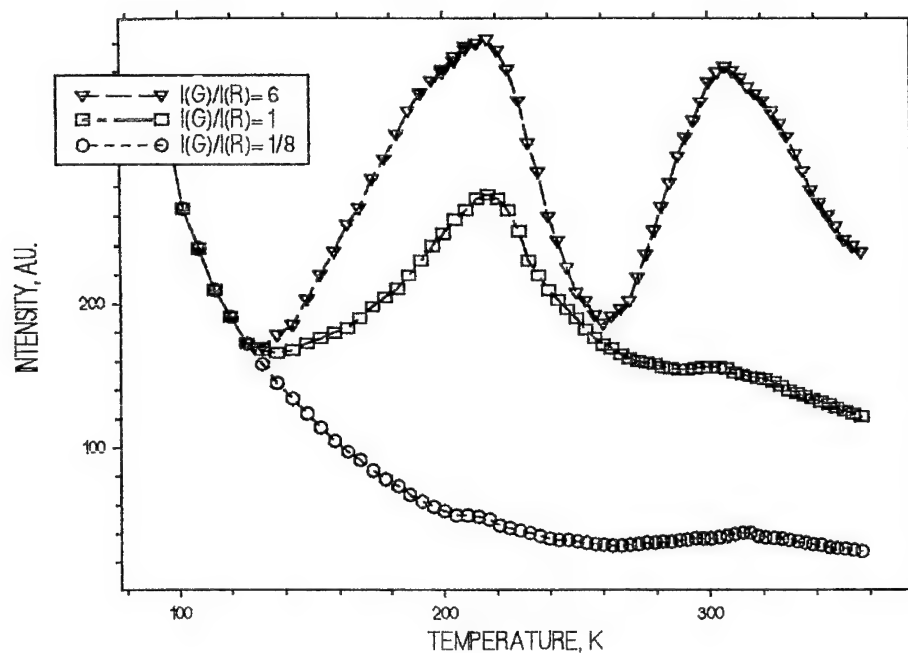


FIGURE 4 Temperature dependences of G-emission of $\text{Cs}_2\text{CdI}_4\text{-Mn}$ single crystals with different ratio of relative intensity of G- and R-emissions.

3 CONCLUSION

The interaction of impurity centres in $\text{Cs}_2\text{CdI}_4\text{-Mn}$ single crystals are caused by its neighboring location in lattice and strongly depend on the mutual positions. The efficiency of interaction reflect the change the mutual positions of centres in lattice and, therefore reflect the motion of atoms (or groups of atoms) during the temperature change and at PT.

ACNOWLEDGMENT

This work was supported by the State Committee on Science and Technology of Ukraine.

REFERENCES

1. Alexandrov K. S. Beznosikov B. V. *Structural phase transitions in crystals (potassium sulphate family)* (Nauka, Novosibirsk, 1993) p. 157.
2. Bolesta I. and Furgala Y. *Ferroelectrics*, **130**, 309 (1992).
3. Bolesta I. and Furgala Y. *Phys. Stat. Sol.*, **142**, 245 (1994).
4. Flerov I. N. *et al. Fiz. tverd. tela*, **30**, 1948 (1988).
5. Mamin R. F. *Zhurn. eksper. teor. Fiz.*, **53**, 499 (1991).

BLUE AVALANCHE UPCONVERSION IN YAG:Tm

S. GUY, M. F. JOUBERT, B. JACQUIER and C. LINARÉS

*Laboratoire de Physico-Chimie des Matériaux Luminescents, Université Claude Bernard
Lyon 1, URA CNRS 442, 43, bd du 11 Novembre 1918, bât. 205, 69622 Villeurbanne
Cedex, France*

We report on the investigation of the photon avalanche effect in YAG: 5 at% Tm at room temperature leading to intense blue emission after pumping at 616.4 nm. A theoretical model based on rate equations reproduces quite well the experimental results under low and intermediate excitation density. Above this, an extra blue intensity is observed and additional terms should be included in the model.

Key words: photon avalanche, upconversion, rare-earth spectroscopy.

1 INTRODUCTION

We have recently demonstrated the first observation of blue upconverted fluorescence via photon avalanche pumping in YAG:Tm³⁺ at any temperature.¹ Blue upconversion emission attributed to the ¹G₄ → ³H₆ transition of Tm³⁺ ions has been observed, in a 5 at% sample, using cw pumping with a single red dye laser at a wavelength resonant with the excited state absorption transition ³F₄ → ¹G₄. The first step is assumed to come from a very weak non resonant absorption in the phonon sideband of the ³F₂ manifold. The rapid non-radiative relaxation populates the ³H₄ metastable state and an efficient cross relaxation fills the ³F₄ reservoir from which the excited state absorption occurs as shown in Figure 1. Different regimes are recognized depending upon a pump power threshold.

Here, we present a theoretical model which was firstly developed for a similar process involving Nd³⁺ ions in YLF.² This model, adapted to the case of Tm³⁺, describes the dynamics of the avalanche below and above the power threshold as well as the power dependence of the blue upconverted fluorescence intensity at room temperature.

2 EXPERIMENTAL

The cw red laser beam was tightly focused into the sample at room temperature. The upconverted fluorescence was spectrally analysed through a monochromator as shown in Figure 2. The transmitted light as well as the upconverted fluorescence intensities have been recorded as a function of time for different pump power. As reported earlier for low temperature,¹ a threshold mechanism is observed, illustrated in Figure 3 by several transient signal records below, above and at the threshold. This behaviour is the known signature of the avalanche process.³ This threshold increases with temperature from 7 mW at 30°K¹ to 15 mW at room temperature. At about twice this threshold power, the upconverted fluorescence shows a new increase and, at the same time, UV fluorescences appear arising from the relaxation of the ¹D₂ and ¹I₆ states. However, these emissions remain weaker than the blue fluorescence from ¹G₄.

Direct excitation into the relevant excited states, namely ³H₄, ¹G₄ and ¹D₂, has been performed on low concentrated thulium doped YAG to reach their respective radiative lifetimes as well as on more highly concentrated samples to get information about the transfer rates.⁴

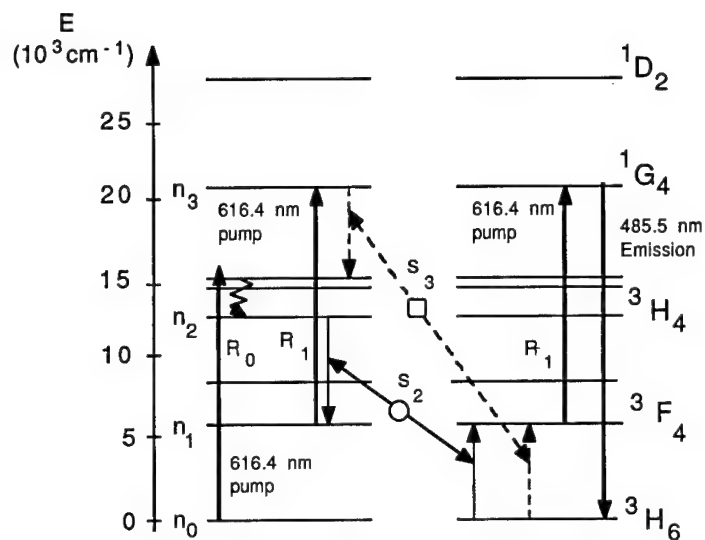


FIGURE 1 Schematic energy level diagram of YAG: Tm illustrating the relaxations and energy transfers involved in the pumping of the blue $1G_4 \rightarrow 3H_6$ emission.

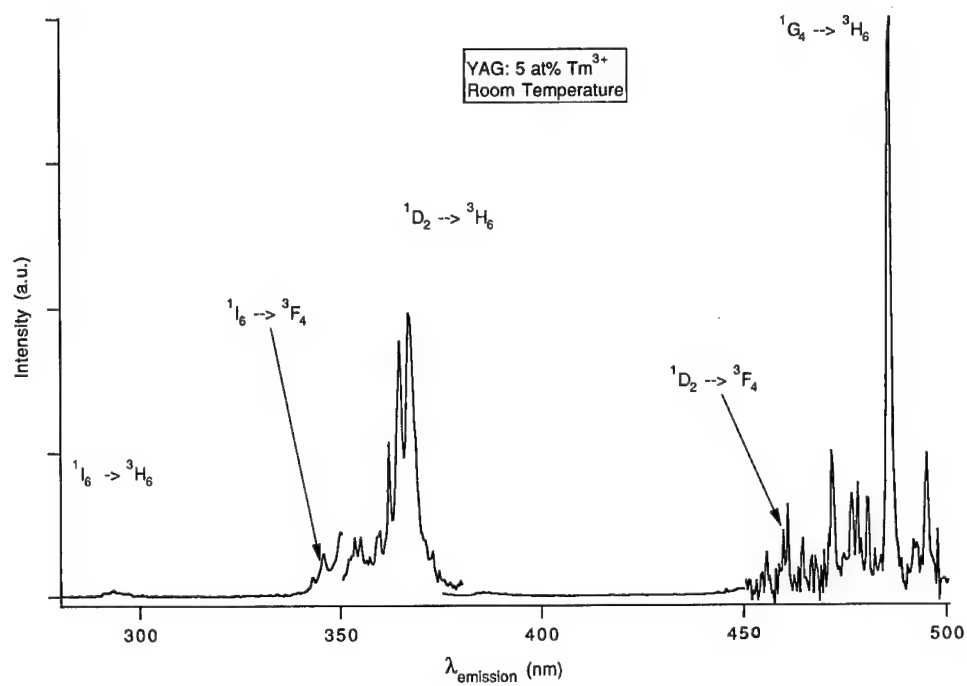


FIGURE 2 Upconverted fluorescence spectrum of Tm³⁺ in YAG after excitation at 616.4 nm.

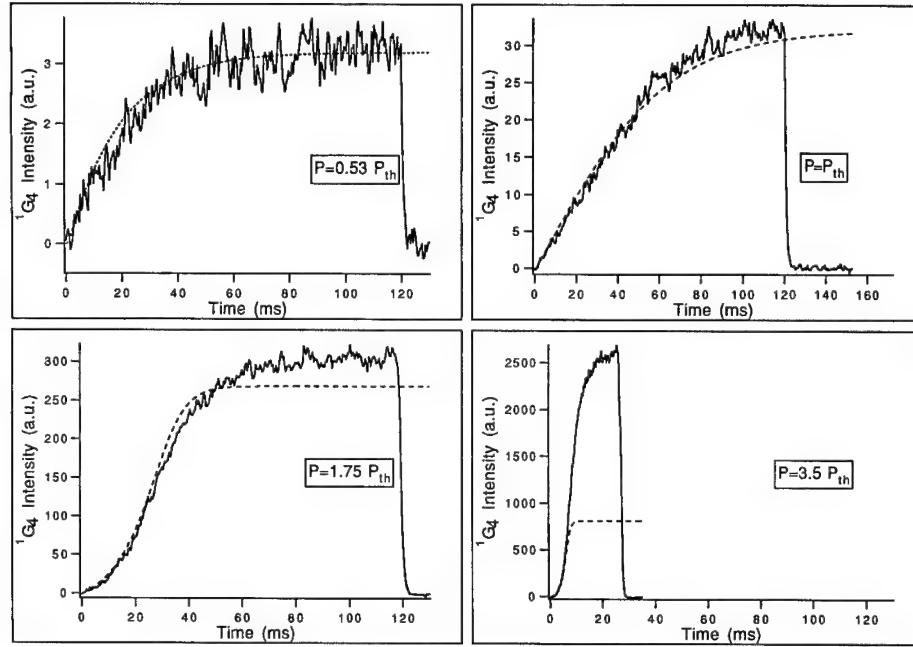


FIGURE 3 Time dependence of the blue upconverted emission:
 ————— experimental curve - - - - - theoretical calculation.

3 THEORETICAL MODEL

These experimental results were analysed using a theoretical model based on population equations of the relevant levels as shown in Figure 1. Taking account of the various relaxations, the rate equations are:

$$\begin{aligned}
 \dot{n}_1 &= -(W_{1r} + R_1)n_1 + (b_{21}W_{2r} + W_{2nr} + 2n_0s_2)n_2 + (b_{31}W_{3r} + n_0s_3)n_3 \\
 &= -(W_{1r} + R_1)n_1 + W_{21}n_2 + W_{31}n_3 \\
 \dot{n}_2 &= R_0n_0 - (W_{2r} + W_{2nr} + s_2n_0)n_2 + (b_{32}W_{3r} + s_3n_0)n_3 \\
 &= R_0n_0 - (W_{2r} + W_{2nr} + s_2n_0)n_2 + W_{32}n_3 \\
 \dot{n}_3 &= R_1n_1 - (W_{3r} + s_3n_0)n_3 \\
 n_0 + n_1 + n_2 + n_3 &= 1
 \end{aligned}$$

where W_{ir} and W_{inr} are the radiative probability and the multiphonon relaxation rate of the i th level, respectively.

Solving numerically the above system leads to the dotted lines represented on the Figure 3. Satisfactory agreement is obtained below the threshold and just above while, at high power, the deviation is quite significant.

The threshold (R_{1th}) is determined by the equilibrium condition between loss and self-storage involving the 3F_4 metastable state:

$$R_{1th} + W_{1r} = R_{1th}(\tau_3 W_{31} + \tau_2 W_{21} \tau_3 W_{32})$$

where τ_i is the measured lifetime of the i th level.

As the 3F_4 level is the most metastable state, that is to say τ_1 higher than τ_3 and τ_2 , and assuming only a weak depletion of the ground state population, the rate equations can be solved analytically:

$$\begin{aligned}n_3 &= \tau_3 R_1 n_1 \\n_2 &= \tau_2 R_0 + \tau_2 \tau_3 W_{32} R_1 n_1 \\\dot{n}_1 &= -W_{1r}(1 - R_1/R_{1th})n_1 + R_0 \tau_2 W_{21}\end{aligned}$$

Then, at the threshold, the time necessary to reach stationary populations is proportional to:

$$\tau_1 \times \sqrt{(\sigma_1/\sigma_0)}$$

where σ_i is the absorption cross section from level i .

4 DISCUSSION

From the experimental results, it is clear that two regimes of absorbed power can be defined:

- (i) at approximately twice the threshold, the transient signals are well fitted by the numerical simulation with the parameters: $s_2 = 40\,000 + / - 5000 \text{ s}^{-1}$, $s_3 = 7000 + / - 1000 \text{ s}^{-1}$ and $R_0/R_1 = 0.04 + / - 0.01$;
- (ii) at higher pump power, an extra blue intensity is not explained at the present time; it could arise from emission from higher excited states which is in resonance with the blue emitting light of the 1G_4 . In that case, additional terms in the theoretical model have to be considered.

Finally, evidence of a photon avalanche has been recently found in Tm^{3+} doped YAG planar waveguides with a threshold even lower than in the bulk material which looks promising for laser application.

5 CONCLUSION

Blue upconverted fluorescence via photon avalanche pumping in YAG:Tm has been demonstrated at room temperature. A theoretical model reproduces quite well the power dependence of the fluorescence signal up to about twice the power threshold. Above this, other relaxations involving higher excited states must be considered to remove the apparent discrepancy.

REFERENCES

1. S. Guy, M. F. Joubert and B. Jacquier *Phys. Stat. Sol. (b)* **183**, K33 (1994).
2. M. F. Joubert, S. Guy and B. Jacquier *Phys. Rev.* **B48**, 10031 (1993).
3. M. F. Joubert, S. Guy, B. Jacquier and C. Linarès Proc. Deuxième Colloque Franco—Israélien sur les Matériaux lasers, Lyon (France) Décembre 1993, to be published in Optical Materials.
4. S. Guy, M. Malinowski, M. F. Joubert and C. Linarès to be published.

NEW SPECTROSCOPIC EFFECTS OF FERROELECTRIC PHASE TRANSITION IN $\text{Li}_2\text{Ge}_7\text{O}_{15}$ CRYSTALS DOPED WITH $3d^3$ -IONS

A. A. KAPLYANSKII, S. A. BASUN and S. P. FEOFILOV

A. F. Ioffe Physico-Technical Institute, 194021 St. Petersburg, Russia

In $\text{Li}_2\text{Ge}_7\text{O}_{15}$ (LGO) crystals doped with Cr^{3+} and Mn^{4+} ions the transformation of luminescence spectra in the region of R-lines at ferroelectric phase transition $D_{2h} \rightarrow C_{2v}$ in LGO was used to determine the point group symmetry and microstructure of $3d^3$ -centers. In experiments on pseudo-Stark splitting of R-lines in external electric field, the phase transition induced polarization of $3d^3$ -ions was observed, the induced dipole moments being directed perpendicular to ferroelectric axis of C_{2v} phase.

Key words: $\text{Li}_2\text{Ge}_7\text{O}_{15}:\text{Cr}^{3+}$, $\text{Li}_2\text{Ge}_7\text{O}_{15}:\text{Mn}^{4+}$, center symmetry, charge compensation, dipole moment, phase transition.

1 INTRODUCTION

Orthorhombic lithium heptagermanate crystals $\text{Li}_2\text{Ge}_7\text{O}_{15}$ (LGO) in paraelectric phase ($T > T_c = 10^\circ\text{C}$) belong to centrosymmetric D_{2h} class, whereas in ferroelectric phase ($T < T_c = 10^\circ\text{C}$)—to polar C_{2v} class.^{1,2} In doped LGO: Cr^{3+} crystals Cr^{3+} ions replace Ge^{4+} in octahedral coordination (GeO_6) and their optical spectra are typical for Cr^{3+} in high octahedral crystal field.³ Narrow R-lines (${}^2\text{E} \rightarrow {}^4\text{A}_2$ transitions) are observed only at low temperatures in the luminescence spectra of LGO ferrophase.

2 MULTISITE LUMINESCENCE SPECTRA OF Cr^{3+} IONS IN LGO

In luminescence spectra of LGO:Cr at $T = 77\text{ K}$ (Figure 1a) two pairs of lines $\text{R}_1 - \text{R}_2$, $\text{R}'_1 - \text{R}'_2$ are observed indicating the existence of two types of Cr^{3+} -centers in ferrophase.³ In spectra of LGO:Cr,Mg crystals containing Mg^{2+} ions, additional R-lines are observed located both in shortwavelength side (pair ${}^m\text{R}_1 - {}^m\text{R}_2$) and in longwavelength side (two pairs ${}^l\text{R}_1 - {}^l\text{R}_2$, ${}^l\text{R}'_1 - {}^l\text{R}'_2$) relative to dominant $\text{R}_1 - \text{R}_2$, $\text{R}'_1 - \text{R}'_2$ lines (Figure 1b). Multisite spectra are typical for doped crystals with heterovalent substitution being connected usually with different mechanisms of local charge compensation of excess impurity charge.

3 POINT SYMMETRY OF Cr^{3+} SITES IN LGO AND PHASE TRANSITION INDUCED SPLITTING OF THEIR R-LINES

In LGO paraphase D_{2h} (axes 'a', 'b', 'c') the point symmetry group of octahedral Ge^{4+} position which is occupied by Cr^{3+} ion belongs to monoclinic group C_2 with only two-fold symmetry axis parallel to rhombic axis 'b' (Figure 2). Any positively charged defect in Cr^{3+} environment which locally compensates the negative excess charge of $\text{Cr}^{3+}(\text{Ge}^{4+})$ should in general case reduce the center symmetry until triclinic C_1 . The possible symmetries of Cr^{3+} -centers (C_2 or C_1) may be determined from the behaviour of optical spectra at ferroelectric phase transition (PT) $D_{2h} \rightarrow C_{2v}$ (see also ⁴). At $D_{2h} \rightarrow C_{2v}$ PT

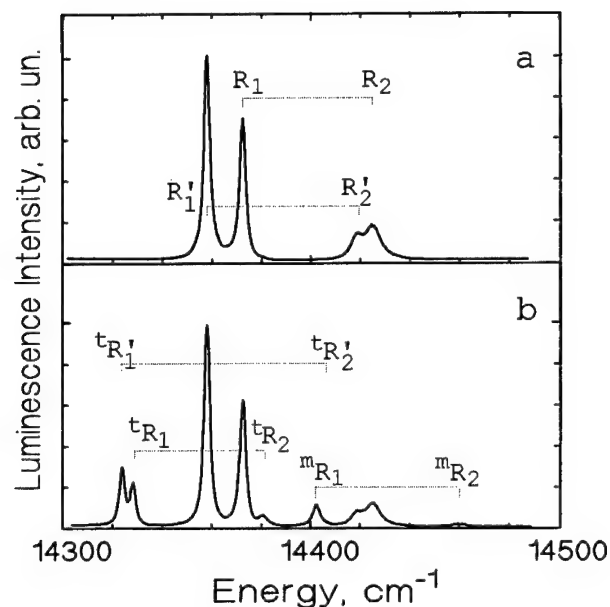


FIGURE 1 Luminescence spectra of samples LGO:0.05%Cr (a) and LGO:0.01%Cr, 0.02%Mg (b) at $T = 77$ K.

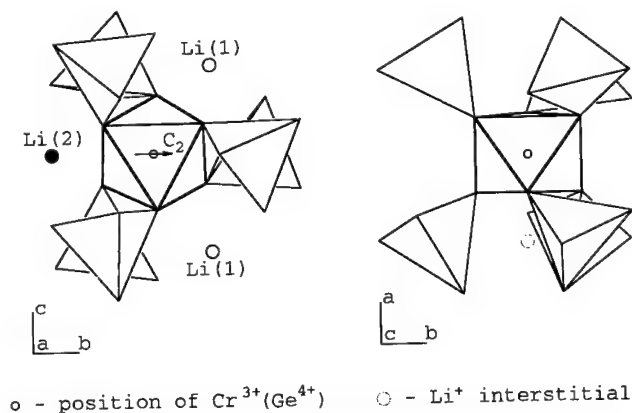


FIGURE 2 Fragments of LGO paraphase lattice in projection on planes 'bc' (a) and 'ab' (b). Octahedron GeO_6 with surrounding tetrahedra GeO_4 is shown. Small open circle—position of octahedral Ge^{4+} substituted by $3d^3$ -ion. Large circles— Li^+ ion positions: regular 1 (open circle), regular 2 (dark circle), and nonstoichiometric interstitial (dotted open circle).

with ferroelectric axis 'c' optical spectra of C_1 -centers should split into doublets whereas no splitting should occur for C_2 -centres.⁴

As it was shown,⁵ pairs of spectra lines $R_1 - R'_1$, $R_2 - R'_2$ which have in ferrophase very close spectral positions, intensities, and decay times, merge into one pair at $T \rightarrow T_c$ which indicates the triclinic C_1 -symmetry of corresponding Cr^{3+} -centers in paraphase. According to^{5,6} the charge compensation in such centers ($\text{Cr}^{3+}\text{Li}^+$ -centers) dominating both in

LGO:Cr and LGO:Cr,Mg is provided by interstitial Li^+ ion located in nearest empty octahedral position (see Figure 2b). Similarly, close doublet ${}^1\text{R}_1$, ${}^1\text{R}'_1$ (and corresponding ${}^1\text{R}_2$, ${}^1\text{R}'_2$ lines) which is observed in LGO:Cr,Mg ferrophase, we interpret as the PT induced doublet splitting of R-spectra belonging to $\text{Cr}^{3+}\text{Mg}^{2+}(1)$ -centers with C_1 -symmetry (in paraphase). The charge compensation in these centers is realized by means of Mg^{2+} ions substituting nearest regular Li^+ -ion in position Li(1) (see Figure 2a). The single pair ${}^m\text{R}_1 - {}^m\text{R}_2$ observed in ferrophase LGO:Cr,Mg spectrum indicates the singlet splitting of spectra at $\text{D}_{2h} \rightarrow \text{C}_{2v}$ PT, which is indicative for monoclinic C_2 -centers in paraphase. We suppose that in these $\text{Cr}^{3+}\text{Mg}^{2+}(2)$ -centers charge compensation is provided by Mg^{2+} ion substituting regular Li^+ in Li(2) position (see Figure 2a).

The interpretation is confirmed by observation of single $\text{R}_1 - \text{R}_2$ pair ($15013 - 15113 \text{ cm}^{-1}$ at 77K) in the luminescence spectrum of isoelectronic Mn^{4+} in LGO ferrophase, which indicates the monoclinic C_2 -symmetry of Mn^{4+} -centers (in paraphase). Namely this point group describes in paraphase the symmetry of Ge^{4+} position which is occupied by isovalent Mn^{4+} when no charge compensation is needed.

To interpret the relative spectral position of R-lines for different Cr^{3+} -centers (Figure 1), the polar (C_2) symmetry of Cr^{3+} -ion in octahedral Ge^{4+} position should be taken into account. Due to C_2 -symmetry, Cr^{3+} has permanent electric dipole moment \vec{D}_b along $\text{C}_2 \parallel b$. The ${}^4\text{A}_2 - {}^2\text{E}$ transition frequency in Cr^{3+} -ions should possess linear Stark shift $\Delta\nu$ in microscopic Coulomb field \vec{E} produced by positively charged compensating defect. From geometric considerations (see Figure 2), $\Delta\nu$ has opposite sign for two Mg^{2+} compensated centers with Mg^{2+} in Li(1) or Li(2) positions relative to nonstoichiometric Li^+ compensated center where $\vec{D}_b \perp \vec{E}_c$ and $\Delta\nu \equiv 0$. This explains the relative spectral position of R-lines belonging to $\text{Cr}^{3+}\text{Li}^+$, $\text{Cr}^{3+}\text{Mg}^{2+}(2)$, and $\text{Cr}^{3+}\text{Mg}^{2+}(1)$ centers.⁴ Similar Stark shift is especially large for UV charge transfer bands of Cr^{3+} center which reveal the giant ($\sim 0.6 \text{ eV}$) difference in spectral position of UV bands belonging to $\text{Cr}^{3+}\text{Li}^+$ and $\text{Cr}^{3+}\text{Mg}^{2+}(2)$ centers.⁴

4 PSEUDO-STARK SPLITTING OF R-LINES AND PHASE TRANSITION INDUCED POLARIZATION OF $3d^3$ -IONS

In paraelectric phase D_{2h} of LGO, the $3d^3$ -ion in monoclinic inversionless sites with point symmetry C_2 has permanent electric dipole moment \vec{D} directed in lattice along two-fold symmetry axis of center $\text{C}_2 \parallel b$. Ferroelectric PT $\text{D}_{2h} \rightarrow \text{C}_{2v}$ with polar axis $c \perp b$ which reduces the center symmetry $\text{C}_2 \rightarrow \text{C}_1$, induces in principle additional 'c' and 'a' dipole moment components

$$\vec{D}^\eta = \begin{pmatrix} \alpha_{xx} & \alpha_{xy} & 0 \\ \alpha_{yx} & \alpha_{yy} & 0 \\ 0 & 0 & \alpha_{xy} \end{pmatrix} \vec{\eta} \quad x \parallel a, y \parallel c, z \parallel b \quad (1)$$

where $\vec{\eta}(0, \eta, 0)$ is order parameter of PT with transformation properties of polar vector $\parallel c$ and α_{ik} is the second rank tensor for C_2 -symmetry. It follows from (1) that values of PT induced dipole components $\sim \eta \sim (\text{T}_c - \text{T})^{1/2}$.

The PT induced dipole moments were observed directly in experiments on pseudo-Stark splitting of R_1 -lines of monoclinic $3d^3$ -centers in ferroelectric phase LGO in external electric field. The prominent doublet linear in field splitting of R_1 -line was observed both for ${}^m\text{R}_1$ -line of $\text{Cr}^{3+}\text{Mg}^{2+}(2)$ center and for R_1 -line of Mn^{4+} center in the external field $\parallel a$. It is interesting that PT induced dipoles D_a are directed in lattice perpendicular to its ferroelectric axis 'c'.

REFERENCES

1. M. Wada and Y. Ishibashi. *J. Phys. Soc. Jpn.* **52**, 193 (1983).
2. Y. Iwata, I. Shibuya, M. Wada, A. Sawada, Y. Ishibashi. *J. Phys. Soc. Jpn.* **56**, 2420 (1987).
3. R. C. Powell. *J. Appl. Phys.* **39**, 4517 (1968); *Phys. Rev.* **173**, 358 (1968).
4. S. A. Basun, A. A. Kaplyanskii, S. P. Feofilov. *Phys. Solid State* (translation from *Fizina Tverdogo Tela*) **36**, 1821 (1994).
5. S. A. Basun, S. P. Feofilov and A. A. Kaplyanskii. *Ferroelectrics* **143**, 163 (1993).
6. A. A. Galeev, N. M. Hassanova, A. B. Bykov, V. M. Vinokurov, N. M. Nizamutdinov and G. R. Bulka, *Spectroscopy, Chemistry and Real Structure of Minerals and Their Analogs* (Kazan University Publishing, Kazan, 1990), p. 77 (in Russian).

EXCITED STATE ABSORPTION IN HOLMIUM DOPED $\text{Gd}_3\text{Ga}_5\text{O}_{12}$ GARNET

A. BRENIER, C. MADEJ, C. PÉDRINI and G. BOULON

*Laboratoire de Physico-Chimie des Matériaux Luminescents, URA CNRS N°442,
Université Claude Bernard-Lyon I, 43 B^d 11 Novembre 1918, 69622 Villeurbanne cédex,
France.*

The purpose of the present work is the direct measurement of the $^5\text{I}_7 \rightarrow ^5\text{S}_2 - ^5\text{F}_4(\text{Ho})$ excited state absorption in $\text{Gd}_3\text{Ga}_5\text{O}_{12}$ garnet with a two beam experiment. The result is compared with the cross-section deduced from the $^5\text{S}_2 - ^5\text{F}_4 \rightarrow ^5\text{I}_7$ emission spectrum, using Mc Cumber relations. The result is also compared to the laser excitation spectrum near 753 nm of the green emission recorded in a previous work [1].

Key words: excited-state absorption, photoluminescence.

1 INTRODUCTION

In a previous work [1] we have obtained the conversion of infrared laser light (near 753 nm) into a green emission from the Ho ions in $\text{Gd}_3\text{Ga}_5\text{O}_{12}:\text{Yb}:\text{Tm}:\text{Ho}$ garnet by a two step process: absorption from the ground states of the ions followed by a looping mechanism. The latter is composed by an excited state absorption from the $^5\text{I}_7(\text{Ho})$ level corresponding to the transition: $^5\text{I}_7 \rightarrow ^5\text{S}_2 - ^5\text{F}_4(\text{Ho})$ and by a positive feedback process involving the Tm ions. In this experiment we recorded the laser excitation spectrum near 753 nm of the green emission: it is the image of the $^5\text{I}_7 \rightarrow ^5\text{S}_2 - ^5\text{F}_4(\text{Ho})$ excited state absorption. The purpose of the present work is the direct measurement of such an excited state absorption with a two beam experiment. The calibration of the cross-section (cm^2) is obtained by measuring the decreasing due to the pump beam of the $^5\text{I}_8 \rightarrow ^5\text{S}_2 - ^5\text{F}_4(\text{Ho})$ absorption from the $^5\text{I}_8$ Ho ground state. The result is compared with the excited state absorption cross-section deduced from the $^5\text{S}_2 - ^5\text{F}_4 \rightarrow ^5\text{I}_7(\text{Ho})$ emission spectrum, using Mc Cumber relations. The result is also compared to the laser excitation spectrum near 753 nm of the green emission recorded in our previous work.

2 EXPERIMENTAL METHODS

We used a Ho(3%)-Yb(5%) doped $\text{Gd}_3\text{Ga}_5\text{O}_{12}$ crystal grown at the laboratory by the Czochralski method. The probe beam, provided by a CW tungsten lamp, was slightly focused on the sample and detected in the 735–765 nm range through a Jobin-Yvon HRS2 monochromator by a Hamamatsu AsGa photomultiplier. The slits were 0.16 mm and the resolution 1.2 nm/mm slit. The pump beam was crossing perpendicularly and overlapping the probe beam inside the crystal. It was expanded and focused after the sample by a cylindrical lens. The pump beam was provided by a pulsed Laser Analytical Systems dye laser pumped by a frequency doubled B. M. Industries pulsed YAG:Nd laser. The pulse duration was a few ns, the wavelength 639 nm corresponding to the $^5\text{I}_8 \rightarrow ^5\text{F}_5(\text{Ho})$ transition, the energy was 54 mJ/pulse. The signal corresponding to the probe beam given by the photomultiplier was sent in two Stanford Research System SR 250 boxcar averages. The gate of the first one was delayed 45 ms. This delay is long enough for all the Ho ions excited by the pump pulse to return to the $^5\text{I}_8$ ground state. So the output signal of the first

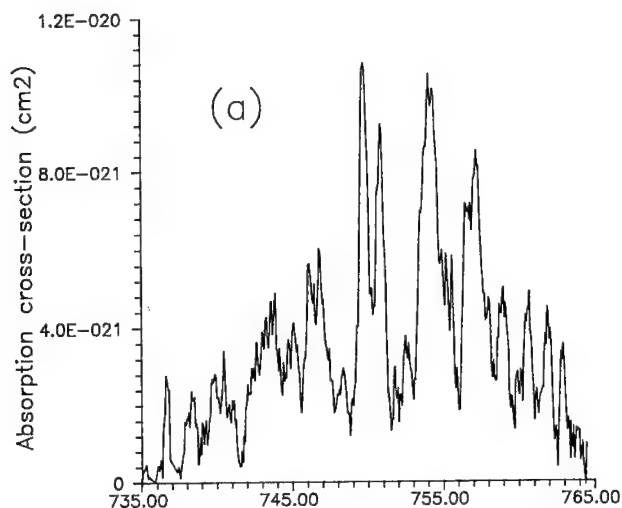


FIGURE (a) ${}^5\text{I}_7 \rightarrow {}^5\text{S}_2 - {}^5\text{F}_4$ excited-state absorption cross-section measured in a two beams experiment.

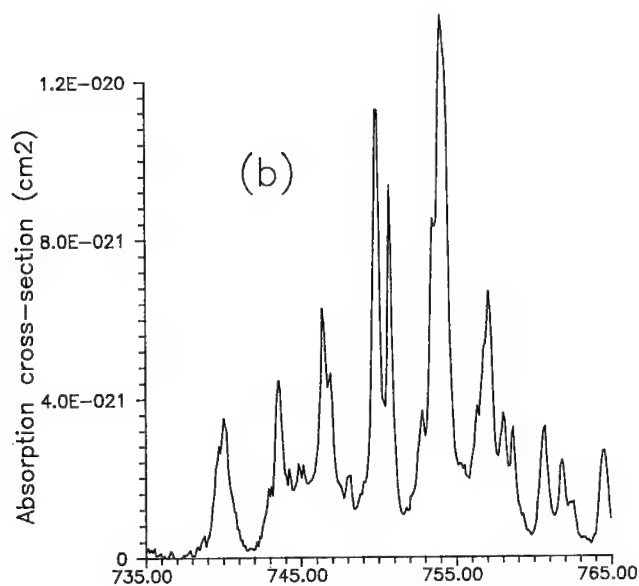


FIGURE (b) ${}^5\text{I}_7 \rightarrow {}^5\text{S}_2 - {}^5\text{F}_4$ excited-state absorption cross-section measured using Mc Cumber relations.

boxcar is nothing else than the baseline of the probe beam. The gate of the second boxcar was delayed 1.56 ms. This delay is long enough for the ${}^5\text{F}_5$ and ${}^5\text{I}_6(\text{Ho})$ populations induced by the pump to return to zero (the ${}^5\text{F}_5$ and ${}^5\text{I}_6(\text{Ho})$ lifetimes are respectively a few tens of μs and 550 μs) and short enough for the ${}^5\text{I}_7$ level was still strongly populated after the pump pulse (the ${}^5\text{I}_7$ lifetime is 10 ms). So the output signal of the second boxcar

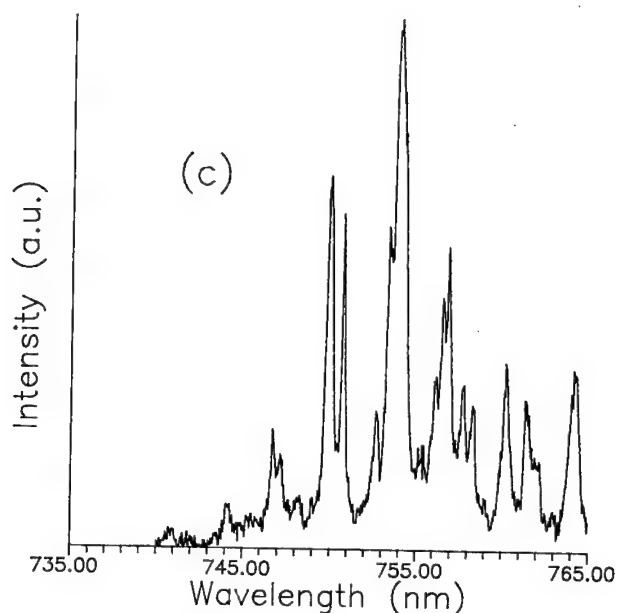


FIGURE (c) Excitation spectrum of the $^5\text{S}_2 - ^5\text{F}_4$ fluorescence measured in a looping mechanism experiment.

corresponds to the probe beam decreased by the $^5\text{I}_7 \rightarrow ^5\text{S}_2 - ^5\text{F}_4(\text{Ho})$ excited state absorption due to the $^5\text{I}_7$ population still existing 1.56 ms after the pump pulse.

3 RESULTS

The intensity of the probe beam when pumping the sample is:

$$(1) \quad I = I_0 e^{-\sigma NL}$$

where I_0 is the intensity of the probe beam without pumping, L is the path length inside the crystal, σ is the $^5\text{I}_7 \rightarrow ^5\text{S}_2 - ^5\text{F}_4(\text{Ho})$ absorption cross-section and N is the concentration (ions/ cm^3) of the $^5\text{I}_7$ population. Expression (1) is valid because there is no absorption of the probe beam from the ground state in the 735–765 nm range. From (1) and exhibiting the λ wavelength dependence we obtain the formula giving the cross-section:

$$(2) \quad \sigma\lambda = (1/NL) \ln(I_0(\lambda)/I(\lambda))$$

The calibration factor NL was obtained by recording the decreasing of the $^5\text{I}_8 \rightarrow ^5\text{S}_2 - ^5\text{F}_4$ absorption from the $^5\text{I}_8$ ground state due to the population N in the $^5\text{I}_7$ level, in the 535–543 nm range:

$$(3) \quad NL = (1/\sigma') \ln(I'/I)$$

where $\sigma'(\lambda')$ is the cross-section of the $^5\text{I}_8 \rightarrow ^5\text{S}_2 - ^5\text{F}_4$ absorption from the $^5\text{I}_8$ ground state known from standard absorption measurements, $I'(\lambda')$ is the probe intensity under

pumping, $I(\lambda')$ the probe intensity without pumping, λ' stands in the 535–543 nm range. The left side of (3) should not depend on the wavelength λ' , so NL was calculated by averaging the right side of (3) in the 535–543 nm range and was found to be $5.11 \times 10^{18} \text{ cm}^{-2}$. Inserting this value in (2) results is the $^5\text{I}_7 \rightarrow ^5\text{S}_2 - ^5\text{F}_4(\text{Ho})$ absorption cross-section represented in Figure (a).

4 DISCUSSION AND CONCLUDING REMARKS

We recorded the normalized emission spectrum $f(\omega)$ of the $^5\text{S}_2 - ^5\text{F}_4 \rightarrow ^5\text{I}_7$ transition and we deduced from it the emission cross-section σ_e of this transition and the $^5\text{I}_7 \rightarrow ^5\text{S}_2 - ^5\text{F}_4(\text{Ho})$ absorption cross-section σ_a by using McCumber relations² connecting emission and absorption spectra. These relations are:

$$(4) \quad \sigma_e(\omega) = f(\omega) (2\pi c/\omega n)^2 \text{ and } (5) \quad \sigma_a = \sigma_e e^{\hbar\omega/kT} (N_2/N_1)_e$$

where n is the index of refraction of the host solid, $(N_2/N_1)_e$ is the ratio of the $^5\text{S}_2 - ^5\text{F}_4$ and $^5\text{I}_7$ populations at thermal equilibrium, calculated according to Boltzman law.¹ The result for $\sigma_a(\lambda)$ is represented in Figure (b). We give also in Figure (c) the CW laser excitation spectrum of the green Ho emission that we obtained in our previous work¹ in the 735–765 nm range.

We conclude that the two $^5\text{I}_7 \rightarrow ^5\text{S}_2 - ^5\text{F}_4$ (Ho) absorption cross-section spectra obtained by two independent ways (Figure (a) and (b)) are in reasonable agreement despite some discrepancy in the values of the peak cross-sections and despite the fact that the spectrum (a) is much more noisy than (b). More the excitation spectrum of the green emission in Figure (c) is the image of the spectra (a) and (b) at least above 750 nm, confirming the interpretation on the origin of the green emission recorded in.¹ Nevertheless below 750 nm a discrepancy exists between (b) and (c) but we have to keep in mind that the relation connecting (b) and (c) is not a simple relation of proportionality.

REFERENCE

1. A. Brenier, L. C. Courrol, C. Pédrini, C. Madej, G. Boulon, *Optical Materials* **3** (1994) 25–33.
2. D. E. McCumber, *Phys. Rev.* vol. **136** n°4A (1964) 954.

LUMINESCENCE OF YTTERBIUM DOPED LiNbO₃:MgO UNDER UV EXCITATION

A. BRENIER, C. MADEJ, C. PÉDRINI and G. BOULON

*Laboratoire de Physico-Chimie des Matériaux Luminescents, URA CNRS N°442,
Université Claude Bernard-Lyon I, 43 B^d 11 Novembre 1918, 69622 Willeurbanne Cédex,
France*

The usual absorption and luminescence of the trivalent ytterbium ions stand in the 900-1100 nm range. Under 355 nm laser excitation in ytterbium doped LiNbO₃:MgO we observed in addition a weak broad band emission extending from 700 to at least 900 nm. Its lifetime is about 1 μ s. Its excitation spectrum is composed of at least one band near 325 nm. This unexpected luminescence has similarities with well-known luminescence in divalent ytterbium doped fluorides.

Key words: photoluminescence, ytterbium, lithium niobate.

1 INTRODUCTION

We have grown at the laboratory by the Czochralski method at ytterbium doped LiNbO₃:MgO crystal from a congruent composition (Li₂O 48.55 molar %) in which we added Yb₂O₃ 1.25 molar % and MgO 5 molar %. The usual absorption and luminescence of the trivalent Yb³⁺ ions stand in the 900-1100 nm range at room temperature and were of course observed. Under 355 nm laser excitation we observed in addition a weak broad band emission extending from 700 to at least 900 nm. Its lifetime is about 1 μ s. Its excitation spectrum is composed of at least one band near 325 nm. This unexpected luminescence has similarities with well-known luminescence in divalent Yb²⁺ doped CaF₂ or SrF₂.

2 EXPERIMENTAL RESULTS

355 nm pulsed excitation from a frequency-tripled BM Industries Nd:YAG laser results in emissions which we recorded with an Hamamatsu R1767 photomultiplier through a Jobin-Yvon monochromator equipped with a 1 μ m blazed grating. Two different lifetimes of the luminescence exist so the emission spectra were obtained sending the signal in a Stanford Research Systems boxcar averager SRS250. Its gate was 2 μ s width and when it was not delayed we obtained the spectrum represented by the solid curve in Figure 1. It correspond to a lifetime of about 1 μ s. The huge peak at 1064 nm is a laser signal which could not be totally eliminated in the excitation beam. The two peaks near 770 and 1010 nm exist also in samples not doped with ytterbium and their origin is unknown. When the gate was 2 ms delayed we obtained the spectrum represented by the dashed curve in Figure 1. It corresponds to a lifetime of about 1 ms. This spectrum stands in the range of the usual Yb³⁺ emission corresponding to the $^2F_{5/2} \rightarrow ^2F_{7/2}$ transition. In Figure 2 we give the comparison with the usual Yb³⁺ emission in the two polarizations obtained under 920 nm excitation. We observe a good similarity if we take into account the fact that the spectrum in dashed line in Figure 1 is a non-polarized one.

We did not observed an increasing of the intensity of the emission by cooling the sample to liquid helium temperature.

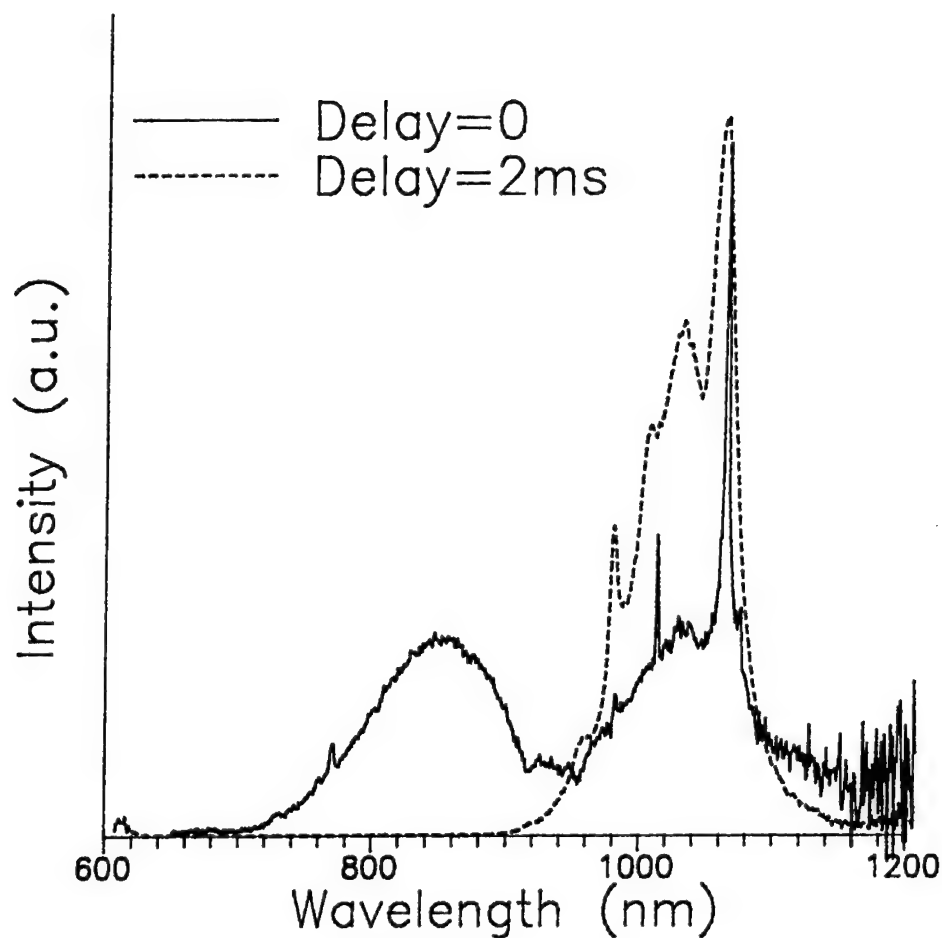


FIGURE 1 Time resolved fluorescence of ytterbium doped $\text{LiNbO}_3\text{:MgO}$ under 355 nm excitation at room temperature. Solid line: short lived component; Dashed line: long lived component.

The excitation spectrum of the emission limited to the range 700–900 nm was recorded with a xenon lamp and a monochromator. It is represented at 10 K in Figure 3. The main peak is situated at 320 nm. The two peaks at 360 nm correspond to $^1\text{D}_2$ absorption of thulium traces.

3 CONCLUSION

We report here the detection of unexpected emission and absorption bands in an ytterbium doped $\text{LiNbO}_3\text{:MgO}$ crystal under uv excitation. The range of wavelengths and the

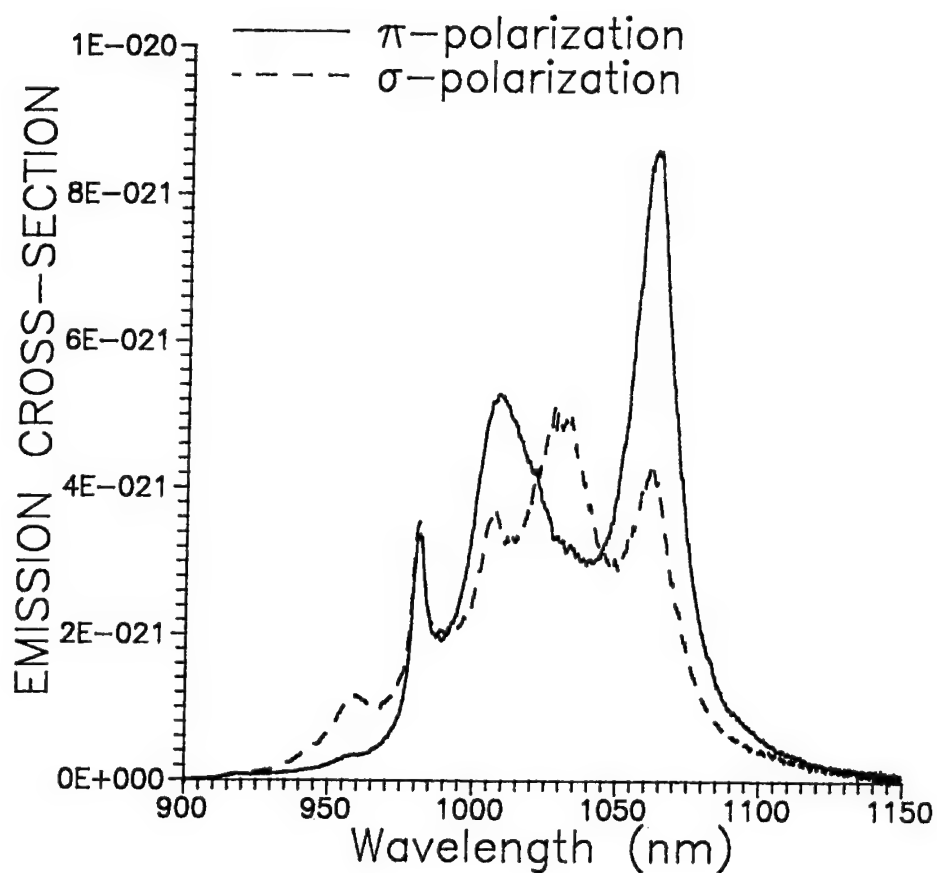


FIGURE 2 Luminescence of ytterbium doped $\text{LiNbO}_3\text{:MgO}$ under 920 nm excitation at room temperature.

lifetime of the emission are very different than the ones of the usual Yb^{3+} emission corresponding to the $^2\text{F}_{5/2} \rightarrow ^2\text{F}_{7/2}$ transition. A possible origin of this emission is traces of divalent ytterbium in the host but a more complete excitation spectrum extending up to 100 nm is needed before giving a definitive interpretation.

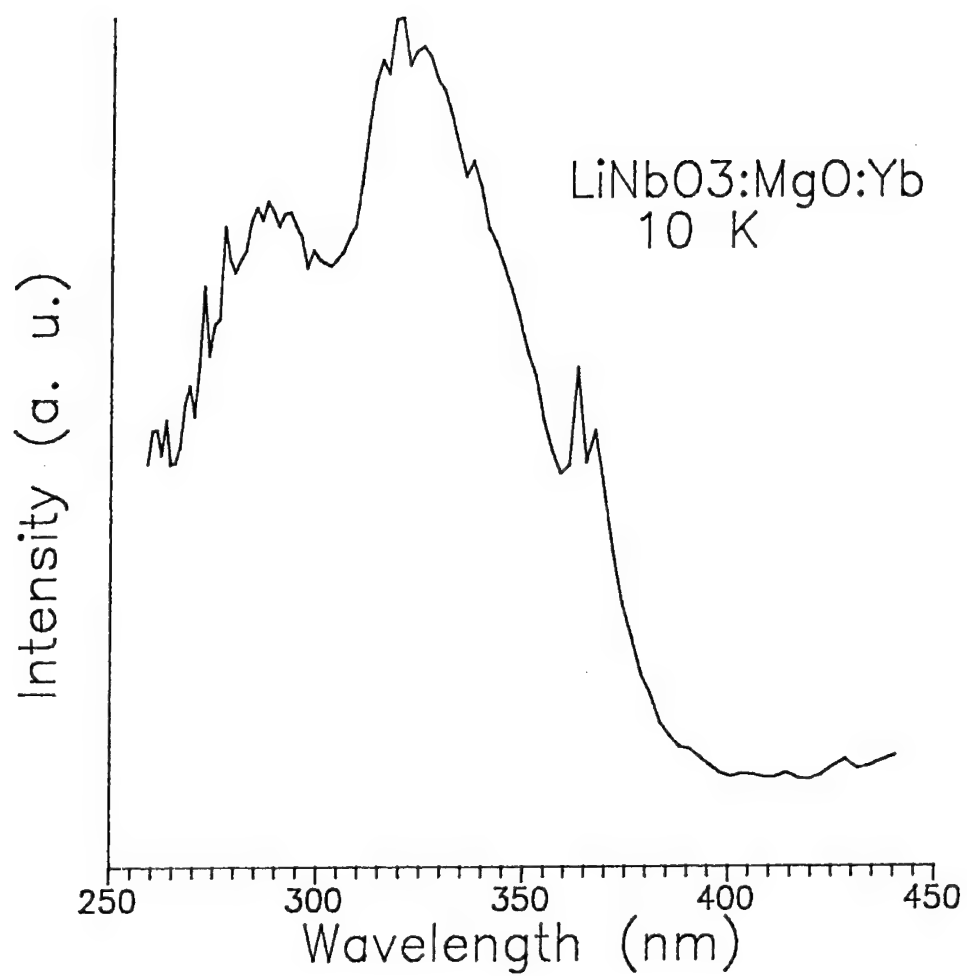


FIGURE 3 Excitation spectrum of the 700–900 nm luminescence of ytterbium doped LiNbO₃:MgO.

OPTICAL DETECTION OF Eu^{3+} SITES IN $\text{Gd}_3\text{Ga}_5\text{O}_{12}:\text{Eu}^{3+}$

L. C. COURROL, L. GOMES, A. BRENIER,* C. PÉDRINI,* C. MADEJ*
and G. BOULON*

*Divisão de Materiais Optoeletrônicos, IPEN/CNEN-SP; *Laboratoire de Physico-Chimie
des Matériaux Luminescents, Université Claude Bernard-Lyon I*

The trivalent rare earth ions occupy the eight-coordinated (dodecahedral) sites (D_2 point symmetry) in $\text{Gd}_3\text{Ga}_5\text{O}_{12}:\text{Eu}^{3+}$ crystal. The fluorescence of Eu^{3+} has been investigated using laser-excited site-selection spectroscopy. It was seen three distinct sites deduced from the spectra, one of them owing to the garnet site. The emission and excitation spectra of non-garnet site are consistent with the low symmetry point of C_{2v} site.

1 INTRODUCTION

Rare-earth doped garnets are considered very important laser materials.^{1,2}

The knowledge of their structures and the determination of the rare earth multisites are essentials to the performance and the technology development of this material as laser light source in the mid-IR.

The $\text{Gd}_3\text{Ga}_5\text{O}_{12}$ (GGG) type garnet has a cubic crystalline structure with eight molecules per unit cell. The Gd^{3+} ions are located in the dodecahedral D_2 site and the Ga^{3+} ions are in S_4 and S_6 sites. The rare earth Eu^{3+} ions are located generally in the Gd^{3+} positions. However, laser-excited site selection spectroscopy can give information about the different sites as well as their local symmetry. This information can be used for a complete understanding of the physical properties of this material.

The Eu^{3+} ions are appropriate for site-selection spectroscopy study, because they have absorption and emission bands in the visible range; the luminescence spectrum is particularly simple since the fundamental 7F_0 level is not decomposed by the crystalline field.

In this paper, laser-excited site-selection spectroscopy has been utilized to determine the Eu^{3+} occupation sites in GGG. The experimental results indicated the existence of three different sites when analysing the emission spectra. Two of them are non-garnet sites.

The GGG: Eu^{3+} sample was grown by Czochralski's technique in the Laboratoire de Physico-Chimie des Matériaux Luminescents (Lyon). The high resolution excitation and emission spectra were measured by exciting the crystal with a tunable dye laser pumped by an excimer laser. The luminescence was detected by a cooled S-20 photomultiplier. The signals were recorded using an SR 400 two-channel gated photon counter and the sample was placed in a closed-cycle He cryostat for low temperature measurements.

2 EXPERIMENTAL RESULTS

We investigated the $^5D_0 \rightarrow ^7F_0$ and $^5D_0 \rightarrow ^7F_1$ fluorescent transitions of Eu^{3+} at 6 K, in GGG. The first transition is forbidden because $\Delta J = 0$, but can appear in the C_n , C_{nv} and C_s symmetries.³ The emission spectra of the $^5D_0 \rightarrow ^7F_1$ transition at 596.3 nm at 6 K, showed the presence of an excitation band centered at 580.2 nm due to the $^7F_0 \rightarrow ^5D_0$ transition as is shown in Figure 1. This excitation band shows the existence of a non-garnet

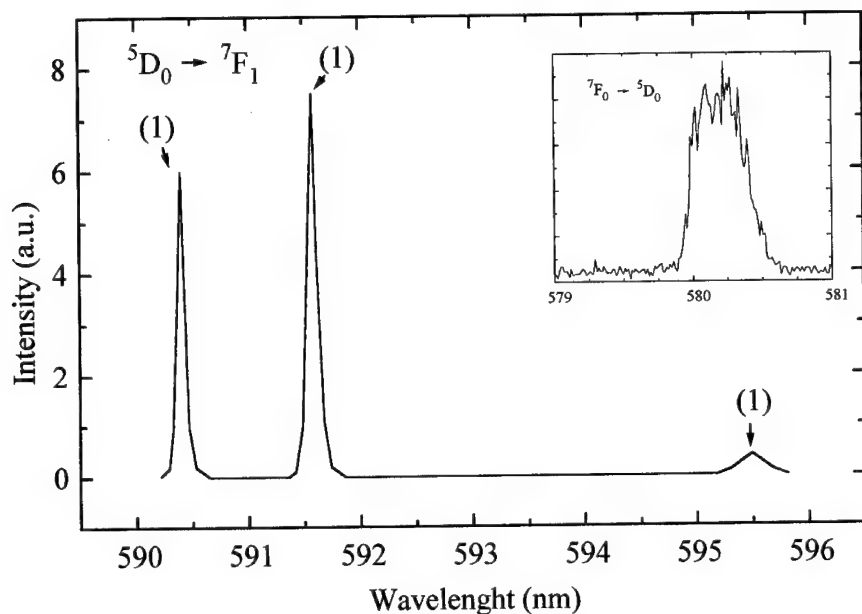


FIGURE 1 Emission spectra of the transition ${}^5D_0 \rightarrow {}^7F_1$ with excitation fixed at 580.2 nm at 12 K. The excitation spectra of the fundamental transition ${}^7F_0 \rightarrow {}^5D_0$ with emission fixed at 596.3 nm at 6 K is shown too.

site probably with a C_{2v} symmetry. The excitation of this transition at 580.2 nm (${}^7F_0 \rightarrow {}^5D_0$) shows the presence of emission bands corresponding to the ${}^5D_0 \rightarrow {}^7F_1$ transition composed of three sharp lines centered at 590.4, 591.6 and 595.5 nm (1 site) (see Figure 1).

This ion when excited at 527.5 nm shows the emission band due to ${}^5D_0 \rightarrow {}^7F_1$ transition which is exhibited in Figure 2. In this spectrum we observe the presence of 6 more lines beside the 3 already identified lines. These lines have peaks at 591, 591.2, 592.2, 592.5, 594.2 and 594.5 nm corresponding to different site symmetries. The identification of these lines with their symmetries could be obtained by specific excitation at different positions, Figure 3. For example, the excitation at 526.86 nm contributes with the lines: 591.2, 592.2 and 594.5 nm (site 3). The excitation at 527.6 nm exhibited lines peaking at 591.0, 592.5 and 594.2 nm (site 2).

The (3) site is the D_2 site, expected for Eu^{3+} , the most abundant site in the lattice.

The (2) site must have the D_{2h} symmetry, showing also 3 lines. It can not be the Ga^{3+} site which has S_4 or S_6 symmetry.

By using second order approximation in the crystalline field effects, it was possible to calculate the A_2^0 and A_2^2 parameters for the ${}^5D_0 \rightarrow {}^7F_1$ transition. We found for the (1) site: 224.28 and 88.9 cm^{-1} ; for the (3) site: 142.03 and 60.28 cm^{-1} and for the (2) site: 126.15 and 54.48 cm^{-1} .

It was observed that the (1) site have the ligand ions closest that the (2) and (3) sites, due to the fact that $A_2^2(1) > A_2^2(2 \text{ and } 3)$.

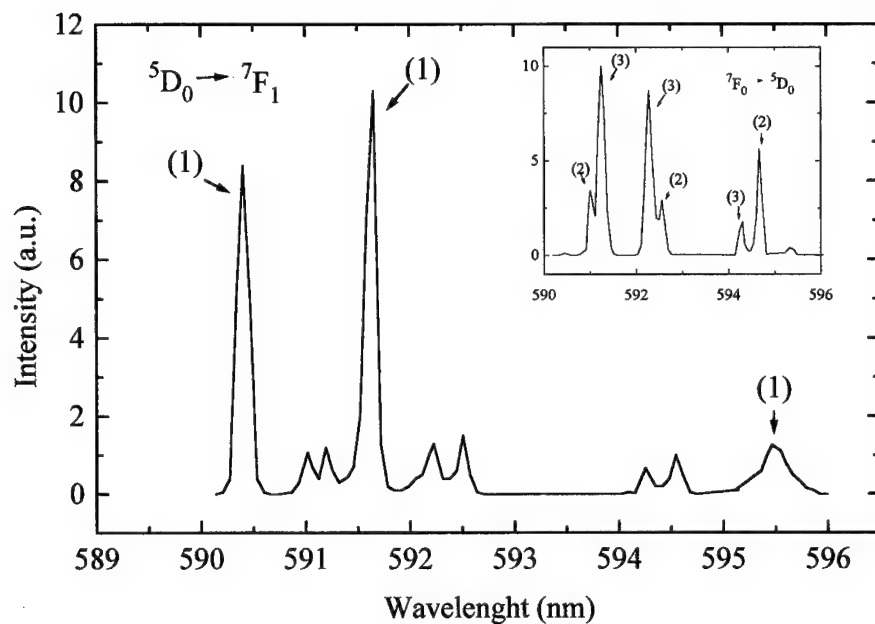


FIGURE 2 Emission spectra of the $^5\text{D}_0 \rightarrow ^7\text{F}_1$ transition with excitation at 527.5 nm at 12 K. Emission spectra of the $^5\text{D}_0 \rightarrow ^7\text{F}_1$ transition with excitation at 527.6 nm at 12 K (inserted figure).

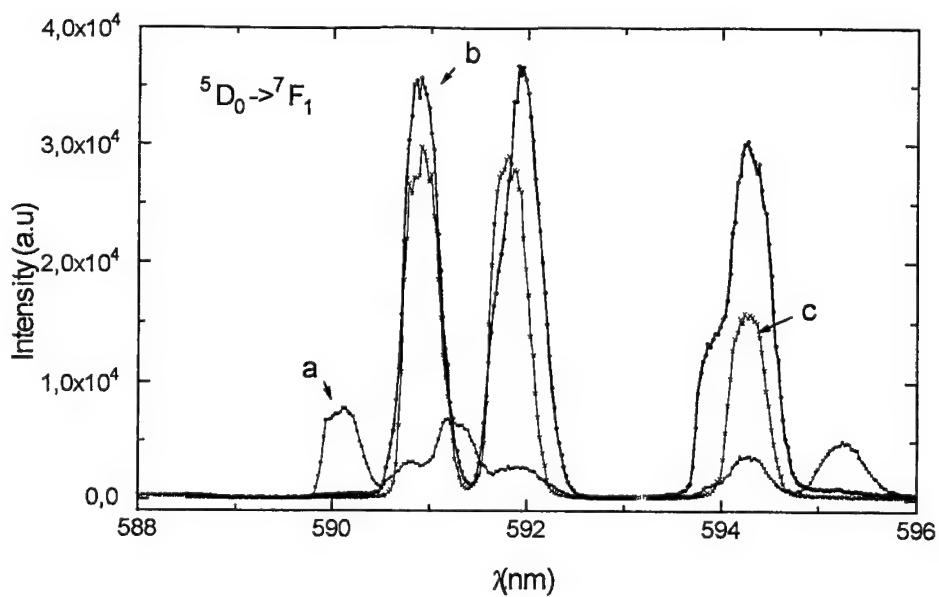


FIGURE 3 Emission spectra of the $^5\text{D}_0 \rightarrow ^7\text{F}_1$ transition with excitation at a) 527.36 nm, b) 527.45 nm and c) 526.86 nm, at 6 K.

3 CONCLUSION

The experimental results showed the presence of 3 non equivalent crystalline sites in GGG:Eu³⁺ crystal. These different sites were named (1), (2) and (3) sites could be identified by their group of emission lines of $^5D_0 \rightarrow ^7F_1$ transition when selectively excited at 580.2 nm and 527.6 nm respectively.

By the observation of fundamental transition $^7F_0 \rightarrow ^5D_0$, we could verify that the (1) site must have one of the C_2 , C_{2v} , or C_s symmetry (most probably, C_{2v} symmetry).

The predominant site D_2 has symmetry that corresponds to site type (3). The (2) site must have D_{2h} symmetry.

REFERENCES

1. H. Lundt, H. Weidner, *Opt. Communications*, **75**, 5 (1990).
2. A. Brenier, L. C. Courrol, C. Pedrini, C. Madej, G. Boulon, *Phys. Review*, **B49**, 0 (1994).
3. G. Blasse, A. Brill, *Philips Res. Repts*, **21**, 368–378 (1966).

STUDY OF BISTABLE (SHALLOW-DEEP) DEFECT SYSTEMS IN $\text{CdF}_2:\text{M}^{3+}$ (M: In, Ga)

YANG CAI and K. S. SONG

Physics Department, University of Ottawa, Ottawa, Ont. Canada K1N 6N5

Bistable (shallow-deep) defect systems associated with trivalent impurities (In, Ga, Y and Sc) in CdF_2 are studied using the extended-ion approach, in which a very large cluster of atoms is treated. Two groups of trivalent impurity centres are found. With In and Ga, there is a low, but clearly identified, potential barrier which separates the deep level from the shallow one. In Sc and Y, only a simple shallow level state is obtained. The analysis of the result shows that the difference is to be attributed to the short range potential of the trivalent impurity centres.

1 INTRODUCTION

Cadmium fluoride, CdF_2 , has the fluorite structure with the lattice constant, a_0 , being 5.365 Å. CdF_2 can be doped with numerous trivalent dopants, Sc, Y, and rare earth elements. Most of the trivalent metals in CdF_2 produce stable shallow hydrogenic donor states. In¹ and Ga² have shown unusual bistable behaviour. In room temperature absorption spectra of $\text{CdF}_2:\text{In}$ two strongly asymmetric bands are seen. One of these is in the visible light range (VIS), peaked at 3 eV, and another in the mid-infrared (mid-IR), at 0.2 eV. According to J. M. Langer *et al.*,¹ the 0.2 eV-band indicates a weakly localized ($\text{In}^{3+} + e^-$) state with a thermal ionization energy of 0.14 eV, while the 3 eV-band indicates a strongly localized In^{2+} state with a thermal ionization energy of only 0.25 eV (all thermal energies refer to 0 K), which means an enormous Stokes shift for the deeper state. The energy barrier separating the two states and leading to the metastable effects is about 0.17 eV. The absorption spectra of $\text{CdF}_2:\text{Ga}$ has similar asymmetric bands peaked at 4 eV and 0.17 eV, respectively.²

The most general framework for the theoretical description of bistability occurring in crystal defects has been developed by Toyozawa.³ In the case of an electron bound to a charged impurity, the electron always has a localized but shallow state, and in addition may have a localized deep minimum stabilized by combined action of the short range impurity potential and the electron-phonon interaction.

In this paper we present a brief report on the structure of the M^{3+} impurity with an excited electron bound to it (with $\text{M}=\text{In, Ga, Sc, and Y}$). The discrete structure of the lattice and detailed interaction between the excited electron and the impurity atom as well as the surrounding atoms of Cd^{2+} and F^- are explicitly taken into account within the approach of the extended-ion method. In order to compare the shallow and deep level states on the same footing, an identical treatment is applied to both states. The adiabatic potential energy is determined as a function of the configuration coordinate (c. c.) chosen (the nearest neighbour $\text{M}^{3+}-\text{F}^-$ distance). As expected, one finds a strongly relaxed lattice environment associated with the shallow (diffuse electron wavefunction) level, and an almost undistorted lattice environment for the deep (compact state) level. The most significant result is that the short range potential of the impurity atom core plays an important role in the appearance of the bistable state.

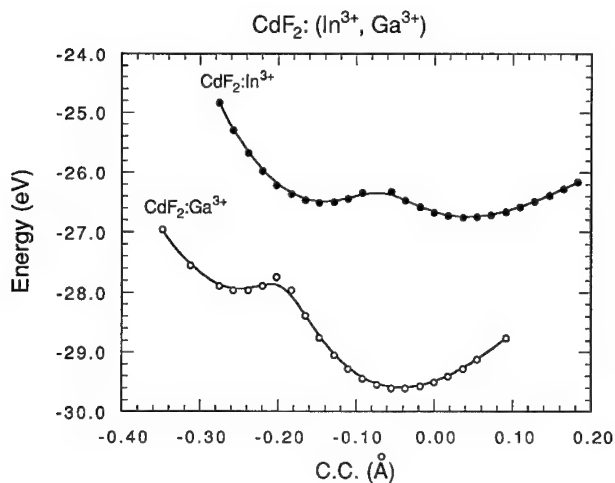


FIGURE 1 Potential energy curve for $\text{CdF}_2:(\text{In}^{3+}, \text{Ga}^{3+})$. Total energy of the system as a function of nearest $\text{M}^{3+} - \text{F}^-$ distance (c.c.).

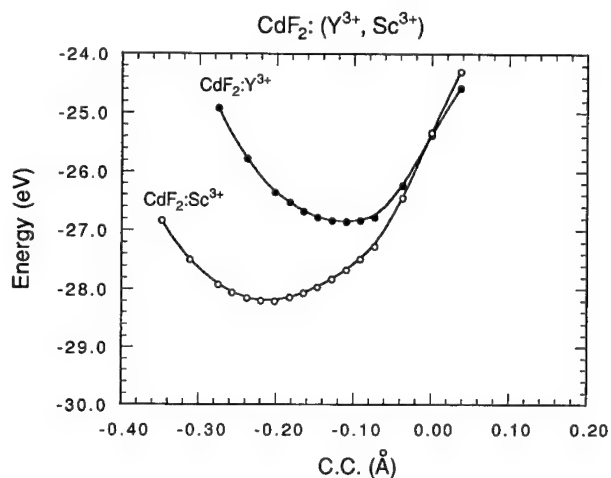


FIGURE 2 Potential energy curve for $\text{CdF}_2:(\text{In}^{3+}, \text{Ga}^{3+})$. Total energy of the system as a function of nearest $\text{M}^{3+} - \text{F}^-$ distance (c. c.).

2 METHOD OF CALCULATION

The total energy is taken to be the sum of the lattice distortion energy, the energy of the defect electron and the polarization energy of the crystal. We minimize the total energy for fixed values of the c.c. by allowing the positions of about 45 atoms to relax.

The energy of the distorted lattice is made up of the Coulomb energy and the short range repulsion of the ions. The interionic potentials were determined with Gordon-Kim⁴ approach.

To calculate the energy (and structure) of the defect electron, we use the extended-ion model.^{5,6} Analytical expressions are derived to calculate the overlap integral, the screened Coulomb and exchange terms of outer *s*, *p* and *d* orbital. A large number of atoms (up to 1800) is considered.

The impurity ion has a net charge of +e. This means that polarization effects will take on an important role in this problem, especially for the shallow state. We calculate this energy by the Mott-Littleton method including monopole-dipole and dipole-dipole terms. The polarizability employed here are from ref. (7)

We have used two diffuse and one compact gaussian bases centred on the impurity to represent the defect electron. The Gaussian damping factors ($\alpha = 0.005 \sim 0.08$ typically) are chosen such that the lowest energies are obtained in either the delocalized or localized state. The surrounding shells are relaxed up to the third. Details will be published later.

3 RESULTS AND DISCUSSION

We have found a bistable defect system for In and Ga and a single shallow level system for Sc and Y in agreement with experimental observations. The calculated adiabatic potential energy is shown for the four impurities in Figure 1–2. Here the c.c. is the nearest $M^{3+}-F^-$ distance.

In all four M^{3+} studies, a shallow level with a very diffuse wavefunction (the gaussian with damping factor $\alpha = 0.005$ (in a. u.) of $\exp(-\alpha r^2)$ has the largest weight) appears. With the shallow state, a large number of atoms which surround the trivalent impurity are subject to partly unscreened Coulomb field. This has been treated, as described above by Mott-Littleton method. Typically, we found the electronic polarization energy of about 1.1 eV. The lattice ‘collapses’ toward the impurity atom by about 0.15 Å (the first shell F^-) due to the Coulomb attraction.

With In and Ga replacing a host Cd atom, we obtained beside the shallow level one deeper level with a compact wavefunction (also s-like). Corresponding to the deep level, the lattice relaxation is almost negligible. The lattice responds as if to a In^{2+} (or Ga^{2+}) ion. The electronic polarization is also quite small, ~ -0.1 eV.

A potential barrier between the shallow and deep levels is seen in both $CdF_2:In$ and $CdF_2:Ga$. It seems rather low, although it is not possible to attach great confidence to the value obtained (~ 0.1 eV). On the other hand, the energy difference between the shallow and deep levels is found to be about 0.2 eV in $CdF_2:In$ from Figure 1. This value is in good agreement with the one reported in Ref(1): 0.11 eV. In the case of $CdF_2:Ga$, there is no reported experimental value available.

We now discuss on the factors which contribute to the appearance of the deep level, such as in In and Ga, but not in Sc and Y. It seems reasonable to associate the deep level with the first s-like level of the free M^{2+} ion. These are the $5s(In^{2+})$, $4s(Ga^{2+})$, $5s(Y^{2+})$ and $4s(Sc^{2+})$ levels. For the first two, In and Ga, the binding energy is about 28 eV and 31 eV, respectively. In CdF_2 lattice this value can be reduced by about 20 eV with the repulsive Madelung potential of the cation site. The resulting energy can be compared to the purely electronic energy of the deep level which is about $(-)$ 8 eV and $(-)$ 9 eV, respectively. Applying the same argument to the case of Sc and Y, one finds that the electron energy in lattice would be about zero. It seems reasonable therefore that the deep level does not show up in the case of Sc and Y due to this internal difference of the two groups of trivalent atoms. We predict that Tl^{3+} would show a deep level beside the shallow donor level in CdF_2 . The present example can be interpreted in terms of the effect of short range potential produced by the impurity atom in the context of the extrinsic self-trapping, proposed by Shinozuka and Toyozawa.³

REFERENCES

1. J. E. Dmochowski, J. M. Langer, Z. Kalinski and W. Jantsch, *Phys. Rev. Letters* **56**, 1735 (1986).
2. J. E. Dmochowski, W. Jantsch, D. Dobosz and J. M. Langer, *Acta Phys. Polon. A* **73**, 247 (1988).
3. Y. Shinozuka and Y. Toyozawa, *J. Phys. Soc. Japan* **46**, 505 (1979).
4. R. G. Gordon and Y. S. Kim, *J. Chem. Phys.* **56**, 3122 (1972).
5. K. S. Song, L. Emery, G. Brunet and C. H. Leung, *Nucl. Instrum. Methods B1*, **456** (1984).
6. K. S. Song and R. T. William, *Self-Trapped Exciton*, Springer-Verlag (1993), Chap. 2.
7. J. R. Tessman, A. H. Kahn and W. Shockley, *Phys. Rev.* **92**, 890 (1953).

POLARIZED CHARGE TRANSFER SPECTRA OF Cu^{2+} DOPED PEROVSKITE LAYERS $(\text{RNH}_3)_2\text{Cd}_x\text{Mn}_{1-x}\text{Cl}_4$ ($x = 0-1$)

B. BATICLE,[†] F. RODRÍGUEZ and R. VALIENTE

D.C.T.T.Y.M. Facultad de Ciencias, Universidad de Cantabria, 39005 Santander, Spain

This work investigates the charge transfer spectra of CuCl_6^{4-} complexes formed in the $(\text{RNH}_3)_2\text{Cd}_x\text{Mn}_{1-x}\text{Cl}_4$ crystal series. For $x = 1$, it is demonstrated that Cu complexes display an elongated D_{4h} symmetry, forming an antiferrodistortive type structure which is similar to that found in the pure copper crystals. The presence of Mn induces an important enhancement of the charge transfer bands as well as significant redshifts. The results are interpreted in terms of distortions of the CuCl_6^{4-} geometry which changes from D_{4h} elongated ($x = 1$) to nearly D_{4h} compressed ($x = 0$). The transition energy, polarization and assignment of the charge transfer bands are analysed.

Key words: CuCl_6^{4-} complex; D_{4h} elongated and compressed symmetries; Charge Transfer spectra; $(\text{RNH}_3)_2\text{Cd}_x\text{Mn}_{1-x}\text{Cl}_4$ crystals.

1 INTRODUCTION

Hexacoordinated CuX_6^{4-} complexes display either dynamic or static Jahn-Teller distortions of tetragonal (D_{4h}) or (D_{2h}) symmetry. Such distortions are associated with electron-phonon couplings $E_g \otimes e_g$ of the parent 2E_g octahedral states. Within a linear approximation, the equilibrium geometry of these complexes would correspond to any point (Q_θ , Q_ϵ) of the potential energy surface minima (mexican hat) which describes a circle in the Jahn-Teller active e_g normal coordinate space. In this situation, either elongated or compressed D_{4h} distortions along x , y or z and other orthorhombic intermediates are equally probable. The occurrence of a given equilibrium geometry is determined by high order couplings. At this stage, the crystal anisotropy of the host matrix can play a fundamental role for determining the kind of distortion displayed by these Cu^{2+} complexes.^{1,2} Consequently, this also affects the nature of the electronic ground state, which can vary from ${}^2B_{1g}(d_{x^2-y^2})$ in a D_{4h} elongated complex to ${}^2A_{1g}(d_{3z^2-r^2})$ in a D_{4h} compressed one, passing through intermediates mixed states for D_{2h} distortions.

These structural modifications have a strong influence not only on the EPR spectra, which are very dependent on the electronic ground state symmetry, but also in their optical properties. In particular, the transition energy and polarization of both crystal field and $\text{Cl}^- \rightarrow \text{Cu}^{2+}$ charge transfer (CT) bands are expected to show significant changes with the complex symmetry.

It must be observed that CuX_6^{4-} complexes formed in either Cu pure or doped insulating crystals usually display the elongated or nearly elongated D_{4h} symmetry. An exception to this behaviour has been found in fluorides such as KCuAlF_6 or $\text{Ba}_2\text{ZnF}_6:\text{Cu}^{2+}$ and $\text{K}_2\text{ZnF}_4:\text{Cu}^{2+}$ ³ where CuF_6^{4-} shows D_{4h} compressed distortions.

In chlorides, this geometry has only been found at our knowledge in $(\text{enH}_2)\text{MnCl}_4:\text{Cu}^{2+}$,⁴ where a compressed D_{4h} distortion around the Cu^{2+} was assumed for explaining the intense CT band at $20\,800\text{ cm}^{-1}$. The existence of such a distortion was

[†] UFR Chimie, Université Joseph Fourier, Grenoble, France.

attributed to the crystal anisotropy of the 2-D layer compound $(enH_2)MnCl_4$, whose Mn^{2+} site with four long Mn-Cl in plane distances (2.65 Å) could largely favour the formation of compressed Cu^{2+} units. Recent investigation devoted to synthesize the compressed complex in other chlorides lattices have been unsuccessful.⁵

The aim of the present work is to investigate on the local structure of the $CuCl_6^{4-}$ complexes formed in the mixed $(RNH_3)_2Mn_{1-x}Cd_xCl_4$ ($x = 0 - 1$; R = Met, Et) crystals doped with 1 mol % Cu^{2+} through the polarized CT spectroscopy. This crystal family provides a wide range of metal-ligand distances for accommodating Cu^{2+} ions in D_{4h} compressed sites: $R_{eq} = 2.65$ Å and $R_{ax} = 2.56$ Å for $x = 1$, and $R_{eq} = 2.58$ Å and $R_{ax} = 2.50$ Å for $x = 0$.^{6,7}

2 EXPERIMENTAL

Single crystals of Cu^{2+} doped $(RNH_3)_2Cd_xMn_{1-x}Cl_4$ were grown by slow evaporation at 36°C of acidified aqueous and methanolic solutions containing stoichiometric amounts of RNH_3Cl , $CdCl_2$ and $MnCl_2 \cdot 4H_2O$. A 1 mol % of $CuCl_2$ was added to the solutions. Square plates habits with well developed (001) planes were obtained. The formation of mixed crystals belonging to the orthorhombic *Abma* space group was checked by X-ray diffraction. The FULLPROF program⁸ was used for analysing X-ray data and for obtaining the lattice parameters. The real Mn, Cd and Cu concentrations were measured by atomic spectroscopy. The real Mn^{2+} fraction, x , is about 50% the nominal value.

The polarized Optical Absorption (OA) spectra different temperatures have been obtained with the experimental setup described elsewhere.⁹

3 RESULTS AND DISCUSSION

3.1 Polarized OA Spectra of $(RNH_3)_2CdCl_4 \cdot Cu^{2+}$

Figure 1 shows the polarized OA spectra of the $(EtNH_3)_2CdCl_4 \cdot Cu^{2+}$ single crystal along the three orthorhombic *a*, *b* and *c* directions at 300 and 10 K. Bands around 26 000 and 36 000 cm^{-1} correspond to $Cl^- \rightarrow Cu^{2+}$ CT transitions of the $CuCl_6^{4-}$ complex formed. These transition energies and the band polarization, clearly indicate that $CuCl_6^{4-}$ displays an elongated D_{4h} symmetry with the axial Cu-Cl bonds, forming an antiferrodistortive type structure in the (001) plane. It should be noted that this situation contrasts with the local structure of the substituted $Cd^{2+}(CdCl_6^{4-} D_{4h} \text{ compressed})$, but it is similar to the corresponding $CuCl_6^{4-}$ complexes in the pure $(EtNH_3)_2CuCl_4$ ¹⁰ crystals.

The present conclusion is supported by the following facts:

- 1) The spectra show two intense bands at 25 770 and 36 460 cm^{-1} which are similar to the $e_u(\pi + \sigma)$ and $e_u(\sigma + \pi) \rightarrow b_{1g}(d_{x^2-y^2})$ CT transitions observed in $CdCl_2 \cdot Cu^{2+}$,¹¹ $(EtNH_3)_2CuCl_4$ ¹⁰ and $TMACdCl_3 \cdot Cu^{2+}$ ¹² where elongated D_{4h} complexes are formed. In fact, these CT bands for the compressed D_{4h} complex should appear at 20 800 cm^{-1} as it was observed in $(enH_2)MnCl_4 \cdot Cu^{2+}$ ⁴ and later confirmed by MS-X α calculations.¹³
- 2) The intensity of the band at 36 460 cm^{-1} which is polarized within the equatorial plane of the complex, is higher in *c* polarization. Obviously, this can not be explained by assuming that there is either a compressed or elongated axial distortion along the *c* axis. Moreover, the fact that the band intensity along *c* is twice the in-plane intensity, strongly suggests that two of the equatorial Cl^- ligands correspond to Cl^- out of the (001) plane.

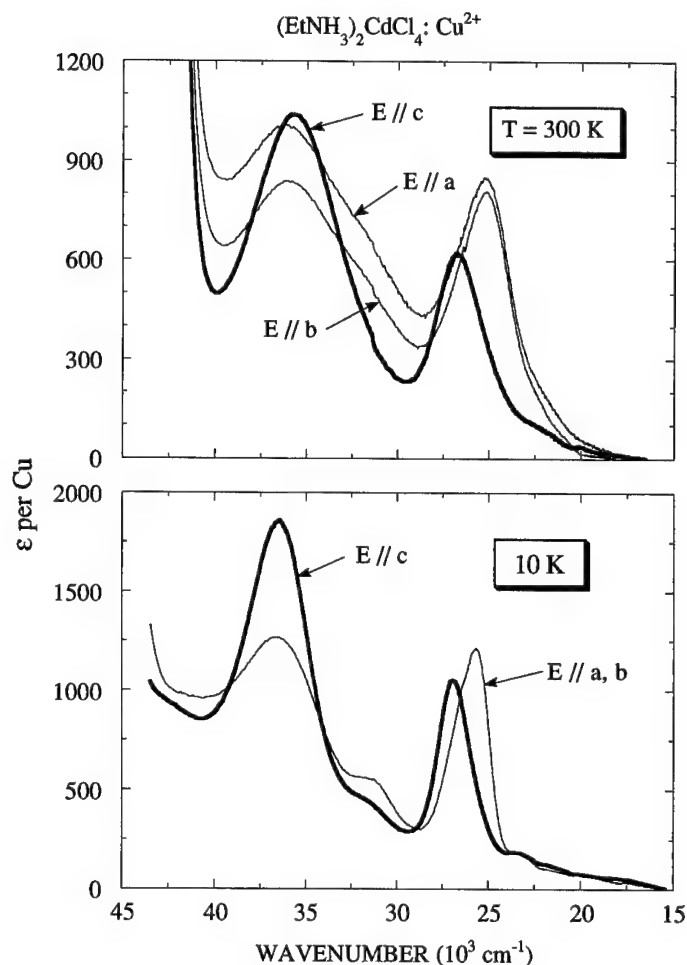


FIGURE 1 Polarized OA spectra of the $(\text{EtNH}_3)_2\text{CdCl}_4:\text{Cu}^{2+}$ single crystal at $T = 300\text{ K}$ and 10 K . Spectra were recorded with \mathbf{E} parallel to the three orthorhombic \mathbf{a} , \mathbf{b} and \mathbf{c} directions.

The spectra of Figure 1 also reveal that these two ligands are not symmetrically equivalent to the two in plane Cl^- equatorial ligands, given that the first $e_u(\pi + \sigma) \rightarrow b_{1g}(x^2 - y^2)$ CT transition (D_{4h} scheme) appears at $27\,000\text{ cm}^{-1}$ in \mathbf{c} polarization and at $25\,770\text{ cm}^{-1}$ in \mathbf{a} , \mathbf{b} polarizations (Table I). This result clearly demonstrates that the real CuCl_6^{4-} symmetry is D_{2h} , like it is expected for orthorhombic crystals.

The presence of two weak bands at $23\,100$ and $31\,200\text{ cm}^{-1}$ in the $T = 10\text{ K}$ spectra is noteworthy. The first band which is assigned to the $a_{2u}(ax; \pi + \sigma) \rightarrow b_{1g}(x^2 - y^2)$ CT transition, should be electric dipole forbidden within an elongated D_{4h} scheme. However, small deviations from this symmetry toward D_{2h} causes the ground state to transform into a_{1g} . This means that the unpaired electron wavefunction, mainly associated with $d_{x^2-y^2}$, can be mixed with $d_{3z^2-r^2}$. Thus CT transitions from the mainly ligand a_{2u} (D_{4h}) levels are

Table I

Transition energy (cm^{-1}), Polarization and Oscillator Strength, f , corresponding to the Charge Transfer bands of several $\text{A}_2\text{Cd}, \text{Mn}_{1-x}\text{Cl}_x\text{Cu}^{2+}$ crystals ($x = 1, 0.7$ and 0 ; $\text{A} = \text{CH}_3\text{NH}_3$). The assignment is made within a D_{2h} scheme of the CuCl_6^{4-} complex. Nearly elongated and compressed D_{4h} symmetries are considered for $x = 1$ and $x = 0$, respectively. a , b and c denote the orthorhombic directions; x , y and z are the local coordinate axes of the complex with z taken along the fourfold axis. The polarization is given in parenthesis. F denotes forbidden transition.

Transition Assignment				$\text{A}_2\text{CdCl}_4\text{:Cu}^{2+}$		$\text{A}_2\text{Cd}_{0.7}\text{Mn}_{0.3}\text{Cl}_4\text{:Cu}^{2+}$		$\text{A}_2\text{MnCl}_4\text{:Cu}^{2+}$	
D_{4h} elongated ${}^2\text{B}_{1g}(x^2-y^2) \rightarrow$	D_{2h} intermediate ${}^2\text{A}_g[\alpha(x^2-y^2) + \beta z^2] \rightarrow$	D_{4h} compressed ${}^2\text{A}_{1g}(z^2) \rightarrow$		observed energy $T = 10 \text{ K}$	f	observed energy $T = 300 \text{ K}$	f	observed energy $T = 300 \text{ K}$	f
${}^2\text{A}_{2u}(\text{ax}; \pi + \sigma)(\text{F})$	${}^2\text{B}_{1u}(z)$	${}^2\text{E}_g(x, y)$		23 100 (a, b, c)	10^{-4}	21 880 (a, b)	5.10^{-3}	20 860 (a, b)	7.10^{-2}
${}^2\text{E}_g(\text{eq}; \pi + \sigma)(x, y)$	${}^2\text{B}_{2u}(y)$	${}^2\text{A}_{2u}(z)$		25 770 (a, b)	8.10^{-3}	25 080 (a, b)	2.10^{-2}	24 730 (a, b)	2.10^{-2}
	${}^2\text{B}_{3u}(x)$			27 000 (c)	7.10^{-3}			26 900 (c)	3.10^{-2}
${}^2\text{B}_{2u}(\pi)(z)$	${}^2\text{B}_{1u}(z)$	${}^2\text{E}_g(x, y)$						30 675 (a, b)	10^{-3}
${}^2\text{E}_g(\text{ax}; \pi)(x, y)$	${}^2\text{B}_{2u}(y)$	${}^2\text{B}_{2u}(\text{F})$		31 200 (a, b)	5.10^{-4}				
	${}^2\text{B}_{3u}(x)$								
${}^2\text{E}_g(\text{eq}; \sigma + \pi)(x, y)$	${}^2\text{B}_{2u}(y)$	${}^2\text{A}_{2u}(z)$		36 460 (a, b)	10^{-2}			36 100 (c)	8.10^{-2}
	${}^2\text{B}_{3u}(x)$			36 460 (c)	2.10^{-2}				
${}^2\text{A}_{2u}(\text{eq}; \sigma + \pi)(\text{F})$	${}^2\text{B}_{1u}(z)$	${}^2\text{E}_g(x, y)$						36 100 (a, b)	7.10^{-3}

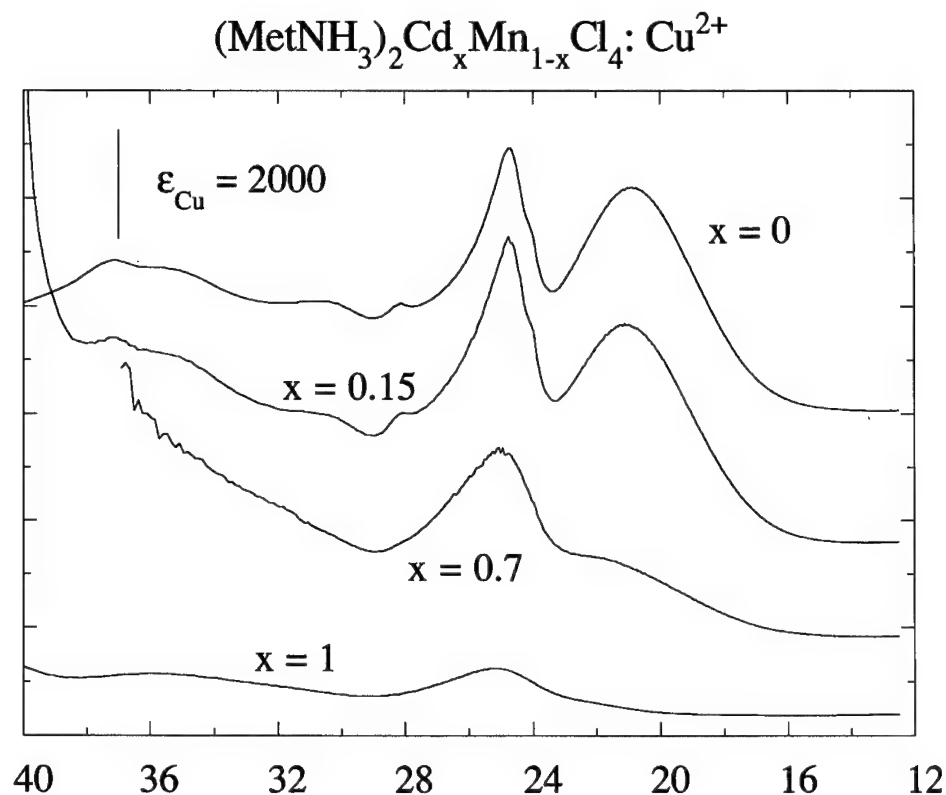


FIGURE 2 Evolution of CT spectra at $T = 300$ K along the $(\text{MetNH}_3)_2\text{Cd}_x\text{Mn}_{1-x}\text{Cl}_4 \cdot \text{Cu}^{2+}$ series from $x = 0$ to $x = 1$. Spectra were taken with E parallel to a .

partially allowed by the electric dipole mechanism. Apart from symmetry, the spin-orbit interaction of the Cl ligands weakly allows this transition.¹²

Table I shows CT band assignment; transition energies and oscillator strength for these crystals.

3.2 Influence of The Chemical Pressure

Figure 2 shows the CT spectra of the isomorphous $(\text{MetNH}_3)_2\text{Cd}_x\text{Mn}_{1-x}\text{Cl}_4$ series. Apart from Mn^{2+} , the effect of diluting Mn in the Cd network is to reduce the cation- Cl^- distances within the (001) plane. This is proved by X-ray diffraction which indicates that this distance changes from $R = 2.65 \text{ \AA}$ ($x = 1$) to $R = 2.58 \text{ \AA}$ ($x = 0$).

It is interesting to observe the enormous enhancement of the $a_{2u} \rightarrow b_{1g}$ CT band on passing from $x = 1$ (D_{4h} elongated) to $x = 0$ (D_{4h} compressed from Ref [4]). Its oscillator strength increases by three orders of magnitude and its energy shifts from $23\,100 \text{ cm}^{-1}$ for $x = 1$ to $20\,860 \text{ cm}^{-1}$ for $x = 0$. The fact that the band intensity is proportional to x rather than to the cell volume, strongly suggests that the change of the complex geometry is mainly governed by the presence of neighbor Mn ions. An elongated geometry for $x = 1$

with in-plane axial bonds, is favoured given that the Cd-Cl distance, $R = 2.65 \text{ \AA}$, is similar to the average Cu-Cl distances of the pure copper compound: $R_{ax} = 2.98 \text{ \AA}$ and $R_{eq} = 2.28 \text{ \AA}$.¹⁰ This situation is hard to be accomplished for $x = 0$ due to the bonding constrain imposed by the Mn. Therefore, the role play by the Mn is mainly to reduce and increase R_{ax} and R_{eq} , respectively, leading to nearly compressed D_{4h} with the axial Cu-Cl bond pointing along c . In this situation the CT band enhancement can be explained qualitatively by the increase of the overlap between the axial Cl^- σ -levels and the unpaired electron level which changes from $x^2 - y^2$ (zero overlap) to $3z^2 - r^2$ or other intermediates. Moreover, this increase is also favoured by the reduction of the axial Cu-Cl distance of the elongated complex. The CT redshift of 2000 cm^{-1} observed for the first CT band from $x = 1$ to $x = 0$ is consistent with previous MS-X α calculation which predict transition energies for the $e_u \rightarrow a_{1g}$ CT transition around $21\,000 \text{ cm}^{-1}$.¹³

Nevertheless, the enormous increase of the whole absorption bands on passing from $x = 1$ to $x = 0$ deserves further investigations. Another transition mechanisms involving Mn-Cu pairs as well as experiments using hydrostatic pressure techniques are currently investigated.

ACKNOWLEDGEMENTS

B.B. participated in this research with the support of an ERASMUS grant. Financial support by Caja Cantabria and the CICYT (Project No. PB92-0505) are acknowledged.

REFERENCES

1. M. A. Hitchman. *Comments Inorg. Chem.* **15**, 197 (1994).
2. D. Reinen and M. Atanasov. *Magnetic Resonance Review* **15**, 167 (1991).
3. K. Finnie, L. Dubicki, E. R. Krauz and M. J. Riley. *Inorg. Chem.* **28**, 3908 (1990).
4. U. Schmid, H. U. Güdel and R. D. Willet. *Inorg. Chem.* **21**, 2977 (1982).
5. P. J. Ellis H. C. Freeman, M. A. Hitchman, D. Reinen and B. Wagner. *Inorg. Chem.* **33**, 1249 (1994).
6. W. Depmeier, J. Felsche and G. Wildermuth. *J. Solid State Chem.* **21**, 57 (1977).
7. N. Lehner, K. Strobel, R. Geik and G. Heger, *J. Phys. C: Solid State Phys.* **8**, 4096 (1978).
8. J. Rodríguez, N. Anne and J. Pannetier, *Internal Report No. 87R014T* (1987). Institut Laue Langevin.
9. M. C. Marco de Lucas and F. Rodríguez. *J. Phys.: Condens. Matter* **5**, 2625 (1993).
10. S. R. Desjardins, K. W. Penfield, S. L. Cohen, R. L. Musselman and E. I. Soloman. *J. Am. Chem. Soc.* **105**, 4590 (1983).
11. K. Kan'no, S. Naoe, S. Mukai and Y. Nakai. *Solid State Commun.* **13**, 1325 (1973).
12. R. Valiente, M. C. Marco de Lucas and R. Rodríguez. *J. Phys.: Condens. Matter* **6**, 4527 (1994).
13. J. A. Aramburu and M. Moreno. *Journal de chimie physique* **86** 871 (1989).

OPTICAL PROPERTIES AND LOCAL STRUCTURE OF MnCl_6^{4-} IN $\text{ABCl}_3:\text{Mn}^{2+}$

M. C. MARCO DE LUCAS, F. RODRÍGUEZ,[§] C. PRIETO*, M. VERDAGUER,^{†a} M. MORENO and H. U. GÜDEL**

*D.C.T.T.YM. Facultad de Ciencias, Universidad de Cantabria, 39005 Santander, Spain; * Instituto de Ciencias de Materiales (C.S.I.C.) Facultad de Ciencias, (C-IV), Cantoblanco 28049 Madrid Spain; †Laboratoire de Chimie des Metaux de Transition, Université Pierre et Marie Curie, 75252 Paris, Cedex 05, France; ^a L.U.R.E., Université Paris-Sud, 91405 Orsay Cedex, France; ** Institut Für Anorganische Chemie der Universität Bern, Freiestrasse 3, CH-3000, Bern 9, Switzerland*

The optical properties of $\text{ABCl}_3:\text{Mn}^{2+}$ crystals are investigated in the 300–10 K temperature range. The variation of the peak energy and the Stokes shift along the series are explained in terms of slight differences in the Mn–Cl distance. The local structure around the Mn is determined by correlating optical spectroscopy and EXAFS techniques. Interestingly, the thermal shift of the ${}^6\text{A}_{1g} \rightarrow {}^4\text{T}_{1g}$ excitation band is much smaller than that experienced by the corresponding emission band. This behaviour is explained by the phonon assisted mechanism involve in these transitions. The influence of the structural phase transition of the $\text{CsCaCl}_3:\text{Mn}^{2+}$ at $T_C = 95$ K upon the thermal band shift is also analysed.

Key words: Excitation and luminescence; $\text{ABCl}_3:\text{Mn}^{2+}$ perovskites; MnCl_6^{4-} complex; Thermal Shift; Local structure around Mn^{2+} ; Influence of bond distances.

1 INTRODUCTION

The investigations devoted to correlate the optical properties of transition metal complexes with the metal-ligand distance, R , are important not only for a microscopic understanding of the variations of such properties with chemical or hydrostatic pressures but also for explaining their temperature dependence. In fact, the temperature dependence of spectroscopic parameters such as the peak energy, Stokes shift and lifetime with the temperature is governed by two main contributions: 1) the explicit contribution which is associated with variations in the thermal population at constant volume, and 2) the implicit contribution which reflects the changes induced by thermal expansion effects. The importance of these contributions can not be revealed unless the variation of these parameters with R has been properly established. In the case of luminescent materials, such correlations are difficult to make in concentrated materials since the emission band is greatly influenced by the exciton dynamics in exchange coupled systems. Though, this problem can be largely overcome using diluted materials, difficulties arise to determine bond distances around the impurity.

The aim of this work is to investigate the excitation and luminescence spectra as well as the lifetime in the 10–300 K temperature range of MnCl_6^{4-} complexes formed in the $\text{ABCl}_3:\text{Mn}^{2+}$ perovskite crystals. In the present case, the selected crystal family provides a wide range of molecular cell volumes¹ ($\Delta a = 0.66$ Å) for accommodating the Mn impurity which is important to establish structural correlations. In this way, we report the first local structural determinations on $\text{KMgCl}_3:\text{Mn}^{2+}$ and $\text{RbCaCl}_3:\text{Mn}^{2+}$ through EXAFS which confirm the previous Mn–Cl distance estimates based on the variation of the

[§] Author for correspondence.

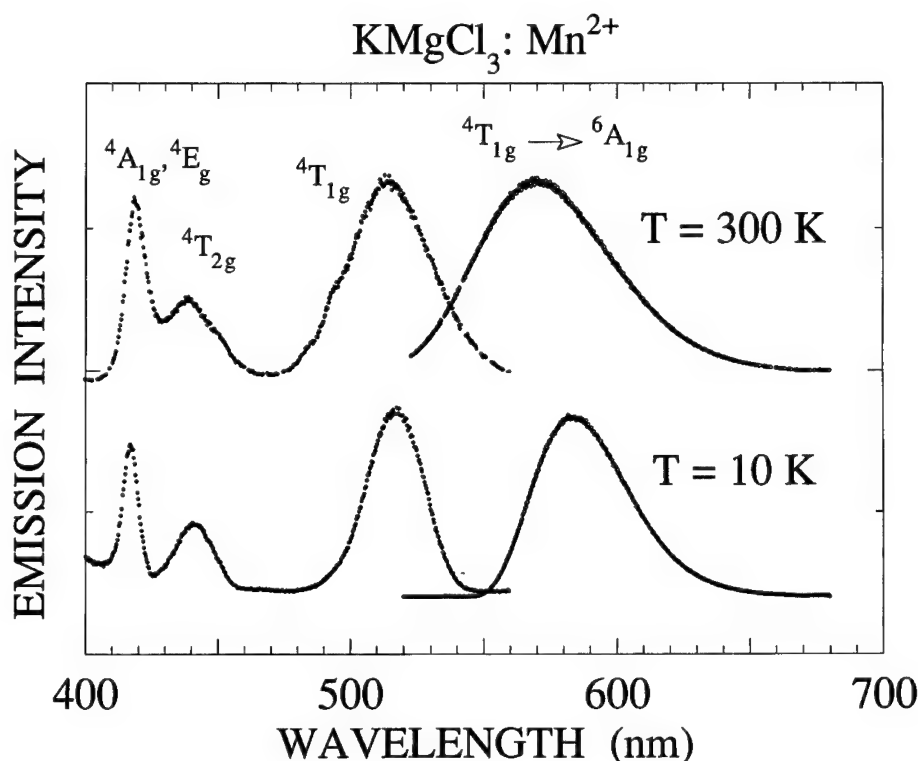


FIGURE 1 Time resolved emission and excitation spectra of the $\text{KMgCl}_3 : \text{Mn}^{2+}$ crystal at 10 and 300 K.

crystal field parameter, $10Dq$, along the whole $\text{ABCl}_3 : \text{Mn}^{2+}$ series.¹ Attention will be also paid on the variations experienced by the peak energy and the Stokes shift with temperature. The results of this investigation are compared with those previously found for MnF_6^{4-} in $\text{ABF}_3 : \text{Mn}^{2+}$.²

2 EXPERIMENTAL

Single crystals of MnCl_2 -doped KMgCl_3 , KCaCl_3 , RbCdCl_3 , RbCaCl_3 , CsSrCl_3 , RbSrCl_3 were grown by the Bridgman technique as described elsewhere.¹ The time resolved emission and excitation spectra as well as the lifetime at different temperatures were obtained by usual procedures.² The EXAFS experiments have been performed in the XAS-3 (DCI) station at LURE (Orsay) using the fluorescence mode. Suitable spectra could be obtained for $\text{KMgCl}_3 : \text{Mn}^{2+}$ and $\text{RbCaCl}_3 : \text{Mn}^{2+}$. No Mn signal was detected for the remainder crystals due to the intense X-ray fluorescence from the Cs and Cd ions as well as to some hydration problems with $\text{KCaCl}_3 : \text{Mn}^{2+}$ and $\text{CsSrCl}_3 : \text{Mn}^{2+}$. EXAFS data were analysed using the Michalowicz software package program,³ kindly provided by the author. In both cases, the EXAFS oscillations associated with the first coordination sphere around Mn are well described by an octahedral MnCl_6^{4-} unit with Mn-Cl distances, $R = 2.51$ and 2.53 \AA ($\Delta R = 0.02 \text{ \AA}$) for $\text{KMgCl}_3 : \text{Mn}^{2+}$ and $\text{RbCaCl}_3 : \text{Mn}^{2+}$, respec-

Table I

Structural and spectroscopic parameters of $ABCl_3:Mn^{2+}$ crystals. Bond distances and peak energies are given in Å and cm^{-1} , respectively. ΔE_{ex} and ΔE_{em} are the thermal shifts from 10 K to 300 K for excitation and emission, respectively. The τ_o and $\hbar\omega_u$ parameters were obtained from data of Figure 2. Units in ms and cm^{-1} , respectively.

Compound	R(Mn-Cl)	$^4T_{1g}$ Excit.		Emission		Stokes shift 300 K	ΔE_{ex}	ΔE_{em}	τ_o	$\hbar\omega_u$
		300 K	10K	300 K	10K					
KMgCl ₃ :Mn ²⁺	2.51	19440	19330	17530	17100	1910	110	430	50	186
KCaCl ₃ :Mn ²⁺	2.54	20010	19940	17920	17260	2090	70	660	57.1	183
CsCaCl ₃ :Mn ²⁺	2.55	20100	19880	18190	17150	1910	220	1040	53.6	181
CsSrCl ₃ :Mn ²⁺	2.57	20240		18080	17300	2160		780	54.3	184

tively. These results must be compared with 2.51 and 2.54 Å derived from the crystal field splitting parameter, $10Dq$.¹

3 RESULTS AND ANALYSIS

Figure 1 shows the emission and the corresponding excitation spectra of KMgCl₃:Mn²⁺ at 10 and 300 K. Similar spectra are found for the remainder crystals of the family.¹ The bands correspond to d^5 intraconfigurational transitions of the octahedral $MnCl_6^{4-}$ complex. The variations of the $^4T_{1g}$ excitation and the emission bands in the 10–300 K temperature range are depicted in Figure 2 together with those of the lifetime, $\tau(T)$, for several $ABCl_3:Mn^{2+}$ crystals. The more relevant spectroscopic and structural parameters are given in Table I.

1) *Influence of the Mn-Cl distance.* The variation of the excitation and emission bands, E_{ex} and E_{em} , and the Stokes shift, ΔE_s , along the $ABCl_3:Mn^{2+}$ series can be explained by the slight variations of the Mn-Cl distance in the $MnCl_6^{4-}$ complex. The R values for the whole series have been derived from $10Dq$ on the assumption that $10Dq \propto R^{-5}$. The estimated R values coincide with those derived from EXAFS and therefore confirm the assumed R-dependence for $10Dq$. It is interesting to point out that the same dependence has been found experimentally^{2,4} for MnF_6^{4-} and also confirmed by MS-X α and Extended Hückel calculations⁵ which demonstrate that $10Dq$ is proportional to R^{-n} with n close to 5 for different transition metal complexes, irrespective of the nature of the halogen ligands. It must be emphasized that this procedure provides an accurate method for determining Mn-Cl distances since accuracies in $10Dq$ of 30 cm^{-1} would lead to accuracies in R of 3×10^{-3} Å, thus improving the present EXAFS resolution. A salient feature of these R estimates concerns the high lattice relaxation around Mn²⁺ found in chlorides. If we denote by ΔR_L the difference between the B-Cl distance in the host lattice and 2.525 Å corresponding to the Mn-Cl distance in the pure NH_4MnCl_3 perovskite,⁶ it is found that the variation of R along the $ABCl_3:Mn^{2+}$ series is $\Delta R = 0.18 \Delta R_L$ whereas $\Delta R = 0.30 \Delta R_L$ for $ABF_3:Mn^{2+}$. This significant difference is likely due to the smaller compressibilities of the fluorides.

As regards Table I, two important facts must be underlined: 1) Both E_{em} and E_{ex} shift to lower energies upon increasing R according to the Tanabe Sugano diagram for d^5 ions.

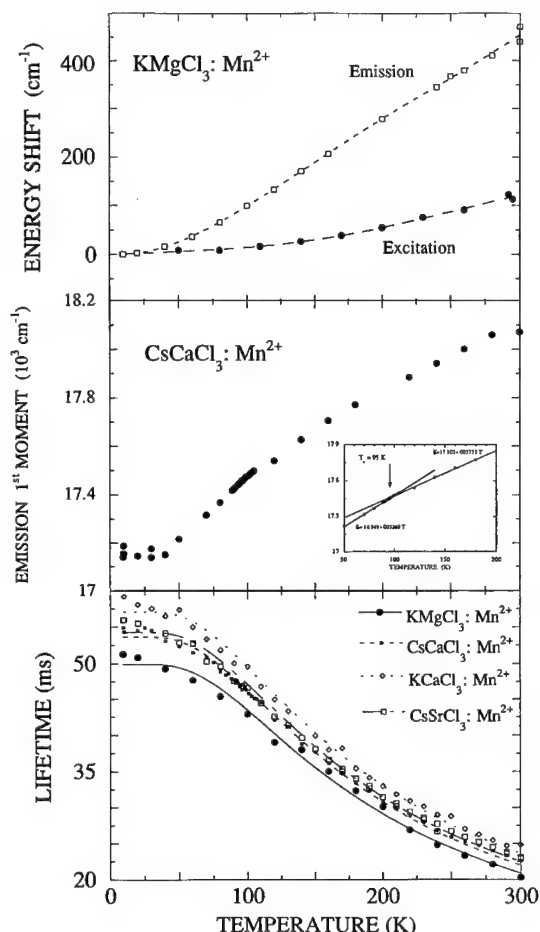


FIGURE 2 (Top): Thermal shifts of the ${}^6A_{1g} \rightarrow {}^4T_{1g}$ excitation and the corresponding emission bands of $\text{KMgCl}_3:\text{Mn}^{2+}$ in the 10–300 K temperature range. The shifts are calculated from first moment analysis and are taken zero at $T=10$ K. (Middle): Variation of the emission first moment of $\text{CsCaCl}_3:\text{Mn}^{2+}$ from 10 K to 300 K. The inset shows a magnification around the phase transition temperature, $T_C = 95$ K. (Bottom): Temperature dependence of the lifetime, $\tau(T)$, for several $\text{ABCl}_3:\text{Mn}^{2+}$ crystals. The curves are fittings to the equation $\tau(T) = \tau_0 T(\hbar\omega_u/2KT)$. The τ_0 and $\hbar\omega_u$ parameters are given in Table I.

2) This shift is quite different for emission and excitation, reflecting an increase of the Stokes shift, $\Delta E_s \propto R^\beta$ with $\beta = 10$ is measured for the present systems while $\beta = 5$ is found for MnF_6^{4-} along the $\text{ABF}_3:\text{Mn}^{2+}$ series. Following the analysis of ref. 5, this difference can be explained on the assumption that the Grüneisen parameter associated with the totally symmetric vibrational mode, increases on passing from fluorides to chlorides.

2) *Temperature dependence of the peak energy and the lifetime.* The spectra of Figure 1 show that the 10Dq-dependent ${}^4T_{1g}$ and ${}^4T_{2g}$ excitation bands and the emission band shift to lower energies upon cooling, like it is expected for a reduction of R by thermal effects. However, it is worth noting that the emission thermal shift is about 5 times

higher than the corresponding excitation shift (Figure 2 and Table I). This behaviour which has also been found in MnF_6^{4-} and other Mn pure- or doped compounds, is responsible for the good sensitivity exhibited by the emission bands to detect structural phase transitions of the host crystal. Previous studies carried out on $RbCaF_3:Mn^{2+2}$ and $RbCdF_3:Mn^{2+7}$ and TMA_2MnCl_4 ⁸ crystals confirm this fact. Furthermore, the emission thermal shift, ΔE_{em} , increases almost twice on passing from $KMgCl_3:Mn^{2+}$ to $CsSrCl_3:Mn^{2+}$ (Table I). This difference is probably related to the higher thermal expansion coefficient of the $MnCl_6^{4-}$ complex in $CsSrCl_3:Mn^{2+}$. Such an interpretation is based on the fact that the room temperature Mn-Cl distance, $R = 2.57 \text{ \AA}$, is far above the equilibrium distance for NH_4MnCl_3 and thus such a situation could facilitate a stronger reduction of R upon cooling. By contrast, smaller variations $R(T)$ should be expected for $KMgCl_3:Mn^{2+}$ since $R(300)$ is significantly shorter than 2.525 \AA .

A noteworthy fact is the high values of ΔE_{em} and ΔE_{ex} measured for $CsCaCl_3:Mn^{2+}$ (Table I). Such *anomalous* shifts are a consequence of the $Pm3m \rightarrow I4/mbm$ phase transition (PT) undergone by this crystal at $T_c = 95 \text{ K}$.⁹ The occurrence of such a PT is well detected through these spectroscopic tools, by the abrupt jump experienced by the slope $\partial E_{em}/\partial T$ around T_c (inset of Figure 2). Moreover, this jump ($1.5 \text{ cm}^{-1}/\text{K}$ for $CsCaCl_3:Mn^{2+}$) is 6 times higher than those measured for $RbCdF_3:Mn^{2+7}$ and $RbCaF_3:Mn^{2+2}$ in the $Pm3m \rightarrow I4/mcm$ PTs at 124 and 193 K, respectively, and therefore reflects the strong influence of these PTs in the Mn^{2+} emission of $MnCl_6^{4-}$.

The different thermal shift observed for excitation and emission for all crystal is mainly related to the odd parity phonon assistance mechanism required to gain electric dipole intensity in centrosymmetric systems. This mechanism would shift $\pm \hbar\omega_u$ the excitation (+) and the emission (−) bands at low temperature. The variation $\tau(T)$ (Figure 2), following the equation: $\tau(T) = \tau_o \text{Th}(\hbar\omega_u/2KT)$, confirms that this mechanism is dominant for the present transitions. The fit $\hbar\omega_u$ and τ_o values for the studied crystals are given in Table I. Note that the effective phonon energy is close to the high energy odd parity modes of the $MnCl_6^{4-}$ complex whereas τ_o is significantly larger than those measured at low temperatures in other chlorides containing isolated- or exchange coupled- $MnCl_6^{4-}$ units in low symmetry sites such as the 1-D $CsMnCl_3(1 \text{ ms})$ ¹⁰ and $(CH_3)_4NMnCl_3(0.8 \text{ ms})$ ¹¹ or the 2-D $CH_3NH_3CdCl_4:Mn^{2+}(12 \text{ ms})$ ¹² and $CH_3NH_3MnCl_4(3.3 \text{ ms})$.¹² On the other hand, τ_o is three times smaller than those measured in $KMgF_3:Mn^{2+}$ and $KZnF_3:Mn^{2+13}$. This reduction of the lifetime when F^- is replaced by Cl^- , is likely associated with the lower energy of the odd parity charge transfer states in $MnCl_6^{4-}$. Apart from the particular values of the vibronic coupling coefficients, the energy difference between the charge transfer states for chlorides and fluorides (about 30000 cm^{-1} according to the optical electronegativity difference for F^- and Cl^- ¹⁴) could account for almost a factor 2 in τ_o .

ACKNOWLEDGEMENTS

Thanks are due to Dr. A. Michalowicz for providing us with the software programs for EXAFS analysis. Financial support from the Swiss National Science Foundation and the CICYT (Project No PB92-0505) is acknowledged.

REFERENCES

1. M. C. Marco de Lucas, F. Rodríguez, H. U. Güdel and N. Furer. *J. Lumin.* **60 & 61**, 581 (1994).
2. M. C. Marco de Lucas, F. Rodríguez and M. Moreno. *J. Phys.: Condens. Matter* **5**, 1437 (1993).
3. A. Michalowicz, 'EXAFS pour le MAC, Logiciels pour la Chimie', Société Française de Chimie. Paris (1991).

4. F. Rodríguez and M. Moreno. *J. Chem. Phys.* **84**, 692 (1986).
5. M. Moreno, M. T. Barriuso and J. A. Aramburu, *J. Phys.: Condens. Matter.* **4**, 9841 (1992).
6. F. Agulló-Rueda, J. M. Calleja, F. Jaque and J. D. Tornero, *Solid State Comm.* **60**, 331 (1986).
7. M. C. Marco de Lucas, F. Rodríguez and M. Moreno. *J. Phys.: Condens. Matter.* **6**, 6353 (1994).
8. M. C. Marco de Lucas and F. Rodríguez. *J. Phys.: Condens. Matter.* **1**, 4252 (1989).
9. Y. Vaills, J. Y. Buzaré, A. Gibaud and C. Launay *Solid State Comm.* **60**, 139 (1986).
10. U. Kambli and H. U. Güdel. *Inorg. Chem.* **23**, 3479 (1984).
11. M. C. Marco de Lucas and F. Rodríguez. *Rev. Sci. Instrum.* **61**, 23 (1990).
12. P. Day, G. Ingleto, T. Low, J. O. R. Norris and B. Stewart *J. Chem. Soc., Faraday Trans. 2*, 1201 (1985).
13. F. Rodríguez, H. Riesen and H.U. Güdel. *J. Lumin.* **50**, 101 (1991).
14. C. K. Jørgensen. *Prog. Inorg. Chem.* **12**, 101 (1970).

PHOTO-EPR STUDIES OF ELECTRON AND HOLE TRAPPING BY $[\text{Fe}(\text{CN})_6]^{4-}$ COMPLEXES IN SILVER CHLORIDE

M. T. OLM and R. S. EACHUS

Eastman Kodak Company, Rochester, New York, USA

$[\text{Fe}(\text{CN})_6]^{4-}$ was incorporated into silver chloride powders precipitated from aqueous solution with all six cyanide ligands intact. The most notable feature of this dopant was its amphoteric behavior, acting as either a deep hole trap or a shallow electron trap. The filled t_{2g} orbital manifold of this complex lies below the Fermi level, which places the vacant e_g levels well above the conduction band minimum. The trapping behavior of $[\text{Fe}(\text{CN})_6]^{4-}$ was determined by whether or not it was closely associated with a charge-compensating silver ion vacancy.

Key words: iron hexacyanide, silver chloride, hole-trap, EPR, vacancy, dopant.

1 INTRODUCTION

Small quantities of transition metal complexes are often used to control the behavior of photocarriers in the silver halide microcrystals that make up conventional photographic film. Electron paramagnetic resonance studies of the photodynamics of doped silver halide single crystals and microcrystals (photo-EPR) have been valuable in understanding these doped systems.

Interest in the dopant $[\text{Fe}(\text{CN})_6]^{4-}$ was initially sparked by the observation of hole-trapping by Fe^{2+} in AgCl single crystals and by the desire to reduce recombination inefficiencies in silver halide photographic systems.^{1,2,3} The studies reported here show that the trapping properties of the $[\text{Fe}(\text{CN})_6]^{4-}$ dopant are more complicated than initially supposed.

2 EXPERIMENTAL

Silver chloride precipitates were prepared doped with between 25 and 50 parts per million of $\text{K}_4\text{Fe}(\text{CN})_6 \cdot 3\text{H}_2\text{O}$, or, where noted $\text{K}_3\text{Fe}(\text{CN})_6$. Some of these powders were treated with chlorine gas prior to examination by EPR. This treatment results in the injection of valence band holes and silver ion vacancies into the AgCl crystallites and was useful in assessing the hole-trapping propensities of the dopants. EPR studies were done with a Varian E-9 EPR spectrometer. Samples were irradiated in situ at 365 nm with the filtered output of a 200 W super pressure mercury lamp. The samples were irradiated at temperatures between 10 and 300 K. Irradiations below room temperature stabilized short-lived intermediates and shallowly-trapped carrier centers.

3 RESULTS AND DISCUSSION

After treatment with chlorine at room temperature or after irradiation with band gap light, an EPR spectrum was obtained, the overall intensity of which was dependent on the nominal $[\text{Fe}(\text{CN})_6]^{4-}$ dopant concentration (Figure 1). The EPR spectrum was made up of

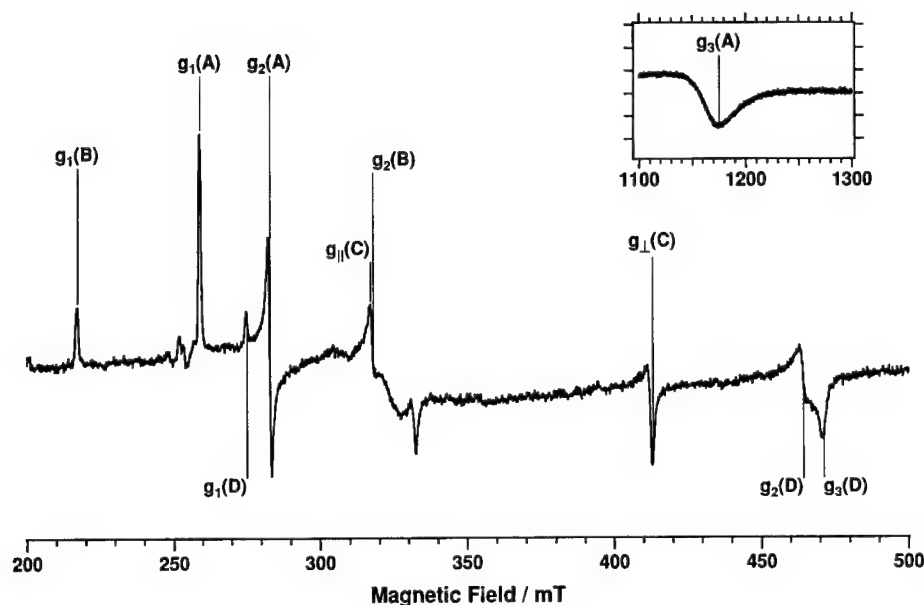


FIGURE 1 EPR spectrum, measured at 20 K, produced by the room temperature, 365 nm irradiation of a $[\text{Fe}(\text{CN})_6]^{4-}$ -doped, AgCl powder.

signals from *four* different paramagnetic species. The g -values measured for these centers are given in Table I. Although, no superhyperfine splittings were resolved, line broadening was detected in AgCl powders doped with $[\text{Fe}^{13}\text{CN}]_6^{4-}$. This indicates that at least several cyanide ligands remained coordinated to each Fe^{2+} ion after incorporation. Indeed, given the high stability of the ferrocyanide ion in aqueous solution, it seems likely that all of the ligands remained associated during incorporation.

The data listed in Table I are similar to those reported for $[\text{Fe}(\text{CN})_6]^{3-}$ centers in $\text{K}_3\text{CoCN}_6^4$ and NaCl^5 host lattices and support the assignment of the species observed to four structurally inequivalent $[\text{Fe}(\text{CN})_6]^{3-}$ centers substituting in the lattice for $[\text{AgCl}_6]^{5-}$. The most likely structural characteristic that would distinguish these centers is the spatial distribution of charge compensating silver ion vacancies (V) around the dopant.⁶ Two silver ion vacancies are required for complete charge compensation.

The single crystals necessary for complete structural studies could not be prepared, since $[\text{Fe}(\text{CN})_6]^{4-}$ decomposes during high temperature growth. Nevertheless, some structural information is available from the powder EPR studies. Complex C (Figure 1) had a powder pattern characteristic of a center with axial symmetry and was therefore amenable to a molecular orbital analysis such as that described by Griffith.⁷ This showed that C was compressed along its symmetry axis. There are a limited number of arrangements of vacancies that would result in this distortion and following the arguments in reference 6, we can assign C to a $[\text{Fe}(\text{CN})_6]^{3-}$ complex with two next nearest neighbor vacancies (V_{nnn}) axially opposed along the $[100]$ distortion axis. The species B was by far the most stable Fe^{3+} center. It was the sole center produced by direct doping with $[\text{Fe}(\text{CN})_6]^{3-}$; oddly, it was produced only in low yield by chlorination or irradiation compared to centers A, C, and D. This must be because B and A, C, D arise from different $\text{Fe}^{2+} \cdot V$ precursors. Since C (and therefore A and D) most likely arise from a $\text{Fe}^{2+} \cdot V_{\text{nnn}}$

Table I
g Factors for $[\text{Fe}(\text{CN})_6]^{3-}$ Centers in AgCl

Center	g_1	g_2	g_3	g_{av}
A	2.565 (7)	2.348 (2)	0.566 (8)	2.035
B	3.056 (0)	2.091 (0)	(a)	—
C	1.607 (8)	1.607 (8)	2.098 (7)	1.787
D	1.413 (0)	1.417 (5)	2.417 (3)	1.812
I				1.783 (0)
E	2.289 (2)	2.091 (1)	(a)	—

(a) Values not obtained experimentally

precursor, B must result from a $\text{Fe}^{2+} \cdot \text{V}_{nn}$ center (nn = nearest neighbor). Once hole trapping at either neutral center occurs, the positively charged product is stabilized by association with a second vacancy.

Hole trapping at $\{[\text{Fe}(\text{CN})_6]^{4-} \cdot \text{V}\}$ occurs because the dopant introduces occupied energy levels into the AgCl bandgap. These levels are derived from the t_{2g} orbital manifold of the $[\text{Fe}(\text{CN})_6]^{4-}$ complex. Since the Fe^{3+} states were observed to be metastable, the levels derived from the t_{2g} manifold must lie below the Fermi level. Since the ligand field splitting for the ferrocyanide ion far exceeds the bandgap energy of AgCl, the vacant e_g derived dopant levels lie above the conduction band edge. Thus, the ferrocyanide complexes cannot act as a deep electron traps to produce $[\text{Fe}(\text{CN})_6]^{5-}$.

The exposure of $[\text{Fe}(\text{CN})_6]^{4-}$ -doped silver chloride powders to band-to-band excitation at temperature below 200 K produced a single, intense symmetric EPR line that has previously been assigned to electrons equilibrating between conduction band and shallow trap states.⁸ This line had a g -value of 1.8781 ± 0.0005 at 20 K. The g -value of the signal increased as the temperature was raised above 50 K and its linewidth narrowed from about 1.5 mT at 13 K. to constant value of 0.15 mT above about 60 K. These spectral changes reflect the excitation of photoelectrons from shallow trap states to conduction band states as the temperature was raised.

The intensity of the low-temperature EPR signal was dependent on the $[\text{Fe}(\text{CN})_6]^{4-}$ concentration and thus must result from electron trapping at defects introduced by doping. Coulombic arguments would suggest that the shallow electron trapping centers are uncompensated $[\text{Fe}(\text{CN})_6]^{4-}$ complexes. These nominally have a positive charge of +1 with respect to the silver chloride lattice. The effective mass model predicts these traps would have a depth in AgCl of the order of 65 meV.²

The presence of uncompensated $[\text{Fe}(\text{CN})_6]^{4-}$ complexes was confirmed with the observation of a symmetric line at $g = \pm 0.001$ in AgCl samples doped directly with $[\text{Fe}(\text{CN})_6]^{3-}$ and irradiated at 20 K. The $[\text{Fe}(\text{CN})_6]^{3-}$ dopant was incorporated as a mixture of $[\text{Fe}(\text{CN})_6]^{3-}$ and $[\text{Fe}(\text{CN})_6]^{4-}$ states. The $[\text{Fe}(\text{CN})_6]^{3-}$ centers acted as deep electron traps at low temperatures and prevented electron trapping by uncompensated $[\text{Fe}(\text{CN})_6]^{4-}$ centers. In the absence of recombination, the uncompensated $[\text{Fe}(\text{CN})_6]^{4-}$ centers acted as hole traps. The high symmetry $[\text{Fe}(\text{CN})_6]^{3-}$ center (I) so produced had a g -value close to the average g -value measured for the anisotropic, vacancy compensated $[\text{Fe}(\text{CN})_6]^{3-}$ centers C and D. A new, anisotropic center, E, was also formed during low temperature exposure of $[\text{Fe}(\text{CN})_6]^{3-}$ -doped samples (Table I). This center is most likely a partially compensated $\{[\text{Fe}(\text{CN})_6]^{3-} \cdot 1\text{V}\}$ center produced by hole trapping at compensated $[\text{Fe}(\text{CN})_6]^{4-}$ centers. Low temperatures quench ionic motion and compensation by a second vacancy was not possible at 20 K. Both E and I decayed on warming above 50 K.

Quenching of ionic motion at low temperatures also precludes the formation of atomic silver clusters (latent image). This extends the lifetimes of electrons associated with the shallow traps to the point where they can be detected by EPR. In doped samples exposed below about 150 K, the electron EPR signal at $g = 1.8781$ did not decay and photoconductivity was persistent. By analogy with the effects of other shallow electron trapping dopants (Pb^{2+} and Cd^{2+}), the room temperature lifetime of the photoelectron, before its permanent removal to form latent image, will also be extended.⁹

In summary, $[\text{Fe}(\text{CN})_6]^{4-}$ was incorporated into silver chloride powders and acted as either a deep hole trap or a shallow electron trap, depending on whether or not it was closely associated with a charge-compensating silver ion vacancy. Hole-trapping is expected to reduce losses from recombination in practical systems. Shallow electron trapping is expected to extend the photoelectron lifetime. Clearly, both must be considered when evaluating the photographic effects of the dopant $[\text{Fe}(\text{CN})_6]^{4-}$.

REFERENCES

1. K. A. Hay, D. J. E. Ingram, A. C. Tomlinson, *J. Phys. C: Solid State Phys.*, **1**, 1205 (1968).
2. J. F. Hamilton, *Adv. Phys.* **37** 359 (1988).
3. J. W. Mitchell, *J. Imaging Sci. Technol.* **37** 33 (1993).
4. J. M. Baker, B. Bleaney, and K. D. Bowers, *Proc. Phys. Soc. B* **69** 1205 (1956).
5. D. M. Wang, S. M. Meijers, and E. de Boer, *Mol. Phys.* **70** 1135 (1990).
6. D. A. Corrigan, R. S. Eachus, R. E. Graves and M. T. Olm *J. Chem. Phys.* **70** 5676 (1979).
7. J. S. Griffith, *The Theory of Transition Metal Ions* (Cambridge University Press, Cambridge, 1964) pp. 363–366.
8. R. S. Eachus, M. T. Olm, R. Janes, and M. C. R. Symons, *Phys. Status Solidi (b)* **152** 583 (1989).
9. J. P. Spoonhower and R. S. Eachus, *Phot. Sci. Eng.* **26** 20 (1982).

SITE SELECTIVE SPECTROSCOPY OF Eu^{3+} AND Eu^{3+} - Ho^{3+} DOPED GLASSES

V. D. RODRÍGUEZ, V. LAVÍN, U. R. RODRÍGUEZ-MENDOZA, I. R. MARTÍN
and P. NUÑEZ*

*Dpto. Física Fundamental y Experimental. Universidad de La Laguna 38206 La Laguna,
Tenerife. SPAIN; *Dpto. de Química Inorgánica. Universidad de La Laguna
38206 La Laguna, Tenerife, SPAIN*

A study of the optical properties of the Eu^{3+} ions in borate glasses and their correlation with the local environment of the ions is presented. From luminescence spectra and emission decay curves with narrow band excitation of the $^5\text{D}_0$ level, the Judd-Ofelt parameters are calculated as a function of the excitation wavelength. In codoped glasses the non radiative energy transfer process from Eu to Ho has been studied; the energy transfer parameter is also found to depend on the wavelength excitation.

Key words: luminescence, site selective spectroscopy, Eu, Ho, borate glasses.

1 INTRODUCTION

Insulating materials doped with Rare Earth ions have been extensively studied by site selective spectroscopy in order to obtain precise information about the local environment of the ions. In these works the Eu^{3+} ion has been the predominant choice because the ground ($^7\text{F}_0$) and the lower emitting ($^5\text{D}_0$) levels are nondegenerate for this ion, then they are not splitted by the crystal field.

The radiative transitions of the Rare Earths occurring in the 4f shell are parity forbidden for electric dipole processes. However, the electric dipole transitions, forced by the odd-parity terms of the crystal field, use to have larger probability than the magnetic dipole transitions.

The electric dipole transition probabilities can be evaluated using the Judd-Ofelt (J-O) theory.^{1,2}

$$A = \frac{64\pi^4 e^2}{3h\lambda^3 (2J+1)} \chi_{\text{ed}} \sum_{\kappa=2,4,6} \Omega_{\kappa} | \langle \| U^{(\kappa)} \| \rangle |^2$$

where Ω_{κ} represents the J-O parameters and $U^{(\kappa)}$ are tensor operators of rank κ .

The physical meaning of the J-O parameters is still not very clear but comparing values of these parameters for different materials it is found that Ω_2 depends strongly on the ion environment while Ω_4 seems to depend on long range effects.^{3,4}

In the emission spectra obtained exciting the $^5\text{D}_0$ level the peaks corresponding to transitions to the different $^7\text{F}_J$ levels are found. The $^5\text{D}_0 \rightarrow ^7\text{F}_1$ transition is magnetic dipole allowed. For $J = 2, 4$ and 6 the transitions are electric dipole; for $J = 2$ the probability of the transition depends on Ω_2 , for $J = 4$ on Ω_4 and for $J = 6$ on Ω_6 .

The probabilities of the transitions from the $^5\text{D}_0$ level to $^7\text{F}_J$ levels can be evaluated with the lifetime of the $^5\text{D}_0$ level and the areas of the emission peaks. With these probabilities the J-O parameters can be obtained.

We have used this method with measurements obtained with narrow band excitation all along the $^7\text{F}_0 \rightarrow ^5\text{D}_0$ excitation spectra. By this way the dependence of the Judd-Ofelt parameters with the environment of the Eu is determined.

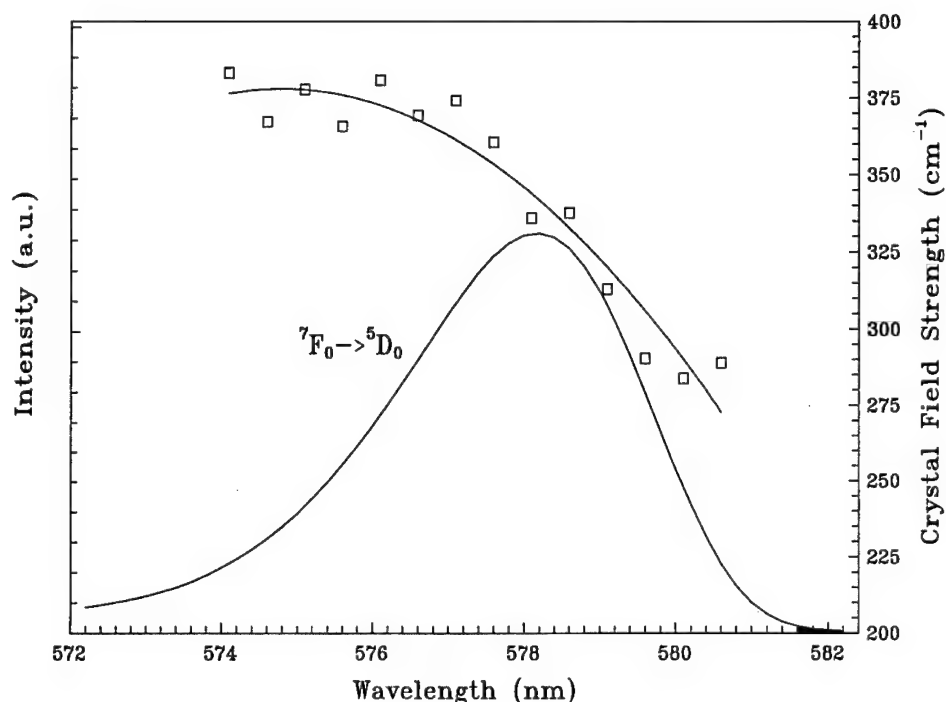


FIGURE 1 Inhomogeneous excitation profile of the transition ${}^7F_0 \rightarrow {}^5D_0$ at 10 K. Crystal field strength for different excitation wavelengths (\square).

2 RESULTS AND DISCUSSION

The glasses used in this work were prepared with the starting composition in mol% 66.6 B_2O_3 and 33.3 CaO and the concentration of Eu and Ho in the range from 0 to 2.5 mol%. All the spectra have been recorded at 10 K in order to avoid the thermalization of the ground state 7F_0 with the excited state 7F_1 .

Figure 1 shows the inhomogeneous excitation profile of the transition ${}^7F_0 \rightarrow {}^5D_0$. Also in this figure the crystal field strength related to the Eu^{3+} ions excited in different wavelengths is included. Details of these calculations were included in a previous work;⁵ C_{2v} symmetry, which allows full splitting of the 7F_1 and 7F_2 levels,⁶ was assumed and the equations given by Lempicki *et al.*⁷ were used; the obtained results, analyzed in the frame of the Brecher-Riseberg model,⁶ indicated the presence of sites in the full range from eight to nine coordinating oxygens.

The lifetimes obtained with narrow band excitation to the 5D_0 are showed in Figure 2. In spite of the known energy transfer process between Eu^{3+} ions, the results for 0.1 and 2.5 mol% of Eu are similar. It is observed that the lifetime is shorter for ions with higher crystal field (See Figures 1 and 2).

In Figure 3 the J-O parameters Ω_2 and Ω_4 for different excitation wavelengths are given. A clear correlation is observed between the dependence of Ω_2 on the wavelength and the behaviour found for the crystal field strength. Although no definitive conclusions

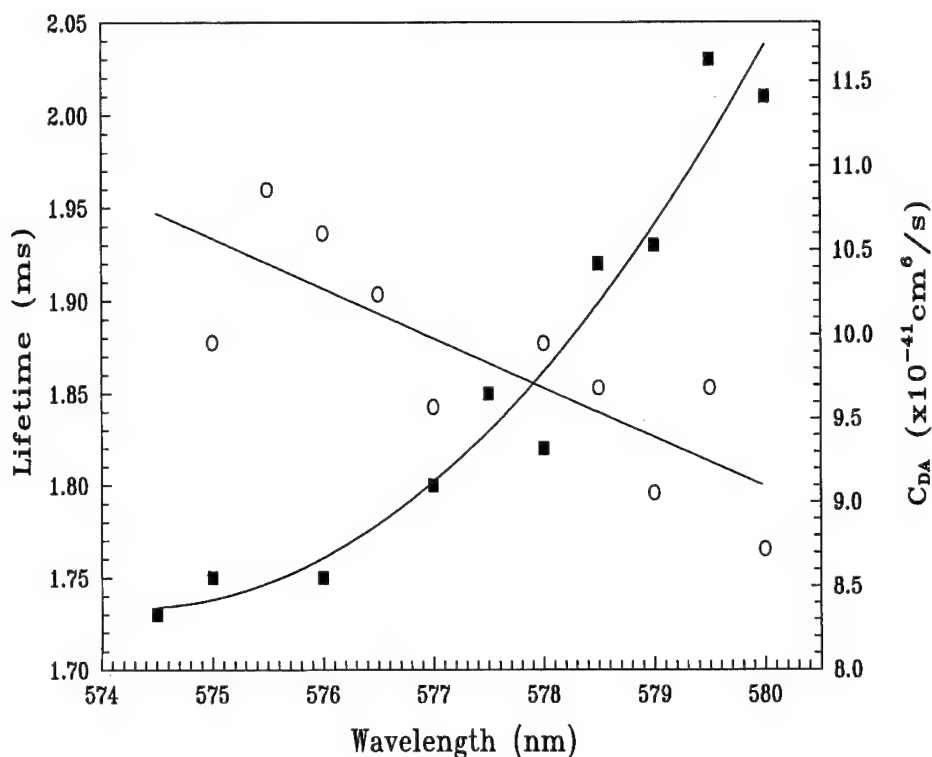


FIGURE 2 Lifetime of the $^5\text{D}_0$ level in Eu^{3+} doped glasses (■) and C_{DA} in Eu^{3+} - Ho^{3+} codoped glasses (○) for different excitation wavelengths.

can be obtained about Ω_4 due to the dispersion presented by the results, these are compatible with the expected scarce dependence on excitation wavelength.

In samples codoped with Eu and Ho the decay curves of the emission from the $^5\text{D}_0$ level have been fitted to the kinetic model of Inokuti-Hirayama.⁸ In Figure 2 the values obtained for the energy transfer parameter C_{DA} as a function of the excitation wavelength are given. The behaviour is the expected considering the dependence of this parameter with the transition probabilities and the overlap between the emission of Eu^{3+} and the absorption of Ho^{3+} .

In conclusion, in the studied glasses of the Eu^{3+} ions seem to occupy a continuum site distribution. The sites are characterized by different transition probabilities and, as a consequence, by different values for the J-O parameter Ω_2 ; a correlation between this parameter and the crystal field strength is found. In glasses codoped with Ho^{3+} the parameter C_{DA} for energy transfer from Eu^{3+} to Ho^{3+} also has different values for Eu^{3+} ions in different sites.

ACKNOWLEDGMENTS

This work has been partially supported by 'Gobierno Autónomo de Canarias' under contract number 226-265/93.

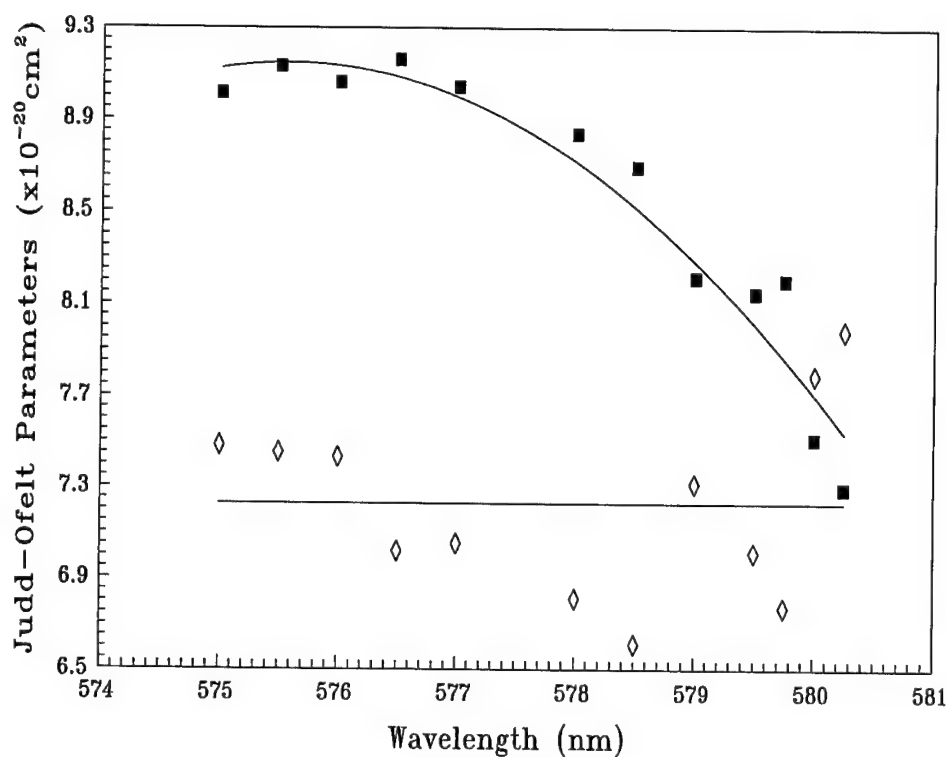


FIGURE 3 Judd-Ofelt parameters Ω_2 (■) and Ω_4 (◇) for different excitation wavelengths.

REFERENCES

1. B. R. Judd, *Phys. Rev.* **127**, 750 (1962).
2. G. S. Ofelt, *J. Chem. Phys.* **37**, 511 (1962).
3. R. D. Peacock, *Structure and Bonding* **22**, 83 (1975).
4. E. W. J. L. Oomen and A. M. A. van Dongen, *J. Non-Cryst. Sol.* **111**, 205 (1989).
5. V. Lavín, V. D. Rodríguez, U. R. Rodríguez-Mendoza, I. R. Martín and P. Nuñez, *International Conference on Luminescence ICL'93*, Storrs, USA (1993).
6. C. Brecher and L. A. Riseberg, *Phys. Rev.* **B13**, 81 (1976).
7. A. Lempicki, H. Samelson and C. Brecher, *J. Mol. Spect.* **27**, 375 (1968).
8. M. Inokuti and F. Hirayama, *J. Chem. Phys.* **41**, 652 (1964).

THERMOLUMINESCENCE OF BRAZILIAN TOPAZ

DIVANÍZIA DO N. SOUZA, JOSÉ F. DE LIMA and MÁRIO ERNESTO G. VALERIO

*Depto. de Física—CCET, Universidade Federal de Sergipe, 49.000-000 Aracaju—SE—
Brazil; e-mail: MVALERIO@BRUFSE.BITNET*

Thermoluminescence measurements were performed on samples of yellowish Brazilian Topaz from Acari, MG. Virgin samples revealed peaks 2 and 4 at about 150 and 300°C, respectively, while in samples with extra dose of γ -rays, we observed another peak at 80°C. When topaz samples were thermally treated, peak 4 vanished and peak 3 at about 180°C, became visible. Isothermal decay of peak 2 performed on virgin samples showed that peak 3 is present on this samples too. The spectra of the first 3 peaks are very similar in the range of 350 to 500 nm indicating that the recombination processes related to these 3 peaks could be the same. The dose dependency of the TL intensity of the first 3 peaks was measured from 0.5 to 400 Gy and it seems to start saturating above 400 Gy.

Key words: Thermoluminescence, Topaz, spectra of TL peaks, thermal treatment, dose dependency.

1 INTRODUCTION

Topaz $[(\text{Al}(\text{F}, \text{OH}))_2\text{SiO}_4]$ is a very stable aluminum silicate mineral with a well-ordered orthorhombic crystalline structure with hardness exceeded only by corundum and diamond. Topaz crystals are normally transparent ranging from colorless to pale colors. The first work employing Thermoluminescence (TL) in this material was done by Moss and McKlveen¹ with samples collected in the Topaz Mountain, Utah, USA. Azorin *et al.*² found that their Topaz from Mexico has a TL response with radiation dose of about 100 times higher than other natural silicates such as Amethyst and Aventurin although it is lower than the commercial TLD-100 dosimeter. Both works found only two TL peaks ranging from 140 to 170°C, for the first one, and 300 to 340°C, for the second. On the other hand, Ferreira Lima *et al.*³ observed 4 TL peaks in their Brazilian Topaz from Governador Valadares, MG. The fade of the TL emission was only 25% of the initial TL signal after a period of time as great as 400 days at room temperature² and the main decrease was found to take place within the first day of storage.³ Apart from these very general results concerning the potentially dosimetric application, there are no other significant study with Topaz and most of its properties are still to be discovered. The mechanism of the thermoluminescence of this material was not studied and the features of the TL emissions are not completely tabulated yet.

The aim of the present work is to study the main characteristics of the thermoluminescent emission of the Brazilian Topaz from Acari, MG. The number of TL peaks in untreated and thermally treated samples was studied as well as the spectra and the dose dependencies of the peaks of the thermally treated samples.

2 EXPERIMENTAL

Topaz samples were obtained from Acari, MG, Brazil. The samples were powdered from yellowish stones and only the grains between 0.075 and 0.149 mm were used. Irradiation was performed with γ -rays from a ⁶⁰Co source. The TL emission was investigated in three groups of samples: **group A**, the virgin samples, **group B**, virgin samples with additional doses and, **group C**, samples that received thermal treatment and then were submitted to

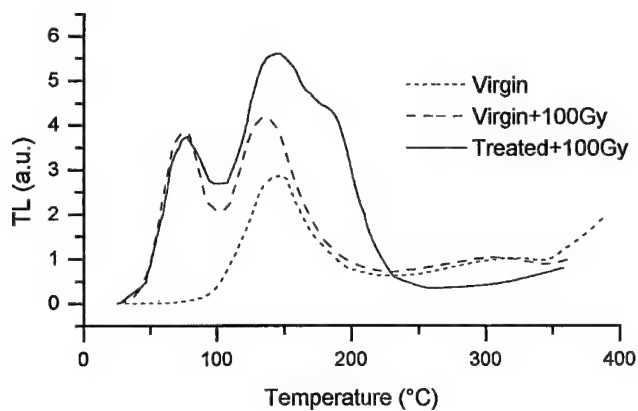


FIGURE 1 TL glow curve of the virgin (A), virgin plus extra dose of γ -rays (B) and thermally treated plus irradiated (C) samples.

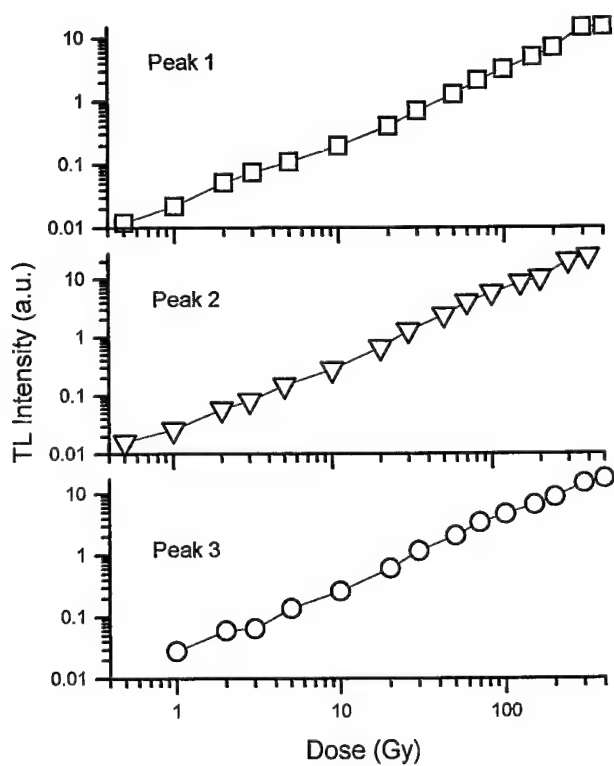


FIGURE 2 Dose dependencies of the peaks 1, 2 and 3 of the thermally treated samples (C). Saturation seems to start only above 400 Gy.

different doses of radiation. The thermal treatments of the C samples were performed in an open-air oven at 400°C for 1 h followed by a quenching back to room temperature. Samples of the C group were irradiated with doses from 0.5 to 400 Gy and the samples in group B received artificial doses ranging from 100 to 400 Gy.

The TL measurements were performed on a home-made TL reader from room temperature up to 450°C. For the measurements of the TL spectra, a monochromator was attached before the photomultiplier and the measured TL intensities of the peaks were then corrected to take into account the spectral response of the photomultiplier and the monochromator.

3 RESULTS AND DISCUSSION

Figure 1 shows the TL glow curve of the A, B, and C samples. Comparing the A and the B samples, it could be seen that peak 1, at about 80°C, had vanished in the virgin sample due to the thermal decay at room temperature. On the other hand, for peak 4, at about 300°C, it was not observed and changes after an extra dose of 100 Gy. Peak 2, at about 150°C, was enhanced by a factor of two due to this extra 100 Gy dose of γ -ray of ^{60}Co .

When a virgin sample of topaz is irradiated with a laboratory dose, the traps related to the first peak is strongly populated again since these traps were all empties. The traps of peak 2 are partially filled so the enhancement of this peak is less pronounced. There are two possible reasons that could explain the behavior of peak 4. The natural dose is enough to saturate this peak and additional doses do not cause any change or the capture cross section of the carriers in the traps associated to this peak is much lower than the corresponding value for the other peaks.

Comparing the TL glow curve of the A and the C samples, one sees that, apart from the increase in the intensities of the peaks 1 and 2, peak 3, at about 180°C, appears quite intense while peak 4 vanished indicating that the thermal treatment of the topaz at 400°C for 1 h. changed the relative concentration of the traps associated to the TL peaks.

The Topaz samples of Moss and McKlveen¹ from the Topaz Mountain, Utah, USA showed only two peaks at 140°C and 300°C, while in the samples of Azorin *et al.*,² obtained from different parts of Mexico, the two peaks were at 180°C and 300°C. Ferreira Lima *et al.*³ found four peaks at 100°C, 130°C, 200°C and 250°C in their samples of topaz from Governador Valadares, MG, Brazil. The TL emission of our samples revealed 4 peaks. These differences in the TL emission of topaz are related to the origin of the samples and consequently to the impurities that can be different from one sample to another.

In Figure 2, it can be seen the dose dependence of the peaks 1, 2 and 3 of the C samples. For these three peaks, the intensities increased with the dose not linearly and we observed that it seems to start saturating only above 400 Gy.

Figure 3 shows the spectra of the first 3 peaks of the samples in group C submitted to a dose of 200 Gy. The spectra of these peaks are very similar displaying several maxima between 330 to 550 nm. This indicates that recombination of carriers is happening in more or less the same way for peaks 1, 2 and 3.

Isothermal decay of peak 2 of the A samples, showed that, after 10 minutes at 150°C, peak 3 became visible revealing that even in the virgin sample this peak exists but hidden by peak 2. Figure 4 shows the TL glow curve of a virgin sample after the isothermal decay of peak 2 at 150°C for 10 min. The difference in peak 3 from the virgin to the thermally treated samples is only on its relative intense compared to peak 2.

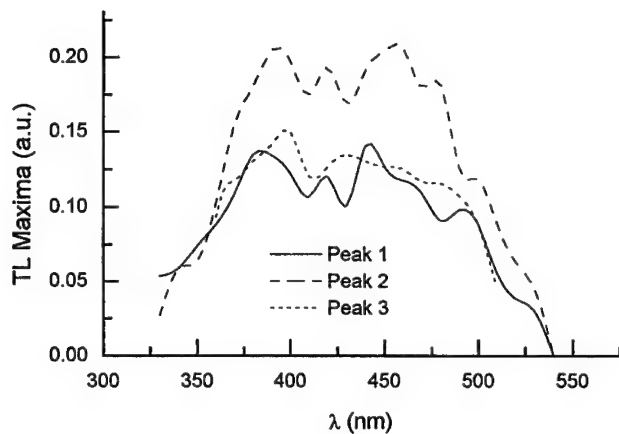


FIGURE 3 Spectral response of peaks 1, 2 and 3 of the thermally treated samples (C). Vertical axis represents the TL intensities of the maxima of the considered peaks.

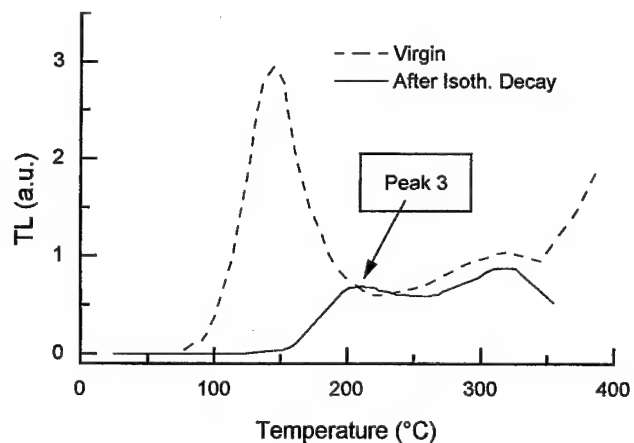


FIGURE 4 TL glow curve of a virgin sample after submitting peak 2 to an isothermal decay at 150°C for 10 min. The original virgin sample TL is also shown for comparison. It can be clearly seen the presence of peak 3 in the virgin samples too.

4 CONCLUSIONS

From these results it is possible to conclude that: i) There are at least 4 traps related to these 4 peaks in topaz; ii) Thermal treatment of the topaz samples seems to modify the original distribution of traps since peak 3, that is not clearly visible in the virgin sample, increases while peak 4 vanishes, and iii) Since the spectra of the first 3 peaks are very similar, the recombination seems to take place in a similar way for these peaks probably related to the same group of luminescence centers.

REFERENCES

1. A. L. Moss and J. W. McKlveen. *Health Physics (GB)* **34**, 137-40, 1978.
2. J. Azorin N., R. P. C. Salvi and A. Gutierrez C. *Health Physics (USA)* **43-4**, 590-5, 1982.
3. C. A. Ferreira Lima, L. A. R. Rosa e P. G. Cunha. *Appl. Radiat. Isot.* **37-2**, 135-7, 1986.

POINT DEFECTS PRODUCED BY GRINDING OF CaS PHOSPHORS: AN ELECTRON SPIN RESONANCE STUDY

D. CAURANT, D. GOURIER, N. DEMONCY and M. PHAM-THI*

*Laboratoire de Chimie Appliquée de l'Etat Solide (URA CNRS 1466), ENSCP, 11 rue
Pierre et Marie Curie, 75231 Paris Cedex 05, France; * Thomson-CSF, Laboratoire
Central de Recherches, Domaine de Corbeville, 91404 Orsay Cedex, France*

Pure and europium-doped CaS powders prepared by the alkaline polysulfides flux method were submitted to grinding and the effect was studied by ESR. The fine structure evolution of Mn^{2+} present as natural impurity has shown that the local order in CaS particles is strongly disturbed by grinding. The ESR signals of F^+ centers induced by grinding can be easily separated from other signals using a 90° out-of-phase detection. A scheme is proposed involving the formation of neutral sulfur vacancies (F centers) and their consecutive reaction with Cr^{3+} , Eu^{3+} or hole centers initially present in CaS to form F^+ centers. Evolution of F^+ centers and formation of new paramagnetic species after thermal treatment in air are studied. The possible cause of the strong decrease of Eu^{2+} fluorescence intensity after grinding is discussed.

Key words: CaS, grinding, Electron Spin Resonance, paramagnetic defects.

1 INTRODUCTION

Calcium sulfide powders are known for their relatively good photo and cathodoluminescence properties when doped with activator ions.^{1,2} For instance, CaS doped with Eu^{2+} which presents a strong red fluorescence near 645 nm has a potential application as phosphor in TV cathode tubes. However the application of mechanical stress (grinding or pressing) to europium-doped CaS powders induces a strong decrease of their luminescent efficiency. Such behavior may be a serious drawback during phosphor powders processing. In this work we have investigated by Electron Spin Resonance (ESR) paramagnetic centers in europium-doped or non-doped native and ground powders. The evolution of grinding induced centers after thermal treatment in air is presented.

2 EXPERIMENTAL PART

CaS powders are elaborated by the alkaline polysulfides flux method.^{3–5} Calcium carbonate is mixed with sodium or potassium carbonate and an excess of sulfur. For europium doped powders, Eu_2O_3 is initially mixed with $CaCO_3$ (Eu 0.1 mol. %). The mixture is then heated at 1273 K during 2 hours. After slow cooling, CaS microcrystals of 10–20 μm diameter and very good crystalline quality are separated from alkaline polysulfides by washing with water.⁵ Depending on chemical composition of the flux (Na_2S_x or K_2S_x), CaS powders will be noted hereafter CaS(Na) or CaS(K). Native powders were ground during 30 min using an attrition apparatus with zirconia balls and anhydrous ethanol. During this process a strong H_2S smell indicates departure of sulfur and the color of undoped powders changes from white to pink. Ground powders are constituted of irregular and agglomerated particles with a mean diameter smaller than 7 μm . Atomic absorption analysis of native products indicates that sodium content ranges

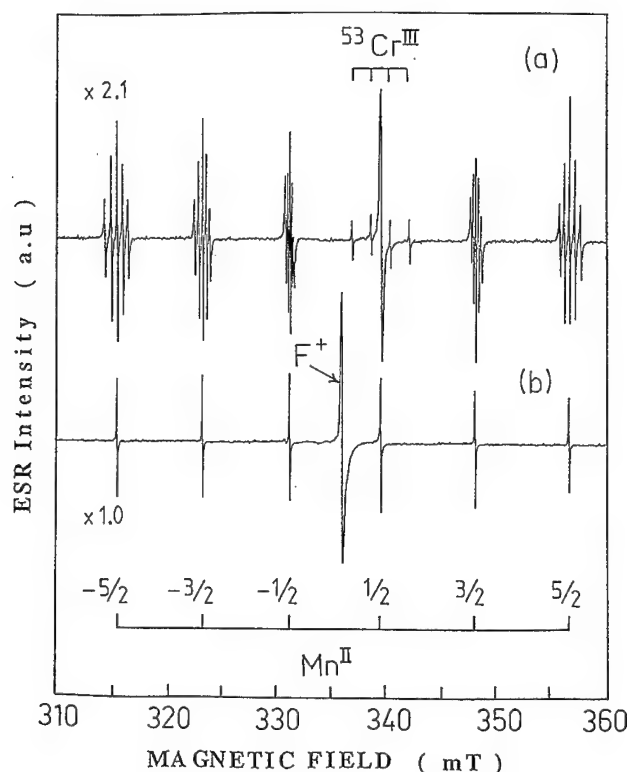


FIGURE 1 ESR spectrum at 110 K of CaS(Na) powder. Microwave frequency $\nu = 9.43$ GHz. Microwave power $P = 2$ mW. (a) native powder (b) ground powder.

between 0.16 and 0.23 mol. % for CaS(Na) whereas potassium content is lower (0.09–0.12 mol %) for CaS(K). Moreover about 1 ppm mol. of chromium and manganese are present as natural impurities. ESR spectra were recorded using an X-band ($\nu = 9.4$ GHz) spectrometer operating in the range $20\text{ K} \leq T \leq 300$ K. Isothermal and isochronal thermal treatments of native and ground powders have been essentially performed in air.

3 RESULTS AND DISCUSSION

3.1 Paramagnetic defects in native powders

ESR spectra of native undoped CaS(Na) and CaS(K) powders are very similar. Figure 1(a) shows an example of a spectrum of CaS(Na). The six intense hyperfine lines separated by about 8 mT and centred near the free electron g factor (g_e) are characteristic of Mn^{2+} ion. Moreover the very well resolved fine structure shows that Mn^{2+} ions are located in very regular octahedral sites.⁶ This fine structure is very sensitive to local disorder around Mn^{2+} which can be considered as a local order probe in CaS grains. $^{52}\text{Cr}^{3+}$ and $^{53}\text{Cr}^{3+}$ ESR lines centered near $g = 1.983$ are also observed (Figure 1a). Moreover two other lines located at $g = 2.016$ and $g = 2.036$ are observed at low temperature and high microwave power.

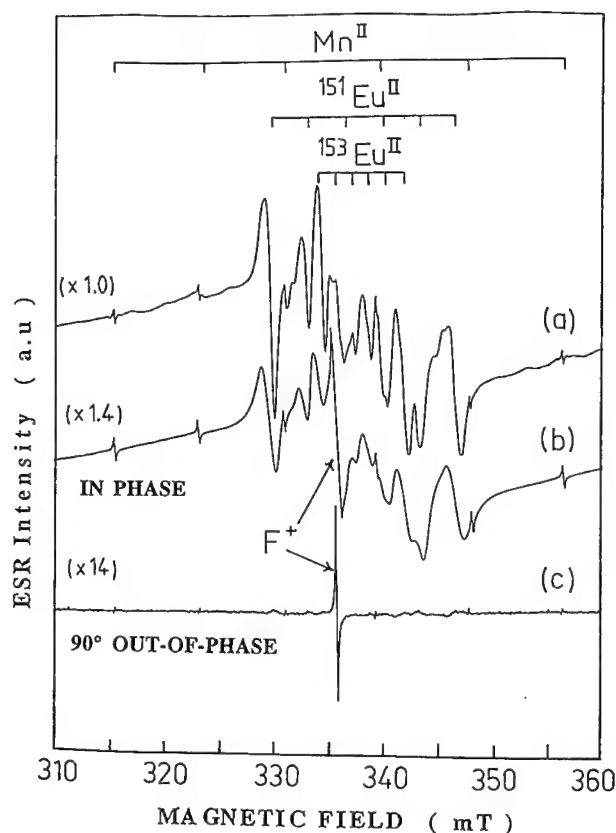


FIGURE 2 ESR spectrum at 300 K of europium doped CaS(K) powder. Microwave frequency $\nu = 9.43$ GHz. Microwave power $P = 2$ mW. (a) native powder (b) ground powder (in-phase detection) (c) ground powder (90° out-of-phase detection).

These signals may be attributed to a hole trapped in the p orbitals of sulfur ions surrounding a cationic defect (a calcium vacancy or a monovalent cationic impurity). ESR spectra of native europium doped CaS(Na) and CaS(K) are totally different. In the case of CaS(K) a strong multicomponent ESR signal associated with $^{151}\text{Eu}^{2+}$ and $^{153}\text{Eu}^{2+}$ is observed⁷ (Figure 2a). For CaS(Na) almost all europium ions are in the diamagnetic trivalent state. Change of europium valence state with alkaline flux nature has been explained by the ease of $\text{Na}^+ - \text{Ca}^{2+}$ substitution and charges compensation phenomena.⁸

3.2 Paramagnetic defects in CaS ground powders

The Mn^{2+} fine structure is suppressed by grinding (Figure 1b), which indicates the occurrence of a crystal field disorder in Mn^{2+} environment attributable to vacancies and dislocations generated during mechanical stress. This feature is accompanied by the growth of a relatively strong ESR line at about the free electron spin g value (Figures 1b, 2b). This signal, which saturates at high microwave power, can be easily isolated from other signals (Mn^{2+} , Cr^{3+} , Eu^{2+}) using a 90° out-of-phase detection (Figure 2c). This feature indicates that the relaxation time T_2 of the grinding induced center is very long

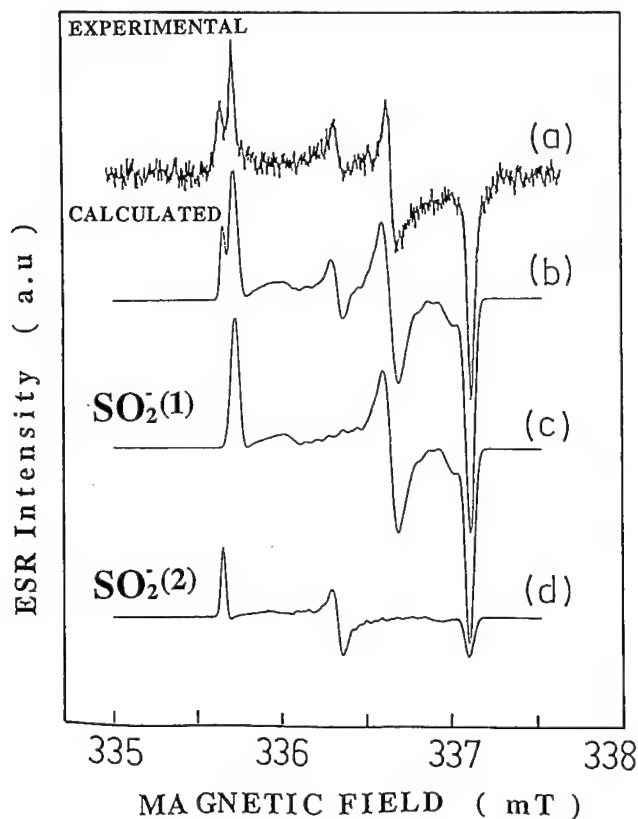


FIGURE 3 Partial view of the ESR spectrum at 20 K of CaS(K) ground powder heat treated in air at 923 K during 2 hours. Microwave frequency $\nu = 9.44$ GHz. Microwave power $P = 2.10^{-3}$ mW. (a) experimental spectrum (b) total simulated spectrum (c) (d) simulated spectra of $\text{SO}_2^-(1)$ and $\text{SO}_2^-(2)$ respectively.

($T_2 \approx 5.10^{-6}$ s). The latter has been attributed to a F^+ center⁹ (a single electron trapped in a sulfur vacancy) at a concentration of about 30–40 ppm. After grinding, Cr^{3+} and hole-center lines completely vanish (Figure 1b), which indicates that they have captured an electron. Moreover in the case of europium-doped CaS(Na), Eu^{2+} ions concentration increases, which shows that Eu^{3+} ions have been partially reduced. All these features imply that the primary defects induced by grinding are neutral F centers. F^+ centers are formed by the following reaction: $\text{F} + \text{A}^{n+} \rightarrow \text{F}^+ + \text{A}^{(n-1)+}$ where A^{n+} represents Cr^{3+} , Eu^{3+} or hole centers. Sulfide vacancies with two trapped electrons (F centers) are supposed to be formed along dislocations or new surfaces following sulfur departure and then to diffuse inside particles where they can react with A^{n+} giving F^+ centers.

3.3 Thermal treatment in air of CaS ground powders

ESR spectra of CaS ground powders strongly change after thermal treatment. For CaS(Na) and CaS(K), the F^+ line rapidly decreases in intensity (and vanishes after about 10 min at 723 K) and is progressively replaced by two multicomponent signals noted $\text{F}_s^+(1)$ and

$F_S^+(2)$ (Table I). Due to the fact that these signals are observed by 90° out-of-phase detection, they can be attributed to surface F^+ centers originating from the diffusion of bulk F^+ centers. F_S^+ centers then react with oxygen, forming O^- centers which in the case of CaS(Na) can be stabilized with Na^+ ions forming neutral (O^-, Na^+) centers at 723 K (Table I). At higher temperatures ($T \geq 973K$), where CaS ground particles have been partially oxidized into $CaSO_4$, two new multicomponent hole-center signals are detected at the same time for CaS(Na) and CaS(K) (Figure 3). We attribute these signals to paramagnetic SO_2^- type centers in CaS phase (Table I). They are probably intermediate species formed when CaS is progressively transformed into $CaSO_4$. After thermal treatment ($T = 723 K$), luminescent properties of europium doped ground powders are partially restored and the pink color of undoped ground powders is bleached. The decrease of europium fluorescence intensity upon grinding can be partly due to competition towards optical absorption between europium ions and grinding induced centers (F and F^+), and to a killing effect of these centers upon Eu^{2+} emission.

TABLE I

Paramagnetic centers generated by grinding (F^+), followed by a thermal treatment in air ($F_S^+(1)$, $F_S^+(2)$, (O^-, Na^+) , $SO_2^-(1)$, $SO_2^-(2)$) of undoped ground CaS powders

Center	F^+	$F_S^+(1)$	$F_S^+(2)$	(O^-, Na^+)	$SO_2^-(1)$	$SO_2^-(2)$
g factor	$g = 2.003(1)$	$g_{//} = 1.997(0)$ $g_{\perp} = 2.000(4)$	$g_{//} = 1.995(5)$ $g_{\perp} = 2.001(7)$	$g_x = 2.015(5)$ $g_y = 2.017(0)$ $g_z = 2.001(2)$	$g_x = 2.004(7)$ $g_y = 2.010(1)$ $g_z = 2.002(0)$	$g_x = 2.006(5)$ $g_y = 2.010(5)$ $g_z = 2.002(0)$

REFERENCES

1. W. Lehmann, *J. Lumin.* **5**, 87 (1972).
2. P. K. Ghosh, B. Ray, *Prog. Crystal Growth and Charact.* **25**, 1 (1992).
3. F. Okamoto, K. Kato, *J. Electrochem. Soc.* **130**(2), 432 (1983).
4. K. Kato, F. Okamoto, *Jpn. J. Appl. Phys.* **22**(1), 76 (1983).
5. M. Pham-Thi, G. Ravoux, *J. Electrochem. Soc.* **138**(4), 1103 (1991).
6. D. Gourier, D. Simons, D. Vivien, N. Ruelle, M. Pham-Thi, *Phys. stat. sol. (b)* **180**, 223 (1993).
7. M. Pham-Thi, N. Ruelle, E. Tronc, D. Simons, D. Vivien, *Jpn. J. Appl. Phys.* (in press).
8. M. Pham-Thi, *Jpn. J. Appl. Phys.* **31**, 2811 (1992).
9. J. E. Wertz, J. W. Orton, P. Auzins, *Discuss. Faraday Soc.* **31**, 140 (1961).

THERMALLY STIMULATED DEPOLARIZATION CURRENT OF MONOVALENT COPPER IONS IN CALCIUM FLUORIDE

L. OLIVEIRA,* O. R. NASCIMENTO,* M. SIU LI,* C. PEDRINI** and H. BILL***

Instituto de Física de São Carlos—USP, Cx.P. 369, 13560—970 São Carlos—S. P., Brazil;* *Laboratoire de Physico-Chimie des Matériaux Luminescents, Unité de Recherche Associée au CNRS 442, Université Lyon 1, 43 Boulevard du 11 novembre 1918, 69622 Villeurbanne, France;* ****Département de Chimie Physique, Université de Genève, 30 quai Ernest-Ensement, 1211 Genève 4, Switzerland*

Thermally stimulated depolarization current (TSDC) measurements of $\text{CaF}_2:\text{Cu}^+$ samples show three different dipolar relaxation bands, with temperature peaks at 52, 144 and 187 K. The two higher temperature bands are more intense and reveal the presence of Cu^+ in probably two different lattice sites. The band at 144 K suggests it is related to the Cu^+ off-center effect, observed through an optical absorption at 328 nm, and it is likely temperature independent. To this Cu^+ off-center effect it is also associated an impurity-vacancy defect, that result from needed charge compensation in CaF_2 . The observed TSDC band at 187 K is attributed to $\text{Cu}_i^+ - \text{F}_i^-$ pair, both ions in interstitial positions. The weakest TSDC at 52 K is assumed to be from a low un-intentional Mn^{2+} doping, sitting in an off-center substitutional position. It is proposed a model to explain the several positions available for the substitutional Cu^+ that response for the TSDC result.

Key words: Alkali halides, Calcium Fluoride, Copper impurity, Dielectric relation.

In an earlier work¹ it was shown through optical absorption measurements that Cu^+ ion occupies an off-center position in CaF_2 crystal. The ultra-violet optical absorption spectrum, from 260 to 385 nm, show three bands, which are attributed to the $\text{Cu}^+ 3d^{10} \rightarrow 3d^9 4s$ transition. The two main bands, at 301 and 328 nm, result from $^1\text{A}(3d^{10}) \rightarrow ^1\text{E}(d^9 4s)$ and $^1\text{A}(3d^{10}) \rightarrow ^1\text{T}_2(3d^9 4s)$ transition, respectively. The weakest band, at 357 nm, is attributed to the spin forbidden $^1\text{A}(3d^{10}) \rightarrow ^3\text{T}_2(3d^9 4s)$ transition. No temperature dependence is observed for integrated absorption bands, as measured from LHeT to RT, which clearly show the off-center effect behavior. Since to the off-center effect is associated an electric dipole, it has an Arrhenius relaxation for classical system and can be investigated through the TSDC technique.

The present work reports the electric dipole relaxation of $\text{CaF}_2:\text{Cu}^+$ as investigated through TSDC technique, reinforcing the off-center behavior deduced from the optical measurements as also propose the possibility for Cu^+ to be in an interstitial position in CaF_2 .

Figure 1 shows a typical TSDC spectrum of $\text{CaF}_2:\text{Cu}^+$. It is observed three different relaxation bands at 52, 144 and 187 K. Each of these bands is well fitted with singular TSDC curve, by using the Prakash method.² The lowest temperature TSDC band is related to the non-intentional Mn^{2+} doped impurity in an off-center substitutional configuration for Ca^{2+} as shown in Figure 1(a). This un-intentional impurity is commonly present in fluorides crystals and its presence in CaF_2 crystal is detected through electron paramagnetic resonance (EPR) measurements. The activation energy for this band is 0.14 eV. Going up to higher temperature, two additional TSDC bands indicate the presence of Cu^+ ions in two different position. The correlation between TSDC and optical absorption¹ results, suggest that the 144 K TSDC band, of higher intensity, is due probably to the electric dipole that results from the Cu^+ off-center defect associated to an impurity-vacancy defect as shown in Figure 1(b). The activation energy for this band is 0.42 eV.

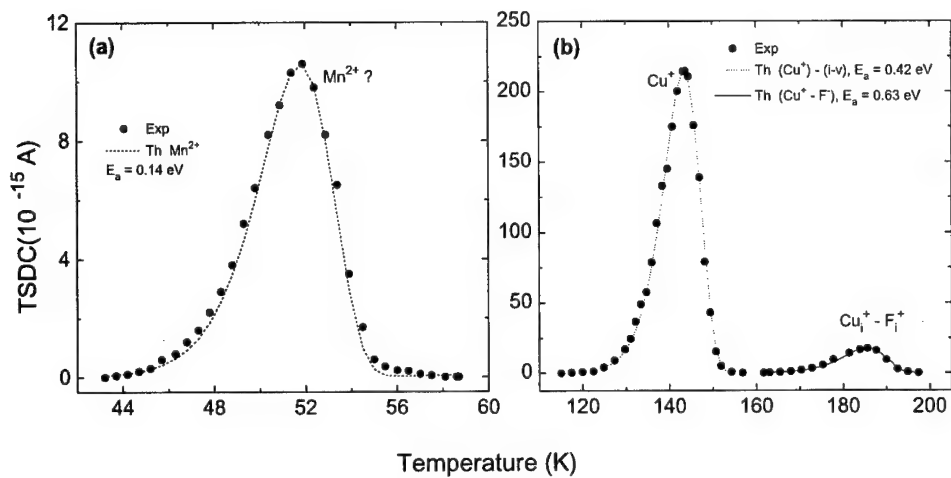


FIGURE 1 TSDC as a function of temperature measurements. (a) Mn^{2+} off-center, (b) Cu^+ off-center with a vacancy defect at 144 K and (c) $Cu_i^+ - F_i^-$ at 187 K.

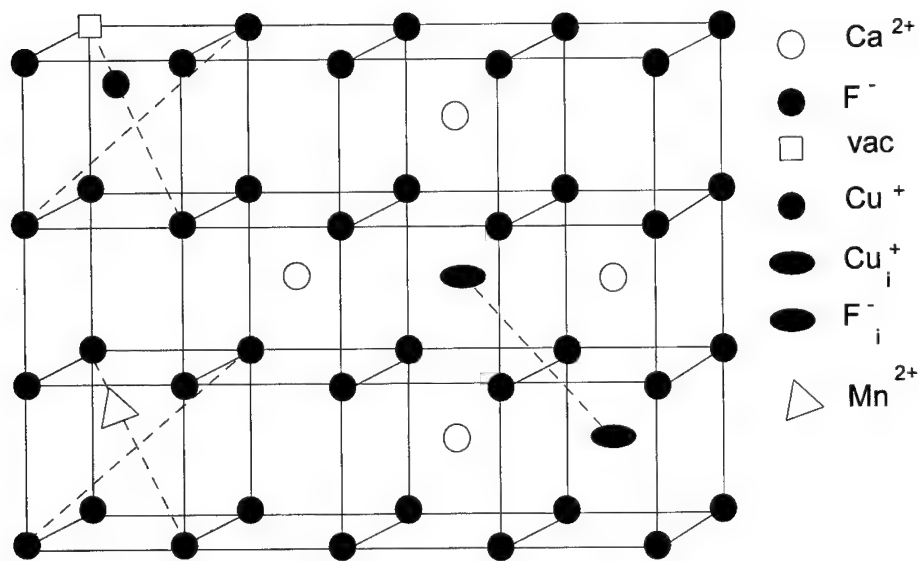


FIGURE 2 Simple model of: (a) Mn^{2+} off-center, (b) Cu^+ off-center and vacancy defect and (c) $Cu_i^+ - F_i^-$ in the CaF_2 crystals.

It is usual to observe that for Cu^+ doped in alkali halides, the off-center effect only exists when the substitutional ion has a larger ionic radii, and usually the electric dipole is larger when TSDC's bands appears at higher temperature, as it is when compared with NaCl, KCl and RbCl host crystals. For NaCl, Na^+ has an ionic radii of 0.97 Å which is close to 0.98 Å from the Cu^+ ion. In this host the Cu^+ is identified as to be in an on-center position, where no TSDC band is observed. While for KCl and RbCl it is observed, since K^+ and Rb^+ ionic radii are 1.33 and 1.47 Å respectively. In the present case Cu^+ substitutes Ca^{2+} , which ionic radii is 0.99 Å and is also close to the Cu^+ ionic radii. But it is necessary to have charge compensation in CaF_2 , that means there must be an anionic vacancy close to the Cu^+ ion. To agree with the optical absorption measurements, where it is observed a temperature independence behavior of the Cu^+ oscillator strength, it is assumed the Cu^+ ion is also displaced from the substituted Ca^{2+} site. Both assumptions suggest we have two superposing electric dipole system, one due to the impurity-vacancy defect and another from the off-center effect. The vacancy allows the Cu^+ ion to have a strong off-center effect, which also agrees with the strong absorption band shift to 328 nm and also the higher TSDC band temperature at 144 K, which usually features the absorption band at below 280 nm and the TSDC band is at below 100 K in several alkali halide host material.

The third TSDC band at 187 K, which is of smaller intensity than the one at 144 K, is attributed to another defect formed from an electric dipole between F_i^- and Cu_i^+ , both in interstitial positions as shown in Figure 2. The calculated activation energy was 0.63 eV. This type of dipole formation has been already studied for Li^+ , Na^+ , K^+ and Rb^+ doped CaF_2 .^{3,4} In both references the off-center effect was not taken into account for electric dipole relaxation, but only impurity-vacancy and interstitial ions. The present sample is unique in showing, both defects together. All the impurities mentioned before have no optical absorption, and it is possible that these impurities should be sitting in an off-center position together with impurity-vacancy defect.

ACKNOWLEDGEMENTS

We acknowledge the financial support from several Brazilian agencies: CNPq, Fapesp, Finep and Capes as also from French agency CNRS.

REFERENCES

1. C. Pedrini, B. Moine and H. Bill; *J. Phys. Condens. Matter* **4**, 1615 (1992).
2. L. Oliveira, P. Magna, N. J. H. Gallo, E. C. Domenicucci and M. Siu Li; *phys. stat. solidi (b)* **171**, 141 (1992).
3. P. W. M. Jacobs, S. H. Ong, A. V. Chadwick and V. M. Can; *J. Sol. State Chem.* **33**, 159 (1980).
4. J. J. Fontanella, A. V. Chadwick, V. M. Can, M. C. Wintersgill and C. G. Andeen; *J. Phys C* **13**, 3457 (1980).

PHOTOSTIMULATED LUMINESCENCE OF KBr-In CRYSTALS

I. PLAVINA,¹ A. I. POPOV² and A. TALE¹

¹*Institute of Physics, Latvian Academy of Sciences, V-2169 Riga, Latvia;* ²*Institute of Solid State Physics, University of Latvia, 8 Kengaraga str., LV-1063 Riga, Latvia*

It is shown that the photostimulated luminescence of the KBr-In crystal at room temperature preliminary irradiated in the exciton absorption band arise from three types of close defect pairs. The stimulation spectra for each pair are investigated. It is shown also that one of these three kinds of defect pairs is {F, In²⁺}, whereas two other pairs have the electron centre of more complicated nature. It is demonstrated that the KBr-In is an effective radiation storage material for both UV- and X-irradiations.

Key words: Alkali halides, photostimulated luminescence, color centers, F-center, storage phosphors.

1 INTRODUCTION

In recent years the photostimulated luminescence (PSL) has the great attention of many scientists because of their application for radiation imaging.^{1,2} For this purposes, a variety of the different PSL phosphors, such as BaFBr:Eu, RbBr-Tl,³ KBr-In⁴ etc have been considered.

In our recent papers⁴⁻⁶ it was shown that {F, In²⁺} defect pairs, which are responsible for the distinctive PSL, are produced under the exciton-band excitation. Furthermore, when the number of the exciton-created photons is less than 5.0×10^{13} photons/cm² only the {F, In²⁺} pairs are formed. In order to excite the PSL of the {F, In²⁺} pairs, the crystal has to be illuminated with light into the F band. As a result, the F center electrons are excited and captured by the nearby In²⁺ centers. This electron transfer from F* to In²⁺ results in the PSL of In⁺ luminescence (420-530 nm).^{4,6}

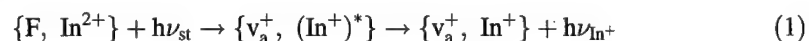
This paper concentrates on the new PSL properties of a KBr-In crystals proposed for UV-⁴ and X-ray radiation imaging.^{4,7}

2 EXPERIMENTAL

Experimental details were presented earlier for the case of UV irradiation in⁴⁻⁶ and for X-rays in^{7,8}.

3 RESULTS AND DISCUSSION

In order to investigate the PSL process after the optical creation of the anion excitons, we measured carefully the kinetics of PSL under constant F-light stimulation. As it was shown in⁴⁻⁶ the PSL of the {F, In²⁺} pairs is exponential in time. This process can be written schematically as



where v_a^+ is the anion vacancy. The appropriate stimulation spectrum is presented in

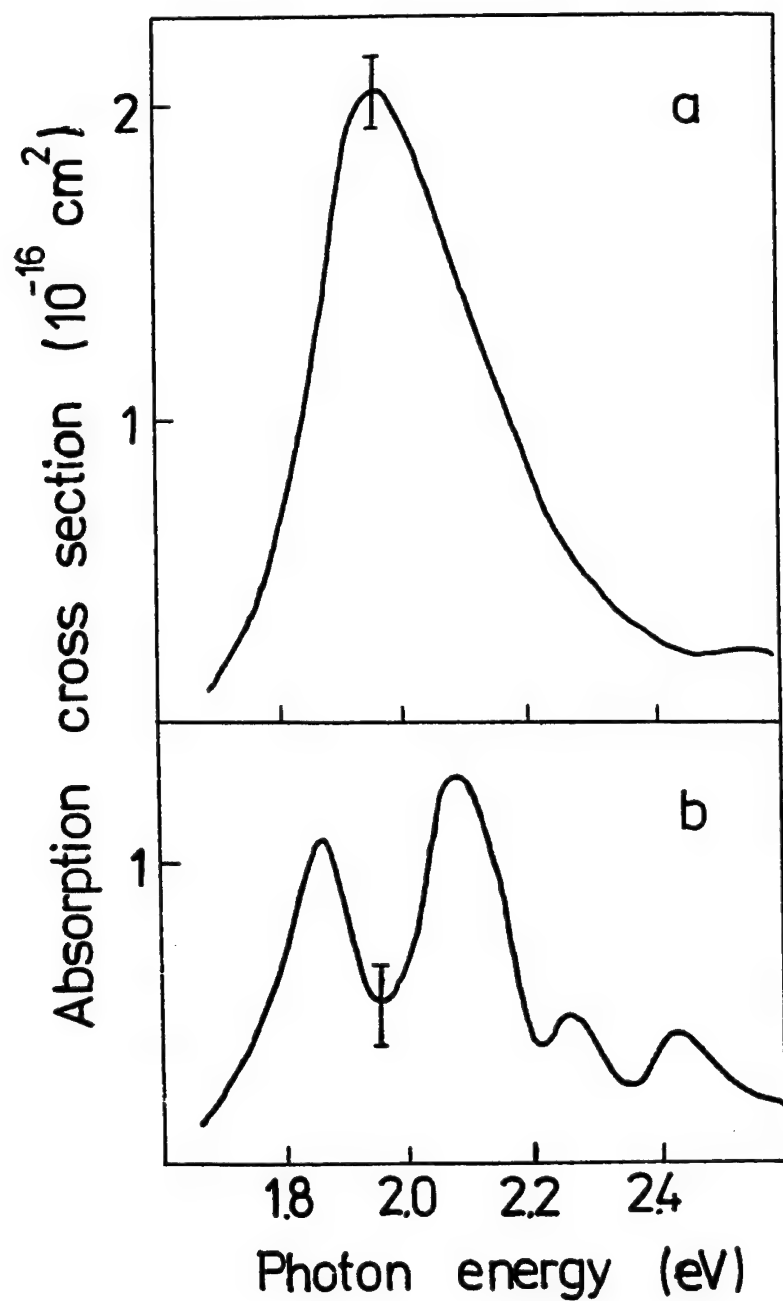


FIGURE 1 Stimulation spectra (in terms of optical absorption cross-section as a function of the stimulating light energy) of the middle and slow components of the PSL.

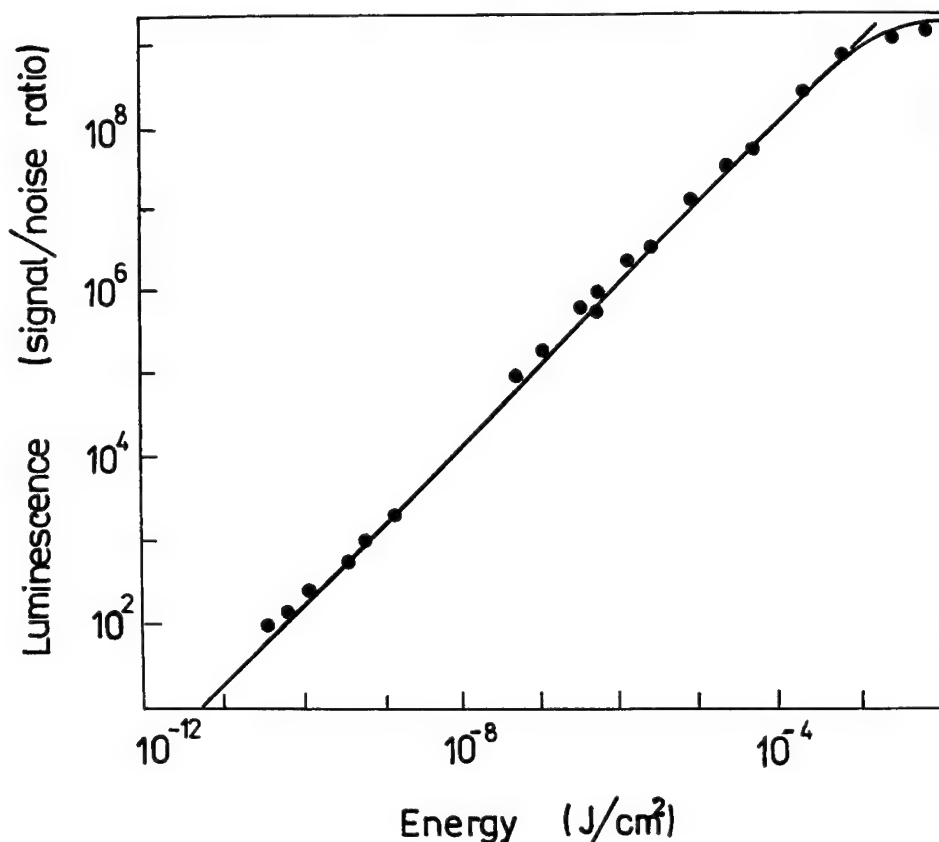
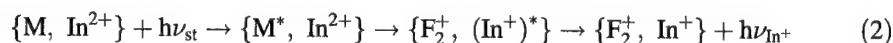


FIGURE 2 Dose dependence of PSL of KBr-In accumulated under UV light ($\lambda = 195$ nm). PSL lightsums magnitude obtained according to a squared signal-to-noise ratio ψ^{24} .

Figure 1. It is similar to the earlier published F-band absorption spectra. Next we have found that the PSL appearing after large dose ($D > 5 \times 10^{13}$ photons/cm²) is the superposition of three exponential components, {F, In²⁺} pairs define the middle of them. The spectral distribution of the absorption cross-section σ of the slow component (Figure 1) looks like the M-centre absorption. It is well known that the F band covers the spectral region of the transition of the M and R centers. In the case of KBr, the M band includes the M₂ and M₂' - transitions ($E_{M_2} = 1.990$ eV, $E_{M_2'} = 2.006$ eV, $\Delta E = 0.016$ eV). Estimation of the σ_{M_2} gives the values of order $1.0 \cdot 10^{-16}$ cm². From the stimulation spectra (Figure 1) it follows that there are two most pronounced bands; $E_1 = 1.87$ eV and $E_2 = 2.08$ eV having $\sigma_{1,2} = 1.05 \cdot 10^{-16}$ and $1.3 \cdot 10^{-16}$ cm², respectively. These σ values are in a good correspondence with the above-mentioned estimation of σ_{M_2} values. The estimated oscillator strengths of the E_1 and E_2 bands are $f_1 = 0.14$ and $f_2 = 0.17$ with good correspondence with data.⁸ Thus we can conclude that the slow component of the PSL of KBr-In crystals is due to {M, In²⁺} pairs and this process can be represented schematically as



The origin of the shortest component of the PSL decay is not so obvious. Appearing under large irradiation doses these centers may have a complex structure. They could be the R centers as well as the F centers perturbed by some defect. The component has a spectrum shifted to the shortwavelength side to 0.1 eV compared with the F band. The pairs responsible for the shortest component will be designated as $\{DF, In^{2+}\}$. Thus we have concluded that the PSL of KBr-In crystals preliminary irradiated in the exciton fundamental absorption is due to three types of the close defect pairs, such as $\{M, In^{2+}\}$ and $\{DF, In^{2+}\}$, in which center-to-center recombination occurs. Recently we show that the resulting $\{V_a^+, In^+\}$ pairs may be converted again into the $\{F, In^{2+}\}$ pairs under the C-absorption band irradiation accompanied with the optical ionization of In^+ ion. The electron capture by the Coulomb field of the near anion vacancy leads to the restoration of the $\{F, In^{2+}\}$ pair.⁶ The same is true for the $\{DF, In^{2+}\}$ defects, but not for the $\{M, In^{2+}\}$ ones. The last fact can be explained by the thermal unstability of the F_2^+ centre at RT. It should be noted that in the case of C-band irradiation the main part of the PSL decays in accordance with the hyperbolic law. As such irradiation leads to the optical ionization of impurity In^+ ions, the released electrons are captured by the Schottky vacancies, thus creating the F centers. Schottky vacancies are randomly distributed (at least in virgin samples!) as well as the F and In^{2+} centers are. The kinetics of the F-destruction of such randomly arranged F and In^{2+} centres differ considerably from that of $\{F, In^{2+}\}$ pairs.^{5,6}

In conclusion, in Figure 2 we demonstrate that KBr-In is an effective UV radiation storage material with a wide dynamic range. A direct proportionality of the PSL intensity to X-ray exposure have been recently established over a wide dose range, viz. from $6 \cdot 10^{-8}$ to 30 R at 44 kV voltage,⁷ that is definitely the outstanding property and is much better than that, reported for BaFBr-Eu.⁹ The comparison of the stimulation energies of numerous storage materials also showed the advantage of the KBr-In.¹⁰

The research described in this publication was made possible in part by Grant LB2000 from International Science Foundation.

REFERENCES

1. I. Plavina, V. Obedkov, V. Chernyak, G. Balandin and B. Sestroretskii, *Izv. Akad. Nauk Latvian SSR, Ser. fiz. tekhn. nauk*, No. 5, 67 (1969).
2. G. Vlasov, R. Kalnins, L. Nagli, V. Obedkov, I. Plavina and A. Tale, *Avtometriya* **1**, 66 (1980).
3. H. von Seggern, A. Meijerink, T. Voigt and A. Winnacker, *J. Appl. Phys.* **66**, 4418 (1989); K. Amitani, A. Kano, H. Tsuchino and F. Shimada, *Konica Technical Report* **1**, 120 (1988).
4. P. Bratslavets, A. Kalnins, A. Popov, B. Rapoport, A. Tale, B. Zeigurs, in: 'The Advancement of Imaging Science and Technology', 1990, Int. Acad. Pub. (A. Pergamon—CNPIEC Joint Venture) p. 474-476.
5. A. Kalnins, I. Plavina, A. I. Popov and A. Tale, *J. Phys. Condens Matter* **3**, 1265 (1991); Proc. Intern. Conf. Luminescence, Lissabon, July 1990, (pp. 280, 281).
6. P. F. Braslavets, A. Kalnins, I. Plavina, A. I. Popov, B. I. Rapoport and A. Tale, *Phys. Status Solidi* **B170**, 395 (1992).
7. A. Kalnins, I. Plavina and A. Tale, *Nuclear Instr. and Meth.* **B84** 95 (1994); I. Plavina, A. Kalnins, A. I. Popov and A. Tale, *Nuclear Instr. and Meth. B* (in press).
8. T. Y. Neubert, Sh. Susman, *J. Chem. Phys.* **43**, 2819 (1965).
9. J. Miyahara, K. Takahashi, Y. Amemiya, N. Kamiya and Y. Satow, *Nucl. Instr. and Meth.* **A246**, 572 (1986).
10. L. E. Trinkler, M. F. Trinkler and A. I. Popov, *Phys. Status Solidi* **B180**, K31 (1983).

ENERGY TRANSFER AND UP-CONVERSION IN Yb-Tm CODOPED FLUORINDATE GLASSES

V. D. RODRÍGUEZ, I. R. MARTÍN, R. ALCALÁ* and R. CASES*

*Dpto. Física Fund. y Experimental. Universidad de La Laguna. 38206 La Laguna,
S/C de Tenerife, Spain; *ICMA, Universidad de Zaragoza-C.S.I.C., San Francisco s/n.
50009 Zaragoza, Spain*

The non-resonant energy transfer Yb \rightarrow Tm in indium based fluoride glasses has been studied in the temperature range 10–300 K. The transfer parameters donor-donor and donor-acceptor have been calculated from the kinetic models and from the Miyakawa-Dexter model. It is concluded that processes with 1, 2 or 3 phonons participate in the energy transfer. The mechanism and the efficiency of the up-conversion Tm³⁺ emission at 800 nm are investigated.

Key words: Energy transfer, up-conversion, Yb, Tm, indium fluoride glasses.

1 INTRODUCTION

Optical properties of heavy metal fluoride glasses doped with rare earth ions have been intensively studied due to the high quantum efficiencies observed in these materials. The Tm³⁺ ions present an emission at 1.8 μ m, which is a good candidate for the development of solid state lasers in the 2 μ m range, and also present an emission at 800 nm which coincides with the window of the silica optical fibre. In a previous paper¹ we studied the luminescence of Tm³⁺ ions by direct excitation of these ions in indium based glasses. In this work we extend the study to glasses with the same composition but codoped with Tm³⁺ and Yb³⁺ in order to excite the Tm³⁺ ions by energy transfer from Yb³⁺ ions.

2 EXPERIMENTAL

The samples used in this study were prepared with the following starting composition in mol%: (40-x-y) InF₃, 20ZnF₂, 20SrF₂, 20BaF₂, xTmF₃ and yYbF₃, with x and y in the range 0–2.5.

Emission spectra were obtained by exciting the samples with light from a 300 W Xe arc lamp passed through a 0.25 m double monochromator. Fluorescence was detected with a photomultiplier for the visible and with a silicon avalanche photodiode for the near infrared range. Emission spectra were corrected by the system spectral response. Emission decays were measured by modulating the exciting light with a mechanical chopper and using a digital storage oscilloscope controlled by a personal computer.

For low temperature measurements a continuous flow cryostat was utilized in the range from 10 K to room temperature (RT).

3 RESULTS AND DISCUSSION

The RT absorption and emission spectra in the near infrared range of a sample with 2.25 mol% of Yb³⁺ are shown in Figure 1; also are included the energy level diagrams of the Yb³⁺ and Tm³⁺ ions.

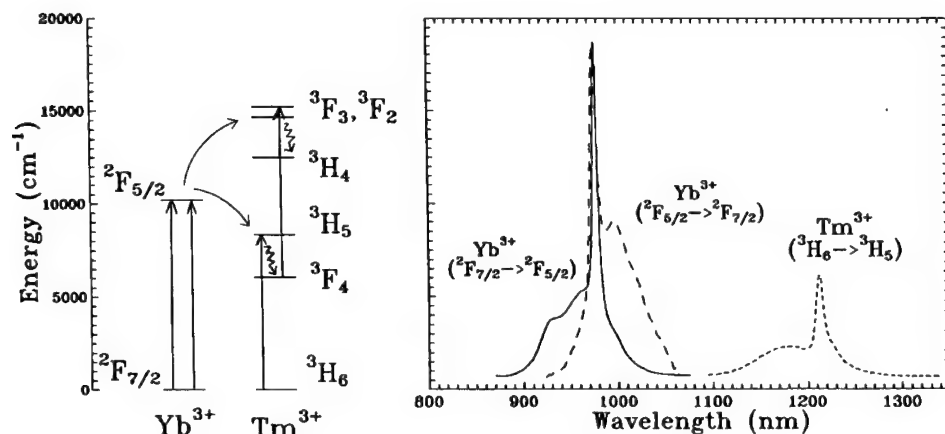
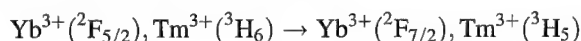


FIGURE 1 Energy levels of Yb^{3+} and Tm^{3+} ions. Absorption (—) and emission (---) spectra of a single doped sample with 2.25 mol% of Yb^{3+} . Absorption spectrum (---) of a single doped sample with 2.5 mol% of Tm^{3+} . All the spectra were obtained at RT. Up-conversion mechanism is depicted.

In glasses single doped with Yb^{3+} the lifetime of the emission at 975 nm increases with the concentration due to an efficient radiative energy transfer. For low concentrations of Yb^{3+} (0.1 mol%) this effect is not appreciable and we obtain a lifetime of 1.66 ms. No temperature dependence of this parameter between RT and 10 K is observed.

In Figure 1 is also included the absorption spectrum of the ${}^3\text{H}_6 \rightarrow {}^3\text{H}_5$ transition of Tm^{3+} , the absorption peak is close to the emission from the ${}^2\text{F}_{5/2}$ level of Yb^{3+} . As a consequence in samples double doped nonradiative energy transfer $\text{Yb}^{3+} \rightarrow \text{Tm}^{3+}$ is observed corresponding to the following process:



With low concentration of Yb^{3+} (0.1 mol%) the energy migration is negligible and a good fitting of the emission decay curves to the Inokuti-Hirayama formula,² assuming dipole-dipole interaction, is obtained. The calculated energy transfer parameter C_{DA} does not depend appreciably on the Tm^{3+} concentration, a mean value of $2.0 \times 10^{-41} \text{ cm}^6 \text{ s}^{-1}$ is obtained at RT. This result is similar but lower than that obtained by Chamarro and Cases ($2.9 \times 10^{-41} \text{ cm}^6 \text{ s}^{-1}$) for fluorohafnate glasses.³ In Figure 2 the dependence of this parameter with the temperature is presented, an appreciable decrease is observed under 150 K.

In Figure 2 are also shown the values of C_{DA} estimated with the Miyakawa-Dexter model⁴ for nonresonant energy transfer considering 1, 2 or 3 phonons of 500 cm^{-1} , which corresponds to the maximum energy phonons in these glasses. These values of C_{DA} decrease when the temperature is increased due to the decreasing of the overlap integral of the donor emission and the shifted acceptor absorption. The values of C_{DA} obtained for 0 or 4 phonons are much more lower. The disagreement between these results and those obtained from the emission decay curves is not too large taking into account the approximations involved in the models, it is concluded that the transfer $\text{Yb}^{3+} \rightarrow \text{Tm}^{3+}$ is non-resonant with participation of processes with 1, 2 or 3 phonons.

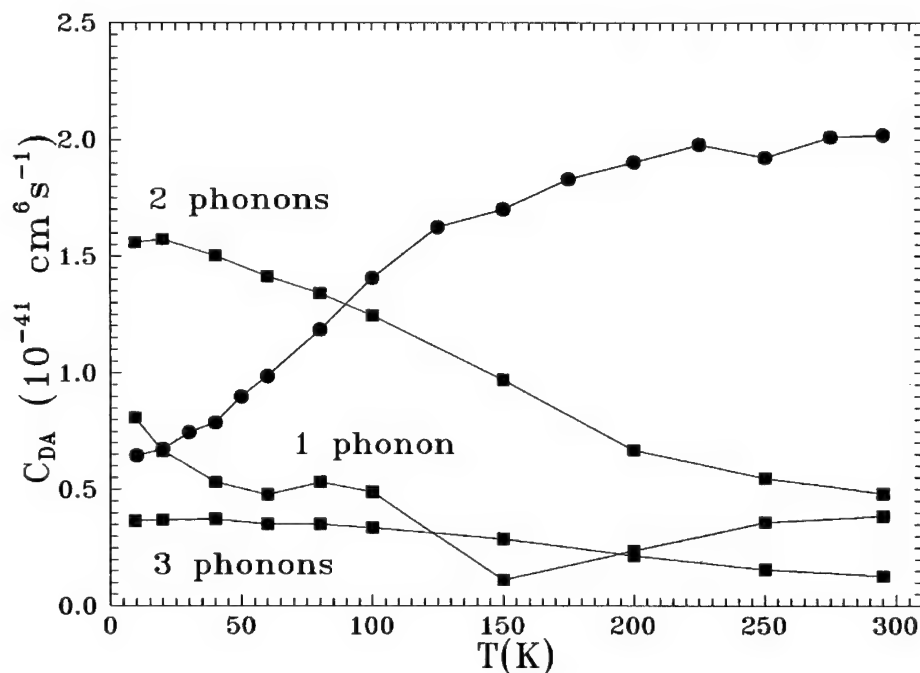


FIGURE 2 Energy transfer parameter C_{DA} obtained from the fits of the decay curves (●) and from the Miyakawa-Dexter model for different number of phonons with energy of 500 cm^{-1} (■).

For Yb^{3+} concentrations of 0.75 and 2.25 mol% the energy migration is appreciable and a better fitting of the emission decay curves is obtained with the diffusion model by Yokota-Tanimoto.⁵ The mean values obtained for the diffusion parameter D at RT are $2.2 \cdot 10^{-12}$ and $2.7 \cdot 10^{-11}\text{ cm}^2\text{s}^{-1}$ for 0.75 and 2.25 mol% of Yb^{3+} respectively. The energy transfer parameter donor-donor C_{DD} , calculated from the diffusion parameter assuming dipole-dipole interaction among donors, is given in Figure 3 in the range 10–300 K. In this figure also the parameter C_{DD} calculated with the Miyakawa-Dexter model is presented. Only a moderate agreement is again observed between the kinetic and the Miyakawa-Dexter model.

Up-conversion luminescence of Tm^{3+} at about 800 nm ($^3\text{H}_4 \rightarrow ^3\text{H}_6$) is observed when Yb^{3+} ions are excited in codoped glasses. The dependence of this up-conversion emission on the excitation intensity indicates that the process involves two photons. Moreover, a quadratic dependence of the up-conversion intensity upon the Yb^{3+} concentration is observed. It is concluded that the up-conversion mechanism involves double excitation of Tm^{3+} by sequential energy transfer from Yb^{3+} ions. This mechanism is depicted in Figure 1. The up-conversion efficiency is almost constant from RT down to 100 K, like it was observed in fluorohafnate glasses,⁶ and then decreases appreciably. This behaviour is in agreement with the similar temperature dependence of the energy transfer parameters obtained from the kinetic models.

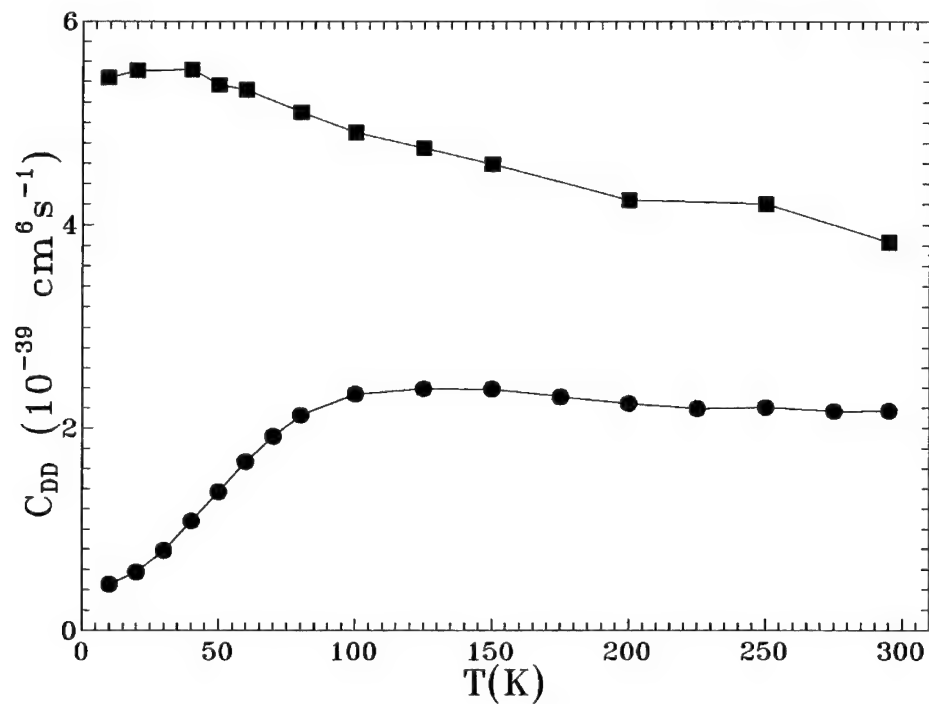


FIGURE 3 Energy transfer parameter donor-donor C_{DD} obtained from the fits of the decay curves (●) and from the Miyakawa-Dexter model for resonant energy transfer (■).

REFERENCES

1. I. R. Martín, V. D. Rodríguez, R. Alcalá and R. Cases, *J. Non-Cryst. Solids* **161**, 294 (1993).
2. M. Inokuti and F. Hirayama, *J. Chem. Phys.* **43**, 1978 (1965).
3. M. A. Chamarro and R. Cases, *Sol. State Comm.* **68**, 953 (1988).
4. T. Miyakawa and D. L. Dexter, *Phys. Rev.* **B1**, 2961 (1970).
5. M. Yokota and O. Tanimoto, *J. Phys. Soc. Jpn.* **22**, 779 (1967).
6. M. A. Chamarro and R. Cases, *J. Lumin.* **42**, 267 (1988).

SPECTRALLY RESOLVED THERMOLUMINESCENCE OF Cu AND Eu DOPED $\text{Li}_2\text{B}_4\text{O}_7$

M. MARTINI,* C. FURETTA, C. SANIPOLI, A. SCACCO and K. SOMAIAH†

**Dipartimento di Fisica, Università di Milano, via Celoria 16, 20133 Milano, Italy;*

Dipartimento di Fisica, Università La Sapienza, P. le A. Moro 2, 00185 Roma, Italy

Thermoluminescence studies are carried out on samples in powder form of $\text{Li}_2\text{B}_4\text{O}_7$ doped with Cu or Eu impurities. Results concerning $\text{Li}_2\text{B}_4\text{O}_7\text{:Cu}$ are found in agreement with data in the literature and show that the emitting defects are of intrinsic nature. In $\text{Li}_2\text{B}_4\text{O}_7\text{:Eu}$ a further emission is attributed to extrinsic aggregate centres.

Key words: Thermoluminescence, Dosimetry, $\text{Li}_2\text{B}_4\text{O}_7$.

1 INTRODUCTION

There is a continuous search for materials showing thermoluminescence (TL) to be used in radiation dosimetry. For this purpose, a phosphor should exhibit several favourable features, such as high sensitivity, effective atomic number Z as close as possible to that (7.42) of the soft biological tissue, flat energy dependence of its response. Up to now, only $\text{Li}_2\text{B}_4\text{O}_7\text{:Mn}$, for which $Z = 7.3$, showed a negligible energy dependence of TL signal, unfortunately coupled to a low sensitivity.¹ Several investigations, devoted to the identification of efficient activators for $\text{Li}_2\text{B}_4\text{O}_7$, showed that very good TL performances are obtained with metal impurities, such as Cu and Ag ions.² Glow curves of all such systems show, besides a low temperature peak (not suitable for dosimetry owing to its high rate of fading), a peak in the range between 185°C and 230°C depending on the activator. Surprisingly, no data were reported so far for $\text{Li}_2\text{B}_4\text{O}_7$ doped with rare earth impurities, which are known to be excellent activators in other materials. In this work, TL features of $\text{Li}_2\text{B}_4\text{O}_7\text{:Cu}$ and $\text{Li}_2\text{B}_4\text{O}_7\text{:Eu}$ are investigated and compared, mostly by the aid of measurements of the wavelength distribution of the emitted light.

2 PREPARATION OF MATERIALS AND EXPERIMENTAL PROCEDURES

Both phosphors were obtained by the sintering method.³ The starting material was $\text{Li}_2\text{B}_4\text{O}_7$ powder, to which solutions of $\text{Cu}(\text{NO}_3)_2 \cdot 3\text{H}_2\text{O}$ or EuBr_3 were added. In this way, samples of $\text{Li}_2\text{B}_4\text{O}_7\text{:Cu}$ contained 0.7 mole % of the impurity, while the dopant concentration in $\text{Li}_2\text{B}_4\text{O}_7\text{:Eu}$ was 0.6 mole %. The resulting powders, sieved to select particles of 100–150 microns, were irradiated with a ^{90}Sr β source and TL was measured with a Toledo TLD reader. The spectral analysis of TL signals was obtained by using a high sensitivity TL spectrometer whose details are reported elsewhere.⁴

† Permanent address: Department of Physics, Osmania University, Hyderabad 500 007, India.

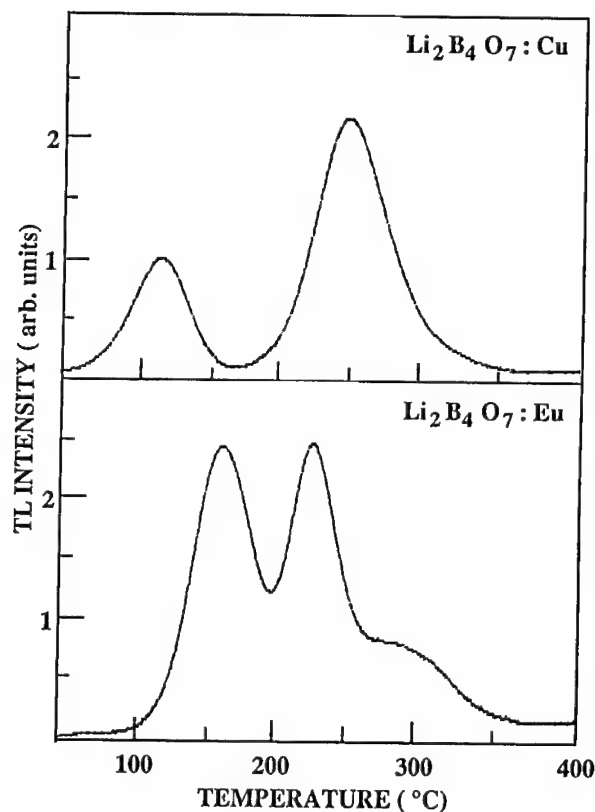


FIGURE 1 Glow curves of $\text{Li}_2\text{B}_4\text{O}_7 : \text{Cu}$ (a) and $\text{Li}_2\text{B}_4\text{O}_7 : \text{Eu}$ (b) after β -irradiation measured with a heating rate of 5°C/s .

3 EXPERIMENTAL RESULTS

Figure 1 shows typical glow curves of both phosphors, measured with a heating rate of 5°C/s . In $\text{Li}_2\text{B}_4\text{O}_7 : \text{Cu}$ two well resolved peaks are observed at about 120°C and 260°C : their positions, shapes and relative intensities are in reasonable agreement with previous findings.² In the case of $\text{Li}_2\text{B}_4\text{O}_7 : \text{Eu}$, the glow curve is composed by three peaks: two of them, at about 140°C and 215°C , show comparable intensities, while a shoulder is observed at about 275°C , namely in the descending side of the high temperature peak. Eu-activated samples exhibit intensities of TL signals comparable with those of $\text{Li}_2\text{B}_4\text{O}_7 : \text{Cu}$. Response to the dose is under investigation for both materials. After preliminary measurements, it is observed that in the case of Cu-activated samples the intensity of the dosimetric peak at 260°C is linearly dependent on the absorbed dose up to about 3.5 Gy, while the dosimetric peak at 145°C in Eu-activated $\text{Li}_2\text{B}_4\text{O}_7$ shows supralinearity starting at about 0.9 Gy.

Spectrally resolved TL, measured with a heating rate of 1°C/s , is shown in Figs 2 and 3 for both phosphors. In $\text{Li}_2\text{B}_4\text{O}_7 : \text{Cu}$ the same emission band at about 375 nm is found for both TL peaks, in good agreement with the results in the literature.² In $\text{Li}_2\text{B}_4\text{O}_7 : \text{Eu}$ the

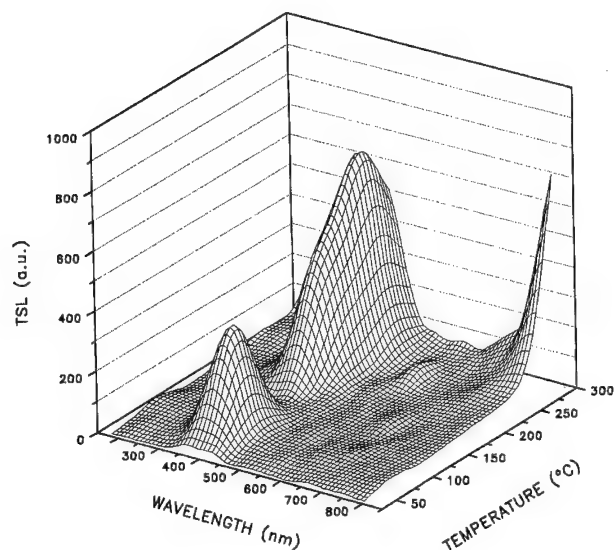


FIGURE 2 Spectrally resolved TL emission of $\text{Li}_2\text{B}_4\text{O}_7:\text{Cu}$ after β -irradiation (2 Gy) measured with a heating rate of $1^{\circ}\text{C}/\text{s}$.

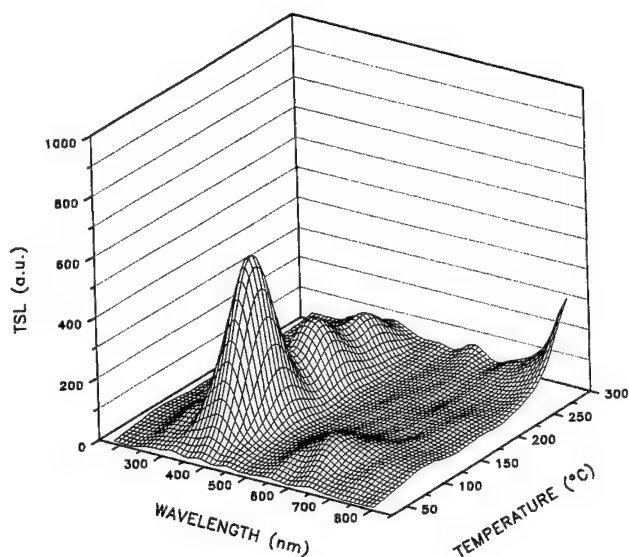


FIGURE 3 Spectrally resolved TL emission of $\text{Li}_2\text{B}_4\text{O}_7:\text{Eu}$ after β -irradiation (2 Gy) measured with a heating rate of $1^{\circ}\text{C}/\text{s}$.

low temperature TL peak is characterised by an intense emission at 375 nm accompanied by a weaker band at about 610 nm, while the high temperature peaks consist only of the 375 nm emission.

4 DISCUSSION AND CONCLUSIONS

Samples of $\text{Li}_2\text{B}_4\text{O}_7$ doped with Cu and Eu impurity, exhibit, after β -irradiation, TL peaks at different temperatures and of different intensities, but with typically coincident emission wavelength at about 375 nm. Therefore such a luminescence, independent of the kind of dopant, strongly suggests the hypothesis of the intrinsic nature of the emitting centres. This interpretation is also supported by the presence of two much weaker TL peaks in the glow curve of the undoped material, which are reasonably coincident with those reported in the literature for variously doped $\text{Li}_2\text{B}_4\text{O}_7$ and with those found in the present work. The defects responsible for the TL emission can be possibly identified as the F and F_2 centres created by the irradiation in the lattice of $\text{Li}_2\text{B}_4\text{O}_7$. Their thermal destabilization, occurring at different temperatures, would produce the same emission. In Eu-doped samples, however, a further emission at low temperature is found at 610 nm. Such a luminescence, undoubtedly related to the dopant, can be attributed to complex defects, formed by aggregation of Eu impurities with colour centres, which are easily destroyed by a moderate increase of the sample temperature. In order to confirm such an interpretation, systematic studies concerning the influence of dopant concentrations on TL signals in $\text{Li}_2\text{B}_4\text{O}_7$ are in progress.

REFERENCES

1. J. Azorin, C. Furetta and A. Scacco: *phys. stat. sol. (a)* **138**, 9 (1993).
2. M. Takenaga, O. Yamamoto and T. Yamashita: *Health Phys.* **44**, 387 (1983).
3. M. Takenaga, O. Yamamoto and T. Yamashita: *Nucl. Instr. Meth.* **175** (1980).
4. M. Martini, S. Paravisi and C. Liguori, to be published.

REVERSIBLE PHOTOIONIZATION PROCESS IN LUMINESCENT Ce^{3+} DOPED ELPASOLITE-TYPE FLUOROINDATES

J. P. CHAMINADE, A. GARCIA, T. GAEWDANG, M. POUCHARD, J. GRANNEC,
and B. JACQUIER*

*Laboratoire de Chimie du Solide du CNRS, Université de Bordeaux I, 33405 Talence
Cédex, France; *Laboratoire de Physico-Chimie des Matériaux Luminescents, URA n°442
CNRS, Université de Lyon I, 69622 Villeurbanne Cédex, France*

Ce^{3+} luminescence was investigated in elpasolite fluoroindates A_2BInF_6 ($\text{A} = \text{K}, \text{Rb}$; $\text{B} = \text{Na}, \text{K}$). All $\text{A}_2\text{BInF}_6:\text{Ce}^{3+}$ have been synthesized by solid state reactions from stoichiometric mixtures in sealed gold tubes at 700°C . Transparent colourless $\text{Rb}_2\text{KInF}_6:\text{Ce}^{3+}$ crystals were grown by Bridgman method in 10% Rh-Pt crucibles sealed under dry argon atmosphere.

At room temperature $\text{Rb}_2\text{KInF}_6:\text{Ce}^{3+}$ presents a blue-green broad-band emission when excited with a 315 nm UV radiation. This emission can be ascribed to the Ce^{3+} ions in In^{3+} site. Two other emissions in the blue and UV can be assumed to originate from Ce^{3+} ions located in the 6 coordinated potassium and 12 coordinated rubidium sites.

Under a steady 315 nm UV excitation the main blue-green Ce^{3+} emission decreases progressively, giving rise to a new emitting centre which exhibits a red emission under 255 nm excitation. This phenomenon is optically reversible and moreover the original state can be thermally regenerated. An hypothesis based on the In(III)-Ce(III) redox couple is proposed to explain this behaviour: photoionization of Ce^{3+} leads to Ce^{4+} with electron transfer on In^{3+} acceptors. This red luminescence is ascribed to the formation of In^+ ions.

Key words: elpasolite fluoroindates, Ce^{3+} luminescence, crystal growth, photoionization process.

1 INTRODUCTION

It has been recently proposed to use single crystal scintillators containing a large amount of ^{115}In for the detection of low energy solar neutrinos according to Raghavan's nuclear reaction.^{1,2} Until now the only cerium-doped indate matrix whose luminescence was studied is the solid solution $\text{In}_x\text{Sc}_{1-x}\text{BO}_3:\text{Ce}^{3+}$; it was shown that the Ce^{3+} luminescence disappears with the increase in indium content due to the position of the 5d states above the bottom of the conduction band.³ Consequently we extended this investigation to fluoroindates and particularly to elpasolite fluoroindates A_2BInF_6 ($\text{A} = \text{K}, \text{Rb}$; $\text{B} = \text{Na}, \text{K}$) which appear attractive ionic host crystals for rare earth.

Fluoroindates with general formula A_2BInF_6 belong to a wide family of crystals whose structures derive from that of the elpasolite (K_2NaAlF_6 prototype structure, $\text{Fm}\bar{3}\text{m}$ with $Z = 4$). The structural arrangement corresponds to that of the perovskite with an additional cationic ordering between the smaller monovalent cations B and trivalent cations M in the octahedral sites.^{4,5}

The present work deals with the synthesis, crystal growth and luminescence properties of $\text{A}_2\text{BInF}_6:\text{Ce}^{3+}$ compounds.

2 EXPERIMENTAL

The alkali fluorides, NaF, KF and RbF were commercial products which were dehydrated under vacuum. CeF_3 and InF_3 trifluorides were synthesized from the corresponding

chlorides or oxides under an HF flow up to 1000°C or under a F₂ stream up to 600°C respectively. All A₂BInF₆ compounds have been prepared by solid state reaction from stoichiometric mixtures of composition 2AF + BF + (1 - x)InF₃ + xCeF₃. The reactions were carried out at about 700°C in sealed gold tubes. Among the different materials Rb₂KInF₆: 1% Ce³⁺ has been selected for crystal growth using a Bridgman method.

The crystal-growth equipment was built up of two independent furnaces separated by an insulating zone. The temperature of each furnace has been separately programmed. The biconal shaped crucibles were sealed under dry argon atmosphere and set in the crystal growth apparatus. Initially heated to T = T_F + 50 K in the upper furnace, the crucible was moved down to the cooler furnace at a rate of 0.15 mm/h to 1.5 mm/h with a thermal gradient of 2.5 K/mm. The temperature was then lowered to room temperature at a rate of 10 K/h to minimize any thermal stresses. Single crystals around 5 × 5 × 5 mm³ were obtained without visible inhomogeneities. They were cut into slices or cubes along the different crystallographic orientations. The luminescence measurements were performed from the liquid helium temperature up to room temperature, using Jobin-Yvon SPEX FL 212 spectrofluorometer equipped with a SMC Air Liquide, liquid helium flow cryostat. Decay measurements were carried out with synchrotron radiation (LURE) as the excitation source.

3 LUMINESCENCE

The luminescence measurements were performed on polished and oriented Rb₂KInF₆:Ce³⁺ 1% single crystals at room temperature. They present a blue-green broad band emission peaking at 480 nm when excited with a 315 nm radiation (Figure 1). This emission can be ascribed to the 5d → 4f transitions of Ce³⁺ ions in In³⁺ sites. The decay constant, 30 ns, is of the order of magnitude of values observed for Ce³⁺.

Two other emissions with lower intensity have also been detected (Figure 1). An ultraviolet one around 320 nm corresponding to an excitation at 245 nm, and a weak blue emission at 424 nm for an excitation at 270 nm. These two other emissions can be assumed

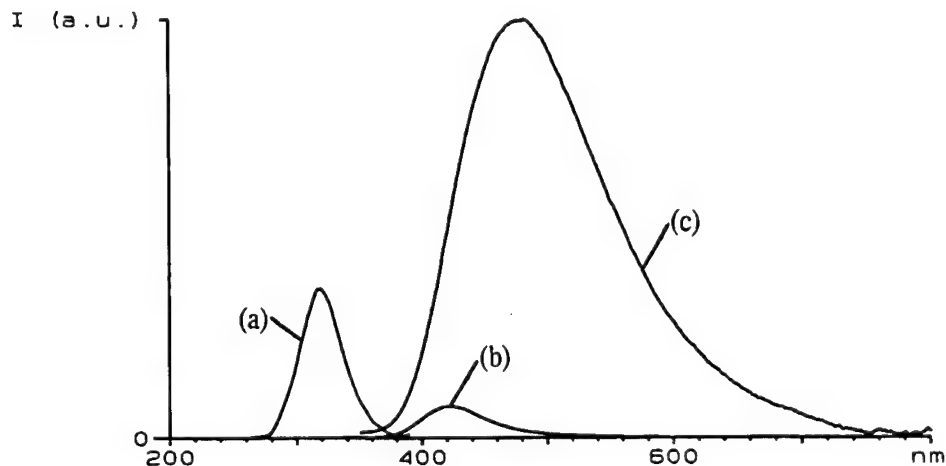


FIGURE 1 Emission spectra of ultraviolet (a) ($\lambda_{\text{exc.}} = 245$ nm), blue (b) ($\lambda_{\text{exc.}} = 272$ nm) and blue-green (c) ($\lambda_{\text{exc.}} = 315$ nm) luminescence of a Rb₂KInF₆:Ce³⁺ 1% single crystal at 300 K (comparable intensities, corrected from the spectral response of the photomultiplier and lamp flux).

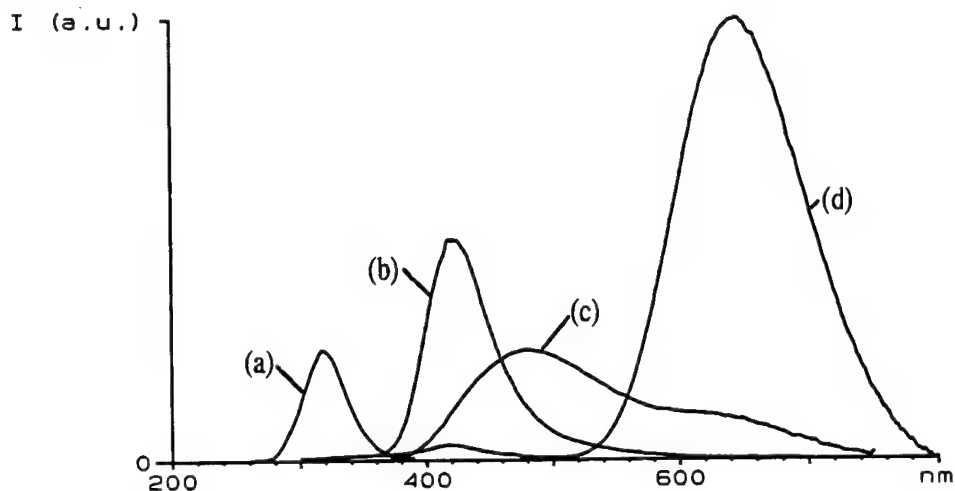


FIGURE 2 Emission spectra of ultraviolet (a) ($\lambda_{\text{exc.}} = 245$ nm), blue (b) ($\lambda_{\text{exc.}} = 272$ nm), blue-green (c) ($\lambda_{\text{exc.}} = 315$ nm) and red (d) ($\lambda_{\text{exc.}} = 255$ nm) luminescence of a previously irradiated ($\lambda_{\text{irr}} = 315$ nm) crystal at 300 K (comparable and corrected intensities. On the figure the red luminescence intensity is divided by four).

to originate also from Ce^{3+} ions but located in other types of sites. The elpasolite-type structure A_2BInF_6 possesses an other 6-coordinated site (B), corresponding to the potassium ions in Rb_2KInF_6 , and a 12-coordinated one (A) occupied by rubidium ions. The latter being very large the ligand field effect is small, inducing a weak splitting of the Ce^{3+} 5d excited levels. The blue and UV emissions are therefore assigned to Ce^{3+} ions in the potassium and rubidium sites.

Under a steady UV excitation at 315 nm the intensity of the main blue-green emission decreases progressively and gives rise to a new emitting centre which luminesces in the red (broad band emission centered at 650 nm) when excited at 255 nm (Figure 2).

This phenomenon is reversible: when steadily excited at 255 nm, the red emission decreases and the centre correlated with the blue-green emission is recreated. Moreover the original state can be thermally regenerated. After 1 hour annealing at 400°C under vacuum in a sealed quartz tube, the red emission excited at 255 nm has completely disappeared and the single crystal shows the original blue-green emission for a 315 nm excitation. At room temperature, the red emitting centre shows very high stability, several months later a 315 nm-irradiated crystal still exhibits a red luminescence when excited at 255 nm.

With yttrium and scandium elpasolites no formation of new emitting centre under irradiation in the cerium $4f \rightarrow 5d$ band was observed. Indium is therefore involved in the process.

An hypothesis based on the In(III)-Ce(III) redox couple is proposed to explain this behaviour. Under a specific 315 nm irradiation the 5d Ce^{3+} levels are populated. Then two mechanisms are in competition:

- a radiative deexcitation of Ce^{3+} with photons emission corresponding to the blue-green fluorescence,
- Ce^{3+} photoionization in Ce^{4+} with a transfer to an acceptor (vacancy, In^{3+} ...).

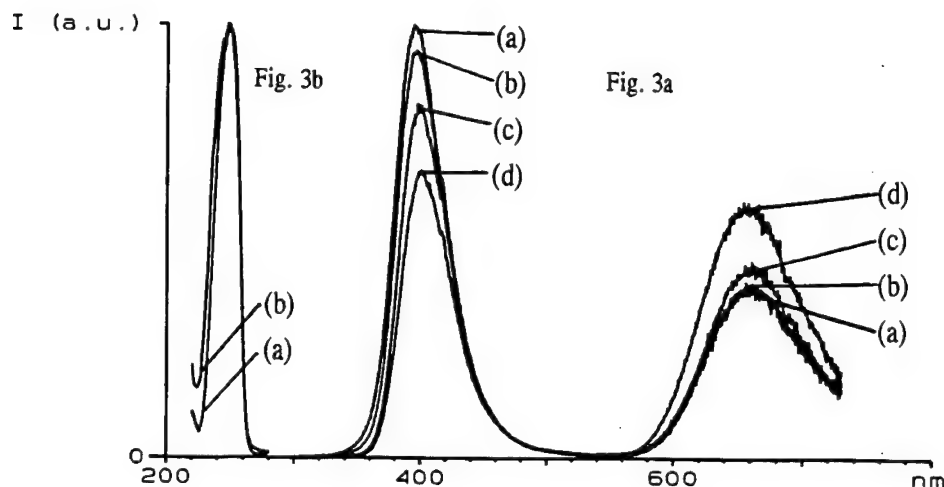
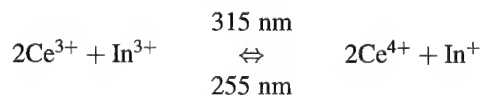


FIGURE 3a Emission spectra of the blue and red luminescence of a $\text{Rb}_2\text{KInF}_6:\text{Ce}^{3+}$ 1% 315 nm irradiated crystal under 255 nm excitation versus temperature. (10 K (a), 40 K (b), 75 K (c), 125 K (d)).

Figure 3b Normalized excitation spectra of the blue (a) and red (b) emission of a $\text{Rb}_2\text{KInF}_6:\text{Ce}^{3+}$ 1% 315 nm-irradiated crystal at low temperature (10 K).

The indium can change its oxidation state and play the acceptor role, therefore we can describe this phenomenon by the following equation:



The intensity lessening of the blue-green emission can be correlated with the decrease of the concentration of Ce^{3+} ions. The mechanism reversibility can be afforded by In^{+} photoionization with electrons transfer on Ce^{3+} under 255 nm excitation. Decreasing the temperature in an irradiated $\text{Rb}_2\text{KInF}_6:\text{Ce}^{3+}$ 1% crystal induces a quenching of the 255 nm excited red emission in favor of a blue one (Figure 3a). This behaviour has been also previously noticed in In^{+} doped alkali-halides.^{6,7,8} At low temperature the blue and the red emissions coexist. Both emission seem to have the same excitation spectrum (Figure 3b). The luminescence characteristics observed at low temperature are consistent with the existence of a two-minima excited state of In^{+} like in alkali-halides.

4 CONCLUSION

It is rather difficult to find luminescent materials containing simultaneously indium and cerium ions due to their oxydo-reduction characteristics. Fluoride host lattices with elpasolite-type structure appear to be a particular case: depending on the excitation way they can exhibit either Ce^{3+} blue-green emission or In^{+} red emission. This phenomenon is optically reversible and involves two photoionization processes leading to two different emitting ions Ce^{3+} (In^{3+}) or In^{+} (Ce^{4+}). The In^{+} ions formed show a good stability at

room temperature. These luminescent properties of cerium doped fluoroindate elpasolite-type compounds make them appropriate for use as storage phosphors.

REFERENCES

1. R. S. Raghavan, *Phys. Rev. Letters*, **37**, 259 (1976).
2. L. Gonzales-Mestres, *Ann de Phys. (Suppl.)* **6**, 181 (1992).
3. T. Gaewdang, J. P. Chaminade, A. Garcia, M. Pouchard and B. Jacquier, *J. Phys. Chem. Solids* (accepted).
4. K. S. Aleksandrov and S. V. Misyul', *Sov. Phys. Crystallogr.* **26**, 612 (1981).
5. D. Babel and A. Tressaud, Crystal Chemistry of Fluorides, in *Inorganic Solid Fluorides*, P. Hagenmuller Ed., Academic Press, New York, **77** (1985).
6. A. Fukuda, S. Makishima, T. Mabuchi and R. Onaka, *J. Phys. Chem. Solids*, **28**, 1763 (1967).
7. A. Fukuda, *Phys. Rev. B*, **1**, 4161 (1970).
8. M. Casalboni, F. Crisanti, U. M. Grassano, C. Manfrocelli, A. Scacco and A. Tanga, *Phys. Stat. Sol. (b)*, **93**, 755 (1979).

EXCITED LEVELS OF THE 2.56 eV EMISSION IN SYNTHETIC DIAMOND

E. PEREIRA, L. PEREIRA, D. M. HOFMANN,* W. STADLER* and B. K. MEYER*

*Departamento de Física, Universidade de Aveiro, 3800 Aveiro, Portugal; *Physik
Department E16, Technical University Munich, D-85747 Garching, Germany*

The 2.56 eV luminescence is found in high pressure synthetic diamond grown in the presence of the Ni-Fe catalyst and presents a multiplet zero phonon line structure. The vibronic analysis of the band using the linear electron-phonon coupling model indicates that the lower energy component of the zero phonon line structure couples preferentially to a near local phonon of 21 meV, while the other components present among themselves a similar vibronic coupling with a weaker coupling to the 21 meV mode. The further splitting that some components present is shown to be due to ground state splitting. These results suggest that the luminescence is due to emission from two electronic levels one of them split in four components to a doubly split ground state. The nature of the centre is discussed.

1 INTRODUCTION

In synthetic diamond several characteristic luminescence bands have been found. Of these the 1.4 eV emission has been unambiguously attributed to Ni, presenting the zero phonon line a splitting due to the different Ni isotopes.¹ Also other bands seen either in absorption or in emission have been attributed to Ni. One of these is the 2.56 eV band that presents an intensity correlated to the Ni content of the samples.² It has also been shown that a resonance at $g = 2.032 \pm 0.001$ is found in the ODMR spectrum of the band.³ This value is identical to the Ni^{2+} g value,⁴ and indeed the EPR spectrum of Ni^{2+} has been found in the same samples. However there is not sufficient evidence to decide if the luminescence is due to Ni^{2+} or if the Ni^{2+} resonance is detectable on the 2.56 eV band by a shunt pass process. The emission has a very complex zero phonon line (ZPL) structure, with five main lines with temperature dependent intensities. In the present work we analyse in detail the vibronic coupling associated with the different lines and the nature of the 0.4 meV temperature independent splitting found in three of these lines, that is shown to be due to ground state splitting. These results coupled with the time dependence of the ODMR signal favours the hypothesis that Ni^{2+} indirectly affects the 2.56 eV luminescence.

2 EXPERIMENTAL RESULTS AND DISCUSSION

Steady state luminescence spectra of the 2.56 eV centre have been recorded at different temperatures using excitation from the 365 nm Hg line. The samples were cooled by a He flow cryostat, with temperatures kept within 0.1 K. The luminescence is viewed through a 1704 Spex monochromator by a RCA C31034 photomultiplier. All spectra are corrected from the spectral response of the detection system. ODMR results were obtained in a magneto-optical cryo-system at temperatures of 1.6 K, with excitation by the 325 nm line of a HeCd laser.

In Figure 1 we show the spectra observed at 4 and 50 K. It is observed that the peak at 21 meV from the ZPL region (marked by an A in the spectra) decreases strongly in intensity upon increasing temperature. In Figure 2 the high resolution higher energy region of the spectra at the same temperatures is shown. It can also be seen that the peak A shifts

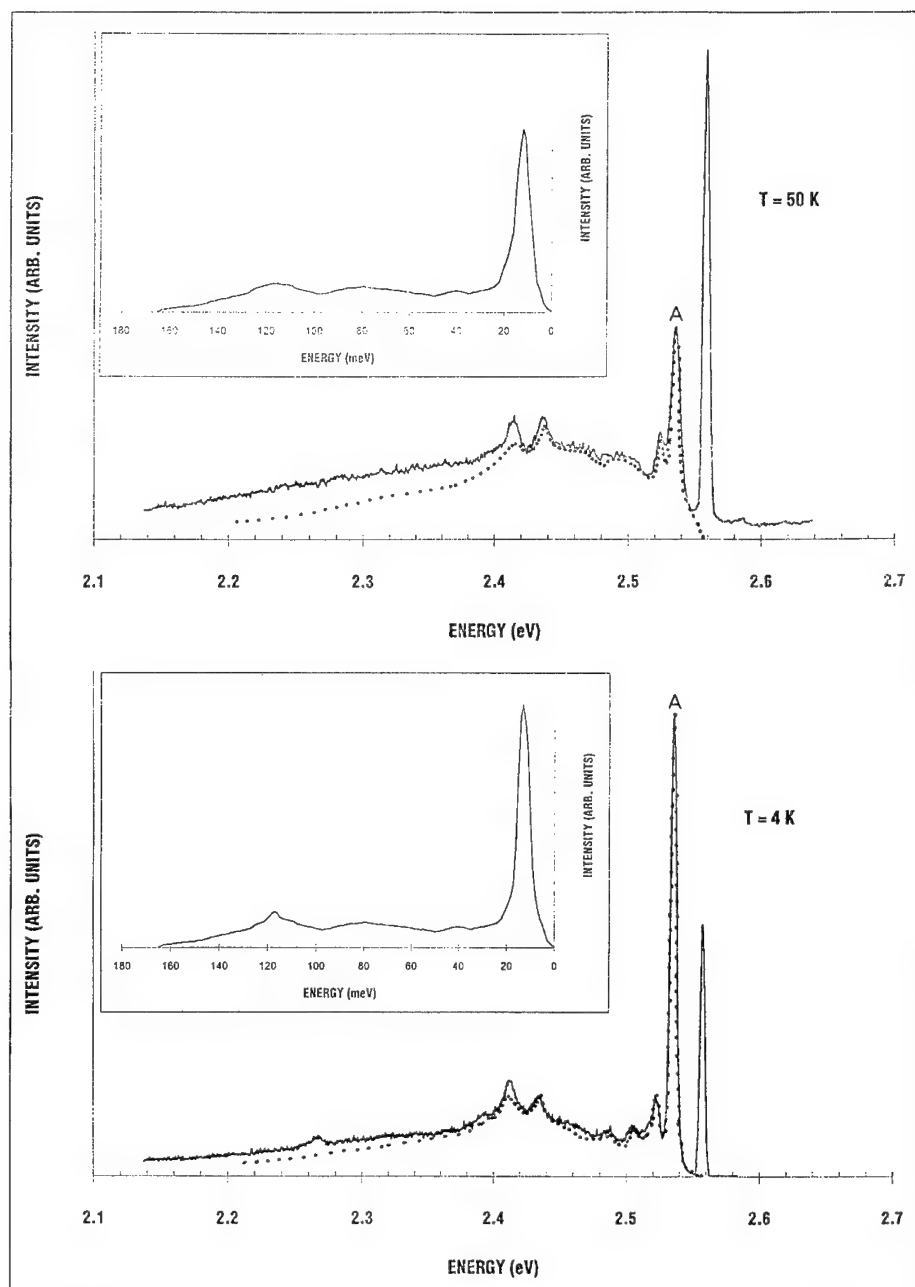


FIGURE 1 Luminescence spectra of the 2.56 eV centre excited by the 365 nm Hg. Line a: 4 K, b: 50 K. Dotted line: reconstructed spectra according to the linear electron-phonon coupling model. Inset: first phonon spectra used in the reconstruction.

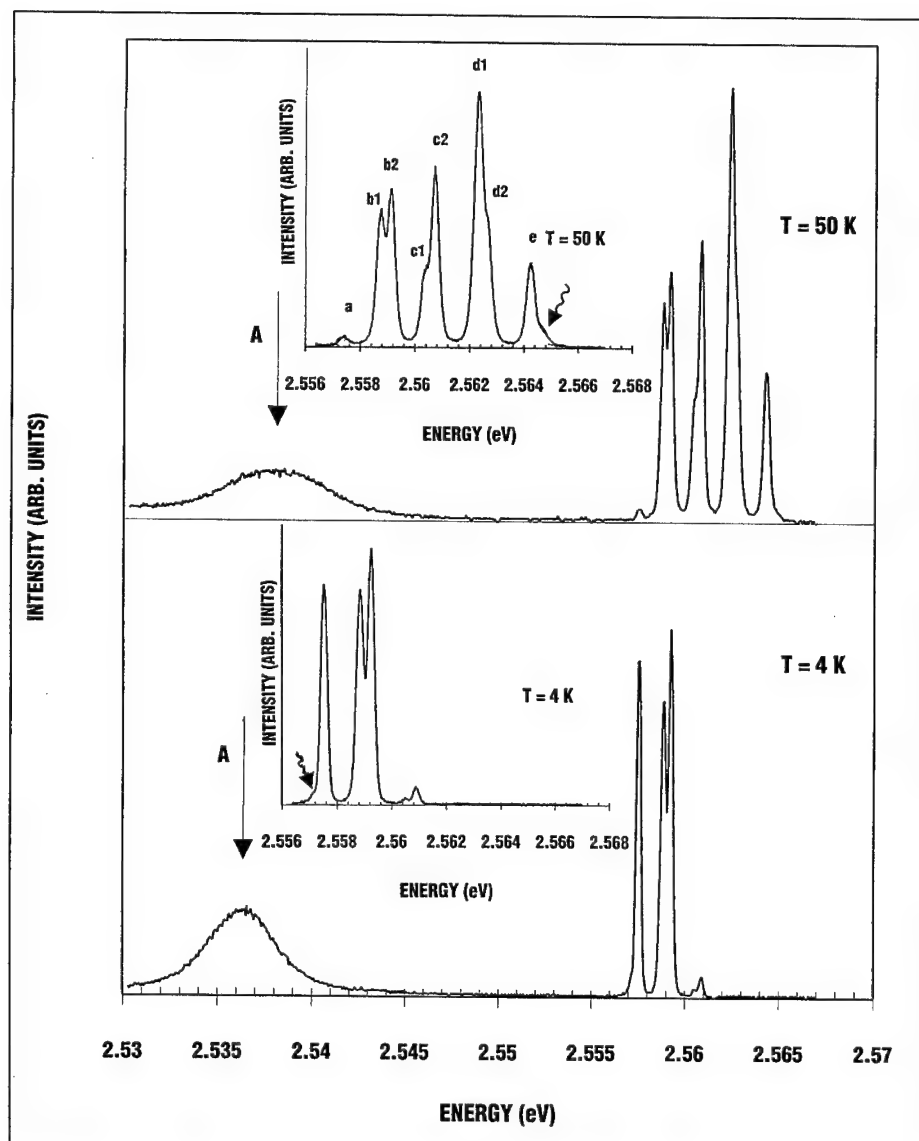


FIGURE 2 The high resolution higher energy region of the spectra for 4 and 50 K. The arrows shows the peak A. Inset: the ZPL region for the same temperatures.

towards higher energies upon increasing temperature. The different components of the ZPL are labelled *a*, *b* (*b1*, *b2*), *c* (*c1*, *c2*), *d* (*d1*, *d2*) and *e*. The relative intensity change of lines *a*, *b*, *c*, *d* and *e* with temperature reveal thermalization, with line *a* showing a 40 times lower transition probability to the ground state than line *b*,³ while the transition probabilities of the other lines are of the same order of magnitude at 50 K.² In the inset of

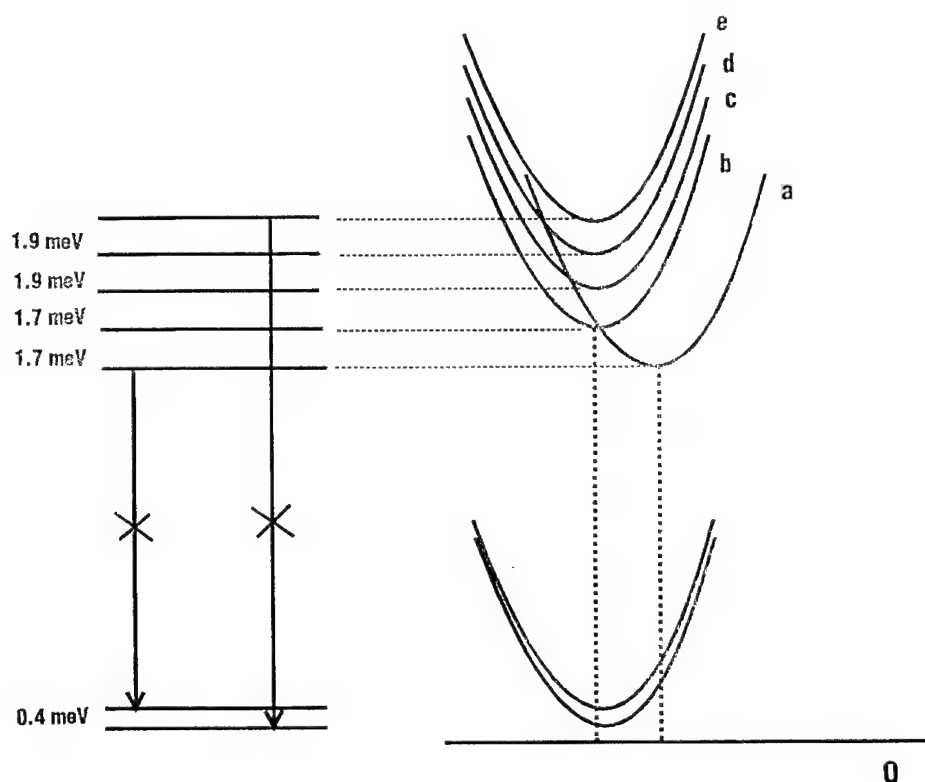


FIGURE 3 Schema of ground and excited levels of the centre. Q is the 21 meV mode coordinate. Transitions marked by X are nearly forbidden.

Figure 2 only the ZPL region is shown. The ratio of lines $b1/b2$, $c1/c2$ and $d1/d2$ is constant in the whole temperature range where it can be observed (due to vibronic coupling broadening the splitting is no longer observed above 70 K) and equal respectively to 5/6, 1/3 and 3/1. Also it is observed that the splitting is equal to 0.4 meV in the three pairs of lines. It can also be seen that lines a and e are asymmetrical, a small shoulder on the low energy side of line a and on the high energy side of line e being observed as indicated by the wavy arrows in the insets. These results may be explained if the emission takes place from 5 excited levels to two ground state levels 0.4 meV apart. The small shoulders in lines a and e may indicate that the transitions from the excited levels to the higher and lower energy ground state levels are nearly forbidden. A schema of the levels and their energy separations is shown in Figure 3. The vibronic spectra may be explained assuming that peak A is a phonon replica of the ZPL, showing a stronger coupling to level a . This explains also the broadening and shift towards higher energies of peak A. Vibronic bands in diamond are usually accounted for by the linear electron-phonon coupling model.⁵ Using this model a vibronic band can be reconstructed by trial and error from an estimated first phonon spectrum and Huang-Rhys (S) factor until agreement between experimental and reconstructed band is achieved.

The n^{th} phonon transition probability is given by

$$M_{0n}^2 = \frac{S^n e^{-S}}{n!}$$

The band intensity at an energy $\hbar\omega$ below the ZPL due to the n^{th} phonon will be given by

$$I_n(\hbar\omega) = \int_0^{\hbar\omega_m} I_1(x) I_{n-1}(\hbar\omega - x) dx$$

where $I_1(x)$ is the first phonon intensity at energy x and $\hbar\omega_m$ is the maximum vibrational energy of the centre.

In the inset of Figure 1 we show the first phonon spectra that reconstruct the bands at 4 and 50 K, with S factors respectively of 2.5 and 1.8. The vibronic coupling is identical in lines b to e . The reconstructed bands are shown by dotted lines in the spectra of Figure 1.

The time dependence of the $g = 2.032$ ODMR signal has been investigated, by varying the on/off modulation frequency of the microwaves. It was found that the maximum signal intensity is achieved up to 1.5 kHz. For higher frequencies the signal intensity shows an exponential decay and vanishes above 5 kHz. The inverse of the frequency corresponds to a life time, the best fit to the experimental data yielding 0.5 ± 0.3 ms. This value approaches the longer lifetime component found in the photoluminescence decay that is attributed to an indirect population of the centre, as its relative intensity increases with temperature and matches the total luminescence intensity increase.³

3 CONCLUSIONS

The different transition probability to the ground state and the different vibronic coupling suggest that line a originates in a different electronic level, while the other four are components of another electronic level, split by spin-orbit or Jahn-Teller interactions. These results however cast doubt on the assignment of substitutional Ni^- to the centre with a $^4\text{A}_2$ ground state and ^2E and $^4\text{T}_2$ excited states, as it would be difficult to explain the ground state splitting of 0.4 meV, as compared with the ground state splitting of Cr^{+++} in ruby, also a $^4\text{A}_2$ level of only 0.04 meV. Another hypothesis is that the centre will suffer a large tetragonal distortion as occurs in Cs_3CoCl_5 , where the spin-orbit splitting of the $^4\text{A}_2$ level is of 1.1 meV.⁶ However the ^2E and $^4\text{T}_2$ levels are much closer than in Cs_3CoCl_5 making unlikely that the ^2E level will not be split, as observed. Also the fact that the ODMR signal has a decay very similar to the decay observed in photoluminescence for the indirect population of the emitting levels supports the idea that Ni^- populates the 2.56 eV centre that is due to other impurities. Further work is needed to clarify the origin of the band.

ACKNOWLEDGMENTS

Financial support from DAAD-CRUP is acknowledged.

REFERENCES

1. M. H. Nazaré, A. Neves and G. Davies, *Phys. Rev.* **B43** (1991) 14196.
2. A. T. Collins, H. Kanda and C. Burns, *Phil. Mag.* **B61** (1990) 797.

3. E. Pereira, L. Santos, L. Pereira, D. M. Hofmann, P. Christmann, W. Stadler and B. K. Meyer, *Diam and Rel. Mat.*, **4** (1994) 53.
4. J. Isoya, H. Kanda, J. Norris, J. Tang and M. K. Bowmann, *Phys. Rev.* **B41** (1990) 3905.
5. G. Davies, *Rep. Prog. Phys.*, **44**, (1981) 787.
6. J. C. Rivoal, C. Grisolia, J. P. Torre and M. Vala, *J. Physique* **46** (1985) 1709.

Er³⁺ ION CONCENTRATION AND ANNEALING TEMPERATURE EFFECT ON THE FLUORESCENCE OF Er³⁺:TiO₂ PLANAR WAVEGUIDES PREPARED BY THE SOL-GEL PROCESS

A. BAHTAT,¹ M. BOUAZAOU,² M. C. MARCO DE LUCAS,¹ M. BAHTAT,³
B. JACQUIER¹ and J. MUGNIER¹

¹Laboratoire de Physico-Chimie des Matériaux Luminescents, URA 442 CNRS, Université Lyon I, 43 Bd du 11 novembre 1918, 69622 villeurbanne (France); ²Laboratoire de Spectroscopie Hertzienne, URA 249 CNRS, Université Lille I, Bat P5, 59655 Villeneuve d'Ascq (France); ³Laboratoire du Traitement du Signal et Instrumentation, URA 842 CNRS, Faculté des sciences, 23 bd du Dr. P. Michelon, 42023 ST-Etienne (France)

The fabrication of Erbium-doped optical planar waveguides using the sol-gel process and the dip-coating procedure is described. The planar waveguides are optically pumped at room temperature using a Ti: sapphire laser with $\lambda = 800$ nm; the observed fluorescence of Er³⁺ ions at 1.53 μ m is investigated. It is shown that the shape of the ⁴I_{13/2} → ⁴I_{15/2} transition depends on the concentration of Er³⁺ ions in TiO₂ monomode waveguides (thickness = 80 nm), indicating that Er³⁺ ions modify the structure of TiO₂ gel network. The dependence on heat treatment of Er³⁺ fluorescence spectra is investigated and preliminary lifetime measurements are presented. The elaboration of erbium-doped optical planar waveguides by the sol-gel process seems an inexpensive route for the realization of integrated devices on planar substrates.

Key words: optical waveguides, Er³⁺ ions, sol-gel.

1 INTRODUCTION

Rare-earth-doped materials have attracted much attention in the fabrication of planar waveguide devices for optical communication and processing systems. To this end, several techniques have been used to produce these waveguides.^{1–3} In this study, we will show that Er³⁺ doped planar waveguides can be prepared successfully using the sol-gel method. Fluorescence spectroscopy is used to demonstrate Er³⁺ incorporation and to characterize the Er³⁺ ions environment. The purpose of this paper is to describe the structural evolution of the sol-gel erbium doped waveguides and the variation of the full width at half-maximum (FWHM) of the ⁴I_{13/2} → ⁴I_{15/2} transition according to rare-earth concentration and annealing temperature.

2 EXPERIMENT

The preparation of TiO₂ optical planar waveguides by the sol-gel process and dip-coating technique has been described elsewhere.⁴ Briefly, the starting solution was prepared using titanium isopropoxide (Ti(OⁱPr)₄-Aldrich), iso-propanol (ⁱPrOH- Merck) and acetic acid (AcOH-Prolabo) with a molar ratio AcOH/Ti = 6. Er³⁺ ions were introduced by adding Er(NO₃)₃ in a molar ratio Er(NO₃)₃/Ti = x (x = 3, 5, 7, 10, and 15%). The mixture obtained was diluted by methyl alcohol. Pyrex substrates (75 mm × 25 mm) were carefully cleaned, then immersed in the solution and withdrawn from the bath at a rate of 40 mm/min. The Er³⁺:TiO₂ layers obtained are first dried at 100°C for 15 min and then heated in the oven at different temperatures (500 and 600°C) under a constant flow of pure

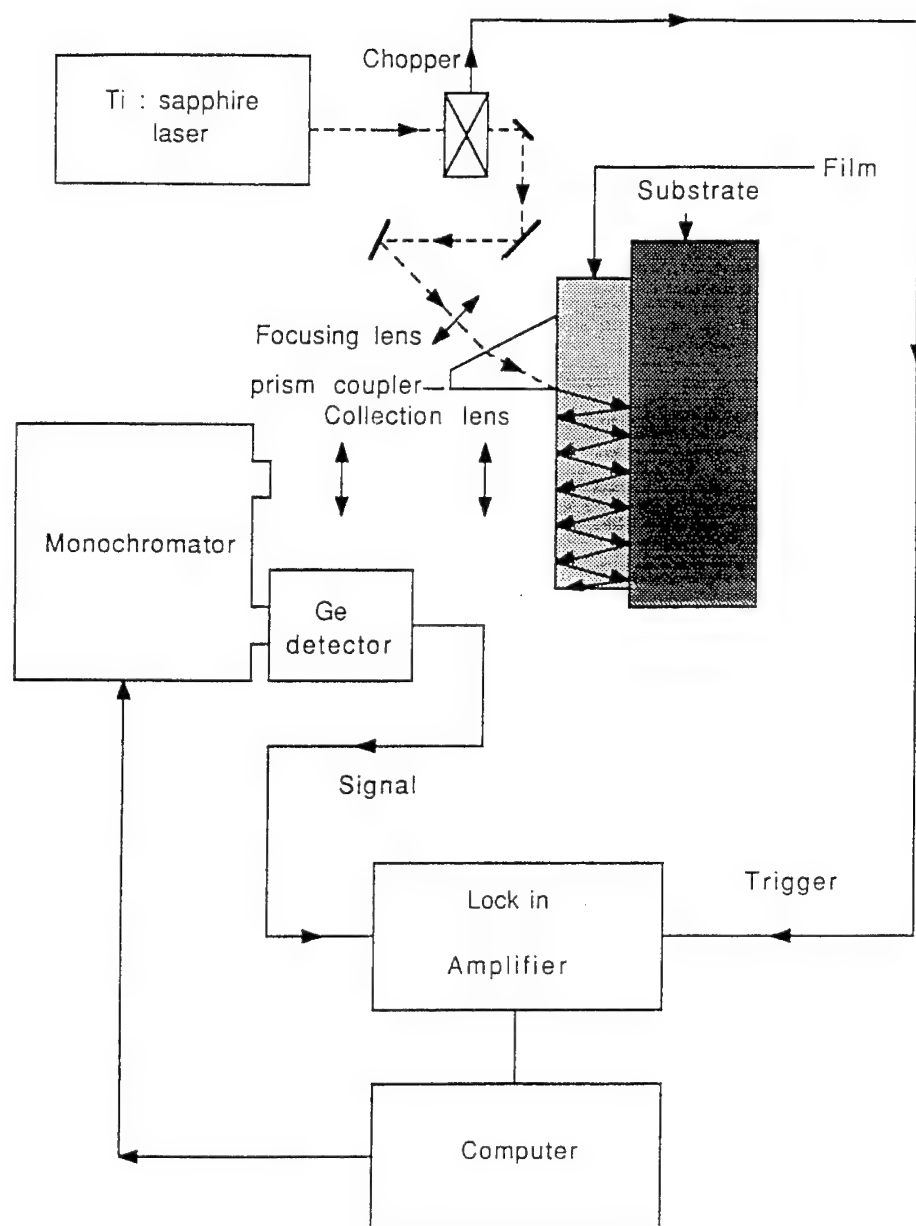


FIGURE 1 Experimental setup.

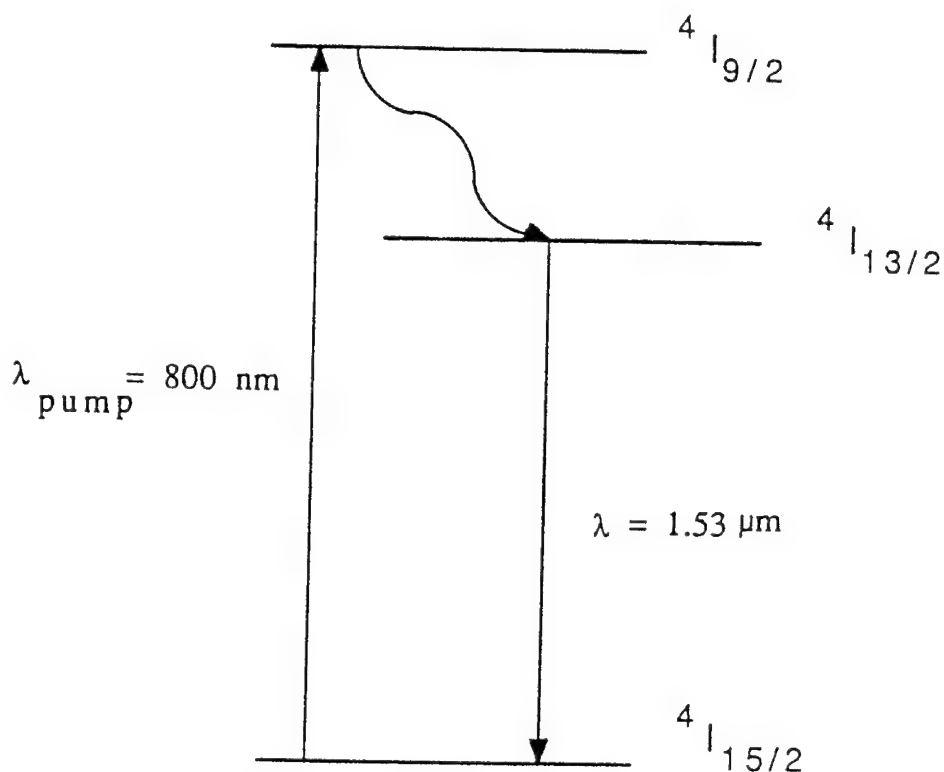


FIGURE 2 Er³⁺ energy level diagram for the fluorescence configuration.

and dry oxygen for one hour. The resulting films are $d \approx 80$ nm thick and their refractive index ranges from 1.8 to 2.1 depending on the annealing temperature. Such a single film is a monomode waveguide for wavelengths in the visible region.

The experimental apparatus used for monitoring fluorescence spectra is shown in Figure 1. A Ti:sapphire laser tuned to 800 nm was used as the pump source. The pump beam is coupled into the film using a heavy glass prism (refractive index = 2). The light emitted at $\pi/2$ rad from the waveguide was analyzed with a Jobin-Yvon HR640 monochromator and detected with a North-Coast liquid-nitrogen-cooled germanium detector. The spectral resolution ranged from 1 to 2 nm. The pump signal was mechanically chopped at 80 Hz and the signal from the Ge-detector was preamplified and passed to a Lock-in amplifier. All the spectra were recorded at room temperature.

3 RESULTS AND DISCUSSION

Figure 2 shows the energy levels involved in the fluorescence pump configuration. The Er³⁺ ion is pumped to the $4I_{9/2}$ excited state by the Ti:sapphire laser tuned to 800 nm,

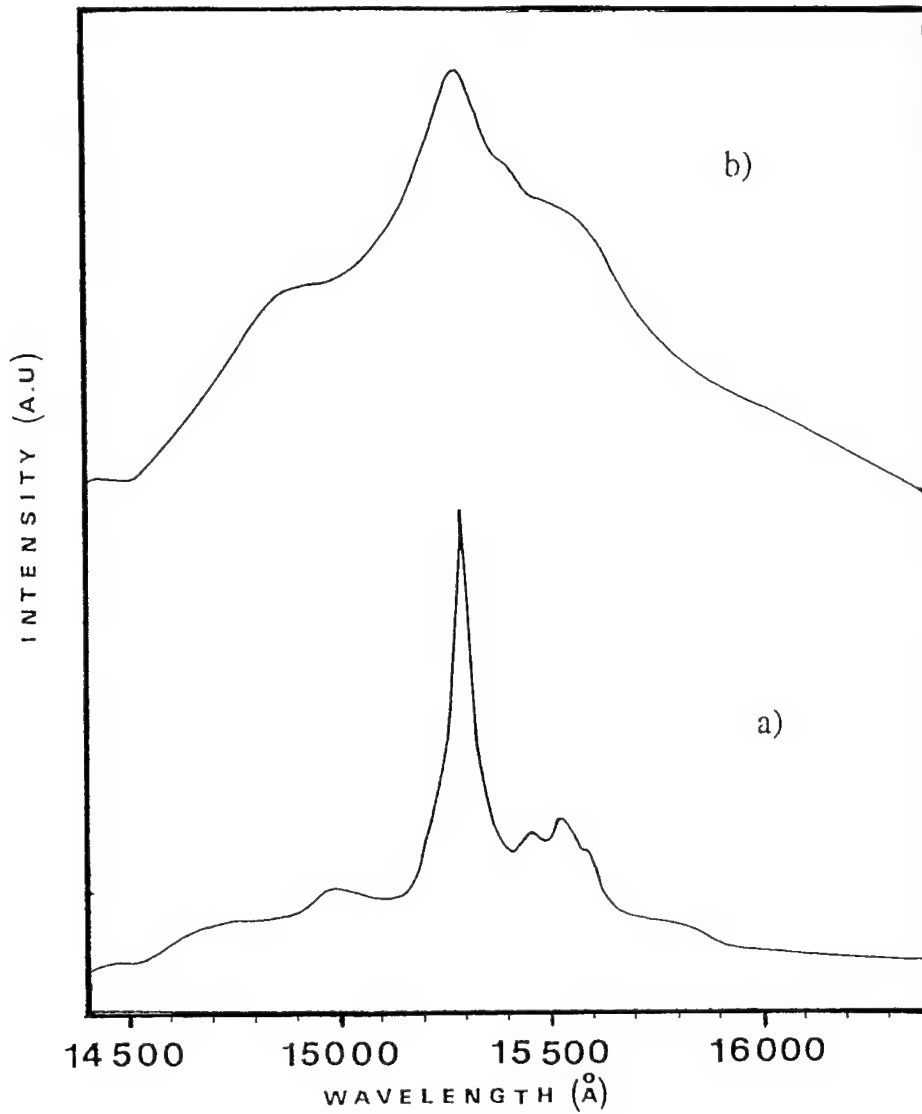


FIGURE 3 Fluorescence spectra of $\text{Er}^{3+}:\text{TiO}_2$ waveguides obtained by excitation in the $^4\text{I}_{9/2}$ state for a) 3-mol% $\text{Er}^{3+}:\text{TiO}_2$ and b) 7-mol% $\text{Er}^{3+}:\text{TiO}_2$ waveguides. Annealing temperature $T = 500^\circ\text{C}$.

whereupon the energy decays through non-radiative processes to the $^4\text{I}_{13/2}$ state. From there the system decays to the ground state $^4\text{I}_{15/2}$ through an optical transition at $\lambda = 1.53 \mu\text{m}$.

$\text{Er}^{3+}:\text{TiO}_2$ waveguides of different Er ion concentrations (3%, 7%, 10% and 15%) were studied. These waveguides were annealed at 500°C for 1 hour. As an example, Figure 3

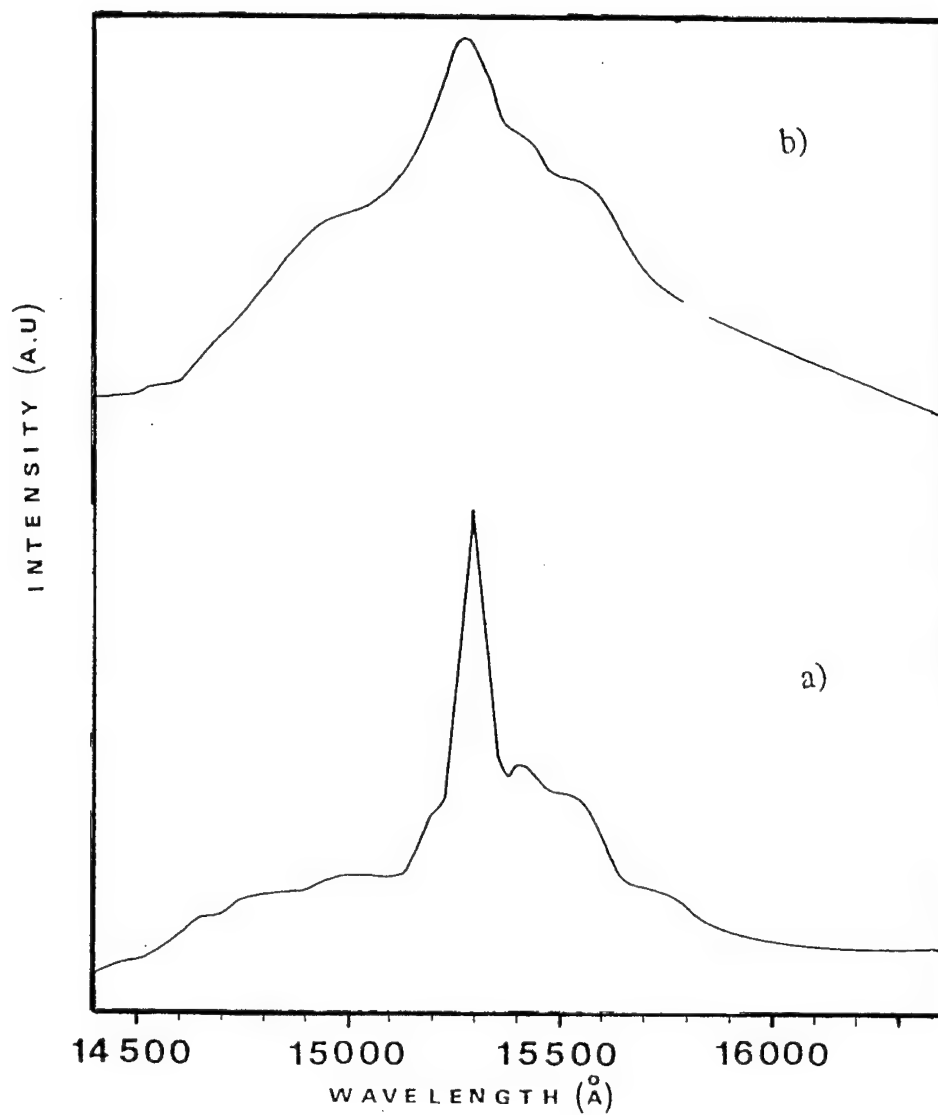


FIGURE 4 Fluorescence spectra of Er³⁺:TiO₂ waveguides obtained by excitation in the ⁴I_{9/2} state for a) 7-mol% Er³⁺:TiO₂ and b) 10-mol% Er³⁺:TiO₂ waveguides. Annealing temperature T = 600°C.

shows the fluorescence spectra of waveguides for Er ion concentrations of 3% and 7%. The two spectra peak at $\lambda = 1.53 \mu\text{m}$, while their shapes are quite different. Indeed, the full width at half-maximum (FWHM) of the ⁴I_{13/2} → ⁴I_{15/2} transition increases with Er concentration. It is found to vary from 7 nm to 65 nm corresponding respectively to 3%

and 15% concentrations (see Table I). Waveguide Raman spectroscopy⁵ is used to confirm the structure of these waveguides. It emerges that guides with 7%, 10% and 15% Er ion concentrations have an amorphous structure. Nevertheless, 3-mol% Er³⁺:TiO₂ and 5-mol% Er³⁺:TiO₂ waveguides have a crystalline structure (anatase). From these results, it appears clearly that the incorporation of Er³⁺ ions changes the TiO₂ gel network and this behaviour affects the fluorescence spectrum. For amorphous structure of the Er³⁺:TiO₂ films, the FWHM of the ⁴I_{13/2} → ⁴I_{15/2} transition is around 65 nm (see Table I) which is the case for 7-mol% Er³⁺, 10-mol% Er³⁺ and 15-mol% Er³⁺:TiO₂ waveguides.

Figure 4 shows the fluorescence spectra of waveguides for 7% and 10% Er ion concentrations annealed at 600°C for 1 hour. In this case, the ⁴I_{13/2} → ⁴I_{15/2} line becomes narrower for the Er ion concentration lower than 10% (see Table I). The 10-mol% Er³⁺ and 15-mol% Er³⁺:TiO₂ waveguides remain amorphous at annealing temperature T = 600°C. The structure of the layers depends on the Er ion concentrations and annealing temperature. An increase of Er ion concentration requires a high annealing temperature to obtain a TiO₂ crystalline structure (anatase).

Fluorescence lifetime measurements were performed at room temperature in waveguiding configuration on samples heat-treated at 600°C. It was found that the lifetime of ⁴I_{13/2} state decreases from around 1.5 ms to around 0.2 ms when increasing Er ion concentration from 1% to 15%. This effect can be attributed to concentration quenching, as a result of energy exchange among closely spaced Er³⁺ ions. Otherwise, the lifetime obtained for 1% Er³⁺:TiO₂ waveguide is comparable to the lifetime reported for Er-implanted soda-lime-silicate glass⁶ with the same Er ion concentration. A comprehensive study of the lifetime evolution as a function of Er ion concentration and annealing temperature is underway.

Table I
The FWHM of the ⁴I_{13/2} → ⁴I_{15/2} transition of Er³⁺ for different Er³⁺ ion concentrations and annealing temperatures.

Er ions concentrations	3%	5%	7%	10%	15%
FWHM (nm) of the ⁴ I _{13/2} → ⁴ I _{15/2} Annealing temperature T = 500°C	7		65	65	65
FWHM (nm) of the ⁴ I _{13/2} → ⁴ I _{15/2} Annealing temperature T = 600°C	6	8.5	11	65	65

4 CONCLUSION

We have shown that it is possible to prepare TiO₂ erbium-doped optical planar waveguides from the sol-gel route. The structure of the waveguiding films (amorphous and/or nanocrystalline form), the full width at half-maximum of the ⁴I_{13/2} → ⁴I_{15/2} transition (from 7 nm to 65 nm) and the lifetime of ⁴I_{13/2} state (around 1 ms) strongly depend on Er ion concentration and annealing temperature. The results of this study indicate that the sol-gel process is an inexpensive route for the production of Er-doped integrated devices on a planar substrate.

REFERENCES

1. S. Honkanen, S. I. Najafi and W. J. Wang. *Electron. Lett.* 1992, 28, p. 746.
2. P. Becker, R. Brinkmann, N. Dinand, W. Sohler and H. Suche. *Appl. Phys. Lett.* 1992, 61, p. 1257.

3. W. J. Wang, S. I. Najafi, S. Honkanen, Q. He, C. Wu and J. Glinski. *Electron. Lett.* 1992, 28, p. 1872.
4. M. Bahtat, J. Mugnier, A. Bahtat, and J. Serughetti. 'Treizièmes Journées Nationales d'Optique Guidée (JNOG)', Marseille (France), 1993.
5. A. Bahtat, M. Bouazaoui, M. Bahtat and J. Mugnier. *Opt. Commun.* 1994, 111, p. 55.
6. E. Snoeks, G. N. van den Hoven and Z.A. Polman. *J. Appl. Phys.* 1993, 73, p. 8179.

EPR AND PHOTOLUMINESCENCE OF Cr^{3+} IONS IN CsCdF_3 AND CsCaF_3

B. VILLACAMPA, R. CASES and R. ALCALÁ

*Instituto de Ciencia de Materiales de Aragón. Univ. de Zaragoza-C.S.I.C.
Pza. S. Francisco s/n. 50009 Zaragoza. Spain*

EPR and photoluminescence measurements of chromium doped CsCdF_3 and CsCaF_3 crystals have been performed. The two main EPR signals are associated with cubic and trigonal Cr^{3+} centers. The g factor, the parameters of the hyperfine (HF) interaction with the ^{53}Cr nuclei and the superhyperfine (SHF) interaction with the six nearest neighbour fluorine nuclei have been derived for the cubic centers. For the trigonal ones the g factor and the zero field splitting parameter have been obtained. Photoluminescence and lifetimes have been measured at 10 K. The observed phonon structure is associated with zero phonon lines (ZPL) and vibrational replicas of both cubic and trigonal centers. The frequencies of the phonon modes of the $[\text{CrF}_6]^{3-}$ complex involved in the structure have been derived.

Key Words: Cr^{3+} ions, fluoroperovskites, EPR, photoluminescence, lifetime.

1 INTRODUCTION

In the search of new materials for tunable solid state lasers in the near infrared the spectroscopic properties of Cr^{3+} ions have been investigated in some cubic fluoroperovskites.⁽¹⁻⁵⁾ Different types of Cr^{3+} centers have been observed and studied by EPR. The photoluminescence results can be explained by taking into account the contributions of the different centers. In KZnF_3 and RbCdF_3 the non exponential decays of the room temperature (RT) photoluminescence after pulsed excitation and the phonon structure observed at 10 K are due to the presence of cubic and trigonal Cr^{3+} defects. However, the assignment of the phonon lines to normal modes of the $[\text{CrF}_6]^{3-}$ complex in RbCdF_3 ³ is not as clear as in KZnF_3 .⁴

On the other hand, some preliminary studies of Cr^{3+} centers in CsCdF_3 ⁵ show some differences with respect to other fluoroperovskites. To check this behaviour and to complete the study of the Cr^{3+} centers that are formed in Cs compounds we have performed an spectroscopic study of chromium doped CsCdF_3 and CsCaF_3 crystals. The spin Hamiltonian (SH) parameters of cubic and trigonal Cr^{3+} centers are obtained and compared with those in similar crystals. The low temperature photoluminescence has been also measured and the results are explained taking into account the contributions of the different Cr^{3+} centers.

2 EXPERIMENTAL RESULTS AND DISCUSSION

Chromium doped fluoroperovskite crystals with a nominal CrF_3 content of 1 mol% were grown in our laboratory by the Bridgmann technique, using a radiofrequency heated furnace and vitreous carbon crucibles. EPR and photoluminescence set-ups were described elsewhere.³

The EPR spectrum of Cr doped CsCdF_3 and CsCaF_3 single crystals are very similar. So we will describe only the spectra corresponding to the Cd compound (although the SH parameters for the two matrices will be given). As shown in Figure 1 two main EPR

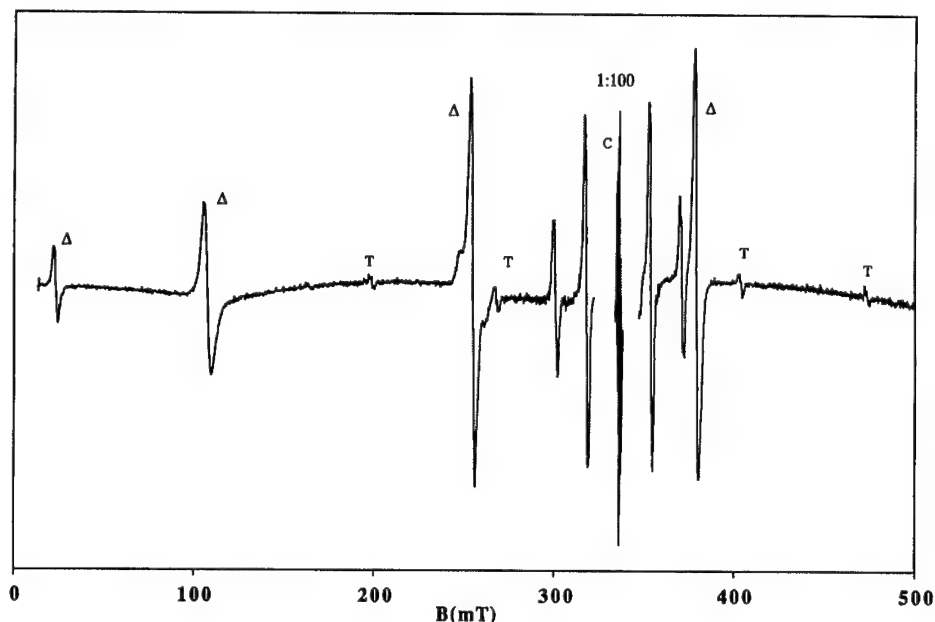


FIGURE 1 EPR spectrum of a $\text{CsCdF}_3\text{:Cr}$ crystal measured with the magnetic field parallel to a $\langle 100 \rangle$ direction. Lines marked with C correspond to cubic centers and those marked with Δ to the trigonal ones. Some small lines due to tetragonal centers are marked with T.

signals are observed which can be associated with Cr^{3+} ions. Signal C is due to cubic Cr^{3+} ions, the structure being associated with the SHF interaction with the six nearest neighbour fluorines. The ^{53}Cr HF structure is also observed. The SHF lines positions can be obtained by using the following SH:

$$H = g\beta S B + aSI + \sum_{j=1}^6 \{A_{\perp}(S_{x_j}I_{x_j} + S_{y_j}I_{y_j}) + A_{\parallel}S_{z_j}I_{z_j}\} \quad (1)$$

with $S = 3/2$, $I = 0$ for ^{52}Cr and $I = 3/2$ for ^{53}Cr , $I_j = 1/2$ and the x, y, z axes along the $\langle 100 \rangle$ directions of the crystal and the z_j axes correspond to the $\text{F}^- - \text{Cr}^{3+}$ bond directions. The g -factor, HF (a in 10^{-4} cm^{-1}) and SHF (A_{\parallel} and A_{\perp} in 10^{-4} cm^{-1}) parameters are: $g = 1.971$, $a = 17.95$, $A_{\parallel} = 8.8$ and $A_{\perp} = 3.1$ for the Cd compound and $g = 1.971$, $a = 18.05$, $A_{\parallel} = 9.3$ and $A_{\perp} = 2.6$ for the Ca one measured at 80 K. Using for the g -factor the expression: $g = 2.0023 - 8\lambda/\Delta$ where λ is the spin-orbit (SO) coupling constant for a single d electron and $\Delta = 10 \text{ Dq}$ (Dq is the cubic field splitting) a value of $\lambda = 55 \text{ cm}^{-1}$ is obtained. This value is much smaller than that of the free ion (91 cm^{-1}) and the reduction can be associated with bonding effects. The SHF interaction parameters are much smaller than those corresponding to other 3d ions. This is due to the

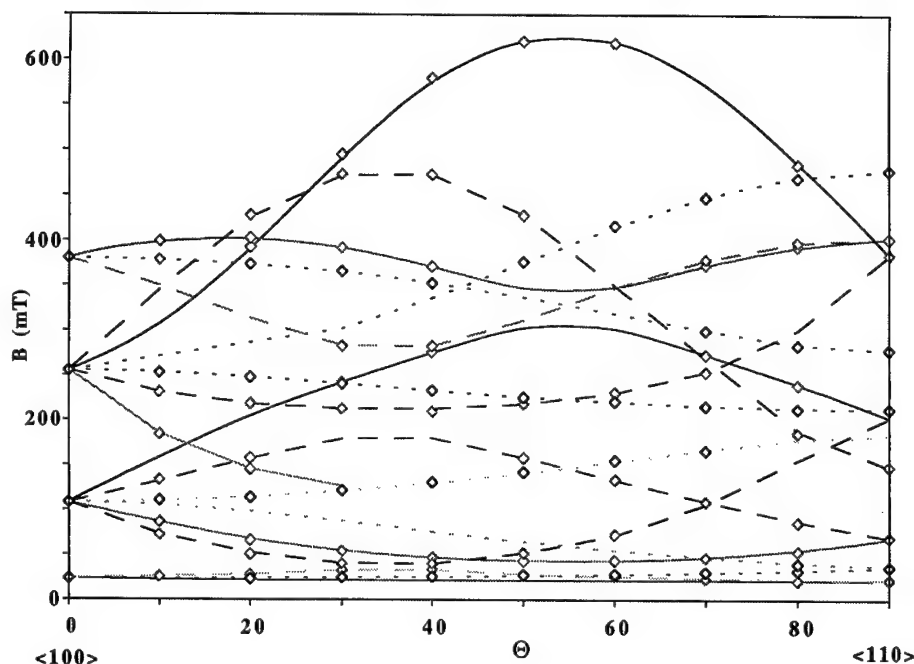


FIGURE 2 Rotational diagram of trigonal Cr^{3+} centers in CsCdF_3 measured at 80 K. Lines correspond to positions calculated with equation [2] and the parameters given in the text.

lack of a first order contribution to the Fermi contact term in the isotropic part of the SHF interaction.^{6,7}

With respect to the signal marked Δ in Figure 1 the lines positions as a function of the magnetic field orientation are given in Figure 2. The signal is due to trigonal Cr^{3+} centers and the lines positions can be calculated using the SH:

$$H = g_{\parallel}\beta B_z S_z + g_{\perp}\beta(B_x S_x + B_y S_y) + D[S_z^2 - \frac{1}{3}S(S+1)] \quad (2)$$

with the z axis along a $\langle 111 \rangle$ direction.

The best fitting of the positions calculated using eq.[2] to the experimental ones (see Figure 2) has been obtained for the following parameters: $g_{\parallel} = 1.971$, $g_{\perp} = 1.972$ and $D = 1350$ (10^{-4} cm^{-1}) for the Cd compound and $g_{\parallel} = 1.970$, $g_{\perp} = 1.971$ and $D = 1445$ (10^{-4} cm^{-1}) for the Ca one. The model for these trigonal centers is a Cr^{3+} ion in a divalent cation position with a Cs^+ vacancy in one of the corners of the cube.

Similar remarks to those for the cubic centers can be made for the g values of the trigonal centers. Concerning the crystal field parameter D, it does not show any clear dependence with the lattice parameter of the matrix although it seems to be smaller in the Cs compounds which have a larger lattice constant than the Rb ones. This behaviour is in contrast with the one reported for the tetragonal centers in which the tetragonal crystal field parameters increases with the lattice constant of the matrix.⁴

The photoluminescence spectrum of $\text{CsCdF}_3:\text{Cr}$ crystals measured at 10 K under excitation with the 470 nm light is given in Figure 3. Similar results appear in the Ca

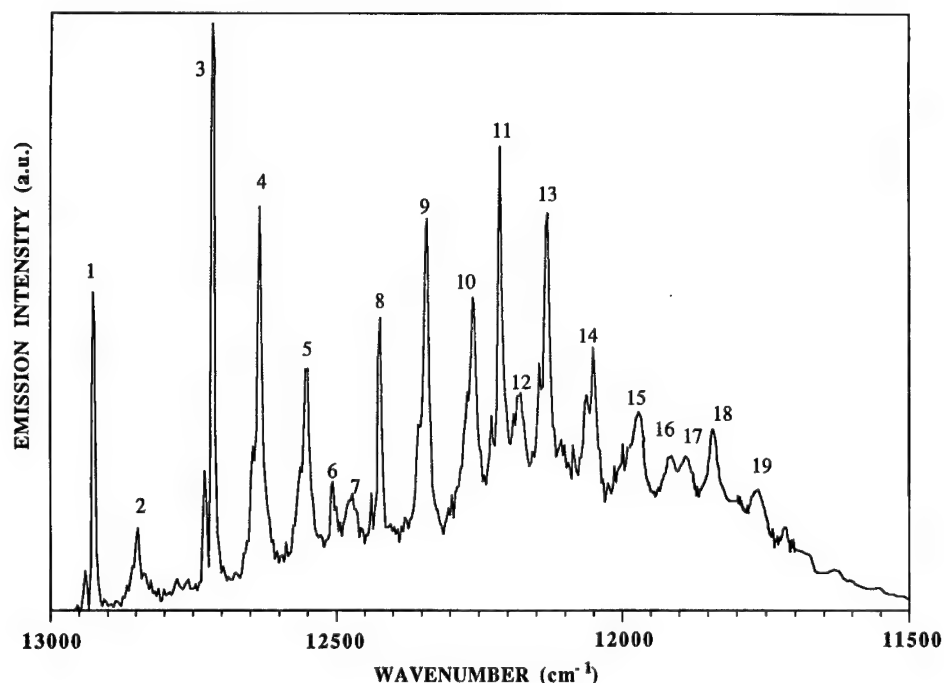


FIGURE 3 Photoluminescence spectrum of a CsCdF₃:Cr crystal under excitation at 470 nm. Measured at 10 K.

crystal. The structure is associated with the ZPL and vibronic replicas of cubic and trigonal Cr³⁺ centers. By comparison with the results in other fluoroperovskites^(3,4,5) line 1 has been assigned to the ZPL of cubic centers.

Decay time measurements have been performed on each of the lines. An exponential decay was observed for line 1. The corresponding lifetime is 560 μ s. Similar exponential decays with the same lifetime have been obtained for lines 4 and 5 indicating that all of them are associated with the cubic centers. The decay in line 3 was non exponential and faster than in line 1. To explain this we propose that both a phonon replica of cubic centers and the ZPL of trigonal centers contribute to line 3.

Time resolved photoluminescence measurements performed at 100 μ s and 1500 μ s after a pulsed excitation confirm this assignments. Taking into account the relative intensities of the lines in both spectra we have been able to assign most of the lines to phonon replicas of cubic and/or trigonal centers. The phonon frequencies involved were about 210, 290, 375 and 500 cm⁻¹ for CsCaF₃ and 210, 295, 380 and 500 cm⁻¹ for CsCdF₃. By comparison with the results obtained for Cr³⁺ in similar environments^{3,4,8} we propose that the two lower frequencies are associated with the t_{1u} and t_{2u} modes of the [CrF₆]³⁻ cluster. The frequencies at about 375 and 500 cm⁻¹ are associated to the e_g and a_{1g} modes of the same complex and the differences with the frequencies found in the literature can be due to the fact that those are stretching modes which are more affected by the change in the Cr³⁺-F distance.

ACKNOWLEDGEMENTS

This work was supported by the CICYT under Project N° MAT 92-1279

REFERENCES

- 1 U. Brauch and U. Dürr, *Optics Communications*, **49**, 61 (1984).
- 2 J. L. Patel, J. J. Davies, B. C. Cavenett, H. Takeuchi and K. Horai, *J. Phys. C.: Solid State Phys.* **9**, 129 (1976).
- 3 B. Villacampa, J. Casas-González, R. Alcalá and P. J. Alonso, *J. Phys.: Condens. Matter*, **3**, 8281 (1991).
- 4 Y. Vaills, J. Y. Buzaré and M. Rousseau, *J. Phys.: Condens. Matter*, **2**, 3997 (1990).
- 5 U. Brauch, *Ph.D Thesis*. University of Stuttgart (1986). (Unpublished).
- 6 A. Abragam and B. Bleaney, *Electron Paramagnetic Resonance in Transition Ions*, Clarendon Press, Oxford (1970), Ch.17.
- 7 J. Owen and J. H. M. Thornley, *Rep. Prog. Phys.* **29** Part II, 675 (1976).
- 8 S. A. Payne, L. L. Chase and G. D. Wilke, *J. Lumin.* **44**, 167 (1989).

SPECTROSCOPIC PROPERTIES OF Mn^{2+} IONS IN MIXED FLUOROPEROVSKITES

F. LAHOZ, P. J. ALONSO, B. VILLACAMPA and R. ALCALÁ

Instituto de Ciencia de Materiales de Aragón. Univ. Zaragoza-C.S.I.C., Pza. S. Francisco s/n, 50009 Zaragoza, Spain

The spectroscopic properties of Mn^{2+} in $RbCd_xCa_{1-x}F_3$ and $Cs_xRb_{1-x}F_3$ have been investigated by EPR and photoluminescence. Only the transitions between the $M_s = \pm 1/2$ Zeeman levels are observed by EPR. Forbidden transitions associated with changes in the M_l of one of the surrounding fluorines are detected. The superhyperfine interaction with the fluorines decreases when the lattice constant increases. The decay of the luminescence emission corresponding to the ${}^4T_{1g}({}^4G) \rightarrow {}^6A_{1g}({}^6S)$ transition of cubic Mn^{2+} has been measured in $RbCa_xCd_{1-x}F_3$ crystals. A continuous change in the lifetime has been found with a minimum at $x \approx 0.3$. These results indicate that there is a distribution of environment for Mn^{2+} in the mixed crystals.

Key words: Mn^{2+} , mixed crystals, EPR, luminescence.

1 INTRODUCTION

It is known that the spectroscopic properties of 3d impurities in crystals are very sensitive to the ion environment and can be considerably changed using different matrices. Mixed crystals allow the possibility to introduce a gradual change in these environments. In some previous works⁽¹⁻³⁾ we have reported on the spectroscopic properties of some 3d ions in different fluoroperovskites such as $RbCaF_3$, $RbCdF_3$, $CsCaF_3$ and $CsCdF_3$. In this communication we present a study of Mn^{2+} ions in $RbCa_xCd_{1-x}F_3$ and $Rb_xCs_{1-x}CaF_3$ crystals ($0 < x < 1$) using EPR and photoluminescence. Changes in the EPR spectra and in the lifetime of the Mn^{2+} emission have been found in the mixed crystals with respect to the non mixed ones. These changes are attributed to a distribution of the Mn^{2+} environments.

2 EXPERIMENTAL RESULTS AND DISCUSSION

Some of the single crystals of $RbCaF_3$, $RbCdF_3$ and $CsCaF_3$ doped with different concentrations of MnF_2 (0.1, 0.3 and 0.6 mol%) were kindly provided by Professor J. M. Spaeth (University of Paderborn). Mixed crystals were grown in our laboratory and doped with different concentrations (0.5 and 2 mol% for optical measurements and 0.05 and lower values mol% for EPR ones) using a Bridgmann technique. The equipment used for EPR and luminescence measurements has already been described in previous papers.¹⁻³

EPR studies of Mn^{2+} in the non mixed crystals ($x = 0, x = 1$) have been previously reported.⁴ The line positions have been calculated using the spin hamiltonian (SH):

$$H = g\mu_B S B + \frac{a}{120} \{O_4^0 + 5 O_4^4\} + A S I + \sum_{j=1}^6 \{A_{\parallel} S_{z_j} I_{z_j} + A_{\perp} (S_{x_j} I_{x_j} + S_{y_j} I_{y_j})\} \quad (1)$$

with $S = 5/2$, $I = 5/2$ and $I_j = 1/2$. The first term represents the Zeeman interaction, the second one the influence of the cubic crystal field, the third one the hyperfine (HF) interaction with the Mn^{2+} nucleus and the last one the superhyperfine (SHF) interaction with the six nearest F^- nuclei. The Mn^{2+} spectra in the mixed crystals are more simple

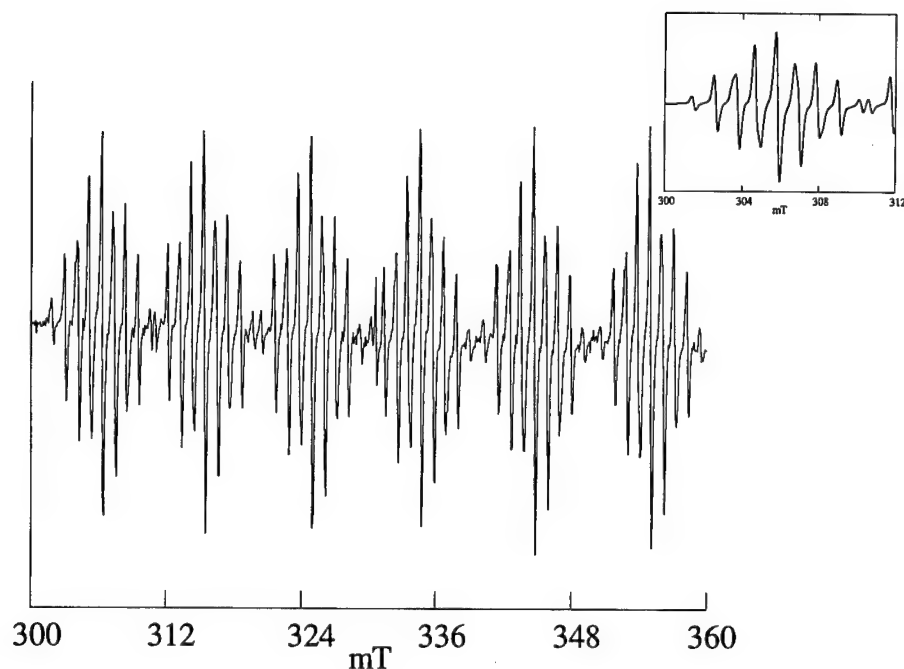


FIGURE 1 EPR spectrum of $\text{Rb}_{0.5}\text{Cs}_{0.5}\text{CaF}_3: \text{Mn}^{2+}$ measured at RT with the applied magnetic field along the (100) direction.

(see Figures 1 and 2) and can be explained using the same SH (eq. 1), but taking into account only the transitions between the $M_s = \pm 1/2$ levels and introducing a term for the fluorine nuclear Zeeman interaction (see below). We can understand this result in the following way. The allowed EPR transitions, according with the selection rule $|\Delta M_s| = \pm 1$, do not have the same positions due to the crystal field terms in eq. [1] and this results in the complicate aspect of the spectrum in the non mixed crystals. In the mixed ones the disorder and the deformations associated with the mixing have to be taken into account and some new crystal field terms of lower symmetry should be included in the SH. The line positions of all the transitions, except the $|+1/2\rangle \leftrightarrow |-1/2\rangle$, are very sensitive to these terms and because of this a large inhomogeneous broadening of these lines is produced in such a way that they can hardly be detected. So, the only observed lines are those corresponding to the $|+1/2\rangle \leftrightarrow |-1/2\rangle$ transitions. In this way it is easy to understand the spectrum in Figure 1 where the six groups of lines are due to the HF interaction with the Mn nucleus and the lines within each group are due to the SHF interaction with the six surrounding fluorines. It should be remarked that we have observed similar spectra (with small changes in the SHF interaction constant) in all our mixed crystals. The inhomogeneous broadening seems to be due to a distribution of deformations of the local environment of Mn^{2+} ions.

Our experiments cannot be interpreted in the same way as those in $\text{Rb}_{1-x}\text{K}_x\text{CaF}_3$ crystal doped with Gd^{3+} .⁵ In this case it has been found that the spectra observed in the mixed crystals for x values up to 0.2 can be explained with a superposition of the spectra of two centers: the one in the non mixed crystal and another where one of the Rb^+ ions has been substituted by a K^+ . The relative intensities of the two spectra are those

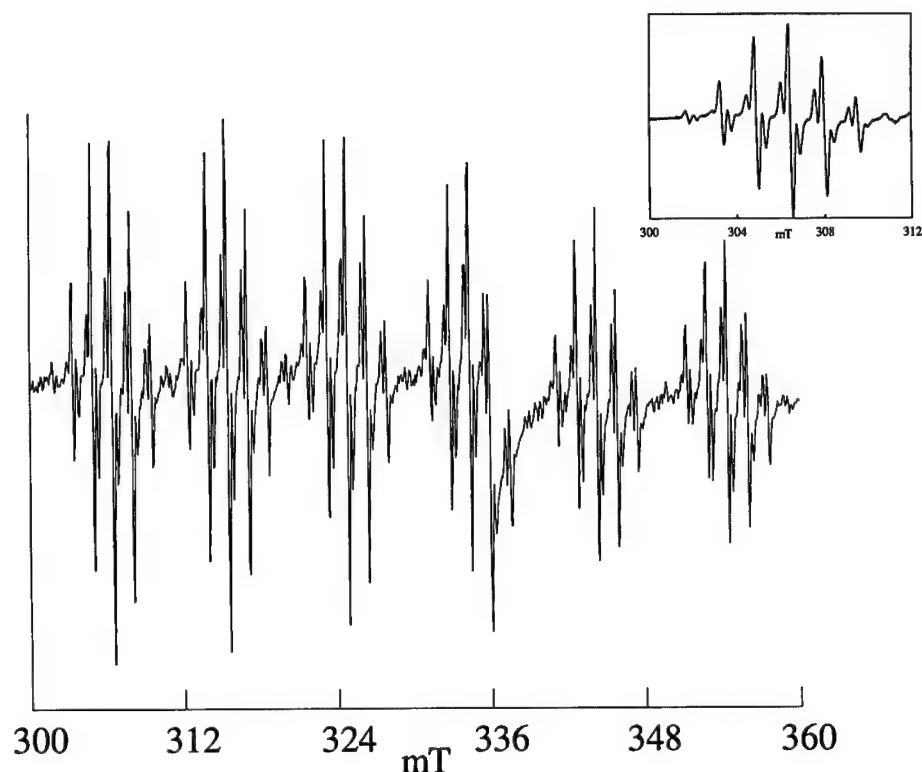


FIGURE 2 EPR spectrum of $\text{Rb}_{0.5}\text{Cs}_{0.5}\text{CaF}_3: \text{Mn}^{2+}$ measure at RT with the applied magnetic field along the $\langle 111 \rangle$ direction.

corresponding to a random distribution of the alkaline ions. In our case it is clear that the superposition of two spectra would not explain the spectrum in Figure 1 where many of the lines observed in the non mixed crystals have disappeared. When the magnetic field is applied in the $[111]$ direction (Figure 2) one expects seven superhyperfine lines in each of the groups corresponding to the $|+1/2\rangle \leftrightarrow |-1/2\rangle$ transition and the SHF interaction with the six equivalent F nuclei that surround the Mn^{2+} ion. However it is found that the seven lines are flanked by satellites of lower intensity. We assign these lines to nuclear Zeeman transitions of one of the surrounding F nuclei. These transitions are forbidden by the superhyperfine selection rule $|\Delta M_I| = 0$. This holds exactly for $H \parallel [100]$. However when H is not along the $\langle 100 \rangle$ direction of SHF tensor is not diagonal and the fluorine nuclear states are mixed. This makes the fluorine Zeeman nuclear transitions partially allowed. This effect has also been observed for the $\langle 110 \rangle$ direction. The positions of the lines can be calculated using the SH of equation [1] and adding the nuclear Zeeman term of the fluorine nuclei.

As we have said the spectra corresponding to different mixture are very similar. The line width presents a slight increase when the percentage of mixture increases. The hyperfine and superhyperfine parameters vary gradually between those of the $x = 0$ and $x = 1$ crystals. This can be associated with a continuous change of the average $\text{Mn}^{2+} - \text{F}^-$ distance.

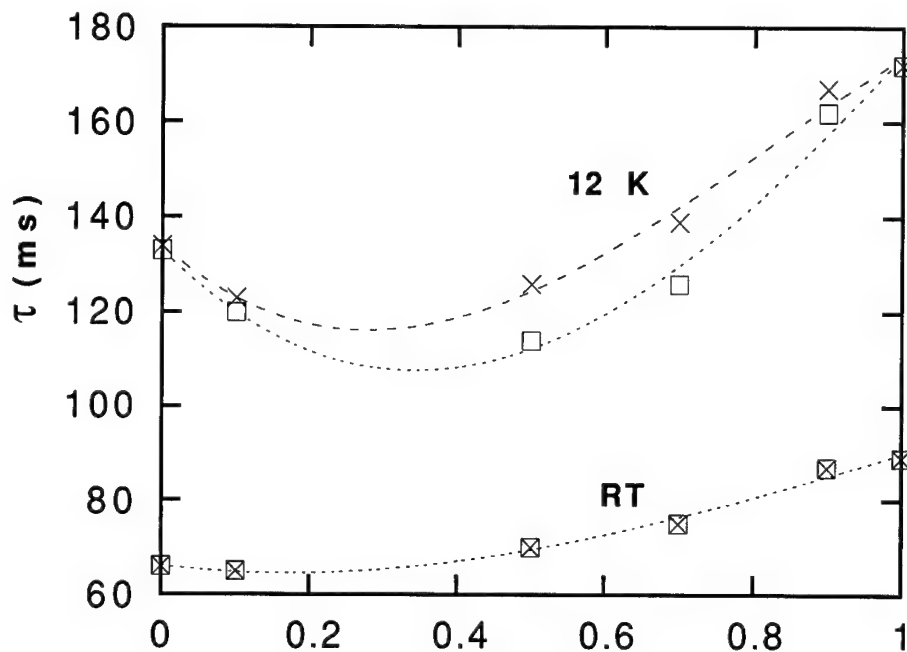


FIGURE 3 Lifetime of the first excited state ${}^4T_{1g}({}^4G)$ of Mn^{2+} in $RbCa_xCd_{1-x}F_3$ at RT and 12 K for different values of x . □ detection at 550 nm and X detection at 620 nm.

Photoluminescence measurements were performed under excitation with 514 nm light. The lifetime (τ) of the first excited state ${}^4T_{1g}({}^4G)$ was measured in $RbCa_xCd_{1-x}F_3$: Mn^{2+} crystals with $x = 0.1, 0.5, 0.7$ and 0.9 and with different MnF_2 concentrations, ranging from 0.5% to 2%. Figure 3 represents the variation of τ with the Ca^{2+} content measured at different temperatures. The temperature dependence of the decay time is due to non-radiative multiphonon processes. The decay time changes continuously between $x = 0$ and $x = 1$ with a minimum at $x \approx 0.3$. The decrease of τ going from $x = 0$ to $x = 0.3$ is due to an increase of the radiative transition probability associated with the lowering of the local symmetry around the Mn^{2+} ions. For $0.3 < x < 1$ there is an increase in τ associated with the increase of the Ca^{2+} content. This effect can be observed at any temperature, but it is more remarkable at low temperature, when the radiative relaxation is the most important one.

As shown in Figure 3, τ depends on the detection wavelength. If we have a distribution of environments around Mn^{2+} ions we measure τ values of different centers when the detection wavelength is changed. At RT this effect is small due to the influence of non radiative processes. At lower temperatures we observe a decrease on τ for smaller detection wavelengths. The electric dipole emission probability (P) of a photon of frequency ω in any direction and with any polarization is proportional to ω^3 and to the square of the matrix element of the transition operator (p_{ij}): $P = K \cdot \omega^3 \cdot |P_{ij}|^2$. When the energy difference between the two states gets bigger, ω increases and at the same time the matrix element of the transition operator becomes smaller. Our results indicate that the influence of the ω^3 factor is dominant in our case.

ACKNOWLEDGMENTS

This work was supported by the CICYT under contract N^o MAT 92-1279.

REFERENCES

1. R. Alcalá, J. Casas-González and B. Villacampa. *Rad. Effects and Defects in Solids* **119-121**, 901 (1991).
2. B. Villacampa, R. Alcalá, P. J. Alonso and J. M. Spaeth. *J. Phys: Condens. Matter* **5**, 747 (1993).
3. B. Villacampa, R. Cases, V. M. Orera and R. Alcalá. *J. Phys. Chem. Solids* **55**, 263 (1994).
4. J. J. Rousseau, A. Leble and J. C. Fayet. *J. Physique* **39**, 1215 (1978).
5. J. Y. Buzaré and P. Foucher. *J. Phys.: Condens. Matter* **3**, 2535 (1991).
6. B. Di Bartolo in *Optical Interactions in Solids*, John Wiley, New York (1968), Ch. 14.

EPR STUDY OF CONCENTRATION DEPENDENCE IN Ce, Ce:La AND Ce:Y DOPED SrF₂

O. DANKERT, D. VAINSHTEIN, H. C. DATEMA and H. W. DEN HARTOG

*Solid State Physics Laboratory, University of Groningen; Nijenborgh 4, 9747 AG
Groningen, The Netherlands*

Experimental results of an EPR-study of the concentration dependence of the doubly integrated intensity and linewidth of the signals associated with tetragonal Ce³⁺-F⁻-dipoles in Sr_{1-x}Ce_xF_{2+x}, Sr_{1-0.005-x}Ce_{0.005}La_xF_{2+0.005+x} and Sr_{1-0.005-x}Ce_{0.005}Y_xF_{2+0.005+x} are presented. Both show a nonlinear behaviour. Besides the tetragonal defects no other symmetries have been found.

Key words: EPR, f-state ions, SrF₂:CeF₃, SrF₂:CeF₃:LaF₃, SrF₂:CeF₃:YF₃.

1 INTRODUCTION

Electron Paramagnetic Resonance (EPR) measurements have been carried out to study the defect states in Sr_{1-x}Ce_xF_{2+x}, Sr_{1-0.005-x}Ce_{0.005}La_xF_{2+0.005+x} and Sr_{1-0.005-x}Ce_{0.005}Y_xF_{2+0.005+x}. These crystals have been grown by the Bridgman-method with Ce-concentrations up to 8.5 mole% in Sr_{1-x}Ce_xF_{2+x} and with La- or Y-concentrations up to 5.1 mole% in codoped SrF₂-crystals containing 0.5 mole% CeF₃. DSC didn't show evidence for dissociation of dipoles; probably the sensitivity of these experiments was insufficient.

2 EXPERIMENTAL RESULTS

2.1 SrF₂:CeF₃

SrF₂-crystals with CeF₃-concentrations between 0.3 and 8.5 mole% have been studied. The orientation dependence of the EPR-signals shows only tetragonal Ce³⁺-F⁻-dipoles in this crystal. The calculated g-factors are: $g_{\perp} = 1.457$ and $g_{\parallel} = 2.848$, the literature values are respectively 1.472 and 2.854.¹ The dependences of the doubly integrated intensity and widths of the EPR-signals versus the concentration of CeF₃ are studied. Figures 1 and 2 show these dependences for the double EPR-Ce³⁺-peak (at g_{\perp}) with $H_0 \parallel [100]$. At low concentrations the intensity depends linearly upon the concentration CeF₃ and reaches a maximum at 2.4 mole%. For higher concentrations (between 2.4 and 5 mole%) the intensity decreases by about 50% and at still higher concentrations (5-8.5 mole%) the intensity is approximately constant. The linewidth increases from 16 Gauss at 0.4 mole% to 60 Gauss at 2.4 mole%; for CeF₃-concentrations of 5 up to 8.5 mole% the linewidth increases from 54 to 154 Gauss. Extra signals from other positions than the tetragonal dipoles have not been recorded by EPR.

2.2 SrF₂: CeF₃ (0.5 mole%): LaF₃ Codoped Crystals

The dependences of the linewidth and the doubly integrated intensity versus the concentration of CeF₃+LaF₃ in SrF₂ of the double Ce³⁺-peak (La is diamagnetic, so it has no EPR-signal) are shown in Figures 1 and 2. The CeF₃-concentration is constant

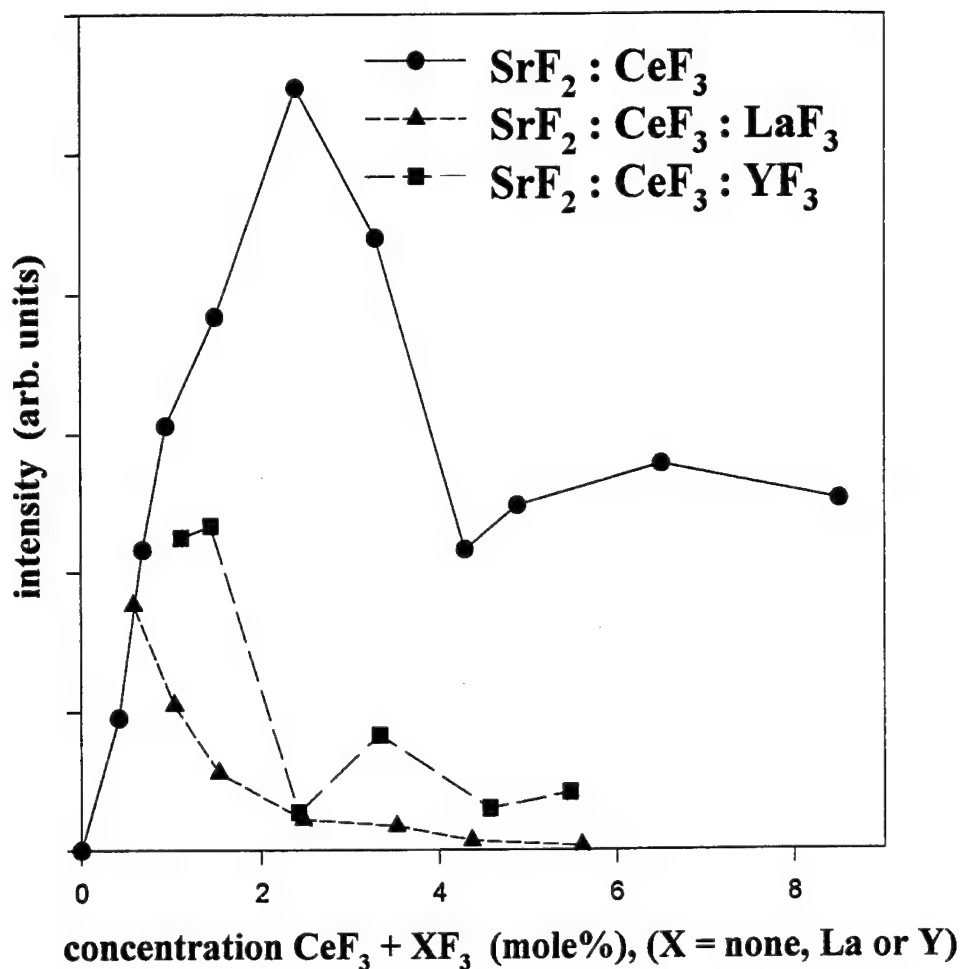


FIGURE 1 The dependence of the doubly integrated intensity of the two-fold degenerate EPR-Ce³⁺-peak (at g_{\perp}) vs. the concentration.

(0.5 mole%) and the concentration LaF₃ varies from 0 to 5.1 mole%. The linewidth shows approximately the same shape as for Sr_{1-x}Ce_xF_{2+x}, at low concentrations (< 1.5 mole%) the linewidth increases from 9 to 39 Gauss and the increases again from 35 Gauss at 3.5 mole% to 76 Gauss at 5.6 mole%. The intensity of the Ce³⁺-peak decreases rapidly with increasing La-concentrations. In contrast with the singly doped samples extra signals are recorded in these codoped crystals. At high concentrations of LaF₃ over 10% of the intensity is related to these signals. There are several signals and it is impossible to obtain accurate angular dependences of these signals, though the general trend suggests that we are dealing with perturbed tetragonal sites.

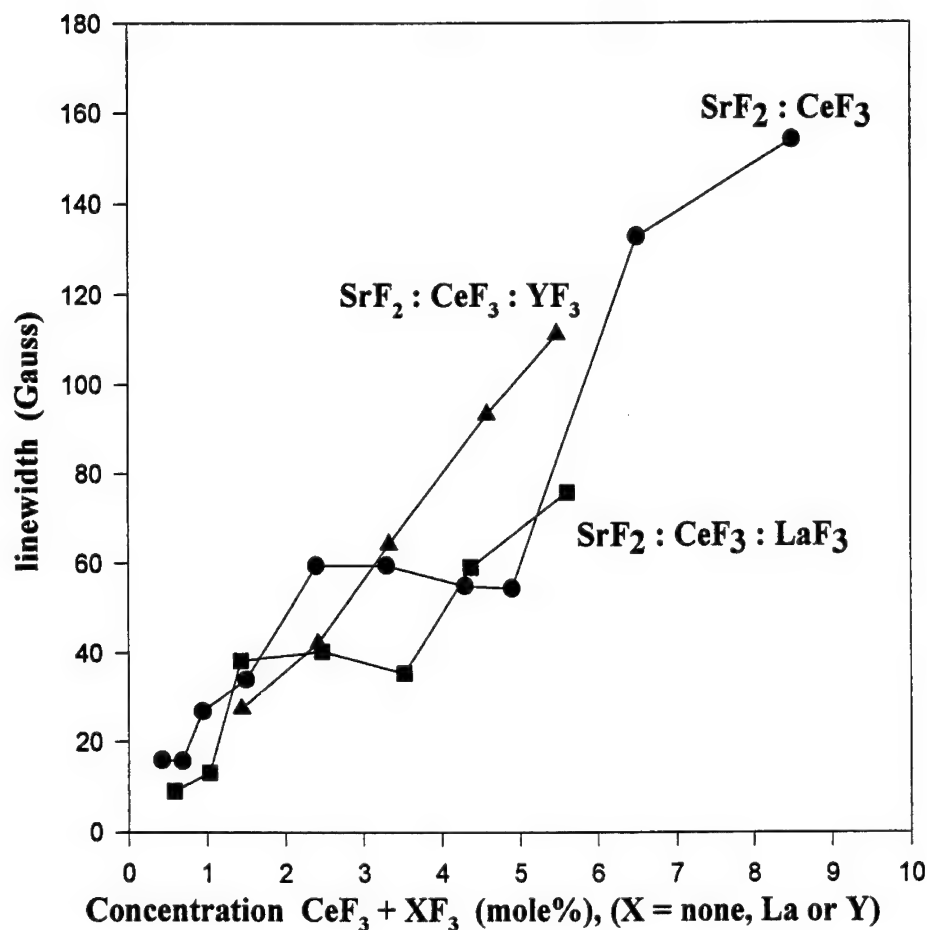


FIGURE 2 The dependence of the linewidth of the two-fold degenerate EPR- Ce^{3+} -peak (at g_{\perp}) vs. the concentration.

2.3 $\text{SrF}_2:\text{CeF}_3$, (0.5 mole%): YF_3 Codoped Crystals

Tetragonal sites in $\text{SrF}_2:\text{CeF}_3:\text{YF}_3$ -crystals have been investigated for a constant CeF_3 -concentration (0.5 mole%) and different concentrations of YF_3 up to 4.9 mole%. The linewidth of the two fold Ce^{3+} -peak ($H_0 \parallel [100]$) increases linearly up to 111 Gauss at 4.9 mole% of YF_3 and the doubly integrated intensity decreases rapidly with increasing YF_3 -concentrations. No extra signals are recorded.

2.4 $\text{BaF}_2:\text{CeF}_3$

ITC-experiments in BaF_2 doped with LaF_3 showed that trigonal and tetragonal defects are formed in this crystal,² so trigonal dipoles are also expected in Ce-doped BaF_2 .

BaF₂-crystals doped with 0.8 and 1.5 mole% CeF₃ have been studied with EPR, only tetragonal signals are found. This implies that trigonal Ce³⁺-sites cannot be observed by means of EPR.

3 CONCLUSIONS

Because of the observed nonlinear behaviour of the EPR intensity versus the concentration of the dopants (in SrF₂:CeF₃ above 2.5 mole% CeF₃ and in all La or Y codoped SrF₂:CeF₃ crystals) one would expect that additional to the tetragonal dipoles other complexes may be present. The decrease of the Ce³⁺-intensity in the codoped crystals is probably due to the forming of other complexes than the tetragonal dipoles. From the observed rotational behaviour of the extra signals observed in some of the samples, we conclude that we are only dealing with perturbed tetragonal dipoles. We didn't observe cubic Ce³⁺-centres nor did we find any of the rhombic lines as observed by J. M. Baker³ in SrF₂ containing 0.1% Ce.

ACKNOWLEDGEMENTS

The crystals used in this experiment were grown by J. E. M. Jacobs.

REFERENCES

1. A. A. Antipin, I. N. Kurkin, G. K. Chirkin and L. Ya Shekun, *Sov. Phys. — Solid State* **6**, 1590 (1965).
2. H. W. den Hartog, K. F. Pen and J. Meuldijk, *Phys. Rev.* **B28**, 6031 (1983).
3. J. M. Baker and D. M. Chaplin, *J. Phys. C: Solid State Phys.* **12**, L129 (1979).

DIFFERENTIAL SPECTROSCOPIC PROPERTIES OF Nd^{3+} IN NdGaO_3 AND LaGaO_3

V. M. ORERA, L. E. TRINKLER* and R. I. MERINO

*Instituto de Ciencia de Materiales de Aragon (CSIC-UZ.), Facultad de Ciencias,
Universidad de Zaragoza, Zaragoza, Spain; *Institute of Solid State Physics, Latvian
University, Riga, Latvia*

The NdGaO_3 and LaGaO_3 crystals are orthorhombic perovskites, belonging to space group D_{2h}^{16} Pbnm. The Nd^{3+} spectroscopic properties including both optical absorption and emission in both compounds were measured at different temperatures between 9 and 300 K. Very high neodymium concentration is the reason for the quenching of the luminescence in the Nd compound but it allows us to observe all possible electronic transitions in the 200–2500 nm region. The spectra are partially polarized. Though the energy level positions in both compounds are essentially the same, there are some unusual aspects of the Nd compound as compared with the behavior of the La one that can not be explained by current single ion theories.

Key words: Optical Properties, Nd^{3+} , NdGaO_3 .

1 INTRODUCTION

Oxide perovskites are simple systems with very interesting magnetic and electronic properties. Since the discovering of the high-temperature superconductivity there are renewed efforts in the study of the properties of these compounds.

In particular NdGaO_3 (NGO) is a magnetic insulator material showing an antiferromagnetic ordering at $T_c = 0.97$ K.¹ The crystals have a good optical quality allowing us to perform optical spectroscopy studies to obtain information on their electronic structure. Additionally these compounds are suitable to study the features resulting from the interactions between absorbers, whose details are not yet fully understood in spite of its crucial importance. For that purpose we have also studied the diluted $\text{LaGaO}_3\text{:Nd}$ (LGO) system and compared the results with those of the concentrated crystal. In this paper we present some preliminary experimental results.

The compounds are orthorhombic perovskites isostructural with GdFeO_3 and they belong to space group D_{2h}^{16} with four formula per unit cell along all the measurement temperature range.² The rare earth ions occupy the 4c sites in the center of strongly distorted oxygen dodecahedra (point group C_s). For a representation of the crystal structure see for example Figure 1 in ref.³ The Nd-O distances range from 2.3 to 3.4 Å and the Nd-Nd ones between 3.8 and 3.95 Å.

2 EXPERIMENTAL DETAILS

NdGaO_3 and 1% at. Nd doped LaGaO_3 compounds used in this study were grown by the Czochralski method. After orientation using the back reflection Laue method thin slabs parallel to the (110) planes of $\approx 100 \text{ mm}^2 \times 0.3 \text{ mm}$ were cut and polished. The LaGaO_3 (LGO) boule was not a single crystal, it consists of a clear grey color polycrystalline material with some small pink colour crystallites (less than 1 mm^3) embedded on it.

We have performed EDX microanalysis on that sample with the following results. The

grey phase corresponds to the $\text{La}_2\text{GaO}_{4.5}$ compound whereas the crystallites have the desired LGO formula. The Nd impurity distributes quite inhomogeneously through the sample its concentration being less than 1.3% at the sensitivity limit, in the crystallites. The index of refraction of the NGO sample 2.13 was measured by the apparent thickness method using an optical microscope and white light.

Optical absorption measurements were made in a Hitachi U-3400 Spectrophotometer. Polarized optical absorption spectra in the 900–300 nm region were obtained using unsupported dichroic polarizers. Photoluminescence spectra were obtained exciting the sample with light from a 1000 W tungsten lamp passed through a 0.5 m double monochromator. Fluorescence was detected through a 0.5 m monochromator with Si diode detector. Lifetime measurements were performed by modulating the exciting light with a mechanical chopper and using a Tektronic 2430 digital oscilloscope. Variable temperatures below 300 K were achieved using a close-cycle cryorefrigerator and with an accuracy of ± 1 K.

3 EXPERIMENTAL RESULTS

In the presence of a crystal field of C_s symmetry each $|J\rangle$ level of the $4f^3 \text{Nd}^{3+}$ configuration splits into $(2J+1)/2$ Kramers doublets. So for example the $^4I_{9/2}$ ground state will be split into 5 Stark levels being the lowest one the only populated at low temperatures.

3.1 Optical Absorption

NGO single crystal absorption edge is at about 220 nm ($45\,500\text{ cm}^{-1}$). Due to the high Nd^{3+} concentration all the possible f-f electronic transitions in that region are clearly seen. Since some of these bands are very narrow (0.2 nm at 9 K) they have to be measured with a high spectral resolution. The energies and labelling of the levels are given in Table I. Some of the absorption bands are partially polarized. The polarization degree of the bands in the 350–900 nm region defined as $P = (P_{\parallel} - P_{\perp}) / (P_{\parallel} + P_{\perp})$ with respect to the c-axis is also given in Table I.

The poor optical quality of the samples enables us to measure only seven absorption bands in LGO:Nd (see Table I). In this compound we could not perform polarization experiments.

The thermal evolution of the absorption spectra of both samples was measured in the 9–300 K temperature range. Increasing the temperature induces a progressive thermal population of the ground state Stark levels which results in a decrease of the low temperature spectrum accompanied by an increase of some absorption bands at their low energy side. We obtain five bands separated by 90, 180, 430 and 545 cm^{-1} . In LGO the splitting is 85, 155, 450 and 535 cm^{-1} .

The oscillator strengths 'f' of the J-J' transitions are given in Table II. For LGO we assumed a Nd^{3+} concentration of 1 at.% as in the melt being this the greater error source in the f determination. Table I clearly shows a differential behaviour between NGO and LGO. In the latter f are almost temperature independent whereas those of most of the bands increase as the temperature rises in the former.

On the other hand the thermal behaviour of the bands around 430 nm in NGO is abnormal. As the shortwave subband does not obey the Boltzman distribution function of the density of states in the ground state throughout the temperature region 9–300 K.

In the case of NGO all the absorption bands besides the electronic zero-phonon

transitions have phonon side bands on their shortwave side. In contrast, only very weak side bands are seen in LGO. The peak positions of this structure approximately coincide with the phonon frequencies obtained by Raman and infrared techniques⁴ (see Table III). It is interesting to realize that the vibronic sidebands appear in the energy region of the phonon modes involving stretching or bending of the Nd-O binding. The ratio of the integrated zero-phonon line intensity I_{zp} to the total integrated area I_0 , $R = I_{zp}/I_0$ is given for those absorption bands where the vibronic spectrum is better resolved in Table II. R is temperature independent.

Table I
Energy levels, polarization degree P at 10 K and increase on the strength of the absorption bands of NGO with temperature.

Level	$\nu(\text{cm}^{-1})$ (NGO)	P (NGO)	$f(300)/f(10)$	$\nu(\text{cm}^{-1})$ (LGO)
$^2F_{5/2}$	37735	—	2.65	—
$^2H_{11/2}$	34130	—	1.3	—
$^2D_{5/2, 3/2}$	32785	—	1.4	—
$^2H_{9/2}$	31645	—	0.5	—
$^2L_{17/2, 15/2}$	—	—	—	—
$^4D_{7/2}, ^2I_{13/2}$	30490	—	1	—
$^4D_{3/2, 5/2}, ^2I_{11/2}$	27933	—	3.8	—
$(^2D, ^2P)_{3/2}$	26042	0	1	—
$^2D_{5/2}$	23753	0.65	0.4	—
	23641	-0.1	—	—
$^2P_{1/2}$	23164	0.3	10.8	23226
$^2K_{15/2}, ^2G_{9/2}$	21276	0.35	1.3	—
$(^2D, 2p)_{3/2}, ^4G_{11/2}$	—	—	—	—
$^2K_{13/2}, ^4G_{7/2, 9/2}$	19194	0.3	2.05	19263
$^4G_{5/2}, ^2G_{7/2}$	17330	-0.1	3.3	17166
$^2H_{11/2}$	15748	0	2	15768
	14916	0.25	—	14948
	14771	-0.1	—	14921
$^4F_{9/2}$	14725	0	3.7	14793
	14684	0	—	14723
	14569	0	—	14579
$^4F_{7/2}, ^4S_{3/2}$	13495	0.2	3.9	13470
$^4F_{5/2}, ^2H_{9/2}$	12422	0	4.4	12400
$^4F_{3/2}$	11521	0	3.6	11542
	11399	0	—	11436
	6602, 6546	—	—	6615, 6548
$^4I_{15/2}$	6320, 6250	—	1.1	6486, 6310
	6193, 5994	—	—	6202, 5999
	5904, 5787	—	—	5934, 5778
	4334, 4248	—	—	4344, 4231
$^4I_{13/2}$	4228, 4142	—	—	4193, 4146
	4047, 3994	—	—	4034, 4018
	3935	—	—	3940

3.2 Emission

No emission has been detected in NGO, in contrast emission spectra corresponding to the $^4F_{3/2} \rightarrow ^4I_{9/2}$ ($11\,200\text{ cm}^{-1}$) and $^4I_{9/2} \rightarrow ^4F_{3/2}$ (9400 cm^{-1}) transitions were detected at temperatures between 9 and 300 K in LGO. The decay curve of the emission is exponential with a temperature independent decay time of $230\text{ }\mu\text{s}$.

4 DISCUSSION

Most of the results presented in the preceding section such as energy level positions, intensity parameters, crystal field structures, etc. can be analyzed on the light of existing theories for non-overlapping lanthanide ions. The absence of any structure that could be related to ion interactions and the close similarity between LGO:Nd and NGO indicates that interionic electronic interactions in the latter are weak, but there are some other aspects which point towards non-localized states in NGO.

Table II
Oscillator strengths f of Nd^{3+} in NGO and LGO (in 10^{-8} units) and R ratio of vibronic to zero-phonon band strengths.

Level	$f_{\text{exp}}(300 \text{ K})$	$f_{\text{the}}^{\text{NGO}}$	R	$f_{\text{exp}}(300 \text{ K})$ LGO	f_{the}
$^2\text{F}_{3/2}$	18.5				
$^2\text{F}_{5/2}$	52.2				
$^2\text{H}_{1/2}$	27				
$^2\text{D}_{5/2, 3/2}$	60				
$^2\text{H}_{9/2}$	5.3				
$^2\text{L}_{17/2, 15/2}$					
$^4\text{D}_{7/2}, ^2\text{I}_{13/2}$	350				
$^4\text{D}_{3/2, 5/2}, ^2\text{I}_{11/2}$	1100				
$(^2\text{D}, ^2\text{P})_{3/2}$	3.7	4.7			
$^2\text{D}_{5/2}$	3.1	3.6			
$^2\text{P}_{1/2}$	43	77.7	0.3	22	13.8
$^2\text{K}_{15/2}, ^2\text{G}_{9/2}$	191	136			
$(^2\text{D}, ^2\text{P})_{3/2}, ^4\text{G}_{11/2}$					
$^2\text{K}_{13/2}, ^4\text{G}_{7/2, 9/2}$	657	546		138	135
$^4\text{G}_{5/2}, ^2\text{G}_{7/2}$	1100	1108		438	438
$^2\text{H}_{11/2}$	14.7	14.3	0.1		
$^4\text{F}_{9/2}$	63.5	51.8		11	14.4
$^4\text{F}_{7/2}, ^4\text{S}_{3/2}$	638	617		182	183
$^4\text{F}_{5/2}, ^2\text{H}_{9/2}$	612	683		179	178
$^4\text{F}_{3/2}$	208	284	0.75	46	54
$^4\text{I}_{15/2}$	28.3	17.3			

First, in NGO the lines are very narrow and their shape more Lorentzian than Gaussianlike. The band intensities increase as the temperature rises. Second, in the concentrated compound, vibronic side-bands are observed in almost all the bands while they are noticeably weaker in the diluted crystal. Third is the differential temperature dependence of the first $^4\text{I}_{9/2} \rightarrow ^2\text{P}_{1/2}$ subband that in NGO does not follow the expected Boltzman equation opposite to the normal behaviour of this transition in LGO.

Neglecting magnetic ordering effects, active only at very low temperatures, and since the crystal structure of NGO and LGO is the same, their lattice parameters very similar and also their phonon spectra, these differences have to be related with the existence of non-localized excitations in the concentrated compound.

REFERENCES

1. F. Bartolomé, M. D. Kuz'min, R. I. Merino and J. Bartolomé, *IEEE Trans. on Magn.*, **30**, 960 (1994).
2. S. Geller, *Acta Cryst.*, **10**, 243 (1957).
3. A. Podlesnyak, S. Rosenkranz, F. Fauth, W. Marti, A. Furrer, A. Mirmelstein and H. J. Scheel, *J. Phys. Condens. Matter* **5**, 8973 (1993).

4. M. C. Saine, E. Husson and H. Brusset, *Spectrochimica Acta* **38A**, 19 (1981).

Table III
Phonon modes in NGO. Frequencies in cm⁻¹.

i.r.[4]	Raman[4]	Vibronic
607	—	—
548	—	—
510	—	—
455	469	—
—	462	—
435	—	—
—	410	406
390	—	—
—	361	—
357	—	—
—	346	—
—	340	340
325	—	—
308	—	308
285	289	277
220	—	222
—	214	—
—	200	—
185	180	184
—	169	—
—	145	148
—	135	—
—	92	98
—	—	56

EPR OF JAHN-TELLER Cr^{2+} IN CaF_2 , BaF_2 AND SrCl_2

P. B. OLIETE, V. M. ORERA and P. J. ALONSO

*Instituto de Ciencia de Materiales de Aragón. C.S.I.C.-Universidad de Zaragoza Pza. San
Francisco s/n, E-50009 Zaragoza, Spain*

We study chromium-doped CaF_2 , BaF_2 and SrCl_2 using EPR. Cr^{2+} ions enter the fluorite structure in a substitutional Jahn-Teller distorted site. In CaF_2 the orthorhombic distortion is produced by two fluorine ions placed in the plane perpendicular to the defect axis. In BaF_2 and SrCl_2 the distortion is tetragonal. Measurements in the three different planes using both X and Q-band and at temperatures between 4 and 300 K allow us to determine most of the spin Hamiltonian parameters including those of hyperfine and superhyperfine interactions.

Key words: EPR, Cr^{2+} Fluorites, Jahn-Teller effect.

1 INTRODUCTION

Chromium doped fluorite-type materials have been the subject of several studies in the past because of the interesting features they present related with the production of monovalent and trivalent chromium charge states by x irradiation.^{1–3} In spite of this interest and except for CdF_2 ,⁴ the divalent chromium valence state has not been yet studied in detail in those crystals.

Cr^{2+} ions (d^4) enter the fluorite structure in a cation site (cubic symmetry). The 5D ground state is split by the cubic field into $^5T_{2g}$ and 5E_g states, $^5T_{2g}$ being the lower one. The orbital degeneracy is lifted by the Jahn-Teller effect (JT). EPR is a suitable tool to study these effects. But in this case the analysis is somewhat complicated by crystal field spin Hamiltonian terms of strength comparable to the microwave frequencies and also by hyperfine and superhyperfine contributions of the order of magnitude of the nuclear Zeeman interaction. Thus in order to solve the problem an exact solution of the spin Hamiltonian as well as measurements at different microwaves are necessary.

2 EXPERIMENTAL DETAILS

Single crystals used in this study were grown in our laboratory using a standard Bridgeman method. The Chromium content in the starting materials ranged from 0.1 to 1%. $\text{CaF}_2:\text{Cr}$ and $\text{SrCl}_2:\text{Cr}$ samples were colourless while $\text{BaF}_2:\text{Cr}$ samples presented a bluish colour.

EPR measurements were performed in a Varian E-112 spectrometer working in the X-band and a Bruker ESP-380 spectrometer working in the Q-band. Liquid-nitrogen temperature measurements were taken using an immersion quartz dewar and the low temperature measurements were made using an Oxford CF 100 continuous flow cryostat. A Varian E-257 continuous flow cryostat was used for measurements between LNT and 300 K. Magnetic field values were determined with a NMR gaussmeter and the DPPH signal ($g = 2.0037 \pm 0.0002$) was used to calibrate the microwave frequency.

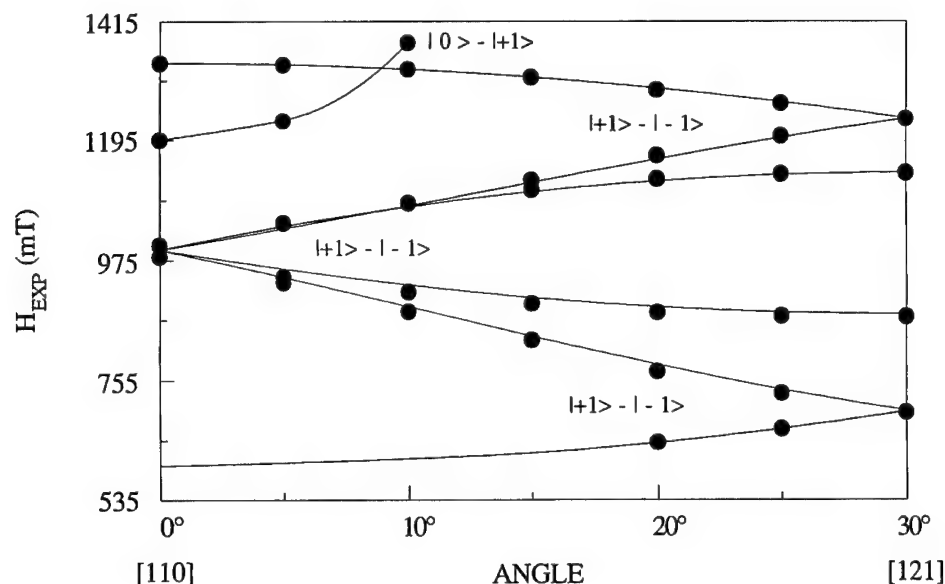


FIGURE 1 Angular dependence of $\text{CaF}_2:\text{Cr}^{2+}$ in the (111) plane measured at 77 K in the Q-band. The points are the experimental and the curves the calculated line positions.

3 EXPERIMENTAL RESULTS AND INTERPRETATION

We have measured the EPR of $\text{SrCl}_2:\text{Cr}$, $\text{BaF}_2:\text{Cr}$ and $\text{CaF}_2:\text{Cr}$ crystals at 9.3 GHz (X-band) and 34.0 GHz (Q-band) as a function of the angle between the crystallographic axes and the external magnetic field \mathbf{B} at temperatures in the 4–300 K range.

In all the cases we have obtained an anisotropic spectrum corresponding to an ion with electronic spin 2 that we associate with Cr^{2+} . The angular dependence of the resonance line positions and their intensities can be explained with the following spin Hamiltonian:

$$H = \beta[g_{\parallel}S_zB_z + g_{\perp}(S_xB_x + S_yB_y)] + D[S_z^2 - (1/3)S(S+1)] + E(S_x^2 - S_y^2) \quad (1)$$

with $S = 2$ and axes to be defined below. The spin Hamiltonian terms have their usual meaning. In all the cases the sign of D was determined by the temperature dependence of the line intensities.

CaF_2

Measurements were performed in the (100), (110) and (111) planes in both X and Q-bands. As an example we give in Figure 1 the angular dependence for a (111) plane in Q-band. It corresponds to an orthorhombic defect whose principal axes are $x = [-110]$, $y = [001]$ and $z = [110]$. The solid lines are the calculated line positions using an exact diagonalization of the spin Hamiltonian of eq. 1 with the values of parameters given in Table I.

At low temperatures and when $B/[100]$ or $[110]$, replicas about 40 times weaker are seen at both sides of the central spectrum. They are due to hyperfine interaction (hf) with

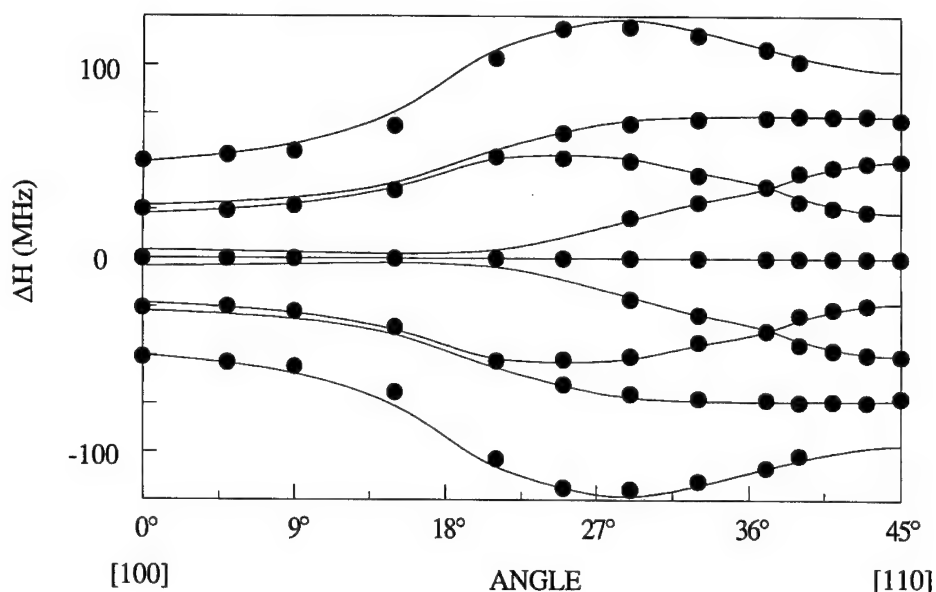


FIGURE 2 Angular dependence of the shf structure in the (100) plane measured at 77 K in the X-band. The points are the experimental and the curves the calculated line positions. The structure corresponds to a defect with the z-axis in the rotation plane.

the ⁵³Cr isotope of 9.5% natural abundance. The hf parameters have been calculated by adding to **H** the following Hamiltonian in the defect axes frame.

$$\mathbf{H}_{\text{hf}} = A_{\parallel}({}^{53}\text{Cr})S_zI_z + A_{\perp}({}^{53}\text{Cr})(S_xI_x + S_yI_y) \quad (2)$$

The hf parameters were obtained using perturbation methods up to first order. They are also given in Table I.

The superhyperfine structure corresponding to interaction with two equivalent fluorine nuclei has also been resolved in all the three measured planes. The angular dependence as measured at 77 K in the X-band is shown in Figure 2. It has been explained by adding the following axial spin Hamiltonian.

$$\mathbf{H}_{\text{shf}+\text{nz}} = \sum_i \{ -g_n \beta_n \mathbf{I}^i \cdot \mathbf{B} + A_{\parallel} S_z' I_z'^i + A_{\perp} (S_x' I_x'^i + S_y' I_y'^i) \} \quad (3)$$

with x'/z and z' at about $27.5 \pm 6^\circ$ from the [110] direction, $A_{\parallel} = 31 \pm 3.2$ MHz and $A_{\perp} = 54.6 \pm 5.4$ MHz. Thus assuming an axial shf interaction along the Cr²⁺-F⁻¹ bonding our results correspond to two nearest neighbour fluorine ions in the plane perpendicular to the defect axis.

BaF₂ and SrCl₂

The angular dependence of the spectrum was measured for the (100) and (110) planes for both X and Q-band. In Figure 3 we show the angular dependence at LNT, for the (100) plane in the X-band. The anisotropic spectrum corresponds to an ion in tetragonal

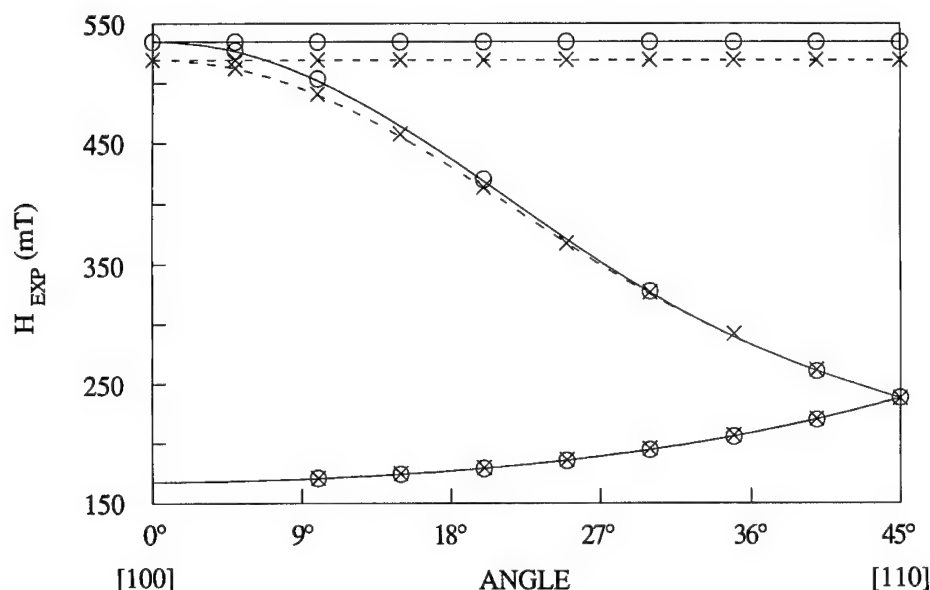


FIGURE 3 Angular dependence of Cr^{2+} EPR lines in the (100) plane measured at 77 K in the X-band. o: BaF_2 . x: SrCl_2 . Solid and dashed curves give the calculated line positions.

symmetry. Now the z-axis in the Spin Hamiltonian (1) is the tetragonal distortion axis. The parameter values, which are independent on the temperature in the measured range, are given in Table I.

The hf structure is resolved for both parallel and perpendicular directions in SrCl_2 but only for the perpendicular one in BaF_2 . The values are also given in Table I. In order to account for the angular dependence of the line intensity a cubic crystal field term $a(S_x^4 + S_y^4 + S_z^4)/6$ has to be added to the Hamiltonian (see Table I).

Table I
Spin Hamiltonian parameters. D, E and a are given in cm^{-1} the hf parameters in MHz.

Crystal	g_{\parallel}	g_{\perp}	D	E	a	$A_{\parallel}^{53}\text{Cr}$	$A_{\perp}^{53}\text{Cr}$
CaF_2	1.965(7)	1.995(2)	-2.237(4)	0.0476(1)	—	36 ± 4	33 ± 3
BaF_2	1.974(3)	1.998(3)	-2.099(3)	—	0.020(2)	—	35.1 ± 2
SrCl_2	1.974(2)	1.997(4)	-1.957(4)	—	0.021(3)	31.2 ± 1.5	43.5 ± 1.5

P. B. Oliete thanks D. G. A. for financial support.

REFERENCES

1. W. Gelhoff and W. Ulrici, *Phys. Stat. Sol.* **B102**,11(1980).
2. R. Alcalá, P. J. Alonso, V. M. Orera and H. W. den Hartog, *Phys. Rev.* **32**, 4158 (1985).
3. V. M. Orera, R. Alcalá and P. J. Alonso, *J. Phys. C* **19**,607 (1986).
4. R. Jablonski, M. Domanska, B. Krukowska-Fulde and T. Niemyski, *Mat. Res. Bull.* **8**, 749 (1973).

Nd^{3+} CENTRES IN HIGHLY NEODYMIUM DOPED LaBGeO_5 CRYSTALS

L. BITAR,* J. CAPMANY,* L. E. BAUSÁ,* J. GARCÍA-SOLÉ,* R. MONCORGÉ** and
A. A. KAMINSKII***

Dpto. Física de Materiales C-IV, Universidad Autónoma de Madrid, Cantoblanco, 28049-Madrid, Spain;* *Laboratoire de Physico-Chimie des Matériaux Luminescents, Université Claude Bernard, Lyon 1, 69622 Villeurbanne Cedex, France;* ****Av. Shubnikov Institute of Crystals, Russian Academy of Sciences, Moscow 117333, Russia*

Site selective spectroscopy has been used to detect the different Nd^{3+} centers in the $\text{La}_{1-x}\text{Nd}_x\text{BGeO}_5$ system as Nd concentration level is increased from 0.2 to 10 at%. For the highest concentration the presence of two Nd^{3+} centers with very different crystal field was detected. Both types of centers are correlated with the two polymorphic phase, LaBGeO_5 and NdBGeO_5 , with a different space group which coexist in the host for these high doping level.

1 INTRODUCTION

At present, research and development on solid state laser crystals is aimed at obtaining new materials capable to act as a laser media as well as non-linear elements. This allows for a certain degree of compactness and integration in the fabrication of devices useful to obtain laser action with self frequency doubling and self-Q-switching.

$\text{LaBGeO}_5:\text{Nd}^{3+}$ crystal appears as a promising non linear material with advantages over the $\text{LiNbO}_3:\text{MgO}:\text{Nd}^{3+}$ system, such as the absence of optical damage by photorefractive effect for high levels of radiation, a higher distribution coefficient for Nd^{3+} ions (close to unity) and a weak concentration quenching of the emission.¹

Previous works report on the basic characteristics of these crystals (spectroscopy, laser parameters and second harmonic generation efficiency) for Nd^{3+} concentrations lower than 2 at%.^{1–4} However, the $\text{La}_{1-x}\text{Nd}_x\text{BGeO}_5$ system shows two polymorphic modifications. Previous X-ray analysis data have shown that the LaBGeO_5 system crystallizes in a stillwellite type structure with a space group $P3_1$. On the other hand, NdBGeO_5 crystals show a different crystalline structure, belonging to the $P2_1/a$ space group. Site selective spectroscopy has been used for the first time to detect the different Nd^{3+} centers in the $\text{La}_{1-x}\text{Nd}_x\text{BGeO}_5$ system which are produced as Nd concentration level is increased up to 10 at%.

2 EXPERIMENTAL

A variety of lanthanum borogermanate crystals doped with Nd^{3+} concentrations ranging from 0.1 to 10 at% were grown by the Czochralski method using oriented seeds and more details are given elsewhere.¹

Samples were mounted in a He cryostat and the fluorescence spectra were taken at low temperature (10 K). Site selective excitation in the 850–900 nm range was performed by using a tunable Ti-sapphire laser. Emission from the samples, monitored in the 1040 to 1090 nm range was focused on a 30 cm focal length monochromator blazed at 1.1 μm . A Si photodiode connected to a vibrating reed electrometer was used for the detection.

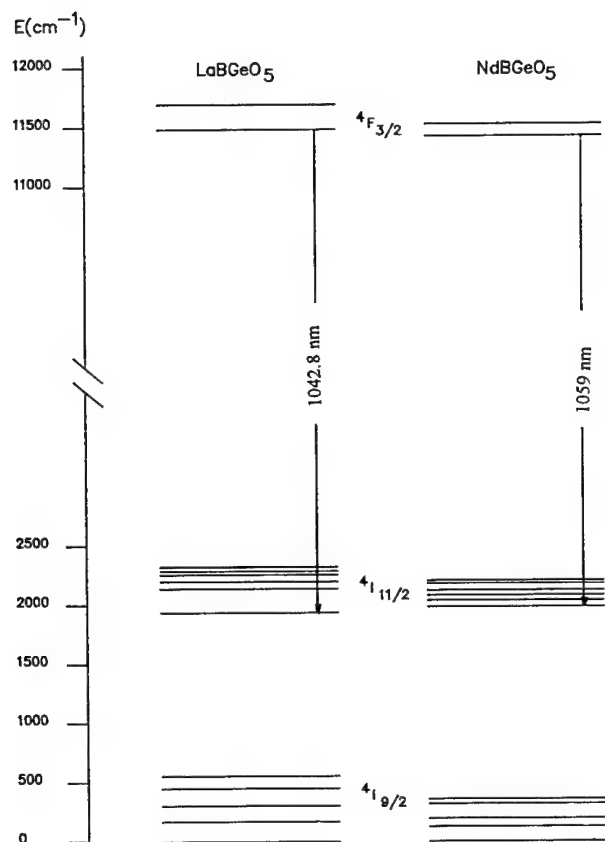


FIGURE 1 Partial scheme of levels and main emissions for Nd^{3+} ions in the two polymorphic modifications of the $\text{La}_{1-x}\text{Nd}_x\text{BGeO}_5$ system (LaBGeO_5 and NdBGeO_5 system).

3 RESULTS AND DISCUSSION

Different optical spectra (absorption and emission) were obtained when studying both, the Nd^{3+} doped LaBGeO_5 (doping level from 0.001 to 0.1 at%) and the NdBGeO_5 crystals.⁵ Figure 1 shows a partial scheme of levels as well as the emissions observed in the laser region for both systems. The positions of the energy levels are shifted, revealing the difference of crystalline environment around the Nd^{3+} ions in both systems. This is specially clear for the ${}^4\text{F}_{3/2}$ multiplet where energy splitting and gravity center are strongly affected.

In order to study the effect of the structural changes produced by increasing Nd doping level, the excitation spectra have been studied for different Nd^{3+} concentrations. Figure 2 shows the compared excitation spectra for two concentrations, 0.2 and 10 at% obtained when monitoring the emissions marked on Figure 1 (${}^4\text{F}_{3/2} \rightarrow {}^4\text{I}_{11/2}$ transition). The spectra were performed at low temperature in order to obtain higher resolution and, for the sake of simplicity only the transition from the fundamental Stark level to the lowest energy

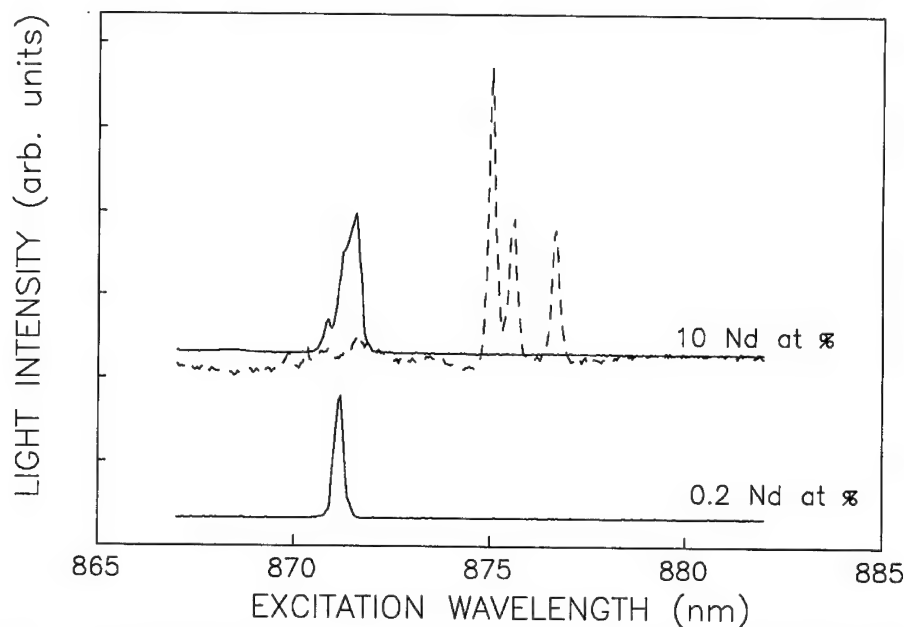


FIGURE 2 Excitation spectra of Nd³⁺ ions in LaBGeO₅ crystals associated with the 1 → R1 transition for two different concentrations at 10 K. Solid line $\lambda_{em} = 1048.2$ nm; dashed line $\lambda_{em} = 1059$ nm.

level of the $^4F_{3/2}$ multiplet (1 → R1 transition) is depicted for it appeared as the most resolved one (wavelength range of study 860–880 nm). As observed, for a 0.2 at% Nd doped sample only the line at 871 nm associated with the 1 → R1 transition is detected in the wavelength range studied. No peaks appear when changing the emission wavelength. The line is associated with the 1 → R1 transition of Nd³⁺ ions substituting for La³⁺ ions in the LaBGeO₅ matrix, in agreement with previous data. The previous results on Nd³⁺:LaBGeO₅ (at lower concentrations) and NdBGeO₅ report the 1 → R1 lines to be sharp and positioned at 871 and 875.5 nm respectively.

In case of higher doped samples, when monitoring the two emissions marked on Figure 1, different excitation lines appear at two different regions as a result of a very different crystal field site for Nd³⁺: the one associated with the Nd³⁺ ions in the LaBGeO₅ phase and the one related to the NdBGeO₅ polymorphic phase. This confirms the coexistence of the two structural phases in the host for this concentration level.

However, in contrast with the aforementioned results for Nd:LaBGeO₅ and NdBGeO₅ a spread of crystallographic sites for Nd³⁺ ions is observed for both phases. For the emission wavelength at 1048.2 nm the excitation peak centered at 871 appears broader and with a certain degree of structure revealing the presence of a distribution of different Nd³⁺ sites with similar crystal fields to that corresponding to La³⁺ cationic positions. For the emission wavelength associated with the NdBGeO₅ crystal (1055.9 nm) at least three excitation lines are clearly detected around the energy position associated with the 1 → R1 transition for Nd³⁺ ions in this structural phase. Thus, a number of nonequivalent centres are then formed in these Nd activated mixed crystals with partially ordered structure. These results could be related to a certain degree of structural disorder in the host due to the coexistence of the two polymorphic phases which induced a certain degree of cationic

lattice disorder. Further work is now under way to obtain a more detailed information on the structure of these multcentres.

4 CONCLUSION

The coexistence of the two polymorphic phases in the $\text{La}_{1-x}\text{Nd}_x\text{BGO}_5$ has been demonstrated for $x = 10$ by means of optical spectra of Nd^{3+} ions. The excitation spectra show two group of lines related to Nd^{3+} ions in very different crystal field related to both structures. The presence of alloy disordered is also evidenced by the observation of Nd^{3+} multcentres whose energy levels are positioned close to those corresponding to each of the aforementioned LaBGeO_5 and NdBGeO_5 phases.

REFERENCES

1. A. A. Kaminskii, A. V. Butashin, I. A. Maslayanizin, B. V. Mill, V. S. Mironov, S. P. Rozov, S. E. Sarkisov, and V. D. Shigorin, *Phys. Stat. Sol (a)* **125**, 6712 (1991).
2. J. Capmany, L. E. Bausá, J. García-Solé, R. Moncorgé, A. V. Butashin, B. V. Mill, and A. A. Kaminskii, *J. of Luminescence* **5819** (1994).
3. R. Moncorgé, Y. Guyot, G. Boulon, J. García-Solé, J. Capmany, A. A. Kaminskii, A. V. Butashin and B. V. Mill, *Journal de Physique IV*, **C4-423** (1994).
4. A. A. Kaminskii, B. V. Mill and A. V. Butashin, *Phys. Stat. Sol (a)* **118**, k59 (1990).

ENERGY LEVELS OF THE Eu^{3+} CENTERS IN LiNbO_3

J. E. MUÑOZ SANTIUSTE,* I. VERGARA* and J. GARCÍA SOLÉ**

*Escuela Politécnica Superior. Universidad Carlos III de Madrid. Avenida del Mediterraneo 20, Leganes 28913, Madrid, Spain; **Departamento de Física Aplicada C-IV, Universidad Autónoma de Madrid, Cantoblanco 28049 Madrid, Spain.

Energy levels of the Eu^{3+} centers formed in LiNbO_3 have been obtained from emission spectra by means of site selective spectroscopy. The crystal field parameters have been then determined for each individual center considering a main C_3 symmetry.

Key words: Luminescence, Site selection, Crystal field.

1 INTRODUCTION

LiNbO_3 (pure and codoped with MgO) is technologically a very important crystal because of its excellent electro-optic, nonlinear and laser host properties. The combination of these properties is of special interest in integrated optical devices.¹

The physical properties of this material are strongly dependent on the presence of dopant ions. The formation of non-equivalent centers has been reported for a variety of rare earth dopant ions by means of optical methods. However the site location and local structure of these centers is still an open question. The optical spectra of the Eu^{3+} ion in LiNbO_3 have been reported to be particularly sensitive to changes in its local environment. In fact the presence of four non-equivalent Eu^{3+} centers has been recently reported by using optical methods.² In this work the energy levels of these Eu^{3+} centers have been experimentally determined by using laser site selective spectroscopy. The crystal field parameters associated to each Eu^{3+} center are then obtained.

2 Eu^{3+} CENTERS IN LiNbO_3

LiNbO_3 is a rhomboedral crystal below the ferroelectric Curie Temperature (1190°C). In this structure three octahedral sites with local C_3 symmetry are candidates to be occupied (Li^+ , Nb^{5+} and a free vacancy site). Recent Monte Carlo simulation of RBS/channeling measurements strongly supports the location of Eu^{3+} ions in Li^+ sites although off-center allocated from regular Li^+ position.³

On the other hand, four Eu^{3+} centers have been previously detected in europium doped LiNbO_3 crystals as a quadruple structure in the $^5D_0(A) \rightarrow ^7F_1(A)$ transition (see inset of Figure 1). These centers are labeled Eu-1 (587.8 nm), Eu-2 (588.7 nm), Eu-3 (589.3 nm) and Eu-4 (590.3 nm) according to the peak position of their $^5D_0(A) \rightarrow ^7F_1(A)$ transition. Therefore, taking into account RBS results these centers may be thought of as being a consequence of the off-center position in the Li^+ octahedral sites.

3 EXPERIMENTAL RESULTS AND CRYSTAL FIELD CALCULATIONS

Taking advantage of the good resolution in the $^5D_0(A) \rightarrow ^7F_1(A)$ transition, the complete emission spectrum of each Eu^{3+} center can be obtained separately under resonant

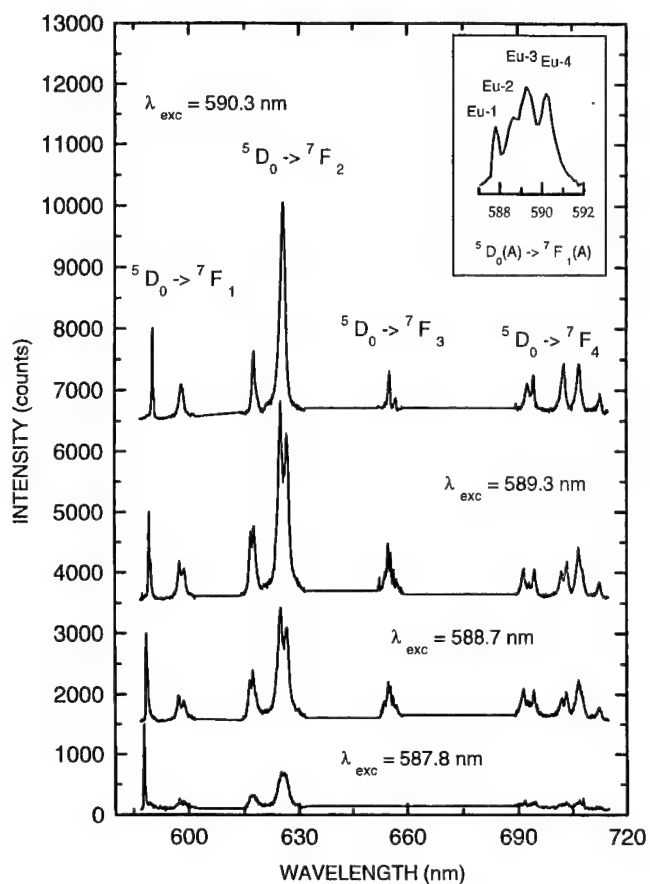


FIGURE 1 Luminiscence spectra taken at 150 K of a congruent sample of $\text{LiNbO}_3:\text{Eu}^{3+}$ under selective excitation in the four europium centers. Inset shows the complete ${}^5D_0(A) \rightarrow {}^7F_1(A)$ transition under excitation at 532 nm.

excitation in the corresponding wavelength peak.

Figure 1 shows the 150 K emission spectra of the Eu^{3+} centers for a congruent ($[\text{Li}]/[\text{Nb}] = 0.94$) $\text{LiNbO}_3:\text{Eu}^{3+}$ sample in the spectral region involving the ${}^5D_0(A) \rightarrow {}^7F_{1,2,3,4}$ transitions. The energy level positions associated to each individual europium center can be obtained from these spectra. The energy levels are listed in Table I. It should be noted that E levels of the Eu-1, Eu-2 and Eu-3 centers are split due to a local symmetry lower than C_3 , as a consequence of non-axial perturbations. This result indicates that the nature of this centers must be complex. On the opposite Eu-4 center is remain in C_3 symmetry.

Crystal field analysis has been made for each europium center, using a zeroth-order approximation. Taking advantage of the fact that levels of the first excited state 5D are far away from the 7F ground state the spin-orbit mixing between these states is not very important and no great error is introduced (less than 5%) if pure LS-type eigenfunctions are used for the 7F_J ground states. This truncate representation gives rise to a 49×49 complex matrix including full J mixing which can be easily diagonalized by using a personal computer.

In spite of the symmetry reduction observed for Eu-1, Eu-2 and Eu-3 centers, a C_3 main symmetry is assumed for all europium centers in order to simplify calculations. In this symmetry, the crystal field Hamiltonian is given by:

$$H_{CF} = \sum_{k=0}^{\leq 6} \sum_{\substack{\leq k \\ \geq -k}} B_q^k [C_q^{(k)} + (-1)^q C_q^{(k)}] + i \sum_{\substack{\leq k \\ \geq -k}} S_q^k [C_q^{(k)} + (-1)^q C_q^{(k)}]$$

which has nine parameters; six real $B_2^0, B_4^0, B_4^3, B_6^0, B_6^3, B_6^6$ and three complex, S_4^3, S_6^3, S_6^6 .

Only the components of the four lowest 7F_J states ($J = 0, -1, 4$) were determined from our fluorescence spectra, and some of them could not be resolved (see Table I). This fact leads to an uncertain determination of some crystal field parameters, as indicated by their high experimental errors.

Table I
Experimental and calculated values of the lowest terms of Eu^{3+} in LiNbO_3 (C_3).

Term	Level position (cm^{-1})							
	Eu-1 Exp.	Calc.	Eu-2 Exp.	Calc.	Eu-3 Exp.	Calc.	Eu-4 Exp.	Calc.
7F_4	3163	3162	3139	3137	3081	3082	3113	3106
	3054	3050	3028	3029	2988	2982	3002	3001
	2980	2971	2958	2950	2968	2950	2922	2927
	2955	2960	2938	2943	2956	2950	2922	2927
	2804	2783	2776	2758	2904	2886	—	2911
	2775	2766	2744	2732	2871	2697	2748	2743
	2750	2766	2715	2732	2718	2673	2712	2717
7F_3	—	1974	1958	1973	—	1969	1928	1960
	—	1898	1921	1909	1898	1899	1888	1902
	—	1856	1907	1876	1863	1857	—	1878
	—	1842	1883	1849	1845	1841	1863	1844
	—	1834	—	1830	1831	1813	—	1824
7F_2	1223	1216	1222	1199	1162	1142	1166	1168
	1205	994	1179	984	1122	943	—	968
	1008	990	980	971	930	918	962	955
	982	990	959	971	906	918	962	955
7F_1	497	474	471	445	419	404	432	433
	466	196	434	201	383	191	211	210
	181	196	187	201	198	191	211	210
7F_0	0	-20	0	-21	0	-20	0	-20

Matrix diagonalization and least square fitting parametrization have been made by using standard techniques. The obtained sets of crystal field parameters are listed in Table II.

It should be noticed that the crystal field parameters of Eu^{3+} centers are not very different from each other. This is, in principle, in agreement with an unique octahedral site occupation (the Li^+ site), according with previous RBS results. An inspection of Table II

shows that the axial crystal field parameter $|B_2^0|$ increases slightly in Eu-1 and Eu-2 centers. This fact indicates that these are the more axially distorted centers. Axial distortion must be a consequence of the off-centered position from regular lattice sites in the Li octahedron. The origin of different displacements must be a consequence of the defects associated to the non-stoichiometry of the LiNbO_3 crystal; Nb antisites (Nb^{5+} ions occupying Li sites),⁴ Nb vacancies or Ilmenite-like occlusions [5, 6] near the dopant ion (along the c axis). The different center models formed at the expense of these defects must give place to small changes in the local environment that support the formation of non equivalent optical centers.

Table II
Crystal Field Parameters (in cm^{-1}) of Eu^{3+} in LiNbO_3 .

	Eu-1		Eu-2		Eu-3		Eu-4	
B_2^0	-963	± 6	-850	± 2	-743	± 2	-776	± 2
B_4^0	213	± 9	59	± 3	-54	± 4	36	± 3
B_4^3	182	± 210	223	± 80	172	± 77	219	± 82
S_4^3	919	± 61	987	± 18	1013	± 13	934	± 19
B_6^0	-215	± 15	-99	± 5	-215	± 5	-139	± 5
B_6^3	-836	± 15	-919	± 4	-887	± 8	-880	± 7
S_6^3	-27	± 187	-24	± 73	-94	± 69	-57	± 78
B_6^6	-530	± 95	-440	± 34	-435	± 57	-380	± 32
S_6^6	217	± 176	211	± 71	371	± 66	179	± 68

ACKNOWLEDGEMENTS

This work has been supported by Comisión Interministerial de Ciencia y Tecnología under project MAT 130/92.

REFERENCES

1. E. Lallier, *Appl. Opt.*, **31**, 5276 (1992).
2. J. E. Muñoz Santiuste, B. Macalik and J. García Solé, *Phys. Rev.* **B47**, 88 (1993).
3. L. Rebouta, P. J. M. Smulders, D. O. Boerma, F. Agulló-López, M. F. da Silva and J. C. Soares, *Phys. Rev.* **B48**, 3600 (1993).
4. S. C. Abrahams and P. Marsh, *Acta Cryst.*, **B12**, 161 (1986).
5. O. F. Schirmer, O. Thiemann and M. Wohlecke, *J. Phys. Chem. Solids* **52**, 185 (1991).
6. H. J. Donenberg, S. M. Tomlinson and C. R. A Catlow, *J. Phys. Chem. Solids* **52**, 201 (1991).

EPR STUDY OF Nd^{3+} IONS IN $\text{Bi}_4\text{Ge}_3\text{O}_{12}$ SINGLE CRYSTALS

D. BRAVO,[†] A. MARTÍN,[‡] A. A. KAMINSKII* and F. J. LÓPEZ[†]

[†]Dpto. Física de Materiales, C-IV, Universidad Autónoma de Madrid, E-28049 Madrid, Spain; [‡]Dpto. Física e Instalaciones ETSAM-UPM, Avda. Juan de Herrera 4, E-28040 Madrid, Spain; *A. V. Shubnikov Institute of Crystallography, Russian Acad. Sci., Moscow 117333, Russia

An electron paramagnetic resonance study of trivalent neodymium in $\text{Bi}_4\text{Ge}_3\text{O}_{12}$ has been carried out at 5 K. The ions are substituting for Bi^{3+} in a crystal field of trigonal symmetry, which agrees with previous crystal-field analysis of the optical spectra. A detailed study of the measured g-factor values indicates that corrections to the existing crystal-field parameters B_n^m should be performed. It is suggested that corrections to the sixth-rank parameters are particularly important.

Key words: EPR, Nd^{3+} , $\text{Bi}_4\text{Ge}_3\text{O}_{12}$, Crystal-field parameters.

1 INTRODUCTION

$\text{Bi}_4\text{Ge}_3\text{O}_{12}$ has found applications in several fields. Undoped single crystals have been commonly used as scintillators.¹ Also, its nonlinear optical properties have attracted considerable attention. Recently, holographic gratings have been induced in undoped samples,² as well as in samples doped with iron-group transition ions.^{3–5} Moreover, $\text{Bi}_4\text{Ge}_3\text{O}_{12}$ (BGO) activated with trivalent rare-earth ions is a potential solid state laser.^{6,7}

The electron paramagnetic resonance (EPR) technique has been applied in the past to determine site symmetries and valence states for a number of impurities in BGO. The results of these studies have shown that Cr^{4+} and Fe^{3+} enter the Ge^{4+} -site,^{8,9} whereas Mn^{2+} , Co^{2+} , Cr^{3+} , Gd^{3+} and Er^{3+} enter the Bi^{3+} -site.⁸ The Ge^{4+} -sites have tetragonal (S_4) symmetry along the $\langle 100 \rangle$ axes of the cubic unit cell of BGO, in contrast to the Bi^{3+} -sites, which have trigonal (C_3) symmetry along the $\langle 111 \rangle$ axes. On the other hand, the crystal-field (CF) analysis of the optical spectra of Nd^{3+} and Er^{3+} carried out by Morrison and Leavitt,¹⁰ satisfactorily explains the observed energy levels for both ions by considering a CF Hamiltonian appropriate to C_3 symmetry.

In the present work we study the EPR spectra of Nd^{3+} ions in single crystals of BGO. The analysis of the spectra provides the spin-Hamiltonian parameters for this ion and confirms the impurity location in the Bi^{3+} -site. Furthermore, we compare the experimental g-factor values to those calculated using the CF parameters obtained by Morrison and Leavitt¹⁰ from the absorption and luminescence spectra.⁶ The comparison suggests that the existing set of CF parameters for Nd^{3+} in BGO,¹⁰ should be improved.

2 EXPERIMENTAL METHODS

Single crystals of BGO have been grown by the Czochralski technique with about 1% of Nd impurities. The details about the crystal growth and crystal structure have been given in Ref. 6. From the boule obtained, a sample of $2\text{ mm} \times 2\text{ mm} \times 8\text{ mm}$ was sawn and oriented by taking a number of Laue x-ray diffraction patterns.

A Bruker ESP 300 E X-band spectrometer with field modulation of 100 kHz was used

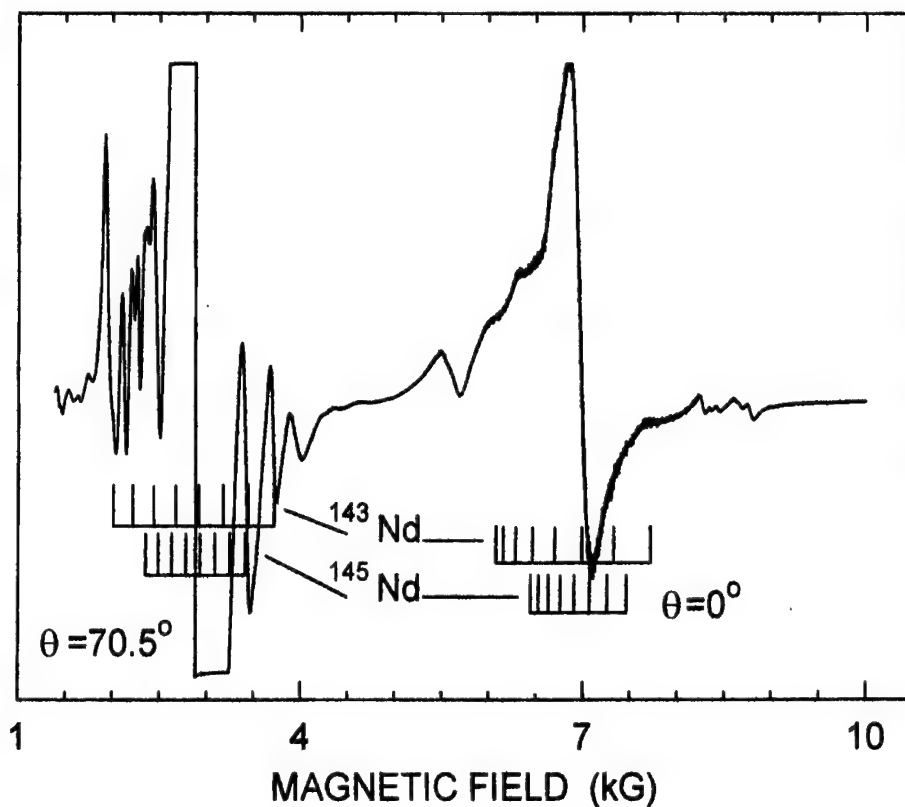


FIGURE 1 EPR first derivative spectrum of $\text{Bi}_4\text{Ge}_3\text{O}_{12}:\text{Nd}^{3+}$, measured at 5 K, with the magnetic field parallel to a $\langle 111 \rangle$ crystal direction. The spectrum consists of one threefold degenerate spectrum for $\theta = 70.53^\circ$ plus one single spectrum for $\theta = 0^\circ$. The stick diagrams depict the resonance field positions for the odd Nd-isotopes.

to record the EPR spectra. The temperature of the sample was controlled with a continuous flow liquid helium cryostat (Oxford Instruments ESR 900).

3 RESULTS

The EPR spectra of Nd-doped samples measured at 5 K consist of a maximum of four groups of lines formed by an intense line and various accompanying lines of much weaker intensity (marked with stick diagrams in Figure 1). Other weak signals are also observed, but they follow different angular dependences and will not be dealt with here. When the magnetic field \vec{H} is parallel to a $\langle 100 \rangle$ direction the four groups of lines collapse into a single one. If \vec{H} is parallel to a $\langle 111 \rangle$ direction two groups of lines are observed whose splitting corresponds to the maximum separation (see Figure 1). These facts and the observed angular dependence of the spectrum give evidence that it is due to a defect with effective spin $S' = 1/2$ and axial symmetry along the $\langle 111 \rangle$ directions of the cubic lattice of BGO.

The lines are quite broad (with a peak-to-peak linewidth of about 200 G), so that the accompanying lines cannot be distinguished for some magnetic field orientations.

However, in the favorable cases it is possible to observe that the signal ratio between the intense and the accompanying lines nearly agrees with the natural abundance ratio of the neodymium isotopes (¹⁴³Nd and ¹⁴⁵Nd are 12.17% and 8.30% abundant, respectively, both having $I = 7/2$). Therefore, we attribute the groups of lines to a neodymium defect, the accompanying lines being due to hyperfine (hf) structure from the odd isotopes.

The EPR spectra have been analyzed with the following spin-Hamiltonian ($S' = 1/2, I = 7/2$):

$$\mathcal{H} = g_{\parallel}\beta H_Z \hat{S}'_Z + g_{\perp}\beta(H_X \hat{S}'_X + H_Y \hat{S}'_Y) + A_{\parallel} S'_Z \hat{I}_Z + A_{\perp}(S'_X \hat{I}_X + S'_Y \hat{I}_Y) \quad (1)$$

where Z is chosen parallel to a $\langle 111 \rangle$ crystal direction. The fitted values for g_{\parallel} and g_{\perp} are given in Table I. No detailed analysis of the hf structure has been done due to the large linewidth of the signals. However, an estimation of the hf parameters A_{\parallel} and A_{\perp} can be made from the experimental g -values taking into account the simple relation $A_{\parallel}/g_{\parallel} = A_{\perp}/g_{\perp} = A_J/g_J$, where A_J and g_J are the magnetic hyperfine constant and the Landé g -factor for the ground level of the free Nd³⁺ ion, respectively.¹¹ Subsequently, we have diagonalized the (16×16) energy matrix of Eq. (1) for various orientations of \vec{H} using the experimental and estimated spin-Hamiltonian parameters. The calculated line positions for \vec{H} parallel to the $\langle 111 \rangle$ direction are shown in Figure 1 with stick diagrams. It is seen that the estimated parameters account satisfactorily for the observed hf structure.

4 DISCUSSION

Nd³⁺ has the 4f³ electronic configuration and a ⁴I_{9/2} free-ion ground level which splits into five Kramers doublets for crystal fields of symmetry lower than cubic.¹¹ EPR signals are observed only for the lowest lying doublet ($S' = 1/2$). Our experimental mean g -value $\bar{g} = (g_{\parallel} + 2g_{\perp})/3 = 1.943$ is similar to those obtained for Nd³⁺ in various hosts.¹² These facts and the observed hf structure support the assignment of the EPR spectra to Nd³⁺ ions.

On the other hand, the observed axially of the defect along the $\langle 111 \rangle$ crystal directions can be explained assuming that Nd³⁺ substitutes for Bi³⁺, because only the Bi³⁺ sites have such symmetry. This agrees with the previous analysis of the optical data.^{6,10}

In order to relate our EPR results to those from optical spectroscopy,^{6,10} the measured g -factor values have been compared to those calculated using the CF parameters given by Morrison and Leavitt.¹⁰ Theoretical principal g -values for a Kramers doublet can be calculated from:¹¹

$$g_{\parallel} = 2g_J \langle + | J_Z | + \rangle, \quad g_{\perp} = g_J \langle + | J_+ | - \rangle \quad (2)$$

where $|+\rangle$ and $|-\rangle$ correspond to the two states of the Kramers doublet which are linear combinations of M_J states as a consequence of the crystal field. The wavefunctions $|+\rangle$ and $|-\rangle$ can be obtained by diagonalizing the (10×10) CF energy matrix (for the $J = 9/2$ ground manifold) constructed from the existing CF parameters B_n^m for Nd³⁺ in BGO.¹⁰ The details of this calculation procedure (approximation G) and the successive approximations (GE and GERS) have been presented in a previous publication.⁸ The calculated g -factor values in the different approximations are given in Table I together with the mean square deviation σ for the energy levels.¹⁰ It is observed that the deviations for the $J = 9/2$ ground manifold (σ_G) and for the $J = 11/2$ manifold (σ_E) are small and comparable to those obtained in ref. 10. On the other hand, the calculated mean g -values are very close to that measured, but the calculated values for g_{\parallel} and g_{\perp} do not agree with the experimental ones in any approximation.

Therefore, we conclude that the lack of agreement between the calculated and observed g -values must be due to the employed CF parameters B_n^m .¹⁰ The same conclusion was achieved in the EPR study of Er^{3+} in BGO.⁸ In that case, it was found that corrections to the sixth-rank CF parameters allow to explain satisfactorily the measured g -values, introducing little misfit in the calculated energy levels. In the present case, we have seen that changes on these parameters allow us to fit the calculated g -values with minor increase for the energy deviations. As an example, the g -values and deviations calculated in the approximation GERS⁸ are given in Table I for a new value of the parameter B_6^0 .

Table I

Experimental and calculated g -factor values for Nd^{3+} ions in BGO. The calculations have been made in the approximations G, GE and GERS,⁸ using the CF parameters given by Morrison and Leavitt.¹⁰ The last column shows the results using a different value for the parameter B_6^0 . The energy level deviations σ_G and σ_E are also listed (see text).

	EXPERIMENTAL VALUES	CALCULATED VALUES USING APPROXIMATIONS			
		G	GE	GERS	GERS with $(B_6^0)' = 0.48B_6^0$
$ g_{\parallel} $	0.958	2.30	2.13	2.11	0.96
$ g_{\perp} $	2.435	1.74	1.90	1.92	2.65
$ \bar{g} $	1.943	1.93	1.98	1.98	2.09
$\sigma_G(\text{cm}^{-1})$	—	5.2	8.8	2.4	17.1
$\sigma_E(\text{cm}^{-1})$	—	—	9.1	11.5	15.1

REFERENCES

1. B. G. Grabmaier, *IEEE Trans. Nucl. Sci.* **NS-31**, 372 (1984).
2. G. Montemezzani, St. Pfändler and P. Günter, *J. Opt. Soc. Am.* **B9**, 1110 (1992).
3. E. Moya, L. Contreras and C. Zaldo, *J. Opt. Soc. Am.* **B5**, 1737 (1988).
4. C. Zaldo and E. Diéguez, *Opt. Materials* **1**, 171 (1992).
5. C. Zaldo, E. Moya, L. F. Magaña, L. Kovács and K. Polgár, *J. Appl. Phys.* **73**, 2114 (1993).
6. A. A. Kaminskii et al., *Phys. Status Solidi (a)* **33**, 737 (1976).
7. A. A. Kaminskii et al., *Phys. Status Solidi (a)* **56**, 725 (1979).
8. D. Bravo and F. J. López, *J. Chem. Phys.* **99**, 4952 (1993), and references therein.
9. D. Bravo, A. Martín, E. Diéguez and F. J. López, (to be published).
10. C. A. Morrison and R. P. Leavitt, *J. Chem. Phys.* **74**, 25 (1981).
11. A. Abragam and B. Bleaney, *Electron Paramagnetic Resonance of Transition Ions* (Clarendon Press, Oxford, 1970).
12. M. M. Abraham, L. A. Boatner, J. O. Ramey and M. Rappaz, *J. Chem. Phys.* **78**, 3 (1983), and references therein.

LIGHT-INDUCED NIR-ABSORPTION IN $\text{Sr}_{0.61}\text{Ba}_{0.39}\text{Nb}_2\text{O}_6 : \text{Ce}$ AT LOW TEMPERATURES

G. GRETEN, S. KAPPHAN, R. PANKRATH

Fachbereich Physik, University of Osnabrück, D-49069 Osnabrück

Absorption measurements of $\text{Sr}_{0.61}\text{Ba}_{0.39}\text{Nb}_2\text{O}_6:\text{Ce}$ under visible light (Ar^+ , $-\text{Kr}^+$ laser or XBO-lamp) illumination show a light-induced broadband NIR-absorption with maximum at $1.6\ \mu\text{m}$. This absorption is very pronounced at temperatures below 150 K. Its lineshape is similar to the broadband absorption which is being observed in reduced SBN crystals. The time dependence of the light induced NIR-absorption after switching off the laser light can be fitted by an addition of two exponentials. The temperature dependence of these time constants is not Arrhenius like indicating several interaction mechanisms.

Key words: Light-induced NIR-Absorption, SBN:Ce, photorefractive properties, charge transfer process.

1 INTRODUCTION

The mixed crystal system Strontium Barium Niobate possesses at room temperature a tetragonal tungsten-bronze structure with partially empty sites.¹ Large homogeneous crystals can be grown of the congruent composition $\text{Sr}_{0.61}\text{Ba}_{0.39}\text{Nb}_2\text{O}_6$ with a ferroelectric phase transition at $T = 80^\circ\text{C}$ (4 mm to 4 mm).² The SBN material displays photorefractive properties being enhanced by doping with ions like cerium or iron, which makes the material interesting for electrooptic applications like volume holographic storage.³ The details of the light induced processes and the lattice sites for dopant ions in the tungsten-bronze structure are not sufficiently well known at present. Light induced absorption processes in the visible under intense laser light irradiation have been reported for the perovskites BaTiO_3 , KNbO_3 and for LiNbO_3 and more recently for SBN.⁴ These measurements lead to the interpretation that two centers are involved, which are each in a different valence state. Recent theoretical calculations for SBN yield a photorefractive mechanism due to an intervalence transition $\text{Ce}^{3+} + \text{Nb}^{5+} \rightarrow \text{Ce}^{4+} + \text{Nb}^{4+}$. The broad dichroitic cerium induced absorption extending from the visible to the NIR-range with a maximum near 550 nm is the starting point for the above mechanism. The simultaneous emergence of an infrared absorption supposed to exist due to the Nb^{4+} centers has not been investigated yet and is the topic of this contribution. We will compare the spectral form of the absorption with that of reduced SBN-crystals, which are known to show the tendency of Nb^{5+} to be reduced to Nb^{4+} .⁵

2 EXPERIMENTAL

SBN crystals of the congruent melting composition have been grown in excellent quality, displaying natural facets using the Czochralski crystal growth method with very small temperature gradient by R. Pankrath at the University of Osnabrück. Cerium dopings of 0.025 to 1.6 weight percent CeO_2 were added to the melt.

The absorption measurements in the NIR-spectral range are performed with a Fourier IR-spectrometer (Bruker 113 Cv) and a conventional double beam spectrometer (Beckmann ACTA VII). The samples were illuminated (approximately $2\ \text{W}/\text{cm}^2$) in the

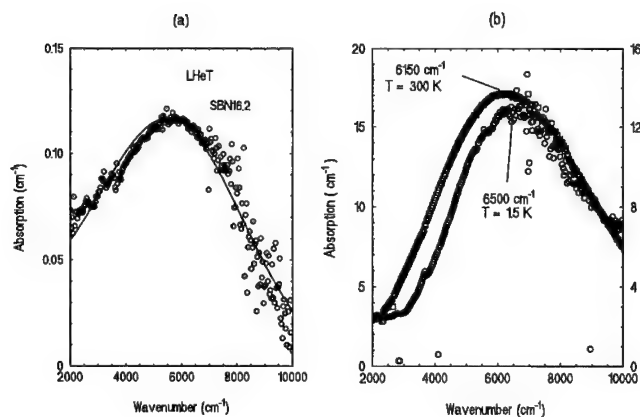


FIGURE 1 (a) Light induced NIR-absorption in SBN:Ce at LHe temperature under illumination with visible light (Ar^+ -Laser).

(b) NIR-absorption in reduced SBN:Ce at two different temperatures (1.5 K and 300 K).

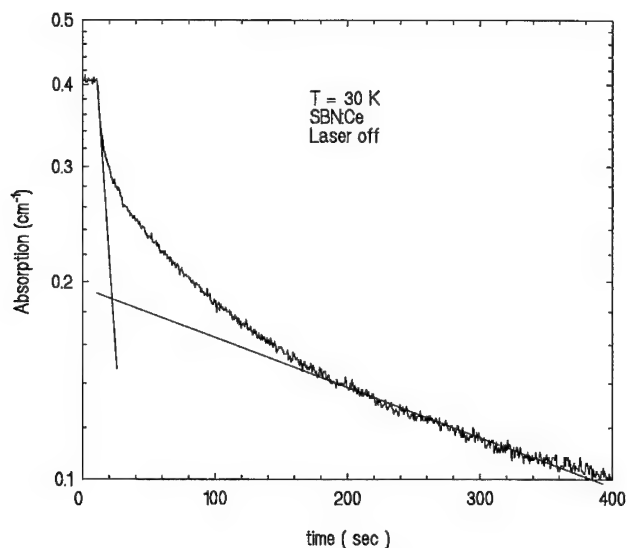


FIGURE 2 Time dependence of visible light induced absorption at 6250 cm^{-1} $T = (30\text{ K})$. Excitation was accomplished with 488 nm Ar^+ -laser light. The absorption is plotted in a logarithmic scale. The decay curves can be fitted by two exponentials.

visible with light from a Ar^+ -laser, a Kr^+ -laser (Spectra Mod. 171) or a XBO-lamp (using broad band-cut off filters).

For the temperature dependent measurements the sample was placed in a LHe-cryostat (Leybold) or in a closed-cycle cryostat (Air Products—Displex System). To reduce some of the SBN crystals, the samples were tempered in Argon-atmosphere for 4 hours at 800°C .

3 RESULTS AND DISCUSSION

Pure or cerium doped as-grown SBN crystals do not show an absorption in the NIR-region around $1.6 \mu\text{m}$ (ca. 6000 cm^{-1}). Tempering the crystals at elevated temperatures in reducing atmosphere gives rise to a broad absorption with maximum (at room temperature) at 6150 cm^{-1} . At low temperatures (1.5 K) the absorption maximum is shifted to 6500 cm^{-1} . The cerium doping is not seen to influence this absorption. The shape and the spectral position (see Figure 1b) resemble Nb^{4+} -polaron absorptions in other niobates,⁶ where also a blue-shift of the Nb^{4+} -polaron absorption with decreasing temperature is observed. The position is in fair agreement with recent theoretical calculations,⁵ confirming the identification of the NIR-absorption in SBN to result from Nb^{4+} -polarons.

Illumination with visible light (Ar^+ -, Kr^+ -laser or XBO-lamp) at low temperature evokes an absorption (see Figure 1a) with similar shape and position. It could be observed at temperatures lower than 150 K. The temperature dependence exhibits a remarkable change at temperatures round 50 K. The light induced NIR-absorption decays with a non-monoexponential dark decay time of the induced absorption after switching off the illumination. Figure 2 shows a typical example of this behaviour at $T = 30 \text{ K}$ for a measuring wavelength of $\lambda = 1600 \text{ nm}$. The time dependence of the absorption decay can be fitted by a superposition of two exponential processes. Measurements at different NIR-wavelength at $T = 15 \text{ K}$ indicate about the same exponential time constants for the absorption decay. The following function is used for a fit:

$$y = a * \exp \frac{t - t_0}{b} + c * \exp \frac{t - t_0}{d} \quad (1)$$

For $T = 15 \text{ K}$ the value of b was $35 \pm 10 \text{ sec}$ and the value of d was $180 \pm 30 \text{ sec}$, t_0 is the time when the laser light was shut off. The constants a and c are the amplitudes of the exponential absorption decay. The temperature dependence of the time constants of the light induced NIR-absorption are not Arrhenius like at low temperatures, see Table I.

Table I
Parameters of above fitting of time dependence for different temperatures. SBN14.2, 488 nm

Temperature in K	a in a.u.	b in sec	c in a.u.	d in sec
15	159	19	113	88
20	124	10	271	95
25	101	10	254	106
35	110	5.82	190	116
40	92	4.3	123	130
45	87	3.5	87	141

In order to exclude coherence effects, the light induced absorption was observed with the same results, under illumination of light from a XBO-lamp as well. As a result, we can conclude that visible light induces a charge transfer from a , up to now unknown, center to the conduction band of SBN, with the electron being trapped successively by Nb^{5+} forming a Nb^{4+} -polaron. Judging from the fact that the visible transition can be enhanced by cerium doping and based upon the calculations of Baetzold⁵ yielding $\text{Ce}^{3+}/\text{Ce}^{4+}$ as stable oxidation states of cerium in SBN, the unknown center is tentatively identified as Ce^{3+} on a Sr^{2+} or Ba^{2+} site.

This work was supported by the DFG (SFB 225, C7).

REFERENCES

1. R. R. Neurgaonkar, W. K. Cory, J. R. Oliver, M. D. Ewbank, W. F. Hall, *Optical Engineering* (1987) **26** 392.
2. R. A. Vazquez, M. D. Ewbank, R. R. Neurgaonkar, *Optics Communications* (1991) **80** (3,4) 253.
3. Tom Parish, *c'T Magazin für Computer Technik* (1991) **1** 54.
4. M. Simon, A. Gerwens, and E. Krätzig, *phys. stat. sol. (a)*, submitted.
5. Baetzold *Physical Review B* (1993) **48** (9) 5759.
6. H. Müller, B. Faust, O. F. Schirmer, *Ferroelectrics* (1994), in press.

SHARP R-LINES IN ABSORPTION AND EMISSION OF Cr^{3+} IN STOICHIOMETRIC (VTE) LiNbO_3

C. FISCHER, S. KAPPAN, XI-QI FENG* and NING CHENG*

*FB Physik, University of Osnabrück, 49069 Osnabrück, Germany; *Shanghai Institute of Ceramics, Academia Sinica, 200050 Shanghai, China*

R-line absorption and luminescence spectra of Cr^{3+} doped LiNbO_3 show a distinct dependence on crystal stoichiometry. In the Cr^{3+} R-line region around 730 nm, up to five transitions can be observed in absorption and emission. In stoichiometric $\text{LiNbO}_3\text{:Cr}$ crystals the line width (FWHM) in both absorption and emission decreases by about a factor of 2.5 in comparison with the same transitions in congruent samples. The emission line at lowest energy in the R-line spectrum ($\lambda = 734.5$ nm) disappears completely in stoichiometric $\text{LiNbO}_3\text{:Cr}$. This results, discussed together with models dealing with charge compensated Cr^{3+} pairs on Li and Nb sites and unpaired Cr^{3+} on Li site, is indicating a vanishing of the unpaired $\text{Cr}_{\text{Li}}^{3+}$ with increasing $[\text{Li}]/[\text{Nb}]$ ratio. Luminescence lifetime measurements in stoichiometric $\text{LiNbO}_3\text{:Cr}$ reveal values similar to results for congruent material of $\tau = 295$ μs for the 731 nm line and $\tau = 268$ μs for the 735 nm line, underlining the R-line character of these transitions.

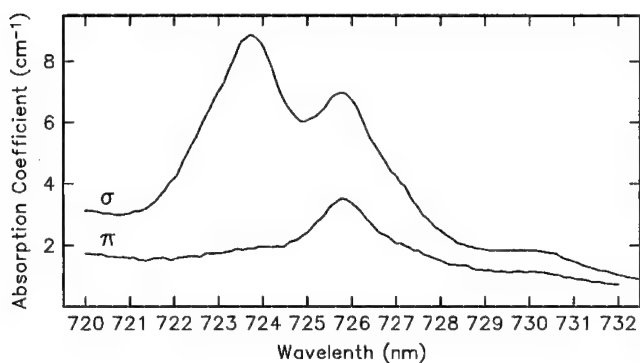
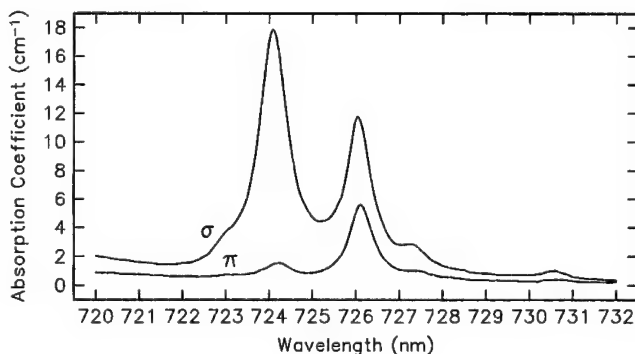
Key words: Cr^{3+} centers, stoichiometric (VTE) LiNbO_3 , R-line absorption and emission, defect lattice sites.

1 INTRODUCTION

LiNbO_3 is an important technological crystal because of its electro-optic, nonlinear and laser host properties. Many applications of this material require the presence of dopant ions, which in most cases are introduced during the crystal growth process. The location of these ions in the host lattice often influences the macroscopic properties of the material and consequently different techniques are used to determine these positions. The dopant ion Cr^{3+} has been successfully used for laser emission in various hosts and recently a lot of spectroscopic studies of $\text{LiNbO}_3\text{:Cr}$ were performed. Cr^{3+} can enter both cationic lattice sites Li^+ and Nb^{5+} with local $\text{C}_{3v}(\text{C}_3)$ symmetry, giving rise to two R-line doublets, $^4\text{A}_2 \leftrightarrow ^2\text{E}(\text{E})$ and $^4\text{A}_2 \leftrightarrow ^2\text{E}(2\text{A})$, with slightly different frequencies. Several authors^{1,2,3,4} proposed a dimerlike incorporation of Cr^{3+} on neighbouring Li and Nb sites to preserve local charge neutrality. On the other hand the observation of more than four R-lines suggests the existence of at least one additional (unpaired) lattice position, where it is not quite clear whether this is a Li or a Nb site. In this paper we investigate the influence of crystal stoichiometry changes on the R-line absorption and emission spectra. Furthermore we investigate samples with different Cr^{3+} concentrations.

2 EXPERIMENTAL

$\text{LiNbO}_3\text{:Cr}$ single crystals were grown using the Czochralski technique with chromium concentrations in the melt ranging from 0.0002 to 0.1 wt%. Stoichiometric crystals were obtained by means of the Vapour Transport Equilibration (VTE) method, i.e. congruent grown samples were treated in Li-rich environment (containing a mixture of LiNbO_3 and Li_3NbO_4) at 1100°C for extended periods (up to 500 hours for a 2 mm thick plate) to obtain a homogeneous stoichiometric composition.⁵ The sample homogeneity was checked by monitoring the spatially resolved second harmonic generation of Nd:YAG laser light⁶ (phase matching temperature $T_{\text{pm}} = 238^\circ\text{C}$). Absorption measurements were performed with a Beckman ACTA VII double beam spectrometer with the samples

FIGURE 1 Polarized R-line absorption spectra of congruent $\text{LiNbO}_3\text{:Cr}$, $T = 10$ K.FIGURE 2 Polarized R-line absorption spectra of stoichiometric $\text{LiNbO}_3\text{:Cr}$, $T = 10$ K.

mounted in a closed circle cryostat. Emission spectra were recorded using a SPEX 1500 single grating spectrometer and a cooled RCA C31034 photo multiplier. The excitation source for these experiments was a XBO 450 lamp with a SPEX Minimate as tunable, variable bandpass filter. In these experiments the samples were mounted in an LHe flow cryostat. An excimer laser (N_2 , $\lambda = 337$ nm) was used as excitation source for the luminescence lifetime measurements, which were recorded with a storage oscilloscope.

3 RESULTS AND DISCUSSION

Figure 1 and 2 show the polarized R-line absorption spectra of congruent and stoichiometric (VTE) $\text{LiNbO}_3\text{:Cr}$ 0.1 wt% at 10 K. In the spectrum of the congruent crystal three rather broad lines are observed, whereas the spectrum of stoichiometric material exhibits more details, i.e. five absorption lines (including the high energy shoulder at 723 nm). The line width (FWHM) is about 2 nm for the congruent sample, but only 0.8 nm for the stoichiometric one. This comparatively strong decrease indicates a much less disordered lattice environment for Cr^{3+} in stoichiometric LiNbO_3 , namely a reduction of intrinsic defects such as antisite defects or structural vacancies. In the emission spectra

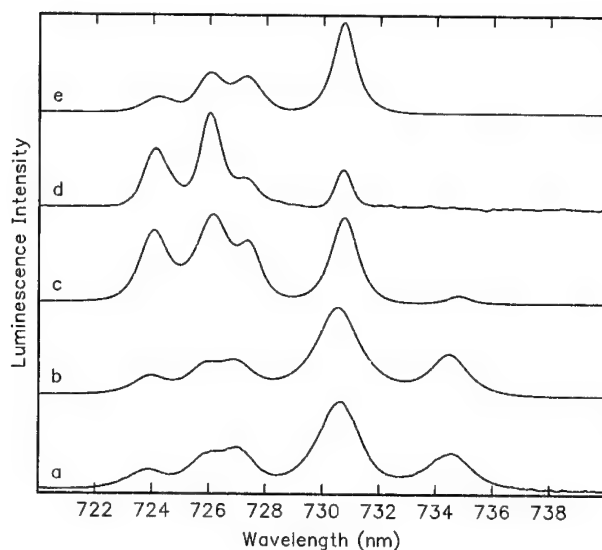


FIGURE 3 R-line emission spectra of $\text{LiNbO}_3\text{:Cr}$ with different $[\text{Li}]/[\text{Nb}]$ ratios and different Cr concentrations, $T = 78 \text{ K}$, $\lambda_{\text{exc}} = 650 \text{ nm}$. The broadband ${}^4\text{T}_2 \rightarrow {}^4\text{A}_2$ emission has been subtracted from the curves.
 a) congruent, 0.1 wt% Cr ; b) congruent, 0.005 wt% Cr ; c) $[\text{Li}]/[\text{Nb}] = 1.1$, 0.0002 wt% Cr ;
 d) stoichiometric, 0.005 wt% Cr ; e) stoichiometric, 0.1 wt% Cr.

in Figure 3 the line narrowing is not so distinct. Here the FWHM decreases only from about 1.5 nm to about 1 nm. A more striking result of these measurements is the dependence of relative line intensities on crystal composition. For congruent $\text{LiNbO}_3\text{:Cr}$ the shape of the complete R-line spectrum does not depend on the Cr concentration in the investigated range (see spectra a. and b.). This is quite different for stoichiometric crystals. In the low doped sample spectrum (curve d.) the main emission intensity lies in the two high energy lines at 724 nm (I and II), whereas in the case of a high doped sample (curve e.) most of the intensity is in the 730.5 nm line (IV), similar to congruent sample spectra. The most important result of the emission measurements is the vanishing of the low energy line at 734.5 nm (V) with increasing $[\text{Li}]/[\text{Nb}]$ ratio. In the spectrum of a sample grown from Li-rich melt (curve c.) this line is already very weak and in stoichiometric $\text{LiNbO}_3\text{:Cr}$ it can not be observed. Our interpretation of this result is the following: Besides the charge compensated $\text{Cr}_{\text{Li}}^{3+} - \text{Cr}_{\text{Nb}}^{3+}$ pairs in congruent $\text{LiNbO}_3\text{:Cr}$ there are unpaired Cr^{3+} that are preferably incorporated on Li site. With increasing Li concentration these $\text{Cr}_{\text{Li}}^{3+}$ are substituted by Li ions. In stoichiometric crystals the 'free' $\text{Cr}_{\text{Li}}^{3+}$ has disappeared completely, so that only the pairs are left.

Luminescence lifetime measurements in stoichiometric $\text{LiNbO}_3\text{:Cr}$ reveal values of $\tau = 295 \mu\text{s}$ for the 731 nm line and $\tau = 268 \mu\text{s}$ for the 735 nm line. These values are very similar to results for congruent materials,³ leading to the conclusion that there is no influence of stoichiometry variations to R-line transition rates.

REFERENCES

1. G. I. Malovichko, V. G. Grachev, S. N. Lukin, *Sov. Phys. Solid State* **28**(4), 553 (1986).
2. V. G. Grachev, G. I. Malovichko, V. V. Troitskil, *Sov. Phys. Solid State* **29**(2), 349 (1987).

3. Weiyi Jia, Huimin Liu, R. Knutson, W. M. Yen, *Phys. Rev.* **B41**, 10906 (1990).
4. G. G. Siu, Zhao Min Guang, *Phys. Rev.* **B43**, 13575 (1991).
5. Y. S. Luh, M. M. Fejer, R. L. Byer, R. S. Feigelson, *J. Crystal Growth* **85**, 264 (1987).
6. N. Schmidt, K. Betzler, M. Grabs, S. Kapphan, F. Klose, *J. Appl. Phys.* **65**, 1253 (1984).
7. Y. M. Chang, T. H. Yeom, Y. Y. Yeung, C. Rudowicz, *J. Phys. Condens. Matter* **5**, 6221 (1993).

CLUSTERING PROCESSES IN $\text{CaF}_2:\text{Gd}+\text{Lu}$ AND $\text{CaF}_2:\text{Gd}+\text{Sm}$

N. SUÁREZ

Physics Department, Universidad Simón Bolívar, Apartado 89000, Caracas 1081, Venezuela

The combined results obtained by ionic thermal currents (ITC) and electron paramagnetic resonance (EPR) techniques on CaF_2 double-doped either with $\text{Gd}+\text{Lu}$ or $\text{Gd}+\text{Sm}$ are presented here. In both systems a fraction of the Gd ions are observed in tetragonal and cubic sites. The $\text{Gd}+\text{Lu}$ systems shows a very weak ITC spectrum in contrast to the $\text{Gd}+\text{Sm}$ samples which present at least eight peaks of dipolar origin. The differences observed are accounted for by the existence in one case of an hexamer structure from the lowest Lu doping level and in the second case by the scavenging of F_i^- by clusters of increasing size with the Sm concentration. The experimental results confirm the predictions from HADES simulations that take into account the ion size effects.

Key words: Thermally Stimulated Depolarization Currents, Paramagnetic Centers, Fluorites, Defect Clustering, Dielectric Relaxation.

1 INTRODUCTION

The variety in the reported results on the fluorite matrices doped with trivalent cations shows the complexity of the equilibrium among the coexisting defects and its dependence on the difference in ionic radius of the dopant ion. Lu is the smallest cation in the lanthanide series while Sm is a middle size ion. In this work, we report ITC and EPR experiments in CaF_2 double-doped either with $\text{Gd}+\text{Lu}$ or $\text{Gd}+\text{Sm}$. The molar fraction of Gd was kept constant in each sample ($y = 0.0001$) and the Lu and Sm concentration were varied from $x = 0.0001$ to $x = 0.02$ and from $x = 0.0001$ to $x = 0.05$ molar fraction, respectively. The two techniques give complementary information as the first one (ITC) is sensitive to dipolar defects while the second one allows to determine the symmetry of the crystalline field around the paramagnetic ion. The Gd, which is midway in the lanthanide series, is used as a paramagnetic probe as its room temperature EPR spectrum should not be broaden dramatically as the Lu or Sm doping levels increases. The comparison of the results obtained by the two techniques will allow to follow the formation of polarizable aggregates and to observe the effects on the symmetry and abundance of the Gd centers coexisting in the matrix as the Lu or Sm concentration increases.

2 EXPERIMENTS AND RESULTS

The ITC experiments were carried in a setup that has previously been described.¹ The system has a sensitivity better than 10^{-16} A and the samples used in the experiments were single crystals purchased from Optovac Inc. The ITC spectra were recorded from 77 to 300K using a heating rate of 0.1Ks^{-1} . The EPR experiments were performed at room temperature in the X-band with a TE_{110} cylindrical cavity² with the magnetic field in the (110) plane.

The ITC spectrum of the Lu-doped crystals² is very weak. It is mainly composed of a low temperature peak located at 137K, corresponding to the superposition of the relaxations of the $\text{Lu}^{3+} - \text{F}_i^-$ and $\text{Gd}^{3+} - \text{F}_i^-$ first neighbor (nn) dipoles; two broader relaxations exist at 200 K and 220 K, about 30 times less intense than the first one. The

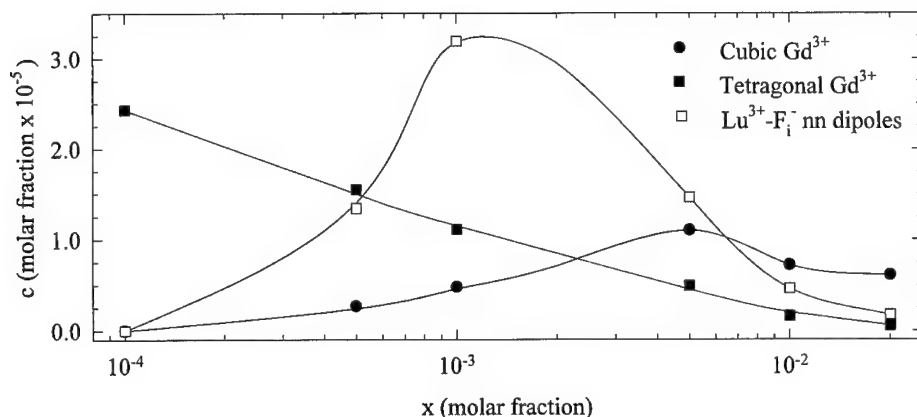


FIGURE 1 Concentrations of cubic and tetragonal centers of Gd^{3+} (filled symbols) and $Lu^{3+} - F_i^-$ nn dipoles (open symbols) versus the Lu concentration in $CaF_2:Gd+Lu$ samples (lines are drawn to guide the eye).

intensities of these 3 relaxation show a maximum for $x = 0.003$. On the contrary the ITC spectrum for the Sm-doped crystals is very rich, exhibiting 8 peaks of dipolar origin whose maxima are located from 97 to 245 K. The peak at 137 K, corresponding to the superposition of the relaxations of the $Sm^{3+} - F_i^-$ and $Gd^{3+} - F_i^-$ nn dipoles, shows an intensity maximum at $x = 5 \times 10^{-4}$. The intensities of another two peaks also show a maximum as x increases while the others are continuously increasing with x .

The EPR results show in both systems the existence of two Gd centers, a tetragonal one due to the $Gd^{3+} - F_i^-$ nn dipole, and a cubic center due to the free Gd^{3+} non-locally compensated. The concentration of Gd nn dipoles can be determined by EPR and then be subtracted from the total concentration of nn dipoles estimated from the corresponding ITC peak intensity to obtain the absolute concentration of Lu or Sm nn dipoles. Figure 1 shows the concentration of cubic and tetragonal centers of Gd as determined by EPR and Lu nn dipoles versus the Lu concentration. A similar graph for the Gd+Sm doped samples is shown in Figure 2. The comparison between the two figures leads to the following observations: a) in both systems the number of Gd tetragonal centers is constantly decreasing as x grows; b) the Gd cubic centers concentration shows a maximum around $x = 5 \times 10^{-3}$ and $x = 10^{-3}$, respectively in the Lu and the Sm doped samples; c) in the Gd+Lu system, the Gd cubic and Lu nn dipoles are not present at $x = 0.0001$; and d) the Lu and Sm nn dipole concentration show a maximum around $x = 10^{-3}$ and $x = 5 \times 10^{-4}$ respectively, with abundances of 3% and 26% relative to the total concentration of the corresponding dopant.

In the Gd+Lu crystals the low number of Lu nn dipoles and the overall weakness of its ITC spectra in the temperature range explored here indicate that the Lu ions must be predominantly either in cubic sites or in more complicate aggregates. These larger aggregates could be either a non-gettered or a gettered cluster, whose relaxation may originate the peak at 20 K in the dielectric spectrum of the Lu doped CaF_2 crystals reported by Andeen *et al.*³ The absence of Gd^{3+} cubic centers as well as the nonexistence of Lu nn dipoles for $x = 10^{-4}$ is an indication that even at this low concentration the trivalent ions must be forming mixed clusters of large size. Since the amount of Gd and Lu centers detected by both techniques is so low, and it is even decreasing in the higher doped samples, the EPR and ITC results show that the existence of a high concentration of Lu ions in cubic sites, that would not be detected by these two techniques, should be

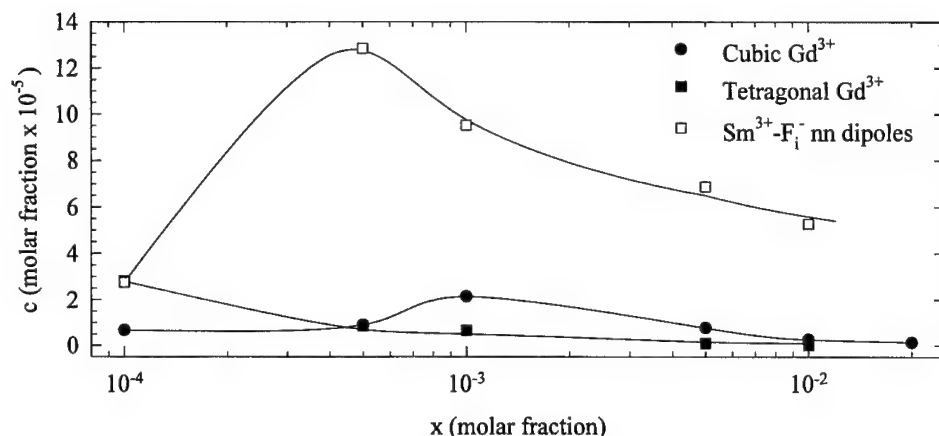


FIGURE 2 Concentrations of cubic and tetragonal centers of Gd^{3+} (filled symbols) and $\text{Sm}^{3+}-\text{F}_i^-$ nn dipoles (open symbols) versus the Sm concentration in $\text{CaF}_2:\text{Gd}+\text{Sm}$ samples (lines are drawn to guide the eye).

discarded. The missing Gd and Lu ions should then exist in defect structures of higher complexity such as the ones predicted by the HADES simulations⁴ for $\text{CaF}_2:\text{Y}^{3+}$. As Lu^{3+} is still smaller than Y^{3+} it should follow a similar behavior in the clustering tendency. Cirrillo-Penn and Wright⁵ have proposed for the smaller rare earths the existence of an enriched F_i^- hexamer structure which could be the origin of the relaxation observed in CaF_2 doped with small rare earths at 20 K, temperature that we could not reach in our experiments.

In contrast, the higher number of Sm nn dipoles, as well as the variety of polarizable entities present in the ITC spectra of the Sm doped samples, evidence the formation of polarizable clusters of increasing size as the number of trivalent cation increases. This behavior is analogous to the one found in the ITC spectra of CaF_2 single doped with Gd in the same intermediate concentration range.² In the CaF_2 matrix the similarity in the ionic radius of Sm^{3+} , Ca^{3+} and Gd^{3+} might account for the tendency of Sm and Gd to form small clusters, which becomes larger as the Sm concentration increases. These clusters could be L-shaped dipoles, gettered dimers, gettered trimers, and so on. In fact, for the CaF_2 doped with Gd, HADES simulations have shown an increased stability for small clusters that have scavenged an F_i^- . In the Gd+Sm double-doped samples studied here the combined ITC and EPR results show that the number of Gd in cubic sites does not change significantly while the intensity of a majority of the ITC cluster-associated peaks increases. This observation implies that the F_i^- contributing to the scavenging of these dipolar clusters should be associated to the Sm and not to the Gd. Therefore, the Sm ions must abundantly exist as cubic defects in the matrix. The higher number of ITC relaxations present in these samples could be due to a greater number of different polarizable clusters or to a variety of relative positions of the extra F_i^- that slightly changes the relaxation times involved.

3 CONCLUSIONS

By using the complementary EPR and ITC techniques in CaF_2 samples double-doped with Gd+Lu or Gd+Sm we were able to follow the variation of the different dipolar defects

and paramagnetic centers, that coexist in these two types of solid solutions, as a function of the Lu or the Sm concentration. In the Gd+Lu doped samples the poor ITC spectrum and the low number of Gd^{3+} ions in tetragonal and cubic symmetry have shown that the clustering process cannot be interpreted as the scavenging of F_i^- by various clusters of increasing size. Here the existence of the proposed hexamer structure, even at low impurity concentration, is the only explanation that takes into account the observed combination of results. In contrast, in the Gd+Sm samples, the rich ITC spectrum and also the low number of cubic and tetragonal Gd centers detected by EPR evidence the tendency to form small polarizable clusters of increasing size as the Sm concentration increases. The analysis of the combined ITC and EPR results show that the F_i^- associated to the Sm^{3+} ions must be the one contributing to the scavenging of these clusters, therefore, there should exist an abundant number of Sm in cubic sites. The fundamental differences found here on the two double-doped crystals are in agreement with the predictions of the HADES simulations that take into account the ion size effects.

ACKNOWLEDGEMENTS

The author gratefully acknowledges financial support from the Consejo Nacional de Investigaciones Científicas y Tecnológicas (Programa de Nuevas Tecnologías Proyecto NM-012).

REFERENCES

1. E. Laredo, M. Puma, and D. R. Figueroa, *Phys. Rev. B* **19**, 2224 (1979).
2. E. Laredo, M. Díaz, N. Suárez, and A. Bello, *Phys. Rev. B* **46**, 11415 (1992).
3. C. A. Andeen, J. J. Fontanella, M. C. Winstergill, P. J. Welcher, R. J. Kimble, and G. E. Matthews, *J. Phys. C*, **14** 3557 (1981).
4. P. J. Bendall, C. R. A. Catlow, J. Corish, and P. W. M. Jacobs, *J. Solid State Chem.* **51** 159 (1984).
5. K. M. Cirillo-Penn and J. C. Wright, *Phys. Rev. B* **41**, 10799 (1990).

NEW SYMMETRY PROPERTIES OF THE CUBIC RARE-EARTH CENTERS IN CRYSTALS

V. LUPEI

Institute of Atomic Physics, 76900 Bucharest, Romania

A method that gives analytical basis functions for the irreducible representations which label the crystal field levels of the rare-earth ions in cubic symmetry, regardless how many times these representations enter in the decomposition of the irreducible representation of the three-dimensional rotation group is presented. The method makes use of the transformation properties of the wavefunctions under rotations around two fourth-order axes of the cube and gives analytical crystal field wavefunctions versus the composition parameter of the cubic crystal field potential.

1 INTRODUCTION

Knowledge of wavefunctions and of energy levels of transition ions in crystals is important for characterization of the crystal field interaction and for calculation of the effect of various external fields. Generally the crystal field interaction of rare-earth f-electron systems (lanthanides and actinides) could be considered as weak, i.e. the total angular momentum quantum number J remains good, although sometimes strong J -mixing by crystal field interaction could take place. In this approximation the energy levels J are split in crystal field (c.f.) components, each of them being characterized by one of the irreducible representations Γ_i of the cubic group to which the irreducible representation of the three-dimensional rotation group is reduced:

$$D^{(J)} \rightarrow \sum_i a_i(J) \Gamma_i \quad (1)$$

Each c.f. component has a residual degeneracy, equal to the dimension of the representation Γ_i and its wavefunctions form a basis for this representation. The c.f. wavefunctions are linear combinations of free-ion wavefunctions:

$$|f_i\rangle = \sum_M C_{JM}^{(j)} |JM\rangle \quad (2)$$

where $j \equiv (\Gamma_i, \tilde{M})$ denotes the irreducible representation Γ_i and the function \tilde{M} inside the basis of representation. The coefficients $C_{JM}^{(j)}$ could be calculated by diagonalization of the crystal field potential in the space of the $(2J + 1)$ functions $|JM\rangle$; in case of cubic symmetry for f-electron systems this Hamiltonian is written (the notations used here are similar to those from¹)

$$\mathcal{H} = B_4 O_4 + B_6 O_6 \quad (3)$$

where O_4 and O_6 are fourth- and respectively sixth-order polynomials in angular momentum operators while $B_4 = \beta A_4 \langle r^4 \rangle$ and $B_6 = \gamma A_6 \langle r^6 \rangle$ characterize the strength of interaction. By introducing² the scaling factors $F(4)$ and $F(6)$ and the energy W and crystal field composition parameter such as

$$B_4 F(4) = Wx \text{ and } B_6 F(6) = W(1 - |x|), \quad (4)$$

the Hamiltonian (3) could be rewritten as

$$\mathcal{H} = Wx \left[\frac{O_4}{F(4)} + \frac{1 - |x|}{x} \frac{O_6}{F(6)} \right] = Wxh; \quad (5)$$

here h is the reduced Hamiltonian which depends on the composition parameter x but not on the absolute values of the c.f. parameters B_4 and B_6 . Other choices for the composition parameter such as $y = A_6 \langle r^6 \rangle / A_4 \langle r^4 \rangle$ or $z = B_6/B_4$ could be made.

The basis functions for representations Γ_i for which $a_i(J) = 1$ do not depend on the composition parameter of the cubic crystal field. However if $a_i(J) > 1$ these functions depend in a very intricate way on this parameter; this dependence is currently calculated numerically. However is a difficult and time-consuming work to extract the value of the composition parameter from the matrix elements of various interactions, measured in experiments. Such a result would also lack a clear and explicit dependence of the effects of these interactions on the composition parameter of the crystal field. The present paper shows that this limitation originates from the incomplete use of the transformation properties of the cubic group in the previous theories and discusses a new method which enables to obtain analytical wavefunctions and energy levels for f-electron systems versus the composition parameter of the cubic crystal field potential regardless the value of $a_i(J)$ in eg. (1). A preliminary discussion of this problem for several particular cases was presented in.^{3,4}

2 TRANSFORMATION PROPERTIES OF THE WAVEFUNCTIONS

For odd f-electron systems the total angular momentum quantum number is a half-integer and the transformation properties of these ions in cubic symmetry are described by the double cubic group which has two two-dimensional representations, Γ_6 and Γ_7 , and one four-dimensional representation, Γ_8 . It is useful to write the half-integer J as a sum $(n + m + 1/2)$, where n is an integer and m is another integer which could take the values n or $(n + 1)$. For even f-electron systems J is an integer equal to $(n + m)$ and the transformation properties are described by the simple cubic group which has two one-dimensional representations Γ_1 and Γ_2 , a bi-dimensional representation Γ_3 and two three-dimensional representations, Γ_4 and Γ_5 .

The properties of the f-ions in crystals could be grouped in four classes according to the following determining factors: (i) the temporal inversion; (ii) the crystal field symmetry transformations; (iii) orthogonality; (iv) the selection rules of the reduced crystal field Hamiltonian h . Each of these factors acts in a specific way on the coefficients $C_{JM}^{(j)}$ from eq. (2); these properties are enough as to determine analytical functions for $C_{JM}^{(j)}$ versus the cubic crystal field composition parameter.

2.1 Transformation Properties Determined by The Temporal Inversion

According to the temporal inversion each wavefunction (2) has a temporal conjugate

$$|\bar{f}_i\rangle = \sum_M (C_{JM}^{(j)})^* (-1)^{J-M} |JM\rangle \quad (6)$$

which is also a wavefunction of the ion in crystal. For odd f-electron systems (Kramers ions) the functions (2) and (6) are distinct; in case of even f-systems this may not be always so. Thus the temporal inversion could reduce the number of $C_{JM}^{(j)}$ coefficients to be determined from other properties.

2.2 Transformation Properties Determined by The Crystal Field Symmetry Group

Essential in determining the properties of the wave functions of the f-ions in cubic sites are the fourth-order rotation axes. Traditionally only one of these rotations (chosen as z-axis) is used; this paper shows that the rotation around a second fourth-order axis (taken as axis y) is also important. These two rotation properties have several important consequences:

A. They impose conditions upon the coefficients $C_{JM}^{(j)}$:

a. Rotation $R_Z(\frac{\pi}{2})$ imposes that the differences between the values of M in eq. (2) are multiples of 4:

In case of odd f-electron systems this leads to a grouping of the wavefunctions in two families:

$$|f^{(1)}\rangle = \{J, (J-4), \dots\}, \text{ with } (n+1) \text{ components } M \quad (7a)$$

this family contains $(n+1)$ functions

$$|f^{(2)}\rangle = \{J-2, (J-6), \dots\}, \text{ with } m \text{ components } M; \quad (7b)$$

this family contains m functions.

The basis of the representation Γ_8 contains a function of family (7a) and one of (7b) and their conjugates while Γ_6 and Γ_7 have the bases either from (7a) or (7b), but not from the same family for both of them.

– For even electron systems three families of wavefunctions could be formed:

$$|f_{(1)}\rangle = \{[J - (n+1-m)], \dots, [J + (n+3-m)]\}, \quad (8a)$$

with m components M and containing m distinct wavefunctions,

$$|f_{(2)}\rangle = \{[J - (m-n)], \dots, [-J + (m-n)]\}, \quad (8b)$$

with $(n+1)$ components M placed symmetrically around $M=0$ and containing $(n+1)$ distinct wavefunctions,

$$|f_{(3)}\rangle = \{[J - (2+m-n)], \dots, [-J + (2+m-n)]\}, \quad (8c)$$

with n components placed symmetrically around $M=0$ and containing n wavefunctions.

b. Rotation $R_Y(\frac{\pi}{2})$ establishes a connection between the coefficients of wavefunctions from different families. The relations obtained this way are then submitted to the restriction that $R_Y(\frac{\pi}{2})$ applied to a function which belongs to the basis of a given representation should not transform it to a function which belongs to the basis of another representation. For instance, if in case of odd systems the basis of Γ_6 belongs to the family (7a) the rotation $R_Y(\frac{\pi}{2})$ should not transform it to a function (7b) which forms the basis for Γ_7 . Then for each $M_{(1)}$ component of a function (7a) we have

$$\langle M_{(1)} | R_Y(\frac{\pi}{2}) | f_{(2)} \rangle = 0 \quad (9)$$

B. Rotations $R_Z(\frac{\pi}{2})$ and $R_Y(\frac{\pi}{2})$ can define for each representation a pseudo- or fictitious angular momentum \tilde{J} . Thus the decomposition (1) shows that for some of the J values (0, 1/2, 1, 3/2), $D^{(j)}$ reduces to a unique cubic point group representation (Γ_1 , Γ_6 , Γ_4 and Γ_8 respectively); this suggests that the basis functions for these representations could be regarded as the wavefunctions of a fictitious angular momentum \tilde{J} , specific for each representation regardless the actual value of J and having similar transformation properties

to \tilde{J} under the rotations $R_z(\frac{\Pi}{2})$ and $R_y(\frac{\Pi}{2})$. Then the basis functions could be labelled by the $(2\tilde{J}+1)$ projections of \tilde{J} and they must satisfy the transformation properties:

$$R_z(\frac{\Pi}{2}) | \tilde{M} \rangle = \exp(-i \frac{\Pi}{2} \tilde{M}) | \tilde{M} \rangle \quad (10)$$

$$R_z(\frac{\Pi}{2}) | \tilde{M} \rangle = \sum_{\tilde{M}'} d_{\tilde{M}\tilde{M}'}^{(\tilde{J})}(\frac{\Pi}{2}) | \tilde{M}' \rangle \quad (11)$$

where $d_{\tilde{M}\tilde{M}'}^{(\tilde{J})}(\frac{\Pi}{2})$ are the reduced matrix elements for the $(\frac{\Pi}{2})$ rotation operator.

Equations (10) and (11) applied to each of the families of wavefunctions enable the determination of the values of \tilde{J} and \tilde{M} to be attached to each of the wavefunctions. The basis functions of representations $\Gamma_1, \Gamma_6, \Gamma_4$ and Γ_8 (for which $a_i = 1$ in eq. (1)) could be thus characterized by the fictitious moments $\tilde{0}, 1/2, \tilde{1}$ and $3/2$ respectively and by the set of corresponding \tilde{M} projections. In case of representations which never show alone in the decomposition (1) it could be shown that: (i) the basis functions of representation Γ_7 could be labelled by the projections $\pm 3/2, \sqrt{\mp \frac{5}{2}}$ of a fictitious momentum $\tilde{J} = 5/2$; (ii) the basis functions of representation Γ_5 could be labelled by the projections $\tilde{1}, -\tilde{1}$ and a combination of projections $\tilde{2}$ and $-\tilde{2}$ of a fictitious momentum $\tilde{J} = \tilde{2}$; (iii) the basis functions of representation Γ_2 correspond to a combination of projections $(|\tilde{2}\rangle - |-\tilde{2}\rangle)$ of a momentum $\tilde{J} = \tilde{3}$; (iv) the basis functions of Γ_3 correspond to projection $\tilde{0}$ and to the combination $|\tilde{2}\rangle + |-\tilde{2}\rangle$ of a momentum $\tilde{J} = \tilde{2}$.

2.3 Orthogonality Properties

The orthogonality conditions

$$\sum_i \langle \Gamma_i^l \tilde{M} | \Gamma_i^{l'} \tilde{M}' \rangle = \delta_{ll'} \delta_{\tilde{M}\tilde{M}'} \quad (12)$$

where i refers to the type of representation and l labels the various representations of the same type provide additional relations between the coefficients C_{JM} .

2.4 Properties Imposed by The Selection Rules of The Crystal Field Hamiltonian

A useful way to reduce the number of parameters to be handled in calculations is to replace the starting coefficients C_{JM} in eq. (2) by orthogonal functions of fictitious angles. This enables to write analytical functions versus only a few such angular parameters for all the coefficients C_{JM} by using the properties described above. Then these fictitious angles could be connected to the composition parameter of the crystals field by using the selection rules for the matrix elements of the reduced Hamiltonian h between functions of the same \tilde{M} belonging to the various representations of the same type:

$$\langle \Gamma_i \tilde{M} | h | \Gamma_i^1 \tilde{M} \rangle = 0 \quad (13)$$

3 EXAMPLES

3.1 $J = 9/2$

$$D^{(9/2)} \rightarrow \Gamma_6 + 2\Gamma_8$$

$$\Gamma_8^{(1)} : |\Gamma_8^{(1)}, \pm 3/2\rangle = \pm(\cos \theta_1 |\mp 5/2\rangle + \sin \theta_1 |\pm 3/2\rangle)$$

$$|\Gamma_8^{(1)}, 1/2\rangle = \pm \frac{1}{4\sqrt{3}} [-(\sqrt{21} \cos \theta_1 + 3 \sin \theta_1) |\pm 9/2\rangle + (\sqrt{6} \cos \theta_1 + \sqrt{14} \sin \theta_1) |\pm 1/2\rangle + (\sqrt{21} \cos \theta_1 - 5 \sin \theta_1) |\pm 7/2\rangle]$$

$$\Gamma_8^{(2)} : \theta_2 = \theta_1 + \frac{\pi}{2}$$

$$\tan 2\theta_1 = \sqrt{\frac{3}{28}} \frac{5 + 336z}{1 - 12z}$$

with $z = (B_6/B_4)$

3.2 $J = 11/2$

$$D^{(11/2)} \rightarrow \Gamma_6 + \Gamma_7 + 2\Gamma_8$$

$$\Gamma_8^{(1)} : |\Gamma_8^{(1)}, \pm 3/2\rangle = \pm \frac{1}{4\sqrt{3}} [\sqrt{33} \sin \theta_1 |\pm 11/2\rangle + (\sqrt{10} \sin \theta_1 - 4 \cos \theta_1) |\pm 3/2\rangle + (\sqrt{5} \sin \theta_1 + 4\sqrt{2} \cos \theta_1) |\mp 5/2\rangle]$$

$$|\Gamma_8^{(1)}, \pm 1/2\rangle = \pm \frac{1}{4\sqrt{3}} [(\sin \theta_1 - 2\sqrt{10} \cos \theta_1) |\pm 9/2\rangle$$

$$+ \sqrt{42} \sin \theta_1 |\pm 1/2\rangle + (\sqrt{5} \sin \theta_1 + 2\sqrt{2} \cos \theta_1) |\mp 7/2\rangle]$$

$$\Gamma_8^{(2)} : \theta_2 = \theta_1 + \frac{\pi}{2}$$

$$\tan 2\theta_1 = \frac{2\sqrt{10}}{33} (1 - 441z)$$

The matrix elements calculated with these wavefunctions will then show an explicit analytical dependence on the composition parameter z of the cubic crystal field potential.

REFERENCES

1. A. Abragam and B. Bleaney, 'Electron Paramagnetic Resonance of Transition Ions', Clarendon Press, Oxford 1970.
2. K. R. Lea, M. J. M. Leask and W. P. Wolf, *J. Phys. Chem. Solids* **23**, 1981 (1962).
3. V. Lupei, C. Stoicescu and I. Ursu, *Bull. Magn. Res.* **5**, 136 (1983).
4. V. Lupei, Proc. XXIII Congress Ampere 'Magnetic Resonance and Related Phenomena', Roma 1986, p. 281.

NONRADIATIVE RECOMBINATION PROCESSES IN WIDE BAND GAP II-VI PHOSPHOR MATERIALS

M. SURMA and M. GODLEWSKI

*Institute of Physics, Polish Academy of Sciences, 02-668 Warsaw, Al. Lotników 32/46,
Poland*

Transition metal ions limit the light emission from wide band gap II-VI phosphor materials. Nickel, iron and chromium deactivate the visible luminescence of ZnSe due to the bypassing and three center Auger processes. For ZnMnS the donor-acceptor pair (DAP) emission is deactivated by spin dependent energy transfer transitions from DAPs to Mn ions.

Key words: ZnS, ZnSe, transition metals, nonradiative processes, bypassing, Auger effect.

1 INTRODUCTION

Transition metal (TM) (e.g. Cu, Mn) activated wide band gap II-VI compounds have found a wide spread application in opto-electronic industry. This is due to an observation of a bright light emission from donor-acceptor pair (DAP) or intra-shell transitions of TMs. The efficiency of an emission from Cu or Mn activated II-VI phosphors is limited by the inadvertent presence of other TM ions, such as iron, chromium or nickel. In ZnS, these ions are known as the most effective deactivators of the visible luminescence.^{1,2} Several processes account for such a role of TM ions in ZnS:Fe: the so-called bypassing process (free carrier trapping via deep impurity level of TM,¹ Fig. 1(a)), energy transfer processes from donor-acceptor pairs to iron,³ including the three center Auger recombination (TCAR) process⁴ (Fig. 1(b)), and formation of iron-copper pairs.^{3,5} In this paper we analyze the role of iron, chromium and nickel in nonradiative recombination processes in ZnSe and that of manganese in ZnS. The results of photo-stimulated electron spin resonance (photo-ESR), optically detected magnetic resonance (ODMR), photoluminescence (PL) and optical absorption are discussed. Several nonradiative processes are shown to be important and their relative role is analyzed. The relative role of these processes is discussed in the present work for Cr, Fe, Ni doped ZnSe and Mn doped ZnS.

2 RESULTS AND DISCUSSION

In ZnS:Fe the most important channels of DAP deactivation are the bypassing and Fe-Cu pair formation processes, with the Auger effect being also active.² We show below that in the case of ZnSe, the bypassing process involving TM centers remains dominant because of the relatively large electron and hole capture cross sections by nickel, iron and chromium. The photo-ESR method was applied, since the bypassing and the TCAR transitions involve a change of the TM charge state, a process readily monitored with use of ESR. The photo-sensitivity of Cr⁺, Fe³⁺ and Ni⁺ ESR signals was studied.

Figure 2 presents the spectral dependence of photo-excitation of the Cr⁺ and Fe³⁺ ESR signals in ZnSe doped with Cr, Fe and Ni. In the case of Fe³⁺, the photo-excitation spectrum is dominated either by the direct chromium ionization transition (band II) or by nickel (2+ → 1+) ionization (band IV), identified in a separate ESR study.^{6,7} In both cases the Fe³⁺ ESR signal is induced by the capture of photo-excited holes by Fe²⁺

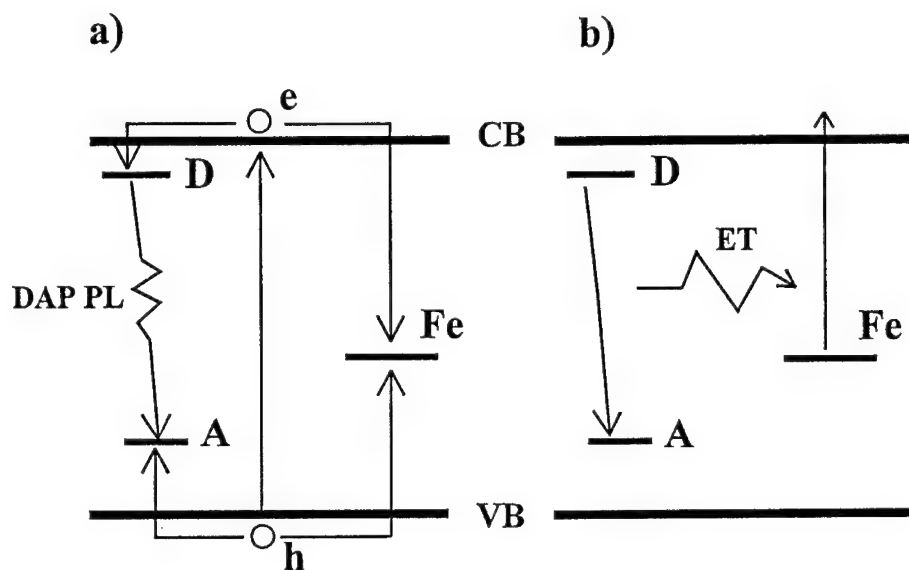


FIGURE 1 Deactivation of the DAP radiative recombination by the bypassing (a) and energy transfer (b) processes. In the bypassing process free carriers recombine via TM level instead being trapped by donor and acceptor centers. The three center Auger recombination process results in TM ionization following energy transfer from the DAP.

centers. We show that the direct Fe ionization (band I) is fairly weak, which indicates a rapid recapture of the photo-generated electrons by Fe^{3+} centers.

In ZnS the Fe^{3+} ESR signal was excited via the TCAR process,⁴ which involves in the first step the ionization of an acceptor with electron being captured by a shallow donor. The so excited DAP decays nonradiatively by energy transfer to iron (Figure 1(b)) resulting in its ionization. The lack of a TCAR band in Fe^{3+} photo-excitation in ZnSe:Fe (Figure 2) is a result of the large electron capture cross section of Fe^{3+} . In intentionally Fe doped samples electrons are efficiently trapped by Fe^{3+} centers resulting in a small occupation of this state observed in the ESR study. It is not the case for Ni doped ZnSe. Here the Fe^{3+} centers created in the TCAR process remain metastably occupied since photo-generated electrons are trapped either by shallow donors or (mostly) by nickel centers. This result indicates a high efficiency of the bypassing process for Ni ion in ZnSe.

The Cr^{3+} photo-excitation spectrum is dominated by (band III) an indirect process which involves acceptors ionization and capture of photo-excited electrons by Cr^{2+} centers. The PL experiments indicate, however, that electron capture rates by chromium in ZnSe are relatively small compared to those by iron and nickel.

In ZnSe and ZnS the energy transfer from DAP to Fe (Cr) resulting in intra-shell excitation of the TM ion was rather inefficient. A different situation occurs for crystals heavily doped with manganese ions. ODMR and PL excitation (PLE) experiments performed on $\text{Zn}_{0.8}\text{Mn}_{0.2}\text{S}$ indicate an efficient energy transfer link between DAPs and Mn ions. This energy transfer is a spin dependent process in a magnetic field, less effective in a singlet state of the donor-acceptor pair state, but very effective in a triplet state when the radiative recombination is forbidden and transfer to Mn is allowed by spin selection rules.

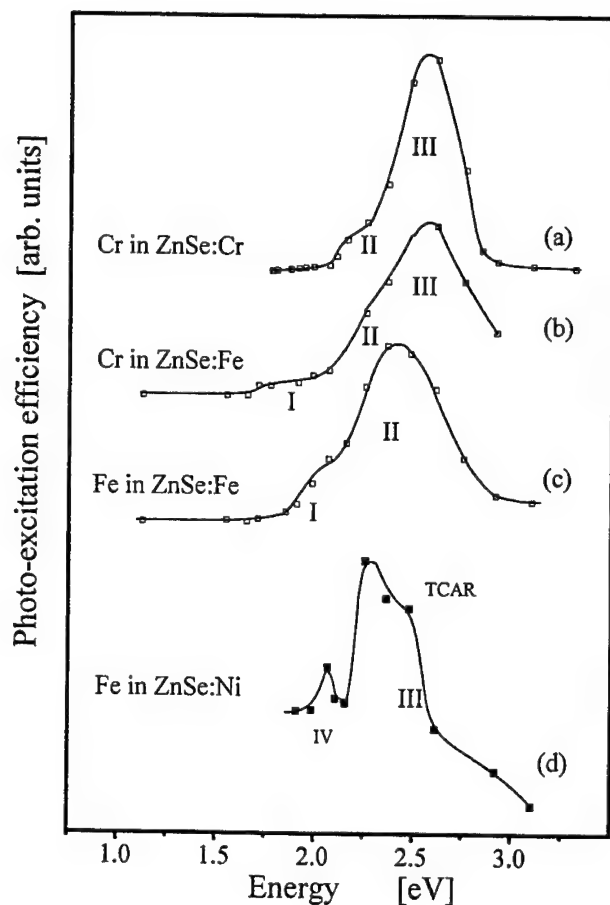


FIGURE 2 Photo-excitation spectra of the Cr^+ (a,b) and Fe^{3+} (c,d) ESR signals in (a) ZnSe:Cr, (b,c) ZnSe:Fe, and (d) ZnSe:Ni.

The present ESR and ODMR investigations do not show formation of the TM complexes with a component of the DA pair. The Fe-Cu pairs detected in ESR and ODMR investigations of ZnS ,^{3,5} were not observed in the case of ZnSe.

Concluding, the present results indicate the deactivation of DAP visible PL in ZnSe by Ni, Fe and Cr. The dominant process is bypassing with the three center Auger transition being also effective. In the case of ZnMnS Mn deactivates DAP transitions by the DAP to Mn energy transfer process.

This work was supported by KBN grants no. 2 0469 91 01 and 2 0476 91 01.

REFERENCES

1. M. Tabei, S. Shionoya, and H. Ohmatsu, *Jpn. J. Appl. Phys.* **14**, 240 (1976).
2. M. Godlewski and A. Zakrzewski, in *II-VI Semiconductor Compounds*, ed. M. Jain (World Scientific, Singapore, 1993), p. 205.

3. M. Godlewski and M. Skowróński, *Phys. Rev.* **B32**, 4007 (1985).
4. A. Zakrzewski and M. Godlewski, *Phys. Rev.* **B34**, 8993 (1986).
5. M. Godlewski, W. E. Lamb, and B. C. Cavenett, *J. Phys.* **C15**, 3925 (1982).
6. M. Godlewski and M. Kamińska, *J. Phys.* **C13**, 6537 (1980).
7. G. Roussos, J. Nagel, and H. -J Schulz, *Z. Phys. B-Condensed Matter* **53**, 95 (1983).

UPCONVERSION LUMINESCENCE PROPERTIES OF Er^{3+} IONS DOPED IN LITHIUM NIOBATE SINGLE CRYSTALS.

H. J. SEO,* T. P. J. HAN, G. D. McCLURE and B. HENDERSON

Department of Physics and Applied Physics, University of Strathclyde, Glasgow G1 1XN, Scotland.

Laser selective excitation is used to study the spectroscopic properties of Er^{3+} ions doped in Lithium Niobate (LNB) single crystals, where it substitutes for the Li^+ or Nb^{5+} sites both having local C_3 symmetry. Excited state absorption resulting in energy upconverted fluorescence are observed (for dopant concentrations range 0.045 to 0.37 mol.%) for temperatures up to 297 K. The upconversion mechanism is dominated by the sequential two photon excitation process. The polarised excitation and emission spectra of the upconverted fluorescence reveal the existence of multiple sites and inhomogeneously broadened energy levels as a consequence of the disordered structure of the LNB lattice.

Key words: Er, LiNbO_3 , upconversion.

1 INTRODUCTION

Lithium niobate, LiNbO_3 (LNB), doped with various admixtures of impurity ions is of great interest on account of the possibility of combining the acousto-optical, electro-optical and non-linear optical properties of the matrix with good luminescence characteristics of the active ions. The aim of this study is to investigate the energy upconverted fluorescence properties of Er^{3+} doped LiNbO_3 by site selective laser spectroscopy.

2 OPTICAL PROPERTIES

Optical absorption and laser spectroscopy have been used to investigate LiNbO_3 crystals doped with Er^{3+} ions. Near-infrared fluorescence from the higher energy, $^4\text{I}_{9/2, 11/2, 13/2}$, multiplets reveals the inhomogeneous nature of this crystal system and the presence of two dominant Er^{3+} sites¹, site 'a' and 'b', within the concentrations limit studied (0.045 to 0.37 mol.% in the melt). Absorption from excited states can be significant in Er ions doped materials. Such a process usually involves an intermediate metastable level with relatively long fluorescence decaytime. It is noted that the probability of energy upconversion process via excited state absorption, ESA, is proportional to the fluorescence decaytime of the intermediate state and dependent on the energy match among the multiplets involved. This paper presents the spectroscopic results of the energy upconverted fluorescence studies of Er ions doped in LiNbO_3 crystals. The temperature, excitation and emission wavelength dependent are analysed and the possible mechanisms of the upconversion process are discussed.

Excited state absorption processes with excitation wavelengths into the $^4\text{I}_{9/2}$ multiplet of the Er^{3+} ions are observed at temperatures from 12 K to 297 K. Figure 1 shows the room temperature upconverted fluorescence spectra under excitation into the $^4\text{I}_{9/2}$

* Permanent address: Department of Natural Sciences, Pusan National University of Technology, Pusan 608–739, Korea.

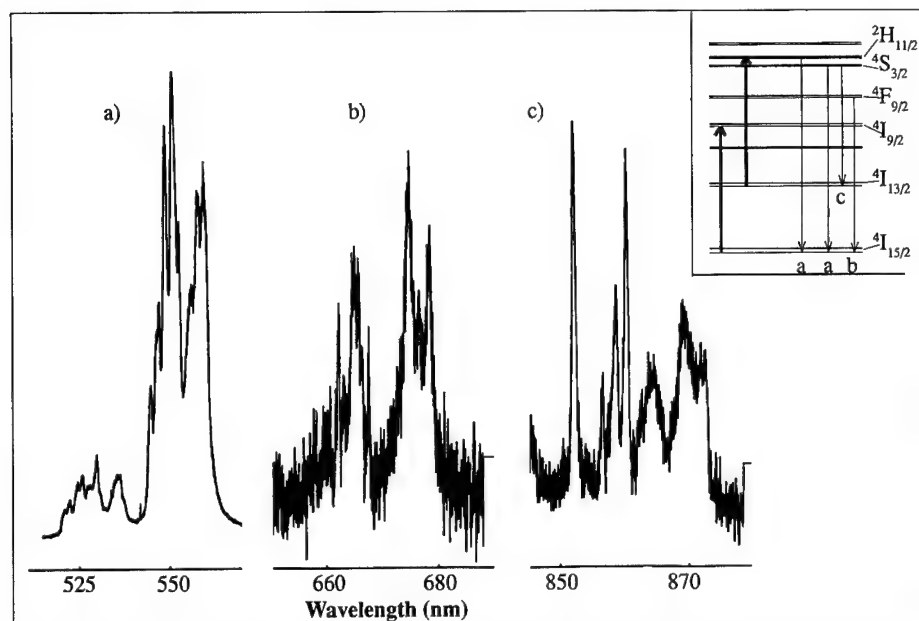


FIGURE 1 Room temperature upconverted fluorescence spectra of the : a) ${}^2\text{H}_{11/2}, {}^4\text{S}_{3/2} \rightarrow {}^4\text{I}_{15/2}$; b) ${}^4\text{F}_{9/2} \rightarrow {}^4\text{I}_{15/2}$; c) ${}^4\text{S}_{3/2} \rightarrow {}^4\text{I}_{13/2}$ transitions.

multiplet. The various transitions involved are indicated in the inset of Figure 1 which also shows the ${}^4\text{I}_{13/2}$ multiplet, with a decaytime of 7.4 ms at room temperature², is involved as the metastable state. The strongest upconverted fluorescence corresponds to the ${}^4\text{S}_{3/2} \rightarrow {}^4\text{I}_{15/2}$ transition. Upconverted fluorescence from the ${}^2\text{H}_{11/2}$ multiplet is only observed at high temperatures as a result of thermal population from the ${}^4\text{S}_{3/2}$ multiplet. This can be shown by plotting the ratio of the integrated fluorescence intensity from the ${}^4\text{S}_{3/2}$ and ${}^2\text{H}_{11/2}$ multiplets to the ground state as a function of inverse temperature. The linear dependency confirmed the Boltzman thermal distribution relationship between these two multiplets and gives an energy separation of 534 cm^{-1} which is in good agreement with the 600 cm^{-1} obtained from absorption data.

The upconverted fluorescence intensity (I) as a function of excitation power (P) is given by the relation $I \propto P^n$, where n is equal to 2. This quadratic dependency indicates the upconversion mechanism involves two photons. Many mechanisms have been proposed to explain the different types of upconversion fluorescence behaviour observed for rare-earth ions in various host materials³. The two processes most commonly invoked for the energy upconversion are the sequential two photon excitation process (STEP) and the energy transfer upconversion process (ETU). Each of these processes requires two incident photons; the first process involves a single ion while the 2nd requires two or more ions. Recent results from lattice site determination of impurity ions in LiNbO_3 by ion beam method⁴ suggest that rare-earth ions have a tendency to favour the Li^+ ion site over the Nb^{5+} ion site. This coupled with the low concentrations of Er^{3+} ions used in this study and the energy match of the two transitions involved; ground state absorption (GSA), ${}^4\text{I}_{15/2} \rightarrow {}^4\text{I}_{9/2}$, and ESA, ${}^4\text{I}_{13/2} \rightarrow {}^2\text{H}_{11/2}$, strongly supports the STEP process as the dominant upconversion mechanism although one cannot discount possible ETU contribution especially at high dopant concentrations. Figure 2 shows the upconverted

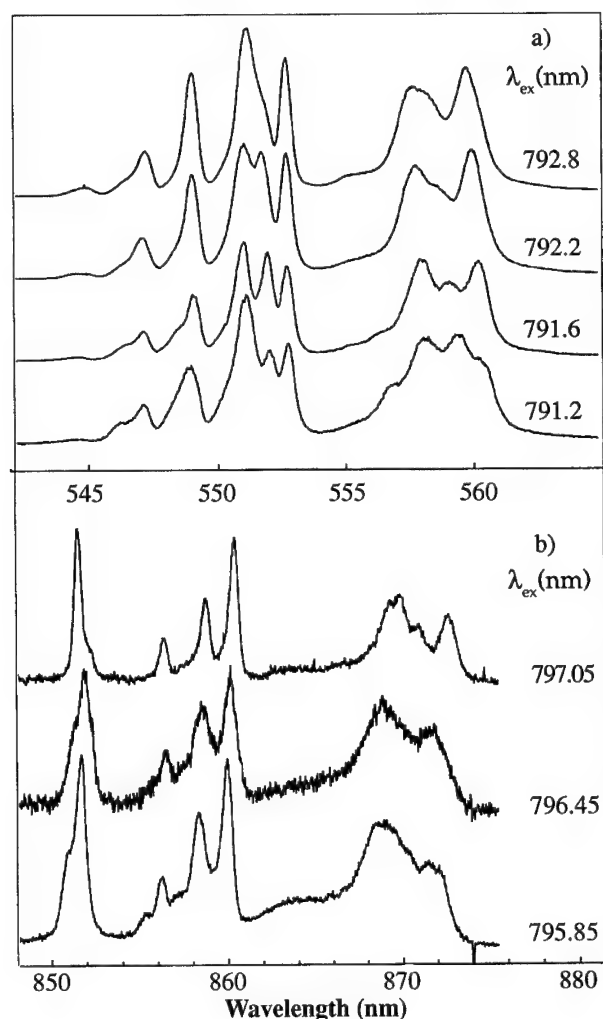


FIGURE 2 Low temperature (12 K) upconverted fluorescence spectra of the a) $^4S_{3/2} \rightarrow ^4I_{15/2}$ and b) $^4S_{3/2} \rightarrow ^4I_{13/2}$ transitions as a function of excitation wavelengths across the inhomogeneously broadened lines (B₁ and B₂) of the $^4I_{9/2}$ multiplet.

fluorescence of the $^4S_{3/2} \rightarrow ^4I_{15/2}$ and $^4I_{13/2}$ transitions at various excitation wavelengths across the inhomogeneously broadened absorption lines (B₁ and B₂) of the $^4I_{9/2}$ multiplet. The observed fluorescence patterns show no resemblance of those of the sites 'a' and 'b' and the emission lines are relatively broad. The position and relative intensity of some of the peaks changes as the excitation wavelength changes. Polarised excitation spectra of the 551 nm and 552 nm emission lines, as shown in Figure 3, reveals that they are originated from different Er³⁺ centres and the greater than expected number of peaks verified the existence of multiple sites. These observations may be explain in terms of the inhomogeneity of this crystal system and that the upconverted fluorescence is the product

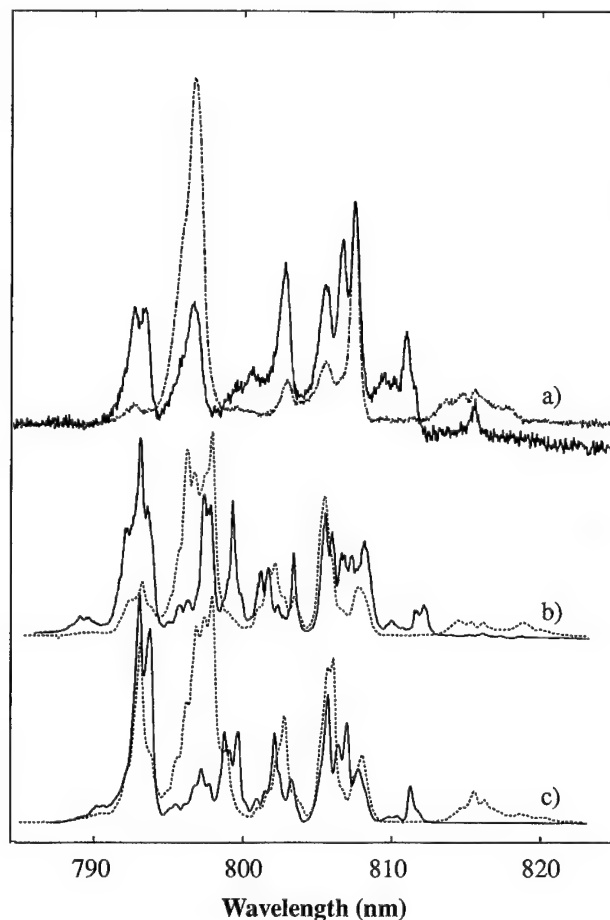


FIGURE 3 Polarised spectra of the ${}^4I_{9/2}$ multiplet: a) absorption spectrum from the, ${}^4I_{15/2}$, ground state at 77 K; b) 12 K excitation spectrum of the 552.0 nm fluorescence line; c) 12 K excitation spectrum of the 551 nm fluorescence line. Dashed line is π -polarised (the E vector is parallel to the c-axis) and the solid line is σ -polarised (the E vector is perpendicular to the c-axis).

of GSA and ESA. The latter contributes to the observed complicated excitation spectra and the additional fine structures as compared to the corresponding absorption spectrum. The energy mismatch between the GSA and ESA transitions is ca. 40 cm^{-1} , as compared to 138 cm^{-1} reported by Gabrielyan *et al.*⁵ due to their mis-assignment of one of the energy levels of the ${}^2H_{11/2}$ multiplet, is very small and can easily be bridged by thermal phonons, for temperatures greater than 20 K, to enable energy upconversion via STEP without invoking ETU processes.

ACKNOWLEDGEMENT

This research is supported by a research grant from EPSRC, UK. One of the authors, HJS, wishes to thank BSRI programme (project #BSRI-94-2411), Korea for support.

REFERENCES

1. H. J. Seo, T. P. J. Han, G. D. McClure, B. Henderson to be published.
2. V. G. Babadzhanyan, S. Georgescu, C. Ionescu, R. B. Kostanyan, V. Lupei, T. V. Sanamyan, V. R. Nikogosyan, *Sov. J. Contemp. Phys. (USA)* **25**(6), 46 (1990).
3. J. C. Wright, *Radiationless Processes in molecules and Condensed Phases*, Topics in Applied Physics, vol. 15. Ed. F. K. Fong.
4. L. Rebouta, M. F. daSilva, J. C. Soares, J. A. Sanz-García, E. Dieguez, F. Agulló-López, *Nuclear Instruments and Methods in Physics Research* **B64**, 189 (1992).
5. V. T. Gabrielyan, A. A. Kaminskii, L. Li. *Phys. Stat. Sol. A* **3**, K37 (1970).

EPR AND OPTICAL SPECTROSCOPY OF Cr^{3+} DOPED CaYAlO_4

M. YAMAGA, H. TAKEUCHI,¹ K. HOLLIDAY,² P. MACFARLANE,²
B. HENDERSON,² Y. INOUE,³ and N. KODAMA,³

Department of Physics, Faculty of General Education, Gifu University, Gifu 501–11, Japan; ¹*Department of Information Electronics, Nagoya University, Nagoya 464–01, Japan;* ²*Department of Physics and Applied Physics, University of Strathclyde, Glasgow G4 0NG, UK;* ³*Tosoh Corporation, Hayakawa, Ayase 252, Japan*

EPR and optical measurements have been carried out on Cr^{3+} doped CaYAlO_4 at 1.6 K, 16 K and 300 K. Q-band measurements revealed a strong, asymmetric EPR line close to $g \approx 2$ for B/c, together with three weak fine-structure lines corresponding to tetragonal symmetry. The R_1 line of Cr^{3+} has an inhomogeneous broadened linewidth of about 100 cm^{-1} at 16 K but a homogeneous width of less than 10 cm^{-1} , the measurement of which was monochromator slit width limited. The large inhomogeneous broadening of the optical and EPR spectra are attributed to the compositional disorder of Ca^{2+} and Y^{3+} in the host lattice.

Key words: transition metal ion, EPR, compositional disorder, fluorescence line narrowing.

Cr^{3+} ions prefer to occupy sites of approximately octahedral symmetry in inorganic crystals and glasses. The microstructure of glasses produces a continuous distribution of the strength of the crystal field experienced by Cr^{3+} ions.¹ Deviation from the stoichiometric composition in perfect crystals may produce several distinct crystal field sites.² Disorder in the oxide perovskite crystal CaYAlO_4 with the space group $I4/mmm$ (D_{4h}^{17}) is produced by the random distribution of Ca^{2+} and Y^{3+} ions on their respective sublattices while keeping the composition ratio of 1:1.

CaYAlO_4 crystals containing 0.1 at. % Cr^{3+} ions were grown in an inert atmosphere by the Czochralski technique. Cr^{3+} ions which preferentially occupy octahedral Al^{3+} sites, act as a probe of the compositional (or substitutional) disorder. EPR measurements of Cr^{3+} were carried out using a Q-band spectrometer ($\nu \approx 34 \text{ GHz}$) with 100 kHz-field modulation at 300 K and 1.6 K. Fluorescence was excited using either an Ar^+ ion laser operating on all lines, or a single mode Ti:sapphire ring laser at temperatures at 16 K and 300 K.

Figure 1 shows an intense asymmetric EPR line at 1.225 T of width 10 mT at room temperature. The angular variation of the weak fine-structure line, observed on both sides of the central feature, indicates a Cr^{3+} center with almost tetragonal symmetry about the c axis. The spin Hamiltonian parameters are estimated to be $g_{\parallel} \approx g_{\perp} \approx 1.983$ and $|D| \approx 85 \times 10^{-4}$. At 1.6 K, the intense asymmetric line at 1.24 T, two more spread fine-structure lines, and the forbidden transitions ($\Delta M = 3, 2$) close to 0.35 T and 0.7 T were observed. The angular variation of these signals suggests that the intense asymmetry EPR line and the weak lines with fine structure are due to Cr^{3+} in low symmetry with $|D| \approx 1500 \times 10^{-4}$ and $|D| \approx (550 \text{ and } 1000) \times 10^{-4} \text{ cm}^{-1}$, respectively.

The room temperature absorption spectrum of Cr^{3+} consists of two bands with peaks at 368 nm and 566 nm, assigned to be $^4A_2 \rightarrow ^4T_1$ and $^4A_2 \rightarrow ^4T_2$ transitions, respectively. The fluorescence excited by a multiline Ar^+ ion laser consists of Cr^{3+} R-lines and accompanying phonon side bands at all temperatures investigated. Figure 2 (a) shows the R_1 line with the linewidth (FWHM) of $\sim 100 \text{ cm}^{-1}$ at 16 K. Fluorescence line narrowing (FLN) can resolve the homogeneous width of the R-line. Excitation and detection of

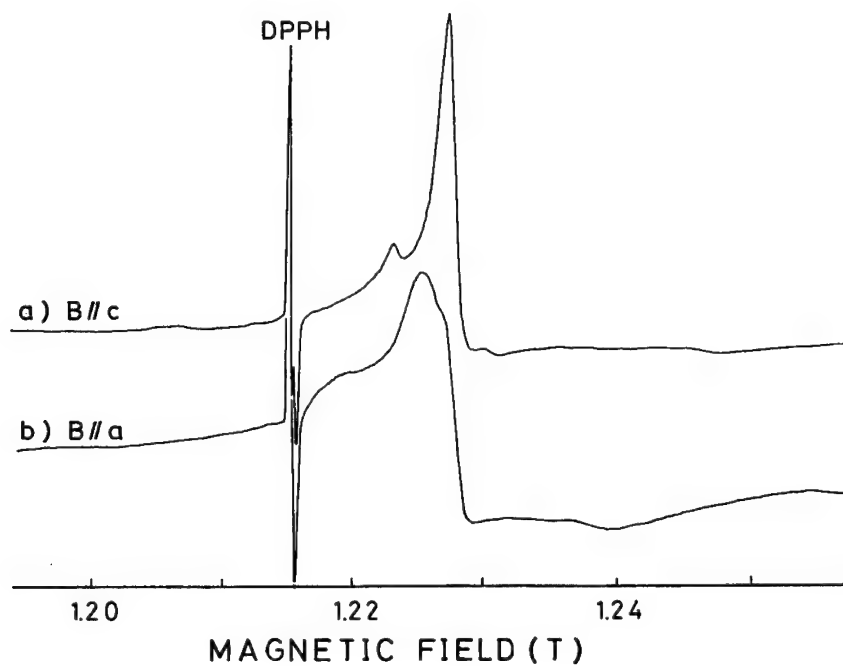


FIGURE 1 Q-band EPR spectra of Cr^{3+} doped CaYAIO_4 at 300 K.

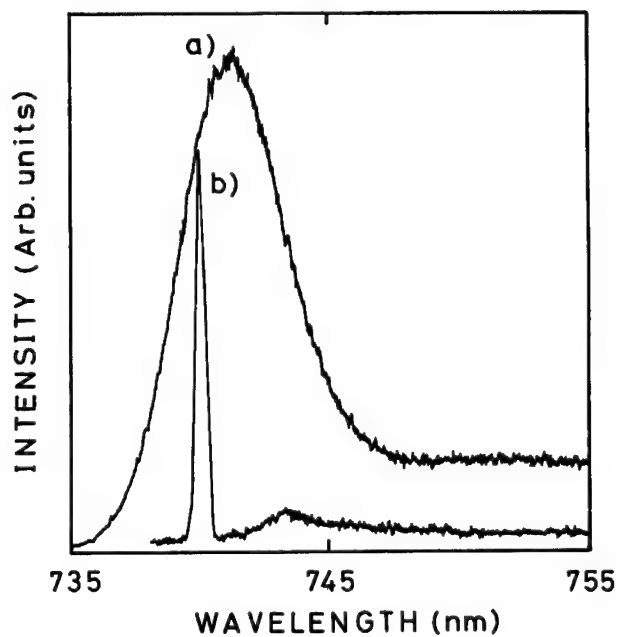


FIGURE 2 (a) The R_1 line of Cr^{3+} doped CaYAIO_4 excited with all lines of an Ar^+ ion laser. (b) The FLN line excited at 740 nm of a Ti:sapphire laser at 16 K.

fluorescence resonant with the R_1 line at 740 nm reveal the FWHM value of the homogeneous linewidth at 16 K to be less than 10 cm^{-1} (Fig. 2(b)). This measurement is limited by the resolution of the monochromator. However, the narrowed fluorescence does not start to broaden beyond the slit width resolution until the sample has been heated to a temperature 100 K. This is contrary to the behaviour observed in Cr^{3+} doped materials such as Al_2O_3 (Ruby) where homogeneous broadening dominates the R-line width at temperatures of 60 K and above.³ The additional source of inhomogeneous broadening in CaYAlO_4 is produced by the random distribution of Ca^{2+} and Y^{3+} ions that leads to a series of slightly different crystal field for the Al^{3+} ions and, consequently, for the Cr^{3+} optically active ions. This compositional disorder is also the cause of the broadening of the EPR lines.

One of the authors (M. Yamaga) is indebted to the University of Strathclyde, the British Council and the Daiwa Anglo-Japanese foundation for financial support of this collaborative research.

REFERENCES

1. B. Henderson, M. Yamaga, Y. Gao and K. P. O'Donnell, *Phys. Rev.* **46** 652 (1992).
2. A. Marshall, K. P. O'Donnell, M. Yamaga, B. Henderson and B. Cockayne, *Appl. Phys.* **A50**, 565 (1990).
3. D. E. McCumber and M. D. Sturge, *J. Appl. Phys.* **34** 1682 (1963).

OPTICAL PROPERTIES OF Cr^{3+} -IONS IN $\text{LaSr}_2\text{Ga}_{11}\text{O}_{20}$

A. LUCI, M. CASALBONI,[†] T. CASTRIGNANÒ, U. M. GRASSANO
and A. A. KAMINSKII[‡]

*Dipartimento di Fisica, Università di Roma Tor Vergata, Via della Ricerca Scientifica, 1,
00133 Roma, Italy;* [‡]*Institute of Crystallography-Russian Academy of Sciences, Moscow-
Russia*

The optical properties of Cr^{3+} ions in the disordered $\text{LaSr}_2\text{Ga}_{11}\text{O}_{20}$ crystal have been investigated through absorption, emission, excitation spectra. Polarized excitation measurements allows us to evaluate the crystal field parameters and to infer the distortion of the octahedral site of Cr^{3+} . In spite of the relatively low value of the crystal field ($Dq/B = 2.26$) obtained from optical data, the emission spectra are constituted by two narrow lines. This behavior, typical of strong field material, is explained by an even lower value of the crystal field corresponding to the ${}^2\text{E}_g$, ${}^4\text{T}_2$ crossing point obtained by means of the Tanabe-Sugano diagram. The value of the splitting and the width of the emission lines, intermediate between crystals and glasses, confirm the disordered structure of this crystal.

Key words: Spectroscopy Cr^{3+} Disordered crystals.

1 INTRODUCTION

Cr^{3+} ion is the active center in several solid state lasers. Crystals or glasses can be doped with Cr^{3+} ion impurities and, depending upon the influence of neighboring atoms, the ion can experience different crystal fields: its emission properties can be very different ranging from narrow line to broad band emission.¹

More recently several investigations have been focused on the properties of doped disordered crystals that represent an intermediate step between crystal and glasses.² In these crystals equivalent crystallographic sites are occupied by different cations of the host crystal with statistical distribution. The crystal field acting on the impurity ion is thus different from site to site, due to the so called *static structural disorder*. The optical properties of the impurity ions in these materials become more similar to those of doped glasses.

In this work we present the first investigation on Cr^{3+} doped $\text{LaSr}_2\text{Ga}_{11}\text{O}_{20}$. From the excitation and the emission spectra it has been possible to construct the Tanabe-Sugano diagram and to derive the crystal field for the Cr^{3+} ion in this crystal.³

2 EXPERIMENTAL

The $\text{LaSr}_2\text{Ga}_{11}\text{O}_{20}$: Cr^{3+} crystals were grown at the Institute of Crystallography of Moscow. The samples studied have a Cr^{3+} concentration of about 0.3% with respect to the structural Ga^{3+} . $\text{LaSr}_2\text{Ga}_{11}\text{O}_{20}$ is a monoclinic insulating crystals (space group C_{2h}^3) with a disordered structure due to the statistical occupation by Sr^{2+} or La^{3+} of a particular lattice site (a seven vertex polyhedron). The Cr^{3+} ion replaces the Ga^{3+} ion in octahedral sites, surrounded by six O^{2-} ions, but experiences also the disordered crystalline field produced by the neighbors ions of the second coordination shell.² Because the absorption spectrum

[†]Permanent address: Dip. Matematica e Fisica-Università di Camerino, Via Madonna delle Carceri, 62032 Camerino-Italy

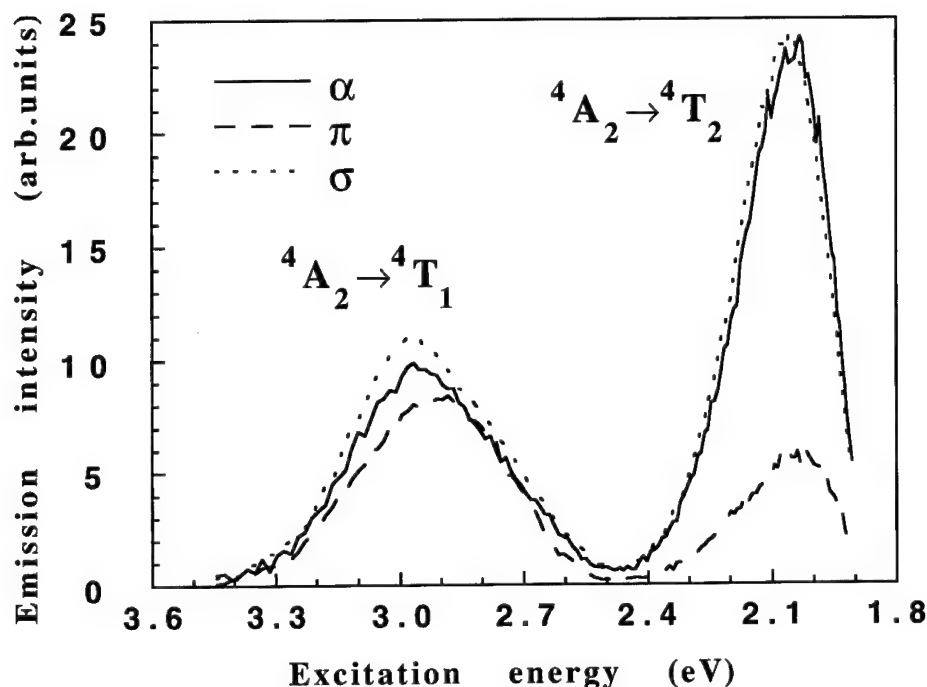


FIGURE 1 Excitation spectra at $T = 77$ K for three different direction of the electric field and propagation vectors of the light with respect to the crystal c -axis.

contains bands not due to Cr^{3+} or at least not related to the optical cycle of the Cr^{3+} ion, we report in Figure 1 the excitation spectrum of the Cr^{3+} emission around 700 nm. The three curves refer to different directions of the electric field and propagation vectors of the light with respect to the crystal c -axis. The so called σ and α spectra are similar and both are different from the π spectrum indicating electric dipole transition.³ In Figure 2 the emission bands, clearly broadened in the disordered crystal, are plotted for different temperatures. At low temperature only one band is visible (peak at 1.775 eV); on increasing temperature two emissions (at 1.775 and 1.790 eV) are present, but above 250 K their intensity decreases and almost vanishes around room temperature.

3 DISCUSSION

The values of the local field parameter Dq and of the Racah coefficients B and C can be derived from the energies of absorption and emission bands that, in octahedral (or nearly octahedral) symmetry, can be assigned to the following transitions:

${}^4\text{A}_2 \rightarrow {}^4\text{T}_2$	absorption	2.06 eV
${}^4\text{A}_2 \rightarrow {}^4\text{T}_1$	absorption	2.94 eV
${}^2\text{E} \rightarrow {}^4\text{A}_2$	emission R_1	1.775 eV
${}^2\text{E} \rightarrow {}^4\text{A}_2$	emission R_2	1.790 eV

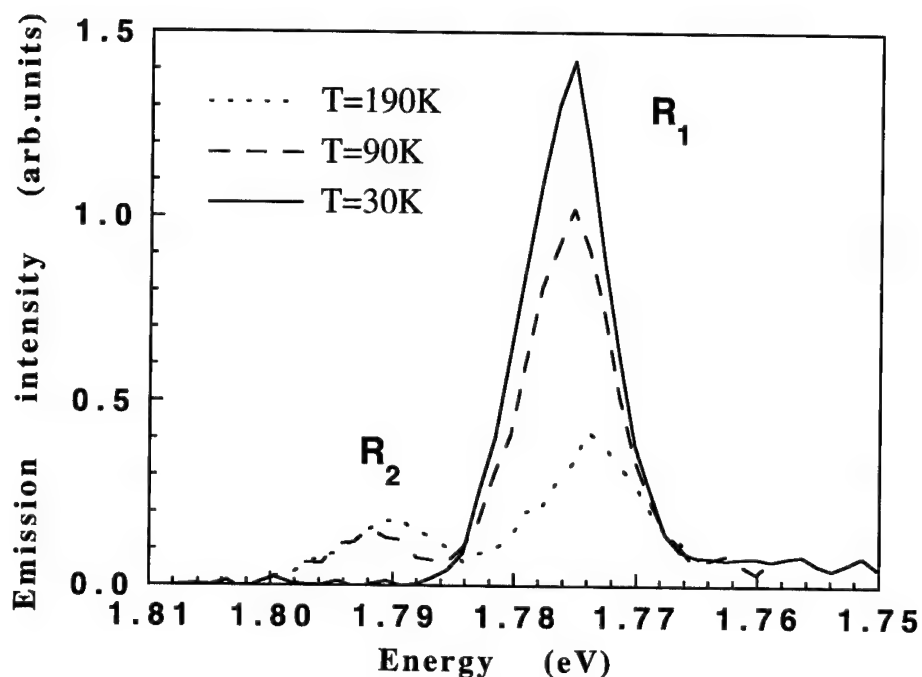


FIGURE 2 Emission spectra for different temperatures.

From easy calculations^{4,5} one obtains the parameters Dq , B and C reported in Table I together with those of few ordered crystals and glasses.

The Tanabe-Sugano diagram calculated from the above obtained values ($C/B = 4.2$) is shown in Figure 3. The arrow indicates the Cr^{3+} ion crystal field $Dq/B = 2.26$. This value is clearly larger than that of the crossing between the 2E and 4T_2 levels, $(Dq/B)_{\text{crossing}} = 1.9$, and this justifies the observed narrow emission lines.

The presence of the two lines (R_1 and R_2) indicates the existence of a tetragonal distortion of the octahedral oxygen cage around Cr^{3+} confirmed by the slight difference in the excitation peaks of the ${}^4A_2 \rightarrow {}^4T_2$ and ${}^4A_2 \rightarrow {}^4T_1$ transitions, measured with the different polarization. Similar results were observed in $\text{La}_3\text{Ga}_5\text{SiO}_{14}$. The parameters of the disordered crystals (Table I) and in particular those of the $\text{LaSr}_2\text{Ga}_{11}\text{O}_{20}$ are closer to those

Table I
Racah parameters and value of crystal field in crystals, disordered crystals and glasses.

	Dq/B	B (cm^{-1})	C (cm^{-1})	[ref.]
$\text{Y}_3\text{Sc}_2\text{Ga}_3\text{O}_{12}$	2.56	630	3248	[1]
$\text{Gd}_3\text{Ga}_5\text{O}_{12}$	2.55	626	3232	[1]
$\text{La}_3\text{Ga}_5\text{SiO}_{14}$	2.50	640	3240	[5]
$\text{LaSr}_2\text{Ga}_{11}\text{O}_{20}$	2.26	734	3060	[*]
Potassium Borate glass	2.25	710	3115	[6]
Silicate glass	2.15	740	3076	[4]

* present work

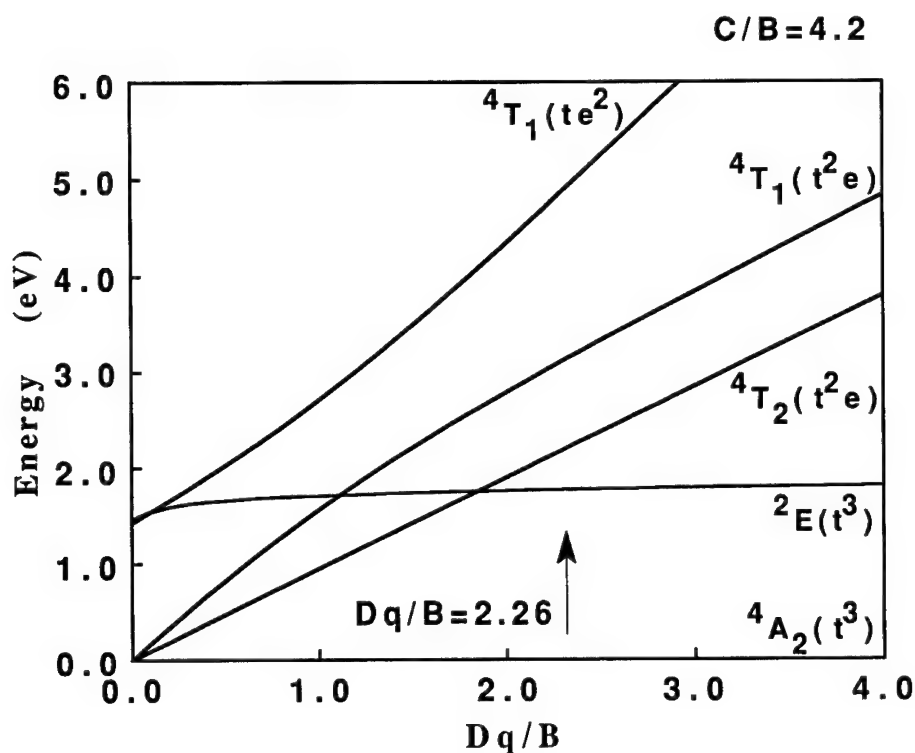


FIGURE 3 Tanabe-Sugano diagram for Cr^{3+} ion in octahedral crystals field calculated for the $\text{LaSr}_2\text{Ga}_{11}\text{O}_{20}$ crystal. The arrow indicates the value of $Dq/B = 2.26$.

of glasses than of other garnets and indeed the halfwidth of the R_1 lines is $\sim 70 \text{ cm}^{-1}$, i.e. much larger than the $\sim 10 \text{ cm}^{-1}$ R lines in $\text{Gd}_3\text{Ga}_5\text{O}_{12}$. This broadening of the line in disordered crystal is almost entirely structural, being independent upon the temperature.

The main, and not small shortcoming, from the point of view of laser operation is the presence of nonradiative deexcitation channels that strongly reduce the emission at room temperature. More complete description of this system derived from the polarized spectra and from the temperature dependence of lifetime emission and quantum yields, will be reported elsewhere.

BIBLIOGRAPHY

1. B. Struve and G. Huber, *Appl. Phys.* **B36**, 195 (1985).
2. A. A. Kaminskii in: *Disordered Solids: Structures and Processes*, ed. B. di Bartolo (Plenum Press, New York, 1989) p. 343.
3. D. S. McClure in: *Solid State Physics*, eds. F. Seitz and D. Turnbull (Academic Press, New York, 1959) Vol. 9, p. 399.
4. F. Rasheed, N. P. O'Donnell, B. Henderson and D. B. Hollis, *J. Phys.: Condens. Matter* **3**, 1915 (1991).
5. M. Casalboni, A. Luci, U. M. Grassano, A. A. Kaminskii, B. V. Mill, *Phys. Rev.* **B49**, 3781 (1994).
6. F. Rasheed, N. P. O'Donnell, B. Henderson and D. B. Hollis, *J. Phys.: Condens. Matter* **3**, 3825 (1991).

NONLINEAR TRANSMISSION IN Cr^{4+} -DOPED SILICATES

V. P. MIKHAILOV, N. I. ZHAVORONKOV, N. V. KULESHOV, A. S. AVTUKH,
V. G. SHCHERBITSKY and B. I. MINKOV*

*International Laser Center, Belarus State University, Minsk 220064, Belarus; *Institute
for Single Crystals, Ukraine Academy of Sciences, Kharkov 310141, Ukraine*

The results of absorption saturation measurements in the visible on chromium doped Y_2SiO_5 , Gd_2SiO_5 and Mg_2SiO_4 crystals are reported. The cross sections for ground state and excited state absorption of Cr^{4+} ion in distorted tetrahedral sites are estimated at 694 nm. Saturable absorber Q-switching of ruby laser using Cr-doped Y_2SiO_5 and Mg_2SiO_4 is described.

1 INTRODUCTION

Tetravalent chromium doped crystals, such as garnets and forsterite, were reported to exhibit saturation of absorption in the near infrared at about $1\text{ }\mu\text{m}$.^{1–6} Absorption cross section was measured for the $^3\text{A}_2 - ^3\text{T}_2$ transition (in T_d approximation) of the Cr^{4+} ion at $1.06\text{ }\mu\text{m}$ wavelength of Nd-YAG laser and was estimated to be $2-5 \times 10^{-18}\text{ cm}^{-1}$ in different hosts. Passive Q-switching and mode-locking in Nd-YAG laser were demonstrated using these materials as saturable absorbers. Moreover, another d^2 -ion—trivalent vanadium was shown to exhibit saturable absorption in the NIR both for the $^3\text{A}_2 - ^3\text{T}_2$ and $^3\text{A}_2 - ^3\text{T}_1$ (^3F) transitions.⁷

In this paper we report on the measurements of saturation of red absorption in a number of Cr^{4+} -doped silicates, namely, Y_2SiO_5 , Gd_2SiO_5 and forsterite. Q-switched operation of ruby laser is demonstrated using Cr-doped silicates as intracavity saturable absorbers.

2 EXPERIMENTAL PROCEDURES

High quality Cr-doped Y_2SiO_5 , Gd_2SiO_5 , and Mg_2SiO_4 single crystals were grown by the Czochralski technique. The Cr-concentration in the raw materials was varied from 0.2 to 2.0 wt %. The polished samples were 15–20 mm in diameter and 3–10 mm in thickness.

Absorption saturation measurements were performed using Q-switched ruby laser with a 100 ns pulse width at 694 nm. The energy of laser pulses was measured with a FNM-2 nanosecond laser photometer calibrated to the absolute energy. The average was taken over 100 laser shots for every experimental point of transmission to enhance the signal-to-noise ratio. The beam area was determined using an optical multichannel analyser with a CCD-system. Systematic errors are estimated as $\pm 30\%$ for the energy fluence measurements.

3 EXPERIMENTAL RESULTS AND DISCUSSION

3.1 Cr^{4+} -doped Y_2SiO_5

The polarized absorption spectra of Cr:YSO were described in refs^{8–10}. The dominant strong absorption bands at $16\,700\text{ cm}^{-1}$ and $14\,000\text{ cm}^{-1}$ and weak absorption at about

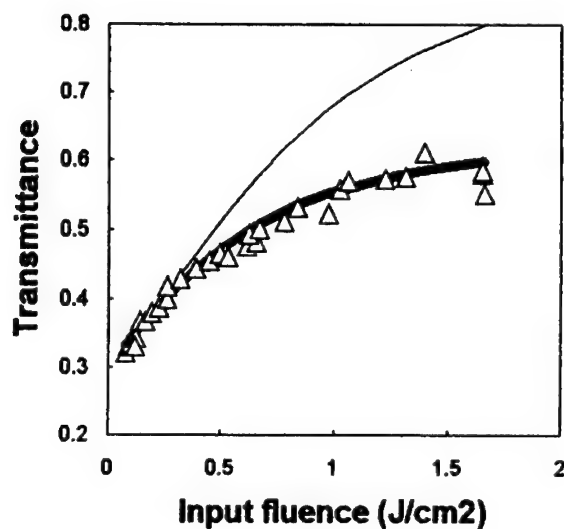


FIGURE 1 Energy transmission of ruby laser pulses through Cr:YSO versus energy fluence. The theoretical curves calculated from Frantz-Nodvik formula (thin line) and from equations (1-5) (thick line) are shown.

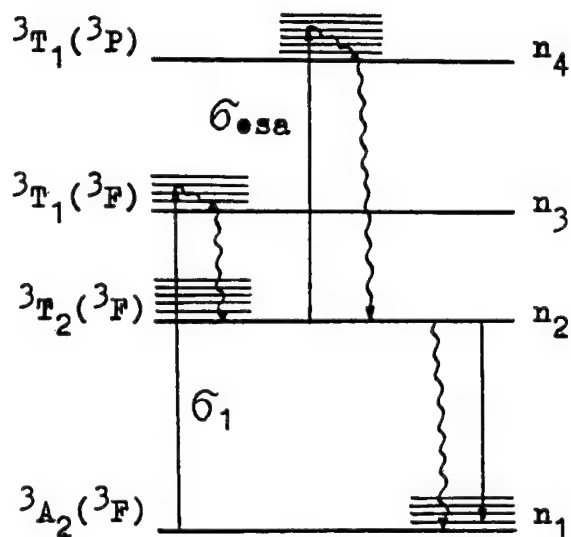


FIGURE 2 Simplified energy-level scheme for Cr^{4+} ion in silicates.

$10\,000\text{ cm}^{-1}$ were assigned to transitions on the Cr^{4+} ions substituting for the Si ions in distorted tetrahedral sites. The weak absorption at about $10\,000\text{ cm}^{-1}$ was assigned to the ${}^3\text{A}_2-{}^3\text{T}_2$ transition, which is electric dipole forbidden in an undisturbed Td symmetry. The strong bands $16\,700$ and $14\,000\text{ cm}^{-1}$ are attributed to the ${}^3\text{A}_2-{}^3\text{T}_1$ (${}^3\text{F}$) transition

splitting due to distortion of the CrO₄⁴⁻ tetrahedron. The lifetime of the ³T₂(³F) excited state was estimated to be 0.65 μs at room temperature from emission decay measurements.

Absorption saturation measurements on Cr:YSO were performed at room temperature. The results for the energy transmission of 100 ns, 694 nm pulses of ruby laser through the sample of Cr:YSO (EIIa, kIIb) versus pump energy fluence is shown in Figure 1. In order to analyse the experimental results on saturation of absorption a simplified energy level diagram shown in Figure 2 was assumed. In this diagram the ¹E(¹D) excited level was assumed to be higher than the ³T₂(³F) level^{9,10} and it was not taken into further consideration. The excitation of the ³T₁(³F) state by the 694 nm laser pulse is followed by the vibrational relaxation intra this state and then nonradiative relaxation occurs to the ³T₂(³F) metastable level. The lifetime of the ³T₂(³F) metastable level is long compared with laser pulse duration. In order to estimate the ³T₁(³F) to ³T₂(³F) relaxation time, the risetime of the luminescence from the ³T₂(³F) level was measured after excitation of the ³T₁(³F) state by the 20 ps-width pulses of second harmonic of a Nd-YAlO₃ laser. This relaxation time was estimated to be less than 5 ns (the temporal response of registration system) at room temperature and at 77 K, that is much shorter compared with the 694 nm pulse duration. So, we attempted to use modified Frantz-Nodvik formula for a slow three-level absorber¹¹ for the analysis of nonlinear transmission data. But this formula exhibited a fairly good fit to the experimental points only at low energy fluences, while strong differences were observed at high fluences (Figure 5). An excited state absorption was assumed to be responsible for this discrepancy. An excited state absorption, to our mind, is associated with transitions from the ³T₂(³F) metastable level, since the relaxation rate from the directly excited ³T₁(³F) state is fast compared with pulse duration and the population of this state is negligible. According to the crystal field calculations the ³T₁(³P) state of the Cr⁴⁺ in YSO was found to be at about 24 000 cm⁻¹. Assuming that the splitting of this level due to symmetry distortion is similar to that of ³T₁(³F) level, we can predict that the ³T₂(³F)–³T₁(³P) transitions can be observed in the spectral range near 13 500–17 000 cm⁻¹. So, we tentatively assign ESA to these transitions (Figure 2). The saturation behaviour of absorber can be described by the following rate equations in which excited state absorption is taken into account:

$$dn_1/dt = -(\sigma_1/h\nu)I + n_2/\tau_{21} \quad (1)$$

$$dn_2/dt = (\sigma_1/h\nu)I - n_2/\tau_{21} \quad (2)$$

$$n_1 + n_2 = n_0 \quad (3)$$

$$dI/dz = -(\sigma_1 n_1 + \sigma_{ESA} n_2)I \quad (4)$$

where $I = I(r, t, z)$ is laser pulse intensity; r is the radial coordinate for the laser beam; z is the pathlength of laser beam in the crystal; n_1 , n_2 and n_0 are the population density of the ³A₂ and ³T₂(³F) states and the total population density, respectively. The nonradiative relaxation rate from the ³T₁(³P) excited state to the ³T₂(³F) metastable level was assumed to be much faster than the laser pulse width (similar to that from the ³T₁(³F) state, thus making the populations of the ³T₁(³P) state also negligible. The energy transmission of laser pulse through the absorber is given by:

$$T_E = \frac{\int_{-\infty}^{+\infty} dt \int_0^{+\infty} I(r, t, L) r dr}{\int_{-\infty}^{+\infty} dt \int_0^{+\infty} I(r, t, 0) r dr} \quad (5)$$

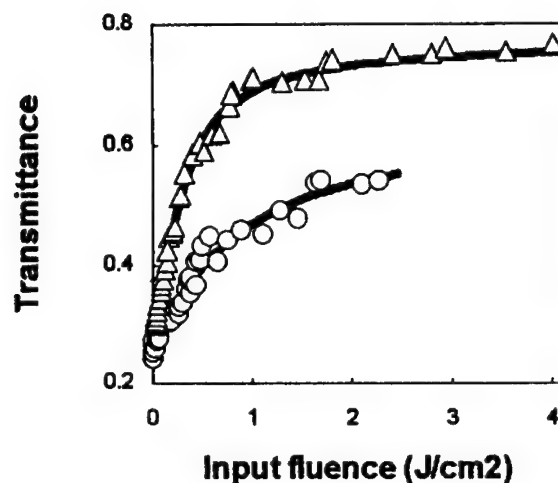


FIGURE 3 Energy transmission of ruby laser pulses through Cr:GSO (circles) and Cr-forsterite (triangles) versus pump energy fluence. The theoretical curves are shown by solid lines.

where L is the thickness of a crystal. The equations were solved numerically for gaussian pulse shape. From the best fit to experimental points (see Figure 1) the values of absorption cross sections were estimated to be $\sigma_1 = 2.1 \pm 0.65 \times 10^{-18} \text{ cm}^2$ and $\sigma_{\text{ESA}} = 7.0 \pm 2.1 \times 10^{-18} \text{ cm}^2$.

3.2 Cr^{4+} -doped Gd_2SiO_5

The strong broad bands at $18\,000 \text{ cm}^{-1}$ and $13\,000 \text{ cm}^{-1}$ and weak absorption at about $10\,500$ and $9\,000 \text{ cm}^{-1}$ are observed in absorption spectrum of this crystal. The strong absorption bands are attributed to the transitions from $^3\text{A}_2$ ground state to the orbital components of the splitted $^3\text{T}_1(^3\text{F})$ state. Weak absorption bands at $10\,500$ and $9\,000 \text{ cm}^{-1}$ are assigned to transitions on the $^3\text{T}_2(^3\text{F})$ level, which is also splitted due to symmetry distortion. The nonradiative relaxation time (which was dominant at temperatures above 150 K) of the $^3\text{T}_2(^3\text{F})$ level was estimated to be 15 ns at room temperature from fluorescence lifetime measurements.

Energy transmission of Q-switched ruby laser pulses throw the Cr:GSO versus input energy fluence is shown in Figure 3. The absorption recovery time of Cr:GSO at room temperature is determined by the lifetime of the $^3\text{T}_2(^3\text{F})$ excited state and much shorter than the pulse width of excitation. As in the case of Cr:YSO, the nonradiative relaxation rates from the $^3\text{T}_1(^3\text{F})$ and $^3\text{T}_1(^3\text{P})$ excited states to the $^3\text{T}_2(^3\text{F})$ metastable level were assumed to be much faster than any other rates. A best fit of the calculated from Equations (1)–(5) T_E values to the experimental results was obtained for the parameters $\sigma_1 = 6.7 \pm 2.0 \times 10^{-18} \text{ cm}^2$ and $\sigma_{\text{ESA}} = 1.9 \pm 0.6 \times 10^{-18} \text{ cm}^2$.

3.3 Cr-doped Mg_2SiO_4

The polarized absorption spectrum of Cr^{4+} -doped forsterite exhibits strong absorption at 694 nm for EIIb and EIIc orientations. The absorption bands at $9\,000$ – $11\,000 \text{ cm}^{-1}$ were assigned to the $^3\text{A}_2 - ^3\text{T}_2(^3\text{F})$ transition and the bands with peaks at $15\,100$ and

13 600 cm⁻¹ were assigned to orbital components of the ³A₂ – ³T₁(³F) transitions, splitted due to symmetry distortion.¹² The lifetime of luminescence from the ³T₂ level was estimated to be of about 3 μs at room temperature. The results for absorption saturation measurements on Cr:forsterite were very similar for both orientations and are shown in Figure 3. The results were analysed using model proposed in Figure 2 and Equations (1)–(5). The values for ground state and excited state absorption cross sections were estimated to be $\sigma_1 = 3.1 \pm 1.0 \times 10^{-18}$ cm² and $\sigma_{ESA} = 6.6 \pm 2.0 \times 10^{-19}$ cm², respectively. The absorption cross section of Cr⁴⁺:forsterite at 1.08 μm was estimated to be 2.3×10^{-18} cm².⁶ The measured value of σ_1 at 694 nm is approximately twice as small as predicted from results of measurements at 1.08 μm. But taking into account the possible systematic errors for measurements of energy fluence the agreement of results seems to be fair.

3.4 Ruby Laser Q-Switch Experiments

Chromium-doped silicates were tested as Q-switch saturable absorbers for ruby laser at 694 nm. The hemispherical laser cavity was formed by 1.0 m radius high reflector and 50% reflectivity flat output coupler. The laser rod was 10 mm in diameter and 120 mm in length. The polished samples of saturable absorber crystals were 2–10 mm in thickness and were not antireflection coated. In the free running operation (without saturable absorber Q-switch) laser pulses obtained were 0.5 J in energy and about 1 ms in duration. At the same pumping conditions single pulses of about 80–100 ns in duration and up to 240 mJ in energy were generated from Q-switched laser using intracavity Cr:forsterite and Cr:YSO saturable absorbers. The absorber was placed near output coupler. Low optical damage threshold of Cr:GSO has made impossible to use this crystal as a passive shutter.

4 CONCLUSION

The saturation of visible absorption in tetravalent chromium doped Y₂SiO₅, Gd₂SiO₅ and Mg₂SiO₄ is investigated. The strong evidence for excited state absorption at 694 nm was observed in these crystals. The ground state and excited state absorption cross sections at 694 nm are calculated from nonlinear transmission data. The excited state absorption is tentatively assigned to the ³T₂ – ³T₁(³P) transitions of tetrahedrally coordinated Cr⁴⁺ ion. Passive Q-switching in a ruby laser is demonstrated using Cr⁴⁺-doped Mg₂SiO₄ and Y₂SiO₅ as intracavity saturable absorbers.

REFERENCES

1. M. I. Demchuk, E. V. Zharikov, A. M. Zabaznov, I. A. Manichev, V. P. Mikhailov *et al.* *Kvant. Electron.* **14** (1987) 423.
2. M. I. Demchuk, N. V. Kuleshov, V. P. Mikhailov *et al.* *Zhurn. Prikl. Spectrosk. (USSR)* **51** (1989) 377.
3. D. M. Andrauskas and C. Kennedy, *OSA Proceedings on Advanced Solid-State Lasers*, edited by G. Dube and L. C. Chase (Optical Society of America, Washington, DC, 1991), vol. 10, p. 393.
4. H. Eilers, K. R. Hoffman, W. M. Dennis, S. M. Jacobsen, and W. M. Yen *Appl. Phys. Lett.* **61** (1992) 2958.
5. K. Spariosu, W. Chen, R. Stults, M. Birnbaum, A. V. Shestakov, *Opt. Letters*. **18** (1993) 814.
6. M. I. Demchuk, V. P. Mikhailov, N. I. Zhavoronkov, N. V. Kuleshov, P. V. Prokoshin, K. V. Yumashev, M. G. Livshits, and B. I. Minkov, *Optics Lett.* **17** (1992) 929.
7. V. P. Mikhailov, N. V. Kuleshov, N. I. Zhavoronkov, P. V. Prokoshin, K. V. Yumashev, V. A. Sandulenko, *Opt. Mater.* **2** (1993) 267.
8. C. Deca, M. Bass, B. H. T. Chai, and Y. Shimony, *J. Opt. Soc. Am. B*, **10** (1993) 1499.
9. U. Hommerich, H. Eilers, S. M. Jacobson, W. M. Yen, and W. Jia, *J. Lumin.* **55** (1993) 1499.

10. N. V. Kuleshov, V. P. Mikhailov, G. V. Shcherbitsky, B. I. Minkov, T. J. Glynn, R. Sherlock, *Opt. Mater.* (to be published).
11. V. Petricevic, S. K. Gayen, and R. R. Alfano, *Appl. Phys. Lett.* **53** (1988) 2590.

PHOTO-STIMULATED X-RAY LUMINESCENCE IN $\text{LiTaO}_3:\text{Tb}^{3+}$ BASED GREEN EMITTING PHOSPHORS

R. BRACCO, C. MAGRO and R. MORLOTTI

3M Italia Ricerche—Medical Imaging Systems Division, 17016 Ferrania (SV), Italia

$\text{LiTaO}_3:\text{Tb}^{3+}$ phosphors, prepared as crystalline powders, exhibit, at room temperature, strong green luminescence both during X-ray exposure (Direct Luminescence, DL) and subsequently, when stimulated in the 400–800 nm range (Photo-Stimulated Luminescence, PSL). Due to the high efficiency of the PSL, similar to that of the well-known UV-blue emitting $\text{BaFCl}_x\text{Br}_{1-x}:\text{Eu}^{2+}$ phosphors, the new storage phosphors based on $\text{LiTaO}_3:\text{Tb}^{3+}$ can find applications as X-ray sensors in Medical Digital Radiography and other radiation sensing fields.

Both the direct and photo-stimulated luminescence efficiencies depend on the Li/Ta ratio, on the Tb^{3+} ions concentration and on the presence of co-dopants like, as in this case, Mg^{2+} alkali earth ions. Mg^{2+} ions improve the D.L. and have also a positive effect on the P.S.L. up to a nominal concentration of 0.015–0.02 at/mol.

The results of the luminescence properties are here interpreted, with the support of diffuse reflectance data and lattice parameter measurements, on the basis of models describing the atomic defectuality situation and the distribution of the luminescence activator Tb^{3+} and of the Mg^{2+} alkali earth ions at lattice sites.

1 PREPARATION AND CHARACTERIZATION

1.1 Phosphor Powder Preparation

The raw materials (4N) Ta_2O_5 , Tb_4O_7 , alkali earth sulfates (if possible), $\text{Li}_2\text{SO}_4 \cdot \text{H}_2\text{O}$, are mixed, dried and fired in the temperature range 1000–1250°C (in air or inert gas) for several hours. Finally they are washed with water, seaved and dried at 120°C.¹

1.2 Crystallographic Properties

According to published data,² the crystal structure, determined by X-ray diffractometry, is hexagonal-rhombohedral with noncentrosymmetric space group $\text{R}\bar{3}\text{c}$. The density of the powder is 7.43 g/cm³. The refractive index, at 632.8 nm, is 2.17.

1.3 Point Defect Situation

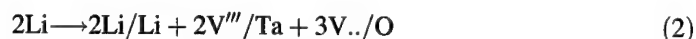
It is controlled by intrinsic deviations from stoichiometry as by the addition of foreign atoms, as Tb^{3+} and alkali earth 2+ ions. Since it is responsible of the main trapping events of the X-ray induced carriers (e' , h^+) it must be preliminarily clarified. We take into account: Li^+ and O^{2-} vacancies, V'/Li and $\text{V}../\text{O}$ respectively;^{3,4,5} Tb^{3+} at Li^+ and Ta^{5+} sites, $\text{Tb}../\text{Li}$ and Tb''/Ta respectively; Mg^{2+} at Li^+ sites, $\text{Mg}./\text{Li}$. The considered defectuality producing processes are:

1.4 $-\text{Li}/\text{Ta}$ Ratio

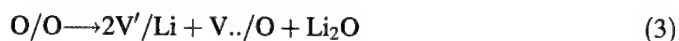
Lithium deficiency: LiTaO_3 can arrange high deviations from stoichiometry; the Li/Ta ratio can range from 0.8 to 1.2, approx., see (6)



Lithium excess:



1.5 Oxygen Deficiency :



1.6 Adding the Luminescence Activator, Tb^{3+} :

Tb^{3+} ions can occupy Li^+ or Ta^{5+} , as Eu^{3+} ions do in LiNbO_3 :⁷



where Tb^{3+} ions occupy Li^+ or/and Ta^{5+} sites.

1.7 Adding Alkali Earth Ions, e.g. Mg^{2+}



2 MEASUREMENTS

Luminescence spectra and intensities were obtained at 40 KV_p, 10 mA and processed by an EG&G Princeton Appl. Res. Optical Multichannel Analyzer OMA III unit. Efficiencies were determined by integrating the overall luminescence, collected by a silicon detector, over the exposure time (2 s).

2.1 Photostimulated Luminescence (P.S.L.)

After exposure to X-rays (40 KV_p, 10 mA, 2 s) and 5 s pause, the phosphor powder was stimulated with a quartz-iodine lamp, provided with suitable optical filters. A He-Ne laser was used for stimulating at 632.8 nm. Light powers were 0.01 micro-Watts/sq.cm; pulse length was 120 ms, the photo-luminescence was collected over 300 ms.

Diffuse reflectance (D.R.). Data were obtained by a Perkin-Elmer Lambda 9 spectrophotometer, in the spectral range 250–750 nm.

3 RESULTS AND DISCUSSION

Figure 1 shows a typical luminescence spectrum of $\text{LiTaO}_3:\text{Tb}^{3+}$; typical 5D4 \longrightarrow 7F_j transitions of Tb^{3+} are evident, where the 5D3 \longrightarrow 7F_j are practically absent, even at the lower Tb^{3+} concentration (see the Tb^{3+} energy levels, at the right side).⁸ The sensitivity

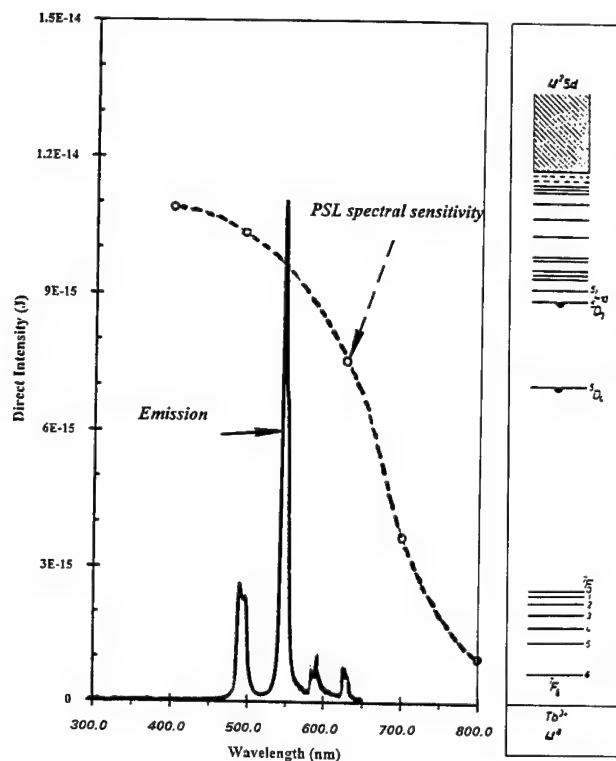


FIGURE 1 Spectral Photostimulability of $\text{LiTaO}_3:\text{Tb}^{3+}$ in comparison with its X-ray Emission Spectrum.

spectrum of the photo-stimulated luminescence (520–580 nm) is also shown, stressing a special feature of this phosphor, i.e. the possibility to get storage signals when photo-stimulated at wavelength lower than that of the emission.

Figure 2 illustrates the dependence of the D.L., of the P.S.L. and of the D.R. on the Tb^{3+} content. It is worth noticing that the maximum of D.L. does not correspond to a maximum of the P.S.L.; this stresses the prevalence, compared to process (4), of a Tb^{3+} incorporation process like (5), producing oxygen vacancies able to trap and store e' , available for the subsequent photo-stimulation but competing with the immediate luminescence process.⁹ The fact that the D.R., between 280 and 650 nm, decreases with Tb^{3+} content, agrees with the considered role of the oxygen vacancies.

Table I illustrates the dependence of D.L., P.S.L., D.R. and the rhombohedral lattice parameter values, respectively, on the Mg^{2+} ion content; for the first three properties, the corresponding values for the sample not Mg^{2+} doped are set to 100, as reference. The positive effect on D.L. and P.S.L. can be understood by assuming that V'/Li , created by the minority Tb^{3+} incorporation process (4), act as non-radiative recombination centers, subtracting e' and $h+$ both to the excitation of Tb^{3+} ions and to the storing at V''/O (being available for the subsequent photo-stimulation). Now, the addition of Mg^{2+} ions, supposed to prefer Li^+ sites, in analogy to the case of $\text{LiNbO}_3:\text{Eu}^{3+}$, Mg^{2+} ,¹⁰ would cause transfer of Tb^{3+} from Li^+ sites to Ta^{5+} sites, accordingly reducing the number of V'/Li . Schematically:

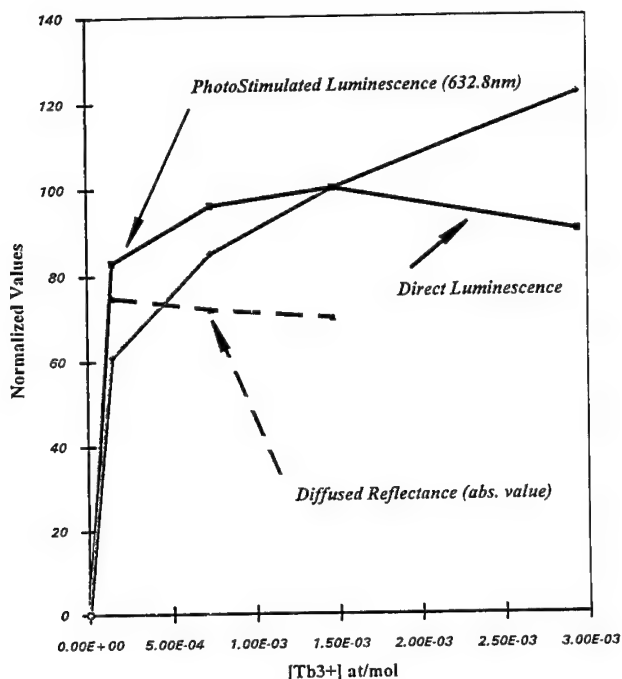
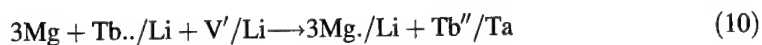


FIGURE 2 Effect of Tb^{3+} concentration on the Diffused Reflectance and on the Luminescence Properties of $LiTaO_3$



After a critical concentration, i.e. 0.02 at/mol, approximately, the Mg^{2+} incorporation mechanism (7), again creating V'/Li , would start to affect negatively the luminescence processes for both D.L. and P.S.L..

Table I
Effect of the Mg^{2+} concentration on the rhombohedral lattice parameter, on the diffused reflectance at 280 nm and on the luminescence properties of $LiTaO_3:Tb^{3+}$.

$[Mg^{2+}]$ (at/mol)	rhomb. Å	diffused reflect.	Direct luminesc.	Photo- stimul.
0	5.47104	100	100	100
1.36E-02	5.47077		230	166
2.24E-02	5.47163	79	83	117
4.48E-02	5.47173	73	54	93

ACKNOWLEDGEMENTS

We wish to thank Dr. P. Salvarani of 3M Italia Ricerche/Analytical Lab. for the determination of the crystal structure and of the lattice parameters.

REFERENCES

1. R. Morlotti, *EP* **597** 311 (filed 26.10.93).
2. S. C. Abrahams, J. L. Bernstein, *J. Phys. Chem. Solids* **28**, 1685 (1967).
3. F. D. Ho, *Phys. Stat. Sol. (b)* **122**, 337 (1984).
4. C. Chen, K. Sweeney, L. Halliburton, *Phys. Stat. Sol. (a)* **81**, 253 (1984).
5. A. Garcia, C. Prieto, L. Arizmendi, *Phys. Stat. Sol. (a)* **100**, k9 (1987).
6. B. Angert, V. Pashkov, N. Soloveva, *Sov. Phys. Jépt*, **35**, (5), 867 (1972).
7. D. Krol, G. Blasse, R. Powell, *J. Chem. Phys.*, **73**, (1), 163 (1980).
8. G. Blasse, *Handbook Phys. Chem. or Rare Earths*, Ed. K. Gschneider and Eyring, North Holland Publ. Comp., p. 237 (1979).
9. R. Morlotti, *et al.*, *Int. Conf. on Defects in Insulating Crystals*, Parma (1988), extended abstr., p. 559.
10. J. Garcia Solle, *et al.*, *J. Electrochem. Soc.* **140**, (7), 2010 (1993).

ABSORPTION AND LUMINESCENCE SPECTROSCOPY OF ZINC BORATE GLASSES DOPED WITH TRIVALENT LANTHANIDE IONS

LUIGI AMBROSI,^a MARCO BETTINELLI,^b GUY CORMIER^c
and MAURIZIO FERRARI^d

^aDipartimento di Chimica Inorganica, Università di Padova, via Loredan 4, I-35131 Padova, Italy; ^bSezione di Chimica, Istituto Politecnico, Facoltà di Scienze, Università di Verona, Strada Le Grazie, I-37134 Verona, Italy; ^cINFM, Dipartimento di Fisica, Università di Padova, Via Marzolo 8, I-35131 Padova, Italy; ^dCNR, Centro di Fisica degli Stati Aggregati ed Impianto Ionico, Via Sommarive 14, I-38050 Povo (TN), Italy.

Absorption and luminescence spectra and decay curves have been measured at temperatures down to 12 K for 4ZnO-3B₂O₃ glasses doped with Pr³⁺ and Eu³⁺. Analysis of the spectra has yielded information about the probability of the radiative transitions in the impurity ions and the strength of the electron-phonon coupling. The strongly non-exponential decay curves indicate the importance of energy transfer and migration processes accounting for the dynamics of the excited states of Pr³⁺.

Key words: Luminescence, Glass, Lanthanide Ions, Energy Transfer.

1 INTRODUCTION

Zn₄O(BO₂)₆ crystals have been intensively studied from a spectroscopic point of view as they are intrinsically luminescent and show efficient thermoluminescence.^{1,2} It is of interest to undertake the study of the optical properties of the same material in the glassy state and as a host for luminescent impurities. Moreover, investigations on the spectroscopy of doped zinc borate glasses have been up to now only sporadic. In this study we report a preliminary spectroscopic study of glasses having composition 4ZnO-3B₂O₃ and containing the trivalent lanthanide ions Pr³⁺ and Eu³⁺ as impurities.

2 EXPERIMENTAL

Glasses of composition 4ZnO-3B₂O₃ doped with 0.5–4% of trivalent lanthanide ion (substituting for Zn²⁺) were prepared by melting appropriate quantities of ZnO, H₃BO₃ and Eu₂O₃ or Pr₆O₁₁ in a Pt crucible at 1250°C for 4 h and quenching the melt in a brass mould. The samples were then annealed at 500°C for 12 h, cut and carefully polished to high optical quality for the spectral measurements. Room temperature absorption spectra were measured using a Cary 5E double beam spectrophotometer.

Emission and excitation spectra were obtained using a dye laser with rhodamine 6G, pumped by excimer laser or using a CW Ar ion laser. The fluorescence was focused onto a model 1401 double Spex monochromator equipped with a cooled RCA C31034A02 photomultiplier tube and was detected by photon counting. Both emission and excitation measurements were performed in time-resolved spectroscopy. Lifetime measurements were performed with a model SR430 Stanford multichannel using a minimum dwell time of 40 ns. An Oxford Instruments flow cryostat was used for low-temperature measurements.

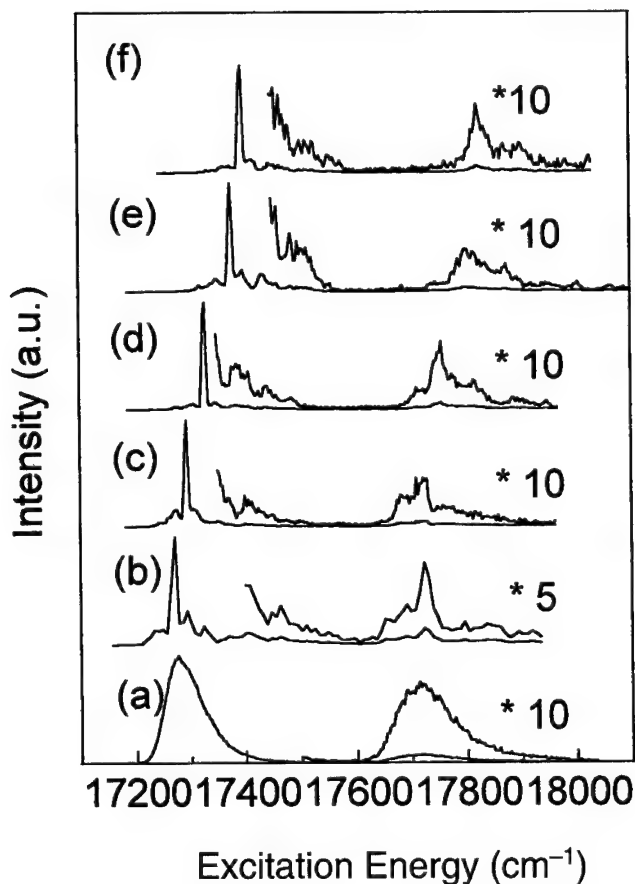


FIGURE 1 $^5D_0 \leftrightarrow ^7F_0$ excitation spectra of the Eu^{3+} in the zinc borate glass obtained at $T = 12$ K. Detection energy is at (a) $16\,270\text{ cm}^{-1}$, (b) $17\,260\text{ cm}^{-1}$, (c) $17\,290\text{ cm}^{-1}$, (d) $17\,320\text{ cm}^{-1}$, (e) $17\,370\text{ cm}^{-1}$, (f) $17\,390\text{ cm}^{-1}$. The amplification factor is shown above the spectra.

3 RESULTS AND DISCUSSION

The inhomogeneous and the resonant site selective excitation spectra of the $^5D_0 \rightarrow ^7F_0$ transition of the glass doped with 0.5% Eu^{3+} are shown in Figure 1. Figure 1(a) features the inhomogeneous excitation spectrum, detecting the $^5D_0 \rightarrow ^7F_2$ transition. Figure 1(b)–(f) show the resonant excitation spectra at different exciting energies, as reported in the caption. All the spectra display well resolved phonon sidebands, all peaking in the region of 450 cm^{-1} from the zero phonon line. The (b)–(f) spectra were measured in site selective conditions. The sidebands are assigned to a Eu-O stretching/ BO_3^{3-} libration localized mode, following the analysis of the vibrational structure of the luminescence spectrum of Eu^{3+} in crystalline ScBO_3 .³ This assignment is confirmed by the presence of a vibrational mode at about 445 cm^{-1} in the Raman spectra of the Eu^{3+} doped glasses, which is not present in the spectra of the undoped host glass.⁴ The structure of the sidebands does not

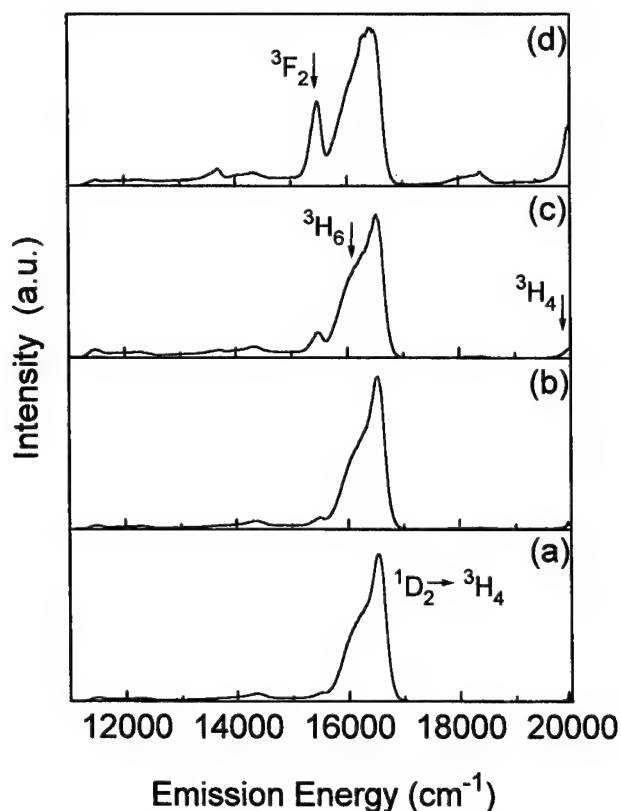


FIGURE 2 Luminescence spectra of Pr^{3+} in the zinc borate glass obtained at $T = 80$ K. The excitation wavelength was 488.0 nm. The concentration of Pr^{3+} was (a) 0.5%, (b) 1.0%, (c) 2.0%, (d) 4.0%. Some transitions originating from the $^3\text{P}_0$ excited state, and the $^1\text{D}_2 \rightarrow ^3\text{H}_4$ transition, are marked in the figure.

appear to change neither with respect to the energy distance from the ZPL, nor to the bandshape. The strength of the electron-phonon coupling g is a crucial parameter in determining important phenomena such as multiphonon relaxation, phonon-assisted energy transfer and upconversion. In the present case we evaluate $g \approx 0.10$ for all sites, an exceptionally high value, compared to the ones ($g \leq 2 \times 10^{-2}$) obtained from the phonon sideband of the hypersensitive $^7\text{F}_0 \rightarrow ^5\text{D}_2$ transition in Eu^{3+} doped borate, silicate and fluorophosphate hosts.⁵⁻⁷ The homogeneous linewidth of the $^5\text{D}_0 \rightarrow ^7\text{F}_0$ transition was measured for the glass doped with 0.5% Eu^{3+} by using the fluorescence line narrowing method, yielding a room temperature value of about 2.5 cm^{-1} at $17\,320 \text{ cm}^{-1}$. This value can be compared with the one obtained for $10\text{Na}_2\text{O}-90\text{B}_2\text{O}_3$ glass⁸ at the same temperature (4 cm^{-1}). No time evolution in the shape of the line at different delay from the excitation was observed, suggesting that energy transfer processes are negligible, although at this temperature the $^7\text{F}_1$ state is thermally populated.

Whilst the spectroscopic study of glasses doped with the Eu^{3+} ion yields valuable information about the static properties of the impurity in the disordered host, especially because it is possible to investigate a $J = 0 \leftrightarrow J = 0$ transition, the dynamic properties concerning the time evolution of the excited states are much more efficiently studied in

systems doped with other lanthanide impurities, such as Pr^{3+} . The Judd-Ofelt intensity parameters Ω_2 , Ω_4 and Ω_6 for the Pr^{3+} ion in the $4\text{ZnO} \cdot 3\text{B}_2\text{O}_3$ glass were obtained from the oscillator strengths of the f-f transitions observed in the room temperature absorption spectrum. A physically meaningful set of parameters ($\Omega_2 = 2.2 \cdot 10^{-19}$, $\Omega_4 = 3.7 \cdot 10^{-20}$ and $\Omega_6 = 1.4 \cdot 10^{-19} \text{ cm}^2$, $\text{RMS} = 2.2 \cdot 10^{-7}$) could be obtained only following the usual procedure⁹ of neglecting the transitions located in the near IR, justified by the different degree of mixing of the various $4f^2$ states with the low lying opposite parity states. The values of the intensity parameters are significantly higher than the ones obtained for the same impurity in a $\text{Zn}(\text{PO}_3)_2$ glass.¹⁰ This behavior is attributed to an enhanced mixing with the opposite parity states, possibly due to a stronger crystal field splitting and/or to a stronger nephelauxetic effect acting on the 5d states. The 80 K luminescence spectra of the glasses doped with Pr^{3+} in the visible region after excitation in the $^3\text{P}_0$ state are shown in Figure 2. They are composed of transitions originating from both the excited states $^3\text{P}_0$ and $^1\text{D}_2$, the latter state populated by non-radiative transitions due to the presence of phonons of 1300 cm^{-1} . Whilst the intensity of the transitions from both the upper $^3\text{P}_0$ and the lower $^1\text{D}_2$ states increase at all temperatures with the Pr^{3+} concentration, the relative intensity from $^3\text{P}_0$ markedly increase with the impurity concentration. Clearly the emission from the $^3\text{P}_0$ state is not concentration quenched, but probably concentration dependent processes, such as energy transfer, are involved in this intensity variation. These processes do not appear to be strongly temperature dependent.

The decay curves of the luminescence from the $^1\text{D}_2$ state after resonant excitation were measured in the range 12–300 K. They are strongly non exponential, the decay becoming distinctly faster when the concentration of Pr^{3+} is increased, and do not show any significant change with temperature. The long time tails of the curves are exponential and characterized by decay constants depending on the Pr^{3+} concentration. The values range from $6 \cdot 10^4 \text{ s}^{-1}$ for the most diluted sample (0.5%) to $3 \cdot 10^5 \text{ s}^{-1}$ for the most concentrated one (4%), and are virtually independent of the excitation and the emission wavelengths. Although the precise values must be considered only as indicative, the behavior seems to indicate the simultaneous presence of cross relaxation and energy migration processes occurring with a comparable rate (intermediate regime). The absence of temperature dependence of the decay curves indicates that the transfer processes do not require the involvement of high frequency phonons and therefore are almost resonant. One of the possible cross relaxations is $^1\text{D}_2 + ^3\text{H}_4 \rightarrow ^1\text{G}_4 + ^3\text{F}_4$ (or $^3\text{F}_3$), in agreement with previous studies.¹¹

Further time resolved measurements are necessary in order to obtain more information about the dynamics of the energy transfer mechanisms responsible for the depopulation of $^3\text{P}_0$ and $^1\text{D}_2$, and to verify the possibility of upconversion emission in these glasses.

REFERENCES

1. A. Meijerink, G. Blasse and M. Glasbeek, *J. Phys.: Condensed Matter* **2**, 6303 (1990).
2. L. Bohatý, S. Haussühl, J. Liebertz and S. Stähr, *Z. Kristallogr.* **161**, 157 (1982).
3. G. Blasse and G. J. Dirksen, *Inorg. Chim. Acta* **145**, 303 (1988).
4. L. Ambrosi, M. Bettinelli, M. Ferrari, M. Casarin and A. Piazza, *J. Phys. IV (Paris)* **C4**, 477 (1994).
5. S. Tanabe, S. Todoroki, K. Hirao and N. Soga, *J. Non-Cryst. Solids* **122**, 59 (1990).
6. S. Todoroki, S. Tanabe, K. Hirao and N. Soga, *J. Non-Cryst. Solids* **136**, 213 (1991).
7. S. Tanabe, S. Yoshii, K. Hirao and N. Soga, *Phys. Rev.* **B45**, 4620 (1992).
8. J. R. Morgan and M. A. El-Sayed, *Chem. Phys. Lett.* **84**, 213 (1981).
9. R. D. Peacock, *Structure and Bonding (Berlin)* **22**, 83 (1975).
10. G. Ingletto, M. Bettinelli, L. Di Sipio, F. Negrisola and C. Aschieri, *Inorg. Chim. Acta* **188**, 201 (1991).
11. J. C. Vial, R. Buisson, F. Madeore and M. Poirier, *J. Phys. (Paris)* **40**, 913 (1979).

OPTICAL ENERGY TRANSFER IN RARE EARTH DOPED SILICA GELS

A. BOUAJAJ,^{1,3} A. MONTEIL,² M. FERRARI,³ and M. MONTAGNA⁴

¹Physico-Chimie des Matériaux Luminescents URA 442 du CNRS, Université Lyon I, 43 bd du 11 Novembre 1918, 69622 Villeurbanne, France; ²Laboratoire POMA, Université d'Angers, 2 bd Lavoisier, 49045 Angers cedex, France; ³CNR-CeFSA, Centro di Fisica degli Stati Aggregati, via Sommarive 14, 38050 Povo, Trento, Italy; ⁴Dipartimento di Fisica, Università di Trento, via Sommarive 14, 38050 Povo, Trento, Italy

In this work we study the time dependence of the Eu^{3+} luminescence from the $^5\text{D}_0$ state in a silica gel. Sample was doped with a 0.2% Eu/Si molar ratio and fully densified by heat treatment at 1050°C . The $^5\text{D}_0 \leftrightarrow ^7\text{F}_0$ transition shows a different lineshape in absorption and luminescence at temperatures lower than room temperature. This effect is due to efficient energy transfer among Eu^{3+} ions with different environments.¹ Energy transfer is studied by detecting the resonant and out of resonance decay profile, after selective excitation within the $^7\text{F}_0 \rightarrow ^5\text{D}_0$ absorption line. The transfer rate is comparable with the radiative decay rate. At low temperature luminescence occurs mainly from the ions in sites having the $^5\text{D}_0 \rightarrow ^7\text{F}_0$ transition frequency in the low tail of the inhomogeneous line.

Key words: Silica gel, rare-earth, energy transfer.

1 INTRODUCTION

Optical energy transfer becomes an undesired effect when one uses the spectroscopic properties of lanthanide ions as a probe of the structural evolution in silica gels. In particular, the energy transfer does not allow to resolve the internal structure of the multiplets by site selection spectroscopy and to measure the homogeneous linewidth by Resonant Fluorescence Line Narrowing (RFLN) measurements.² On the other hand, the detailed understanding of the excitation transfer among the optical centers embedded in sol-gel materials is important for applications and can provide relevant information about the rearrangement of the matrix during the gel-to-glass transition, and in particular about the rare earth clustering.

This work presents a study of the time dependence of the luminescence from Eu^{3+} ions embedded in a silica sol-gel matrix. In particular energy transfer is studied for the fully densified sample.

2 EXPERIMENTAL

Silica gels were obtained by hydrolysis and copolymerization of tetramethylorthosilicate (TMOS), methanol and water with the molar ratios: $\text{TMOS}/\text{MeOH}/\text{H}_2\text{O} = 1/6.2/10$. An acid aqueous solution of $\text{Eu}(\text{NO}_3)_3$ was then added in order to reach a concentration of $\text{Eu}/\text{Si} = 0.2\%$. The heat treatments were performed in air for 10 h, at different temperatures from room temperature (R.T.) up to 1050°C . In this work we study the fully densified sample. RFLN measurements were performed in Time Resolved Spectroscopy (TRS) using photon counting detection. Lifetimes measurements were performed by a Stanford S430 multichannel analyzer with 80 ns minimum dwell time. A detailed description of the preparation of the samples and of the experimental setup can be found elsewhere.^{1,3,4}

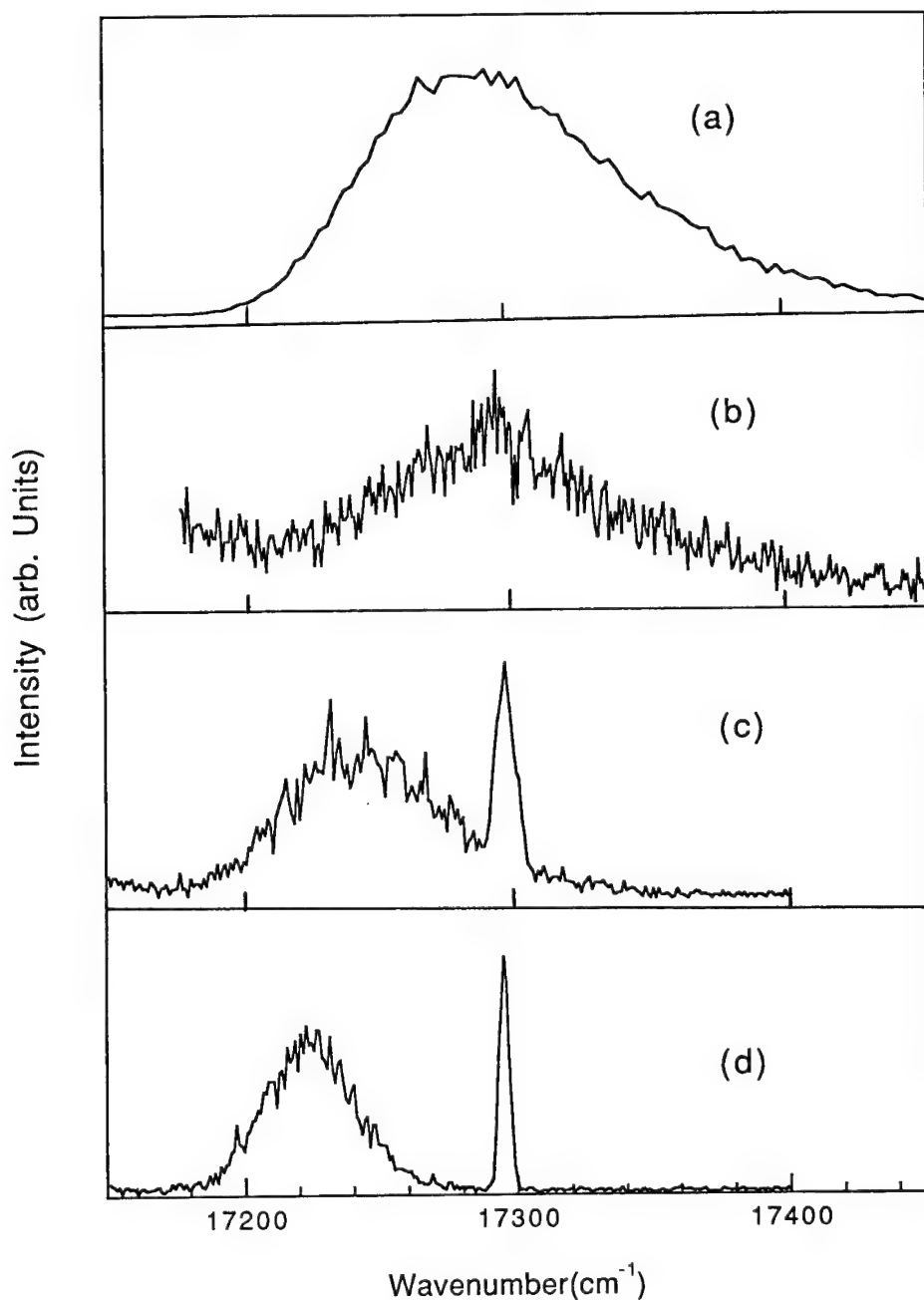


FIGURE 1 (a) Excitation spectrum at $T = 15$ K of the ${}^7F_0 \rightarrow {}^5D_0$ obtained by detecting at $16\,200\text{ cm}^{-1}$ in the ${}^5D_0 \rightarrow {}^7F_2$ band. (b), (c), (d) Luminescence spectra at $T = 300$ K, $T = 30$ K and $T = 15$ K respectively after excitation at $17\,295\text{ cm}^{-1}$, at about the center of the inhomogeneous absorption profile. The data were in all cases acquired using a detection window between 30 and $300\text{ }\mu\text{s}$ after the laser pulse.

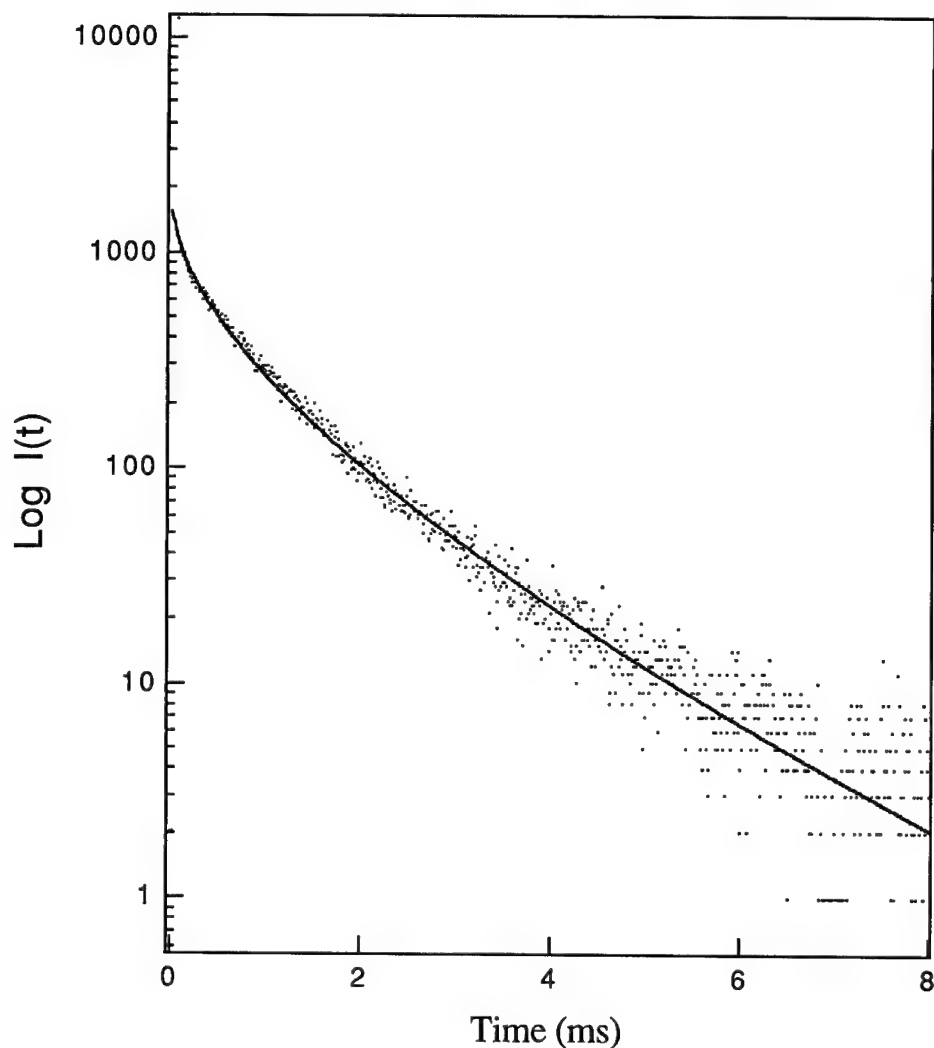


FIGURE 2 Decay curve of the luminescence from the $^5\text{D}_0$ level, after excitation at $17\,295\text{ cm}^{-1}$ and resonant detection at $T = 15\text{ K}$. The continuous line is the result of the fit using a stretched exponential (see text).

3 RESULTS AND DISCUSSION

The low temperature excitation spectrum of the $^7\text{F}_0 \rightarrow ^5\text{D}_0$ band, obtained by detecting in the $^5\text{D}_0 \rightarrow ^7\text{F}_2$ band is shown in Figure 1(a). The band presents a FWHM of about 100 cm^{-1} and reflects the large distribution of sites for Eu^{3+} in densified xerogel. At this temperature the homogeneous linewidth of the transition is completely negligible.⁵ By exciting with a narrow laser within the inhomogeneous profile (Figure 1(b), (c), (d)), the luminescence band is narrowed. At low temperature (c), (d) we observe a sharp resonant line whose linewidth is limited by the experimental setup. A broader band appears on the

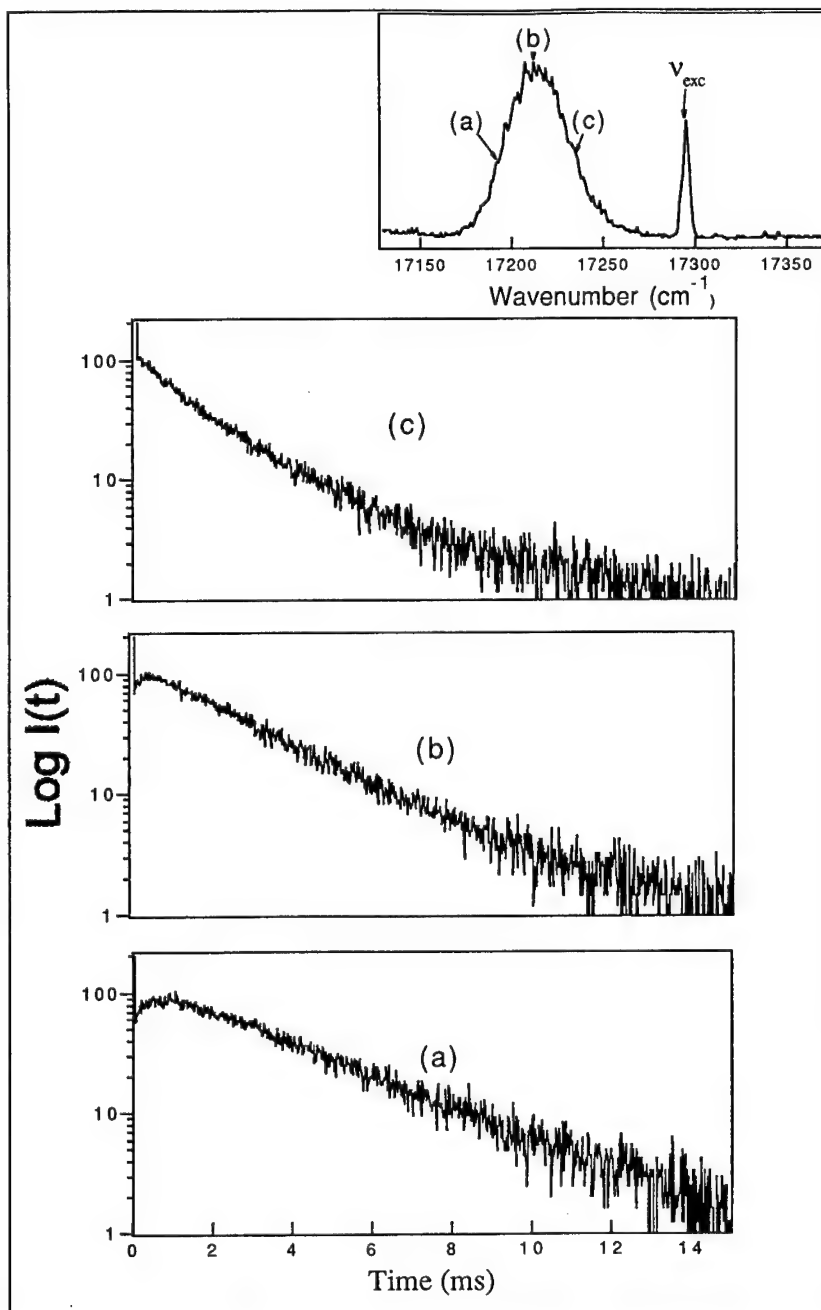


FIGURE 3 Decay curves of the luminescence from the 5D_0 level performed at $T = 15$ K by exciting at $17\,295\text{ cm}^{-1}$ and detecting at different emission energies: (a) $17\,193\text{ cm}^{-1}$, (b) $17\,212\text{ cm}^{-1}$, (c) $17\,235\text{ cm}^{-1}$, as shown in the inset which shows the spectrum of Figure 1(d).

low energy tail of the inhomogeneous profile. The relative intensity of the line with respect to the band decreases with the delay of detection. The linewidth of the band is temperature dependent and does not depend very much on the excitation frequency. The data are compatible with a fast energy transfer among the Eu^{3+} ions in different sites. By assuming thermal equilibrium in the population of the energy levels, the calculated line shape fits well the data as a function of the temperature.¹ In the room temperature spectrum (b), the energy transfer is very fast and the resonant line is no more detectable after a delay of 30 μs .

More detailed information about the transfer rate are given by lifetime measurements. The resonant decay of the luminescence from the donor ions is shown in Figure 2. It has a non exponential profile that reflects the energy transfer process dynamics. The decay can be fitted using a stretched exponential function⁶ with a stretching exponential of 1/2 for dipole-dipole interaction:

$$I(t) = I(0) * \exp[-t/\tau_R - \beta * t^{1/2}].$$

τ_R is the radiative lifetime of the $^5\text{D}_0$ state, assumed to be site independent. β is a parameter related to the transfer rate and to the dependence of the interaction on the distance between the ions. The best fit gives $\tau_R = 4$ ms and $\beta = 53.4 \text{ s}^{-1/2}$. The critical distance is $R(15\text{K}) = 22 \text{ \AA}$ and the average transfer rate is $W(15\text{K}) = 930 \text{ s}^{-1}$. This transfer is comparable with the inverse radiative inverse lifetime.

This is better evidenced in Figure 3 which shows the decay curves of the luminescence for non resonant excitation. The population of the acceptor ions increases through energy transfer from the excited donor ions. An estimation of the risetime gives 348 μs for the sites emitting at lowest energy (Figure 3 (a)), 178 μs for the sites emitting at intermediate energy (Figure 3 (b)) and it is not detectable for the sites emitting at higher energy (Figure 3 (c)). The relatively long time needed to populate the ions which give the luminescence in Figure 3(a), (b) has a simple interpretation which is also independent of the effective transfer mechanism. At low temperature the thermal equilibrium population involves few sites which emit in the very low energy tail of the inhomogeneous profile. The donor levels are quickly depopulated but many steps of transfer are needed to reach the thermal equilibrium.

More detailed measurements as a function of the temperature, of the excitation and the detection frequencies will be necessary to understand in detail the transfer mechanism.

ACKNOWLEDGMENTS

The authors are indebted to M. Bettinelli for his critical reading of the manuscript and his constructive remarks. We acknowledge fruitful discussions with E. Duval and A. Piazza. We thank C. Bovier for his invaluable advice about the preparation of the samples. This work was performed within a CNRS (France) - CNR (Italy) cooperation.

REFERENCES

1. A. Bouajaj, A. Monteil, C. Bovier, M. Ferrari, A. Piazza, *J. de Physique IV*, **C4-579** (1994).
2. R. Camprostrini, G. Carturan, M. Ferrari, M. Montagna, O. Pilla, *J. Mater. Res.* **7**, 745 (1992).
3. A. Bouajaj, A. Monteil, C. Bovier, J. Serughetti, M. Ferrari, *J. Sol-Gel Science and Technology* (1994) in press.
4. A. Bouajaj, *PhD Thesis Lyon* (1994).
5. R. M. Macfarlane and R. M. Shelby, *J. Lumin.* **36**, 179 (1987).
6. M. Inokuti and F. Hirayama, *J. Chem. Phys.* **43**, 1978 (1965).

SAMARIUM DOPED ALKALINE EARTH HALIDE THIN FILMS AS SPECTRALLY SELECTIVE MATERIALS FOR HOLE BURNING?

A. MONNIER, M. SCHNIEPER, R. JAANISO and H. BILL

Department of Physical Chemistry, University of Geneva, 30 Quai E. Ansermet, CH-1211 Geneva 4, Switzerland

Optical hole burning, a potential technique for spectrally selective recording, was demonstrated in Sm-doped MBE-grown thin films of $\text{CaF}_2/\text{Si}\langle 111 \rangle$. The inhomogeneous broadening of the corresponding $\text{Sm}^{2+} 5d(T_{1u}) \leftarrow 4f(^7F_0, A_{1g})$ transition (690 nm) was investigated as a function of substrate temperature and film thickness. The MBE apparatus is briefly described as well as the thin film growth procedure.

Key words: Calciumfluoride: Samarium, thin films, MBE, hole burning.

1 INTRODUCTION

Materials engineering for optical hole burning¹ applications has mainly been directed towards designing bulk matrices. The present study was undertaken to extend such studies to thin MBE-grown films doped with suitable photochromic systems. Sm-doped CaF_2 films grown on $\text{Si}\langle 111 \rangle$ were selected as our model systems because fluorites have properties similar to those of the materials used in high temperature hole burning,² and further, growth and characterization of such films is to some extent known.³ The possibility to grow them under partially nonequilibrium thermodynamic conditions allows to influence the inhomogeneous broadening of electronic transitions. In turn the application of hole burning may be useful for the characterization of the insulating CaF_2 layers in Si technology.⁴

2 RESULTS

Film-growth: Molecular Beam Epitaxy (MBE) has been selected because it offers high flexibility through choice of the growth conditions. Then, it presents extended possibilities to govern the chemical vapor composition in the growth chamber and allows for relatively easy control of the growth parameters. A complete MBE apparatus was designed to suit our needs and then built in our laboratory. Its construction allows for five effusion cells. The device includes a sample exchange system together with a sample holder which can be heated to 1000°C, a quadrupole mass spectrometer, a film thickness meter and a RHEED setup which enables to follow the structural evolution of the film during growth. A typical growth procedure was as follows. Substrates of dimensions 10 × 10 mm were cut from 0.2 mm thick polished Si plates, carefully cleaned according to a modified Shiraki procedure⁵ and then heated to 1000°C in situ immediately before film deposition. The RHEED pattern presented after this heat treatment the 7 × 7 Si superstructure. The CaF_2 films (doped with nominally 1% Sm) were grown at a typical rate of 0.05 nm/sec. The superstructure rapidly disappeared and only the streaks due to the CaF_2 film were observed. Four substrate temperatures (100, 300, 500, 700°C) and four film thickness' (100, 200, 500, 1000 nm, all realized on the same substrate) were selected as growth

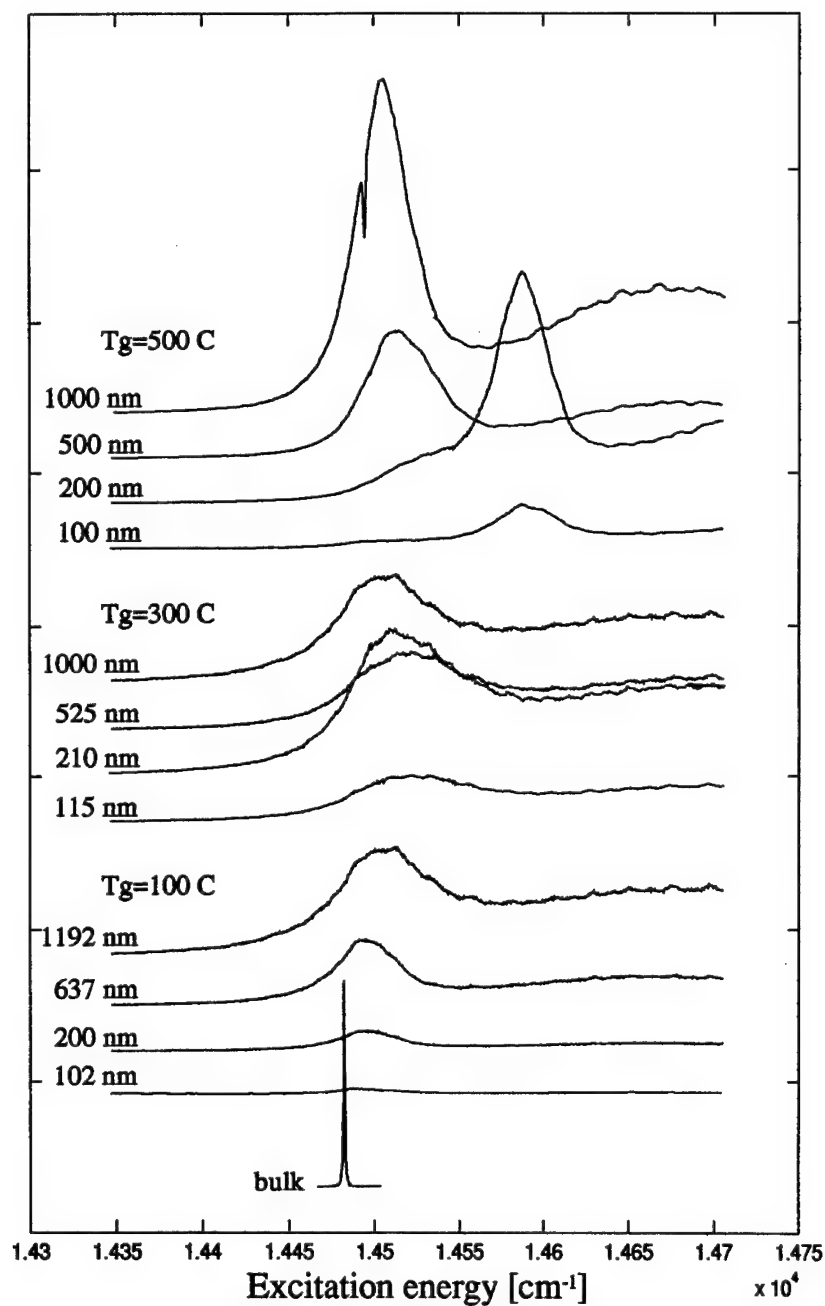


FIGURE 1 Excitation spectra of the $\text{Sm}^{2+} 5d(T_{1u}) \leftarrow 4f(^7F_0, A_{1g})$ transition in $\text{CaF}_2/\text{Si} (111)$ films as a function of growth temperature and film thickness. Temperature: 7 K. Spectrum at the top shows a hole burnt during set up of the experiment.

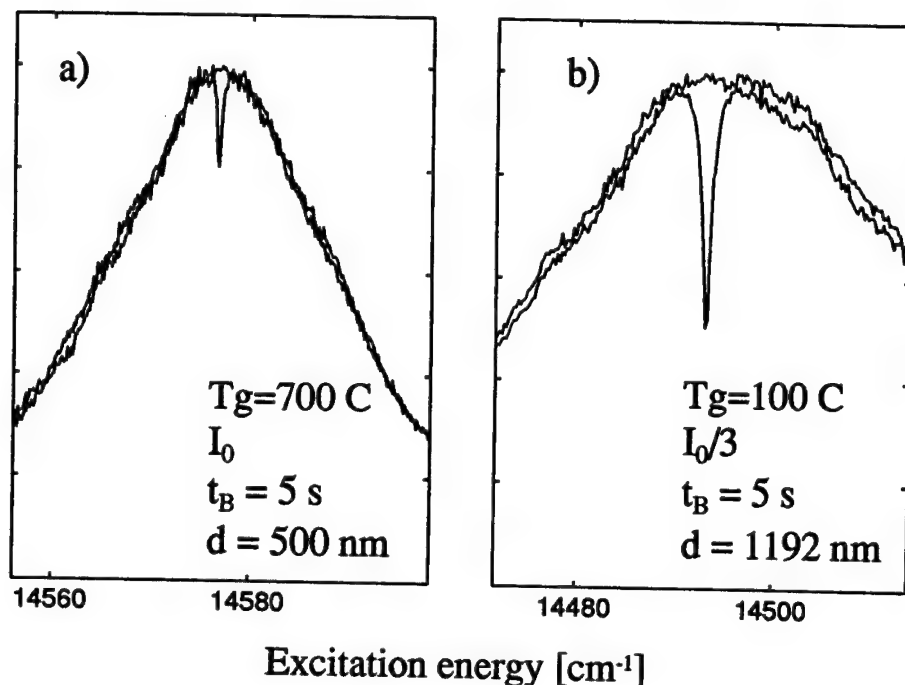


FIGURE 2 Holes burnt into $\text{CaF}_2:\text{Sm}^{2+}$ thin films at 7 K.
 a) Substrate temperature 700°C.
 b) Substrate temperature 100°C.

parameters. The film thickness was determined with a SYCON film thickness monitor. The equipment was calibrated with the aid of the white light interference method. The films obtained were of high optical quality as checked by investigating their scattering properties in a laser beam.

Excitation spectra and hole burning: excitation spectra of the $\text{Sm}^{2+} 5d(T_{1u}) \leftarrow 4f(A_{1g})$ transition were obtained with a tunable dye laser (line width 3–5 GHz) by monitoring the red shifted fluorescence of the zero phonon line (ZPL) through a color filter (R9G). Films corresponding to every pair of the growth parameter set were prepared and investigated. Part of the results are shown in Figure 1. Note that the corresponding spectrum of Sm^{2+} in bulk CaF_2 was added as a marker to this Figure. The Huang-Rhys factor was determined to have the same value (≈ 0.3) in the bulk and in the films, indicating essentially the same electron-phonon coupling strength in both cases. The feasibility of spectral hole burning (see spectrum in Figure 1) clearly shows that the observed broadening of the thin film spectra is essentially of inhomogeneous origin. The behavior of the inhomogeneous ZPL line as a function of substrate temperature and film thickness is as follows, where $\Delta[\text{cm}^{-1}] = (\text{position maximum ZPL in film} - \text{position maximum ZPL in bulk})$, and b [a number] = (ZPL width film/ZPL width bulk).

T [°C]	100	200	500	1000 [nm]
100	no marked thickness dependence			$\Delta = 9 \text{ cm}^{-1}$, $b \approx 36$
300	\Rightarrow increasing width \Rightarrow			$\Delta = 24.6 \text{ cm}^{-1}$, $b \approx 53$

At higher film temperatures strong thickness dependence.

$$\begin{array}{ccc}
 500^\circ & \Delta \approx 109 \text{ cm}^{-1} \leftarrow \text{'phase transition'} \Rightarrow & \Delta \approx 25 \text{ cm}^{-1} \\
 & b \approx 30 & b \approx 33
 \end{array}$$

For comparison a film (1000 nm thick) was grown at 600°C, homoepitaxially, onto a CaF_2 (111) substrate. Small shift Δ ($< 0.2 \text{ cm}^{-1}$) but important broadening b (≈ 32) was observed.

At low substrate temperature epitaxial growth is bad because of low lateral diffusion. But tensile strain is almost absent, resulting in an inhomogeneous line shape determined by point defects⁶. The inverse situation is observed at high substrate temperatures. The important tensile strain gives rise to sizable shifts of the line. The strong thickness dependence found indicates a reorganization to the 'bulk' CaF_2 structure as soon as the film is thick enough to overcome the forces due to the interface mismatch. The most interesting films were grown at 300°C because they show both, the strong shift and important disorder. This transition region is favorable to strong inhomogeneous broadening. Spectral holes were burnt into two samples (Figure 2). A 700°C sample presented hole widths of $\approx 8 \text{ GHz}$, similar to values obtained in bulk matrices.⁷ Deeper and wider holes (same laser intensity (1 W/cm^2) and burning time (5 sec)) were burnt into the 300°C samples.

3 CONCLUSION

Out-of-equilibrium film growth at rather low temperatures is useful for obtaining both, the wide inhomogeneous broadening of the optical line and efficient hole burning, under no loss of the optical quality of the film.

REFERENCES

1. W. E. Moerner, W. Length, G. C. Borklund, *Topics Current Physics* 44, Springer Berlin (1988).
2. R. Jaaniso, H. Bill, *Europhys. Lett.* **16** (1991) 569.
3. N. S. Sokolov et al., *Jpn. J. Appl. Phys.* **33** (1994) 2395.
4. V. Mathet et al., *J. Crystal Growth* **132** (1993) 241.
5. A. Ishizaka et al., *J. Electrochem. Soc.* **133** (1986) 666.
6. A. M. Stoneham, *Rev Mod. Phys.* **41** (1968) 82.
7. R. M. Macfarlane, R. M. Shelby, *Opt. Letters* **9** (1984) 533.

5 EXCITED STATES

UPCONVERSION IN $\text{CsCdBr}_3:\text{Pr}^{3+}$

J. NEUKUM, N. BODENSCHATZ and J. HEBER

Institute of Solid State Physics, Technical University of Darmstadt, 64289 Darmstadt, Germany

In CsCdBr_3 the trivalent Pr ions substitute the divalent Cd ions. Charge compensation leads to three Pr-vacancy centers. The first one is the well known symmetric pair center Pr^{3+} -Cd vacancy— Pr^{3+} the second one is the asymmetric pseudopair center Pr^{3+} - Pr^{3+} -Cd vacancy, and the third one finally is a Pr^{3+} single ion with a Cs vacancy nearby. Only the Pr^{3+} - Pr^{3+} -Cd vacancy center showed upconversion emission from 3P_0 and 3P_1 under 1D_2 excitation. The dynamics of the upconversion process is studied. It cannot be explained in the standard picture of phonon-assisted cross relaxation in the energy level scheme of the rare-earth ions. In our interpretation it is made up by a cooperative energy transfer from the doubly excited pair state $^1D_2 \times ^1D_2$ to lattice excitons followed by a back transfer of the energy exciting the pair into the states $^3P_1 \times ^3H_4$, $^3P_0 \times ^3H_4$, and $^1D_2 \times ^3H_6$. First experiments on $\text{CsCdBr}_3:\text{Pr}^{3+}$ confirm the picture of exciton-mediated upconversion.

Key words: Upconversion, CsCdBr_3 , Pr^{3+} , Tm^{3+} excitons.

Upconversion¹ is a process in which two excited ions redistribute their energy so that one ion goes into a higher excited state on the expense of the other one. This process is not only interesting from a physical point of view but also for applications: It offers the opportunity to make an upconversion laser, a laser which can be pumped at a lower quantum energy than it emits.

Since upconversion is a pair process it is very useful to study this process in crystals into which the active ions enter predominantly by pairs. Such a crystal is CsCdBr_3 doped with rare-earth (RE) ions. CsCdBr_3 crystallizes in the hexagonal CsNiCl_3 structure² with linear chains of confacial $(\text{CdBr}_6)^{4-}$ octahedra arranged along the threefold crystallographic axis and separated by Cs^+ ions. The trivalent RE ions substitute the divalent Cd ions. Charge compensation in the linear Cd^{2+} chain gives rise to three different Pr centers which have been identified spectroscopically³. Only the asymmetric pair center Pr^{3+} - Pr^{3+} - Cd^{2+} vacancy shows upconversion^{3,4} under 1D_2 excitation and will be discussed further. This upconversion is mediated by lattice excitons as sketched in Figure 1: Both ions of the pair have to be excited by the incident light. Due to the strong ion-ion coupling in the asymmetric pair the ions can cooperatively transfer their excitation energy to the lattice exciton. After relaxation into its metastable state the exciton can transfer its energy to one of the pair partners or to a single RE ion, which can be excited to a higher excited state compared with the initial ones. Finally, this ion can emit the upconverted light quantum $\nu_2 \leq 2\nu_1$.

The energy levels and transitions of the excitons are usually much broader than of the RE ions. So for the energy transfer between the exciton and the RE ions good resonance conditions can be expected for overlapping energies. This is true for the cooperative energy transfer from the doubly excited pair to the exciton as well as for the transfer from the exciton to the RE ion in the final step of upconversion. For the first energy transfer from the ion pair to the exciton (Figure 2) no back transfer is expected because of the usually fast relaxation of the exciton down to its metastable excited state. But for the second transfer from the relaxed exciton to the emitting RE ion a limited number of fast energy transfers back and forth can be expected for smaller Franck-Condon shifts (Figure 2) leading to a common decay of the exciton and RE ion. If the energy of the exciton is higher than the energy of the accepting level of the RE ion, energy transfer with phonon assistance is necessary for reasons of energy conservation. At low temperatures this means

Upconversion via electronic lattice excitations

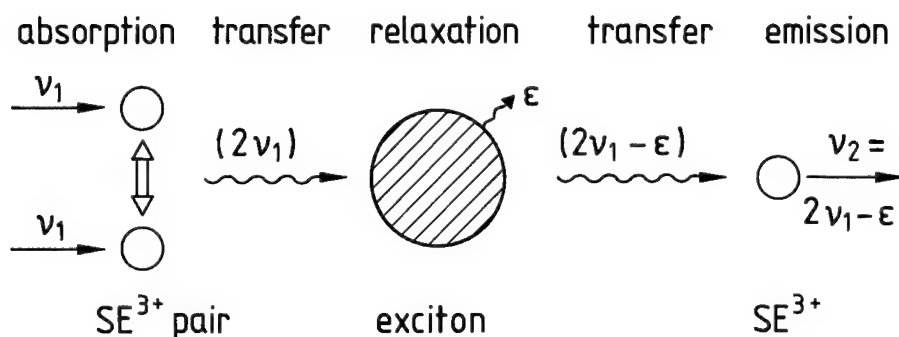


FIGURE 1 Scheme of the upconversion process mediated by excitons.

that the energy transfer is a one-way process from the exciton to the RE ion (Figure 2). This kind of transfer is responsible for the 3P_0 emission (Figure 3). Its fluorescence rises with its intrinsic lifetime of $22\ \mu\text{s}$ and decays with the decay time of the feeding exciton of $136\ \mu\text{s}$ as expected from a simple rate-equation model.

The decay of the 3P_1 emission is different (Figure 3). The 3P_1 level obviously couples resonantly to the faster decaying exciton but not to the slower one. If the fast exciton is decayed the 3P_1 level stays with some residual population and decays with an own lifetime.

The fluorescence transient of the 1D_2 level can be interpreted as a superposition of both processes. At short times the pair level $^1D_2 \times ^3H_6$ is coupled resonantly to the S_1 level giving rise to the fast 1D_2 rise and decay, but for longer times we get a phonon assisted feeding from the T level of the exciton resulting in the slower $136\ \mu\text{s}$ decay.

The red impurity emission of the undoped host lattice (Figure 3) obviously shows a similar coupling to the exciton. The origin of the exciton is not clear to us yet and needs further investigation. A direct emission from it was not found yet. It seems to decay preferentially nonradiatively.

Another fingerprint for the role of excitons in the upconversion process was found by us recently in Tm^{3+} doped CsCdBr_3 . Again the risetime of the upconverted fluorescence is very short. It is $4 \pm 1\ \mu\text{s}$ (Figure 4b), almost the same value as for $\text{Pr}^{3+}:\text{CsCdBr}_3$. But the more interesting fact is that we found a strong upconverted Ho^{3+} fluorescence (Figure 4a) although Ho^{3+} was present in the crystal only as an impurity ($\text{Ho}/\text{Tm} < 10^{-2}$). At lower excitation energies this upconverted fluorescence has been even the stronger one. For reasons of the excitation wavelength the upconversion has to happen on the Tm^{3+} pairs. From here the upconverted excitation energy has to be transferred to the Ho^{3+} ions over mean distances of the order of $100\ \text{\AA}$ in times of the order of $4\ \mu\text{s}$ or even less. This can be concluded from the risetime of the upconverted Ho^{3+} fluorescence. This is far out of the range of the transfer times and transfer distances for direct RE-RE interactions, and can be

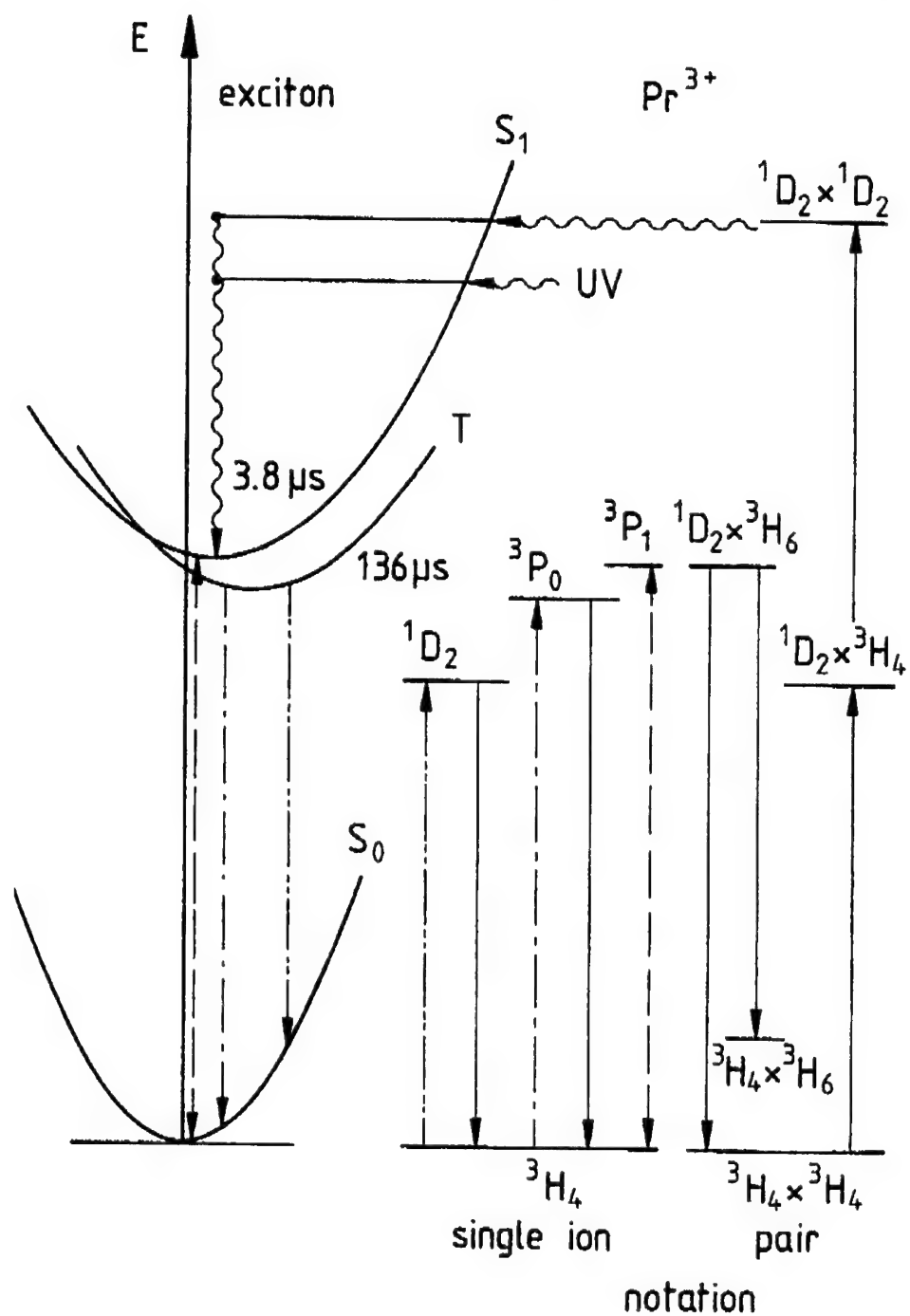


FIGURE 2 Energy-level scheme for the upconversion process in $\text{CsCdBr}_3:\text{Pr}^{3+}$. Full lines represent radiative transitions, dotted lines—energy transfers. UV excitation was accomplished by a nitrogen laser ($\lambda = 337 \text{ nm}$), resonant excitation by a tunable pulsed dye laser.

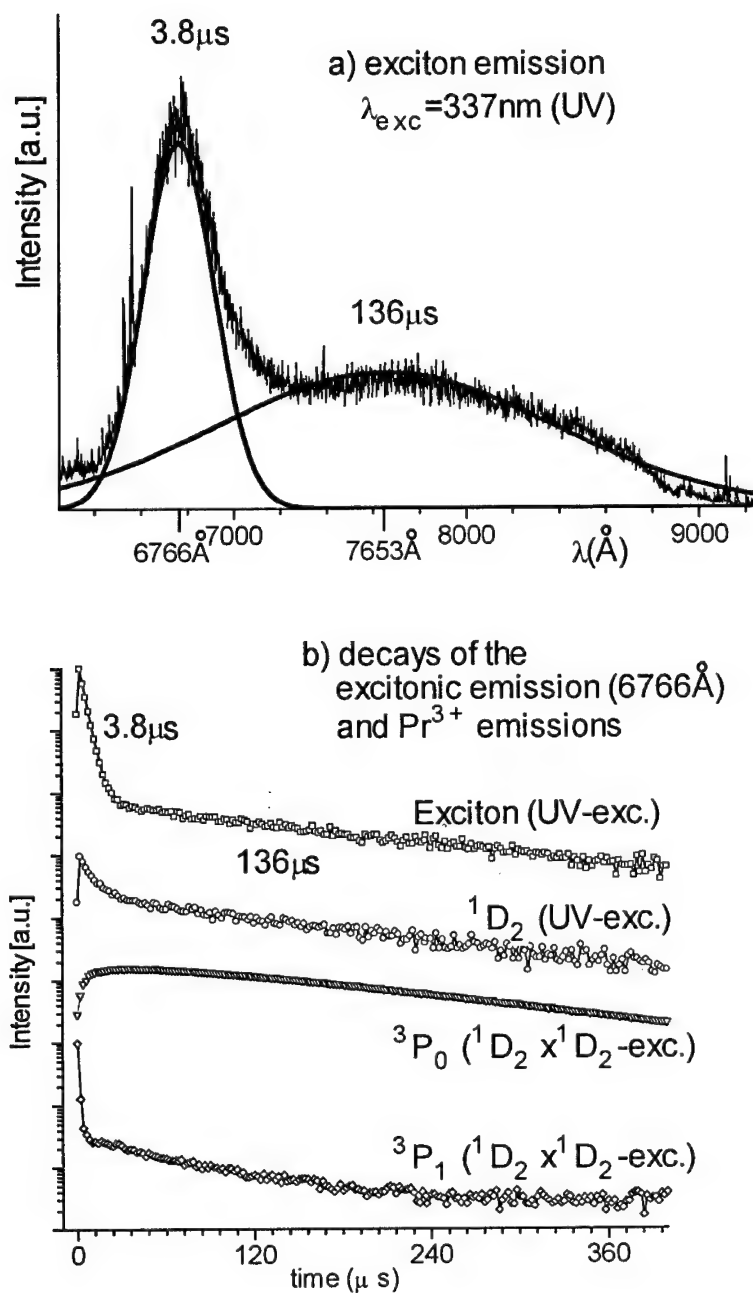


FIGURE 3 (a) Fluorescence spectrum of the red lattice impurity emission fed by the excitons relevant for the upconversion. Undoped crystal. $T = 4.2\text{ K}$.
 (b) Fluorescence decays of the impurity emission ($\lambda = 677\text{ nm}$) and of the Pr^{3+} levels excited via the exciton. $T = 4.2\text{ K}$.

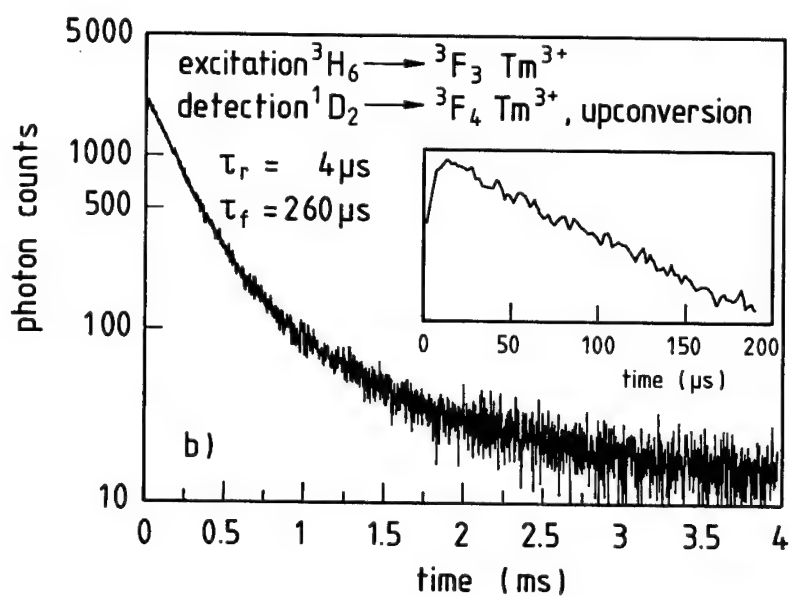
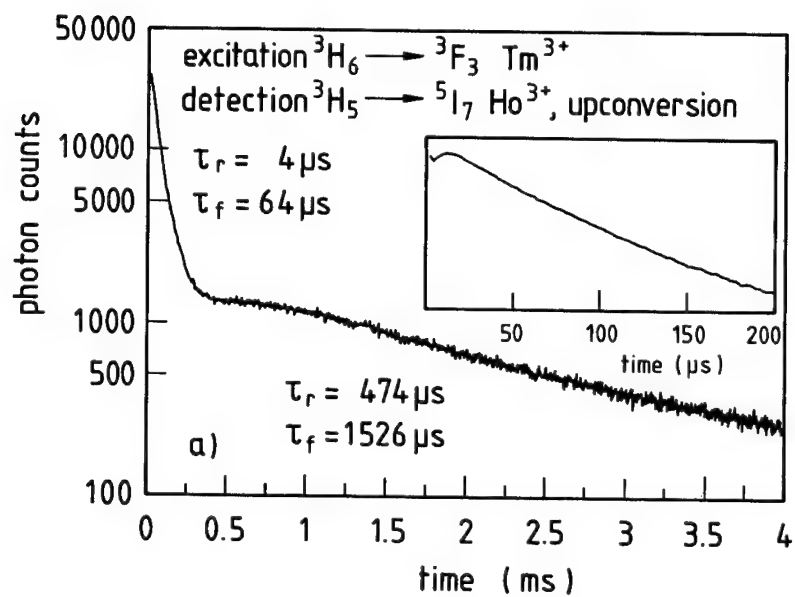


FIGURE 4 Upconversion dynamics of CsCdBr₃:Tm³⁺, Ho³⁺, Tm³⁺ concentration is 0.5%
 (a) Upconverted Ho³⁺ emission
 (b) Upconverted Tm³⁺ emission.

explained reasonably only through the intermediary of an extended excited state like an exciton. There are several excitons discussed in the literature for CsCdBr_3 ^{5,6} and similar compounds,^{7,8} but the origin of the mediating excitons needs further investigation to understand the discussed fast upconversion in more detail.

REFERENCES

1. F. Auzel, C. R. Acad. Sci. (Paris) **262**, 1016 (1966); **263**, 819 (1966).
2. L. M. Henling and G. L. McPherson, *Phys. Rev. B* **16**, 4756 (1977).
3. J. Neukum, N. Bodenschatz, and J. Heber, *Phys. Rev.*, **B50**, 3536 (1994).
4. U. Schäfer, J. Neukum, N. Bodenschatz, and J. Heber, *J. Lumin.* **60/61**, 633 (1994).
5. C. Andraud, F. Pelle, J. P. Denis, and B. Blanzat, *J. Phys.: Condens. Matter* **1**, 1511 (1989).
6. A. Wolfert and G. Blasse, *J. Solid State Chem.* **55**, 344 (1984).
7. C. Dujardin, B. Moine, and C. Pedrini, *J. Lumin.* **54**, 259 (1993).
8. B. Moine, B. Courtois, and C. Pedrini, *J. Phys. France* **50**, 2105 (1989).

METASTABLE ONE-HALIDE SELF-TRAPPED EXCITONS IN ALKALI HALIDES

A. LUSHCHIK, CH. LUSHCHIK, F. SAVIKHIN and E. VASIL'CHENKO

Institute of Physics, Estonian Acad. Sci., Riia 142, EE2400 Tartu, Estonia

Fast ($\tau < 2$ ns) short-wavelength emissions have been detected overlapping the continuous intraband luminescence on exciting KBr, RbBr, KCl and RbCl crystals by an electron beam. These emissions are attributed to the radiative decay of metastable one-halide self-trapped excitons. The weak 5.8 eV emission can effectively be excited in a KBr crystal in the region of the formation of excitons (6.73–7.3 eV).

Key words: luminescence, self trapped excitons, alkali halides.

The emission of relaxed two-halide self-trapped excitons (STE) is dominant in the spectra of intrinsic emission of alkali halides (AH), while the weak emission of free excitons (FE) can also be observed. Other kinds of exciton emission have not been studied in detail. In principle, a metastable state of a one-halide STE could exist as an intermediate one between those of the FE and of the two-halide STE. Broad bands tentatively ascribed to metastable one-halide self-trapped excitons (OSTE), have been detected in the VUV region of cathodoluminescence spectra for KCl, KBr at 80 K¹ and NaCl, RbCl, RbBr crystals at 10 K².

The aim of the present study is to select the OSTE emission among other weak emissions excited in AH by VUV-radiation or by an electron beam. Mainly KBr crystals grown by the Stockbarger or by the Kyropoulos method in helium atmosphere were studied. The KBr salt was preliminarily treated in Br₂ gas flow and additionally refined by manyfold recrystallization from the melt. The content of impurity ions in KBr was on the level of 0.01 to 3 ppm (only the amount of Cl[−] was about 20 ppm).

Main attention was paid to the detection of fast ($\tau < 2$ ns) emissions on exciting a crystal by electron beam pulses (the experimental setup has been described in Ref. 3). Special experiments were carried out in order to distinguish the fast emission of OSTE from the fast continuous temperature-independent intraband luminescence (IBL) detected for the first time in AH by Vaisburd.⁴ The separation of intrinsic and impurity-defect emissions was made by measuring the excitation spectra by using VUV-radiation from a deuterium lamp or synchrotron beamline in MAX-Lab, Lund.⁵

Figure 1 presents the spectra of fast ($\tau < 2$ ns) luminescence of a KBr crystal measured at 295 and 85 K on exciting the crystal by single electron pulses (300 keV). The continuous luminescence in the region of 6 to 1.8 eV (limit of the apparatus) at 295 K is due to indirect electronic transitions between various branches of the conduction band. In the 4–1.8 eV region the IBL spectrum is affected by the reabsorption of fast luminescence by short-lived F and H centres (absorption maxima at 2.05 and 3.25 eV, respectively). It should be remarked that IBL cannot be excited by photons the energy of which only slightly exceeds the value of the energy gap $E_g = 7.5$ eV. A weak σ emission of STE (maximum at 4.4 eV) overlaps the IBL. The excitation spectra of the 4.0 and 5.48 eV emissions have been measured at 295 K in KBr by using the synchrotron radiation. These emission ranges were selected within the IBL region. The STE and the impurity emissions (e.g., Tl⁺ emission in KBr:Tl) increase strongly by increasing the exciting photon energy from 15 to 20 eV due to the formation of secondary excitons or electron-hole pairs by hot photoelectrons.⁵ On the contrary, the process of multiplication of electronic excitations causes the decrease of the intensity of IBL at 4 and 5.48 eV.

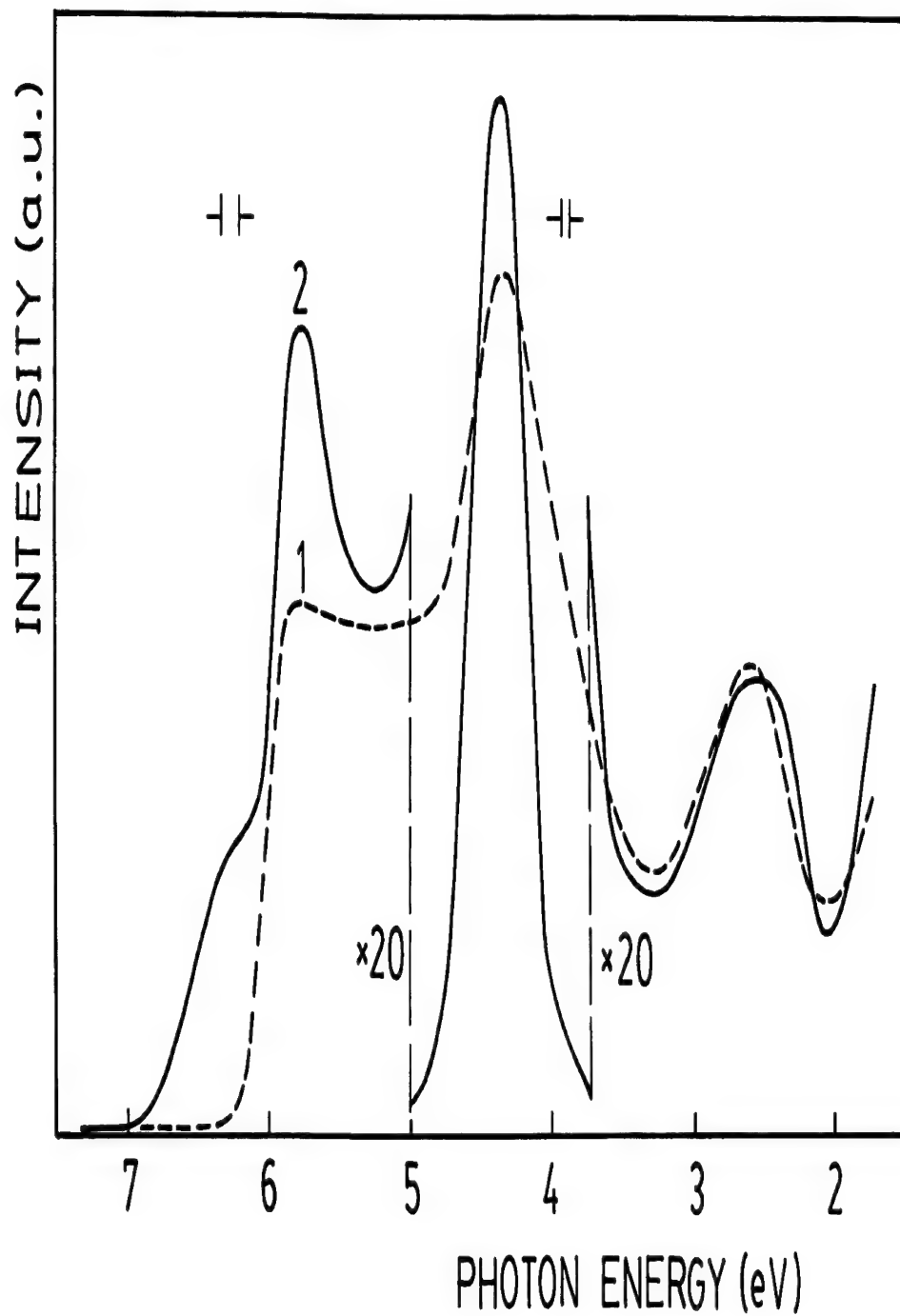


FIGURE 1 Emission spectrum of the fast ($\tau < 2$ ns) luminescence of a KBr crystal on excitation by a 300 keV electron beam at 295 (1) and 85 K (2).

If the sample is cooled to 85 K the fast IBL intensity does not change, while that of STE σ emission increases remarkably and a weak emission in the range 5.5–6.0 eV appears, see Figure 1, curve 2. The last was observed in the steady luminescence spectrum by exciting the KBr sample with 6 keV electrons and it was tentatively interpreted as OSTE luminescence.¹ We have observed analogous fast emissions (overlapping the IBL background) at 85 and 10 K in the spectra of some other AH. If the emission is excited by an electron beam, the maxima of the emissions for chlorides (NaCl, KCl, RbCl and CsCl) are situated in the region of 6.8–7.3 eV, while for KBr and RbBr, 5.5–6.2 eV. Thus, the emissions are connected with the radiative decay of anion electronic excitations and not cation ones. The relative Stokes shifts $\mu = (E^A - E^I)/E^A$ for these emissions are in the range 0.15–0.08 for alkali chlorides and bromides (the maximum of long-wavelength exciton absorption band is taken as the E^A and E^I is the maximum of emission band), i.e. the μ values are considerably smaller than those for the two-halide STE. The intensities of VUV-emissions are 30–300 times lower than that of two-halide STE. The introduction of homologous impurities (I^- , Br^- , Na^+) into KCl and RbCl does not enhance these emissions.

We made an attempt to detect the OSTE emission in case of photoexcitation of KBr. Figure 2 shows the excitation spectrum of STE π emission (2.28 eV) obtained by using VUV-radiation with a resolution of 10 meV at LHeT (curve 1). The spectrum was not corrected for the reflection losses. The excitation efficiency for the π emission is high in the whole spectral region related with the formation of the $\Gamma(1/2, 3/2)$ excitons with $n = 1$ (6.73–7.3 eV) including the Urbach tail of exciton absorption (6.73–6.8 eV), where the direct optical creation of OSTE takes place. Besides π emission of STE, extremely weak emissions at 2.5, 2.85 and 3.5 eV related to Cl^- , Na^+ and I^- impurity ions can be excited by photons of $h\nu \leq 6.75$ eV at LHeT in a KBr crystal. Figure 2 presents also the excitation spectra of the 3.55 (curve 2) and 5.5 ± 0.3 eV (curve 3) emissions. The luminescence attributed to OSTE can effectively be excited in the Urbach tail of exciton absorption as well as in the short-wavelength region of the exciton absorption band. The 5.8 eV emission intensity does not change if the sample is heated to 60 K but is reduced by a factor 2–3 at 90 K. Such an emission can be excited also by 15–17 eV photons due to the creation of secondary excitons by hot photoelectrons.

The measured excitation spectra of short-wavelength emission in KBr at LHeT support the hypothesis that the emission at 5.8 eV is due to OSTE and suggest that OSTE and STE can coexist in AH. Unfortunately, small amounts of impurity ions are present in our KBr crystals. The excitation spectra of impurity emissions can partly overlap the weak OSTE luminescence. The energy transfer by excitons (polaritons) to luminescent impurity centres is possible in KBr. The mean free path of FE before self-trapping does not exceed 10 lattice constants in KCl and RbCl at 5 K. Thus the fast emission at 6.8–7.2 eV (assumed as the OSTE emission in such crystals) should not be due to the energy transfer to luminescent centres in these crystals. Further investigations of the nature of the short-wavelength emissions are needed. In perspective it is necessary to use the subpicosecond technique as in the case of one-halide holes.⁶

In KCl and KBr crystals the efficiency of the creation of F, H pairs with large interdefect distances in pairs as well as of α , I pairs (anion vacancy + interstitial anion) is high on optical generation of excitons, being by 10 to 20 times lower on the recombination of electrons with V_K centres.⁷ OSTE and STE coexist in KBr and KCl as a consequence of the optical formation of excitons, while OSTE does not arise on the recombination of an electron with a relaxed hole (V_K centre). Significant changes in the equilibrium positions of surrounding anions and cations take place during non-radiative transitions $OSTE \rightarrow STE$. This circumstance leads to a dynamic increase of 'cation gates' and

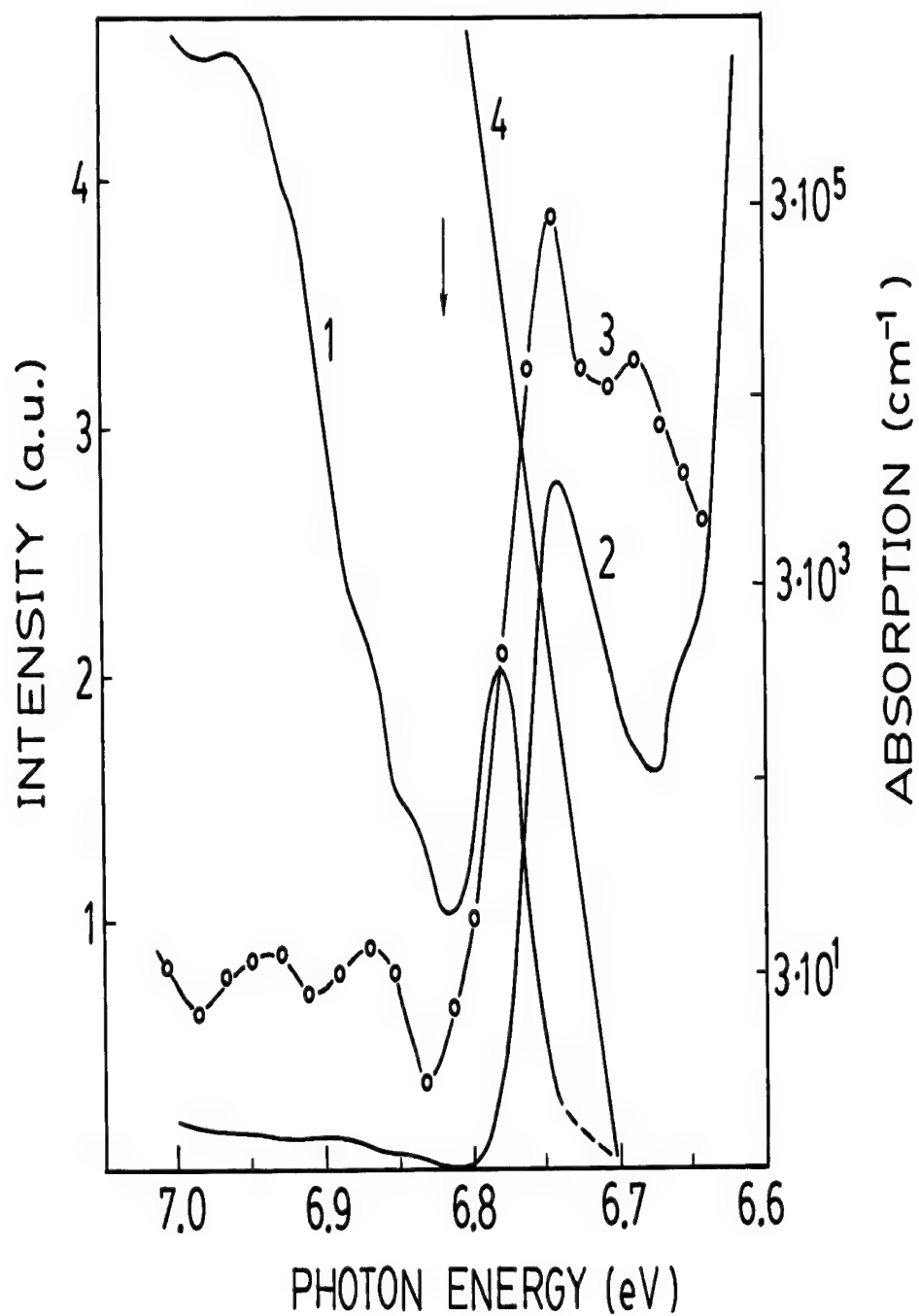


FIGURE 2 Excitation spectra (scale on the left) of steady photoluminescence of the 2.28 (1), 3.55 (2) and 5.5 ± 0.3 eV (3) emission for a KBr crystal at 4.2 (1, 2) and 8 K (3). The spectra are measured by using deuterium discharge (1, 2) or synchrotron radiation (3) with a resolution of 0.5 (1, 2) or 0.33 nm (3). The Urbach tail of KBr at 26 K as reported by T. Tomiki *et al.*, 1974 (4) is shown by comparison, scale on the right.

facilitates the crowdion displacement of X_2^- configuration along [110] direction by several interanion distances. This mechanism of a stable α , I pair creation has been discussed in detail.⁷

REFERENCES

1. I. L. Kuusmann and Ch. B. Lushchik, *Bull. Acad. Sci. USSR. Phys. Ser. (USA)* **40**, 14 (1976).
2. A. Lushchik, Ch. Lushchik, F. Savikhin and E. Vasil'chenko, *Phys. Solid State* **37**, 525 (1995).
3. K. U. Ibragimov and F. A. Savikhin, *Phys. Solid State* **35** 744 (1993).
4. D. I. Vaisburd and B. N. Semin, *Bull. Russ. Acad. Sci., Phys. (USA)* **56** 211 (1992).
5. M. Kirm, I. Martinson, A. Lushchik, K. Kalder, R. Kink, Ch. Lushchik and A. Lohmus, *Solid State Commun.* **90** 741 (1994).
6. K. Tanimura, T. Makimura, T. Shinata, N. Itoh, T. Tokizaki, S. Iwai and A. Nakamura, *Defects in Insulating Materials* ed O. Kanert and J. M. Spaeth (World Scientific, Singapore, 1993) vol. 1, p. 84.
7. A. Ch. Lushchik and Ch. B. Lushchik, *Bull. Russ. Acad. Sci., Phys. (USA)* **56** 201 (1992).

OPTICAL STUDIES OF SELF-TRAPPED HOLES AND EXCITONS IN BERYLLIUM OXIDE

S. V. GORBUNOV, S. V. KUDYAKOV, B. V. SHULGIN and V. YU. YAKOVLEV

*Experimental Physics Department, Urals State Technical University,
620002 Ekaterinburg, Russia*

Time-resolved spectra, decay kinetics, degree of polarization of the luminescence and transient optical absorption induced by irradiation of BeO with an electron, synchrotron and subsequent laser pulses have been studied. It is found that the two pairs of slowly and fastly decaying intrinsic luminescence bands at 6.7, 4.9 and 4.4 eV are associated with the two different types of the self-trapped excitons. The 1.7 eV transient optical absorption band and the ultra-violet absorption band at 3.6 eV are attributed to the electron and hole components of the self-trapped excitons, respectively. The transient optical absorption band with decay time of 6.5 ms is found to be due to the self-trapped holes. The models of self-trapped excitons and holes are discussed on the basis of the present experimental results.

1 INTRODUCTION

The phenomenon of self-trapped excitons and holes has been observed in insulating solids with strong electron-phonon interactions. The structure of self-trapped excitons and holes has been well characterized in alkali halide crystals by means of experimental studies of the luminescence, transient optical absorption, both of electron spin and optically detected magnetic resonances. In cubic alkaline-earth oxides (for ex. MgO) free excitons have been found and studied. However, no data on the existence of self-trapped excitons (STE) in them are available. Experimental results suggesting self-trapping of excitons in non-cubic oxides SiO₂, Y₂O₃, Al₂O₃ have been accumulated. However, up to now the structure of STE remains vague due to the lack of any spectroscopic ESR and optical evidence of self-trapped holes (STH) in oxides.

2 EXPERIMENTAL TECHNIQUE

We have studied pure BeO crystals grown by the temperature gradient and Czochralski-Kyropoulos methods from a BeO solution in sodium tungstate melt. Total concentration of Li, B, Al, Mg and Zn impurities did not exceed 10–50 ppm. The mentioned impurities have been discovered by a laser-induced mass-spectrographic method. We measured the luminescence and the transient optical absorption induced by pulsed irradiation with an optical detection system consisting of a monochromator, a photomultiplier and storage oscilloscopes. For registration of fast processes stroboscopic method of electron-optical chronography with a picosecond time resolution based on LI-602 dissector has been used. Electron pulses with parameters (Energy 200 keV, duration of 10 ns, maximum fluence of 0.25 J·cm⁻²) were generated with a GIN-600 accelerator. Synchrotron X-ray pulses with parameters (Gaussian shape $\sigma = 0.43$ ns, flux density 10^{14} – 10^{16} s⁻¹·cm⁻², frequency 4 MHz, photon energy 3–62 keV) were generated with a VEPP-3 storage ring. Laser pulses of 851 nm (1.46 eV) were obtained using a YLiF₄-Er laser (parameters: duration of 70 ns, pulse energy of 30 mJ). Frank-Ritter and Raushan polarizers were used to analyze luminescence and transient optical absorption.

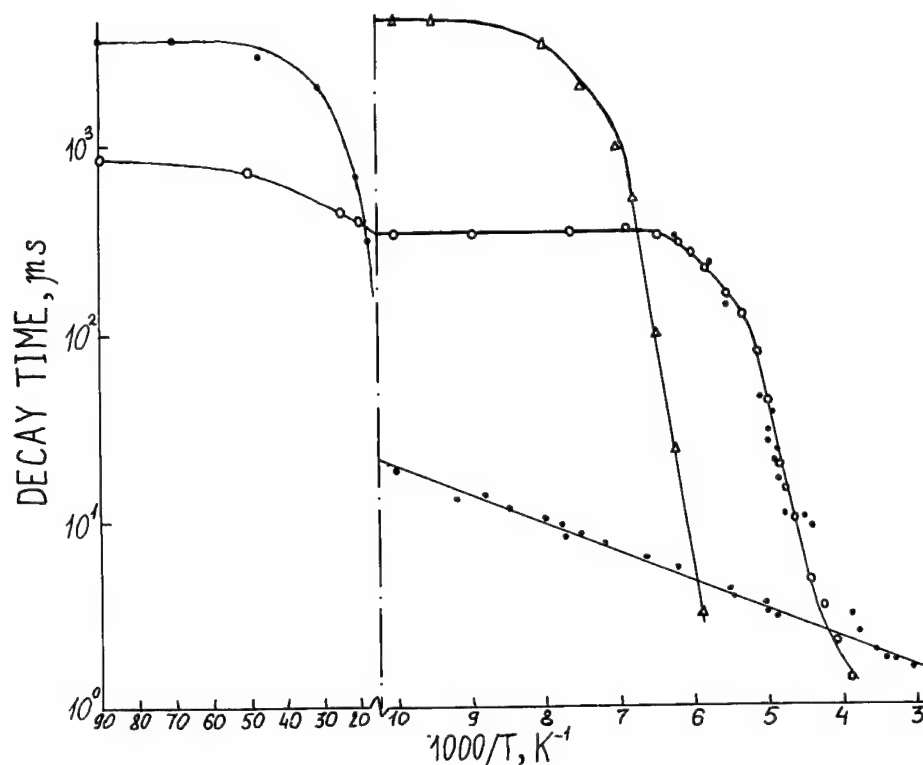


FIGURE 1 Temperature dependences of the decay times of transient optical absorption at 3.6 eV (triangles), luminescences at 4.9 eV (closed circles) and at 6.7 eV (open circles).

3 EXPERIMENTAL RESULTS AND DISCUSSION

The decay kinetics of the 6.7 luminescence at 6 K can be described by the sum of two exponents with time constants of 190 and 850 μ s. These components possess temperature dependent lifetimes and we observed only one exponential component with time constant of 340 μ s. at 80 K. These data show 6.7 eV luminescence (we called it π_1 luminescence according to analogous slowly decaying luminescence of STE in alkali halides) to be associated with transitions from spin levels of splitted triplet state of STE₁ in BeO. The π_1 luminescence polarization degree ($P = (I_{\parallel} - I_{\perp}) / (I_{\parallel} + I_{\perp})$ - where I_{\parallel} and I_{\perp} denote the intensities of the components parallel and perpendicular to the optical c-axis, respectively) was found to be -0.75.

The spectrum of the second slowly decaying luminescence (we called it π_2 luminescence) exhibits a broad band with the maximum at 4.9 eV. At 5 K exponential component with a time constant of 3.6 ms were detected in the π_2 luminescence decay kinetics. We assumed that the π_2 luminescence exponential component is related to triplet-singlet transitions in another STE₂. We found a number of peculiarities in the temperature dependence of π_2 luminescence decay, Figure 1. In the 20–160 K temperature range the behaviour of decay and decay time are typical of a simple process of temperature quenching with an activation energy of 13 meV. In the 160–220 K range in the 4.9 eV luminescence kinetics the second slower exponential component appears. Its value and

temperature dependence of decay time are correlated with those of π_1 luminescence at 6.7 eV. At the subsequent temperature increase in π_2 luminescence decay is clearly manifested growth stage was found. It disappears above 260 K and again there is only one exponential component whose temperature behaviour is described by the quenching process with an activation energy of 13 meV. All these facts can be explained by non-radiative transitions from the triplet state of STE_2 as well as transitions between the triplet states of STE_1 and STE_2 . The value of P for π_2 luminescence was found to be -0.60.

In addition to slowly decaying luminescence bands two fast luminescences were found. One of them has the same spectrum as the π_2 luminescence. This fast emission that called σ_2 luminescence shows a single exponential decay with a time constant of 30 ns. On the other hand, we obtained the σ_2 luminescence polarization degree as -0.46. The second fastly decaying emission at 4.4 eV called π_2 luminescence has an exponential decay with a time constant of 2 ns. It should be emphasized that σ_1 luminescence is strongly polarized along the C-axis. Its degree of polarization was found to be +0.67. According to the obtained results we assumed that both of the fastly decaying luminescences arise from the singlet excited states of the two types of STE in BeO. They have high stability of the initial intensity and decay time at least in the temperature range of 80 - 600 K.

We suggested two types of STE models in BeO using transient absorption. In time resolved spectra of BeO transient optical absorption induced by electron pulse at 80 K two bands at 1.7 and 3.6 eV have been observed. Detailed studies of transient absorption decay showed that the relaxation in 1.7 eV band was described by single exponential dependence with a time constant of 340 μs , typical of 6.7 eV luminescence. Besides, absorption decay in the range of 3.6 eV can be fitted by summation of three exponential curves with constants $\tau_1 = 340 \mu\text{s}$, $\tau_2 = 6.5 \text{ ms}$, $\tau_3 = 450 \text{ ms}$. The intensity of absorption of centers linked with components 340 μs and 6.5 ms increases proportionally to the fluence of electrons while the intensity of a component 450 ms has a saturation dependence. The latter indicates that transient absorption decaying with time 450 ms is due to impurities or nominal defects.

The comparison of decay times of the first component of transient optical absorption and 6.7 eV luminescence demonstrated that their values coincide rather well. The mentioned result are allowed to conclude that the absorption band at 1.7 eV and the main part of the band at 3.6 eV are due to STE_1 . As it is seen from Figure 2 ultra-violet band of STE_1 absorption at 3.6 eV is a two-band superposition with maxima 2.9 eV ($\vec{E} \perp \text{C}$) and 3.9 eV ($\vec{E} \parallel \text{C}$) and long-wave band 1.7 eV is observed only for the electric vector \vec{E} perpendicular to the C-axis. The component with $\tau_2 = 6.5 \text{ ms}$ manifests only one peak at 3.6 eV coinciding with UV-band of STE_1 absorption. However, this band is superposition of two bands with maxima at 3.5 eV ($\vec{E} \perp \text{C}$) and 3.7 eV ($\vec{E} \parallel \text{C}$). Thus, there is similarity in absorption of the second component and a short-wave range of STE_1 absorption alongside several characteristic features. The latter are due to a smaller splitting value (0.2 eV) for the bands with different polarization compared to that of STE_1 .

It is known that in alkali-halide crystals in spectra of transient absorption of STE bands resulting from optical transitions both in exciton hole and electron components¹ have been found. The experimental data mentioned above can be explained assuming that the absorption band at 1.7 eV is due to optical transitions in STE electron component and UV-band at 3.6 eV is linked with optical transitions in an exciton hole component. At subsequent laser excitation in the band 1.7 eV an intensive luminescence of both STE types in BeO has been found. The intensity dependence of this luminescence on the laser pulse delay time relative to the electron pulse coincides with the decay time of luminescence and optical transient absorption of triplet STE_1 . It proves that excitation of transitions in an electron component of STE_1 causes its luminescence as well as transformation into another type of STE_2 .

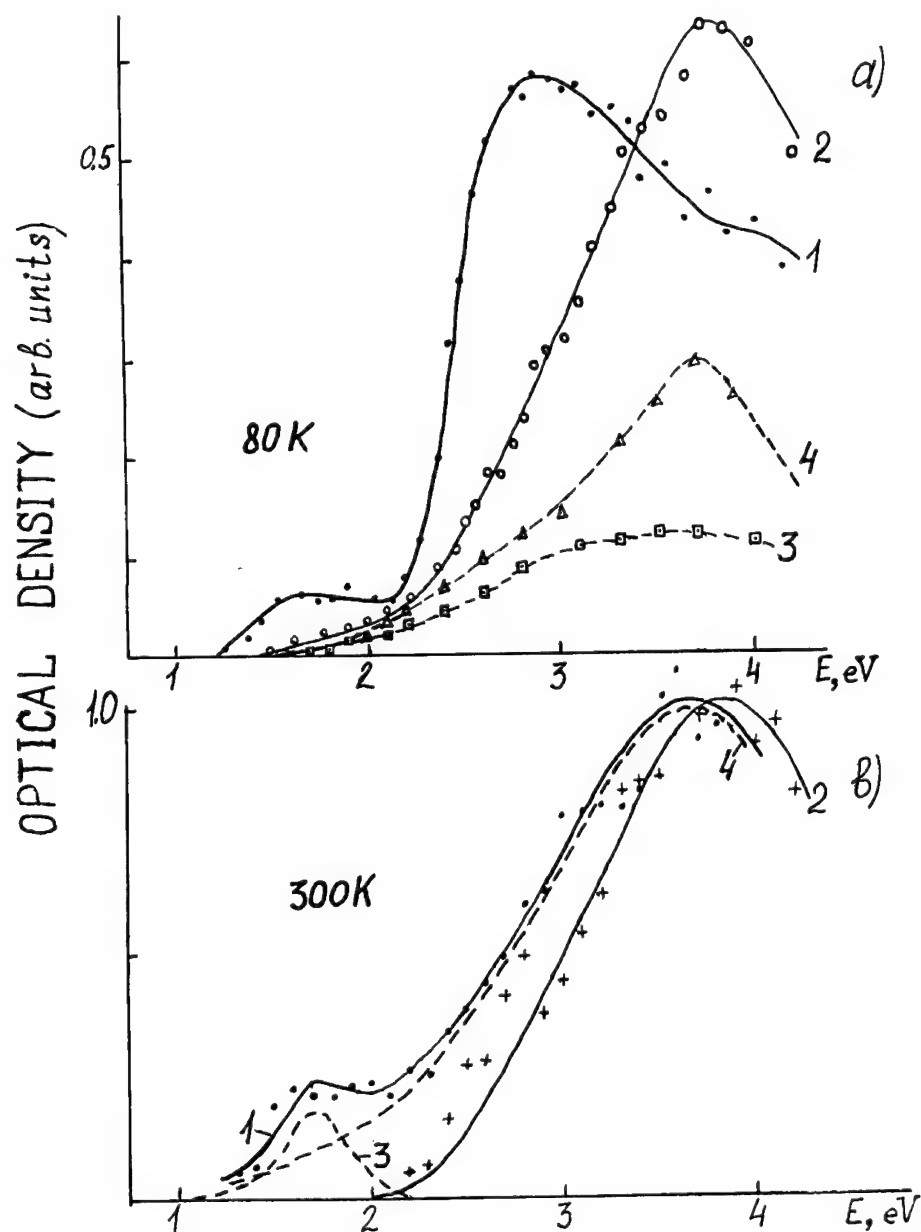


FIGURE 2 a) Polarized transient absorption spectra of BeO crystal taken 50 ns (1, 2) and 5 ms (3, 4) after irradiation with an electron pulse at 80 K. Closed circles and squares (1, 3) and open circles and triangles (2, 4) denote the data measured with \vec{E} perpendicular and \vec{E} parallel to C-axis, respectively. b) Polarized transient absorption spectra of BeO crystal taken 1500 ns after irradiation with an electron pulse at 300 K. Closed circles (1) and crosses (2) denote the data measured with \vec{E} perpendicular and \vec{E} parallel to C-axis, respectively. Solid curves (1, 2) are the calculated spectra and broken curves (3, 4) is a result of decomposing the (1) into two Gaussian shape curves.

The above-cited experimental data allow to adduce a hypothesis that component of the transient optical absorption with a lifetime of 6.5 ms is related with the STH since in its spectrum the band at 1.7 eV has not been found. A model of STH in oxides has been proposed in Ref.2. As opposed to V_k -centers in alkali-halide crystals the motion of STH in oxides can't be **frozen** completely as STH are small polarons being O⁻ ions. This assumption is based on optical and ESR studies of holes in alkaline-earth oxides **trapped** near a cation vacancy or impurity ions.³ According to these data at liquid helium temperature the hole tunnels from anion to anion around a defect for 10-1000 times per second. From this standpoint we studied the temperature dependences of the transient optical absorption decay. Based on the behaviour of decay of components 340 μ s and 6.5 ms we made a conclusion that STH absorption decay in BeO goes on according to the scheme: motion of STH to traps \rightarrow tunnel recombination with electron \rightarrow formation of STE \rightarrow radiative decay of STE. This scheme can be described by the following equation:

$$D = [D_{STE} + D_{STH}\{1 - \exp(-t/\tau_{STH})\}]\exp(-t/\tau_{STE}) + D_{STH} \bullet \exp(-t/\tau_{STH}) + D_s \bullet \exp(-t/\tau_s),$$

where τ_{STE} , τ_{STH} , τ_s , D_{STH} , D_s are decay times and optical absorption amplitudes of STE, STH and traps, respectively. The calculated curves correlate very well with experimental data. The 80-100 K range where the decay time of STH absorption does not depend on temperature can be considered to be an interval of their tunnel motion, Figure 1. At $T > 100$ K the process of thermally activated motion of hole polarons with the activation energy of 0.21 eV begins. In BeO STH and STE generation efficiency do not depend on temperature in the range 80-160 K which is due to the absence of competitive channels in comparison with alkali-halide crystals.

In the decay of optical absorption induced by electron pulse at 300 K a component coinciding in temperature-time parameters with triplet luminescence (π_2) of STE₂ has been found. It turned out to be so because in the range of $T > 260$ K a transformation of one STE type into another takes place. Figure 2 shows BeO transient optical absorption spectrum taken 1.5 μ s after irradiation with an electron pulse at 300 K. The comparison of optical absorption spectra of two STE types helps to make a conclusion that transitions in the electron components in the form of a 1.7 eV band with \vec{E} perpendicular to the c-axis are of similar origin. At the same time transient optical absorption in the hole component of STE₂ is shifted to the short-wave region and is more isotropic than that for STE₁. In order to interpret optical absorption of hole components of STE and STH in BeO we have chosen a model of small polarons in the form of O⁻ ion earlier used by Schirmer.⁴ Dichroism of short-wave bands of hole-trapped centers is related to different symmetry of two excited states, however, for STE and STH the succession of these states is inverse. Polaron transitions have oscillator strength about 0.3-0.4. The weakness of electron component absorption band is indicative of oscillator strength that is considerably less than the one which could be expected for spin-allowed transitions unlike the allowed transitions in STE electron component in alkali-halides.

In BeO wurtzite lattice there are two types of bonding, i.e. Be-O axial and Be-O non-axial having different directions relative to the optical C-axis of the crystal. We assumed the hole component of one STE to be a small polaron in the form of O⁻ ion occupying an axial position. Since luminescences π_1 and σ_1 are strongly polarized perpendicular and parallel to the C-axis we ascribed them to triplet and singlet transitions in STE₁ whose axis is almost parallel to O axial-Be bond directed along C-axis. There is unexpected inversion of STE₁ singlet and triplet levels in BeO compared with alkali halides. Additional support for this effect may be experimental evidence of the inversion of the normal ordering of the valence band spin-orbit splitting found earlier in MgO,⁵ not long ago theoretically

explained in Ref.6. At the same time the σ_2 and π_2 luminescence may be related to the STE₂ singlet and triplet transitions. The similar singlet and triplet luminescence spectra have been found for STE in rare gas crystals. Polarization degree analysis of the σ_2 luminescence shows that STE₂ axis is almost coincident with the O non-axial-Be direction. We suggested that STE₂ hole component is of the form of an O⁻ ion occupying non-axial position. From the point of view of the STE₁ and STE₂ models the non-radiative transitions from STE₁ triplet state to STE₂ triplet state can be explained by thermally activated jump of the hole component of the STE from O axial- to O non-axial.

REFERENCES

1. R. T. Williams, M. N. Kabler, *Phys. Rev.* **B.9**, N4, 1897 (1974).
2. R. T. Cox, *Recent Dev. Condens. Matter. Phys. (New- York-London)* **3**, 355 (1981).
3. B. Henderson, J. E. Wertz, *Defects in the alkaline earth oxides with application to radiation damage and catalysis* (Taylor and Fransis, London, 1977), 159.
4. O. F. Schirmer, *J. Phys. Chem. Sol.* **29**, 1407 (1968).
5. R. C. Whited, Ch. J. Flaten, W. C. Walker, *Solid State Commun.* **13**, 1903 (1973).
6. V. A. Lobatch, *Fizika tverdogo tela.* **33**, N9, 2632 (1991).

THE EXPERIMENTAL OBSERVATION OF THE POTENTIAL BARRIER FOR SELF-TRAPPED EXCITON DECAY INTO F-H PAIR IN KCl-Na CRYSTALS

S. A. CHERNOV and V. V. GAVRILOV

*Institute of Solid State Physics, University of Latvia 8 Kengaraga st., LV-1063, Riga,
Latvia*

The optical absorption induced by the electron pulse irradiation of Na⁺ doped KCl has been measured. Transient optical absorption band of F_A centers was observed at 80 K (LNT). The temperature dependence of F_A center formation was studied. It is proposed that the obtained activation energy originates from the potential barrier between the STE perturbed by the cation impurity and the nearest neighbour F_A-H pair. The mechanism of the suppression of the defect formation by the monovalent cation impurity in alkali halide crystals is discussed.

Key words: transient absorption, self-trapped exciton, Frenkel defects, potential barrier, cation impurity, KCl-Na.

1 INTRODUCTION

Color center production in alkali halide crystals doped with the homologous cation impurities has been intensively studied.¹⁻⁵ However, the detailed mechanism of the influence of the impurity cation on the radiation defect formation is not clear yet. It has been shown that the STE is trapped near the impurity cation site such as KBr:Li and KBr:Na resulting in a significant potential barrier on the way toward further separation of the F-H pair. The presence of a potential bump is expected to influence the low temperature F center creation.⁶ In this paper we shall analyze from this point of view our experimental data on defect generation of KCl-Na crystals.

2 EXPERIMENTAL

Single crystal of KCl with Na⁺ ion concentration ≈ 0.5 mol% have been investigated.

The experiment was performed under irradiation with nanosecond electron pulses. The high-power electron accelerator was able to produce single electron pulses with the following parameters: electron energy 300 keV, pulse duration 5 ns, current density 100 A/cm.² The transient absorption was detected by the fast photomultiplier and oscilloscope using monochromator DMR-4.

3 RESULTS AND DISCUSSION

We have shown that at 15 K the absorption spectrum of KCl:Na crystals measured just after electron pulse is the same as in the case of pure KCl crystals. At 80 K the F-absorption band measured just after the electron pulse has a larger halfwidth than in pure crystals and a shoulder at its longwave length side. However, the F-band absorption spectra measured 100 ns after the electron pulse are again identical in both crystals. Figure 1 shows the spectrum of F centers, which recombined during 100 ns. As it is seen from Figure 1, the absorption spectrum consists of the F and F_A absorption bands. Thus, it can

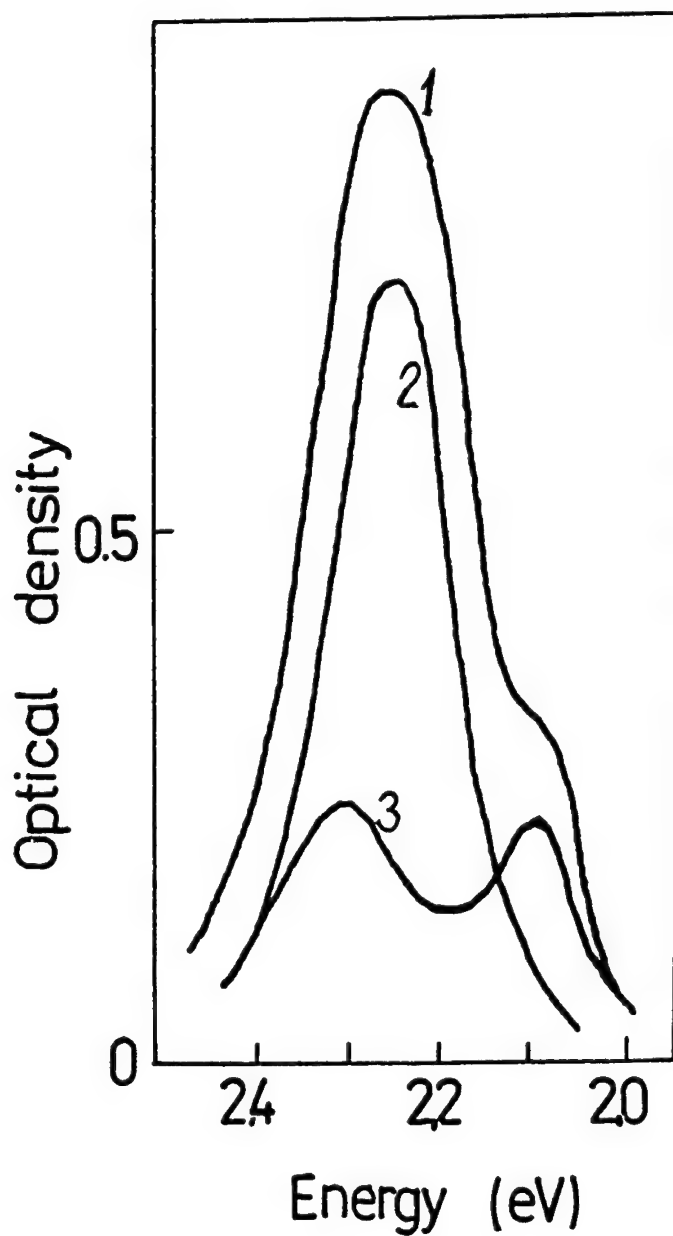


FIGURE 1 Transient absorption spectra due to F centers produced in KCl:Na at 80 K after irradiation by an electron pulse:

- 1) the difference between the optical absorption change measured with delay 2 ns and 100 ns after the electron pulse;
- 2) the absorption spectrum due to F centers;
- 3) the absorption spectrum due to F_A centers.

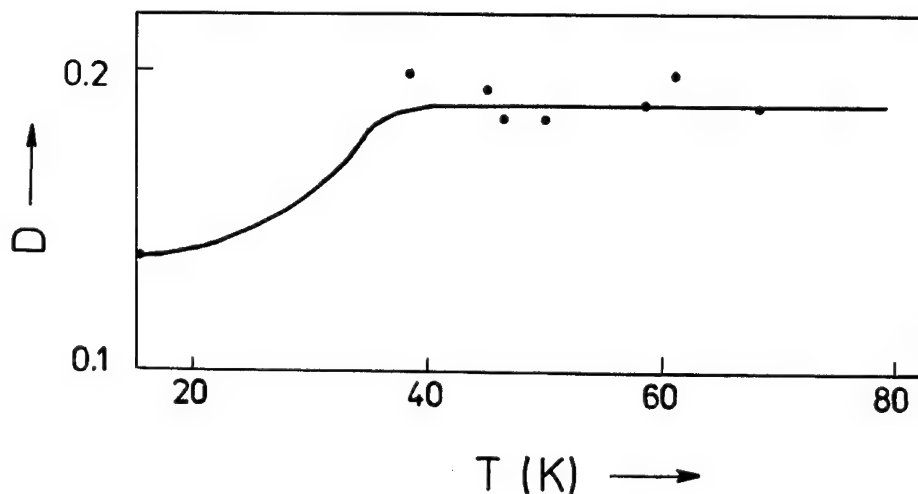


FIGURE 2 Temperature dependence of the optical density at 2.075 eV produced in KCl:Na after electron pulse irradiation.

be concluded that the F_A -H centers are indeed produced due to the impurity—*perturbed* self-trapped exciton (STE) decay.^{7,8}

Next, let us discuss briefly the temperature dependence of the optical absorption at 2.075 eV observed under electron irradiation. This band is known to be the absorption peak due to F_A centers.⁹ As it is seen from Figure 2, when irradiation temperature increases from 15 K to 40 K, the appreciable growth of the F_A centers concentration measured just after electron pulse is observed. Therefore, it is reasonable to conclude that results of Figure 2 indicate that the probability of the perturbed-exciton decay into F_A -H defect pair increases with the temperature rise. From the temperature dependence of $\ln OD$ as a function of inverse temperature (Figure 3), one can easily obtain the activation energy of $E = 12$ meV. In our opinion it is reasonable to ascribe this activation energy to the potential barrier between the first (perturbed STE) and the second nearest neighbor F_A -H pair configuration on the APES.

It is also very interesting, to study the kinetics of annihilation of these F_A centers. At LNT the kinetics of F center decay in pure KCl crystals can be described by the superposition of three exponentials with the distinctive parameters: $\tau_1 = 15$ ns, $\tau_2 = 70$ ns and $\tau_3 = 5$ μ s and about 50% of total F center concentration are destroyed in the former component. In the case of F_A center decay in KCl:Na up to 80–90% of the F-centers are destroyed in the former component. Since the annihilation of F-H pairs at LNT in this range of times is due to the electron tunneling, decay times are determined

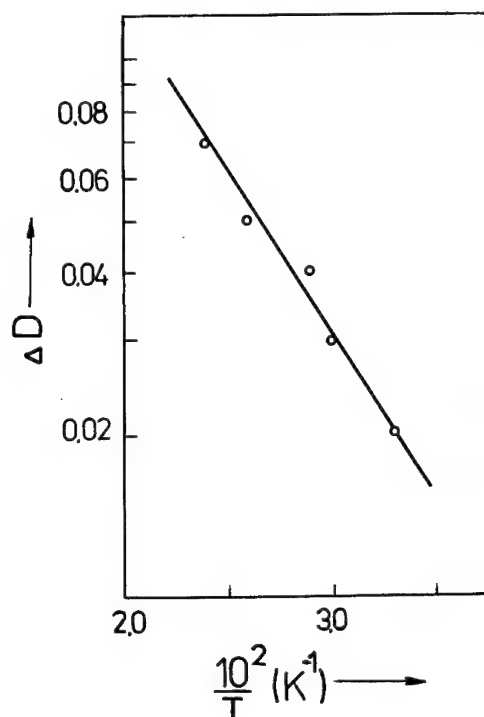


FIGURE 3 Arrhenius plot of the optical density at 2.075 eV produced in KCl:Na after electron pulse irradiation.

directly by the distances between F and H centers. Thus, the qualitative increase in a number of the F centers recombining with the fast component could be explained by a predominant creation of the nearest F-H pairs, created in the case of the perturbed-exciton decay in KCl:Na crystal, compared with STE decay in the perfect lattice. From this point of view it is possible to explain the F_A center absence in the absorption spectra of the stable defects and the suppression of the stable defects formation by Na^+ and Li^+ impurity in KCl and KBr at low temperature (LHeT and LNT). The exciton state which is responsible for the creation of the F-H pair is trapped by the Na^+ or Li^+ impurity. The return of this state of the perturbed exciton to the ground state is accompanied with the emission of phonons at LHeT or formation of the short lived transient F_A -H pair at LNT, which results in the decrease of the production efficiency of stable F centers.

REFERENCES

1. Ch. B. Luschnik, R. J. Gindina, N. E. Luschnik, M. M. Tairov and K. Sh. Shunkeev, *Trudy Inst. Fiz. Akad. Nauk ESSR* **53**, 146 (1982).
2. A. K. Dauletbdkova, A. T. Akilbekov, A. A. Elango, *Fiz. Tverd. Tela (USSR)* **24**, 2920 (1982).
3. K. Tanimura, T. Okada, *Phys. Rev.* **B13**, 1811 (1976).
4. K. Tanimura, *J. Phys. Chem. Solids* **39**, 735 (1978).
5. M. Saidoh, N. Itoh, *J. Phys. Soc. Jap.* **29**, 156 (1970).
6. K. S. Song, Y. Cai, *J. Phys. Soc. Jap.* **60**, 3172 (1991).

7. S. A. Chernov, V. V. Gavrilov, A. A. Malishev, *Fiz. Tverd. Tela (USSR)* **26**, 289 (1984).
8. S. S. Etsin, *Izv. Akad. Nauk Latv. SSR* No. 5, 36 (1985).
9. F. Luty. In *Physics of Color Centres*, ed. by W. B. Fowler 182, Acad. Press (1968).

LUMINESCENCE OF ON- AND OFF-CENTER STE IN ABX_3 CRYSTALS

A. S. VOLOSHINOVSKIY, V. B. MIKHAILIK and P. A. RODNYI

*Lviv State University, Lviv, 290005, Ukraine,
State Technical University, St.-Petersburg, 195251, Russia*

The study of spectral and decay parameters of self-trapped exciton emission in crystals $NaMgF_3$, $KMgF_3$, $RbMgF_3$, $CsMgF_3$, $KMgCl_3$, $KCaCl_3$ and $RbCaCl_3$ is carried out. It is established that in all crystals the intrinsic luminescence contains spectrally-unresolved fast (nanoseconds) and slow (about 1 μs) components.

The self-trapped excitons (STE's) have been observed in a wide variety of ionic crystals.¹ The STE luminescence bands in alkali halide crystals have been classified into three groups I, II and III, in order of increasing Stokes shift. A simple model for the initial state of type I emission is an on-center STE with $V_k + e^-$ configuration. Types II and III come evidently from two different off-center configurations, which resemble more or less the nearest-neighbour F–H pair. The luminescence bands with decay time shorter than 5 ns (σ -bands) belong to type I. The bands of type III usually have a much longer decay time (π -bands). The degree of the off-center relaxation in the STE correlates with Rabin-Klick parameter S/D (S is the space between adjacent halogen ions, and D is the diameter of halogen atom).¹ In crystals with large S/D value ($S/D > 0.35$) the σ -bands are located approximately 1–2 eV above the π -band. In case $NaBr$ and NaI ($S/D < 0.35$) fast and slow components have the same spectral position.

It is interesting whether the STE model is valid for crystals with more complicated structure, such as ternary halide compounds ABX_3 . Here we made the attempts to perform a detailed study of luminescence of some fluorides and chlorides with perovskite structure. The intrinsic luminescence was studied early only in $KMgF_3$ ² and $RbMgF_3$.³

Spectra and decay time of luminescence are measured under pulsed X-ray excitation (1 ns, 35 kV) at 77 K. The ABX_3 luminescence spectra contain the broad single bands which are shifted from absorption edge by nearly 5 eV in chlorides and more than 8 eV in fluorides. The spectrum of $RbMgF_3$ is in a good agreement with short-wave emission band of the crystal at 10 K.³ In $KMgF_3$ the 3.7 eV luminescence band of STE reported in² was not observed at 77 K due to temperature quenching. We detected only long-wave tail of luminescence band which is attributed to radiative core-valence transitions in $KMgF_3$.⁴

The luminescence of the studied ABX_3 crystals contains two components, namely the fast σ -component with decay time less than 10 ns and the slow π -component with that about 1 μs . As example the decay profiles of luminescence in $NaMgF_3$ and $RbMgF_3$ are presented in Figure 1.

In all crystals the fast component has a considerable intensity—this fact allowed us to carry out the measurements of time-resolved spectra of luminescence. It was found that the spectra of fast and slow components coincide. It means a slight splitting of the initial singlet and triplet states of STE or their mixing.

Measured luminescence parameters are summarized in Table I.

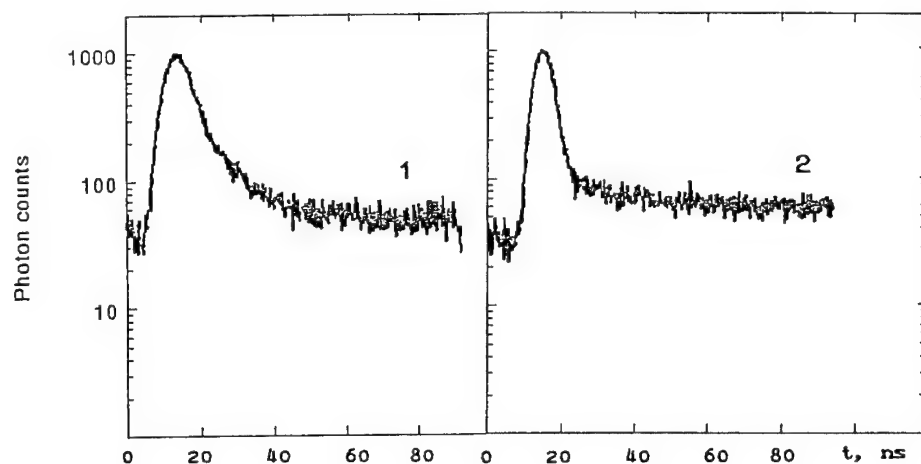
FIGURE 1 Luminescence decay curves of NaMgF₃ (1) and RbMgF₃ at 77 K.

Table I

crystal	1s exciton peak (eV)	STE emission band (eV)	band width (eV)	decay time (ns)
KCaCl ₃	8.0	2.75	0.65	5.2
RbCaCl ₃	7.3	2.65	0.5	3.9
KMgCl ₃		3.25	0.75	3.7
NaMgF ₃	11.6	3.25	0.9	4.1
KMgF ₃	11.8	3.7		0.9
RbMgF ₃		4.25	0.95	2.0
CsMgF ₃		3.3	1.25	2.4

The relative Stokes shifts of ABX₃ are bigger than 0.6 and by analogy with alkali halides these crystals should be related to group III in which the coincidence of σ - and π -bands was not observed. Alternatively, the ABX₃ have large variance of Rabin-Klick parameter S/D. In chlorides this parameter is small $S/D < 0.3$ caused by densified anion packing. Thus the on-center STE can be realized in chlorides studied. The condition for off-center STE has to be proper for fluorides having $S/D > 0.3$. There is an important feature of the crystals with perovskite structure: the point symmetry of V_k-center (and on-center STE) in C_{2v}.

We can use a new approach based on Jahn-Teller effect to explain the mutual spectral position of the σ - and π -bands of the crystals.¹ Since each luminescent state corresponds to a minimum of the adiabatic potential-energy surface (APES) of the lowest state of the STE, the capability of classifying of the excitons into three cases appear. This situation is illustrated in Figure 2. Three possible variants of schematic representation of the singlet and triplet states of the lowest APES are shown. Q₂ represents the off-center relaxation. Figure 2a shows the case when Jahn-Teller effect has not appear. The coincidence of σ - and π -emission in Q₂ = 0 (on-center STE) is displayed (the case of ABCl₃ crystals).

The other cases of energy instability caused by Jahn-Teller effect are presented in Figure 2b and 2c. In case 2b the energy instability exists only for triplet state. Here triplet STE slides down toward the off-center position and separated σ - and π -bands may be

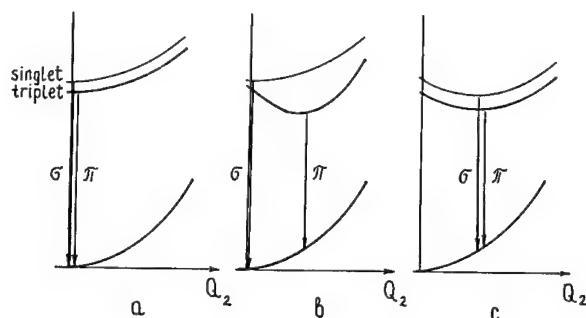


FIGURE 2 Schematic representation of adiabatic potentials for STE's (see text).

observed (some alkali halides). Figure 2c shows the situations of mutual mixing of singlet and triplet levels resulting in energy instability for both singlet and triplet states. Additional minima at a nearly parallel APES's arise. Relaxed excitons occupies the off-center position too, however σ - and π -emissions have almost the same spectral shape (perhaps the case of ABF₃ crystals). Since the spectral and decay time peculiarities of STE luminescence observed in Figure 2a and 2c are very close, only more essential Stokes shift may be a characteristic of the off-center STE in case 2c.

REFERENCES

1. K. S. Song, R. T. Williams, Self-Trapped Excitons, *Springer Series in Solid State Sciences* vol. 105 (Springer-Verlag, Heidelberg, Berlin) 1993.
2. W. Hayes, I. B. Owen, G. I. Pilipenko, *J. Phys. C*, **8**, L407 (1975).
3. K. S. Song, C. H. Leung and R. W. Williams, *J. Phys. Soc. Jap.* **59**, 1881 (1990).
4. P. A. Rodnyi and M. A. Terekhin, in: *Synchrotron Radiation and Dynamic Phenomena/Particles and Fields Series* **49**, 317 (1992).

PHONON ASSISTED EXCITONIC LUMINESCENCE IN CsPbCl_3

I. BALTOG,^a S. LEFRANT,^b C. DIMOFTE,^a and L. MIHUT,^a

^aInstitute of Atomic Physics, IFTM, Lab 13, P. O. Box MG7, R-76900, Bucharest, Romania; ^bInstitute des Matériaux de Nantes, Lab de Physique Cristalline, 2, rue de la Houssinière, F-44072 Nantes Cedex, France

This work presents new data concerning CsPbCl_3 crystal luminescence under high excitation intensity. Six maxima are evidenced in the low temperature (LNT) spectrum. Using two geometries of measurement, particular features of the complex emission spectrum were pointed out which allowed us to associate some bands with phonon shifted free exciton lines, and one of them, located at 23880 cm^{-1} was attributed to a stimulated emission due to an exciton-free electron inelastic collision process.

The researches regarding the optical properties of perovskite-type compounds of chemical formula AMX_3 ($A = \text{Cs, Rb}; M = \text{Pb, Sn, Cd}; X = \text{Cl, Br}$) aroused lately a great interest. This interest is generated both by the understanding and correlation of optical properties variations with the specific phase transitions and by the possible applications in optoacoustics and scintillation techniques.

For CsPbCl_3 crystals the X-ray measurements and the ultraviolet photoelectron spectra suggest that the first absorption peak is due to exciton absorption, closely related to the intra-ionic $6s \rightarrow 6p$ transition in Pb^{2+} ions.¹ The few results reported so far on CsPbCl_3 crystal luminescence conclude that its low temperature emission spectrum is dominated by a complex excitonic emission, dependent on both the excitation energy and intensity.^{2,3}

This paper presents new data concerning the gradual generation of a phonon structure in the CsPbCl_3 luminescence spectrum at 77 K by increasing the excitation intensity. For a certain measuring geometry an excitonic stimulated emission is also emphasized.

The samples were cleaved from a monocrystal grown by the Bridgman method using an equimolar CsCl and PbCl_2 mixture. The emission spectra were measured in a right angle geometry, in a nanosecond time scale, with a double monochromator. The excitation source was a nitrogen laser with a FWHM of 4 ns, operated at 15 Hz repetition rate. Two excitation methods were used: the first with a circular focalization of the radiation onto the surface of the sample, at 45° incidence angle (Figure 1a), adequate to the spectral analysis of the emission, and the second with a linear focalization (cylindrical lens) along the observation direction, at 9° incidence angle (Figure 1b); this geometry minimizes the autoabsorption losses, allows the separation and points out a stimulated emission. The maximum excitation density used ($I_{\text{excit}} = 100\text{ a.u.}$) was 400 kW/cm^2 .

In Figure 1 a complex emission, strongly dependent on the excitation intensity is presented. The assignation of the emission bands was made by combining the deconvolution analysis of emission spectra with the cleaning of spectra by temperature rising, the last procedure being illustrated in Figure 2. Thus, in the spectra presented in Figure 1, 6 maxima were identified with a $\pm 10\text{ cm}^{-1}$ precision: $E_0 = 24\,290\text{ cm}^{-1}$, $E_1 = E_0 - 110$, $E_2 = E_0 - 200$, $E_3 = E_0 - 310$, $E_4 = 23\,880\text{ cm}^{-1}$ and $E_5 = 23\,790\text{ cm}^{-1}$.

The $I_{\text{emis}} \approx (I_{\text{excit}})^{1.1}$ dependence of E_0 emission band confirms its association to the free exciton. This band presents at higher temperatures an almost symmetric broadening relative to the position of its maximum, which presents a Stokes shift less than 30 cm^{-1} .

The Stokes shifts of E_1, E_2 and E_3 maxima do not depend on temperature. The correlation of luminescence spectra with Raman spectrum (obtained at 77 K, under

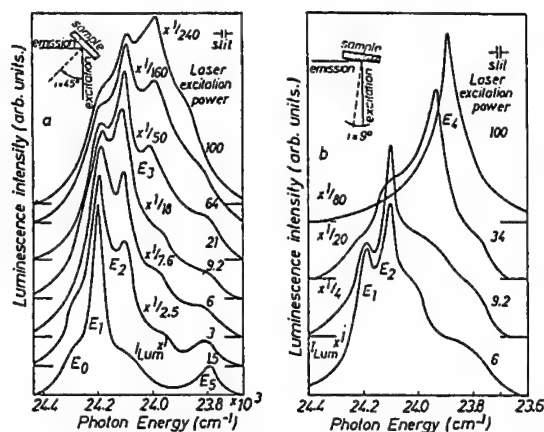


FIGURE 1 Luminescence spectra of the CsPbCl₃ crystal at 77K under various excitation densities ($\lambda_{\text{excit.}} = 337.1 \text{ nm}$).

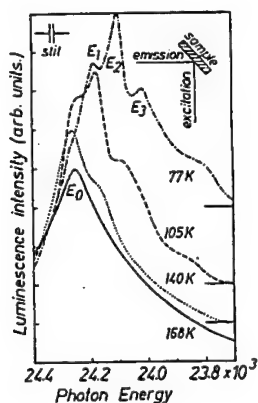


FIGURE 2 Temperature effect on the luminescence spectrum of CsPbCl₃ crystal.

$\lambda = 514.5 \text{ nm}$ excitation and in X(YX)Z measuring configuration) presented in Figure 3 shows that the Stokes shifts of E₁, E₂ and E₃ maxima relative to E₀ are connected with $\omega_{\text{TO}} = 110 \text{ cm}^{-1}$, $\omega_{\text{LO}} = 200 \text{ cm}^{-1}$ and $\omega_{\text{TO}} + \omega_{\text{LO}} = 310 \text{ cm}^{-1}$ respectively. The integrated intensity I_{area} of the complex emission spectrum (Figure 1a) depends on the excitation intensity with a law $I_{\text{area}} \approx (I_{\text{excit}})^{\alpha}$, where α lies in the range 2.0–1.8.

For the E₅ band the dependence on the excitation intensity is similar to that observed for E₀ band. A tempting explanation is to consider this band as a phonon replica of the free exciton line involving the vibrational modes at 480 cm^{-1} identified by Raman spectroscopy (Figure 3).

E₄ peak, well observed in the second measuring geometry (Figure 1b), has a totally different behaviour: it presents an almost quadratic dependence on the excitation intensity,

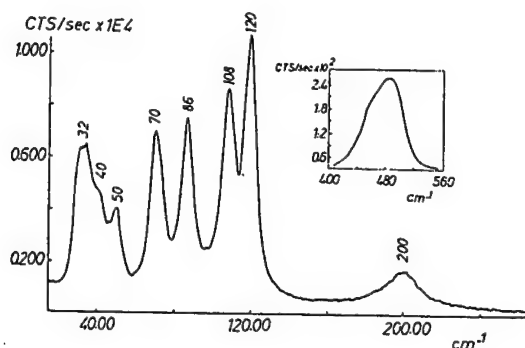


FIGURE 3 Raman spectrum of CsPbCl₃ crystal at 77 K.

$I_{lum} \approx (I_{excit})^{1.9}$, accompanied by a gradual Stokes shift and a decrease of its FWHM. Unlike the E_1 , E_2 and E_3 maxima—for which a gradual decrease of the exponent α to a value slightly sublinear can be observed at high excitation intensities—for the E_4 maximum a growing tendency of this exponent exists at high excitation intensities. This peak is fastest quenched when temperature is rising; it also presents an exponential enhancement with respect to the length of the excited area in the crystal.

These peculiarities of E_4 band lead us to the conclusion that it has to be associated to a stimulated emission probably due to an exciton-electron inelastic collision process. The well-marked increased of this band at high excitation intensities results from the growth of free electron density in volumn unit. The subsequent increase of the inelastic collisions rate generates a gradual Stokes shift of peak's position. The second observation geometry (Figure 1b)—suitable for luminescence radiation observation along the excited volume—points out a spectral self-selecting process of the emission, specific to an optical stimulation process, experimentally emphasized by a decrease of FWHM and by a higher directivity of the luminescence radiation.

REFERENCES

1. Ito, H., Omuki, H. and Onaka, R., *J. Phys. Soc. Japan*, **45**, 2043 (1978).
2. Fröhlich, D., Heidrich, K. and Kunzel, H., *J. Luminescence*, **18/19**, 385 (1979).
3. Pashuk, I. P., Pidzyrilo, N. S. and Matsko, M. G., *Fiz. Tverd. Tela*, **23**, 2162 (1981).

OPTICAL PROPERTIES OF Pb^{2+} -BASED AGGREGATED PHASE IN NaCl AND CsCl ALKALI HALIDE HOSTS

M. NIKL,^{*} K. POLAK,^{*} K. NITSCH,^{*} G. P. PAZZI,^{**} P. FABENI^{**}
and M. GURIOLI,^{***}

^{*}*Institute of Physics, Cukrovarnicka 10, 16200 Prague, Czech republic;* ^{***}*IROE, Via
Panciatichi 64, 50127 Florence, Italy;* ^{**}*LENS, University of Florence, Largo E. Fermi 2,
50125 Florence, Italy*

The absorption and steady state emission properties of Pb^{2+} -aggregated phase in NaCl and CsCl matrices are found to be close to those of the PbCl_2 and CsPbCl_3 bulk crystals, respectively. Much shorter picosecond decay times have been found for CsPbCl_3 -like aggregates in CsCl host with respect to the bulk CsPbCl_3 . It is ascribed to microscopic superradiance effect and together with the achieved high energy shift of the exciton absorption peak proves that the quantum confinement effect takes place in the observed emission in CsPbCl_3 -like aggregates. The autolocalisation of the cation exciton in PbCl_2 -like aggregates is considered to explain the absence of similar effects in Pb^{2+} -doped NaCl crystals.

Key words: alkali halides, lead aggregates, time-resolved luminescence, quantum confinement.

1 INTRODUCTION

Optical properties of foreign aggregated phases in crystal and glass matrices are the subject of the intensive research during the last years in connection with the study of quantum size effects, which can be well demonstrated in these systems.¹ The semiconductor microcrystallites with the structure of the known bulk materials dispersed in a dielectric matrix are the most suitable systems for such a study. Observed optical properties are strongly influenced when the dimensions of these aggregates (quantum dots QD) are less than about $10 \times R_B$, where R_B is the radius of the exciton in QD. Namely the broadening and high energy shift in the optical spectra were reported e.g. for CuCl QD in NaCl matrix² and extremely fast picosecond components were reported in similar system³ and explained by microscopic excitonic superradiance in the aggregates. Many of the observed phenomena can be explained as the consequence of the spatial confinement of the Wannier exciton motion in the aggregates.

It is our aim to introduce two new systems suitable for such studies— PbCl_2 -like phase and CsPbCl_3 -like phase in NaCl and CsCl host crystals, respectively.

2 EXPERIMENTAL

The crystals of NaCl:Pb (0.05% of PbCl_2 in the melt), CsCl:Pb (0.01% of PbCl_2 in the melt) and CsPbCl_3 were grown by Bridgman technique from chemicals purified by multiple zone melting. The samples of dimensions about $7 \times 7 \times 2$ mm were cleaved or cut from as grown crystal and polished. Thin film of CsPbCl_3 was obtained by evaporation of CsPbCl_3 bulk crystal from platinum crucible on quartz substrate in the vacuum. The details about experimental apparatuses used are reported elsewhere.⁵

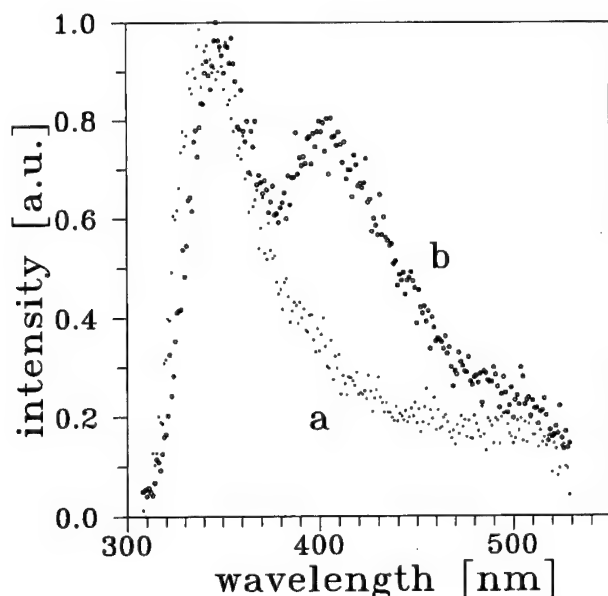


FIGURE 1 Emission spectra of long stored NaCl:Pb, $\lambda_{\text{ex}} = 275$ nm.
a) $T = 4.2$ K, b) $T = 20$ K.

3 EXPERIMENTAL RESULTS AND DISCUSSION

Absorption of NaCl:Pb (as received and long stored at 295 K (RT)) is very close to that of PbCl_2 thin film deposited on NaCl substrate. The Pb^{2+} cation exciton absorption peak is situated at about 272 nm at RT. Under 275 nm excitation two wide emission bands are observed in NaCl:Pb (peaking at ~ 340 and 410 nm) and energy transfer from the 340 to the 410 nm band is evident in the 10–80 K temperature range, see Figure 1. These observed characteristics are similar to the situation in PbCl_2 , where energy transfer is observed between the bands peaking at 330 and 420 nm in the 12–25 K temperature range.⁴ The decay kinetics in both systems is qualitatively similar, too. For NaCl:Pb at 4.2 K in the 330 nm wavelength emission, a fast (a few ns) and a slow (several tens of μs) components are observed and more than 90% of emission intensity is contained in the slow component. These results are comparable with the data reported for PbCl_2 crystal.⁴ These data allow the conclusion that small aggregates of PbCl_2 -like phase can be created in NaCl host.

Absorption of CsCl:Pb (as received sample) at $\lambda > 320$ nm is similar to that of CsPbCl_3 thin film, which shows sharp Pb^{2+} cation exciton absorption peak at 407 nm at RT. Just mentioned absorption structure for $\lambda > 320$ nm can be erased by quenching ($T > 400^\circ\text{C}$ for at least 30 min and fast cooling to RT) and reproduced again by annealing at $200 < T < 250^\circ\text{C}$. At the lower annealing temperatures clear high energy shift (up to 7 nm) of the sharp exciton absorption peak was achieved with respect to the as received or heavily annealed samples.

The emission spectra of CsCl:Pb and CsPbCl_3 in Figure 2 are quite similar peaking at about 419 nm at 10 K (the peak at the low energy side of the bulk CsPbCl_3 spectrum was

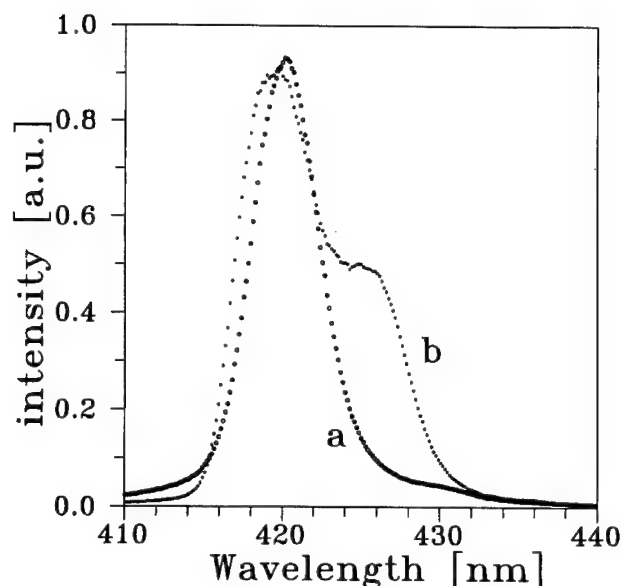


FIGURE 2 Emission spectra of CsCl:Pb and CsPbCl_3 single crystals.

a) CsCl:Pb , $\lambda_{\text{ex}} = 337 \text{ nm}$ (N_2 laser), $T = 10 \text{ K}$

b) CsPbCl_3 , $\lambda_{\text{ex}} = 337 \text{ nm}$ (N_2 laser), $T = 10 \text{ K}$

ascribed to the emission of Pb^{2+} perturbed sites mainly at the surface of the sample).⁵ The emission found in bulk CsPbCl_3 is ascribed to the radiative decay of Wannier exciton in Pb^{2+} sublattice as the top of CsPbCl_3 valence band and the bottom of conduction band are created by 6s and 6p wavefunctions of Pb^{2+} cations, respectively.⁶ Hence we can state that the microcrystallites of CsPbCl_3 are created in the CsCl host during the final cooling of the crystal in the growth process. However, the decay kinetics of the CsPbCl_3 aggregates is completely different from that observed in the bulk CsPbCl_3 . While in the bulk three decay times are observed at 418 nm (0.5, 2.8 and 12 ns),⁵ the luminescence decay in the CsPbCl_3 -like aggregates is single exponential with the decay time of about 30 ps only at 418 nm in as received samples. This effect can be explained under the assumption that the dimensions of the aggregates are less than about 10 nm (radius of Pb^{2+} cation exciton $R_B = 1 \text{ nm}$ in CsPbCl_3) and microscopic excitonic superradiance takes place enhancing the oscillator strength of the radiative transition. In Figure 3 the temperature dependence of the decay times is given at three different wavelengths within the emission band CsPbCl_3 -like QD. This temperature dependence can be tentatively explained as follows. At sufficiently low temperature, when exciton motion is possibly coherent throughout a QD, only the lowest-energy exciton state is significantly populated and the observed decay time is constant and characteristic of this level. At higher temperatures, because of the interaction of exciton with the acoustic phonons, the temporal and spatial coherence^{7,8} of macroscopic transition dipole moment is degrading and the decay time is increased. With the rising temperature also the nonradiative quenching processes are intensified (the overall luminescence intensity decreases with the temperature reaching at 180 K 5–10% of its value at 4.2 K). In case that these processes occur in the relaxed exciton excited state, they shorten the emission decay time, which may lead (because of competition with the previously mentioned process) to the maximum of the $\tau(T)$ dependence.

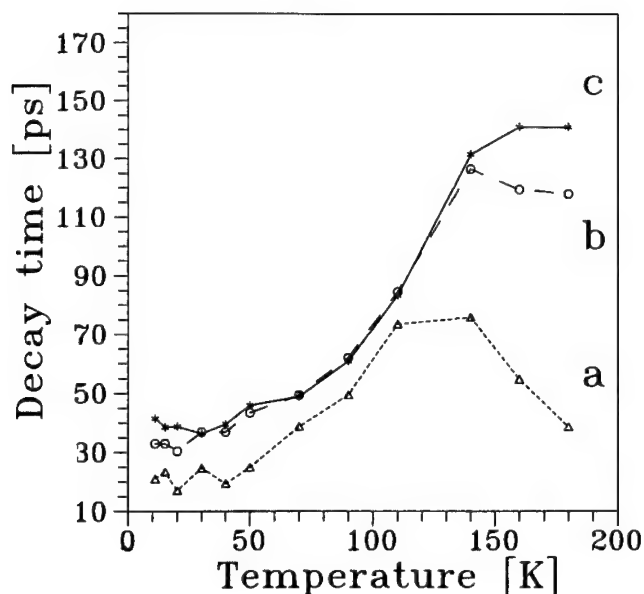


FIGURE 3 Temperature dependence of observed decay times of CsPbCl_3 -like QD at three different wavelengths, $\lambda_{\text{ex}} = 400$ nm. Because of the shift of the emission band with rising temperature, the wavelength was adjusted at every temperature to keep its relative position with respect to the maximum of emission band a constant:

- a) $\lambda_{\text{em}} = 413$ nm at 10 K
- b) $\lambda_{\text{em}} = 419$ nm at 10 K
- c) $\lambda_{\text{em}} = 426$ nm at 10 K.

The main reason for the different aggregate structure for Pb^{2+} -doped NaCl and CsCl host crystals is probably connected with the different structure of the host lattice (f.c.c. in NaCl and b.c.c. in CsCl crystal) and with the fact that there exists no stable ternary compound in Na-Pb-Cl system. The fact that no microscopic superradiance effect is observed in PbCl_2 -like aggregates in NaCl could be explained under the assumption that the exciton is immediately autolocalized after creation and at the lowest temperatures does not move through the aggregate at all. Autolocalization of cation exciton in PbCl_2 was generally accepted in the earlier works⁴ and big Stokes shift between the maximum of excitation and emission (~ 0.8 eV) also strongly supports this hypothesis. As for the difference in the temperature dependence of the energy transfer between 340 and 410 nm bands in PbCl_2 -like aggregates and equivalent process in the bulk PbCl_2 it is not clear, if the only reason is a slightly different structure of the aggregates with respect to the bulk material induced possibly by non-homogeneous pressure of the surrounding NaCl lattice. Also the quantum confinement effect can play some role, as thermally induced hopping of the localized exciton was proposed to explain the energy transfer between the 330 and 420 nm band in the bulk PbCl_2 .

ACKNOWLEDGEMENT

One of the authors (M. Nikl) undertook this work with the support of ICTP Programme for Training and Research in Italian Laboratories. The financial support of NATO grant under ref. HTECH.LG 931435 is also gratefully acknowledged. The authors are grateful to D. Citrin for fruitful discussion and to A. Cihlar for the growth of the crystals.

REFERENCES

1. F. Henneberger, *J. Puls: Optical Properties of Quantum Dots Embedded in Glass; in Optics of Semiconductor Nanostructures*, ed. by F. Henneberger, S. Schmitt-Rink, E. Gobel, Akademie Verlag 1993, p. 497-545.
2. T. Itoh, Y. Iwabuchi, T. Kiriara, *Phys. Stat. Sol. (b)* **146**, 531 (1988).
3. T. Itoh, M. Furumiya, T. Ikehara, *Sol. St. Comm.* **73**, 271 (1990).
4. K. Polak, D. J. S. Birch, M. Nikl, *Phys. Stat. Sol. (b)* **145**, 741 (1988) and *Phys. Stat. Sol. (b)* **165**, 611 (1991).
5. M. Nikl, E. Mihokova, K. Nitsch, K. Polak, M. Rodova, G. P. Pazzi, P. Fabeni, M. Gurioli: *Chem. Phys. Lett.* **220**, 14 (1994).
6. K. Heidrich, H. Kunzel, J. Treusch, *Sol. St. Comm.* **25**, 887 (1978).
7. D. S. Citrin, *Sol. St. Comm.* **84**, 281 (1992); *Phys. Rev. B* **47**, 3832 (1993).
8. F. C. Spano, J. R. Kuklinski, S. Mukamel, *Phys. Rev. Lett.* **65**, 311 (1990).

DYNAMICAL PROCESSES OF ORTHO- AND PARA-EXCITONS IN ALKALI IODIDES

KOICHI TOYODA, TORU TSUJIBAYASHI and TETSUSUKE HAYASHI*

*Department of Physics, Osaka Dental University, 1-4-4 Makino-honmachi, Hirakata, Osaka 573, Japan; *Faculty of Integrated Human Studies, Kyoto University, Kyoto 606-01, Japan*

Energy-transfer and self-trapping processes of orthoexcitons and paraexcitons in alkali iodides are studied. Intensities of emission bands caused by TI^+ impurities and the self-trapped excitons are measured with varying temperature and excitation photon-energy. It is clarified that free excitons participating in the energy transfer to TI^+ in KI and RbI are mainly paraexcitons. The intensity of the σ band increases gradually with elevating temperature in KI. The increase of the intensity will be attributed to a thermally activated process over a potential barrier.

Key words: orthoexciton, paraexciton, alkali iodide, self-trapped exciton, energy-transfer, TI^+ .

1 INTRODUCTION

In alkali iodides free exciton luminescence is observed in addition to the luminescence of self-trapped excitons (STEs). There exists a potential barrier between the free exciton (FE) state and the STE state,¹ and the barrier height for self-trapping was estimated at $10 \sim 30$ meV.² It has recently been clarified that the luminescence of FE in KI and RbI originates from paraexciton (total angular momentum $J = 2$) state,^{3,4} and that of NaI from orthoexciton ($J = 1$) state.⁵ The population distribution between $J = 2$ and $J = 1$ states is governed by the rate of relaxation via LO phonon scattering in these crystals.⁵ The result leads us that the role of spin multiplicity of FE must be considered for understanding the dynamical processes of FEs. It is well known that energy-transfer of FE to impurities occurs under excitation in the $n = 1$ exciton absorption band. However, it has not been examined how the two states, orthoexciton and paraexciton states, participate in the energy-transfer process.

The rate of energy-transfer of FE is influenced by the self-trapping rate. The dynamical processes of self-trapping have been intensively studied both theoretically and experimentally.⁶ In this paper we study the energy-transfer to TI^+ and self-trapping of FE in KI and RbI. A crystal of KI doped with TI by 0.03 mol% was grown by the Kyropoulos method. A single crystal of KI was obtained from the University of Utah, which crystal is referred to undoped KI below. We used a deuterium lamp as the excitation light source filtering with a single-path monochromator. An excimer laser pumped dye laser (Lambda Physik EMG103MSC and FL3002) was also used for the measurement of the intensity of the σ emission band.

2 RESULTS AND DISCUSSION

KI has two emission bands due to STE, σ and π bands. The σ band, which is observed at 4.13 eV, is mainly composed of a singlet component, and the π band, which is observed at 3.31 eV, is composed of a triplet component. Another band called Ex appears at 3.00 eV

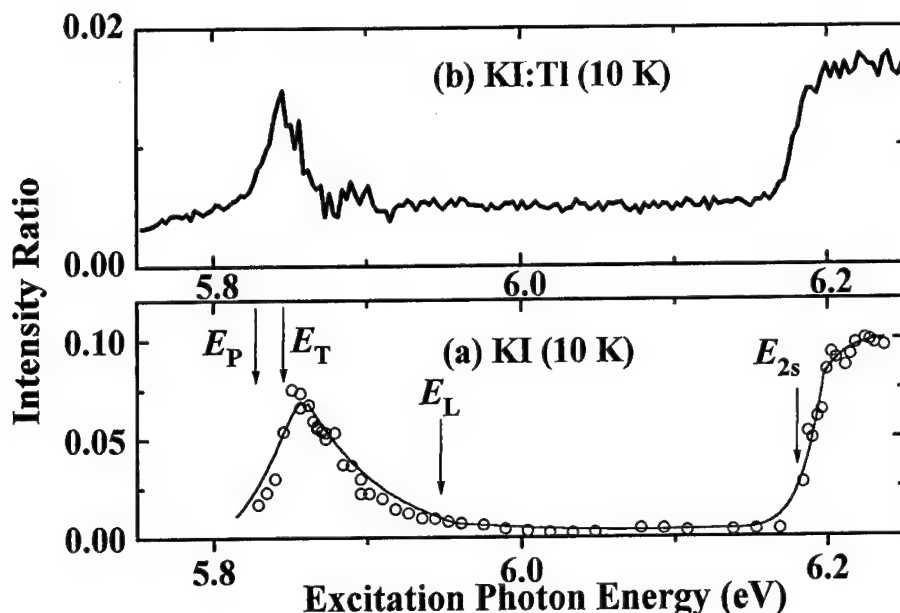


FIGURE 1 (a) The intensity of σ emission relative to that of the sum of π and Ex bands versus excitation photon-energy in undoped KI at 10 K. E_P , E_T , E_L , and E_{2s} indicate paraexciton, orthoexciton, longitudinal exciton, and the edge of the $n = 2$ exciton energies. (b) The intensity of σ emission relative to the total intensity of Tl^+ bands versus excitation photon-energy in KI:Tl at 10 K.

under excitation in the $n = 1$ exciton absorption band. The origin of the Ex band is identified as a Na-perturbed STE.⁷ Figure 1 (a) shows the intensity of the σ relative to the sum of intensities of the π and Ex bands in undoped KI.⁵ E_P , E_T , E_L , and E_{2s} indicate paraexciton, orthoexciton, longitudinal exciton, and the edge of the $n = 2$ exciton energies. The relative intensity decreases at E_{2s} with the decrease of the excitation energy, and it remains small between E_{2s} and E_L . It increases for a further decrease of the excitation energy and reaches a peak value around E_T . We revealed in a preceding paper⁵ that the σ band originates from the orthoexciton, and the π and Ex bands from the paraexciton in undoped KI. The small intensity between E_{2s} and E_L is attributed to an efficient scattering of FE from the orthoexciton state to the paraexciton state via LO-phonon emission. The increase toward E_T is interpreted as the reduction of the number of the scattering events to the paraexciton state.

KI doped with Tl has emission bands originating from Tl^+ at 2.9 eV and 3.7 eV under excitation in the $n = 1$ exciton absorption band of KI. The intensities of the bands are much larger than those of σ and π bands at 10 K, which exhibits an efficient energy-transfer of FE to Tl^+ . Figure 1 (b) shows the intensity of the σ band relative to the sum of intensities of the Tl^+ bands in KI doped with Tl by 0.03 mol% at 10 K. The spectral profile in Figure 1 (b) is quite similar to that in Figure 1 (a) although the peak value at E_T in Figure 1 (b) is somewhat smaller than that in Figure 1 (a). The similarity of the two spectra suggests that the paraexciton rather than the orthoexciton participates in the energy-transfer to Tl^+ . We obtained a similar result in RbI.

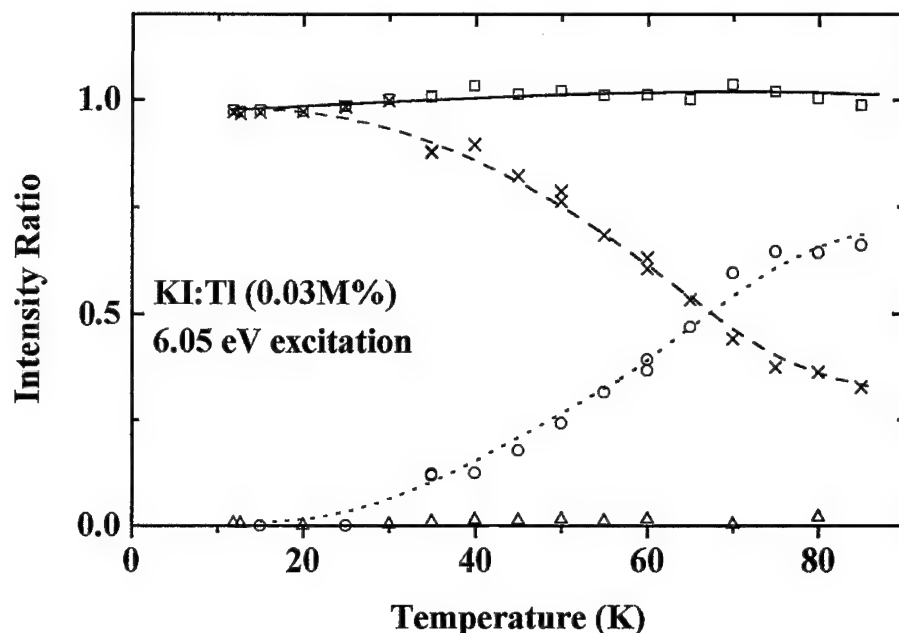


FIGURE 2 The intensities of emission bands in KI:Tl under excitation of 6.05 eV as a function of temperature. Crosses, triangles, circles, and squares indicate the intensities of the sum of Tl^+ bands, σ band, π band, and total emission, respectively.

In Figure 2 are shown intensities of σ , π , and Tl^+ (2.9 eV and 3.7 eV) bands by triangles, circles, and crosses, respectively, as a function of temperature under excitation at 6.05 eV. The sum of these emission bands is shown by the squares. The total yield of the luminescence remains constant with the change of temperature. The sum of the intensities of the Tl^+ bands decreases for the rise of temperature, which is compensated by the increase of the intensity of the π band. The fact can be interpreted as the increase of the self-trapping rate of FE and the consequent reduction of the energy-transfer rate to Tl^+ with elevating temperature as already discussed by Nishimura.⁸ The intensity of the σ band remains small, which is quite different from the behavior of the intensity of the π band. These facts support the result mentioned above that the paraexciton exclusively participates in the energy-transfer to Tl^+ . Most orthoexcitons will be scattered to the paraexciton state in a short time after photo-excitation. The paraexcitons will move in a crystal by diffusion to perform energy-transfer to Tl^+ . In undoped KI energy-transfer to residual Na impurities induces Ex emission.⁷ According to this interpretation, so far experimentally obtained value of the height of the adiabatic potential barrier from the FE state to the STE state, 20 ~ 30 meV in KI, should be that from the paraexciton state to the triplet STE state.

Figure 3 shows the intensity of the σ band in undoped KI as a function of temperature under excitation at 6.046 eV. It increases gradually with the rise of temperature from 10 K up to 70 K. A similar behavior was observed for σ band in the Tl^+ -doped KI in the temperature range above 20 K. The increase will be attributed to thermal activation of the orthoexciton over an adiabatic potential barrier to the singlet STE state. The residual

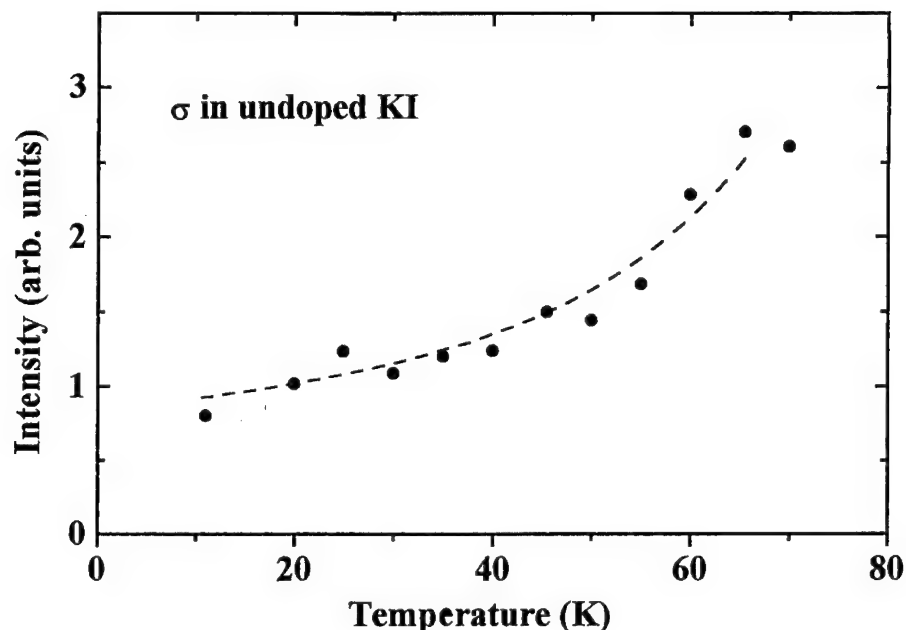


FIGURE 3 The intensity of σ band in undoped KI as a function of temperature. The excitation energy is 6.046 eV.

intensity at low temperatures indicates the existence of a component of which intensity is independent of temperature. Tunneling through the barrier and self-trapping by hot orthoexcitons are the candidates for the processes inducing such a component.

3 SUMMARY

The paraexcitons rather than the orthoexcitons participate in the energy-transfer to TI^+ in KI and RbI. The intensities of the TI^+ bands decrease for the increase of temperature, and the intensity of the π band increases complementarily. The intensity of the σ band remains small and increases only gradually with increasing temperature. The increase indicates the existence of a potential barrier between the orthoexciton state and the singlet STE state. Tunneling through the barrier and self-trapping of hot orthoexcitons may also contribute to the σ emission.

REFERENCES

1. K. Nasu and Y. Toyozawa, *J. Phys. Soc. Jpn.* **50**, 235 (1981).
2. Ch. B. Lushchik, *Excitons*, ed. E. I. Rashba and M. D. Sturge (North-Holland, Amsterdam, 1982) Chap. 12, and references therein.
3. K. Tanimura and N. Itoh, *Phys. Rev.* **B45**, 9417 (1992).
4. T. Kishigami-Tsujibayashi, K. Toyoda, and T. Hayashi, *Phys. Rev.* **B45**, 13737 (1992).

5. T. Tsujibayashi-Kishigami, *J. Phys. Soc. Jpn.* **63**, 335 (1994).
6. K. S. Song and R. T. Williams, *Self-trapped Excitons* (Springer, Berlin, 1993), and references therein.
7. T. Hayashi, T. Yanase, T. Matsumoto, K. Kan'no, K. Toyoda, and Y. Nakai, *J. Phys. Soc. Jpn.* **61**, 1098 (1992).
8. H. Nishimura, *Defect Processes Induced by Electronic Excitation in Insulators*, ed. N. Itoh (World Scientific, Singapore, 1989), and references therein.

DEFECTS AND LUMINESCENCE IN PURE AND I-DOPED AgBr CRYSTALS

L. NAGLI, A. SHMILEVICH, A. KATZIR and N. KRISTIANPOLLER

School of Physics and Astronomy, Tel-Aviv University, 69978, Israel

A main emission band appeared in the pure and lightly I-doped samples at 2.5 eV. The decay times of the luminescence pulse were 16 and 30 μsec in the pure and doped samples respectively. The temperature dependence of the decay time, the thermal activation energy and the halfwidth of the 2.5 eV emission of the doped samples also differed from those of the pure crystals. These difference indicate that the process responsible for the emission in the pure crystals differs from that in the I-doped samples. The 2.5 eV emission in the pure crystals may be due to a radiative decay of an exciton bound to an intrinsic defect. This is supported by the recorded effects of thermal treatment and of plastic deformation on this emission in the pure crystals.

Luminescence methods were applied for the study of optical properties and of defects induced in silver halides by impurities and by thermal and mechanical treatment. Pure and I-doped AgBr crystals were investigated. Some practical motivation for this study was that IR-transmitting fibers are extruded from silver halide crystals and that the properties of the starting materials are of importance for the properties of the resultant fibers.^{1,2}

The pure and I-doped crystals, used for our studies, were grown in our laboratory by the Bridgman-Stockbarger method using ultrapure starting materials. For the study of the effects of heating on the optical properties, the samples were heated to 350°C in a dry N₂ atmosphere and then either rapidly quenched (3–5 min) or slowly cooled (~ 5 hours) to room temperature (RT). The luminescence was excited between 15 and 120 K by monochromatic light using either a continuous 150 W high pressure xenon lamp or a pulse source and a grating monochromator. The rise and decay times of the exciting pulse were about 20 nsec and 0.1 μsec respectively.

The main emission band appeared in the pure AgBr crystals at 15 K at 2.5 eV and an additional band at 2.15 eV (Figure 1, curve a). In the slightly I-doped samples (up to 0.01 mol%) the main band also appeared at 2.5 eV but its half-width was 0.15 eV compared to 0.13 eV in the pure crystals. For higher iodine concentrations the emission maximum shifted to lower energies (2.34 eV for 4 m%); the half-width was in this case 0.18 eV (Figure 1, curve b).

Heating of the pure AgBr samples to 650 K in a nitrogen atmosphere and fast recooling to RT caused a strong decrease in the intensities of the 2.5 and 2.15 eV bands and the appearance of an additional band at 1.7 eV (Figure 1, curve c); the I-doped samples were not affected by this thermal treatment.

Our time resolved luminescence measurements have shown, that the decay time of the emission near 2.5 eV in the I-doped samples is 30 μsec , compared to 16 μsec in the pure crystals, and does not dependent on the I-concentration. These results fit previously reported data.^{3,4} The temperature dependence of the decay time of the I-doped samples also markedly differed from that in the pure AgBr crystals (Figure 2). The thermal activation energy of the decay was evaluated from the decay curves and was found to be 0.09 eV and 0.038 eV for the pure and I-doped samples respectively (Figure 2).

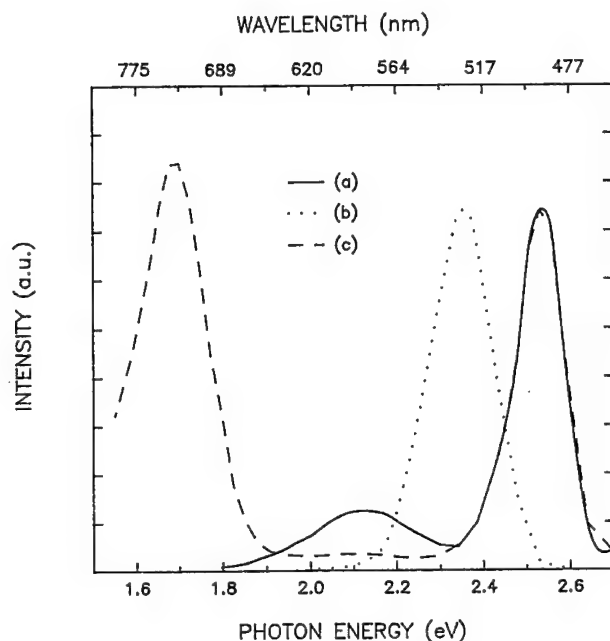


FIGURE 1 Emission spectra at 15 K of: (a) a pure untreated AgBr crystals; (b) an I-doped (4 m%) sample and (c) an pure crystal after thermal treatment at 650 K; the luminescence intensities in curve c are enlarged by a factor of 10.

It has previously been suggested that the main emission band at 2.5 eV is due to a radiative decay of an exciton bound to an I-ion in the nominally pure as in the I-doped AgBr crystals (e.g. 3–5). The here observed differences in the decay time, in its temperature dependence and in the thermal activation energies as well as in the halfwidth of the 2.5 eV emission band indicate that the process, responsible for this band in the pure crystal, differs from that in the I-doped AgBr crystals. The exciton responsible for the 2.5 eV emission in the pure AgBr crystals may be bound to an intrinsic defect, such as a cation vacancy, interstitial silver ion or dislocation, rather than to a casual I-impurity. This is supported by the finding that the thermal treatment caused significant changes in the intensity and in the spectral composition of the emission in the pure samples, but did not influence the emission of any of the I-doped samples. It is well known that thermal treatment as well as plastic deformation may strongly influence the concentration of intrinsic crystal defects.^{6,7} Preliminary results of our recent investigations on effects of pressure on the 2.5 eV emission have shown that in pure AgBr crystals the intensity of this band notably decreases with plastic deformation, while in the I-doped samples no such effect was observed.

REFERENCES

1. D. Gal and A. Katzir, IEEE, *J. Quant. Elect.* **QE-23**, 1827 (1987).
2. F. Moser, N. Barkay, A. Levite, E. Margalit, I. Paiss, A. Sa'ar, I. Schnitzer, A. Zur and A. Katzir, *Proc. SPIE* **1228**, 28 (1990).

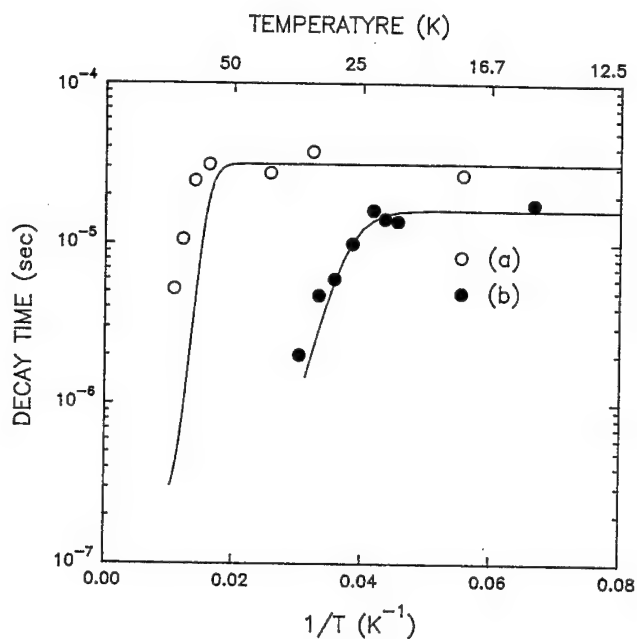


FIGURE 2 The temperature dependence of the decay time of the luminescence pulse for: (a) AgBr:I (4 m%); (b) pure AgBr. The solid lines are best fits of theoretical equations to the experimental data.

3. F. Moser and S. Lyu, *J. of Luminesc.* **3**, 447 (1971).
4. M. Tsukakashi and H. Kanzaki, *J. Phys. Soc. Japan*, **30**, 1423 (1971).
5. A. Marchetti and M. Burberry, *Phys. Rev. B.*, **28**, 2130 (1983).
6. R. Mott and R. Gurny, *Electronic Processes in Ionic Crystals*, Dover Pub. Inc., NY, 1964.
7. D. Jones and J. Mitchell, *Phil. Mag.*, **8**, 1047 (1957).

6 SCINTILLATORS

SCINTILLATION MECHANISMS IN RARE EARTH ORTHOPHOSPHATES

A. J. WOJTOWICZ,^{1,2} D. WISNIEWSKI,^{1,2} A. LEMPICKI,² and L. A. BOATNER³

¹*Institute of Physics, N. Copernicus University, Grudziadzka 5, 87–100 Torun, Poland;*

²*Chem. Dept., Boston University, 590 Commonwealth Ave. Boston, MA 02215, USA;*

³*Solid State Division, Oak Ridge National Laboratory, P. O. Box 2008, Oak Ridge, TN 37831–6056, USA*

Although conversion efficiency of orthophosphate materials is limited by the high frequency vibrations of the PO₄ group, some of them show remarkably promising scintillation properties. In order to understand that behavior, we have studied the orthophosphates of Lu and Yb in various combinations both with and without Ce as an activator. We conclude that, although both Ce and Yb ions scintillate, they also show strong tendency toward mutual quenching. The mechanisms and consequences of this quenching are discussed.

Key words: scintillation mechanism, orthophosphate scintillators, nonradiative processes.

1 INTRODUCTION

Cerium-activated lutetium orthosilicates (LSO) and orthophosphates (LOP) have recently been identified as outstanding scintillators.^{1,2} The role played by lutetium has not yet been elucidated and since it is relatively expensive, a cheaper alternative would be desirable.^{2,3} Ytterbium would seem to be a viable candidate since its 4f¹³ electronic configuration produces only low energy *f-f* transitions ($\sim 10\,000\text{ cm}^{-1}$) while the free ion 4f¹³–4f¹²5d transition energies, at $88\,195\text{ cm}^{-1}$, are almost as high as those of Lu ($100\,000\text{ cm}^{-1}$).⁴ However, Yb³⁺ activated orthophosphates (LuPO₄ and YPO₄) have been found to produce luminescence assigned to transitions connecting the charge transfer state (CTS, Yb²⁺ + h_v, a bound valence hole) with two states (²F_{7/2} and ²F_{5/2}) of the Yb³⁺ 4f¹³ configuration.⁵ The corresponding absorption band peaks at about 204 nm. The absorption edge in LuPO₄ lies at about 8.6 eV,⁶ allowing the unrelaxed 2+ charge state energy level of Yb ion about 2.5 eV below the conduction band to be stable. The presence of the stable 2+ charge state has been related in earlier work to inefficient scintillation in Ce-activated materials.^{7,8}

2 EXPERIMENTAL RESULTS

The samples used in this study were characterized previously,⁹ and also the growth method,² and experimental details⁷ have already been described. The emission spectra under γ -excitation are shown in Figure 1. Spectrum *a* (LuPO₄, sample 10, 6 ppm Ce, 14 ppm Yb) shows two peaks at 334 and 360 nm (2160 cm^{-1} apart), characteristic of the Ce³⁺ ion. On the other hand spectrum *d* (YbPO₄:Ce, sample 1, 1.4 ppm) shows two peaks, at 300 and 430 nm ($10\,070\text{ cm}^{-1}$ apart), due to the charge transfer transition involving Yb ion.^{5,14} Spectra *b* and *c* (Yb_xLu_{1-x}PO₄:Ce, 0.18 wt%, $x = 0.01$ and 0.1 , samples 7 and 8, respectively) show a dip in the Yb 300 nm emission band at about 320 nm obviously due to absorption by Ce ions. Although this indicates efficient radiative energy transfer processes from Yb to Ce and, possibly, nonradiative as well, the detectable Ce emission unexpectedly diminishes with increasing Yb content (compare spectra *b* and *c*).

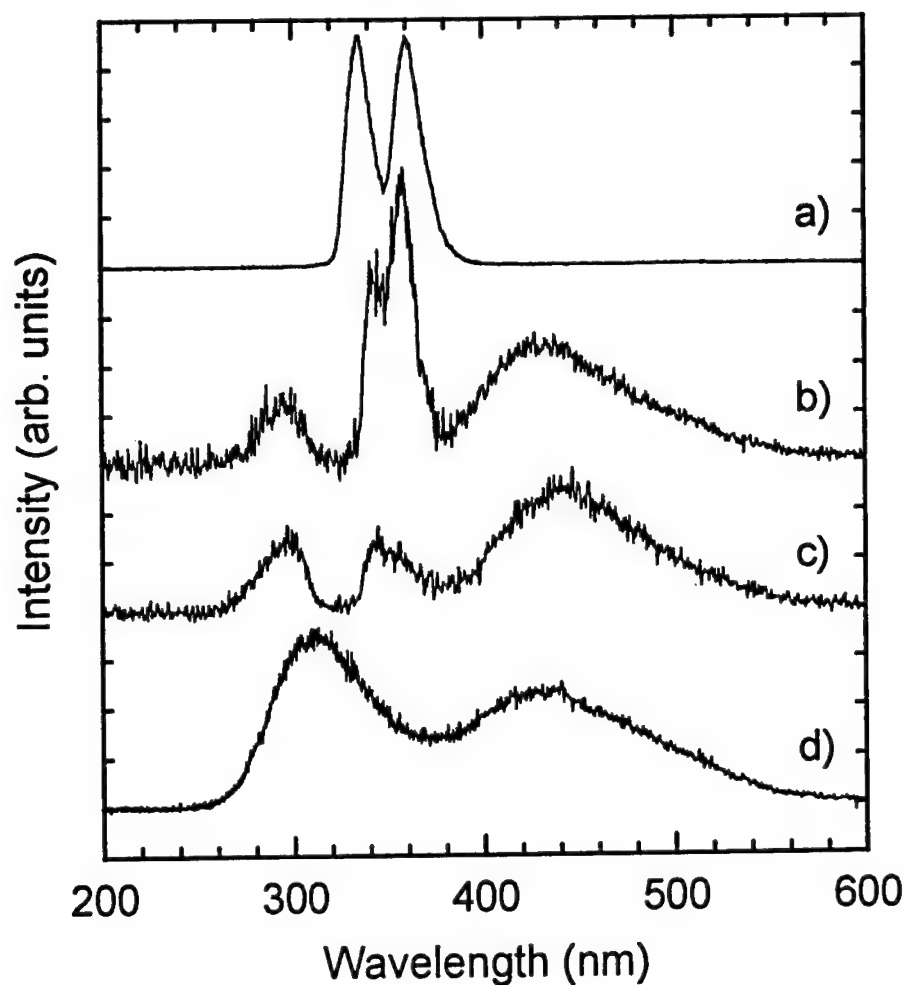


FIGURE 1 Room temperature emission spectra under γ -excitation (see text).

In Figure 2 we show scintillation light output vs Ce content for YbPO_4 crystals. Although the Yb scintillation efficiency diminishes with increasing Ce concentration no corresponding increase in Ce emission is seen in the scintillation spectra. Therefore we conclude that in addition to the quenching of Yb emission by Ce ions, the emission from Ce must also be quenched by Yb ions.

In Figure 3 we present scintillation pulse shapes under γ -excitation at room temperature for different emission wavelengths. As shown by trace *a* the Yb emission ($\text{LuPO}_4\text{:Yb}$, 1.0 wt %, 10^{-3} wt % of Ce, sample 6) exhibits both a rise time and a relatively long decay time, neither of which is shown by Ce emission.^{2,9} At $\lambda = 430$ nm the rise and decay

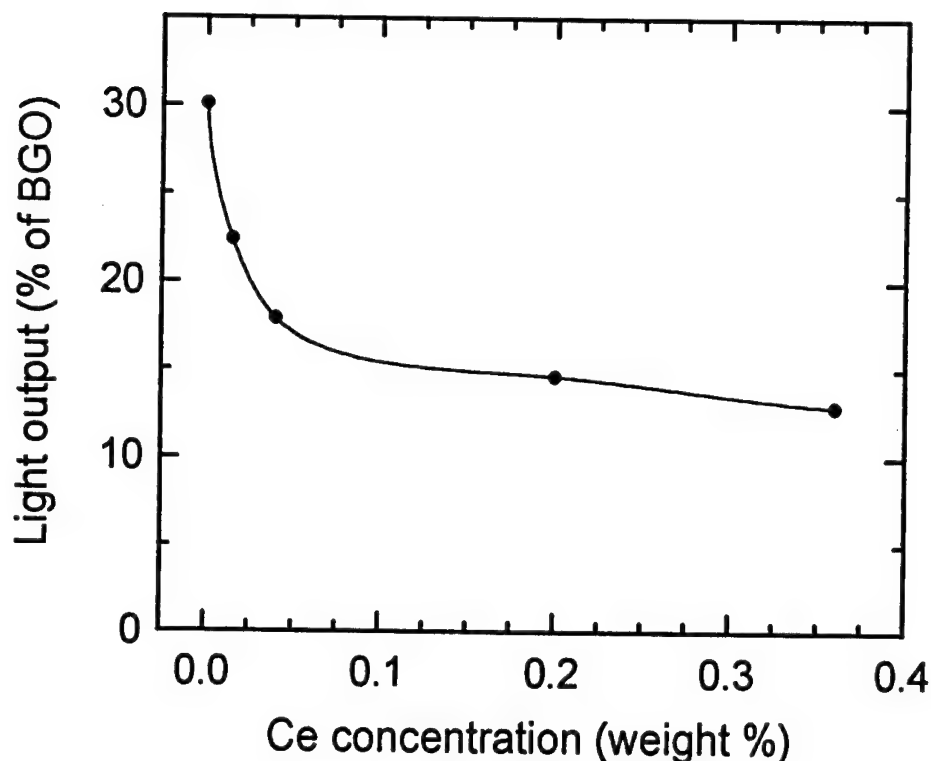


FIGURE 2 Scintillation light output under γ -excitation (compared to BGO) of YbPO_4 vs Ce concentration.

times are about 3.3 ns and 125 ns, respectively. However, with increased Ce doping the decay time of the Yb emission decreases (compare traces *b*, *c*, and *d*). In addition, a new faster decaying component becomes evident; some of which may be due to overlapping emission from the partially quenched Ce ions but most of it very likely reflects a quenching of the Yb emission by nonradiative energy transfer to Ce ions. Further examples are shown in traces *b* and *c*, taken for sample 7 ($\text{Yb}_x \text{Lu}_{1-x} \text{PO}_4 \cdot \text{Ce}$, 0.18 w%, $x = 0.01$). Trace *b* was measured at $\lambda = 430$ nm; it shows no rise time and two components, 15.7 ns (21% zero-time amplitude) and 100 ns (79% zero-time amplitude). Trace *c* was taken at $\lambda = 360$ nm; it again shows no rise time and two component, 12 ns (63% zero-time amplitude) and 90 ns (37% zero-time amplitude). The scintillation pulse of sample 8 ($\text{Yb}_x \text{Lu}_{1-x} \text{PO}_4 \cdot \text{Ce}$, 0.18 w%, $x = 0.1$), shown as trace *d*, was measured at $\lambda = 360$ nm. Again, there is no rise time and there are two components, 19 ns (36% zero-time amplitude) and 84 ns (64% zero-time amplitude). In all cases the emission attributable to both Ce and Yb are less than would be expected in the absence of interaction between them.

3 DISCUSSION AND CONCLUSIONS

Perhaps the most important consequence of the simultaneous presence of Yb and Ce is their mutual quenching. This observation can be explained in terms of the mechanism

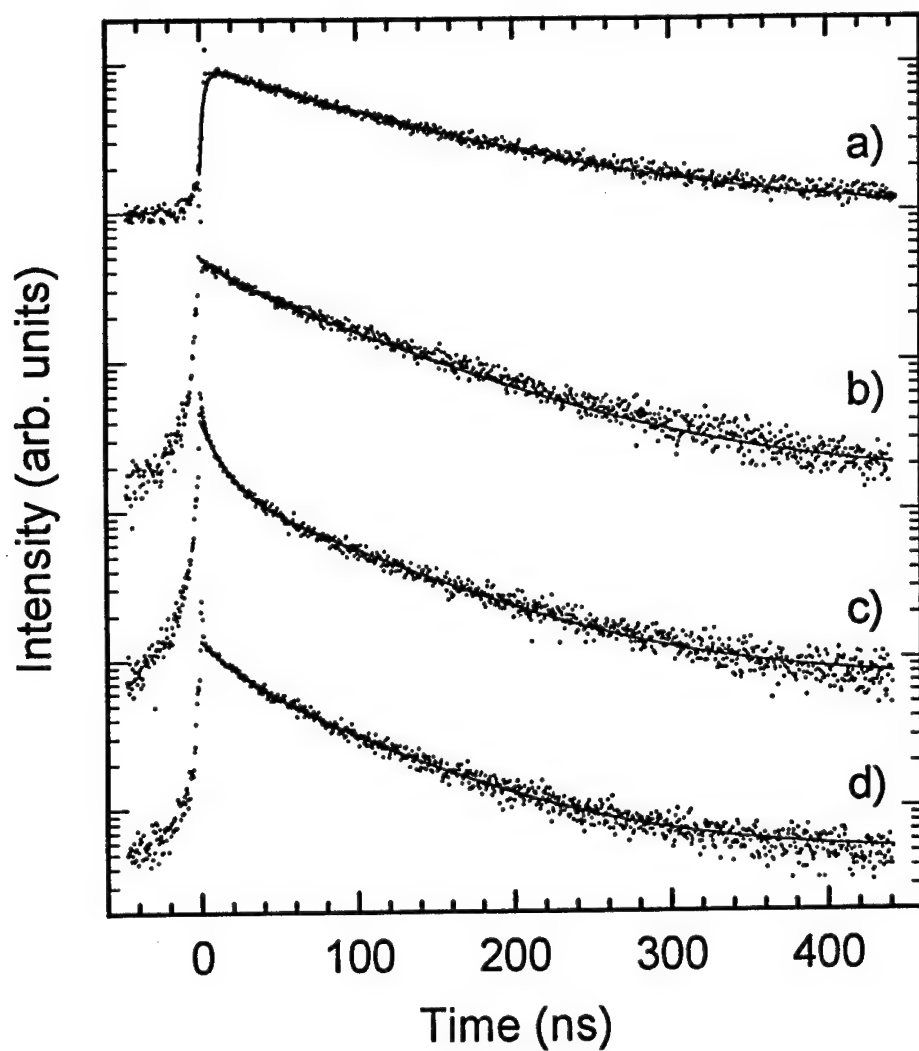
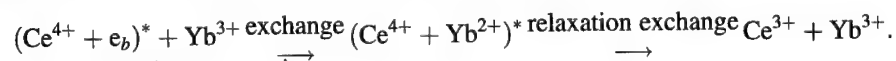


FIGURE 3 Spectrally resolved pulse shapes of γ -excited scintillations taken at room temperature (see text).

proposed earlier for another rare earth combination, Ce and Eu,¹⁰ and for the Ce self-quenching in CeF₃.¹¹ Whenever one of the ions (e.g. Eu, Yb or even Ce itself) has a stable 2+ state, then the emission from the other ion (Ce) can be severely quenched by the formation of a metal-metal charge transfer state which decays nonradiatively to the ground state as shown in Figure 4. This process can be described as follows:



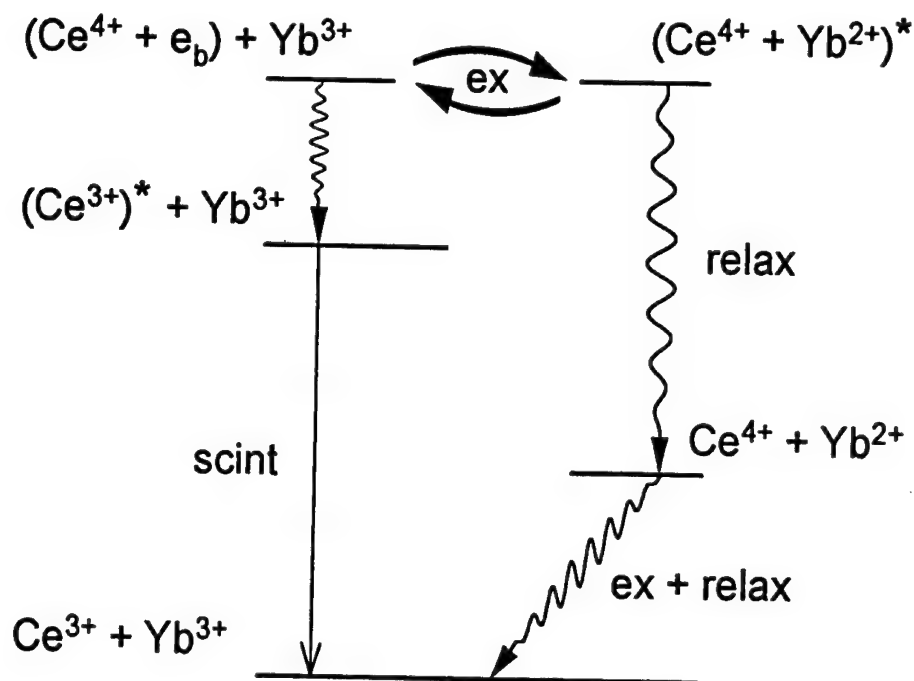


FIGURE 4 The proposed mechanisms of radiative and nonradiative decays of the excited Ce^{3+} ion by interaction with the close neighbor Yb^{3+} ion. The nonradiative decay requires the stability of the Yb 2+ charge state and efficient exchange of an electron between highly excited Ce^{3+} and Yb^{2+} ions as necessary conditions.

The exchange of electron between two neighboring ions, a highly excited Ce^{3+} ion (designated as Ce^{4+} plus loosely bound electron e_b) and an unexcited Yb^{3+} , leads to formation of the oppositely charged metal-metal ion pair far from the equilibrium point in the configuration coordinate space. After relaxation there will be a repeated electron exchange leaving two ions in unexcited 3+ charge states. In this way the Ce^{3+} ion preserves a high quantum efficiency when excited directly into its lower excited states but, after ionization, the new nonradiative recombination channel is open, where the energy of Ce^{3+} electronic excitation is carried away by lattice and/or local vibrations. Therefore, if the Yb concentration is high enough, the energy gathered by Ce ions is lost nonradiatively. Also, the preceding radiative and nonradiative energy transfer from excited Yb ions to Ce ions will, by virtue of the same process, waste the energy gathered by Yb ions. The final conclusion is that intentional or unintentional codoping of Ce and Yb ions into the lattice of a scintillator material has to be carefully avoided. For this reason ytterbium does not provide a cheaper substitute for lutetium in orthophosphate crystals activated with Ce.

ACKNOWLEDGEMENTS

We gratefully acknowledge the support of the US Department of Energy under grant DE-FG02-90ER61003 and contract DE-AC05-84OR21400 with Martin Marietta Energy Systems, Inc. and of N. Copernicus University under grant 385-F/94.

REFERENCES

1. C. L. Melcher and J. S. Schweitzer, *IEEE Trans. Nucl. Sci.* **NS-39**, 502 (1990).
2. A. Lempicki, E. Berman, A. J. Wojtowicz, M. Balcerzyk, and L. A. Boatner, *IEEE Trans. Nucl. Sci.* **40**, 384 (1993).
3. H. Suzuki, T. A. Tombrello, C. L. Melcher, and J. S. Schweitzer, *Nucl. Instr. Meth.* **A320**, 263 (1992).
4. L. Brewer, *J. Opt. Soc. Am.* **61**, 1666 (1971).
5. E. Nakazawa, *Chem. Phys. Lett.* **56**, 161 (1978) and *J. Lumin.* **18/19**, 272 (1979).
6. E. Nakazawa and F. Shiga, *J. Lumin.* **15**, 255 (1977).
7. A. J. Wojtowicz, M. Balcerzyk, E. Berman, and A. Lempicki, *Phys. Rev.* **B49**, 14880 (1994).
8. A. J. Wojtowicz, M. Balcerzyk, D. Wisniewski, A. Lempicki, C. L. Woody, P. W. Levy, J. A. Kierstead and S. Stoll, *IEEE Trans. Nucl. Sci.* **41**, 713 (1994).
9. A. J. Wojtowicz, A. Lempicki, D. Wisniewski and L. A. Boatner, *Mat. Res. Soc. Symp.* **348** 123 (1994).
10. G. Blasse, *Phys. Stat. Sol.* **A75** K41 (1983).
11. A. J. Wojtowicz, A. Lempicki, D. Wisniewski, C. Brecher, R. H. Bartram, C. Woody, P. Levy, S. Stoll, J. Kierstead, C. Pedrini, D. Bouttet, and Cz. Koepke, *Mat. Res. Soc. Symp.* **348**, 455 (1994).

SCINTILLATION PROPERTIES OF $\text{Lu}_3\text{Al}_{5-x}\text{Sc}_x\text{O}_{12}$ CRYSTALS¹

N. N. RYSKIN, P. DORENBOS, C. W. E. VAN EIJK and S. KH. BATYGOV*

*Delft University of Technology, Faculty of Applied Physics, c/o IRI, Mekelweg 15, 2629 J B Delft, The Netherlands; *General Physics Institute 117313, Vavilov str. 38, Moscow, Russia*

The scintillation properties of $\text{Lu}_3\text{Al}_{5-x}\text{Sc}_x\text{O}_{12}$ single garnet crystals doped with different concentrations of Sc^{3+} were investigated. The best scintillation properties were obtained for the crystal with $x = 0.2$ in the melt. This crystal has a broad (FWHM ~ 1 eV) ultraviolet emission band with a maximum at 275 nm. An energy resolution of 7% is observed for the 662 keV photopeak. The main decay component of the scintillation pulse has an exponential decay time of about 600 ns and accounts for 90% of the total light yield. The total scintillation light yield was found to be about 22,500 ph/MeV. Within 10% a linear response was obtained in the energy interval from 8 keV to 1.3 MeV.

Key words: Scintillation, garnet, isoelectronic impurity.

1 INTRODUCTION

$\text{Lu}_3\text{Al}_5\text{O}_{12}$ garnet crystals (LAG), due to their high density (6.67 g/cm³) and other physical properties such as shock-resistivity, nonhygroscopicity, chemical and radiation stability are quite promising host crystals for scintillating materials. Earlier,¹ scintillation properties of LAG crystals doped with Ce^{3+} ions were reported.

It was shown² that substitution of Al^{3+} ions by Sc^{3+} in the LAG lattice gives rise to a broad (FWHM ~ 1 eV) ultraviolet (UV) band located near 280 nm. This band was assigned to isoelectronic impurity centres formed by Sc^{3+} ions substituting Al^{3+} ions in the LAG lattice. In this paper, results of an investigation of the scintillation properties of LAG doped with Sc^{3+} ions are presented. The $\text{Lu}_3\text{Al}_{5-x}\text{Sc}_x\text{O}_{12}$ (LAG-Sc) crystals were grown by the horizontal directed crystallization technique. Details on the experiments carried out in this paper can be found in³.

2 RESULTS AND DISCUSSION

Five LAG-Sc crystals with different x (0.001; 0.04; 0.2; 0.5; 2.0 in the melt) were investigated at room temperature. Some scintillation parameters of the LAG-Sc crystals as a function of the scandium concentration are compiled in Table I. The highest light yield values were obtained for LAG-Sc at a concentration x of 0.2 and 0.5 both under X-ray (25 mA, 35 kV, Cu anode) and 662 keV gamma ray excitation. Decay curves can be fitted quite well with a sum of two exponential components $I = \sum I_i \exp(-t/\tau_i)$, where I_i is the initial intensity and τ_i is the decay time. As can be seen from Table I, the LAG-Sc ($x = 0.2$) crystal is the most interesting from the standpoint of application as a scintillation detector. We therefore focus on the scintillation properties of this sample. The emission, excitation, and absorption spectra of LAG-Sc ($x = 0.2$) are shown in Figure 1. The 275 nm

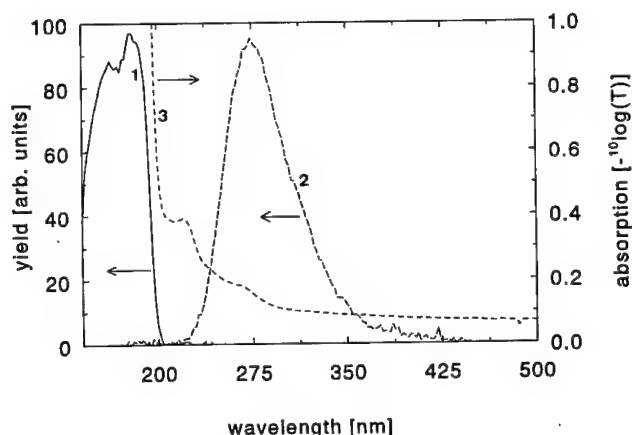


FIGURE 1 The excitation (1), emission (2), and absorption (3) spectra recorded for the 1 mm thick LAG ($x = 0.2$) crystal at 300 K: (1) - $\lambda_{\text{emission}} = 275$ nm, $\lambda_{\text{excitation}} = 140\text{--}250$ nm; (2) - $\lambda_{\text{emission}} = 200\text{--}450$ nm, $\lambda_{\text{excitation}} = 180$ nm;

UV excited emission band (Figure 1, curve 2) looks the same as under X-ray excitation. The excitation spectrum (Figure 1, curve 1) starts at energies where the optical absorption rises strongly (Figure 1, curve 3) and depicts two relatively broad bands with maxima at about 160 and 180 nm. A pulse height spectrum of a ^{137}Cs source obtained with LAG-Sc ($x = 0.2$) using an electronic shaping time of 2 μs and an XP2020Q photomultiplier tube is shown in Figure 2. An energy resolution of 7% with a photoelectron yield of 3490 photoelectrons/MeV (phe/MeV) was obtained. The spectrum was fitted in the range from 530 keV to 750 keV with two Gaussian peaks and a background. Together with the photopeak at 662 keV, the characteristic X-ray escape peak of Lu can be seen at an energy of 608 keV. The main Lu X-ray emission energy is 54.07 keV. Figure 2 also shows two peaks within the energy interval from 100 keV to 250 keV. The one at an energy of about 195 keV is due to Compton backscattering. The one at about 136 keV is again the X-ray characteristic escape peak of Lu but now due to absorption by the crystal of the Compton backscattered γ -rays. The best energy resolution obtained with LAG-Sc ($x = 0.2$) in our experiments was 6.3%. Despite the two times smaller light yield of LAG-Sc ($x = 0.2$) compared to NaI(Tl $^{+}$) the energy resolution is about the same. This can be explained by the fact that the linearity of LAG-Sc ($x = 0.2$) is better than that of NaI-Tl. Actually,

Table I.
Some properties of $\text{Lu}_3\text{Al}_{5-x}\text{Sc}_x\text{O}_{12}$ garnet crystals at 294K.

x	λ_{max} , nm	FWHM, eV	Light yield, ph/MeV		τ_1 , ns	τ_2 , ns	Decay parameters	
			X-ray excitation	γ -ray excitation			I_1 , %	I_2 , %
0.001	293	1.43	14400	9750	1000	4500	70	30
0.04	273	1.10	18500	12250	750	5000	85	15
0.2	275	1.01	22400	20750	610	3300	98	2
0.5	282	1.09	23800	19500	760	5000	92	8
2.0	340	1.03	17600	5000	850	7500	90	10

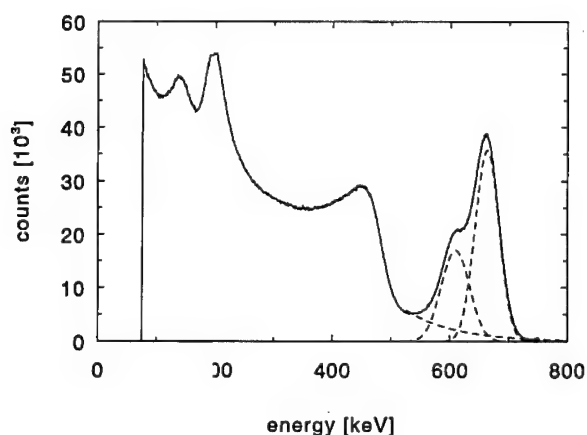


FIGURE 2 Pulse height spectrum of ^{137}Cs ($E_\gamma = 662 \text{ keV}$) measured with the $1.0 \times 10 \times 15 \text{ mm}^3$ LAG-Sc ($x = 0.2$) crystal at room temperature using a shaping time of $2 \mu\text{s}$.

within the energy interval from 8 keV to 1.3 MeV we observe within less than 10% a linear response. This linearity is much better than those of CsI-Tl, NaI-Tl, $\text{Lu}_2\text{SiO}_5\text{-Ce}$, and $\text{Gd}_2\text{SiO}_5\text{-Ce}$. Further studies are carried out to find a correlation between the linearity and other features of a scintillator. Such investigations will give a better understanding of the mechanisms affecting scintillation efficiency and energy resolution.

ACKNOWLEDGEMENTS

The authors wish to thank D. I. Melikhov and A. A. Kuryukhin for growth of the crystals, as well as J. Th. M. de Haas, M. J. Knitel, H. van't Spijker, and D. R. Schaart for assistance during the experiments.

REFERENCES

1. C. W. E. van Eijk, J. Andriessen, P. Dorenbos, and R. Visser, *The 3rd London conference on Position-Sensitive Detectors*, Sept. 6–10, Brunel Univ., London (1993).
2. S. Kh. Batygov, Yu. K. Voronko, A. A. Kuryukhin, N. G. Margiani, D. I. Melikhov, N. N. Ryskin, and V. M. Tatarintsev, *Abst. of the IX All Union symp.*, May 19–26, Leningrad, P. 219 (1990).
3. P. Dorenbos, J. T. M. de Haas, R. Visser, C. W. E. van Eijk, R. W. Hollander, *IEEE Trans. on Nuclear Sci.*, Vol. 40, No. 4, pp. 424–430 (1993).

MONTE-CARLO SIMULATION OF THE CREATION OF EXCITED REGIONS IN INSULATORS BY A PHOTON

R. A. GLUKHOV and A. N. VASIL'EV

*Synchrotron Radiation Laboratory, Physics Department, Moscow State University,
Moscow, 117234 Russia*

Different approaches to solution of the kinetic equations for relaxation of electronic excitations (analytical, numerical solution of integro-differential equations, and Monte-Carlo simulation) display the properties and evolution of the excited region created by the absorption of a high-energy photon. The relaxation at the final stages of inelastic electron-electron scattering determines the number of low-energy excitations in CeF_3 . The number of close excitations around a core hole in BaF_2 rapidly increases after the absorption of photons with energy above 32 eV, which results in a faster decay of crossluminescence.

Key words: Electron relaxation, scintillations, crossluminescence, inelastic scattering, Monte-Carlo.

1 INTRODUCTION

The computer simulation of the fast stages of energy relaxation in insulators after the VUV or XUV photon absorption is useful for evaluation of the yield of different secondary processes (luminescence, scintillation, defect production, etc.). The absorption of a high-energy photon results in the creation of the excited region in an insulating crystal after the absorption of VUV or X-ray photon. This region consists of a number of electrons, holes, excitons and fast defects, if the photon has energy sufficient for producing of several electronic excitations. Therefore the kinetic equations should include all types of interactions between excitations.

2 KINETIC EQUATIONS

The dynamics of excited region created in insulators after the absorption of high-energy photon can be described using polarization approximation for kinetic equation. Such kinetic equation can be derived using Klimontovich's technique.¹ The number of electrons, holes, and excitons created after inelastic electron-electron scattering followed by a photon absorption changes in time. This problem is problem of finite, but large, number of particles. Thus the total set of kinetic equations consist of a large (but finite) chain of kinetic equations for multi-particle distribution functions. The set is rather cumbersome, so Figure 1 shows only one equation for electron energy distribution function. Each term in this equation has an evident sense which is illustrated by the scheme of the process at the right part of the Figure. The following notations are used: $f_\alpha(E, t)$ is the energy distribution function for particles of α -type ($\alpha = e, h$), E is their energy, t is the time, $n(\omega)$ is the refractive index, $g_\alpha(E)$ is the density of states, $I(\omega, t)$ is the intensity of external radiation, $\varepsilon(\omega, \mathbf{k})$ is the complex dielectric permittivity with account for spatial dispersion (the first term in the bracket describes the interaction accompanied by an exchange of longitudinal photon, the second one, by transversal photon; the latter is negligible for most cases),

$$M_{\mathbf{k}}^{\alpha\beta}(E', E) \equiv \frac{1}{k^2 g_{\alpha}(E') g_{\beta}(E)} \sum_{m,n} (|\rho_{nm}|^2)_{-\mathbf{k}} \delta(E' - E_m) \delta(E - E_n)$$

is the mean value of dipole matrix element for transition between states (α, E') and (β, E) with momentum transfer $\hbar\mathbf{k}$, ρ is the density-of-charge operator,

$$S_{\alpha}^E(E) = \frac{\hbar^2}{2\pi^2 k_B T} \int_0^{\Omega_{\max}} d\Omega \int d^3k \operatorname{Im} \left(-\frac{1}{\varepsilon(\Omega, \mathbf{k})} \right) \\ \times \Omega^2 \left[(\bar{n}_{\Omega, \mathbf{k}} + 1) M_{\mathbf{k}}^{\alpha\alpha}(E, E - \hbar\Omega) g_{\alpha}(E - \hbar\Omega) + \bar{n}_{\Omega, \mathbf{k}} M_{\mathbf{k}}^{\alpha\alpha}(E, E + \hbar\Omega) g_{\alpha}(E + \hbar\Omega) \right]$$

is the rate of phonon relaxation, $\bar{n}_{\Omega, \mathbf{k}}$ is the mean number of phonons with frequency Ω and wavenumber \mathbf{k} for temperature T , Ω_{\max} is the maximal phonon frequency.

Other equations in this set have the analogous structure.

3 EXAMPLES OF SOLUTION

3.1 Analytical Solution

Such complicated set of equations can be solved analytically only for the oversimplified cases. The case of the only narrow valence band and random distribution of secondary

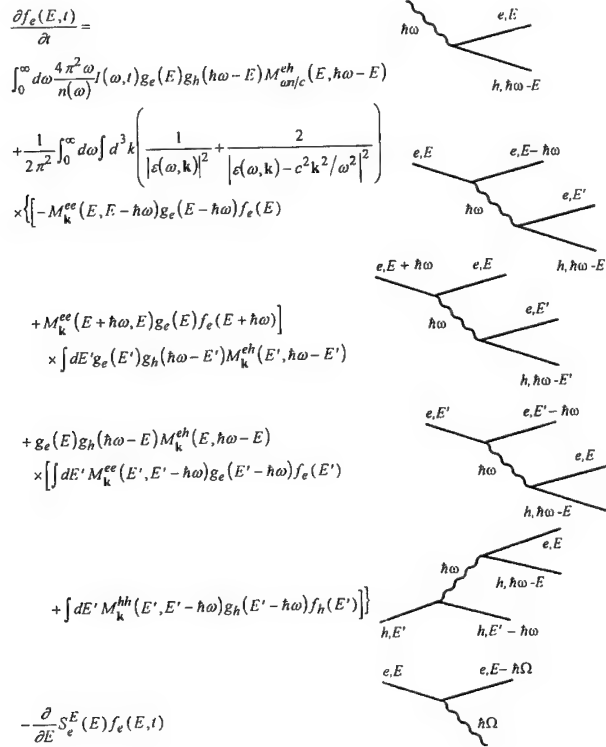


FIGURE 1 The schemes of different elementary processes for electron production and scattering and corresponding kinetic equations. See notations in the text.

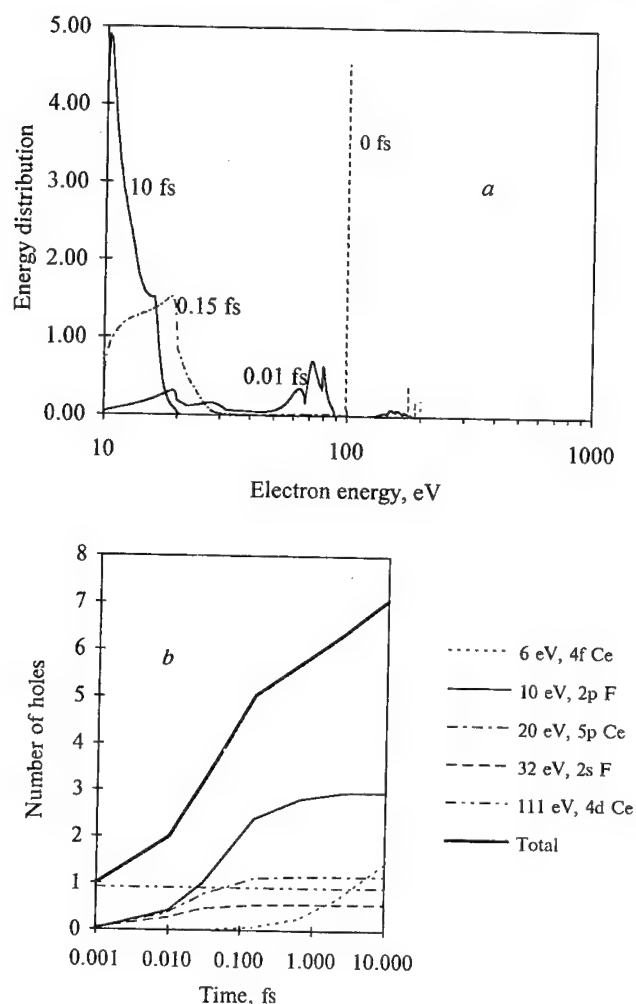


FIGURE 2 The energy distribution of electrons (a) and holes (b) at different time after the absorption of 200 eV photon for CeF_3 band parameters. Only electron inelastic scattering was taken into account.

electrons after the scattering was presented earlier.² The mean energy for the production of an electron-hole pair was estimated there as $(1.4 + 0.55\sigma^{1/2})E_g$, where E_g is the forbidden gap and σ is the dimensionless rate of phonon relaxation. The energy distribution of secondary electrons has logarithmic singularity for low energies just above the bottom of conduction band ($E = E_g$) and smoothly decreases for energies up to $E = 2E_g$.

3.2 Estimating of Electron Energy Distribution in CeF_3

The second approach to the solution of kinetic equations for energy distribution function is the numerical solution of integro-differential equation. The result of the simulation is given in Figure 2. We used the band scheme parameters similar to that of CeF_3 crystal. The valence and core levels are supposed to be flat, and electrons in the conduction band are

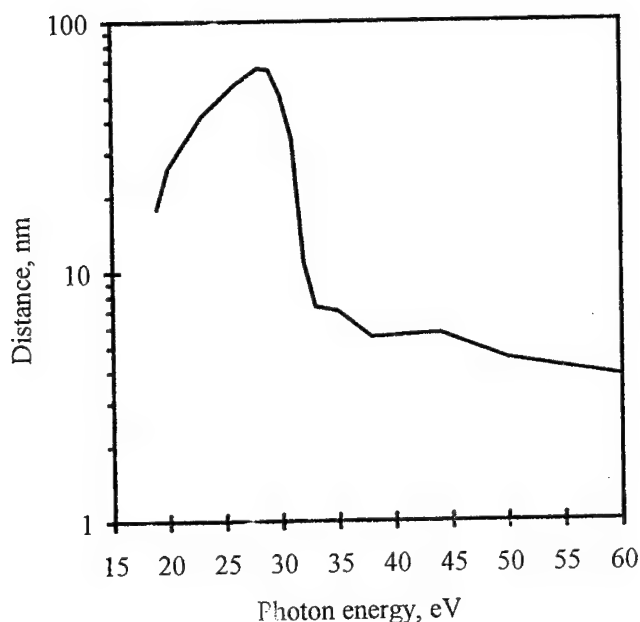


FIGURE 3 The dependence of the mean distance from a core hole to the closest excitation on the photon energy for BaF_2 .

described by free-electron dispersion law. The analytical expression for dielectric permittivity was based on the suggestion of hydrogen-like transitions from core levels, and the amplitude of each contribution was normalised to satisfy sum rules for dielectric function. The rate of relaxation is overestimated in about two times since we neglect spatial dispersion of the permittivity. We simulate only electronic relaxation, and the account of Auger relaxation of core holes should increase the total number of electron-hole pairs in ≈ 1.5 times. The electron distribution at final stages of relaxation is close to that which was obtained for analytical solution.

This simulation demonstrates the role of low-energy stage of inelastic electron-electron scattering. The yield of CeF_3 scintillations is determined mainly by the number of ionized and excited Ce^{3+} ions. Holes at the $4f - \text{Ce}^{3+}$ level are produced mainly at the final stage of electron-electron scattering due to impact ionization of cerium ions. Their yield is strongly determined by the details of electronic distribution at energies between the threshold of such ionization (about 16 eV) and that of ionization of fluorine ion (about 20 eV) and by the rate of thermalization $S_e^E(E)$.

3.3 Spatial Distribution of Excitations in BaF_2

Another approach to solution of kinetic equations is the Monte-Carlo simulation (see e.g.).⁴ This kind of simulation allows to receive much more information, since two- and even three-particle space and energy distribution functions can be evaluated. The simulation was based on the set of kinetic equations similar to that displayed in Figure 1 but with account for spatial motion of excitations (in gas-kinetic approximation for stage of inelastic scattering and in diffusion one for thermalization). The main attention focuses

on the spatial distribution functions of excitations, i.e. one-particle and two-particle distribution functions. One-particle distribution represents the spatial shape of the concentration of excitations in the excited region produced by a photon absorption, whereas two-particle distribution function describes the spatial correlations between different excitations. The latter function determines the energy transfer at final stages of energy relaxation and is important for different quenching processes and the acceleration of the luminescence.⁵

The Monte-Carlo simulation was performed for BaF₂ crystal for photon energies from 20 eV to 100 eV. The possibility of existence of long-living outermost core holes increases the number of excitation types in the crystal (such core holes decay through transversal photon emission, which is described by the second term in the brackets with dielectric permittivities in Figure 1, for details refer).⁶ The kinetics of crossluminescence is determined by the correlation between a core hole and any other excitation (electron, valence hole or valence exciton). Figure 3 shows that the two-particle distribution functions and thus the kinetics are strongly changed with photon energy. For photon energies above 32 eV the mean distance to the nearest excitation strongly decreases. Starting from this energy the spatial distribution of secondary excitations becomes strongly non-homogeneous. For such type of distribution the mean distance between a core hole and the closest excitation occurs to be much less than the mean distance between arbitrary excitations. This situation can be interpreted as creation of separated groups of secondary excitations.

4 CONCLUSION

Three different approaches to solving of kinetic equations for electronic excitations demonstrates that all stages of energy conversion and transfer in crystals are tightly connected. The total yield of secondary processes depends not only on the number of electron-hole pairs but on the energy and spatial distribution of excitations as well.

REFERENCES

1. Yu. L. Klimontovich, *Kinetic theory of Nonideal Gases and Nonideal Plasmas* (Pergamon Press, Oxford: 1982).
2. A. N. Vasil'ev and V. V. Mikhailin, *Bull. of the Akad. of Sciences of the USSR, Phys. series*, **50**, N3, 113 (1986).
3. R. A. Glukhov and A. N. Vasil'ev, *Proceedings of MRS Spring Meeting* **94**, San Francisco, 4-8 April 1994, to be published.
4. A. Ausmees, M. Elango, A. Kikas, and J. Pruulmann, *Phys. stat. sol.(b)* **137**, 495 (1986).
5. A. N. Belskiy, V. V. Mikhailin, A. L. Rogalev, S. Stizza, A. N. Vasil'ev, and E. I. Zinin, in *2nd European Conference on Progress in X-Ray Synchrotron Radiation Research*, Conference Proceedings, **25** (Bologna: SIF) (1990).
6. I. Davoli, V. V. Mikhailin, S. Stizza, and A. N. Vasil'ev, *J. Luminescence* **51**, 275 (1992).

SCINTILLATION PROPERTIES OF $\text{GdAlO}_3\text{:Ce}$ CRYSTALS¹

P. DORENBOS, E. BOUGRINE, J. T. M. DE HAAS, C. W. E. VAN EIJK
and M. V. KORZHIK*

*Delft University of Technology, Faculty of Applied Physics, c/o IRI, Mekelweg 15, 2629
JB Delft, The Netherlands; *Institute of Nuclear Problems, 11 Bobruiskaya, 220050
Minsk, Belarussia*

The scintillation properties of GdAlO_3 single crystals doped with different concentrations of Ce^{3+} are reported. Dipole allowed transitions in Ce^{3+} ions from the lowest 5d to the two 4f levels cause luminescence between 320 and 400 nm.

Key words: Scintillation, 5d-4f luminescence, Ce^{3+} .

1 INTRODUCTION

In this work we report on the scintillation properties of Ce^{3+} doped GdAlO_3 (GAP) single crystals which were grown by means of the horizontally oriented crystallization technique. Four crystals with different Ce concentrations were studied. They are not optically perfect; some crystals are hazy causing substantial scattering of light. The material has a density of 7.5 g/cm^3 and an effective atomic number $Z_{\text{eff}} = 56.2$. The luminescence properties under optical excitations were reported already in 1975 by Fava *et al.*¹ and recently by Mares *et al.*² We focus on the luminescence properties under X-ray and gamma ray excitation. Details on the experimental set-ups employed in this work can be found elsewhere.³

2 RESULTS AND DISCUSSION

Figure 1 shows the X-ray excited emission spectra of the Ce doped crystals. Near 340 and 360 nm one observes two Ce^{3+} emission bands caused by transitions from the lowest 5d level ($^2\text{D}_{3/2}$) to the $^2\text{F}_{5/2}$ and $^2\text{F}_{7/2}$ levels of the $4f^1$ configuration, respectively. Luminescence due to unwanted Tb^{3+} impurities can also be seen; i.e. near 382 nm, 415 nm, and 436 nm. The optical absorption spectrum shows at 288 and 306 nm bands due to $4f \rightarrow 5d$ transitions in Ce^{3+} and at 276 nm an absorption line caused by Gd^{3+} . Similar bands appear in the excitation spectrum of 350 nm luminescence. Table I compiles the optical attenuation coefficients, μ , due to Ce^{3+} absorption at 306 nm. Based on these values, we estimated the Ce concentration in the crystals. Because the precise relation is not known the true Ce concentration may deviate by a factor of two.

The integrated light yield of the Ce^{3+} luminescence bands in photons/(MeV of absorbed X-ray energy) increases with the Ce concentration up to values of 9000, see Table I. Light yield values obtained with 662 keV gamma ray excitation and employing electronic shaping times of 2 and 3 μs are also compiled.

Figure 2 shows the gamma ray excited decay time spectra of the GAP:Ce crystals. Each crystal shows a small fast component in the first 20 ns of the spectrum, but the dominant

¹These investigations in the program of the Foundation for Fundamental research on Matter (POM) have been supported by the Netherlands Technology Foundation (STW).

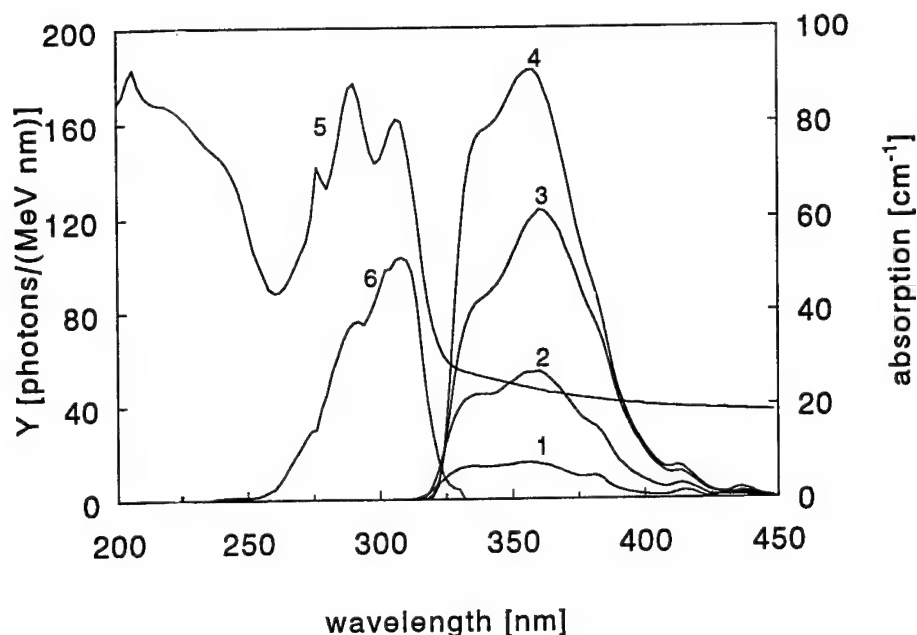


FIGURE 1 Curves 1, 2, 3, 4) X-ray excited emission spectra Y in photons/(MeV·nm) of the GAP crystals doped with 0.02, 0.22, 0.44, and 0.75 mol% Ce^{3+} , respectively. 5) optical absorption A in cm^{-1} of the crystal with 0.22 mol% Ce and 6) $\lambda_{em} = 350$ nm luminescence excitation spectrum η in arb. units of the crystal with 0.02 mol% Ce.

decay is caused by a slow process. We have fitted the decay curve with a sum of two exponential decay curves ($I(t) = \sum \frac{N_i}{\tau_i} \exp(-t/\tau_i)$ with τ the decay time and N the intensity). The fit parameters are compiled in Table I. The main decay component of the 0.02 mol% Ce doped crystal is 1700 ns, and it shortens with almost an order of magnitude for the 0.75 mol% doped crystal ($\tau = 180$ ns). Note that the dominant decay time is considerably longer than the lifetime of the 5d level responsible for the luminescence which is about 60 ns.¹ This indicates a slow transfer rate of the excitations of the host lattice (i.e. the Gd^{3+} sublattice) to the Ce luminescence centers.

In conclusion, the combination of a high density (7.5 g/cm^3), reasonable light yield (6000–9000 photons/MeV), and reasonable decay time (≈ 180 ns) merits further investigation of GAP:Ce crystals. Considering that the optimal Ce concentration has not been established yet, and the sometimes poor optical quality of the crystals, one may expect to be able to improve their scintillation properties.

Table I
Properties of $\text{Gd}_{1-x}\text{Ce}_x\text{AlO}_3$ crystals.

x mol%	μ (306 nm) cm^{-1}	photons/MeV (X-ray exc.)	photons/MeV (γ -ray exc.)	$\frac{N_1}{N_2}$	decay parameters	
					τ_1 (ns)	τ_2 (ns)
0.02	11	840	1120 (3 μs)	0.17	240	1700
0.22	110	2900	2800 (3 μs)	0.16	60	500
0.44	220	6200	3350 (2 μs)	0.12	30	260
0.75	370	9000	6000 (2 μs)	0.14	30	180

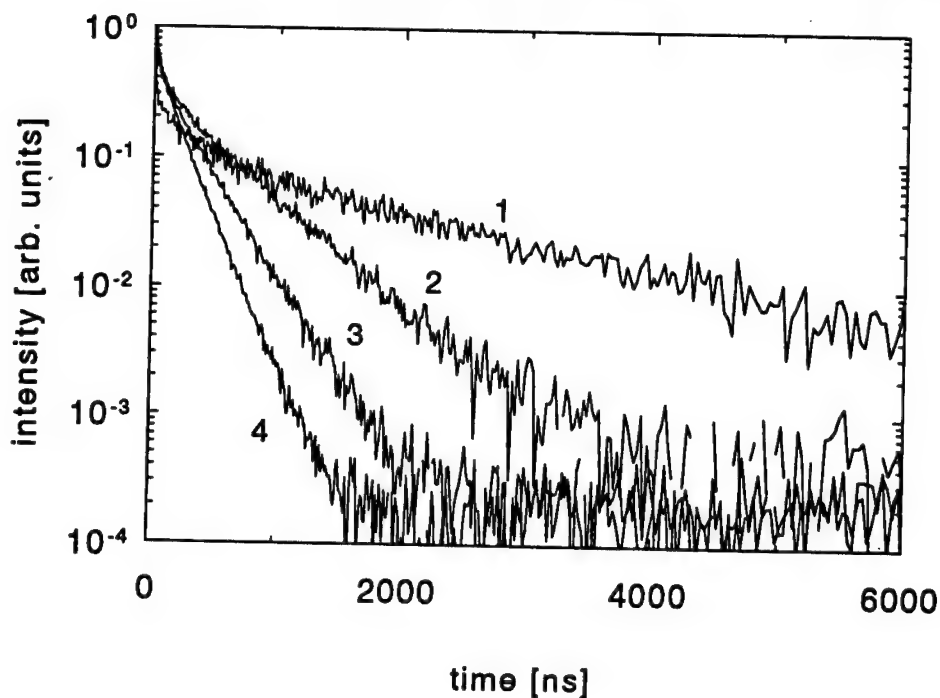


FIGURE 2 Curves 1, 2, 3, 4) scintillation decay spectra of the GAP crystals doped with 0.02, 0.22, 0.44 and 0.75 mol% Ce^{3+} , respectively. The spectra are normalized to unity at time $t = 0$.

ACKNOWLEDGEMENTS

The authors are grateful to S. Smirnova for growth of the crystals, and to Hako Botma for performing the EPMA experiments.

NOTE

With Electron Probe Microanalysis (EPMA) the absolute Ce^{3+} concentration was determined to be: 0.02, 0.16, 0.40 and 0.66 mol %.

REFERENCES

1. J. Fava, G. Le Flem, J. C. Bourcet, F. Gaume-Mahn, *Mat. Res. Bull.* **11**, 1 (1976).
2. J. A. Mares, C. Pedrini, B. Moine, K. Blazek, J. Kvapil, *Chem. Phys. Lett* **206** (1, 2, 3, 4), 9 (1993).
3. P. Dorenbos, J. T. M. de Haas, R. Visser, C. W. E. van Eijk, R. W. Hollander, *IEEE Trans. on Nucl. Sci.* **40**, 424, (1993).

SCINTILLATION PROPERTIES OF $\text{Y}_2\text{SiO}_5\text{:Pr}$ CRYSTALS¹

P. DORENBOS, M. MARSMAN, C. W. E. VAN EIJK,* M. V. KORZHIK,**
and B. I. MINKOV***

**Delft University of Technology, Faculty of Applied Physics, c/o IRI, Mekelweg 15,
2629 JB Delft, The Netherlands; **Institute of Nuclear Problems, 11 Bobruiskaya,
220050 Minsk, Belarussia; ***Institute for single crystals, 60 Lenin av., Kharkov, 310001,
Ukraine*

We report on the scintillation properties of Y_2SiO_5 (YSO) single crystals doped with different concentrations of Pr^{3+} . Dipole allowed transitions from the lowest $4f5d$ level of Pr^{3+} to $4f^2$ levels cause a fast scintillation emission component ($\tau \approx 30$ ns) in the wavelength range 260–350 nm.

Key words: Scintillation, 5d-4f luminescence, Pr^{3+} .

1 INTRODUCTION

The Ce^{3+} doped oxy-orthosilicates Y_2SiO_5 , Gd_2SiO_5 , and Lu_2SiO_5 have been studied widely for their scintillation properties.¹ Instead of Ce^{3+} , one may also consider Pr^{3+} as a luminescence center. Generally, the $4f5d$ - $4f^2$ luminescence of Pr^{3+} is located at energies 1.3 eV ($10\,000\text{ cm}^{-1}$) higher than the luminescence of Ce^{3+} if doped in the same host crystal. Consequently, one may expect a decay time even faster than in the case of Ce^{3+} doping due to the λ^{-3} dependence of the transition rate on the emission wavelength λ .

Figure 1 shows the energy levels of Pr^{3+} in YSO as has been deduced from its optical absorption, emission, and excitation spectra. One observes that the bottom of the $4f5d$ band is located below the $^1\text{S}_0$ state of the $4f^2$ configuration; this is essential for fast $4f5d$ - $4f^2$ luminescence to occur.

The YSO:Pr single crystals were grown by means of the Czochralski method by one of us (B. I. Minkov). We studied three single crystals containing Pr concentrations of 0.3, 0.8, and 2.5 wt% Pr^{3+} and dimensions of about $8 \times 8 \times 6\text{ mm}^3$. The YSO host crystal has a density of 4.45 g/cm^3 with an effective atomic number of $Z_{\text{eff}} = 33.6$ and a refractive index of $n = 1.8$.

2 RESULTS AND DISCUSSION

The broad Pr^{3+} emission bands, see Figure 2, located between 260 nm and 370 nm are caused by transitions from the bottom of the $4f^15d^1$ configuration to levels of the $4f^2$ configuration; i.e. to the $^3\text{H}_J$ and $^3\text{F}_J$ states. The faint emissions in the 490 nm region are caused by transitions from levels of the $^3\text{P}_J$ states down to the $^3\text{H}_4$ ground state of Pr^{3+} . Transitions from the ground state up to the $^3\text{P}_J$ and $^1\text{I}_6$ excited states are responsible for the optical absorption lines between 440 and 500 nm. From the strength of the absorption line at 452 nm ($^3\text{H}_4 \rightarrow ^3\text{P}_2$), we calculated relative Pr^{3+} concentrations of 0.34 : 0.8 : 2.7 for the crystals doped with 0.3, 0.8, and 2.5 wt % Pr^{3+} , respectively.

¹ These investigations in the program of the Foundation for Fundamental research on Matter (FOM) have been supported by the Netherlands Technology Foundation (STW).

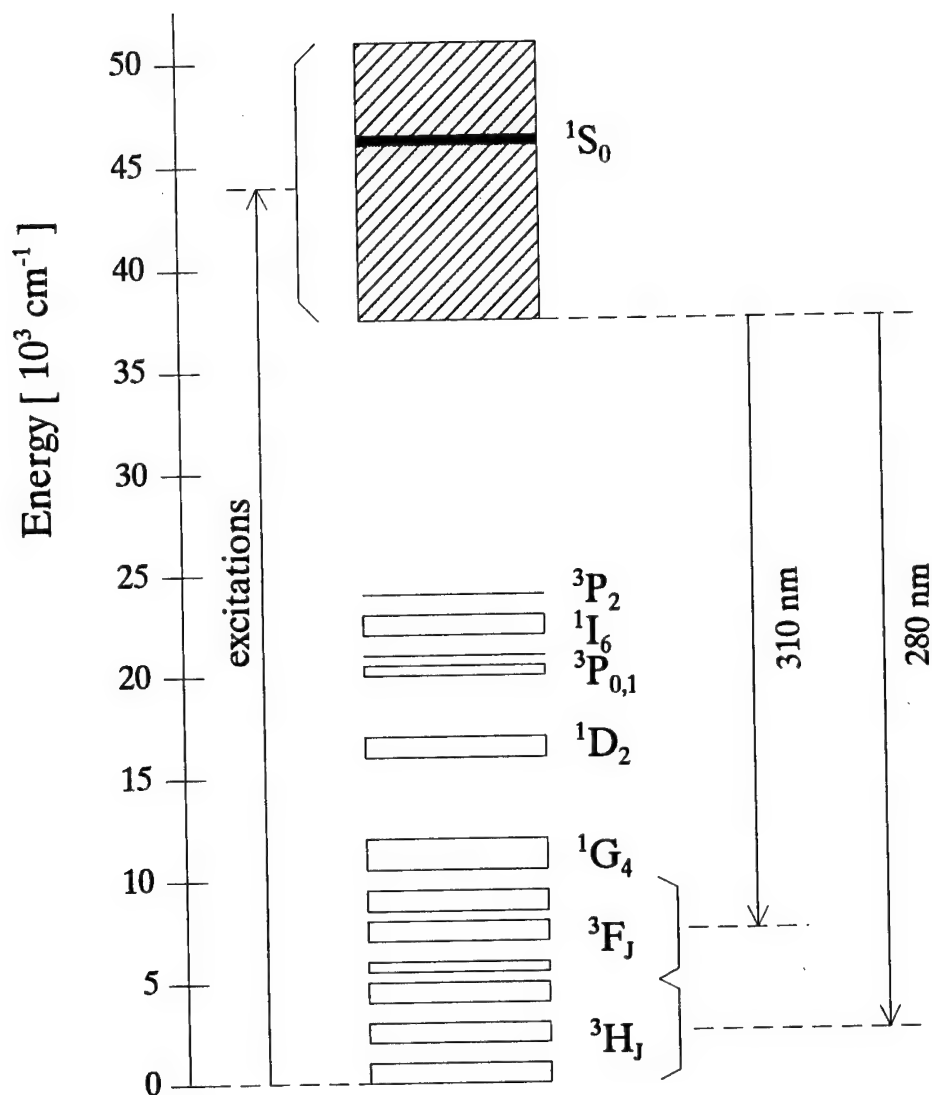


FIGURE 1 Energy levels of the $4f^2$ and $4f5d$ configuration of Pr^{3+} in Y_2SiO_5 single crystals. The shaded region represents the location of levels of the $4f5d$ configuration.

The rapid drop in transmission near 260 nm is caused by the onset of $4f^2 \rightarrow 4f5d$ transitions in Pr^{3+} . The excitation bands between 190 and 260 nm are also attributed to the levels of the $4f5d$ configuration.

In addition to Pr^{3+} , there appears to be small concentrations of Ce^{3+} and Gd^{3+} present in the crystals. The presence of Gd^{3+} is evidenced by the characteristic emission line of

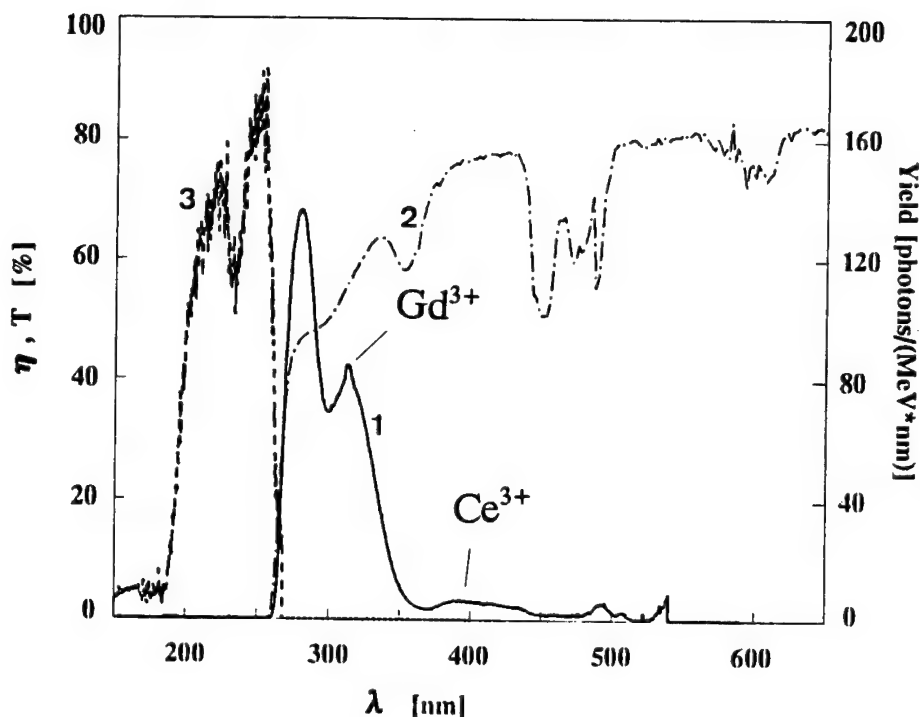


FIGURE 2 1) X-ray excited emission light yield Y in photons/(MeV·nm). 2) optical transmission T in %. 3) $\lambda_{em} = 280$ nm luminescence excitation quantum efficiency (η) of the 6 mm thick $\text{YSO}:0.8$ wt.% Pr^{3+} . η is expressed as a percentage of the quantum efficiency of Na-Salicylate powder.

Gd^{3+} near 312 nm (${}^6\text{P}_{7/2} \rightarrow {}^8\text{S}_{7/2}$) which can be observed in Figure 2. The presence of Ce^{3+} causes the 5d-4f emission bands between 370 and 450 nm and the 4f-5d absorption bands at 290 and 358 nm.

The light yields of the crystals under X-ray irradiation (total) and with 662 keV gamma radiation employing an electronic shaping time of 0.5 μs are compiled in the second and third column of Table I, respectively. We refer to² for details on the experimental methods used. There appears to be no clear dependence of the light yield on the Pr^{3+} concentration. A fast scintillation component with decay time of 27 to 47 ns is responsible for the light yield observed employing 0.5 μs shaping time. The difference between the total light yield is caused by the presence of a component of several hundreds of μs decay time. We note that similar features have been observed for the scintillation properties of Pr^{3+} doped K_2YF_5 crystals.³

In conclusion, YSO crystals have been studied with different amounts of Pr doping. The crystals show the anticipated luminescence due to 4f5d \rightarrow 4f² transitions in Pr^{3+} . Unfortunately only a small part of this emission appears as fast luminescence ($\tau = 30\text{--}50$ ns). The dominant part (75%) is very slow. Consequently, the crystals are less suited for application as a scintillation detector.

Table I
Scintillation properties of Y_2SiO_5 crystals doped with x wt.% Pr^{3+} .

x (wt.%)	photons/MeV (total)	photons/MeV (0.5 μs)	τ_{fast} (ns)
0.3	5500	1600	47
0.8	7000	1600	33
2.5	6400	1900	27

REFERENCES

1. H. Suzuki, T. A. Tombrello, C. L. Melcher, J. S. Schweitzer, *Nucl. Instr. and Meth.* **A320** 263 (1992).
2. P. Dorenbos, J. T. M. de Haas, R. Visser, C. W. E. van Eijk, R. W. Hollander, *IEEE Trans. Nucl. Sci.* **40** (4) 424 (1992).
3. P. Dorenbos, R. Visser, C. W. E. van Eijk, N. M. Khaidukov, M. V. Korzhik, *IEEE Trans Nucl. Sci.* **40** (4) 388 (1993).

SCINTILLATION MECHANISM IN $\text{CsGd}_2\text{F}_7\text{:Ce}^{3+}$ AND $\text{CsY}_2\text{F}_7\text{:Ce}^{3+}$ CRYSTALS[†]

D. R. SCHAART, P. DORENBOS, C. W. E. VAN EIJK, R. VISSER, C. PEDRINI,*
B. MOINE* and N. M. KHAIDUKOV**

*Delft University of Technology, Faculty of Applied Physics,
c/o IRI, Mekelweg 15, 2629 JB Delft, The Netherlands; *Universite Lyon I—Batiment 205,
43, Boulevard du 11 Novembre 1918, 69622 Villeurbanne Cedex—France; **N. S.
Kurnakov Institute of General and Inorganic Chemistry, Moscow, Russia*

The scintillation properties of CsGd_2F_7 and of isostructural CsY_2F_7 crystals doped with Ce^{3+} together with the energy migration mechanisms to the Ce ions are reported. $\text{Ce}^{3+} \rightarrow \text{Gd}^{3+}$ as well as $\text{Gd}^{3+} \rightarrow \text{Ce}^{3+}$ energy transfer, both dependent on temperature and Ce concentration, strongly influence the scintillation properties.

Key words: Scintillation, energy migration, 5d–4f luminescence.

1 INTRODUCTION

Recently we reported on the scintillation properties of CsGd_2F_7 crystals doped with Ce^{3+} concentrations between 0.1 and 10 mol% Ce^{3+} .^{1,2} The intensity of a fast scintillation component, due to 5d–4f luminescence of the Ce^{3+} ions, appeared to increase with the Ce concentration. On the other hand, a slow component becomes less dominant and its decay time becomes shorter at high Ce concentration. With the expectation to obtain better scintillation properties, crystals with 20 and 30 mol% Ce were studied. To understand the scintillation excitation mechanisms, we also studied the luminescence properties of the isostructural CsY_2F_7 crystals doped with Ce.

For details on the method of crystal growth and the experimental techniques to study scintillation properties, we refer to.^{1,3} Two experimental set-ups were used for determining excitation spectra in the vacuum ultra violet (VUV): i) a set-up installed at the SA61 line of the SUPER-ACO synchrotron facility at LURE (laboratoire pour l'utilisation du rayonnement) in Orsay, France, and ii) a set-up employing a D_2 lamp, a VUV-monochromator, and MgF_2 optics in Delft, The Netherlands.

2 RESULTS AND DISCUSSION

CsY_2F_7 and CsGd_2F_7 crystals have an orthorhombic structure with probably 8 inequivalent sites for the Y and Gd ions.⁴ Ce^{3+} is expected to enter the crystal at Y or Gd sites. Optical absorption, luminescence, and excitation spectra indicate the presence of two inequivalent Ce^{3+} centers, hereafter referred to as Ce_I and Ce_{II} . Ce_I centers luminesce near 310 nm and Ce_{II} near 332 nm. Based on optical excitation spectra of these bands and optical absorption spectra, we arrived at the level schemes shown in Figure 1. The main features are: i) the Ce_I luminescence band overlaps the $\text{Gd}^{3+} {}^8\text{S} \rightarrow {}^6\text{P}$ absorption line causing complete energy transfer from Ce_I to neighboring Gd ions, ii) due to a small overlap of the Ce_{II} emission band at 332 nm with the Gd 312 nm absorption line,

[†] These investigations in the program of the Foundation for Fundamental research on Matter (FOM) have been supported by the Netherlands Technology Foundation (STW)

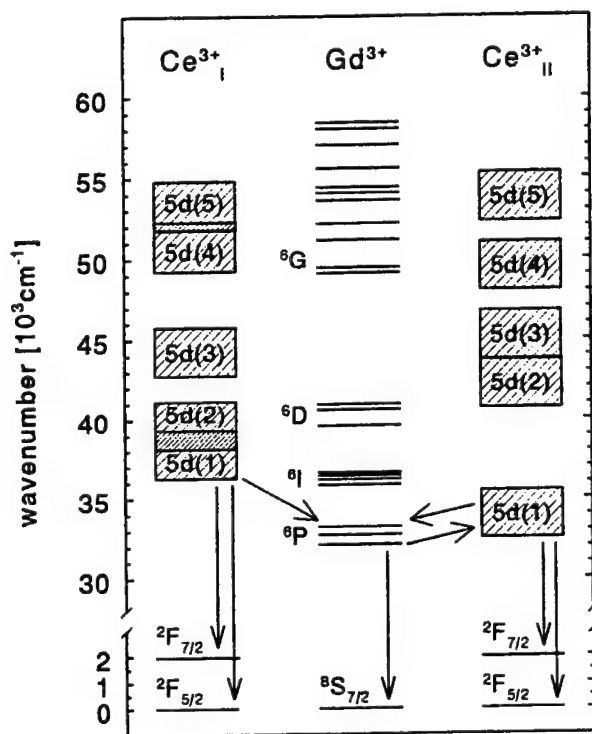


FIGURE 1 Energy level schemes of Gd^{3+} , Ce_I and Ce_{II} centers in $CsGd_2F_7$ and CsY_2F_7 crystals.

$Ce_{II} \rightarrow Gd$ transfer is also possible iii) energy migration is possible over the Gd sublattice, iv) energy transfer is possible from the Ce_I 5d(1) and Gd (6P) levels to the 295 nm Ce_{II} absorption band.

At room temperature, the X-ray excited emission spectrum of $CsGd_2F_7:0.1 \text{ mol\% } Ce^{3+}$ shows a Gd^{3+} emission line at 312 nm and a Ce_{II} type emission band at 340 nm, see Figure 2. The excitation bands at 295 nm and 235 nm are ascribed to the 5d bands of the Ce_{II} centers. The narrow line at 312 nm ($^8S \rightarrow ^6P$ of Gd^{3+}) in the excitation spectrum indicates that $Gd \rightarrow Ce_{II}$ energy transfer takes place. Excitation at room temperature in the Ce_I 5d(1) band near 265 nm leads to Ce_{II} luminescence due to $Ce_I \rightarrow Gd \rightarrow Ce_{II}$ transfer.

At temperatures of 95 K a narrowing of the Ce_{II} 5d(1) band occurs; the overlap with the 312 nm Gd line disappears, and consequently there is no $Gd(^6P) \rightarrow Ce_{II}$ energy transfer. Both the 312 nm Gd line and the 265 nm Ce_I 5d(1) band then disappear from the excitation spectrum; see spectrum b in Figure 2. Excitation at 160 nm produces in both CsY_2F_7 and $CsGd_2F_7$ a broad emission band near 450 nm which is attributed to self trapped exciton luminescence. The band which was also observed under X-ray excitation is quenched at room temperature.

Based on excitation spectra as a function of Ce concentration, temperature, and wavelength we arrive at the following model for the scintillation mechanism. Details on this model and a justification for it will be presented elsewhere.⁵ In $CsY_2F_7:Ce$ the energy transfer from the host crystal to Ce is quite inefficient resulting in a light yield of only

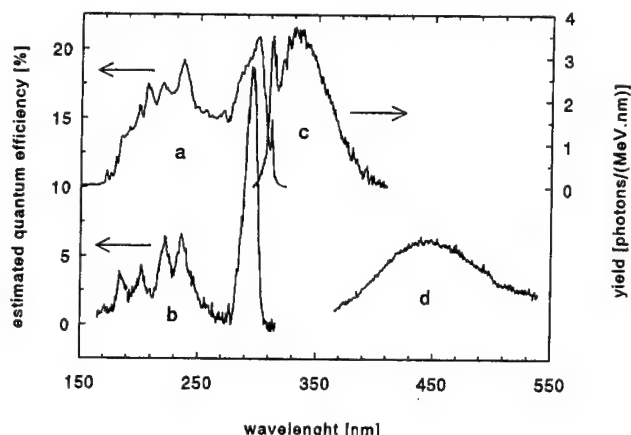


FIGURE 2 a), b) excitation and c), d) emission spectra of $\text{CsGd}_2\text{F}_7: 0.1\% \text{Ce}^{3+}$. a) $\lambda_{em} = 340 \text{ nm}$ and $T = 295 \text{ K}$. b) $\lambda_{em} = 340 \text{ nm}$ and $T = 95 \text{ K}$. c) X-ray excited luminescence (photons/(MeV·nm)) at 295 K . d) $\lambda_{ex} = 160 \text{ nm}$ and $T = 95 \text{ K}$ in arbitrary units. For illustration purposes, spectrum a) has been shifted upwards by 10

1400 photons/MeV at 5 mol% Ce. Due to fast $\text{Ce}_I \rightarrow \text{Ce}_{II}$ transfer the scintillation emission spectrum of this crystal shows mainly Ce_{II} luminescence with a decay time of 32 ns. The Gd sub-lattice in CsGd_2F_7 crystals causes a more efficient energy transfer from the host lattice to the Ce ions resulting in a light yield of 7300 ± 700 photons/MeV for crystals doped with 20% Ce. The fast nonexponential scintillation component of CsGd_2F_7 ($\tau \approx 25 \text{ ns}$) is ascribed to luminescence of directly excited Ce_{II} ions. The dominating slow component (τ of the order of μs) is attributed to Ce_{II} ions excited via the Gd sublattice.

ACKNOWLEDGEMENTS

We wish to thank J. de Haas for his technical assistance during the experiments.

REFERENCES

1. P. Dorenbos, R. Visser, C. W. E. van Eijk, N. M. Khaidukov, M. V. Korzhik, *IEEE Trans. on Nucl. Sci.* **40**(4) (1993) p. 338.
2. P. Dorenbos, R. Visser, C. W. E. van Eijk, N. M. Khaidukov, *Proceedings of the 'Crystal2000' international workshop on Heavy Scintillators*, edited by F. de Notaristefani, P. Lecoq, M. Schneegans (Editions Frontieres, Gif-sur-Yvette Cedex, France, 1993), p. 335.
3. P. Dorenbos, J. T. M. de Haas, R. Visser, C. W. E. van Eijk, R. W. Hollander, *IEEE Trans. on Nucl. Sci.* **40**(4) (1993) p. 424.
4. A. Ellens, S. J. Kroes, J. Sytsma, G. Blasse and N. M. Khaidukov, *Mater. Chem. Phys.* **30** (1991) p. 127.
5. D. R. Schaart, P. Dorenbos, C. W. E. van Eijk, C. Pedrini, B. Moine, N. M. Khaidukov, *J. of Phys. Cond. Mat.* **7** (1995) p.1.

NANOSECOND UV-SCINTILLATION IN CESIUM IODIDE CRYSTALS

S. CHERNOV and V. GAVRILOV

*Institute of Solide State Physics, University of Latvia,
8 Kengaraga st., LV-1063, Riga, Latvia*

The fast UV-luminescence of CsJ have been investigate by nano- and subnanosecond time-resolved spectroscopy. The decay time and yield of fast luminescence are determined. The temperature dependence of fast UV-luminescence intensity under subnanosecond irradiation have been investigated. A most probable nature of fast high temperature UV-luminescence in CsJ cristals is discussed.

Key words: luminescence, rise time, decay time, yield, time-resolved spectroscopy, CsJ.

1 INTRODUCTION

In the last few years fast UV emission in CsJ crystals at room temperature was investigated.^{1–8} The increasing interest in pure CsJ is mainly caused by possible application of this crystals as radiation resistant scintillators with very good timing characteristics. Although the study of the UV-luminescence of CsJ at room temperature has a long histroy (see e.g. ref.),⁷ the mechanism which leads to the UV emission is not clear. There are discrepancies in the definition of the spectral parameters and decay rate of the UV band. It is very likely that the contradictions are caused by the different impurities levels in the CsJ samples and by the use of different sources excitation.

In the present work experiments on the emission in CsJ, especially high resolution temporal measurement, have been carried out under electron pulse excitation.

2 EXPERIMENTAL

Single CsJ crystals, both pure and doped with Br, Cl and Rb were grown in Kharkov Institute of Single Crystals. The emission was excited by single pulses of electron accelerators. Two kinds of accelerators were used: (1) pulse duration 5 ns, electron energy 300 keV, pulse current density 20 A cm⁻² and (2) 50 ps, 200 keV 100 A cm⁻².

The luminescence was detected through a prism monochromator by streak-camera 'Agat-SFI' (time resolution 10 ps) or by means of a 18ELU-FM photomultiplier and S7-19 high speed oscilloscope. The experimental procedure has been discussed elsewhere.^{9,10}

3 RESULTS AND DISCUSSION

The maximum of the fast luminescence band is observed within the region of 305–340 nm at room temperature, and it depends on the types of structural and impurity crystal defects. The major fraction of the centers responsible for the UV luminescence at room temperature decays within 1 ns and the slow component have decay time of 10–15 ns. The quantum yield of the fast luminescence was found to be 0.1–0.5%.

In order to clarify the origin of the fast luminescence emitting state, picosecond spectrscopy will be a useful method of investigation. The decay curve of the 300 nm

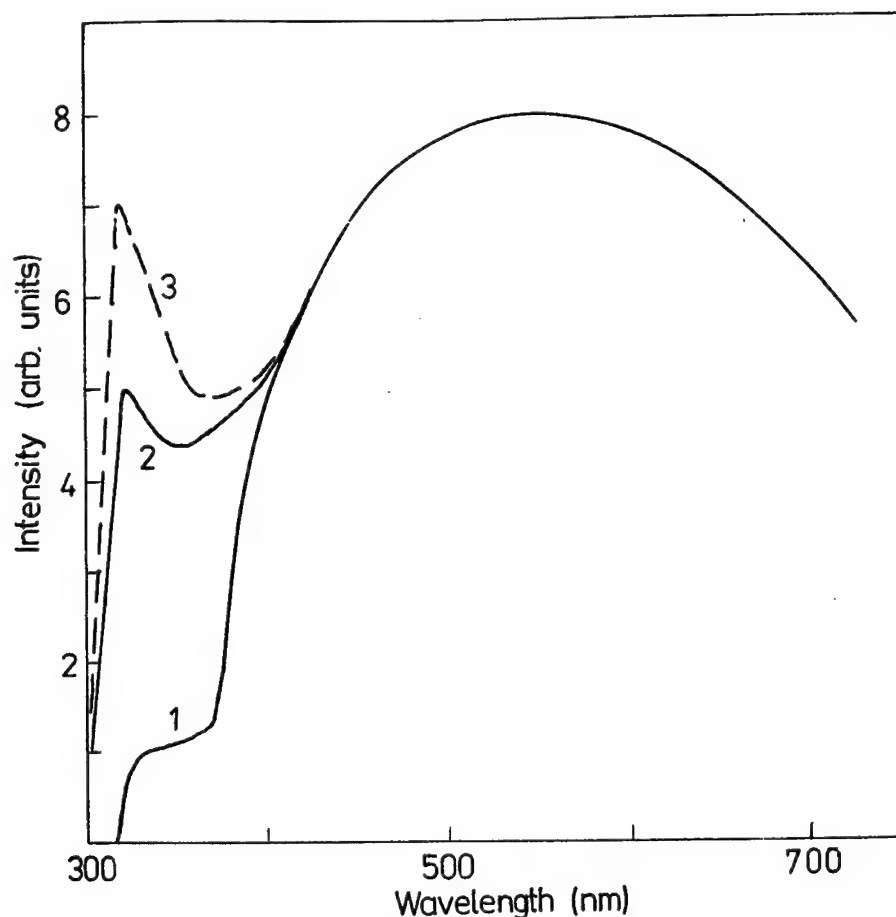


FIGURE 1 Decay kinetics of CsJ luminescence after excitation by 50 ps electron pulses: fast UV emission (305 nm) at 293 K (1), luminescence of triplet STE (337 nm) at 80 K (2) and electron pulse shape (3).

emission intensity in pure CsJ at the room temperature can be decomposed into a fast ($\tau_f = 1$ ns) and a slow ($\tau_s = 10$ ns) exponential component. It can be seen from Figure 1, that at high temperatures the emission intensity decays mainly in the fast component. The rise time of the emission coincides with the excitation pulse duration (see 3, Figure 1) and was obtained to be $\tau_r < 50$ ps. It should be stressed that the τ_r value is much smaller than the growth time of the triplet STE emission in CsJ (see 2, Figure 1).⁹⁻¹¹ The fast emission appears in the temperature region $T > 150$ K. The intensity increases up to room temperature and then remains nearly constant up to 420 K.

The most outstanding feature of the present data is that the rise time of the fast emission τ_r is less than 50 ps, i.e. is considerably smaller than the free electron lifetime in CsJ. It was shown in refs.^{9,10}, that the creation times of the STE and F-centers are controlled by free electron recombination with a self-trapped hole and have values of hundreds of

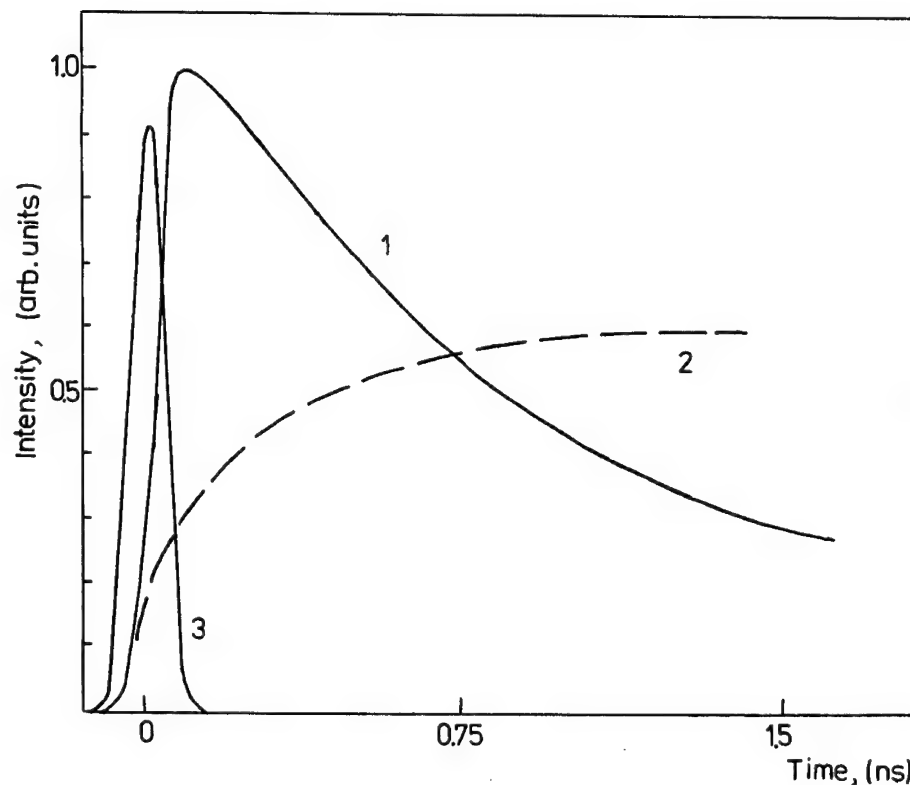


FIGURE 2 Emission spectra of CsI (Tl) crystals with Tl concentration (0.002–0.006) mol% at the excitation by ionizing particle of various types: 1–30 keV X-ray,⁴ 2–1.4 MeV protons; 3–2 MeV α -particles.⁷

picoseconds under presents experimental conditions. Therefore the recombination mechanism of the fast emission can be excluded from consideration, i.e. the emitting state cannot be formed via trapping and recombination of electrons and self-trapped holes.

We suggest that the emitting state arises from the free exciton (FE) or the complex comprising an unrelaxed hole and an electron ($X^0 + e$)¹² capture in the regions perturbed by the lattice defect and STE.

From this viewpoint it is possible to explain the high threshold of excitation (>20 eV) of the fast UV-luminescence which has been observed in experiments with synchrotron irradiation.^{5,6} It is necessary to produce two or more electron excitations simultaneously by one VUV photon to observe fast UV-luminescence.^{5,6} The possibility such as events must be increases with an increase of excitation density. It was shown⁴ that the relative intensity of 2 ns component-luminescence is larger for α -particle than for γ -rays.

From Figure 2 it can be observed that in CsI crystal with the small Tl dope intensity of UV-luminescence is increase with increasing excitation density.⁷

We propose that the emission center mentioned above should be formed as a result interaction of several located electronic excitation: FE + STE, FE + ($X^0 + e$) complex, ($X^0 + e$) complex + STE etc.

The localization of the emission center in lattice sites perturbed by impurities could give rise the probability of the radiative transition and a displacement of the luminescence band to the long-wave region.

4 CONCLUSIONS

A fast UV-luminescence appears in the spectral region 300–340 nm at high temperatures in pure and doped CsJ crystals. The luminescence rise time is less than 50 ps and the decay time of fast emission component 1 ns at the room temperature.

It is proposed that the emission arises as a result interaction of several located electronic excitation.

REFERENCES

1. C. H. Chen, M. P. McCann, and J. C. Wang, *Solid State Commun.* **61**, 559 (1987).
2. S. Kubota, Sh. Sakuragi, S. Hashimoto, and J. Z. Ruan, *Nucl. Instrum. and Meth.*, **A268**, 275 (1988).
3. S. Kubota, H. Murakami, J. Z. Ruan, N. Iwasa, Sh. Sakuragi, and S. Hashimoto, *Nucl. Instrum. and Meth.*, **A273**, 645 (1988).
4. P. Schotanus, R. Kamermans, and P. Dorenbos, *IEEE Trans. Nucl. Sci.*, **37**, 177 (1990).
5. A. N. Belskiy, A. V. Gektin, V. V. Mikhailin, A. L. Rogalev, N. V. Shiran, A. N. Vasilev, E. I. Zinin, Preprint ISK-90-26, Kharkov, Institute of Single Crystals (1990).
6. A. N. Belskiy, A. V. Gektin, V. V. Mikhailin, A. L. Rogalev, N. V. Shiran, A. N. Vasilev, E. I. Zinin, Preprint ISK-91-3, Kharkov, Institute of Single Crystals (1991).
7. R. Gwin and R. B. Murray, *Phys. Rev.*, **131**, 501 (1963).
8. S. Keszthelyi-Landori, I. Foldvari, R. Voszka, Z. Fodor, Z. Seres, *Nucl. Instrum. and Meth.*, **A303**, 377 (1991).
9. A. E. Aluker, R. G. Diech, and G. S. Dumbadze, *Izv. Acad. Nauk Latvian SSR, Ser. Phys. and Techn. Nauk*, **4**, 17 (1987).
10. E. D. Aluker, V. V. Gavrilov, R. G. Deich, and S. A. Chernov, *Fast Radiation Stimulated Processes in Alkali Halide Crystals*, Zinatne, Riga (1987).
11. A. E. Aluker, R. G. Deich, and G. S. Dumbadze, *Pisma Zh. Techn. Fiz.*, **14**, 27 (1988).
12. K. Tanimura, T. Makimura, T. Shibata, N. Itoh, T. Tokizaki, S. Iwai, A. Nakamura, *Proceeding of the XII Intern. Conf. on Defects in Insulating Materials*, Ed. O. Konert, J. P. Spach, **1**, 84 (1992).

DEFECTS INDUCED BY IRRADIATION AT ROOM TEMPERATURE IN CERIUM FLUORIDE

E. AUFRAY, I. DAFINEI, P. LECOQ and M. SCHNEEGANS*

*CERN, Geneva, Switzerland; *LAPP, Annecy, France*

One of the crucial parameters of Cerium Fluoride (CeF_3) which is currently among the best candidates for large electromagnetic calorimeters in future High Energy Physics experiments is the radiation hardness. Several Cerium Fluoride crystals from different producers and with different doping conditions have been irradiated at room temperature with γ -rays at different doses. The behaviour of induced radiation damage has been studied by systematic measurements of absorption spectra with non polarised and polarised light. The saturation of radiation damage in function of the dose, the recovery at room temperature, the optical and thermal bleaching of the damage have been investigated. Based on these experimental results, a tentative explanation of the defects induced by irradiation at room temperature will be given.

Key words: CeF_3 , radiation damage, colour centres, electromagnetic calorimeters.

1 INTRODUCTION

Cerium Fluoride (CeF_3), since the discovery of its fast scintillation,^{1,2} is currently one of the best candidates for large electromagnetic calorimeters in High Energy Physics experiments because of its high density (6.16 g/cm^3), small radiation length (1.68 cm), small Molière radius (2.6 cm). Furthermore because of the high luminosity and high radiation level at the future accelerators, a good radiation hardness is a crucial parameter for the choice of crystals for an electromagnetic calorimeter.

Since 1991, The Crystal Clear Collaboration has undertaken a systematic evaluation of CeF_3 properties and particularly of its radiation hardness. This paper will give a summary of CeF_3 behaviour when exposed to γ radiation at room temperature, based on the study of several CeF_3 crystals from different producers and with different doping conditions.

2 EXPERIMENTAL RESULTS

The radiation damage on CeF_3 has been investigated for more than 200 samples, grown by 8 different producers from all over the world and using different raw materials. The dimension of the studied crystals varies from few cm^3 to 150 cm^3 . The different samples were irradiated at room temperature with the ^{60}Co source (4400Ci) from the radiotherapy unit of Geneva Cantonal Hospital with a dose rate of 3Gy/min .

After a gamma irradiation at room temperature, two different behaviours are observed on the CeF_3 crystals which show some damage. For some crystals, generally grown with bad quality raw material, a pink coloration appears after irradiation due to the presence of 2 absorption bands at 320 nm and at 500 nm (Figure 1). For other crystals, two strong UV absorption bands at 340 nm and 385 nm appear. In some cases two additional weak bands at about 450 nm and 550 nm are observed (Figure 1).

The studies of the recovery at room temperature, of optical and thermal bleaching show that the two kinds of damage observed on CeF_3 are certainly associated with different defects. Indeed, for the first behaviour the damage recovers slowly but continuously at room temperature, and can be annealed by optical or thermal bleaching. For the second

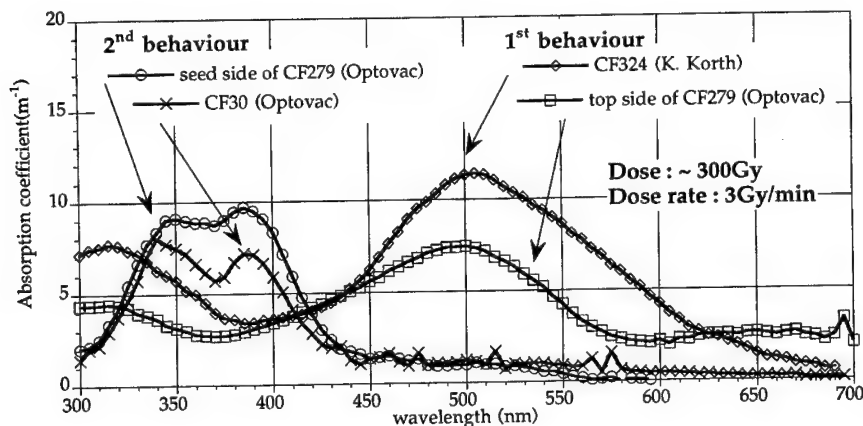


FIGURE 1 Different behaviours of CeF_3 crystals under γ irradiation.

one, after a more or less fast recovery in the first hours after irradiation, a very stable residual damage remains at room temperature. It can be only partially annealed with temperature, and optical bleaching is quite inefficient.³

The fact that the two kinds of damage have been observed in the same crystal, the first one at the top of the crystal and the second one at the seed side, allows to assume that these damages are associated with different impurities having different segregation coefficients.

Moreover the measurements of the absorption spectra with linear polarised light on oriented crystals confirm the different nature of the defects associated to the two kinds of damage. Indeed for the second behaviour, the absorption bands are stronger when the polarisation is parallel to the *c*-axis, whereas for the first behaviour, the absorption at 500 nm is also higher for polarisation parallel to the *c*-axis, but the absorption at 320 nm is stronger for polarisation perpendicular to the *c*-axis. The polarisation dependence of absorption of radiation induced defects suggests they are oriented in preferential directions in the lattice.³

It has been also observed that for long CeF_3 crystals a strong gradient of the damage is observed along the growth axis. This effect, larger at the top of the crystal reflects the segregation of the impurities which occurs during the growth process.

3 DISCUSSION

It is well known that the presence of the impurities lowers the radiation hardness of crystals, as well as the presence of intrinsic defects in the lattice. In the CeF_3 the most probable point defect is the fluorine vacancy which can trap an electron to form an F centre. In some cases, this defect can be associated to impurities present in the crystal, forming perturbed F centre which are generally more stable than F centre only. Moreover, in the CeF_3 structure (tysonite), three types of fluoride sites exist with different Cerium coordinations. The mobility of one of these fluoride ion is higher, creating a preferential site for fluorine vacancies. This can result in the creation of oriented defects as it has been

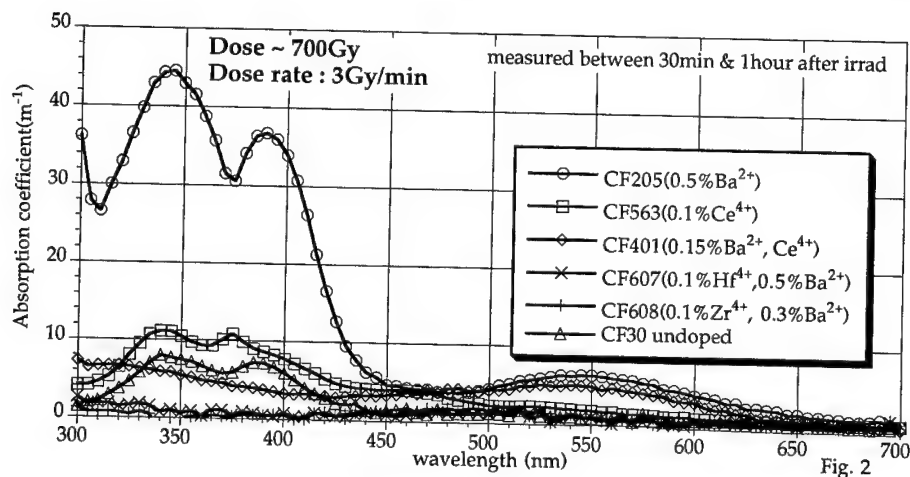


FIGURE 2 Comparison of absorption coefficient of several samples with different dopings.

observed. As it is likely that both fluorine vacancies and impurities play an important role on the radiation damage of CeF_3 , different tests have been made to study their influence.

In order to study the influence of fluorine vacancies on the radiation damage of CeF_3 , some crystals doped with divalent or tetravalent cations have been tested under γ irradiation. The divalent cation doping increases the number of fluorine vacancies (for charge compensation of cation impurities), whereas tetravalent cation doping should reduce it. The irradiation of barium doped crystals shows⁴ that the damage is higher (Figure 2), but recovers very quickly at room temperature proving the role of fluorine vacancies in the radiation damage of CeF_3 . The irradiation of Ce^{4+} doped crystals doesn't show a reduction of the damage (Figure 2), but an important gradient of damage is observed along the crystal with no or little effect on one side. The density of CeF_4 is much lower than CeF_3 (4.8 g/cm^3 vs. 6.13 g/cm^3) which can induce a migration of Ce^{4+} ions to the part of the crystal where no effect is observed. Some crystals doped with both tetravalent and divalent cations have been also irradiated. The observed damage (first type) is small (Figure 2) and recovers quickly at room temperature.

As it has been already said, an important factor for the radiation damage on CeF_3 is the presence of impurities in the raw material. A strong effort has been made to improve the purity of the raw material and particularly in reducing oxygen contamination. Recently several long CeF_3 crystals grown with raw material which had undergone specific treatment have been irradiated. An important improvement in the radiation hardness of CeF_3 has been observed. Indeed, several recent crystals grown with different raw materials show no radiation effect (Figure 3), after a strong gamma irradiation at high dose up to 5000 Gy .³ These results show that CeF_3 could be intrinsically radiation hard at room temperature. And even for the crystals of the new generation which still present some radiation effects, the intensity of the damage is very low and no gradient is observed due to the good uniformity of the quality all along the crystal. It has been also observed that the improvement of the purity of the raw material decreases the saturation dose of CeF_3 . Whereas for the first generation of crystal the saturation was reached after about 1000 Gy , for the latest crystals, the saturation dose is less than 100 Gy . It shows that the reduction of impurities decreases the number of potential defects in CeF_3 .

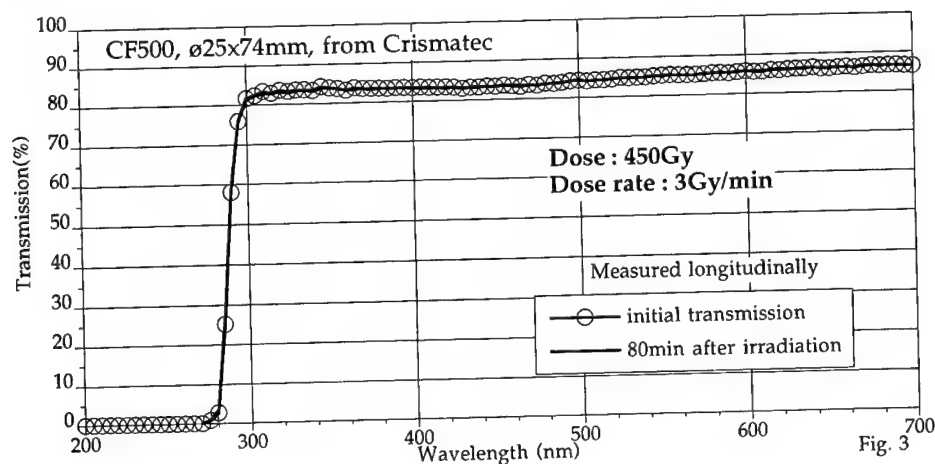


FIGURE 3 Radiation effect on a CeF_3 grown with a specific purification treatment.

This result confirms that a good control of purity of the raw material allows to reduce radiation effects and that CeF_3 could be intrinsically radiation hard at room temperature. This fact seems to confirm that the damage observed on CeF_3 at room temperature is not simply due to the formation of F centres, but probably more complex colour centres involving fluorine vacancies with oxygen or diverse impurities. This is coherent with the results obtained by irradiation at low temperature.^{5,6,7}

4 CONCLUSION

The precise nature of the defects created by irradiation at room temperature on CeF_3 is not yet known. But the different studies made on CeF_3 grown with different raw materials and different dopings, show that the fluorine vacancies intrinsically present in the material play a role, but not alone (damage created is not simply F centre). The purity of the raw material is the crucial parameter to obtain radiation hard crystals. The latest results obtained with the new crystals allow to consider CeF_3 as a suitable candidate for application in High Energy Physics, provided the raw material and growth conditions are correctly chosen.

ACKNOWLEDGEMENTS

The authors want to thank all the members of the Crystal Clear collaboration, as well as the companies Harshaw QS (France), Karl Korth (Germany), NKK (Japan), Optovac (USA), Preciosa Monocrystal (Czech Republic), the Shanghai Institute of Ceramics (China) and the Vavilov State Optics institute (Russia) for the procurement of samples.

REFERENCES

1. W.W. Moses and S.E. Derenzo, *IEEE Trans. Nucl. Sci.* NS-36, 173 (1989).
2. D.F. Anderson, *IEEE Trans. Nucl. Sci.* NS-36 (1989) 137, NIM A287, 606 (1990).
3. E. Auffray *et al.*, to be published in the proceedings of MRS Spring meeting 94, San Francisco, April 4–8, 1994.
4. Further results on Cerium Fluoride crystals, Crystal Clear collaboration, NIM A332, 373 (1993).
5. L.E. Halliburton, to be published in the proceedings of MRS Spring meeting 94, San Francisco, April 4–8, 1994.
6. R.T. Williams *et al.*, 15th Crystal Clear Collaboration meeting CERN, Geneva, June, 27–28 1994.
7. V. Topa *et al.*, to be published in the proceedings of Eurodim 94, Lyon, July, 5–8 1994.

LOCAL TRAP CENTRES IN PbWO_4 CRYSTALS

E. AUFRAY, I. DAFINEI, P. LECOQ and M. SCHNEEGANS*

*CERN, Geneva, Switzerland; *LAPP, Annecy, France*

This paper reports on PbWO_4 trapping centres analysis by the thermally activated luminescence (TSL) method as an attempt to explain the nature of luminescence and quenching processes in PbWO_4 crystals.

At least four trapping centres were identified with energy values of $E_1 = 0.183$ eV; $E_2 = 0.297$ eV; $E_3 = 0.518$ eV; $E_4 = 0.525$ eV and activation temperatures of $T_1 = -154^\circ\text{C}$; $T_2 = -107^\circ\text{C}$; $T_3 = -54^\circ\text{C}$; $T_4 = +8^\circ\text{C}$ respectively. The excitation and emission spectra of thermoluminescence are given. The possible nature of the trapping centres is discussed.

Key words: luminescence, thermally activated luminescence, PbWO_4 .

1 INTRODUCTION

Although the light yield is quite low ($\cong 100$ photons/MeV), PbWO_4 is considered a promising scintillator particularly because of its very high density ($d = 8.2$ g/cm³) leading to a short radiation length ($\chi_0 = 0.87$ cm) and a small Molière radius ($R_m = 2.2$ cm). It also has a good radiation hardness, is not hygroscopic and the decay time constant is particularly fast (80% of scintillation in 20 ns). This low value is due to the strong temperature quenching of several emitting centres and may be connected with the presence of electron levels in the forbidden band.

Though very intensively studied in the last few years, there is no general agreement in the PbWO_4 luminescence centres origin and no systematic work has been done on PbWO_4 thermoluminescence despite the high sensitivity of this method in revealing energy levels associated with radiative recombination. Virtually nothing is known about the local centre parameters although the energy levels which govern the PbWO_4 luminescence lie in the forbidden band. The aim of this work was to examine the trapping centres in PbWO_4 and to determine their parameters by thermally activated luminescence (TSL) method.

2 EXPERIMENTAL RESULTS

The investigated crystals were obtained from Dr. M. Korzhik from the Institute of Nuclear Problems in Minsk, Belarussia, and were grown by Czochralski method in platinum crucibles in atmosphere close to air in composition with some abundance of W in the initial mixture. The crystals were transparent and had no visible defects.

A thermoluminescence bench has been specially designed for the PbWO_4 studies. It allowed TSL spectrum recording with wavelength control both in excitation and in emission. Each 1 cm³ PbWO_4 sample was held in a commercially available TRG/TBT cryostat with quartz windows free of oil vapour. A BT200/TBT temperature controller heated the crystal at a typical rate of $5^\circ\text{C}/\text{min}$ with an accuracy of 0.1°C in the range -190°C to $+60^\circ\text{C}$. The TSL signal was read with a Hamamatsu R446 photo multiplier and recorded on an X-Y plotter as a function of temperature. A 150W Xenon lamp and a Jobin-Yvon H20UV monochromator with a resolution of 2 nm were used as exciting source.

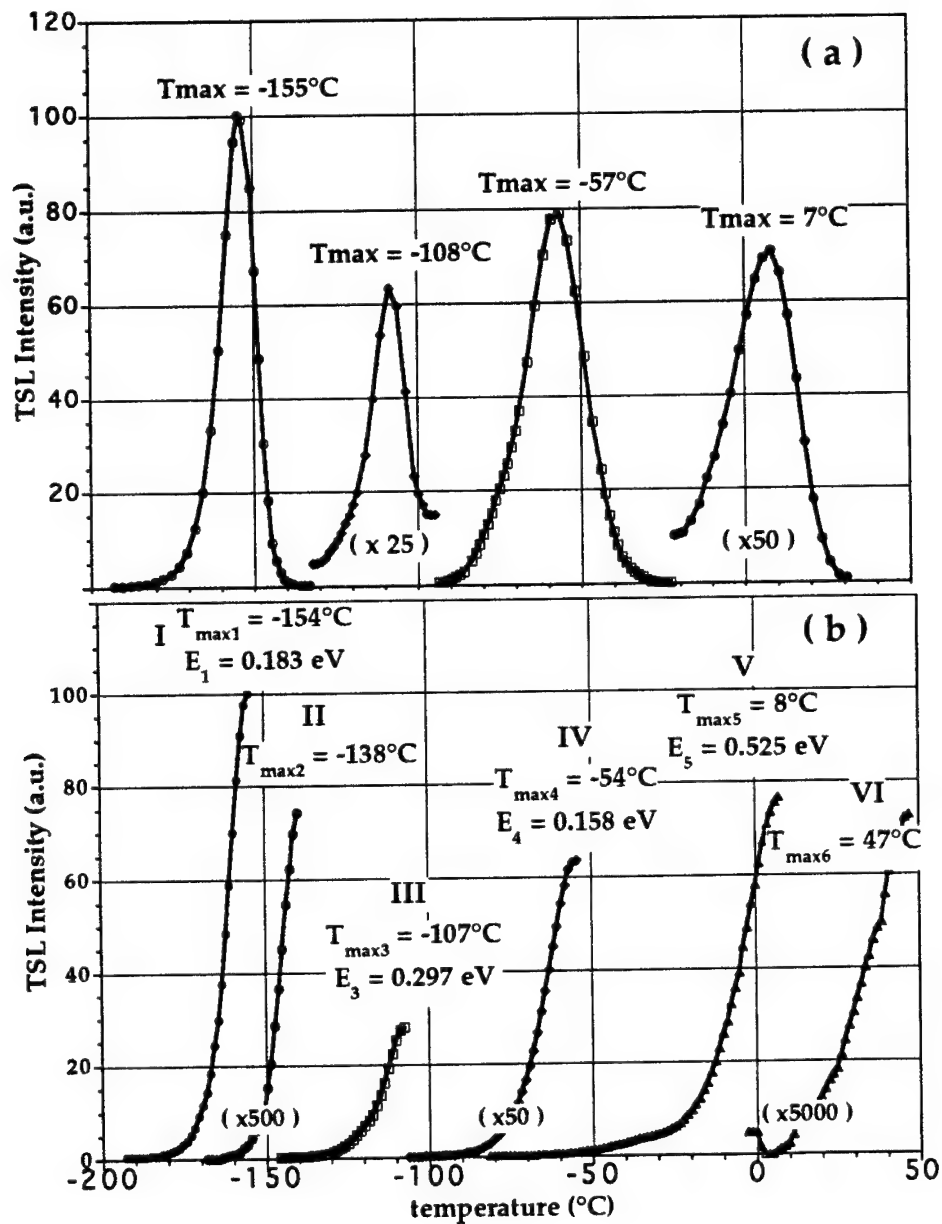


FIGURE 1 (a) TSL spectrum of a PbWO_4 crystal.
 (b) rising part of TSL peaks obtained by the thermal bleaching method.

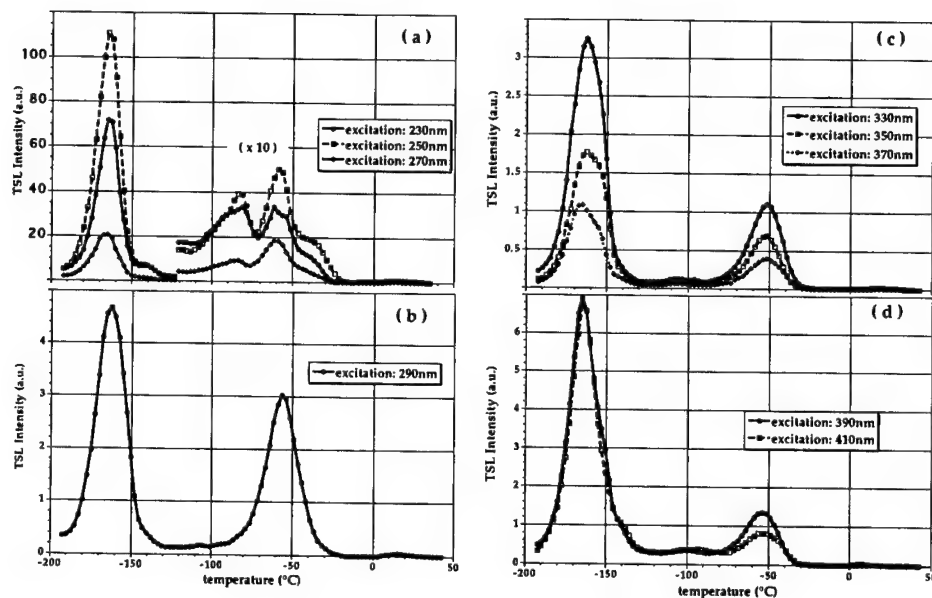


FIGURE 2 PbWO₄ glow peak dependence on the excitation wavelength in the 230 nm–290 nm (a. and b.) and 330 nm–410 nm (c. and d.) spectral range.

For energy calculations the initial rise method was used. During the first portion, the glow curve can be expressed as:

$$I = F \cdot \exp(-E/kT)$$

where F is approximately constant. Plotting $\log I$ vs $1/T$ will result in a straight line. From its slope $-E/k$, the thermal activation energy for the trapped carriers, E , can be extracted. Since the method is applicable only to well defined peaks, a 'cleaning-up' of those having a complex structure was tried by thermal bleaching. To do this, the sample was warmed-up to a temperature just below that of the considered peak and then quickly re-cooled. As a consequence, the traps which complicate the peak in question are emptied and after warming the sample the low temperature side of the peak appears clean.

Several PbWO₄ samples were studied and all of them presented four major glow peaks within the temperature range mentioned above after typically 20 min of Xe lamp exposure at -192°C (Figure 1a). A detailed analysis of the glow peaks for an arbitrarily chosen sample proved that the TSL spectrum is more complicated and at least six peaks were identified (labelled in Figure 1b from I to VI). The thermal activation energy was calculated for four of them. The peaks II and VI have a more complicated structure and their activation energy could not be calculated through the initial rise method. For the V peak, though strongly perturbed at the beginning by a second peak, it was still possible to evaluate the activation energy by this method. The values of the glow peak position and their activation energy are given in Figure 1b. Figure 2 give the TSL spectra obtained for monochromatic excitation and illustrate the complex nature of both major peaks at $\cong -150^\circ\text{C}$ and $\cong -50^\circ\text{C}$. All these spectra are corrected for the spectral characteristic of the Xe

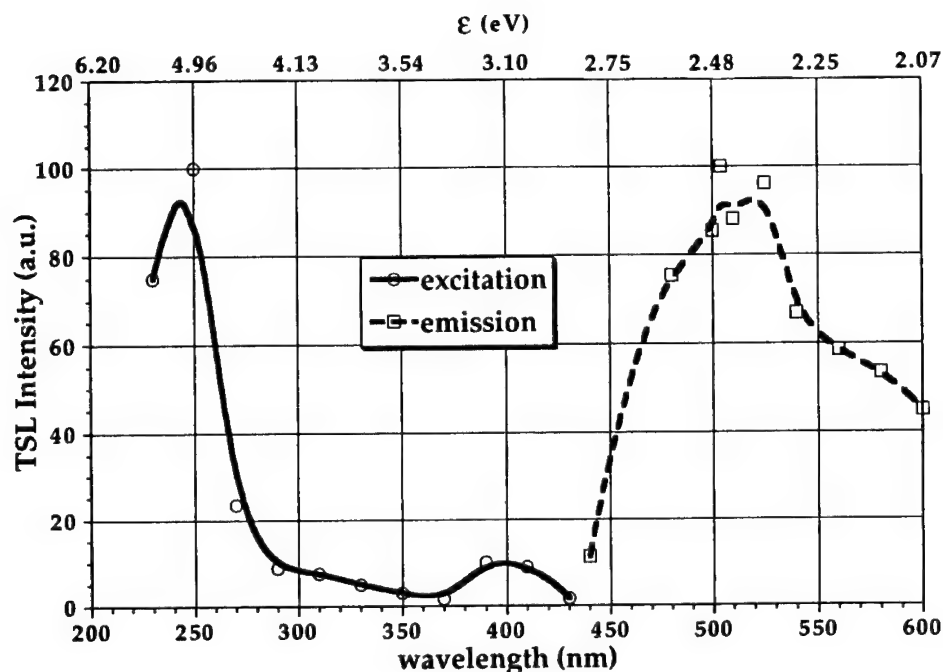


FIGURE 3 PbWO₄ thermoluminescence excitation and emission spectra.

lamp and were plotted in the same arbitrary units. The spectral analysis of the TSL signal, corrected for the quantum efficiency of the R446 photomultiplier, is given in Figure 3 together with the TSL excitation spectrum.

3 DISCUSSION

The PbWO₄ photoluminescence emission spectrum at low temperature is composed of two large overlapping bands peaking at 420 nm and 495 nm and a third weaker band at 600 nm. At room temperature the emission is almost entirely quenched. Under γ excitation, the observed spectra are the superposition of the above mentioned bands. The relative intensities of the blue and green bands and their contribution to the total spectrum depend strongly on the crystal purity and its growing conditions. As a result, the position of luminescence spectrum maxima varies from 430 nm to 530 nm.

Although the spectral dependence of the TSL signal given in Figure 3 is not as reliable as that obtained from photoluminescence or radio luminescence measurements,¹ it seems that only the 504 nm emitting centre is responsible of the thermoluminescence emission. On the other hand, the TSL excitation spectrum, correlated with the photoluminescence and reflectivity spectra² in PbWO₄, suggest that the photoexcited electrons enter the conduction band and after thermalisation pass either to the scintillating centres or to the trapping centres. In this last case, by thermal activation two processes are possible: the

return of trapped carriers to the initial state followed by radiative recombination at the centre(s) active in fluorescence or the direct transfer to the scintillating centre(s) followed by radiative desexcitation.

Thermostimulated conductivity (TSC) measurements will identify which of the two processes is responsible of each TSL peak. They will also help in finding out the signs of the recombination and trapping processes in PbWO₄, which for the moment we consider to be due solely to electrons as free carriers. Indeed, when PbWO₄ crystals are grown, some loss of oxygen occurs. Thus an oxygen deficient crystal is pulled from the melt. We assume that oxygen vacancies are the predominant ionic defects in PbWO₄ crystals. Local charge compensation of these vacancies will create different kinds of defect which act as electron traps. The electronic nature of the traps responsible of the I and II overlapping TSL peaks is proved by the evolution of their relative amplitude dependence on the excitation wavelength (Figure 2c). For the other TSL peaks, the situation is much more complex (Figure 2a, b) and any statement on their nature is impossible for the moment.

4 CONCLUSIONS

The first low temperature TSL measurements on PbWO₄ prove the existence of at least six trapping centres in this crystal. The evaluation of the thermal activation energy of the trapped carriers was made through the initial rise method for four of these peaks.

Only the 495 nm luminescence centre is responsible for the TSL signal.

The excitation of TSL occurs mainly through a Pb²⁺ (¹S₀ – ¹P₁) band to band transition but other kind of excitation might also be possible.

Apparently only electronic traps participate to TSL process in PbWO₄.

REFERENCES

1. I. Dafinei, E. Auffray, P. Lecoq, M. Schneegans, *Lead tungstate for high energy calorimetry*, MRS Spring Conference, San Francisco, April 1994.
2. R. Grasser, A. Scharmann, K. Vlachos, *A renewed investigation of the luminescence of PbMoO₄ and PbWO₄*, report.

TEMPERATURE DEPENDENCE OF CROSSLUMINESCENCE CHARACTERISTICS IN CsCl AND CsBr IN THE 20–300 K RANGE

V. MAKHOV,³ J. BECKER,¹ L. FRANKENSTEIN,¹ I. KUUSMANN,² M. RUNNE,¹
A. SCHRÖDER¹ AND G. ZIMMERER¹

¹*II. Institut für Experimentalphysik der Universität Hamburg;* ²*Institut für Physik, Tartu,*
Estland; ³*Lebedev Physical Institute, Moscow, Russia*

Crossluminescence characteristics of CsCl and CsBr crystals were studied in the temperature range 20–300 K under excitation by synchrotron radiation with photon energies 13–20 eV. Temperature dependences of parameters of high-energy bands in crossluminescence spectra of both crystals show sharp changes at temperature $T < 100$ K. Data are analyzed on the basis of the hypothesis of coexistence in the crystal of different states of core hole separated by an activation barrier.

Key words: crossluminescence, temperature dependence, core hole, activation barrier, synchrotron radiation.

1 INTRODUCTION

Fast intrinsic emission observed in some wideband insulating crystals which is caused by radiative recombination of valence band electrons with relaxed uppermost core (cation) holes is studied during about ten years since its discovery.^{1,2} We shall refer to it as the crossluminescence (CRL) as proposed in ref.³ Many recent theoretical and experimental investigations^{4–8} show that CRL is a local phenomenon: a wideband emission is due to recombination of localized excitations in the local region of the crystal and can be adequately described by a molecular cluster approach.^{5–8} Nevertheless in cesium halide crystals besides wide emission bands predicted by calculations the extra narrow lines are observed which were not found theoretically.⁸ In some cases CRL properties strongly depend on temperature that is not consistent with the existing simple model of CRL. The purpose of the present paper is to study temperature dependence of CRL characteristics in CsCl and CsBr in the temperature range 20–300 K under excitation by synchrotron radiation with photon energies 13–20 eV right after the threshold of CRL excitation.

2 EXPERIMENT

Experiments were performed at the SUPERLUMI station⁹ of HASYLAB at DESY. Two secondary monochromators were used for measurements in different spectral ranges (in fact for different samples): 0.5-meter Czerny-Turner-type monochromator (visible and UV ranges; CsCl crystal) and 0.5-meter Pouey-type vacuum monochromator (vacuum UV and UV ranges; CsBr crystal). In the first case emission spectra were analyzed using position-sensitive detector Photec IPDM 18 having a magnesium fluoride window and a thin S20 photocathode. For our measurements we used its internal ADCs (2*10 bits) and a Target TMCA-2 multi-channel analyser. The best spectral resolution for the PSD system with this monochromator is 0.8 nm. In the second case the solar-blind photomultiplier was used to detect emission spectra.

Crystals were grown in Tartu by the Stockbarger method after a special purification cycle and were polished before the installation into the helium cryostat. Samples were

mounted on the sample holder using silver solution in acetone for better thermal contact. Pressure in the vacuum chamber of the cryostat was about 10^{-9} Torr.

Measured emission spectra were recalculated per unit photon energy interval and were corrected on spectral sensitivity of the detect or used and spectral transmittance of the secondary monochromator. Due to specific peculiarities of used set-up and specimens we could analyze only relative intensities of the peaks in CRL spectra. At low temperatures we have also observed monotonic decrease of CRL intensity with the irradiation dose. This effect is obviously due to quenching of CRL by defects created in the crystal under irradiation.

3. RESULTS

In Figures 1 and 2 emission spectra of CsCl and CsBr measured at different temperatures and their deconvolution into subbands simulated by Gaussians are shown. At 20 K CRL

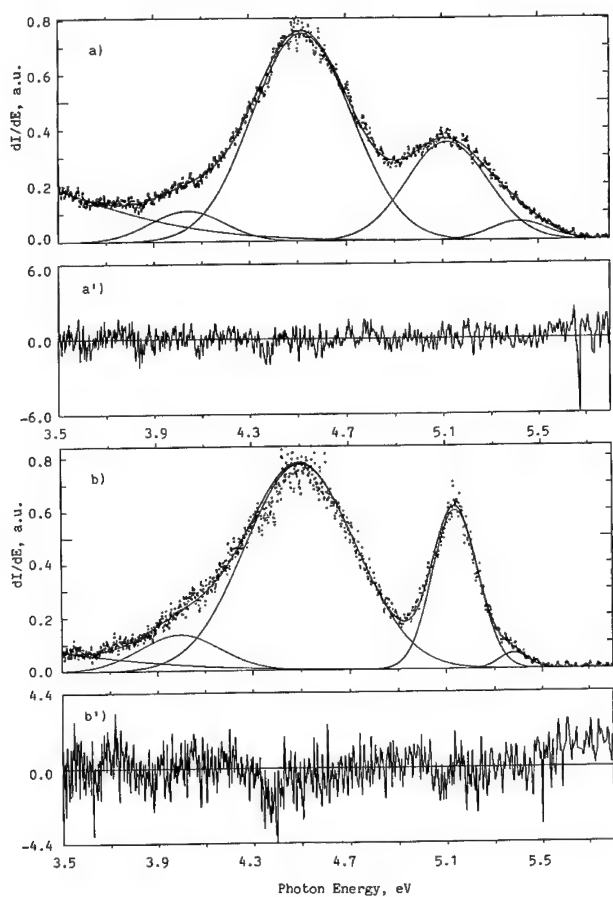


FIGURE 1 Crossluminescence spectra of CsCl crystal measured at 300 (a) and 20 (b) K and their deconvolution into Gaussians (a' and b' — residuals). Excitation photon energy is 14.6 eV. Spectra are normalized to their maxima at 4.5 eV.

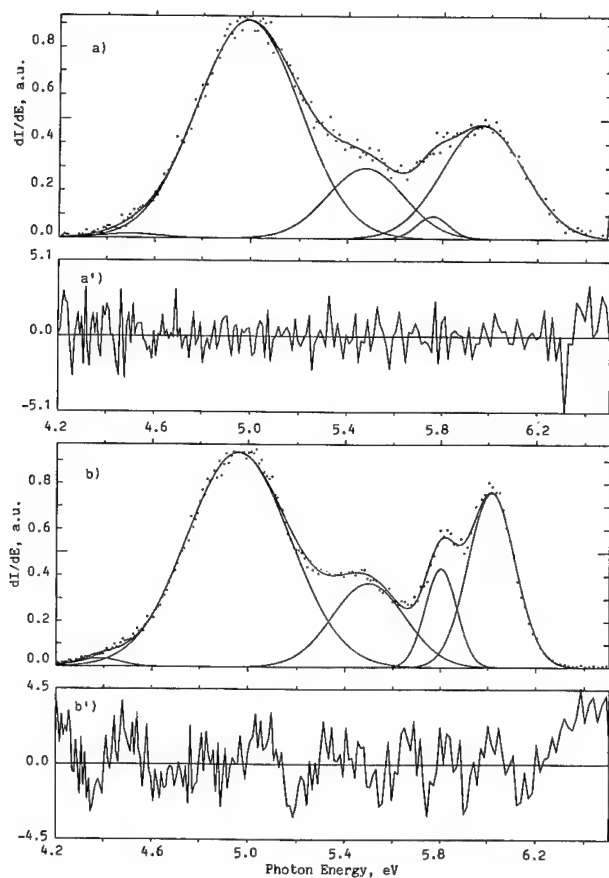


FIGURE 2 Crossluminescence spectra of CsBr crystal measured at 150 (a) and 20 (b) K and their deconvolution into Gaussians (a' and b' — residuals). Excitation photon energy is 14.7 eV. Spectra are normalized to their maxima at 5.0 eV.

spectrum of CsCl consists of two main bands centered near 4.50 and 5.15 eV. High-energy band in CRL spectrum of CsCl can be decomposed at least into two subbands centered near 5.15 and 5.4 eV. CRL spectrum of CsBr has four bands at 4.96, 5.50, 5.80 and 6.02 eV. High-energy edge of CRL spectra shifts monotonically to lower energy with the decrease of temperature that is consistent with the decrease of valence band width and increase of band gap in the crystals as it was found earlier in ref.¹⁰ The shapes of spectra are independent on the excitation energy in the studied spectral region. In accordance with well-known data^{3,4} CRL in CsBr is quenched at temperature $T > 150$ K due to competing radiationless Auger-decay of core holes.

It was found that intensity and spectral parameters of high-energy bands in CRL spectra of CsCl and CsBr show sharp changes at temperature $T < 100$ K (see Figure 3 where temperature dependences of intensity ratios and FWHM for different bands as parameters of spectra deconvolution procedure are shown). FWHM of high-energy band in CRL spectrum of CsCl changes from 0.40 eV at 300 K to 0.22 eV at 20 K and in that of CsBr

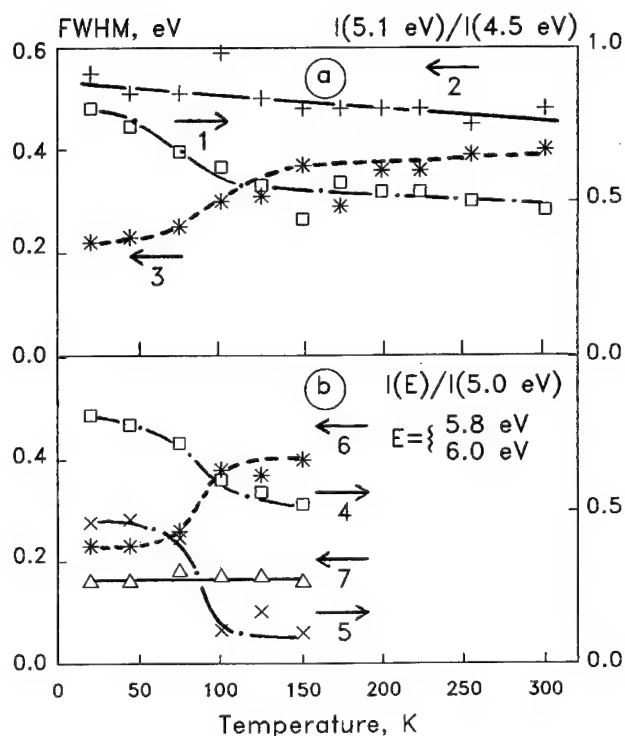


FIGURE 3 Temperature dependences of crossluminescence characteristics in CsCl (a): ratio of intensities (amplitudes) of 5.1 and 4.5 eV bands (1), FWHM of 4.5 (2) and 5.1 (3) eV bands; and CsBr (b): ratios of intensities (amplitudes) of 6.0 and 5.0 eV bands (4), 5.8 and 5.0 eV bands (5), FWHM of 6.0 (6) and 5.8 (7) eV bands. Lines are drawn only for the better visualization of data.

(6.0 eV) — from 0.40 eV at 150 K to 0.23 eV at 20 K. In the same temperature ranges the relative intensities (amplitudes) of these bands increases by a factor of 1.7 in CsCl and 1.55 in CsBr. Temperature dependences of high-energy bands in CRL spectra of CsCl and CsBr can be treated as an appearance at low temperature of 'new' narrow bands with 'new' spectral parameters which are similar for both crystals. The relative intensity of a narrow (FWHM = 0.16 eV independent on temperature) band centered near 5.8 eV in CRL spectrum of CsBr increases by a factor of 4.5 between 100 and 50 K. Characteristics of low-energy bands in CRL spectrum of CsCl (4.5 eV) and CsBr (5.0 and 5.5 eV) depend very slightly on temperature in the same range.

4 DISCUSSION

Several hypothesis were proposed about the nature of narrow lines in CRL spectra of cesium halides. In ref.¹¹ it was suggested that in CRL spectrum an inverted Rydberg-like series of narrow lines and wideband continuum should exist due to radiative transitions to bond and unbond final hole states (hole was supposed to be self-trapped in both cases). Following ref.⁸ parity-forbidden transitions or spin-orbit splitting are responsible for the extra narrow lines. In ref.¹² narrow and wide emission bands in CRL spectrum were

attributed to recombination of valence electron with free (with momentum in the vicinity of a high-symmetry point of the Brillouin zone) and localized (self-trapped) core hole.

Coexistence of emission bands due to free and localized states is possible if an activation energy barrier exists between these two states, otherwise localization of core hole will occur within $10^{-12} - 10^{-14}$ s. The possibility of existence of an activation barrier between free and localized states of core hole was mentioned earlier in ref.¹³ In the presence of an activation barrier a specific temperature dependence of emission intensity should take place that we really observe in CsCl and CsBr for narrow bands which are quenched (or transform into wider emission bands) at $T > 100$ K. Wideband emission of localized excitations is well described by molecular cluster calculations. In fact in this case we should consider the bond state of relaxed core hole and electron from valence band. Probably it would be fruitful to introduce a new term 'core-valence exciton' describing the bond state of core hole and valence electron. In principle such excitation can exist both in localized and mobile (free) state.

One more consequence of possible coexistence of free and localized states is the possibility of migration of free excitations before self-trapping. Migration process results in radiationless losses of excitations near the surface of the crystal that can lead in particular to the non-exponential decay (quenching) of CRL at excitation energies where absorption coefficient is high. The effect was observed in ref.^{14,15} and can be explained both by migration of core excitations and the resonant energy transfer to the surface states. Following our suggestions in the first case the effect should be more pronounced at low temperature. This was really observed in ref.¹⁶ for decay kinetics of CRL in CsCl. Detailed time-resolved measurements at low temperatures are necessary to check this suggestion.

The disadvantages of the proposed model is that the width of narrow emission bands seems to be too large (about 0.2 eV) for the transitions to free states of core hole (it should be of the order kT). So one more possible explanation of the temperature behaviour of CRL emission spectra can be proposed: there exist two different but localized states of core hole also separated by an activation barrier. These states can originate from different local maxima of core band. In principle radiative lifetimes of core holes can be different for these states. So the complicated temperature-dependent CRL decay kinetics should take place that was really observed in fact for all CRL crystals (see for example ref.¹⁴⁻¹⁶)

5 CONCLUSIONS

Till now there is no full understanding of all processes involved in CRL phenomenon. Measurements of temperature dependences of CRL characteristics can give new information about the relaxation and possible migration of core hole excitations. When performing such measurements for CsCl and CsBr crystals it was found that spectral parameters of high-energy bands in CRL spectra of these crystals show sharp changes at temperature $T < 100$ K. Experimental results can be well described in the framework of the model of coexistence in the crystal of different states of core hole separated by an activation barrier. Time-resolved measurements at low temperatures are necessary to study the observed effects in detail.

ACKNOWLEDGEMENTS

The authors wish to thank A. N. Vasil'ev for valuable discussions. One of us (V. M.) would like to thank the German Academic Exchange Service (DAAD) for a fellowship.

REFERENCES

1. Yu. M. Aleksandrov, V. N. Makhov, P. A. Rodnyi, T. I. Syrejschikova and M. N. Yakimenko, *Sov. Phys.-Solid State* **26**, 1734 (1984).
2. J. A. Valbis, Z. A. Rachko and J. L. Jansons, *Sov. Phys.-JETP Letters* **42**, 172 (1985).
3. J. L. Jansons, V. J. Krumins, Z. A. Rachko and J. A. Valbis, *Phys. Stat. Sol.(b)* **144**, 835 (1987).
4. Yu. M. Aleksandrov, I. L. Kuusmann, P. Kh. Liblik, Ch. B. Lushchik, V. N. Makhov, T. I. Syrejschikova and M. N. Yakimenko, *Sov. Phys.-Solid State* **28**, 587 (1987).
5. I. F. Bikmetov and A. B. Sobolev, *Sov. Phys.-Solid State* **33**, 155 (1991).
6. J. Andriessen, P. Dorenbos and C. W. E. van Eijk, *Mol. Phys.* **74**, 535 (1991).
7. A. S. Voloshinovskii, V. B. Mikhailik, S. V. Syrotyuk and P. A. Rodnyi, *Phys. Stat. Sol. (b)* **173**, 739 (1992).
8. J. Andriessen, P. Dorenbos and C. W. E. van Eijk, *Nucl. Tracks Radiat. Meas.* **21**, 139 (1993).
9. G. Zimmerer, *Nucl. Instr. and Meth.* **A308**, 178 (1991).
10. I. Kuusmann, T. Kloiber, W. Laasch and G. Zimmerer, *Radiation Effects and Defects in Solids* **119-121**, 21 (1991).
11. Y. Toyozawa, *Proc. Taniguchi Symposium on Core Level Spectroscopy in Condensed Systems* (Berlin: Springer-Verlag, 1987) p. 231.
12. A. N. Belsky, I. A. Kamenskikh, V. N. Makhov, V. V. Mikhailin, I. H. Munro, A. L. Rogalev, M. A. Terekhin and A. N. Vasil'ev, *Techn. Digest Int. Conf. on Lumin* (Connecticut, 1993) p. M5-100.
13. N. Yu. Kirikova and V. N. Makhov, *Sov. Phys.-Solid State* **34**, 1557 (1992).
14. S. Kubota, M. MacDonald and I. H. Munro, *J. Lumin.* **48-49**, 589 (1991).
15. I. A. Kamenskikh, M. A. MacDonald, V. N. Makhov, V. V. Mikhailin, I. H. Munro and M. A. Terekhin, Preprint DL/SCI/P882E Daresbury Laboratory (1993) p. 10.
16. S. Kubota, Y. Nunoya, J. Ruan (Gen) and S. Hashimoto, UVSOR Activity Report (1991) p. 134.

TIME-RESOLVED STUDIES OF FAST SCINTILLATING CRYSTALS UNDER VUV AND X-RAY SYNCHROTRON RADIATION EXCITATION

E. G. DEVITSIN,¹ N. M. KHAIDUKOV,² N. YU. KIRIKOVA,¹ V. E. KLIMENKO,¹
V. A. KOZLOV,¹ V. N. MAKHOV¹ and T. V. UVAROVA³

¹*Lebedev Physical Institute, Moscow, Russia;* ²*Kurnakov Institute of General and Inorganic Chemistry, Moscow, Russia;* ³*Institute of General Physics, Moscow, Russia*

Time-resolved luminescence studies of several new multi-component crossluminescence crystals as well as $\text{La}_{1-x}\text{Ce}_x\text{F}_3$ ($x = 0.4 \div 0.9$) crystals have been carried out under vacuum UV ($10 \div 30$ eV) and soft X-ray ($h\nu \sim 1$ keV) synchrotron radiation excitation. The band structure parameters of the studied crossluminescence crystals have been estimated by using the spectral data obtained. The non-monotonic dependence of the light yield on x has been observed for $\text{La}_{1-x}\text{Ce}_x\text{F}_3$, the optimum value of x being near 0.7. The result is discussed on the basis of different models of Ce^{3+} emission quenching.

Key words: fast scintillators, crossluminescence, cerium fluoride, synchrotron radiation, emission quenching.

1 INTRODUCTION

Crystals having crossluminescence (CRL), i.e. fast ($\tau < 3$ nsec) intrinsic emission due to radiative recombination of uppermost core holes with valence band electrons,¹ are now considered as promising fast scintillators for high counting-rate detectors of ionizing radiation. Composition variation of complex CRL crystals permits one to obtain emission characteristics required for particular applications. Therefore synthesis and investigations of new multicomponent CRL crystals seem to be a topical problem.

The second family of the crystal scintillators which is now widely discussed for application in fast scintillation detectors is stoichiometric Ce^{3+} compounds, like cerium fluoride. However the nature of complicated emission spectrum and decay kinetics of CeF_3 is still under discussion. Besides, the disadvantage of CeF_3 is also relatively low light yield and strong dependence of emission properties on the crystal quality. Obviously further investigations are necessary to find out the nature of processes forming the spectrum and kinetics of Ce^{3+} emission centers in cerium compounds.

In the present work time-resolved luminescence characteristics of some new complex fluoride CRL crystals as well as $\text{La}_{1-x}\text{Ce}_x\text{F}_3$ ($x = 0.4 \div 0.9$) crystals have been studied using pulsed vacuum UV and soft X-ray synchrotron radiation (SR) excitation at the S-60 SR source.

2 EXPERIMENT

At the S-60 SR source the experimental facility for luminescence studies of solids consists of two stations: 1) station for time-resolved luminescence excitation spectra, reflection spectra and decay kinetics measurements under vacuum UV ($5 \div 30$ eV) excitation; 2) station for time-resolved emission spectra (in the range $2 \div 11$ eV) and decay kinetics measurements under 'white' soft X-ray ($h\nu \sim 1$ keV) excitation. In case of X-ray excitation, when one absorbed photon creates hundreds of electronic excitations the

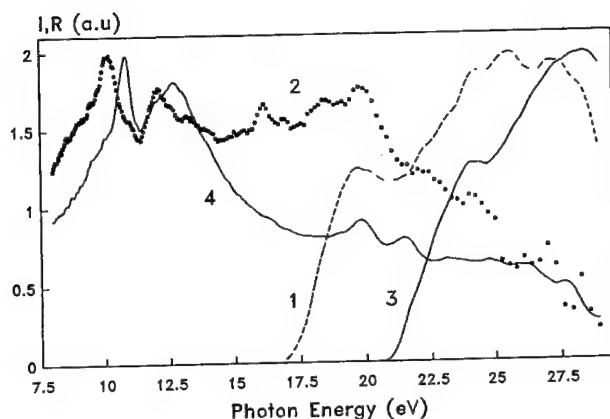


FIGURE 1 Crossluminescence excitation (1, 3) and reflection (2, 4) spectra of Rb_3ScF_6 (1, 2) and KLiYF_5 (3, 4) crystals.

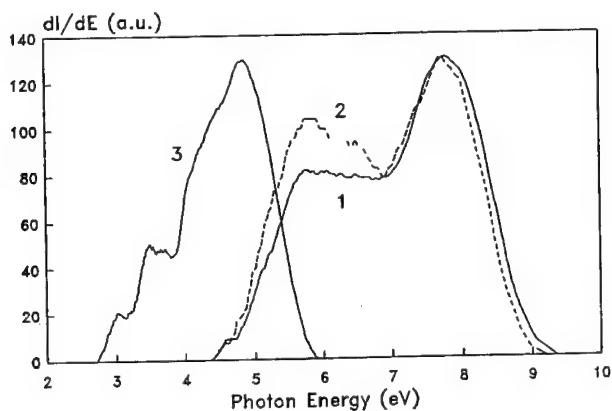


FIGURE 2 Crossluminescence spectra of KLiYF_5 (1), KLiLuF_5 (2) and Rb_3ScF_6 (3) crystals.

conditions existing in the excited region of the crystals are close to those in the 'real scintillator' after high-energy particle absorption.

In all cases measurements were performed on freshly cleaved samples with thickness of several mm. At soft X-ray excitation the emission spectra were detected from both the irradiated surface of the sample ('surface' geometry) and the opposite site of the crystal, i.e. transmitted through the crystal ('bulk' geometry).

The KLiYF_5 , KLiLuF_5 and Rb_3ScF_6 crystals were synthesized by hydrothermal technique. KLiYF_5 and KLiLuF_5 crystallize in their own structure type (monoclinic system, s.g. $P2_1/c, z=4$) with lattice parameters $a = 6.292 \text{ \AA}$, $b = 11.747 \text{ \AA}$, $c = 6.467 \text{ \AA}$, $\beta = 113.715^\circ$, $\rho = 3.49 \text{ g/cm}^3$ and $a = 6.220 \text{ \AA}$, $b = 11.676 \text{ \AA}$, $c = 6.387 \text{ \AA}$, $\beta = 113.837^\circ$; $\rho = 4.98 \text{ g/cm}^3$, respectively.² Rb_3ScF_6 crystallizes in the

tetragonal β -(NH₄)₃ScF₆ structure with lattice parameters $a = 6.477 \text{ \AA}$, $c = 9.222 \text{ \AA}$; $\rho = 3.59 \text{ g/cm}^3$.

La_{1-x}Ce_xF₃ crystals were grown in the Institute of Crystallography of the Russian Academy of Sciences. The growth has been carried out by means of vertically directed crystallization technique (Stockbarger-Bridgeman method) in a fluorine atmosphere.

3 RESULTS AND DISCUSSION

3.1 Crossluminescence Crystals

Measured reflection and excitation spectra for studied crystals are shown in Figure 1. These crystals have CRL excited by photons with $h\nu > 21.2 \text{ eV}$ for KLiYF₅ and KLiLuF₅ and $h\nu > 17.2 \text{ eV}$ for Rb₃ScF₆. For former two crystals the energies of the direct optical creation of anion and cation excitons (from data of reflection spectra measurements) lie at $E_{ex}^a = 11.0 \text{ eV}$ and $E_{ex}^c = 20.1 \text{ eV}$ respectively and for Rb₃ScF₆ — $E_{ex}^a = 10.3 \text{ eV}$ and $E_{ex}^c = 16.4 \text{ eV}$.

CRL emission spectra for these crystals are shown in Figure 2. Since the spectra were measured in the 'bulk' geometry, some peculiarities of the spectra can be due to self-absorption of CRL in the crystal volume. For KLiYF₅ and KLiLuF₅ crystals the CRL characteristics are similar. Their CRL spectra lie in the range $4.3 \div 9.2 \text{ eV}$ and have two bands centered at 5.8 and 7.8 eV. CRL spectrum of Rb₃ScF₆ lies in the range $2.7 \div 5.9 \text{ eV}$ and has the main peak centered at 4.9 eV.

Though theoretical and experimental investigations show that CRL takes place after complete electronic and lattice relaxation of the excited region of the crystal, nevertheless, in most cases correlation between CRL spectra and band structure parameters is rather good.^{3,4} Thus measurements of CRL emission and excitation spectra can be used for the estimation of the band structure parameters of the crystal, namely, valence band width ΔE_v (width of CRL emission spectrum), energy distances between the top of core band and the bottom of conduction band E_{cc} (threshold of CRL excitation) and between the tops of core and valence bands E_{vc} (high energy edge of CRL emission spectrum), band gap $E_g = E_{cc} - E_{vc}$. The bond energies of anion and cation excitons E_b^a and E_b^c can be estimated combining data of CRL excitation and reflection spectra measurements.

From the spectral data the following estimations of band structure parameters were obtained. For KLiYF₅ (KLiLuF₅) these parameters are as follows (core band-K⁺3p): $\Delta E_v = 4.9 \text{ eV}$, $E_{cv} = 9.2 \text{ eV}$; $E_{cc} = 21.2 \text{ eV}$, $E_g = 12.0 \text{ eV}$; $E_b^a = 1.0 \text{ eV}$, $E_b^c = 1.1 \text{ eV}$. For Rb₃ScF₆ corresponding values are (core band-Rb⁺ 4p): $\Delta E_v = 3.2 \text{ eV}$, $E_{cv} = 5.9 \text{ eV}$; $E_{cc} = 17.2 \text{ eV}$, $E_g = 11.1 \text{ eV}$; $E_b^a = E_b^c = 0.8 \text{ eV}$.

3.2 La_{1-x}Ce_xF₃ Crystals

It is well-known that the emission spectrum of CeF₃ consists of two bands: 1) shortwavelength band (SWB) with two maxima at 285 and 305 nm which is due to the radiative transition from the lowest excited 5d state to the spin-orbit split ground 4f state of Ce³⁺ ions situated in regular lattice sites; 2) longwavelength band (LWB) centered near 350 nm which is usually attributed to 5d → 4f transition of Ce³⁺ ions being in defect sites.^{5,6} The decay law for SWB of CeF₃ is non-exponential and has an initial fast ($\tau \sim 2 \div 3 \text{ nsec}$) stage which is due to quenching of Ce³⁺ emission having radiative lifetime $\tau \sim 30 \text{ nsec}$ (the slow stage of the decay).^{6,7}

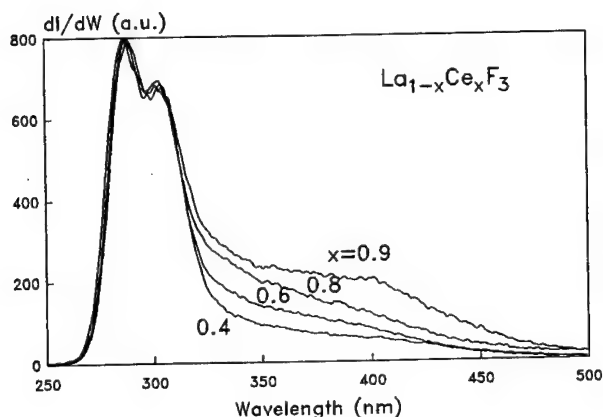


FIGURE 3 Emission spectra of $\text{La}_{1-x}\text{Ce}_x\text{F}_3$ crystals for $x = 0.4, 0.6, 0.8$ and 0.9 .

Emission spectra measured for $\text{La}_{1-x}\text{Ce}_x\text{F}_3$ crystals with different concentrations of Ce^{3+} ions are shown in Figure 3 (the spectra are normalized to their maxima). Both relative and absolute intensity of LWB increases with x while the absolute intensity of SWB (and the total light yield) has a maximum near $x = 0.7$ (the intensity of SWB is about 3 times higher for $x = 0.7$ than for $x = 0.4$ and 0.9). Decay curves measured for 290 nm emission of $\text{La}_{1-x}\text{Ce}_x\text{F}_3$ are shown in Figure 4. The quenching of SWB decreases with the decrease of x . The optimum value of x corresponding to the maximum light yield and relatively fast decay seems to be near 0.7 .

Three main mechanisms of Ce^{3+} SWB emission quenching were proposed so far: 1) non-radiative energy transfer from regular to perturbed Ce^{3+} sites;⁷ 2) non-radiative near-surface recombination as a result of the energy transfer to the surface states;^{5,8} 3) interaction of adjacent excited Ce^{3+} ions in the small volume of the crystal after the absorption of one high-energy photon (or particle).⁹ The first mechanism is efficient in heavily doped CeF_3 and in crystals with high concentration of defects. In principle this mechanism does not decrease the total light yield of CeF_3 . The second mechanism is important only at vacuum UV excitation when the penetration length of radiation is very small (of the order 10^{-6} cm). This mechanism can explain some peculiarities of the spectral dependence of decay kinetics in the vacuum UV excitation region.⁸ The third mechanism is valid only at high-energy excitation and seems to have a threshold near the edge of electronic excitation multiplication in CeF_3 at about 17 eV.¹⁰

The qualitative analysis of our results permits one to conclude that the increase of quenching of SWB with x seems to be directly related with the increase of the non-radiative energy transfer between regular and perturbed Ce^{3+} sites. Since rather small amount of La^{3+} ions strongly suppresses quenching of SWB (La^{3+} ion cannot take part in the energy transfer and be the quencher in this mechanism) the critical radius of the energy transfer is close to the distance between neighbouring Ce^{3+} ions in CeF_3 . Nevertheless, the third mechanism should be also taken into account to explain the increase of the total light yield with x changing from 0.9 to 0.7 . For $x > 0.7$ the decrease of the light yield is obviously due to the decrease of Ce^{3+} emission centers concentration. Thus additional studies are necessary to find out the role of different mechanisms of Ce^{3+} emission

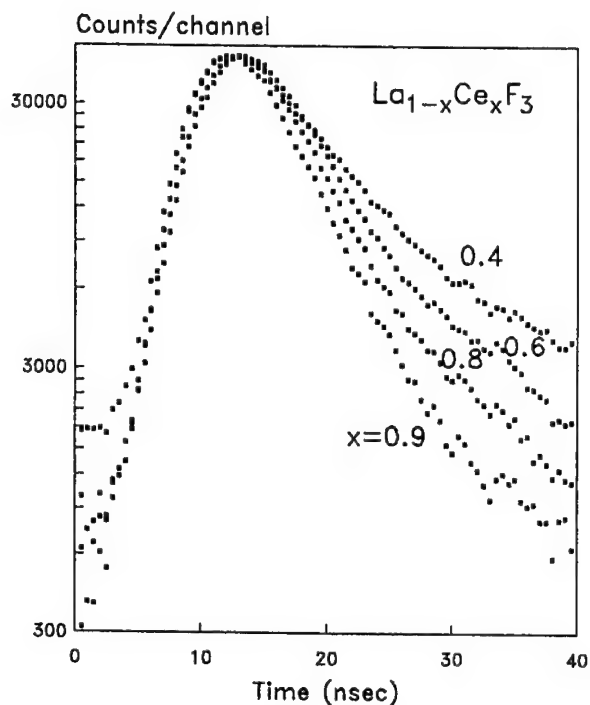


FIGURE 4 Decay curves of 290 nm emission of $\text{La}_{1-x}\text{Ce}_x\text{F}_3$ crystals for $x = 0.4, 0.6, 0.8$ and 0.9 .

quenching.

4 CONCLUSIONS

The use of SR permits one to obtain new information about the emission properties and electron structure of scintillating crystals. By combining spectral data obtained from measurements of emission, excitation and reflection spectra one can estimate the band structure parameters for crystals having CRL. The procedure was successfully used for KLiYF_5 , KLiLuF_5 and Rb_3ScF_6 crystals.

The light yield of $\text{La}_{1-x}\text{Ce}_x\text{F}_3$ ($x = 0.4 \div 0.9$) crystals shows non-monotonic dependence on x . The optimum concentration of Ce^{3+} ions seems to be near 0.7. The value of quenching of Ce^{3+} SWB emission decreases with the decrease of x and correlates to some extent with the decrease of the energy transfer from regular to perturbed Ce^{3+} sites.

REFERENCES

1. Yu. M. Aleksandrov, V. N. Makhov and P. A. Rodnyi, T. I. Syrejschikova and M. N. Yakimenko, *Sov. Phys. -Solid State* **26**, 1734 (1984).
2. A. V. Goryunov, A. I. Popov, N. M. Khaidukov, P. P. Fedorov, *Mater. Res. Bull.* **27**, 213 (1992).

3. J. L. Jansons, V. J. Krumins, Z. A. Rachko and J. A. Valbis, *Phys. Stat. Sol. (b)* **144**, 835 (1987).
4. P. A. Rodnyi and M. A. Terekhin, *Phys. Stat. Sol. (b)* **166**, 283 (1991).
5. C. Pedrini, B. Moine, J. C. Gacon and B. Jacquier, *J. Phys.: Condens. Matter* **4**, 5461 (1992).
6. A. J. Wojtowicz, E. Berman, Cz. Koepke and A. Lempicki, *IEEE Trans. Nucl. Sci.* **39**, 494 (1992).
7. B. Moine, C. Pedrini, D. Bouttet and P. Martin, *Proc. Int. Workshop 'Crystal-2000', Chamonix, France* (September 22–26, 1992), p. 173.
8. A. N. Belsky *et al.*, in press.
9. C. Pedrini, B. Moine, D. Bouttet, A. N. Belsky, V. V. Mikhailin, A. N. Vasil'ev and E. I. Zinin, *Chem. Phys. Lett.* **206**, 470 (1993).
10. I. A. Kamenskikh, M. A. MacDonald, V. N. Makhov, V. V. Mikhailin, I. H. Munro and M. A. Terekhin, Preprint DL/SCI/P882E Daresbury Laboratory (1993).

ODMR OF CD IMPURITY CENTERS IN GG IRRADIATED BaF₂ CRYSTALS

U. ROGULIS, J. TROKŠS, Ā. VEISPĀLS, I. TĀLE, P. KŪLIS and M. SPRINĢIS

Inst. of Solid State Physics, University of Latvia, 8 Kengaraga Str., LV-1063, Rīga, Latvia

The magnetic circular dichroism of the optical absorption (MCD), optically detected magnetic resonance (ODMR) as well as ESR and luminescence in Cd-doped BaF₂ crystals γ -irradiated at RT were investigated. MCD signals centered at 295 nm, 290 nm and 365 nm are observed, together with corresponding radiation induced optical absorption bands in the same wavelength regions. The ODMR detected in all these bands is caused by hyperfine (hf) interaction of unpaired spin with Cd-nucleus. Three types of different Cd-related defects have been separated: 1) Cd⁺_c represented by the MCD of derivative type centered at 295 nm and hf constant $A_{Cd} = 480$ mT, 2) Cd⁺_c-center having lowered symmetry of the nearest neighbours and represented by derivative-type MCD centered at 290 nm and $A_{Cd} = 370$ mT. The nature of perturbation is not clear yet. The ESR spectrum of perturbed Cd⁺_c-center significantly differs from that of the regular Cd⁺_c-center. 3) Center represented by the MCD around 365 nm and the hf constant $A_{Cd} = 380$ mT which is attributed to Cd⁺(1)-type center.

Key words: BaF₂-Cd; Impurity defects; MCD; ODMR; Optical absorption; Luminescence

BaF₂ single crystals find widespread use as fast scintillators, however, only the lead and oxygen—impurity bands have been identified in UV spectral region so far. The optical properties of Cd-related defects are not known. Substitutional Cd⁺_c-defects in alkaline-earth fluorides were recently studied by the ESR technique.¹ ODMR due to Cd-centers detected by tunnelling—recombination luminescence have been observed in CaF₂.² ODMR spectra of Cd⁺_c and A_F(Cd) defects have been detected in KCl and NaCl crystals.³

We studied Cd-defects in BaF₂-Cd crystals using the MCD, ODMR, ESR, optical absorption and luminescence techniques. Cd-doped BaF₂ crystals were grown in vacuum and contained approximately 0.02 at.% Cd. Part of the crystals (denoted as type I) contained at least an order of magnitude less impurities. The impurity content of the other crystals (type II) was comparable to or exceeding (up to 10⁻¹ at.% for alkali metal ions) the Cd concentration. The impurity content was controlled by atomic absorption and mass-spectrometry.

Samples were γ -irradiated at room temperature (doses 10⁵–10⁸ rad). MCD measurements were performed in helium-immersion cryostat ($T = 2$ –4.2 K) in the spectral range 205–530 nm, the applied magnetic field being up to 3.4 T. Frequency range 38–53 GHz (microwave power on the sample in nonresonance system ~ 5 mW) were used for ODMR measurements.

Characteristic γ -induced absorption band of the type I crystal (Figure 1a), located at ~ 295 nm has a derivative type line shape MCD spectrum (Figure 1b). The spectrum of the MCD of the type II crystal (Figure 1c) is shifted to shorter wavelengths ~ 290 nm in respect to that of the type I. The distortion of the line-shape is due to excessive optical density in the type II samples. Additionally, another MCD band located at ~ 365 nm with a shoulder at long wavelength side occurs.

The observed ODMR signals are qualitatively the same for all MCD bands (located at 290, 295 and 365 nm) in both types of samples (Figure 2a, Figure 2b). In the frequency range from 38 GHz to 53 GHz the ODMR spectrum has a central line at $g \sim 2$, the splitting of the side lines is frequency-independent and evidently is the hf splitting (hfs). Analysis indicates that the observed hf splitting is due to Cd-isotopes Cd¹¹¹ (12.8% nat. abundance) and of Cd¹¹³ (12.2%) both having spin $I=1/2$. The average values of hfs for

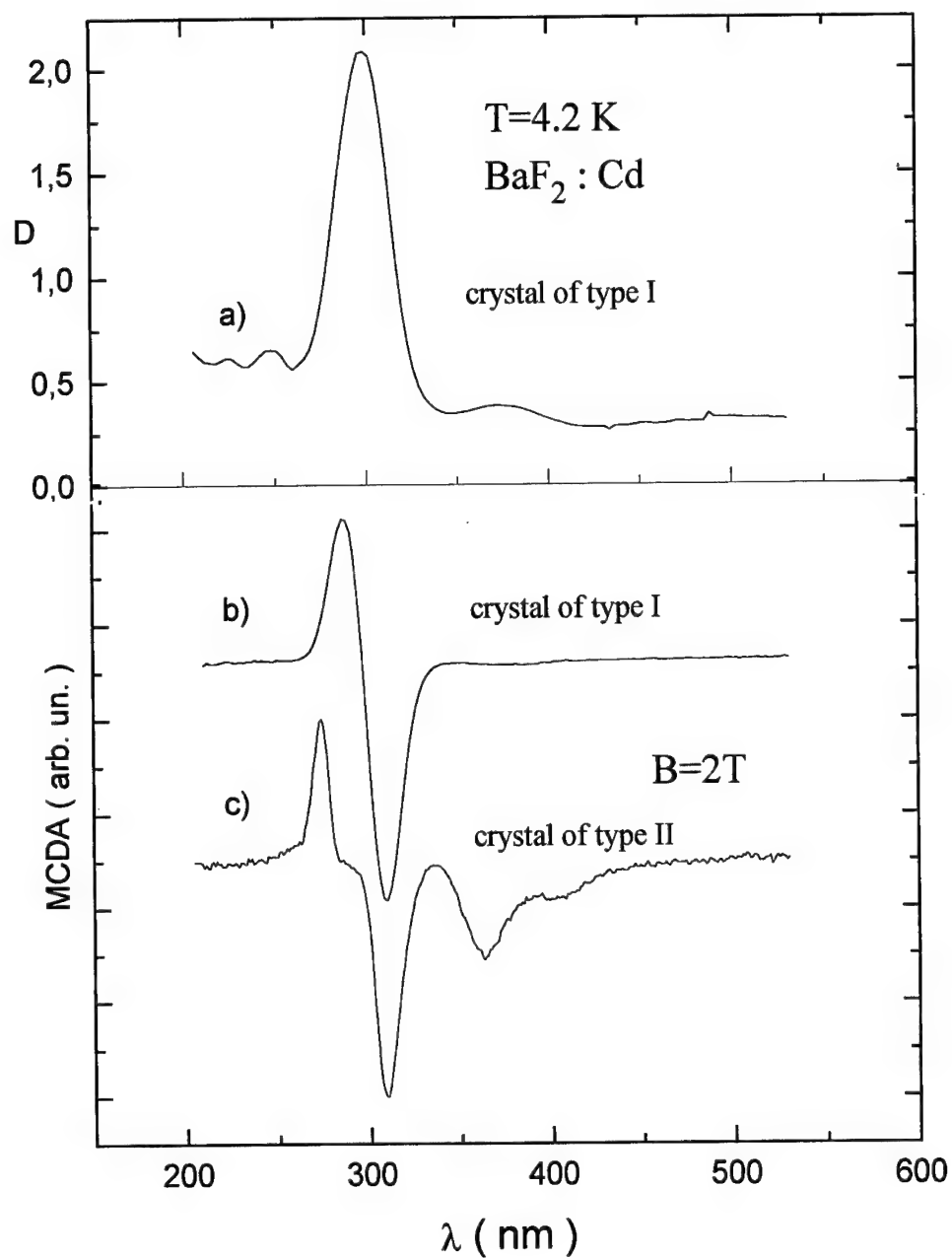


FIGURE 1 The spectrum of the γ -ray induced absorption of the $\text{BaF}_2\text{-Cd}$ (0.02 at.%) crystal of type I (curve a) and the spectrum of the magnetic circular dichroism of the crystal of type I (curve b) and of type II (curve c).

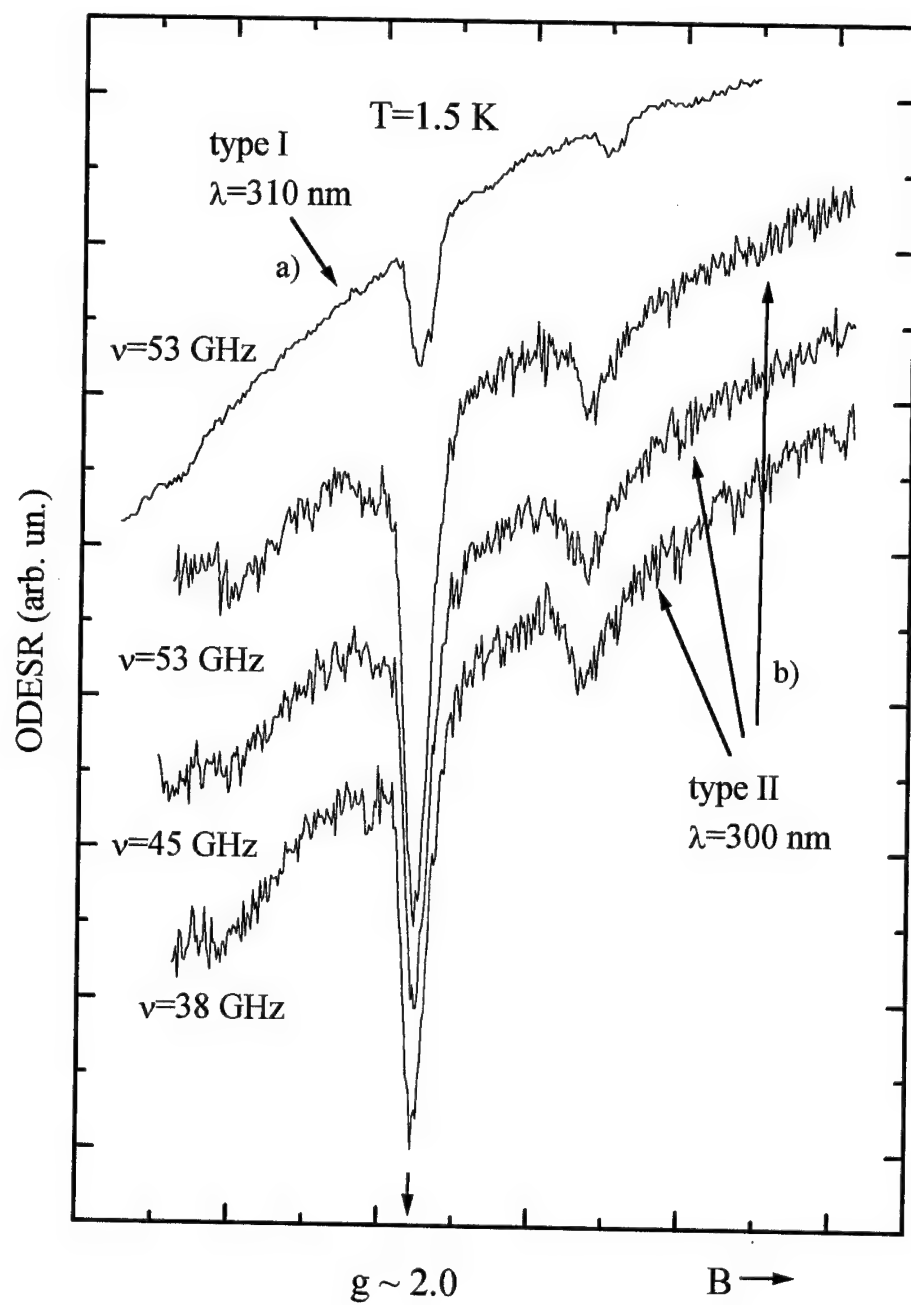


FIGURE 2 The spectrum of the ODESr of the BaF₂-Cd crystal of type I, detected at 310 nm MCD band (curve a), of the crystal of type II, detected at 300 nm MCD band (curves b).

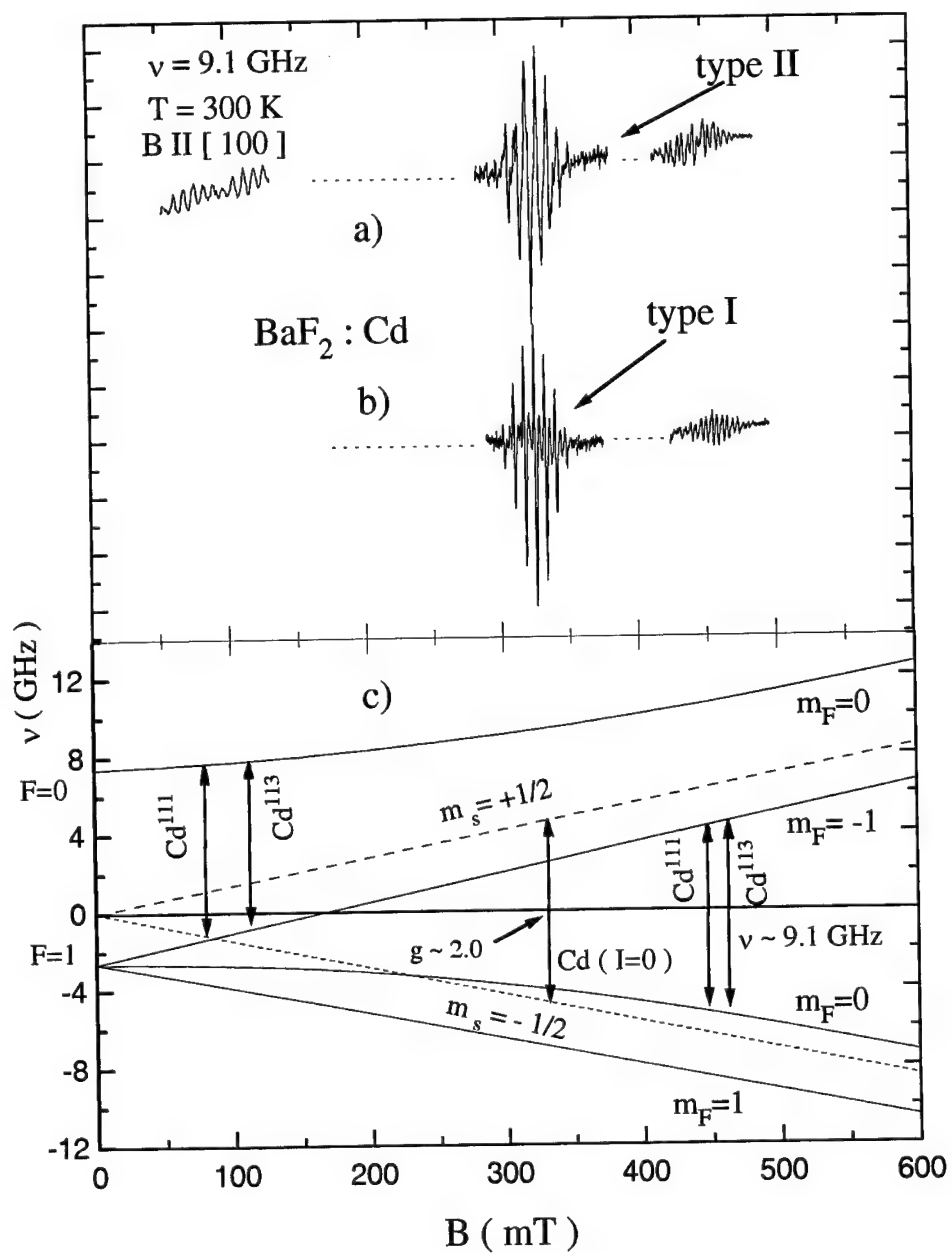


FIGURE 3 The spectrum of the conventional ESR of the $\text{BaF}_2\text{-Cd}$ crystal of the type II (curve a) and, for comparison, the ESR spectrum of the crystal of the type I (curve b), which has the same parameters as the ESR of the Cd^{+}_{c} center known from the literature.¹ Curve c—Breit-Rabi diagram for the ESR spectrum of the sample of type II.

different MCD bands differ, the expected slight difference between the hfs due to Cd¹¹¹ and Cd¹¹³ is not resolved because of the large width of the ODMR lines. Although the hf splitting for 290 nm ($A = 370$ mT) and for 365 nm ($A = 380$ mT) MCD bands of type II crystals has close values, the difference in thermal annealing kinetics of the corresponding optical absorption bands indicate their different nature.

The spectrum of the conventional ESR of the BaF₂-Cd crystal of the type I (Figure 3b) is consistent with the parameters observed earlier for Cd⁺-centers:¹ hf interaction is isotropic with $A(^{111}\text{Cd}) = 12.51$ GHz and $A(^{113}\text{Cd}) = 13.06$ GHz, the isotropic g-factor is $g = 1.9846$ at 300 K. Two significant differences are observed in the ESR spectrum of the crystals of the type II (Figure 3a): (i) The central group no more has correctly 'binomial' shf interaction with 8 equivalent fluorine nuclei, nature of the perturbation causing this deviation is not clear at now. (ii) A low-field ESR group from Cd-hf interaction occurs. The hf parameter values obtained from the ESR spectrum are $A(^{111}\text{Cd}) = 10.04 \pm 0.03$ GHz and $A(^{113}\text{Cd}) = 10.51 \pm 0.03$ GHz at 300 K.

The values of hf splitting parameter A , estimated by ODMR both for the 290 nm band and for the 365 nm band, within the measurement accuracy coincides with those obtained by ESR (taking into account characteristic changes of the hf constant A with the temperature).¹ Because in the samples of type II the 290 nm MCD band strongly dominates and no other ESR signal can be separated, we attribute the obtained ESR signal to the 290 nm MCD band.

So, there are at least three types of Cd-defects, which occur in BaF₂-Cd crystals after irradiation: a) Cd⁺-defect, b) perturbed Cd⁺-defect, nature of perturbation is not clear at now, c) following the peculiarities of the activator-vacancy associate centers observed in alkali-halides³ we attribute the center with the 365 nm MCD band to Cd⁺ (1) type center which involves adjacent anion vacancy, where the unpaired spin is mostly localised at Cd⁺ ion.

Excitation in the region of the discussed absorption bands at 290 nm and 295 nm results as well in photoluminescence bands at $E \sim 730$ nm and 750 nm respectively, both with approximately the same half-width ~ 0.35 eV. The intensity of this luminescence increases insignificantly upon cooling from 300 K down up to 77 K.

REFERENCES

1. V. F. Krutikov, N. I. Silkin and V. G. Stepanov, *Sov. Phys. Sol. State*, **18**, 2958 (1976).
2. P. G. Baranov, V. A. Vetrov, N. G. Romanov, *Sov. Phys. Sol. State*, **25**, 1364 (1983).
3. N. G. Romanov, V. V. Dyakonov, V. A. Vetrov and P. G. Baranov, *Phys. Stat. Sol.*, **B147**, K171 (1988).

COLOUR CATHODOLUMINESCENCE FROM $\text{Bi}_4[\text{GeO}_4]_3$ CRYSTALS

T. A. NAZAROVA, M. V. NAZAROV, G.V. SAPARIN* and S. K. OBYDEN*

*Technical University of Moldova, Kishinev, Moldova; *Department of Physics Faculty
Moscow State University, Moscow, Russia*

The regions of homogeneous and heterogeneous capture of impurities, point and linear defects, affected the luminescence from the undoped $\text{Bi}_4[\text{GeO}_4]_3$ (BGO) and doped BGO:V, BGO:Yb, BGO: Cr^{3+} , BGO:Fe as grown single crystals, were studied. A rapid cathodoluminescence (CL) spectral analysis, based on the panchromatic CL-images in scanning electron microscopy (SEM), was used. Depending on the doped impurities and dislocation configuration, changes in the intensity and wavelength of CL from BGO were found.

Key words: BGO, defects, cathodoluminescence, electron microscopy, dislocations.

1 INTRODUCTION

$\text{Bi}_4[\text{GeO}_4]_3$ (BGO) single crystals are of interest as modulators, based on the linear electro-optic effect,¹ and scintillator for X-ray and positron detectors. Besides, doped BGO crystals have also found application as a new photorefractive (PR) material.² Defects in BGO are responsible for PR response and for decrease of the luminescence output.³

The influences of doped impurities and dislocation configuration on the intensity and spectral band of cathodoluminescence (CL) emission from undoped BGO and doped BGO:V, BGO:Yb, BGO: Cr^{3+} , BGO:Fe were investigated by using colour images in the scanning electron microscopy (SEM).

2 METHOD

The experiments were carried out in the 'Stereoscan' SEM using standard attachment for colour CL described by Saparin.⁴ Accelerating voltage of the device and beam current density remained unchanged during the investigations ($V = 20 \text{ kV}$, $I = 0.5 \text{ A/cm}^2$). Some regions of every sample have been indented on a (001) surface with the standard diamond pyramid by quasistatic loading at 200 gf before the SEM studies.

3 MATERIALS

The undoped BGO and BGO:V, BGO:Yb, BGO: Cr^{3+} , BGO:Fe, used in this study, have been grown from the melt in the Institute of Physics and Technology of Materials, Bucharest, under the direction of Dr. Topa, using the Czochralski method.

Structure of $\text{Bi}_4[\text{GeO}_4]_3$ can be presented as a 3-dimensional chain of BiO_3 -groups, named Bi-umbrellas, and GeO_4 -groups, named Ge-tetrahedra.⁵ The GeO_4 group may be considered as a tightly bound unit, which does not undergo a translation and rotation in the crystal.^{5,6} It has been established,^{7,8} that intrinsic absorption and luminescence in the undoped BGO are due to the intraionic transition of Bi^{3+} . We suppose, that a distortion (for example, along the axis of dislocation) in Bi-sublattice may induce a change of CL from undoped and doped BGO. The presented structure and spatial symmetry of

BGO $\overline{143d}$, (T_d^6) allowed us to suppose that Burgers vector (b) of dislocation loops in BGO is $b = \frac{a}{2} \langle 111 \rangle$, i.e. the translations take place mainly in the $\langle 111 \rangle$ crystallographic direction.

4 RESULTS AND DISCUSSIONS

Regions of homogeneous capture of impurity We have revealed, that a homogeneous capture of Yb-; V-; Fe-impurity leads to decreasing of CL intensity and to shift of its wavelength peak position from blue region of spectrum to green one, in comparison with undoped BGO. We assume, that one of the possible reasons of this change is that the donors, being intrinsic defect in the undoped BGO, provide the emission in blue spectral band. However, the impurity ions of V, Yb and Fe, localized on the Ge or Bi sites, can provide the extrinsic CL in green spectral band.

Regions of deformation-induced defects We observed a decay of CL from all the samples in the centre of indentation. This phenomenon can be attributed to a high concentration of different point and linear defects in these regions as a result of plastic deformation. Besides, we revealed a deformation-enhanced CL emission around all the indentations in the regions created by equilibrium configuration of dislocations with $b = \frac{a}{2} \langle 111 \rangle$. The spectral band of this CL is wider in comparison with undeformed regions. Enhanced CL can be explained by an increase of traps created by multivalent impurity ions in the vicinity of dislocations.

Regions of growth defects The decay of CL in the growth defects has been revealed in BGO:Yb; BGO:Cr and BGO:V. However, two types of growth defects have been revealed in BGO:Fe: one of them provides the decay of CL and the other one provides an intensive CL emission in a wide spectral band, analogous to CL around the indentation. These phenomena can be attributed to different configurations of point and linear defects induced by growth procedure.⁹

5 CONCLUSIONS

The extrinsic CL from BGO depends on the doped impurities and dislocation configuration. A significant increasing of CL intensity and broadening of spectral band were found in the dislocation zones, created around microindentations on doped BGO:Fe and BGO:Yb crystals.

REFERENCES

1. R. Nitsche. *J. Appl. Phys.* **36**, 8, 2358 (1965).
2. E. Moya, L. Contreras, C. Zaldo. *J. Opt. Soc. Am.* **B5**, 1737 (1988).
3. O. Kanert & J.-M. Spaeth, *Defects in Insulating Materials*, World Scientific, **2**, 1157 (1992).
4. G. V. Saparin & S. K. Obyden. *European microscopy and analysis*. **22** 7, (1993).
5. N. V. Belov N. V. Ocherki po strukturnoi mineralogii, M. Nedra, (1976).
6. W. Wojdowski, T. Lukasiewicz, W. Nazarewicz and J. Zmija. *Phys. Stat. Sol.*, **B94**, 649 (1979).
7. M. J. Weber and R. R. Monchamp. *J. Appl. Phys.* **44**, 5495, (1973).
8. E. Dieguez et al. *J. Phys.*, **C18**, 4777, (1985).
9. T. A. Nazarova et al. *Scanning*, **16**, 91, (1994).

FURTHER RESULTS ON $\text{GdAlO}_3\text{:Ce}$ SCINTILLATOR

J. A. MAREŠ,* M. NIKL,* C. PEDRINI,** D. BOUTTET,** C. DUJARDIN,**
B. MOINE,** J. W. M. VERWEIJ** and J. KVAPIL

Institute of Physics, Czech Academy of Sciences, Cukrovarnická 10, 16200 Prague 6, Czech Republic;* *LPCML, Université Lyon I, 43, bd du 11 Novembre 1918, 69622 Villeurbanne, France; Preciosa a.s., Division Monokrystaly, Palackého 175, 51119 Turnov, Czech Republic*

Spectroscopic properties of Ce^{3+} ions in GdAlO_3 crystal are presented. At least three Ce^{3+} nonequivalent centres (multisites) are present in this crystal. Energy transfer from the Ce^{3+} main in the UV emitting centres to the Ce^{3+} green emitting centres is observed. Ce^{3+} fluorescence decays are either fast (1.5–20 ns) or slower due to complicated processes of energy transfer and migration (Ce^{3+})_i → (Gd^{3+})_n-steps → (Ce^{3+})_j (energy transfer through Gd^{3+} sublattice).

Key words: $\text{GdAlO}_3\text{:Ce}$ (GAP:Ce), multisites, Gd^{3+} sublattice, energy transfer, migration, scintillator.

1 INTRODUCTION

The latest applications of scintillators (in medical imaging, high performance electromagnetic calorimeters etc.) require high density, fast and radiation hard scintillators.¹ One of the attractive materials is $\text{Gd}_2\text{SiO}_5\text{:Ce}$ (GSO) with very good light yield (three times higher than that of BGO) and suitable density ($\rho = 6.71 \text{ g/cm}^3$).^{1,2} GSO belongs to the group of the so called Gd^{3+} -concentrated compounds. Some of these materials may offer simultaneously high density, good light yield or even good radiation hardness, which are the main reasons for their intensive studies at present. A disadvantage of Gd^{3+} -concentrated compounds are various transfer processes and interactions in Gd^{3+} sublattice or between Gd^{3+} and impurity ions,^{2,3} which can influence fluorescence processes of scintillation ions.

$\text{GdAlO}_3\text{:Ce}$ (GAP:Ce) is another crystal from the group of Gd^{3+} -concentrated compounds, which is under study as for scintillation applications.^{4–6} Its density is higher than that of GSO ($\rho = 7.5 \text{ g/cm}^3$) and recent studies have shown that Ce^{3+} 5d → 4f emission in GAP:Ce occurs in the UV ($\lambda_p \sim 360 \text{ nm}$) and its decay is very fast ($\tau \sim 1.5 \text{ ns}$).⁴ Similarly as in the other Gd^{3+} -concentrated compounds, one may expect also in GAP:Ce fluorescence processes that Gd^{3+} sublattice will take part in the processes of energy transfer to and from Ce^{3+} ions i. e. $\text{Gd}^{3+} \rightarrow \text{Ce}^{3+}$ energy transfer, migration through Gd^{3+} ions, transfer to unwanted impurity ions or various defects.^{2,3,7}

This paper deals with time-resolved emission spectroscopy of GAP:Ce crystal. Ce^{3+} multisites, energy transfer processes and Gd^{3+} - Ce^{3+} interactions are discussed. For the first time we present results of the studies of Ce^{3+} fluorescence decays (different components are observed) including their temperature dependences.

2 EXPERIMENTAL

Three GAP:Ce crystal samples having Ce concentrations between 0.02 and 0.07 at. % have been studied. Unfortunately, the growth of GAP:Ce crystals has not been satisfactorily solved yet and the studied crystals contain frequent cracks. These cracks

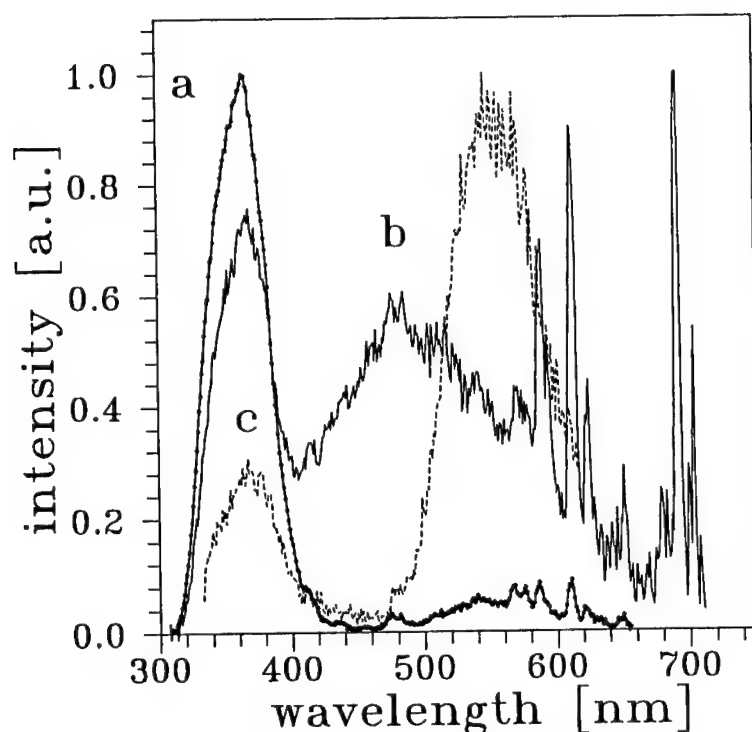


FIGURE 1 Emission spectra of GAP:Ce crystal at 80 K under excitation wavelengths 275 nm (curve a), 220 nm (curve b) and 320 nm (curve c).

arise during cooling down of the crystals during their growth. It seems that a major part of GAP crystals studied have a local distorted cubic structure (distorted octahedron around Gd^{3+} lattice ions).⁷

Different methods have been used for the spectroscopic studies of GAP:Ce crystals. Classical and laser excited time-resolved spectroscopies were used together with the excitation under synchrotron radiation at LURE (in Orsay, France).⁴ Electron microanalysis of the crystals were carried out at the Institute of Physics in Prague, Czech Republic (electron excited x-ray analysis).

3 EXPERIMENTAL RESULTS AND DISCUSSION

Emission and Excitation Spectra of GAP:Ce

Ce^{3+} emission spectra of GAP:Ce crystal are given in Figure 1. Under different excitation wavelengths several UV and visible emission bands are observed. Apart from the line spectrum in the red, which is due to the presence of unwanted Eu^{3+} impurity, the other

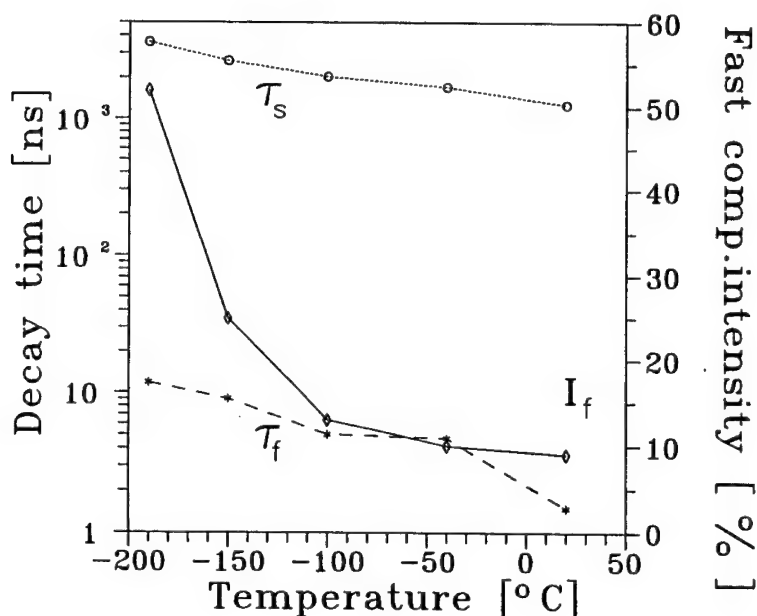


FIGURE 2 Temperature dependence of the fast component mean decay time (τ_f), slow component mean decay time (τ_s) and the percentage of the fast component emission intensity (I_f) in the overall emission (solid line); all given for the main Ce^{3+} UV emission band (360 nm) in GAP:Ce crystal.

broad emission bands are ascribed to $\text{Ce}^{3+} 5d \rightarrow 4f$ transitions. The main Ce^{3+} emission band is peaking in the UV at 360–365 nm and can be decomposed to two gaussians with the maxima at about $\lambda_1 = 360$ nm and $\lambda_2 = 335$ nm at room temperature (this is due to the Ce^{3+} transitions from the lowest 2D excited level to $^2F_{7/2}$ and $^2F_{5/2}$ ground state levels). Ce^{3+} emission is slightly shifted to the high energy side with temperature increasing (from ~ 80 K to room temperature).

Much less intense visible Ce^{3+} emission bands are peaking at 480 and 560 nm (see Figure 1). The main Ce^{3+} UV emission band at $\lambda_p \sim 360$ nm is most efficiently excited at ~ 300 – 305 nm and ~ 285 – 290 nm maxima, while the visible Ce^{3+} emission bands (apart from the UV excitation maxima just mentioned) have still excitation bands peaking at $\lambda \sim 325$ nm and $\lambda \sim 380$ nm. This is an evidence that GAP:Ce crystals contain various nonequivalent Ce^{3+} centres (Ce^{3+} multisites).

Ce^{3+} Fluorescence Decays

The presence of Ce^{3+} multisites can be clearly seen from Ce^{3+} fluorescence decays. Ce^{3+} fluorescence decays in GAP crystal consist of fast (ns) and slow (μs) components, the decays deviate from single exponential behaviour. This behaviour shows that the

processes of energy transfer are present in this crystal. The observed fast Ce^{3+} decays have different lifetimes ranging from 1.5 to 20 ns. The temperature dependences of the mean Ce^{3+} decay times τ_f and τ_s for fast and slow components, respectively are given in Figure 2 (dashed curves). Furthermore, the percentage of the fast component intensity I_f in the overall emission is given by solid line (in Figure 2).

Under $\lambda_{\text{ex}} = 380$ nm the Ce^{3+} visible emission bands show only the fast, exponentially decaying components with lifetimes in the time range 15–20 ns at $T = 80$ K. Under $\lambda_{\text{ex}} = 287$ nm (both Ce^{3+} UV and visible emission bands are excited), the decay of Ce^{3+} green emission shows risetime, which is roughly equal to mean decay time of the main Ce^{3+} UV emission band ($\tau_{\text{UV}} = 6.2$ ns) and the slow component is also present. This behaviour can be interpreted as that the radiative energy transfer from the main Ce^{3+} UV centres to the Ce^{3+} green emitting centres takes place.

$\text{Gd}^{3+} - \text{Ce}^{3+}$ Interactions

Under UV excitation at about $\lambda \sim 300$ nm we excite mainly Ce^{3+} ions (the intense Gd^{3+} absorption lines are around 277 nm).⁴ The fast ns decay components can be undoubtedly ascribed to allowed Ce^{3+} $5d \rightarrow 4f$ transitions, the observed slow components of the decays are most probably connected with $\text{Ce}^{3+} \rightarrow \text{Gd}^{3+}$ energy transfer followed by energy migration through Gd^{3+} sublattice and subsequent trapping at some other Ce^{3+} centres {i.e. delayed Ce^{3+} fluorescence or processes $(\text{Ce}^{3+})_i \rightarrow (\text{Gd}^{3+})_n\text{-steps} \rightarrow (\text{Ce}^{3+})_j$ }.

The high energy shift of the Ce^{3+} UV emission with the increase of temperature might be the reason of intensifying the nearly resonant energy transfer between Ce^{3+} and Gd^{3+} ions at higher temperatures (the lowest Gd^{3+} excited states are in the 310–314 nm range⁴). This assumption can consistently explain the observed temperature dependences of Ce^{3+} fast τ_f and slow τ_s mean decay times and I_f from Figure 2.

4 CONCLUSIONS

Detailed time resolved emission spectroscopy of GAP:Ce crystals and other studies can be summarized as the following:

1. At least three Ce^{3+} nonequivalent centres (multisites) are present having maxima at 360 (the main one), 480 and 560 nm.
2. The fast components of Ce^{3+} decays are due to $5d \rightarrow 4f$ transitions of Ce^{3+} ions (the mean decay lifetimes are in the time range 1.5–20 ns).
3. The slow components of Ce^{3+} decays (delayed fluorescence) are due to processes of $\text{Ce}^{3+} \rightarrow \text{Gd}^{3+}$ energy transfer followed by energy migration through Gd^{3+} sublattice and subsequent trapping at Ce^{3+} ions.
4. Ce^{3+} multisites emitting in the visible are also excited by radiative energy transfer from the main Ce^{3+} UV emitting centres.

REFERENCES

1. P. Lecoq, M. Schlusser and M. Schneegans. *Nucl. Instr. Meth. Phys. Res.* **A315**, 337 (1992).
2. V. G. Baryshevsky, D. M. Kondratiev, M. V. Korzhik, V. B. Pavlenko and A. A. Fedotov. To be published in *J. Lumin.* (1994).
3. A. J. de Vries, W. J. J. Smeets and G. Blasse. *Mat. Chem. Phys.* **18**, 81 (1987).
4. J. A. Mareš, C. Pedrini, B. Moine, K. Blazek and Jos. Kvapil. *Chem. Phys. Lett.* **206**, 9 (1992).

5. J. Fava, G. Le Flem, J. C. Bourcet and F. Gaume-Mahn. *Mat. Res. Bull.* **11**, 1 (1976).
6. R. Visser, *Energy Transfer in Fluoried Scintillators* (PhD thesis), Delft University Press, Delft 1993, Chap. 9, 153.
7. S. J. N. Padua, L. A. O. Nunes and J. C. Castro. *J. Lumin* **43**, 379 (1989).

MULTIPLICATION OF ANION AND CATION ELECTRONIC EXCITATIONS IN ALKALI HALIDES

M. KIRM,¹ A. FRORIP,² R. KINK,² A. LUSHCHIK,² CH. LUSHCHIK²
and I. MARTINSON¹

¹*Department of Physics, Lund University, Sölvegatan 14, S-22362 Lund, Sweden;*

²*Institute of Physics, Estonian Academy of Sciences, Riia 142, EE2400 Tartu, Estonia*

Excitation spectra of intrinsic emissions have been measured for NaCl, RbBr and CsBr crystals at 8 K. The excitonic and electron-hole mechanisms of multiplication of electronic excitations have been detected. The processes of radiative decay of cation electronic excitations and the non-radiative decay with the formation of a double amount of anion electronic excitations will be discussed.

Keywords: multiplication of electronic excitations, excitons, photoluminescence, alkali halide crystals.

Irradiation of wide-gap crystals by γ -rays leads to the formation of a large number of emission quanta per one absorbed quantum. The elementary act of this process, i.e. the creation of two emission quanta by one photon with the energy of 12–21 eV has been investigated in doped alkali iodides.¹ During the last thirty years voluminous information has been obtained for the process of multiplication of electronic excitations (MEE) in various solids (see e.g., Ref. 2). During 1993–94, the process of MEE has been studied for a number of alkali halide crystals (AHC) at 8 K by using synchrotron radiation of 6–32 eV energy (MAX-Lab, Lund). The first results have been published for KCl, CsCl³ and KBr.⁴

The aim of the present study is to obtain new information about MEE processes in NaCl, RbBr and CsBr crystals at 8 K by means of luminescence methods. Special attention will be paid to the formation of secondary excitons and electron-hole pairs by hot photoelectrons and also to the process of radiative and non-radiative decay of cation electronic excitations (CEE). CEE can be formed by photons of 16–22 eV in RbBr⁵ and 13–20 eV in a CsBr crystal.⁶ Single AHC were grown by the Stockbarger method after a special purification cycle involving manifold recrystallization from the melt. The intrinsic luminescence of self-trapped excitations (STE) and cross-luminescence (CL) were recorded through a MDR-12 monochromator and using additional optical filters. Excitation spectra were measured with a spectral resolution 0.25 nm at equal quantum intensities of the excitation falling onto the crystal.

Figure 1 presents the excitation spectrum of STE σ emission for a NaCl crystal. Only anion electronic excitations (AEE) can be created in the region of intrinsic absorption of a crystal. The intensity of STE emission rises by a factor of three when the photon energy increases from 17 to 32 eV. This fact testifies to the realization of excitonic and electron-hole MEE mechanisms in NaCl. Figure 1 also shows the intensity ratio for π (3.4 eV) and σ (5.5 eV) emissions of STE (I_π/I_σ) measured for NaCl at 8 K. The maximum of I_π/I_σ at 19 eV can be assigned (analogous to a KBr crystal)⁴ to the realization of the excitonic mechanism of MEE in NaCl. It involves the formation of a secondary exciton by a hot photoelectron. Typical STE (mainly the π component) emission arises from the radiative decay of this secondary exciton. A subsequent recombination of an electron with a self-trapped hole leads to the appearance of a second quantum of STE emission (mainly the σ component). The hot photoelectrons create mainly secondary electron-hole pairs at $h\nu > 20.5$ eV.

Figure 2 presents the excitation spectra of the σ component of STE emission in RbBr (4.15 eV), π emission of STE in CsBr (3.5 eV) and of 5–6 eV emission in a CsBr crystal at

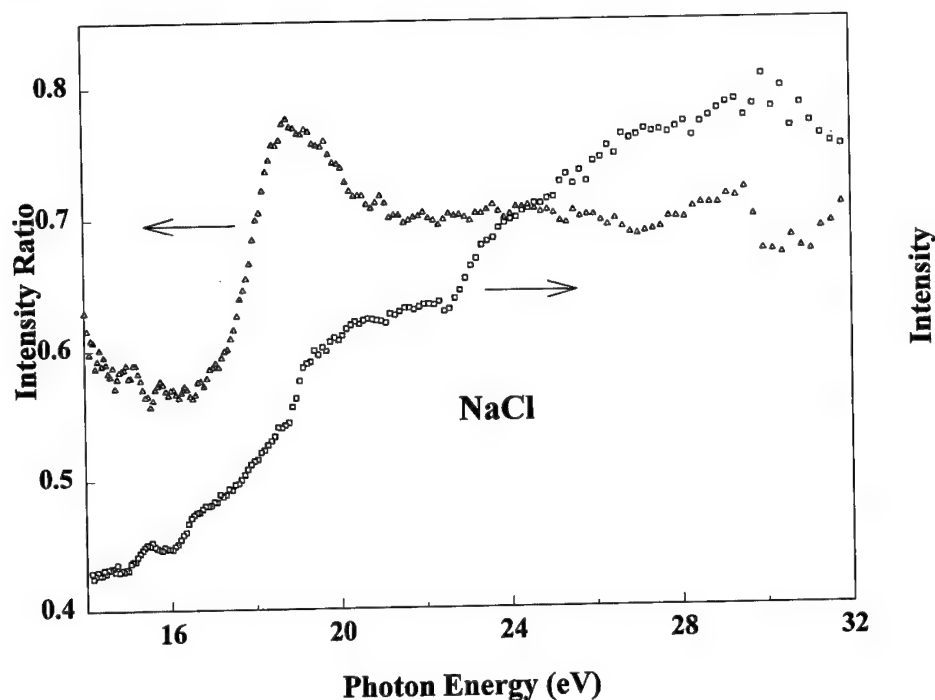


FIGURE 1 The excitation spectra for STE σ emission (\square) (5.5 eV) and the intensity ratio (Δ) for π (3.4 eV) and σ emissions of a NaCl crystal at 8 K.

LHeT. The threshold energy of the 5–6 eV emission excitation is about 13.9 eV. This emission has been interpreted⁶ as a result of the radiative recombination of electrons from the anion valence band with the holes (probably, self-trapped holes) from the $5p^6$ shell of the Cs^+ ion. The intensity of σ emission of STE in RbBr becomes doubled in the region between 14 and 16 eV (see Figure 2(b)). The ionization of anions takes place at the excitation energies $h\nu < 16$ eV in RbBr, where the hot photoelectrons create secondary anion excitons (a peak at 14.8 eV in Figure 2(b)) and electron-hole pairs (15–16 eV). A high-efficiency STE luminescence is observed from 16 to 20 eV, where the photocreation of CEE takes place. In RbBr the ratio of the formation energies of cation and anion excitons $E_{ec}/E_{ea} = 2.25$ and one CEE decays with the formation of two AEE. The increase of STE luminescence intensity at $h\nu > 24$ eV is connected with the formation of secondary excitons and electron-hole pairs by hot electrons created on the photoionization of cations.

In a CsBr crystal at 8 K the value of E_{ec}/E_{ea} equals 1.92 and, because of energetic considerations, the Auger decay of one CEE with the formation of two electron-hole pairs is impossible (no doubling of STE emission intensity in the region of 13–20 eV). Instead of that an intensive CL is observed in CsBr. When the crystal is heated up to 300 K, the value of E_{ea} decreases, while the value of E_{ec} remains approximately the same. Thus at 300 K, E_{ec}/E_{ea} equals 2.02 in CsBr and the decay of CEE with the creation of a double number of AEE can be dominant. We have observed this phenomenon by detecting a sharp increase (doubling) of 2.9 eV impurity emission intensity in the region from 13 to 15 eV in

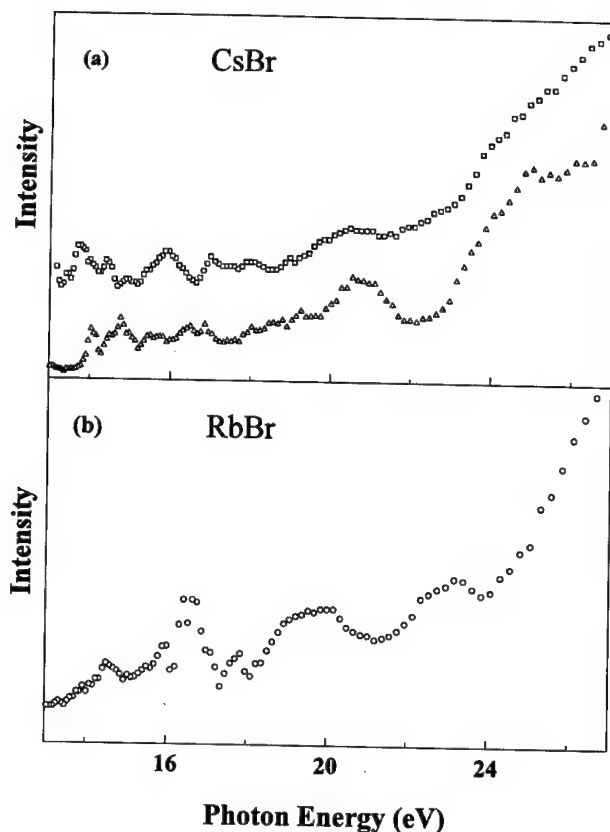


FIGURE 2 (a) The excitation spectra for STE π emission (\square) (3.5 eV) and crossluminescence (\triangle) (5–6 eV) of a CsBr crystal at 8 K. (b), The excitation spectra for STE σ emission (\circ) (4.15 eV) of a RbBr crystal at 8 K.

CsBr at 295 K. The formation of anion excitons and as well the recombination of electrons with self-trapped holes leads to the excitation of STE emission at LHeT. The intensity of π emission and the intensity ratio for π and σ emissions increase sharply in the region $h\nu > 22$ eV. The secondary anion excitons are formed by the hot photoelectrons created at the ionization of cations in CsBr.

The Table I summarises data for the formation energies of anion and cation excitons (E_{ea} and E_{ec}), the minimum ionization energies of anions (E_{ga}) and cations (E_{gc})^{3–7} and as well our experimentally determined values for the threshold energies of the excitonic (E_{th}^o) and the electron-hole (E_{th}^{\pm}) mechanisms of MEE in AHC at LHeT. The values of E_{th}^o and E_{th}^{\pm} are estimated with the accuracy of ± 0.2 eV. Using luminescence methods, the decay of CEE with the formation of a double number of AEE has been observed for four investigated alkali halide crystals (KCl, KBr, RbCl, RbBr) with the ratio $E_{ec}/E_{ea} > 2$. An intensive CL has been detected for CsCl and CsBr crystals with the ratio E_{ec}/E_{ea} less than 2.

A special interest will be paid to the effect of a high local density of AEE that arise due to the process of MEE in the further research. This effect had been discovered for the first

time already in 1964,¹ but not quantitatively investigated. In a NaCl crystal the values of I_{π}/I_{σ} at $h\nu > 21$ eV are considerably higher than at $h\nu < 17$ eV (see Figure 1). The recombination probability of electrons with partly relaxed or non-relaxed holes in quartets of carriers ($h\nu > 20$ eV) is higher than that of the recombinations in electron-hole pairs that are spatially separated from each other ($h\nu < 17$ eV).

Table I

Formation energies of anion (E_{ca}) and cation (E_{ec}) excitons, minimum ionization energies of anions (E_{ga}) and cations (E_{gc}), threshold energies for excitonic (E_{th}^o) and electron-hole (E_{th}^{\pm}) mechanisms of MEE in AHC at 8 K (all values are in eV).

Crystal	E_{th}^o	E_{th}^{\pm}	E_{ca}	E_{ga}	E_{ec}	E_{gc}	E_{ec}/E_{ca}
KCl	16.5	18	7.78	8.69	19.7	20.6	2.53
RbCl	16.0	17.5	7.54	8.5	16.2	≈ 17	2.15
CsCl	20.5	21	7.86	8.4	13.2	14.1	1.68
KBr	15.4	17.0	6.82	7.5	19.9	20.6	2.92
RbBr	14.5	15.5	6.65	7.25	16.2	16.6	2.44
CsBr	20.5	21.5	6.83	7.3	13.1	13.8	1.92

REFERENCES

1. E. R. Ilmas, G. G. Liidya and Ch. B. Lushchik, *Opt. Spectrosc. (USA)* **18**, 255; 359 (1965).
2. M. Casablani and U. M. Grassano, *J. Phys. Chem. Solids* **51**, 805 (1990).
3. M. Kirm, I. Martinson, A. Lushchik, K. Kalder, R. Kink, Ch. Lushchik and A. Löhms, *Solid State Commun.* **90**, 741 (1994).
4. A. Lushchik, E. Feldbach, Ch. Lushchik, M. Kirm and I. Martinson, *Phys. Rev. B* **50**, 6500 (1994).
5. V. Saile, N. Schwentner, M. Skibowski and W. Steinmann, *Phys. Letters A* **46** 245 (1973).
6. Yu. M. Aleksandrov, I. L. Kuusmann, P. Kh. Liblik, Ch. B. Lushchik, V. N. Makhov, T. I. Syreishchikova and M.N. Jakimenko, *Sov. Phys. Solid State (Leningrad)* **29**, 587 (1987).
7. K. S. Song and R. T. Williams, *Self-Trapped Excitons* (Springer Verlag, Berlin, 1993).

PECULIARITIES OF THE TRIPLET RELAXED EXCITED STATE STRUCTURE IN THALLIUM-DOPED CESIUM HALIDE CRYSTALS

V. NAGIRNYI, A. STOLOVICH, S. ZAZUBOVICH, V. ZEPELIN, M. NIKL,*
E. MIHOKOVA* and G. P. PAZZI**

*Institute of Physics, Riia 142, EE2400 Tartu, Estonia; *Institute of Physics, Cukrovarnicka
10, 16200 Prague, Czech Republic; **Institute of Electromagnetic Waves (IROE del CNR),
Florence, Italy*

Four bands, all belonging to the main thallium centre, are detected in the triplet luminescence spectrum of thallium-doped cesium halides under excitation in impurity absorption bands. Their spectral, polarization and kinetics characteristics are studied at 0.35 to 360 K. The parameters of the corresponding relaxed excited states (RES) minima are calculated. Two ultraviolet emission bands are ascribed to electronic transitions from trigonal and tetragonal Jahn-Teller minima of the triplet RES of Tl^+ ion. Two visible bands are assumed to arise from two different off-centre configurations of a self-trapped exciton perturbed by Tl^+ ion.

Key words: self-trapped exciton, luminescence polarization, decay kinetics 'Thallium-doped cesium halides'.

Absorption spectrum of Tl^+ -doped cesium halides differs essentially from that of ns^2 -ion-doped f.c.c. alkali halides.¹ It consists of several almost equidistant bands whose intensities differ not more than two times. The analysis of its shape and temperature dependence allows a conclusion that only the narrow lowest-energy band is similar to the A absorption band of Tl^+ centres in f.c.c. crystals. Broad higher-energy bands are most probably connected with some mixed Tl^+ and excitonic states. This mixing grows in the row of crystals $CsCl \rightarrow CsBr \rightarrow CsI$.

Usually various Jahn-Teller minima of impurity triplet RES have been considered to be responsible for the triplet luminescence of ns^2 -ion-doped alkali halides.² In particular, three emission bands of $CsI:Tl$ (3.09, 2.55 and 2.25 eV) have been connected^{3–5} with three minima of various symmetries coexisting in the triplet RES of Tl^+ . We have found that in cesium halides the triplet emission spectrum of the main thallium centre consists of four bands (Figure 1). The halfwidths and Stokes shifts of two ultraviolet bands are about twice as small as those of two visible bands (Table I). In $CsI:Tl$ all four bands are excited in the A absorption band region. In the row of $CsI \rightarrow CsBr \rightarrow CsCl$ the relative intensity of visible bands, observed at A excitation, decreases, while that of ultraviolet bands, observed at higher-energy excitation, increases.

The characteristics of two ultraviolet bands are analogous to those of triplet A_X and A_T emission of Tl^+ centres in other alkali halides (Table I). They are polarized along the $\langle 111 \rangle$ and $\langle 100 \rangle$ axis of the crystal, respectively.⁶ The polarization degree P is positive, and it grows as the excitation energy decreases. Fast (FC) and slow (SC) components are observed in their low-temperature decay kinetics. The values and temperature dependences of the decay times τ_{SC} and τ_{FC} point to the fact^{4,6} that the structure and the parameters of the triplet RES responsible for ultraviolet emission are similar to the ones observed for the triplet RES of Tl^+ centres in f.c.c. crystals.

The characteristics of two visible bands differ drastically from the ones described above. These emissions are polarized under excitation not only in the A band region but also in the higher-energy absorption bands. In $CsI:Tl$ at 4.2 K P changes from 14% at

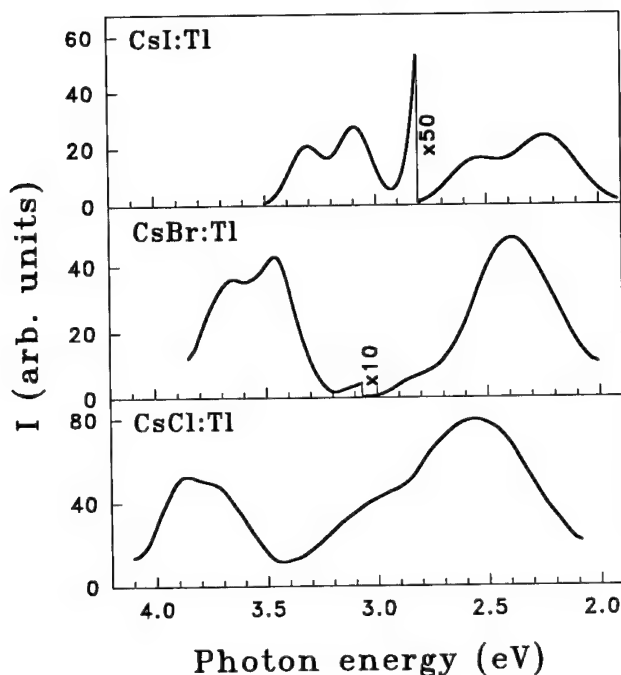


FIGURE 1 Emission spectra of CsCl:Tl, CsBr:Tl and CsI:Tl at 4.2 K.

$\alpha = 0^\circ$ to -14% at $\alpha = 45^\circ$ for the 2.55 eV emission, while $P(\alpha) \sim \text{const}$ for the 2.25 eV emission (α is the angle between \vec{E}_{exc} and [001] axis of the crystal). At 80 K $P(\alpha)$ of the 2.55 and 2.25 eV bands are characteristics of the electronic transitions occurring along the $\langle 100 \rangle$ and $\langle 111 \rangle$ axis, respectively; due to that we label these bands as A_T' and A_X' . At 4.2 K the decay times of A_T' and A_X' bands in CsI:Tl are about two orders shorter than the ones usually observed for triplet emission of Tl^+ centres. As the temperature decreases from 20 to 1 K, τ of A_T' band rises from 25 to 410 μs , while τ of A_X' band decreases from 65 to 48 μs . At $T > 30 - 40$ K a rapid decrease of τ is observed for both emission bands, which is accompanied by changes in the sign of P and in $P(\alpha)$.

Similar features are observed for the visible emission in CsCl:Tl and CsBr:Tl crystals. None of these features have ever been observed for isotropic centres in ns^2 -ion-doped f.c.c. crystals. However, they are very similar to those of the triplet emission of self-trapped excitons (STE) in alkali halides.^{7,8} A careful analysis of the experimental data have lead us to an assumption that the visible emission of Tl^+ -doped cesium halides should be considered as the triplet luminescence of STE perturbed by Tl^+ ion, and that in the systems studied there exist two types of perturbed STE excited state manifold. In both manifolds, the lower excited levels are composed of a split triplet state (t) and a singlet state (s), the energy distance between them being ΔE_{s-t} (Figure 2). Each triplet state consists of almost doubly degenerate emitting level (e) and a metastable level (m), the energy between them being δ .

The decay kinetics of A_T' emission points to the fact that in this case the metastable minimum is located below the emitting one. Only metastable minimum is populated optically, and it emits at extremely low temperatures. As the temperature rises, thermal transitions between metastable and emitting minima start taking place, and τ decreases.

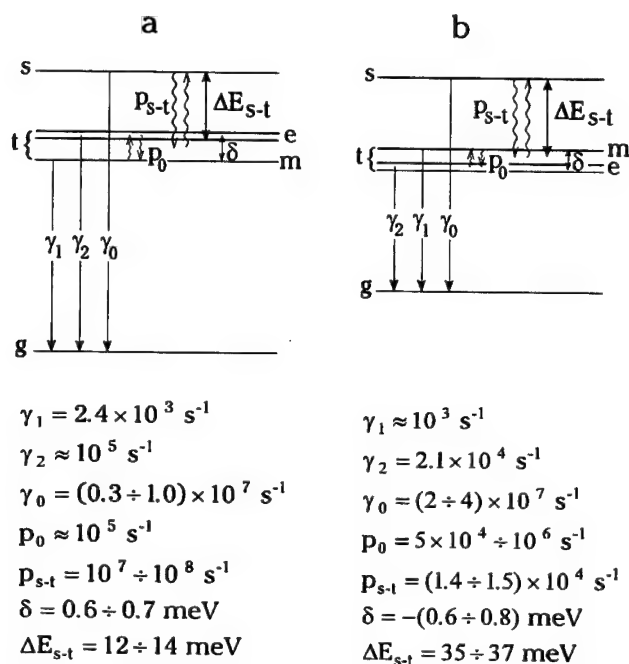


FIGURE 2 Energy levels and parameters of the singlet and triplet excited states responsible for the 2.55 eV (a) and the 2.25 eV (b) emission of CsI:TI.

The increase of τ of A_X' emission of CsI:TI with the temperature rise can be caused by the opposite order of the emitting and the metastable minimum ($\delta < 0$) as compared with the previous case. Indeed, in this case only the lowest, the emitting minimum of the triplet state is optically populated at $T < 1.7 \text{ K}$, and it emits with $\tau = 48 \mu\text{s}$. As the temperature grows, the upper, the metastable minimum becomes thermally populated; it results in the increase of τ .

At $T > 30 - 40 \text{ K}$ thermal transitions from the triplet to the singlet state occur, which lead to a rapid decrease of τ and to changes in polarization properties of both emissions. From $\tau(T)$ dependences the parameters of the corresponding excited states were calculated (Figure 2). They are similar to the ones obtained for STEs in alkali halides.⁸

The emission spectrum of STE may consist of several bands related with on-centre and two different ('weak' and 'strong') off-centre configurations of STE (see, e.g.,^{7,8}). We assume that A_T' band is connected with a 'weak' off-centre STE, while A_X' band, with a 'strong' one, both perturbed by TI^+ ion. Similar to 'strong' off-centre STE, for A_X' emission the Stokes shift is larger, but the probabilities of the radiative and nonradiative transitions are smaller than those for A_T' emission. Negative δ may also point to a 'strong' off-centre configuration responsible for A_X' band in CsI:TI.⁸ The behaviour of A_T' and A_X' bands under high hydrostatic pressure⁹ is also characteristics of a 'weak' and 'strong' off-centre STE, respectively.

In spite of the different nature of the minima responsible for four emission bands, they all are most probably located on the same APES.

Really, they all are populated due to relaxation from the same nonrelaxed state, and thermally stimulated transitions occur between these minima as well. No such 'four-minima' structure of the triplet RES has ever been observed for any ns^2 -ion-doped crystal. It may be caused by the mixing of the excited states of the impurity ion and STE. The excitonic-like nature of visible emission could explain a high scintillation efficiency of CsI:Tl.

ACKNOWLEDGEMENTS

This work was supported by the NATO Grant HTECH.LG No. 931435 and the Estonian Science Foundation Grant No. 355.

REFERENCES

1. K. Maier. Ph. D. Thesis, Frankfurt am Main University, 1970.
2. S. Zazubovich. *Int. J. Modern. Phys.* **B8**, 985 (1994).
3. V. S. Sivasankar, P. W. M. Jacobs. *Phil. Mag.* **B51**, 479 (1985).
4. M. Nikl, J. Hlinka, E. Mihokova, K. Polak, P. Fabeni, G. P. Pazzi. *Phil. Mag.* **B67**, 627 (1993).
5. G. P. Pazzi, M. Nikl, M. Bacci, E. Mihokova, J. Hlinka, P. Fabeni, L. Salvini, *J. Lumin.* **60-61**, 527 (1994).
6. V. Nagirnyi, S. Zazubovich, N. Jaanson. *Phys. stat. sol. (b)* **175**, 155 (1993).
7. K. Kan'no, K. Tanaka, T. Hayashi, *Rev. Solid State Science* **4**, 383 (1990).
8. K. S. Song and R. T. Williams. *Self-Trapped Excitons* (Springer, Berlin 1993).
9. K. Asami, S. Emura, M. Ishiguro, *J. Lumin.* **18/19**, 227 (1979).

TABLE I
Characteristics of triplet emission of Tl^{+} -doped cesium halides

Crystal	Emis- sion	E_m^I , eV	δ_m^I , eV	E_{exc} , eV	S, eV	τ_{SC} , ms	τ_{FC} , ns	$P_{\alpha=0^\circ}$, %	$P_{\alpha=45^\circ}$, %
CsCl:Tl	A_X	3.88	0.28	5.17	1.29	9.0	24.6	0	40
	A_T	3.65	0.22	5.15	1.50	1.5	25.0	15	0
	A_T'	~ 3.00	~ 0.56	6.14	3.14				
	A_X'	2.55	0.60	6.14	3.59				
CsBr:Tl	A_X	3.65	0.26	4.86	1.21	6.6	17.8	0	
	A_T	3.48	0.21	4.86	1.38	1.85	10.6	12	0
	A_T'	2.87	0.40	5.50	2.63	0.67		-25	
	A_X'	2.42	0.48	5.50	3.08		230000	-6	
CsI:Tl	A_X	3.31	0.20	4.32	1.01	1.2	15.1		
	A_T	3.09	0.19	4.22	1.13	1.5	20.0	17	0
	A_T'	2.55	0.35	4.29	1.74	0.4		14	-14
	A_X'	2.25	0.35	4.28	2.03		48000	7	7

THE ROLE OF CATION VACANCIES IN EXCITATION MECHANISM OF RE-IONS IN ALKALINE-EARTH SULPHIDES

A. N. BELSKY, V. V. MIKHAILIN and A. N. VASIL'EV

*Synchrotron Radiation Laboratory, Physics Department, Moscow State University,
117234 Moscow, Russia*

The VUV-excitation spectra and thermostimulated emission for intrinsic and impurity luminescence of alkaline-earth sulphides doped by cerium have been investigated. The intensity of activator emission is higher in samples with artificially created cation vacancies. The role of cation vacancies is displayed as a result of the common analysis of the temperature dependence of impurity luminescence with the curves of the thermostimulation of the hole traps created due to the presence of the cation vacancies. For room temperatures the hole traps on cation vacancies become unstable. Therefore the trap level of cation vacancy serves as a bridge for the capture of holes from the valence band to 4f RE level.

Key words: energy transfer, luminescence center, cerium, cation vacancy.

1 INTRODUCTION

The problem of energy transfer of the electronic-excitation from the crystal matrix to rare-earth (RE) impurities with different valence is studied during several years (see e.g. ¹). Co-activators and intrinsic defects are important for luminescent properties of activated crystals. Nevertheless, their role and the structure of such centers are not revealed by details till now. For instance, 20 years ago there was established the fact that the usage of halide fluxes increases the efficiency of CaS-Ce^{3+} and CaS-Eu^{3+} cathodoluminescence.² Nevertheless, there is no adequate explanation of halogen role.

One probable mechanism of energy transfer to RE emission center in alkali-earth sulphides is discussed in the present paper. Hole traps are the critical stage in such type of energy transfer.

2 HOLE TRAP CENTERS IN ALKALI-EARTH SULPHIDES

Cation vacancies (V-centers) can serve as hole trap centers. The cation vacancies concentration in alkali-earth sulphides is small enough for standard preparation conditions, and their influence on luminescence properties is negligible. Luminescence³ and ESR⁴ studies show that cation vacancies are easily created in alkali-earth sulphides during the roasting with halide-containing fluxes and are stabilized as associates with halide ions (V_{hal} -centers). The efficiency of vacancy creation by halide ions decreases with increase of the cation atomic weight. Holes trapped by V_{hal} -centers in CaS and SrS are stable till temperatures about 200 K. This capture level becomes metastable for higher temperatures. Figure 1 displays the curves of thermostimulated luminescence, the peaks of which correspond to the loosing holes from V-centers, and the curves of the temperature quenching of V-center stationary luminescence in alkali-earth sulphides.

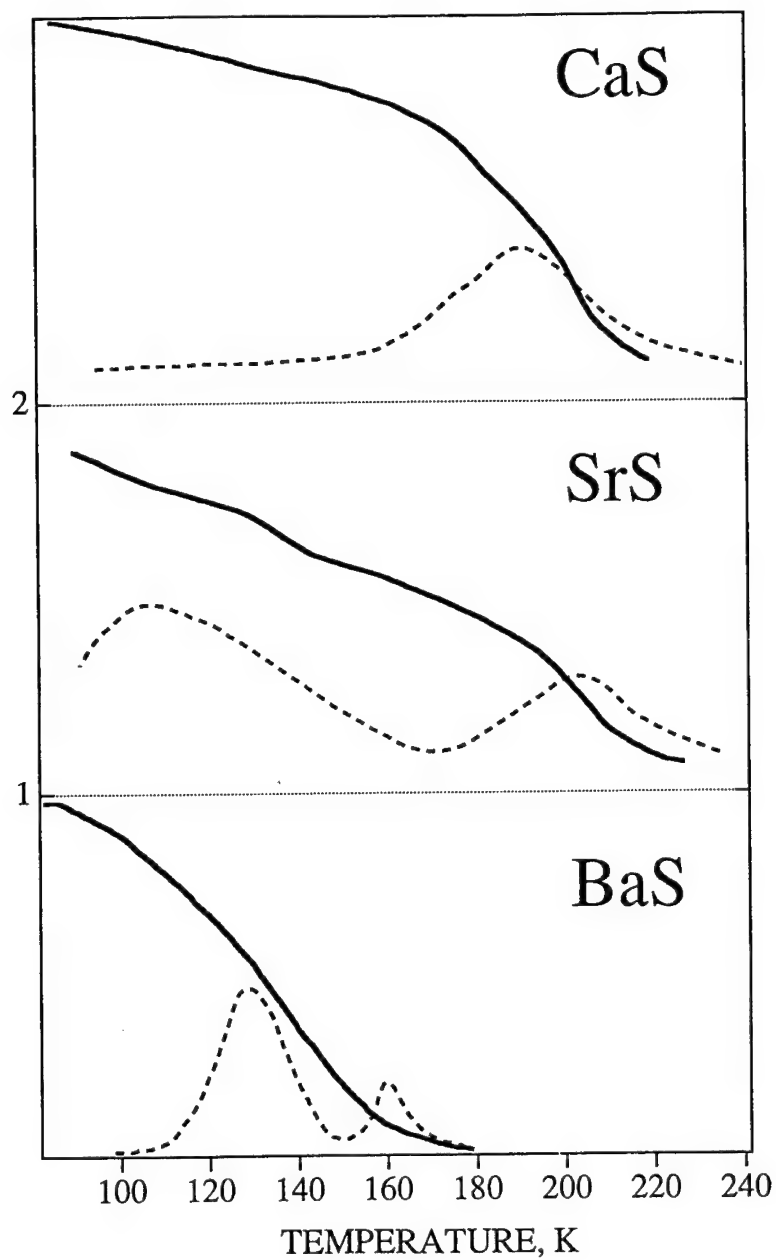


FIGURE 1 Thermostimulated luminescence (dashed curves) and stationary luminescence of V_{Cl} centers vs. temperature (solid).

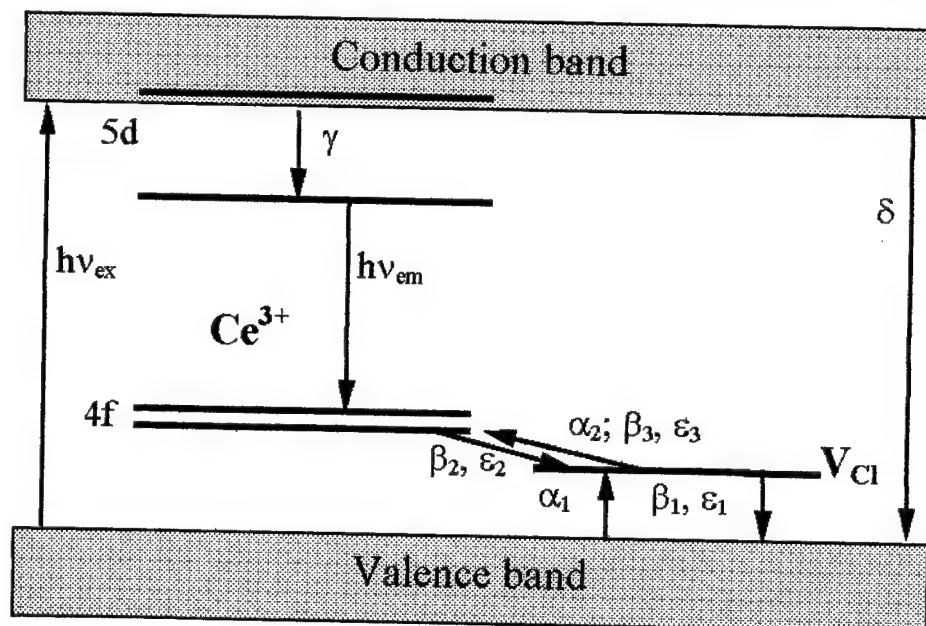


FIGURE 2 Scheme of the processes in the $\text{Ce}^{3+}\text{-V}_{\text{Cl}}$ center.

3 EXCITATION MECHANISM

Substitution of a matrix cation by a RE ion results in the creation of complicated emission centers due to charge and volume compensation. It may be shown that the activator ion and V-center associated with it are the emission centers in alkali-earth sulphides. Mechanism of the luminescence excitation for such centers can be illustrated by the scheme plotted in Figure 2a. The following set of equation corresponds to this mechanism:

$$\begin{aligned}\frac{\partial n_h}{\partial t} &= I - \alpha_1 n_V^0 n_h + \beta_1 n_V e^{-\epsilon_1/kT} - \delta n_e n_h = 0, \\ \frac{\partial n_V}{\partial t} &= \alpha_1 n_V^0 n_h - \beta_1 n_V e^{-\epsilon_1/kT} + \beta_2 n_{\text{Ce}} e^{-\epsilon_2/kT} - \alpha_2 n_V = 0, \\ \frac{\partial n_e}{\partial t} &= I - \gamma n_{\text{Ce}} n_e - \delta n_e n_h = 0, \\ \frac{\partial n_{\text{Ce}}}{\partial t} &= \alpha_2 n_V + \beta_3 n_V e^{-\epsilon_3/kT} - \beta_2 n_{\text{Ce}} e^{-\epsilon_2/kT} - \gamma n_{\text{Ce}} n_e = 0, \\ \frac{\partial n_{\text{Ce}}^*}{\partial t} &= \gamma n_{\text{Ce}} n_e - n_{\text{Ce}}^*/\tau = 0.\end{aligned}$$

Here I is the rate of excitation light quanta absorption by unit volume of the crystal n_e and n_h are the concentrations of electrons and holes, n_V is the concentration of holes at the

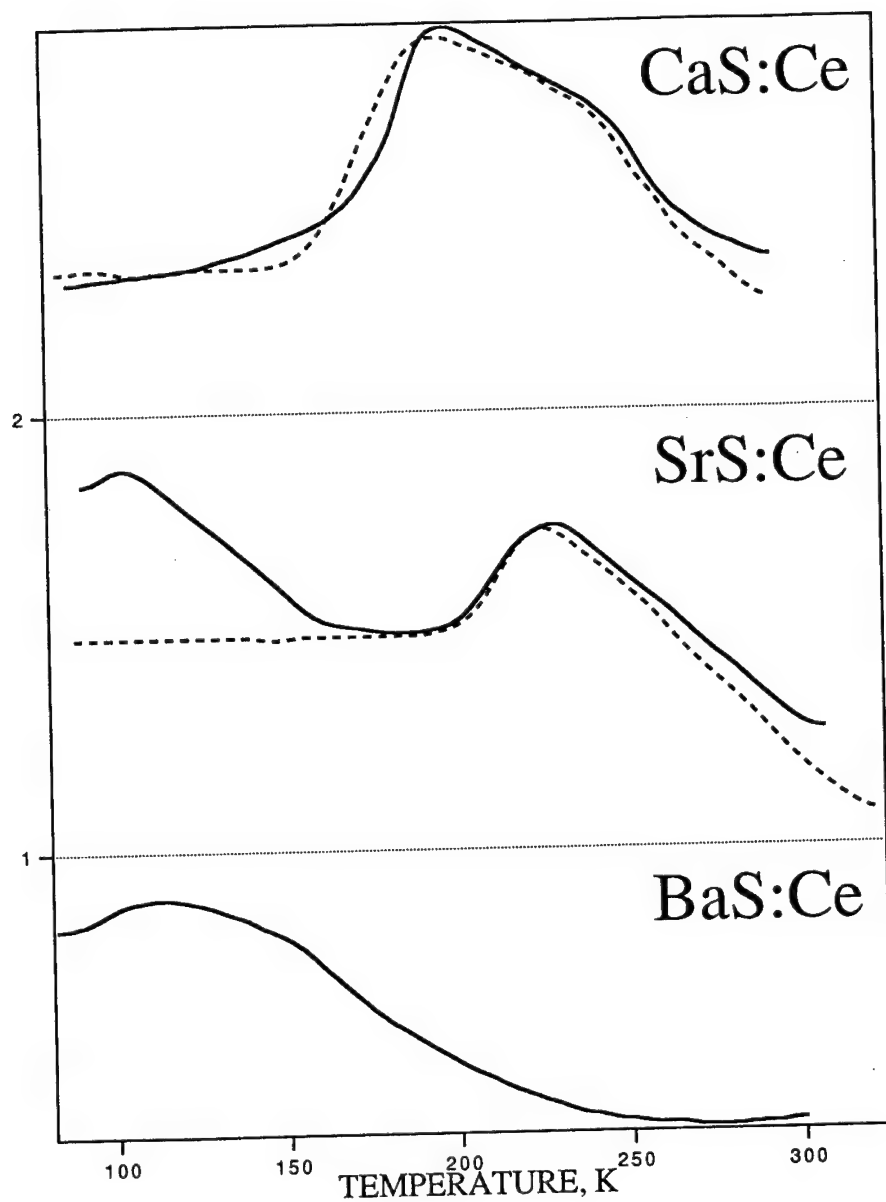


FIGURE 3 Ce^{3+} luminescence intensity vs. temperature for X-ray excitation (solid curve) and the simulation based on the set of equations and experimental data for V_{Cl} centers (dashed).

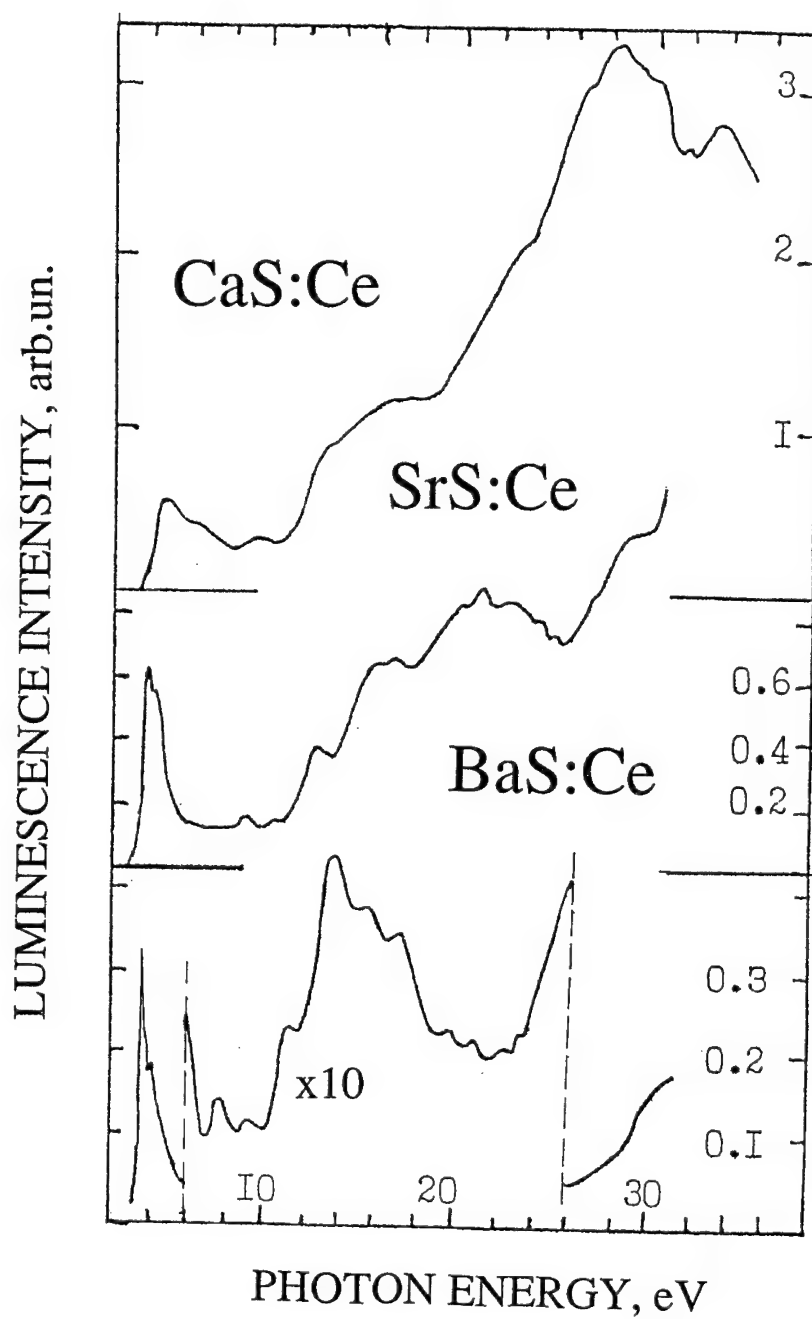


FIGURE 4 Luminescence excitation spectrum.

cation vacancy levels (V^0 and V_{Cl} centers), n_{Ce} is the concentration of holes at cerium ions; n_V^0 is the total concentration of V-centers associated with cerium ions. α , β , δ are probabilities of electron transfer for different processes and ε are the thermal energy of electron levels. Quantum yield of cerium emission $\eta = \gamma n_{Ce} n_e / I$ can be estimated from this set of equations.

Let us notify only some peculiarities of the present model. The direct transition of the electron from $4f$ Ce^{3+} level into the valence hole is not considered, since the efficiency of luminescence in crystals without halide ions is extremely small (this transition is the only possible transition of a valence hole into cerium ion in such crystals). This small probability can be explained by the fact that $4f$ Ce^{3+} level is at least 2 eV above the top of the valence band in alkali-earth sulphides. On the contrary, the capture of an electron from the conduction band by $5d$ cerium level is rather probable, since several sub-levels of the splitted $5d$ level are situated in the conduction band. Secondly, for simplicity we choose the direct inter-band recombination as the recombination channel competitive to cerium luminescence. The most probable type of such channel is the recombination of a valent hole with an electron captured by a F-center.

Figure 3 shows the Ce^{3+} luminescence intensity for alkali-earth sulphides vs. temperature for X-ray excitation and the simulation of these functions based on the set of equations and experimental data for V_{Cl} centers. The proposed model of the excitation energy transfer adequately describes experimental data in temperature range 150 to 300 K. The maximal excitation efficiency is for the temperature about the thermoactivation threshold for V_{Cl} center. Peaks at lower temperatures are connected with emission centers, which consist of a cation vacancy and cerium ion and should correlate with temperature behaviour of V_0 centers.

4 VUV EXCITATION SPECTRA

Excitation spectra of alkali-earth sulphides are plotted in Figure 4. These spectra have the behaviour similar to that discussed in⁵ for excitonic channel of luminescence and in⁶ for recombination luminescence in the presence of two recombination channels. It was shown in⁶ that the shape of the excitation spectrum depends on the capture radius of different types of centers. Here we have the situation with one electron capture center and one hole capture center, and thus the results of⁶ cannot be used without modification. The capture radius R_0 of an electron from the conduction band to a cerium center depends on the time τ , when a hole is located at the cation vacancy, and increases with this time: $R_0 \approx \sqrt{D\tau}$, D is the diffusion coefficient. The excitation spectrum has small decrease in the photon energy range from E_g to $2E_g$ for CaS-Ce and rather prominent one for BaS-Ce, whereas the case of SrS-Ce is the intermediate one. This fact can be explained by the supposition that the activation energy ε decreases in this row, and therefore the time τ when the hole is captured by a cation vacancy, decreases as well. Therefore we conclude that the capture radius for the hole capture by the complex center decreases from CaS-Ce to BaS-Ce. The concentration of F-centers in this row is significantly higher for BaS, and D decreases.

REFERENCES

1. G. Blasse, B. C. Grabmaier, *Luminescence Materials* (Springer-Verlag, Berlin, 1994).
2. W. Lehmann, *J. Luminescence*, **5**, 87 (1972).
3. A. N. Belsky, Ph.D thesis 'Investigation of the electronic structure of XS ($X = Ca, Sr, Ba$) doped by rare earth elements using synchrotron radiation', Moscow State University, 1987.

THE ROLE OF CATION VACANCIES IN EXCITATION MECHANISM OF RE-IONS [887]/389

4. M. I. Danilkyn, I. Riiv, V. Seeman, A. N. Belsky, S. N. Soldatov, *Transactions of the Instituts of Physics of the Estonian Acad. Sci.*, **67**, 97 (1990).
5. V. V. Mikhailin, *Nuclear Instruments and Methods in Physics Research A***216**, 107 (1987).
6. A. N. Belsky, I. A. Kamenskikh, V. V. Mikhailin, I. N. Spinkov, A. N. Vasil'ev, *Physica Scripta*, **41**, 530 (1990).

LSO-Ce FLUORESCENCE SPECTRA AND KINETICS FOR UV, VUV AND X-RAY EXCITATION

I. A. KAMENSKIKH,¹ V. V. MIKHAILIN,¹ I. H. MUNRO,²
D. Y. PETROVYKH,¹ D. A. SHAW,² P. A. STUDENIKIN,³ A. N. VASIL'EV,¹
I. A. ZAGUMENNYI³ and YU. D. ZAVARTSEV³

¹*Physics Department, Moscow State University, 117234 Moscow, Russia;* ²*Daresbury Laboratory, Warrington WA4 4AD, UK;* ³*General Physics Institute, Vavilov str. 38, 117924 Moscow, Russia*

LSO-Ce fluorescence emission and excitation spectra and decay kinetics have been measured for UV, VUV and X-ray excitation at RT and 80 K. The features of the fluorescence excitation spectra of two types of cerium centres in the region 3 to 6 eV are analysed in the assumption of competitive absorption between them. It is shown that the centres can have similar absorption bands. Forbidden energy bandgap for LSO is evaluated to be not less than 6.5 eV.

Key words: lutetium oxyorthosilicate (LSO), scintillator, cerium-doped.

1 INTRODUCTION

High fluorescence yield, fast decay and high density make cerium-doped lutetium oxyorthosilicate ($\text{Lu}_2(\text{SiO}_4)\text{O}:\text{Ce}$) or LSO an attractive candidate for a number of applications.^{1–3} Unlike many other cerium-containing compounds, it has a high efficiency of fluorescence excitation at high energies of excitation. Measurements in the VUV region can be helpful for the understanding of the mechanisms of the energy transfer involved.

2 EXPERIMENTAL

Single crystals of cerium doped Lu_2SiO_5 and $\text{Lu}_{2-x}\text{Gd}_x\text{SiO}_5$, where $x = 1$ (50 at.% of Gd) and 0.4 (20 at.% of Gd), were grown by the Czochralski technique in iridium crucibles of 40 mm diameter and 40 mm height. The oxides of lutetium, gadolinium and cerium were of 99.99% purity, silicon oxide was 99.9% purity. The as-grown crystals were of 16 to 18 mm diameter and ~ 80 mm long. The cerium concentration in the melt was 1 at.%, in the crystal it is expected to be lower due to the low distribution coefficient of cerium ($k_{\text{Ce}} = 0.25$).²

The measurements of fluorescence emission and excitation spectra and fluorescence kinetics have been performed using the synchrotron radiation from the SRS storage ring, DRAL, UK. Fluorescence excitation in the region 3.5 to 30 eV was measured using 1-meter Seya-Namioka monochromator of the station 3.1 at RT and 80 K. The emission bands were separated by interference filters or a secondary monochromator allowing for the measurements of the emission spectra as well. X-ray measurements (emission spectra and fluorescence decay) at RT were performed at the X-ray monochromator of the station 9.3. Fluorescence decay kinetics was studied using the single-photon counting technique in the single-bunch mode of SRS operation (bunch width ~ 200 ps, repetition rate ~ 320 ns).

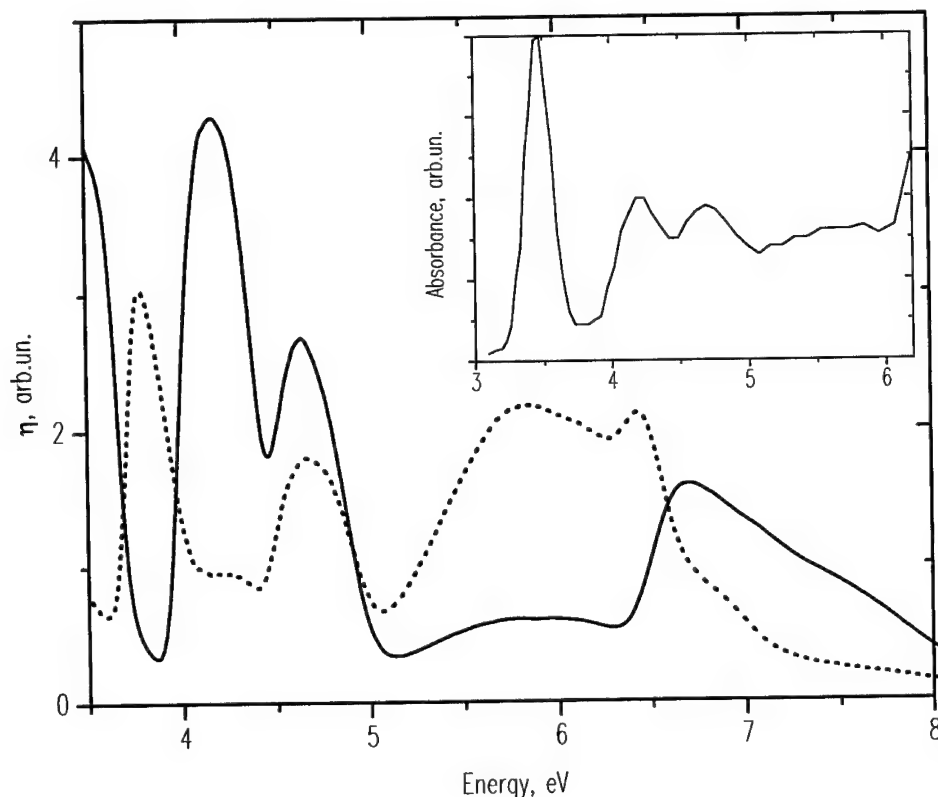


FIGURE 1 Fluorescence excitation spectra for 400 nm (solid curve) and 520 nm emission (dotted curve, multiplied by 10) of LSO-Ce at 80 K. In the insert the absorption spectrum of LSO-Ce from² is reproduced (distortions were not intentional).

3 EXPERIMENTAL RESULTS AND DISCUSSION

Figure 1 presents the fluorescence excitation spectra of two bands of LSO-Ce emission. A typical fluorescence emission spectrum of the LSO crystals at 80 K for the VUV excitation is presented by the solid curve on the left of Figure 2. In a good accord with,³ the emission spectrum consists of two overlapping bands, the first one at 80 K showing as a double peak centered around 400 nm (dotted curve in Figure 2) and a longerwavelength shoulder with the maximum at ~ 460 nm (dashed curve). In³ they were attributed to $5d \rightarrow 4f$ transitions within the Ce^{3+} ions substituting for lutetium in two different crystallographic sites. The doublet structure of the higher-energy band is due to the spin-orbit split Ce^{3+} 4f-level, the splitting is not resolved in the lower-energy band. The excitation of the lower-energy band was measured at 520 nm to minimize the contribution of the higher-energy one. The features of the excitation spectrum of the 400 nm band coincide with those of the absorption² (see the insert in Figure 1), while the low-energy peaks of the excitation

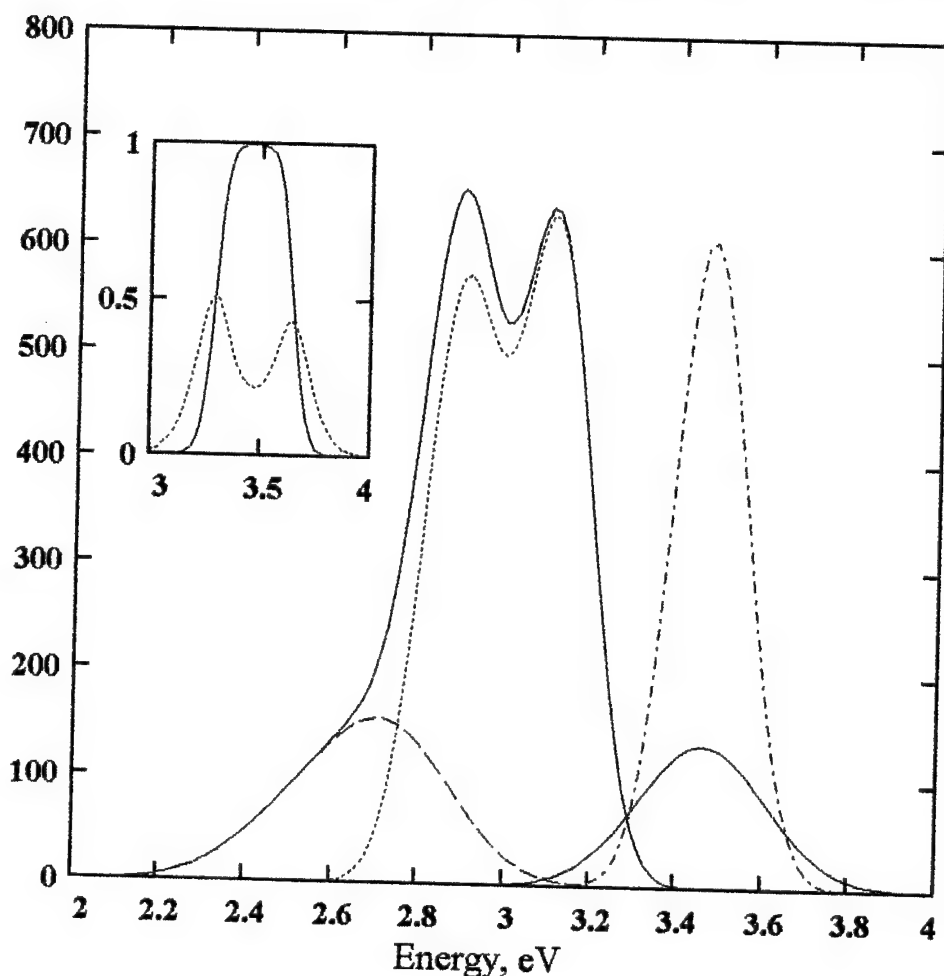


FIGURE 2 Simulated emission and absorption spectra for two types of cerium centres in LSO: dotted and dashed-dotted curve—emission and absorption of the I centre; dashed and solid curve on the right - of the II centre; solid curve on the left is the resultant emission spectrum. In the insert the excitation spectrum of the I centre is presented by the solid curve and of the II centre by the dotted curve. Parameters of the simulation are provided in the text.

spectrum of the 520 nm emission do not show in it (see also Figure 1 in³). The excitation peaks of this emission are anticorrelated with the absorption in the region up to 4.5 eV and are correlated with it at higher excitation energies. As the yield of the 520 nm emission is quite low in the whole spectral range, it makes us think that the features of its excitation spectrum are formed by the competition between the absorption in other centres. If we have a crystal with several types of centres, the observed quantum yield of the i -th centre will be given by the formula:

$$\eta_i^{\text{exp}}(h\nu) = [1 - \exp(-\alpha(h\nu)d)] \cdot \eta_i \cdot \frac{\alpha_i(h\nu)}{\alpha(h\nu)},$$

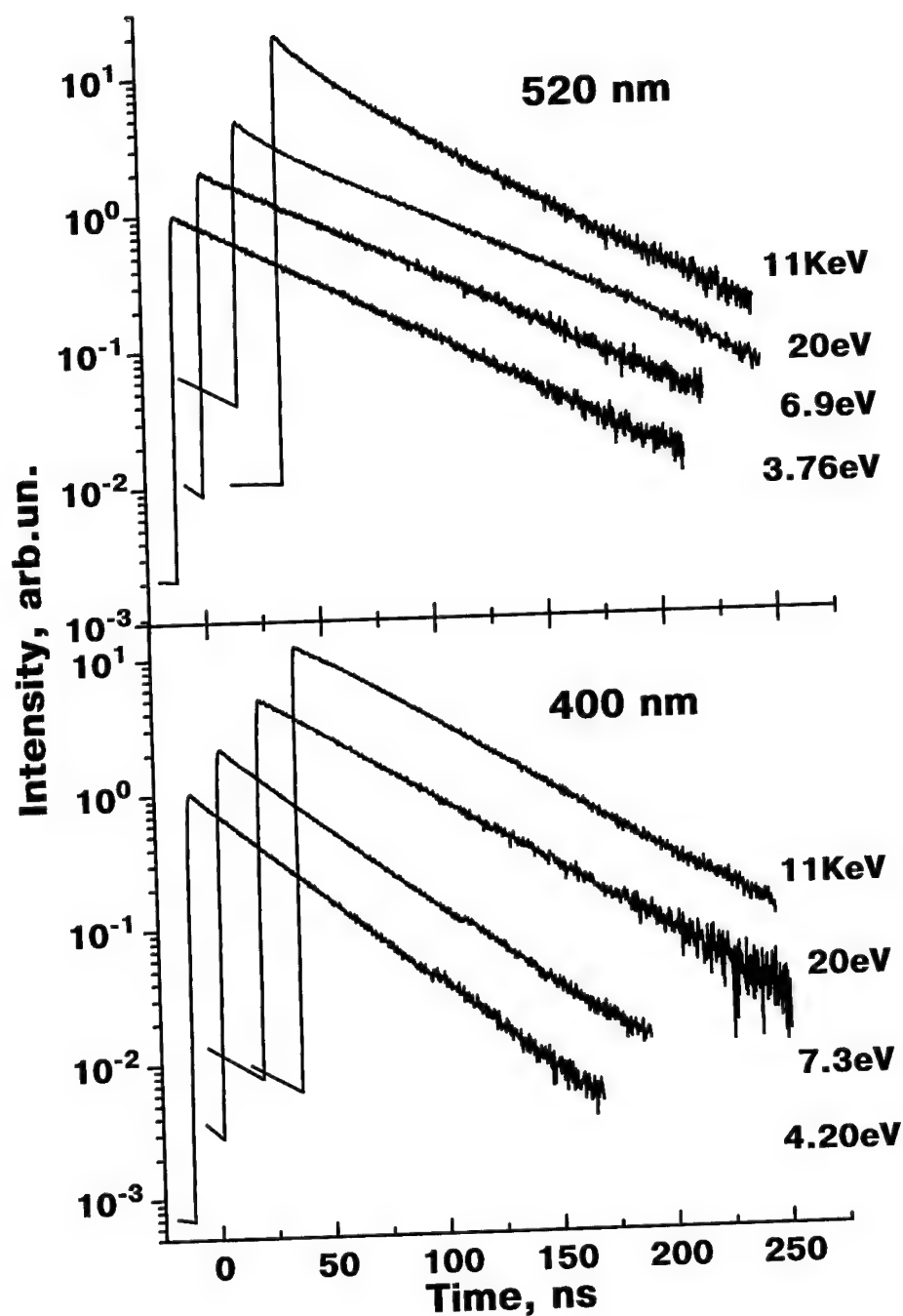


FIGURE 3 Fluorescence decay curves measured for 520 and 400 nm emission of LSO-Ce at 80 K for VUV excitation and at RT for 11 KeV excitation. The noise in the prebunch region is removed not to mask the picture.

where α_i and η_i are the partial absorption and the fluorescence yield of the i -th centre, and $\alpha(h\nu) = \sum_i \alpha_i(h\nu)$ is the total absorption of all the centres. In the case of two centres only with $\alpha_1 \gg \alpha_2$, so that $\alpha \sim \alpha_1$, the excitation spectrum of the strong component will be mainly presented by the first type of the centres, whereas the spectrum of the weak component is proportional to the ratio of the partial absorptions. If there is a third component in the absorption, making $\alpha \gg \alpha_1$, the yield of both types of the centres will be proportional to their partial absorption. We tried to simulate the former case for the first $4f \rightarrow 5d$ absorption peak in the assumption of the presence of two different types of cerium centres, both with the radiative transition $5d \rightarrow 4f$ in Ce^{3+} ions. We simulate the first absorption peak for each of the centres by a Gaussian corresponding to the transition from the lowest of the $4f$ spin-orbit split levels to the lowest term of the $5d$ level split by the crystal field. The emission spectrum is presented for each centre as a pair of Gaussians corresponding to the transitions from the lowest $5d$ level to two $4f$ levels. The Gaussians are given by the standard formula:

$$g(h\nu, S, \Omega, h\nu_0) = \frac{1}{\Omega\sqrt{2\pi S}} \exp \left[-\frac{1}{2S} \left(-\frac{h\nu - h\nu_0 \pm S\hbar\Omega}{S\hbar\Omega} \right)^2 \right]$$

(‘+’ corresponds to the emission and ‘-’ to the absorption). The splitting of the $4f$ level is 0.22 eV for both types of the centres, the other parameters were as follows:

	I centre	II centre
position of the zero-phonon line, $h\nu_0$	3.29 eV	3.1 eV
Huang-Rhys factor	4.5	6.0
local phonon energy, Ω	0.04 eV	0.06 eV

The result of the simulation is shown in Figure 2. The absorption peaks of two centres almost coincide in position, but for the II centre the peak is broader. The excitation for the II centre appears as a pair of peaks on two sides of the I centre excitation band, very similar to the spectrum presented in,³ high-energy part of which can be seen in Figure 1 as well. By altering the ratio of partial absorption of two centres, the gap between two peaks shown by the dotted line can be made more pronounced. The flat top of the I centre excitation peak is formed by the total absorption of the exciting radiation in the crystal.

The peaks at ~ 4.2 and 4.7 eV of the experimental absorption spectrum, which we assign to the transitions from cerium $4f$ level to higher lying $5d$ terms, are superimposed on a broad absorption band of unknown origin. It can be due to the transitions involving cerium levels and those of defects or matrix. At 4.2 eV the contribution to the total absorption due to these transitions is still small, so the situation is similar to the discussed above, when due to the stronger absorption of the I type of the centres, the absorption peak of the II type centre does not form a peak of the excitation. At 4.7 eV the total α becomes larger than both of the partial α_i , so the profile of η_i^{exp} reproduces α_i , and the peaks of both excitation spectra coincide.

Thus we have an interesting situation when the position of the absorption peaks of two types of cerium centres seem to coincide, but the width of the peaks is different. This means that the transition of the cerium ion to the excited state results in different relaxation of the nearest neighbours, depending on the type of the centre. This can be the case if the configuration of the next-neighbours is different for two types of the centres, affecting the relaxation of the nearest neighbours, or if there are two minima of the potential energy surface in configurational coordinates. So far we can't provide an adequate explanation of the processes involved, the question requires further experimental and theoretical investigation.

A remarkable feature of the excitation spectrum of the 520 nm band at RT is a sharp peak at ~ 6.3 eV, at 80 K it's relative intensity decreases and it shifts towards higher energies. The position of the peak coincides with the tail of the fundamental absorption of undoped crystal, so it can be linked to the defects of the matrix, probably of oxygene type. The knowledge of the origin of this defect with high efficiency of the energy transfer to the type II cerium centres can provide a clue to the understanding of the origin of this type II centre itself.

The profile of the excitation spectra for two fluorescence bands, their temperature dependence and kinetics suggest that the forbidden energy bandgap of LSO is about 6.5 eV. The yield of the long-wavelength fluorescence goes down after 6.5 eV, indicating that the probability of the energy transfer to the related centre by separated electron-hole pairs is not high. Our preliminary measurements show an increase of the yield of the 400 nm emission at higher excitation energies up to 30 eV.

Typical decay curves for both fluorescence bands are presented in Figure 3. After low-energy excitation up to ~ 7 eV the decay curves are well described by a single exponential with characteristic time of ~ 30 ns and ~ 50 ns for 400 and 520 nm bands, respectively. In this region there is no evidence of energy transfer between two types of the centres. Decay curves for the excitation in the fundamental absorption region and X-rays have a complicated profile with a 'beak', characteristic of quenching (more pronounced for lower-energy band but visible for 400 nm band at larger scale as well), and a 'hump' or rise-on time, corresponding to the delayed, relative to the excitation pulse, energy transfer to the emission centres. In case of 400 nm emission it shows as slowing down of the decay.

Quite unexpectedly, in the energy range 3.5 to 10 eV the excitation spectra of the mixed crystals $\text{Lu}_{2-x}\text{Gd}_x\text{SiO}_5\text{-Ce}$ were exactly the same as those of LSO-Ce , indicating that there was no energy transfer between gadolinium and cerium. Emission spectra were similar, but broader. The level of phosphorescence was quite high. For the crystals studied the addition of gadolinium did not improve any of the properties of the LSO.

REFERENCES

1. C. L. Melcher, U. S. Patent No 4,958,080, (1990) and 5,025,151 (1991).
2. C. L. Melcher and J. S. Schweitzer, *IEEE Trans. Nucl. Sci.* **39**, 502 (1992).
3. H. Suzuki, T. A. Tombrello, C. L. Melcher and J. S. Schweitzer, *IEEE Trans. Nucl. Sci.* **40**, 380 (1992).

LUMINESCENCE AND SCINTILLATION PROPERTIES OF $\text{In}_2\text{Si}_2\text{O}_7$

A. GARCIA, T. GAUSDANG, J. P. CHAMINADE, C. FOUASSIER, B. VARREL,*
B. JACQUIER,* M. MESSOUS,** B. CHAMBON** and D. DRAIN**

*Laboratoire de Chimie du Solide du CNRS, Université de Bordeaux I, 33405 Talence Cedex, France; *Laboratoire de Physico-Chimie des Matériaux Luminescents URA n°442 CNRS, Université Lyon I, 69622 Villeurbanne Cedex, France; ** Institut de Physique Nucléaire de Lyon, Université Lyon I, 69622 Villeurbanne Cedex, France.*

We report the physical properties of a new fast indium-based scintillator. The technique of elaboration and the crystal structure of indium disilicate ($\text{In}_2\text{Si}_2\text{O}_7$) are presented as well as the analysis of an intense ultraviolet photoluminescence at low temperature. A complex fast fluorescence decay is recorded with two time domains separated by more than one order of magnitude. Scintillation was measured showing a rather good quantum efficiency comparable to $\text{Bi}_4\text{Ge}_3\text{O}_{12}$.

Key words: indium disilicate, crystal growth, Ce^{3+} luminescence, scintillation.

1 INTRODUCTION

It has been recently proposed to use single crystal scintillators containing a large amount of ^{115}In for detection of low energy solar neutrinos according Raghavan's nuclear reaction (1, 2). Research of indium-rich lattices led us to investigate the luminescence properties of various mixed indium oxides such as $\text{In}_6\text{WO}_{12}$ (3), In_2TiO_5 (4). We showed that the optical transitions responsible for the luminescence of indium tungstate are of charge transfer type within isolated octahedra tungstate groups while they arise from the $(\text{In}_2\text{O}_4)_n^{2n-}$ ribbons running along the b-axis of the In_2TiO_5 structure. The present work deals with the synthesis, crystal growth, structure, luminescence and scintillation properties of $\text{In}_2\text{Si}_2\text{O}_7$.

2 EXPERIMENTAL

- $\text{In}_2\text{Si}_2\text{O}_7$ was prepared by a conventional solid state reaction, using In_2O_3 and SiO_2 (Grade 1, Johnson Matthey). The stoichiometric mixture was intimately ground and then pressed into a pellet at 100 MPa. This pellet was fired at 1400°C for 24 h in air. The recovered sample was reground and fired again under the same experimental conditions. The presence of a single phase was controlled by X-ray powder diffraction.
- $\text{In}_2\text{Si}_2\text{O}_7$ single crystals were grown by a flux method using $\text{Li}_2\text{Mo}_2\text{O}_7$ as solvent. The initial constituents In_2O_3 (6 mole %) and SiO_2 (13 mole %) were mixed together with $\text{Li}_2\text{Mo}_2\text{O}_7$ solvent (81 mole %) and introduced in a platinum crucible. The thermal cycle was the following: heating up to 1250°C at 100°C/h, soaking at 1250°C for 12 h, slow cooling to 800°C at 3°C/h, and finally cooling to room temperature at 50°C/h. Single crystals with platelet and needle shapes were removed by dissolving the flux in hot distilled water. An $\text{In}_2\text{Si}_2\text{O}_7$ platelet with the b axis perpendicular to the principal plane, with dimensions $3 \times 3 \times 1 \text{ mm}^3$, was used for scintillating measurements.

TABLE I
Some data on the luminescence of $\text{In}_2\text{Si}_2\text{O}_7$ with thortveitite-type structure at 4.2 K

	$\text{In}_2\text{Si}_2\text{O}_7$
Optical absorption edge (nm) at 300 K	240
Excitation maximum (nm)	225
Emission maximum (nm)	335
Stokes shift value (cm^{-1})	14600
Decay time* (τ) (μs)	6
T_q (K)	200

T_q : thermal quenching temperature of the luminescence

* λ_{exc} : 228 nm for $\text{In}_2\text{Si}_2\text{O}_7$

3 STRUCTURAL DESCRIPTION

The structural refinement of $\text{In}_2\text{Si}_2\text{O}_7$ (5) confirmed that it was closely related with thortveitite i.e. $\text{Sc}_2\text{Si}_2\text{O}_7$ (6).

The lattice can be described as stacking of alternating parallel sheets of InO_6 octahedra and of isolated Si_2O_7 groups. InO_6 octahedra share edges in a nearly hexagonal arrangement in the *ab*-plane forming a distorted honeycomb arrangement of $(\text{In}_2\text{O}_6)^{6-}$ composition. An isolated Si_2O_7 group consists of two SiO_4 tetrahedra sharing one corner in a staggered configuration with a linear Si-O-Si bridge. The silicate groups are packed in such a way that an Si atom on one side of the Si_2O_7 group shares one oxygen atom from the InO_6 sheet above and two from that below in the *c*-direction. The Si atom from the opposite side is in a reverse situation.

4 LUMINESCENCE

The $\text{In}_2\text{Si}_2\text{O}_7$ powder is white. The optical absorption edge derived from the diffuse reflectance spectrum at 300 K lies at 240 nm. For excitation at shorter wavelengths than the absorption edge $\text{In}_2\text{Si}_2\text{O}_7$ gives an intense luminescence in the ultraviolet at 4.4 K. The emission spectrum consists of a broad structureless emission band peaking at 335 nm. Luminescence characteristics are listed in Table I. The corresponding excitation band has its maximum at about 225 nm. The Stokes shift amounts to $15\,000\text{ cm}^{-1}$. With increasing temperature the band shifts slightly to longer wavelengths and decreases in intensity. The luminescence disappears at about 200 K. For excitation at longer wavelengths than the absorption edge, very weak emission bands due to defects are also observed in the blue. At 4.4 K the decay curve of the UV emission consists of a non exponential initial component and an exponential part characterized by a decay constant of $6\text{ }\mu\text{s}$.

Each InO_6 octahedron shares edges with three others with an average In-In distance of $3.45\text{ }\text{\AA}$. Such a structural feature led us to give the same interpretation for the luminescence of $\text{In}_2\text{Si}_2\text{O}_7$ as recently for In_2TiO_5 and for YbFe_2O_4 -type indium oxides (6, 7). Optical transitions can be considered as charge transfer processes from O^{2-} to In^{3+} within the InO_6 octahedra (8, 9). The energy of the absorption edge of $\text{In}_2\text{Si}_2\text{O}_7$ is expected to exceed that of InMgGaO_4 as a consequence of lowering of the interactions between In atoms (due to the smaller number of In nearest neighbors: 3 instead of 6). It was confirmed experimentally: the energy of the excitation band maximum of $\text{In}_2\text{Si}_2\text{O}_7$ is found to be around $11\,000\text{ cm}^{-1}$ above that of InMgGaO_4 .

5 SCINTILLATION

The scintillation of the crystal has been observed at room temperature under alpha radiations namely from a Th alpha source with energies of 6.02 and 8.8 MeV; the small size of the sample did not allow to perform experiments with a gamma source. Measurements of light intensity and decay were performed at temperatures ranging from 4 K up to room temperature. The signal were digitized at a sampling rate of 140 MHz.

As for the fluorescence decay, two components have been detected:

- a fast one, less than 20 ns, independent of temperature and easy to use for time reference in neutrino's experiments,
- a slow one of few μs which lengthens with decreasing temperature and exhibits a maximum intensity at 50 K, decreasing drastically at lower temperature.

The total light intensity is increased by a factor 3.5 when lowering the temperature to liquid nitrogen. A comparison of light output of different current used scintillators shows a factor 8 less with a CaF_2 crystal and a better efficiency than a BGO crystal but recorded at room temperature.

6 CONCLUSION

We have reported the physical properties of a new fast indium-based scintillator, namely indium disilicate ($\text{In}_2\text{Si}_2\text{O}_7$). It exhibits an intense laser induced ultraviolet luminescence which decays with two rather fast components. Under irradiation by alpha particles a quantum efficiency comparable to BGO has been measured with a very small sample. It is thus planned to improve the size of the sample and the way to collect the maximum of light output from the scintillator to the detector. Unfortunately the low quantum efficiency at very low temperature is unfavorable for its use as a bolometer at a few mK.

REFERENCES

1. R. S. Raghavan, *Phys. Rev. Letters*, **37**, 259 (1976).
2. L. Gonzales-Mestres, *Ann. de Phys. (Suppl.)* **6**, 181 (1992).
3. T. Gaewdang, J. P. Chaminade, A. Garcia, C. Fouassier, M. Pouchard, P. Hagenmuller, B. Jacquier, *Material Letters* **18**, 64 (1993).
4. T. Gaewdang, J. P. Chaminade, P. Gravereau, A. Garcia, C. Fouassier, P. Hagenmuller, R. Mahiou, *Mat. Res. Bull.* **28**, 1051 (1993).
5. T. Gaewdang, J. P. Chaminade, P. Gravereau, A. Garcia, C. Fouassier, M. Pouchard, P. Hagenmuller, B. Jacquier, *Z. anorg. allg. Chem.* (to be published).
6. D. W. J. Cruickshank, H. Lynton, G. A. Barclay, *Acta Crystallogr.*, **15**, 491 (1962).
7. G. Blasse, G. J. Dirksen, N. Kimizuka, T. Mohri, *Mat. Res. Bull.*, **21**, 1057 (1986).
8. G. Blasse, *Chem. Phys. Lett.*, **175**, 237 (1990).
9. G. Blasse and L. H. Brixner, *Mater. Chem. Phys.*, **28**, 275 (1991).

THERMOLUMINESCENCE OF DOPED $\text{Gd}_3\text{Ga}_5\text{O}_{12}$ GARNET CERAMICS

A. JAHNKE,^{*} M. OSTERTAG,^{*,**} M. ILMER^{**} and B. C. GRABMAIER^{*}

^{*}*Siemens AG, Corporate Research and Development, 81730 München, Germany;*

^{**}*Institut für Kristallographie und Mineralogie, Universität München,
Theresienstr.41, 80333 München*

Gadolinium gallium garnet ceramics (GGG) doped with Cr^{3+} , Pr^{3+} and Bi^{3+} have efficient luminescence. Excited by X-rays some of the investigated scintillators show an afterglow which is detrimental to an application in medical radio diagnostics. Thermoluminescent measurements between 50 K and 600 K gave results that allow to estimate the trap concentration in these materials. Only shallow traps could be found in GGG:Cr. It seems that these traps are caused by lattice defects relative to oxygen deficiency. The thermoluminescence at higher temperatures of GGG:Pr and GGG:Bi reveals deep traps which determine the afterglow in these luminescent materials.

Key words: thermoluminescence, doped garnet ceramics, chromium, praseodymium, bismuth.

1 INTRODUCTION

Gadolinium gallium garnets $\text{Gd}_3\text{Ga}_5\text{O}_{12}$ (GGG) doped with chromium (Cr^{3+}) are well known as a luminescent material. If these scintillators are manufactured as translucent ceramics they can be used in X-ray computed tomography.¹ The most important requirements for this application are high light output, moderate decay time and low afterglow.

The chromium ions fit quite well into the octahedral B-site of the GGG-lattice (ionic radius of $\text{Ga}^{3+} = 0.62 \text{ \AA}$, that of $\text{Cr}^{3+} = 0.61 \text{ \AA}$)² and give a broad band emission in the infra-red due to the $^4\text{T}_2 \rightarrow ^4\text{A}_2$ transition. The luminescent properties of GGG-ceramics with other dopants like Pr^{3+} and Bi^{3+} are investigated. These materials show a rather high light output and an afterglow even far above room temperature.

Afterglow is a phenomenon that occurs if charge carriers in scintillators are trapped. By thermal or optical activation these charges may leave the traps and recombine radiatively so that light emission is delayed. This detrapping process can be enhanced by rising the temperature. After a certain period of excitation at low temperature this effect is used to measure the retarded light output as a function of the rising temperature, the so-called thermoluminescence.

The investigation of the thermoluminescent behaviour gives information about the existence of trap states, their energy and the afterglow of the scintillator material.

2 EXPERIMENTAL

Doped powders were prepared following the hydroxide precipitation method described in reference.¹ Starting materials were high purity oxides: 99.99% Ga_2O_3 and 99.999% Gd_2O_3 .

The prepared compositions are listed in the following scheme:

Gd ₃			Ga _{4.959}	Cr _{0.041}	O ₁₂
Gd _{2.993}		Ce _{0.007}	Ga _{4.959}	Cr _{0.041}	O ₁₂
Gd _{2.950}	Pr _{0.050}		Ga ₅		O ₁₂
Gd _{2.997}	Pr _{0.003}		Ga ₅		O ₁₂
Gd _{2.994}	Pr _{0.003}	Ce _{0.003}	Ga ₅		O ₁₂
Gd _{2.973}	Bi _{0.027}		Ga ₅		O ₁₂

The dried and calcined garnet powder was mixed with an organic binder and then uniaxially pressed at 2000 kp/cm² into pellets of 15 mm in diameter. These pellets were sintered in air or pure oxygen at 1650°C for 10 hours.

The sintered ceramic samples have a density of nearly 100% of the theoretical value and exhibit translucent to transparent optical quality.

3 MEASUREMENT

The measurements of the thermoluminescence are performed in a helium refrigerator cryostat with a temperature range from 15 K to 320 K, whereas a heating chamber is used for the range from 295 K to 700 K. In the latter case a 3 mm thick heat-absorbing filter glass SCHOTT KG 5 protects the photomultiplier tube HAMAMATSU R 1104 from infra-red radiation.

The thermoluminescent characteristics of the GGG ceramics are studied after cooling the samples to 15 K. During a short test exposure at a reduced X-ray dose (40 kV, 5 mA) the total light yield is measured as a standard. For trap filling the specimens are exposed to X-rays from a tube with a tungsten anode operated at 50 kV and 20 mA for 5 minutes.

Two minutes after the end of X-irradiation the spontaneous emission of light has decreased to a negligible amount. If the sample is now heated at a constant rate of 5 K/min, the thermoluminescent glow curve of the ceramic is recorded by the photomultiplier. During the heating the thermal induced light emission is registered after each temperature step of 1 K.

At 320 K the equipment must be changed. The specimen is now measured in a heating chamber. It is necessary to know the light yield in this set-up at the same reduced X-ray dose as at 15 K. Both standards make it possible to obtain a continuous glow curve over the whole temperature range from 15 K to 700 K.

The procedure to measure the glow curve from 300 K to 700 K is similar to that at low temperature. Samples which show thermoluminescence far above room temperature have been annealed at 773 K for 2 hours and kept in the dark before they were measured.

4 RESULTS AND DISCUSSION

4.1 Glow Curves of GGG:Cr- and GGG:Cr,Ce-Ceramics

The thermoluminescent glow curves of GGG:Cr and GGG:Cr, Ce are shown in Figure 1. The glow curves exhibit peaks at 110 K, 160 K, 250 K, 350 K, and at about 510 K. The presence of cerium reduces the peak height of those peaks which are present below room temperature. Cerium lowers the peak at 250 K so much, that an additional peak at 220 K can be seen.

The peaks below room temperature can be correlated to electron traps. The respective trapping mechanism has been investigated and published.³ The mechanism can be

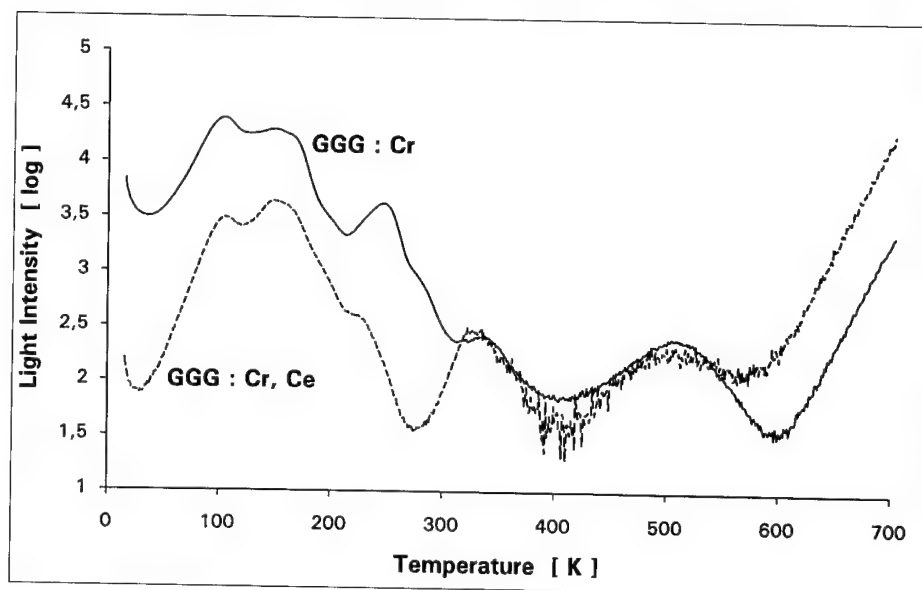


FIGURE 1 Thermoluminescent glow curves of GGG-ceramics doped with 0.041 mol Cr^{3+} showing the influence of codoping with cerium.

explained in the following way: X-rays create electrons and holes. A part of the electrons will be trapped by oxygen vacancies. Their presence in garnets has been proven.³ After escaping from their traps these electrons recombine with the trapped holes at the Cr^{3+} . The oxygen-firing atmosphere and the presence of Ce^{4+} will reduce the oxygen vacancy concentration. The influence of the cerium on the peaks at 350 K and 510 K is not directly evident. So these peaks are not correlated to oxygen vacancies.

4.2 Glow Curves of GGG:Pr- and GGG:Pr,Ce-Ceramics

Pr^{3+} with its ionic radius of 0.99 Å fits well in the dodecahedral Gd^{3+} -site (1.05 Å). Also Ce^{3+} (0.97 Å) fits better on the A-site than on the smaller B-site.

site	A ₃	B ₂	(CO ₄) ₃
e.g. GGG	Gd ₃	Ga ₂	(GaO ₄) ₃
coordination to oxygen	8	6	4
site symmetry	dodecahedral	octahedral	tetrahedral
radii for GGG [Å]	Gd ³⁺ 1.05	Ga ³⁺ 0.62	Ga ³⁺ 0.47
radii of dopants [Å]	Ce ⁴⁺ 0.87	Cr ³⁺ 0.61	Cr ³⁺ 0.61
	Ce ³⁺ 0.97		
	Pr ³⁺ 0.99		
	Bi ³⁺ 1.17		

The glow spectra in Figure 2 show peaks at the following temperatures: 80 K, 110 K, 150 K, 220 K, 350 K, 480 K and 510 K. The peaks at 80 K, 110 K and 150 K are rather low. The dominant peak is that one at 350 K followed by the peaks at 480 K and 510 K.

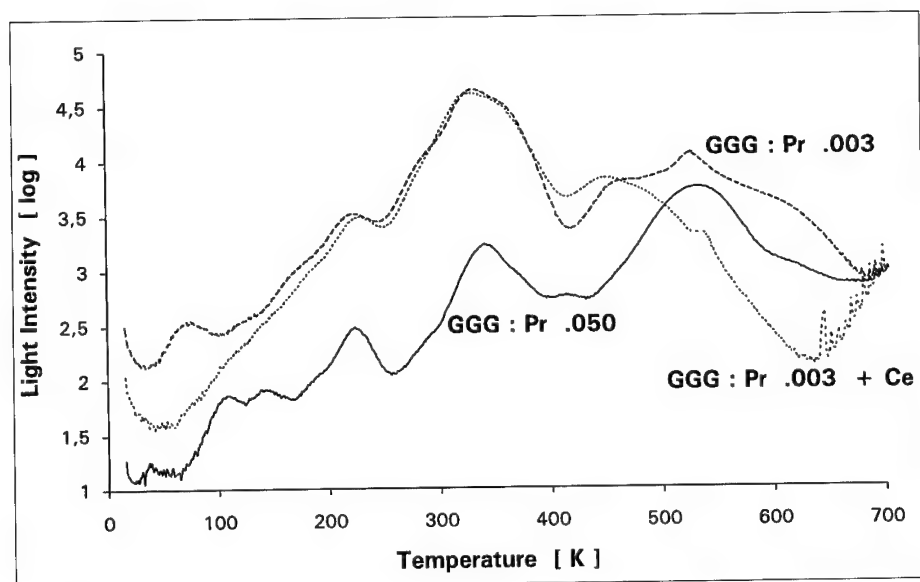


FIGURE 2 Thermoluminescent glow curves of GGG-ceramics doped with Pr^{3+} showing the influence of Pr concentration and Ce codoping.

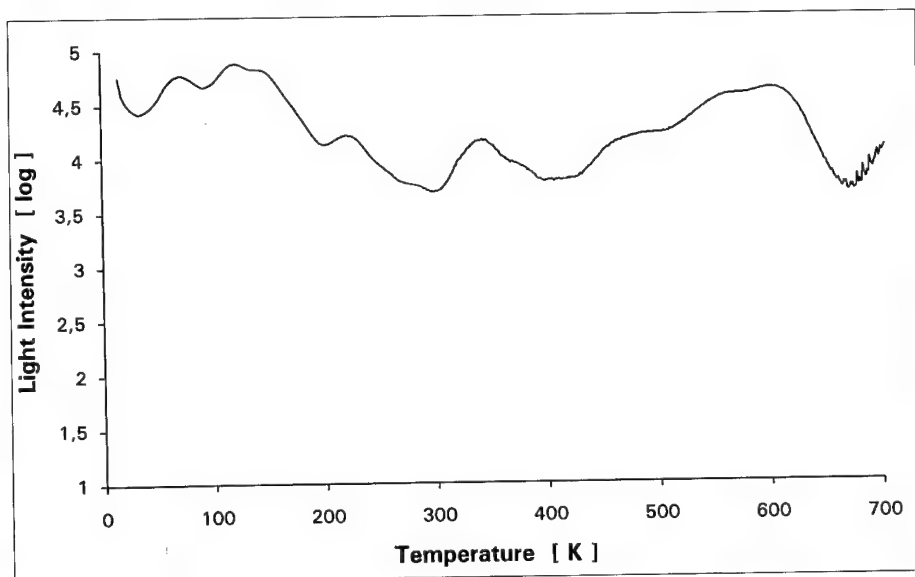


FIGURE 3 Thermoluminescent glow curve of GGG-ceramic doped with 0.027 mol Bi^{3+} .

The peaks at 350 K and 510 K can also be seen in Figure 1. They are related to traps in the GGG host lattice doped with Cr^{3+} . Neither the peak height nor the peak position are influenced by the codopant Ce^{4+} . With respect to this fact the incorporation of

praseodymium must be detrimental to the host lattice. The Pr-ion on its assumed dodecahedral A-site induces deep traps. The peak at 350 K must be related to the very long afterglow mentioned in the introduction. Up to now the luminescence mechanism is unknown.

4.3 Glow Curves of GGG:Bi-Ceramics

Figure 3 shows the glow curve of GGG:Bi. All trap levels have a very high trap concentration and the main peaks found in GGG:Cr and in GGG:Pr are active in Bi-doped GGG, too. The peaks of the glow curve at 80 K, 110 K, 150 K and 220 K correspond to traps related to a high oxygen deficiency. High glow peaks at 350 K and 480 K, and two additional peaks at 570 K and 610 K reveal a high concentration of deep traps. Assuming Pr^{3+} to be detrimental to the GGG host lattice, we see in Figure 3 that Bi^{3+} is even worse. This material has a long intensive afterglow which has been published together with a model for the luminescence mechanism.⁴

5 CONCLUSIONS

An ideal gadolinium gallium garnet single crystal is at room temperature an electrical insulator and is transparent. The band gap was measured by light absorption at 250 nm giving an energy gap of 4.96 eV.⁵ Therefore electronic transitions from the valence band to the conduction band do not occur in the visible wavelength range. After X-ray irradiation of a sample at low temperatures most of the traps are filled with charge carriers. By slowly heating up this sample the electrons gradually move around and find a recombination centre. Summarising, all GGG samples show thermoluminescent glow curves with a peak at 350 K but in different heights. Related to these peaks at least one charge trap in the host lattice was found to be responsible for the same afterglow properties of all differently doped samples. Pr^{3+} enhances the activation of this trap level corresponding to a glow peak at 350 K.

The measurement of this thermal stimulated light emission has proven to be a suitable tool for relating the energy depth of traps to the respective temperature. The height of the glow peaks corresponds to the trap concentration at a certain energy level in the forbidden band gap.

The trap concentration and the necessary ionisation energy for trapped electrons give important information concerning the afterglow of the investigated luminescent material.

REFERENCES

1. V. C. Tsoukala and C. D. Greskovich, GENERAL ELECTRIC COMPANY European Patent Application 0 467 044 A2, 22.01.1992.
2. M. Grinberg, A. Brenier, G. Boulon, C. Pedrini and C. Madej, *J. Lumin.*, **55**, 303 (1993).
3. G. Blasse, B. C. Grabmaier, M. Ostertag, *J. Alloys Comp.*, **200**, 17 (1993).
4. M. Ilmer, B. C. Grabmaier and G. Blasse, *Chem. Mater.*, **6**, 204 (1994).
5. M. Lammers, J. Severin and G. Blasse, *J. Electrochem. Soc.*, **134**, 2356 (1987).

LUMINESCENCE DECAY OF RARE EARTH IONS IN AN ORTHOPHOSPHATE MATRIX

B. FINKE and L. SCHWARZ

*FB Chemie, Ernst-Moritz-Arndt Universität Greifswald, Soldtmannstr. 16, D-17489
Greifswald, Germany*

Investigations of the luminescence decay of Ce^{3+} - and Tb^{3+} -ions in solid solutions of the system $\text{K}_3\text{La}_{1-x-y}\text{Ce}_x\text{Tb}_y(\text{PO}_4)_2$ were carried out at 298 K and 10 K using a laser pulse spectrometer or synchrotron radiation as excitation sources. A comparison of the decay times determined in the host absorption range (160 nm) and in the Ce^{3+} - and Tb^{3+} - ion levels shows a delayed decay of the host excitation. The results are discussed in regard to energy transfer.

1 INTRODUCTION

Solid solutions of potassium lanthanum orthophosphate $\text{K}_3\text{La}(\text{PO}_4)_2$ with analogous double phosphates of cerium and/or terbium have been described earlier.¹ The structure of these compounds is monoclinic (SG $\text{P2}_1/\text{m}$) and corresponds to the unit cell of $\text{K}_3\text{Nd}(\text{PO}_4)_2$ described by Hong and Chinn² as a laser material too. Powders and single mixed crystals of the system $\text{K}_3\text{La}_{1-x-y}\text{Ce}_x\text{Tb}_y(\text{PO}_4)_2$ are luminophors of high efficiency under UV excitation and show the characteristic emission of the inserted Ce^{3+} - and Tb^{3+} -ions.¹ The optical properties of these compounds were studied by VUV- and UV/VIS-spectroscopy.³

Furthermore the luminescence decay of cerium and terbium in the $\text{K}_3\text{La}(\text{PO}_4)_2$ host lattice has been investigated using a laser pulse spectrometer or synchrotron radiation as excitation sources. This paper presents the results of the measurements.

2 EXPERIMENTAL

The samples have been prepared from stoichiometric mixtures of KHCO_3 , RE_2O_3 ($\text{RE} = \text{La}, \text{Ce}, \text{Tb}$), and $(\text{NH}_4)_2\text{HPO}_4$ at 1300 K (powders) or were grown from a flux of $\text{K}_4\text{P}_2\text{O}_7$ (crystals).

The investigations of the luminescence decay of Tb^{3+} -ions were carried out using a nitrogen laser pulse spectrometer ($\lambda_{\text{exc}} = 337.1$ nm; pulse duration ≤ 500 ps) based on LIS 200 (Zentrum für wissenschaftlichen Gerätebau der Akademie der Wissenschaften der DDR)⁴ by direct excitation in the Tb^{3+} levels. The measurements were completed by excitation in the host lattice absorption range (160 nm) using synchrotron radiation at the experimental station SUPERLUMI⁵ of the DORIS storage ring of HASYLAB at DESY. The pulse duration was approximately 130 ps.

The fast decay of Ce^{3+} -ions was also determined by using synchrotron radiation and the equipment of the HIGITI experimental station.⁶

3 RESULTS AND DISCUSSION

3.1 Luminescence decay of Tb^{3+} -ions in $\text{K}_3\text{RE}(\text{PO}_4)_2$

The transient luminescence of Tb^{3+} -ions measured using the LIS 200 and synchrotron radiation was determined for the transitions $^5\text{D}_3, ^5\text{D}_4 \rightarrow ^7\text{F}_5$ in the systems

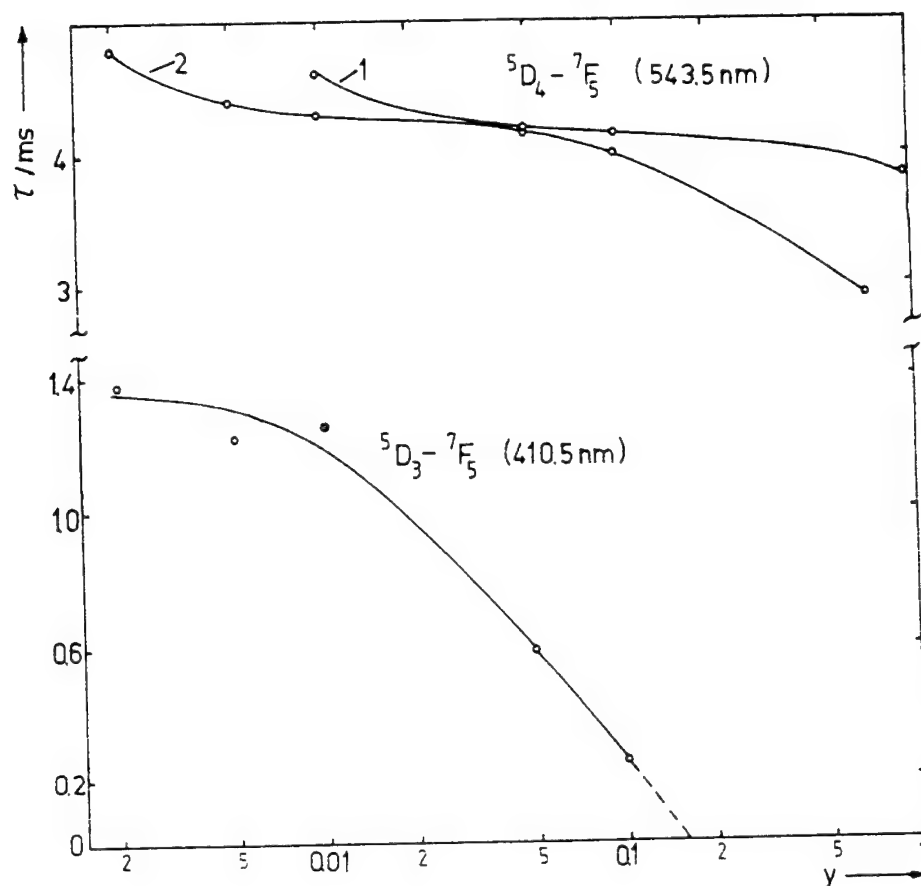


FIGURE 1 Lifetime of the $^5D_4-^7F_5$ transition in $K_3La_{1-y}Tb_y(PO_4)_2$ (curve 1) and $K_3La_{0.75-y}Ce_{0.25}Tb_y(PO_4)_2$ (curve 2) and the lifetime of the $^5D_3-^7F_5$ transition in $K_3La_{1-y}Tb_y(PO_4)_2$ phosphors as a function of the molar fraction y (excitation at 337 nm).

$K_3La_{1-y}Tb_y(PO_4)_2$ ($0.002 \leq y \leq 1$), $K_3La_{0.75-y}Ce_{0.25}Tb_y(PO_4)_2$ ($0.002 \leq y \leq 0.1$)⁷ and $K_3Ce_{1-y}Tb_y(PO_4)_2$ ($0.002 \leq y \leq 1$) for powders and also some crystals (see Table I, Figure 1). In general it could be found that the depopulation of the 5D_3 level of the Tb^{3+} -ion occurs very rapidly but the depopulation of the 5D_4 level is a little delayed because the maximum population of this level is only reached after about 1 ms. Both transient processes show an exponential decay.

The lifetimes of the $^5D_3-^7F_5$ (410.5 nm) and the $^5D_4-^7F_5$ (543.5 nm) transitions of the Tb^{3+} -ion were determined in dependence on the molar fraction y of the Tb content. According to the general statement for compounds with a molar fraction $y \geq 0.01$ a rapid decrease of the $^5D_3-^7F_5$ lifetime was observed. This fact can also be proved by a change of the emission colour of the compounds from blue to green with increasing y . Cross relaxation processes due to $Tb^{3+}-Tb^{3+}$ ion interactions lead to a quick depopulation of 5D_3 levels at higher terbium concentrations by participation of the ground term multiplet 7F_6 .

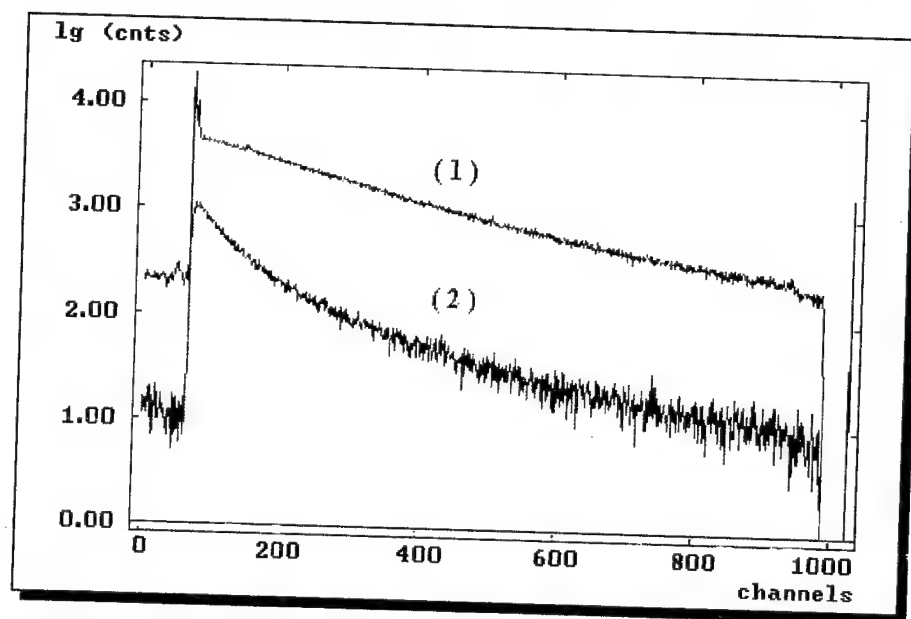


FIGURE 2 Decay curves of $K_3La_{0.9}Ce_{0.1}(PO_4)_2$ (curve 1) and $K_3La_{0.65}Ce_{0.1}Tb_{0.25}(PO_4)_2$ (curve 2) at about 10 K.

However the 5D_4 - 7F_5 lifetime shows only a little dependence on the composition of the compounds and lies between 3 and 4 ms. That applies to $K_3La_{1-y}Tb_y(PO_4)_2$, $K_3La_{0.75-y}Ce_{0.25}Tb_y(PO_4)_2$ as well as $K_3Ce_{1-y}Tb_y(PO_4)_2$.

Lifetime τ decreases slowly due to the absence of concentration quenching of the 5D_4 - 7F_j emission of the Tb^{3+} -ion in $K_3RE(PO_4)_2$ type lattices (see Figure 1).

Table I
Terbium decay time in the system $K_3La_{1-y}Tb_y(PO_4)_2$, measured at 300 K and about 10 K for the terbium transitions 5D_4 - 7F_5 (413 nm) and 5D_4 - 7F_5 (545 nm), exc. 160 nm (SUPERLUMI)

compound	300 K			≈ 10 K		
	5D_3 τ_1 μs [%]	τ_2 μs [%]	5D_4 τ_3 ms	5D_3 τ_1 μs [%]	τ_2 μs [%]	5D_4 τ_3 ms
crystals						
y = 0,1	12.4[10]	1026[90]	4.08	27.3[22]	849[78]	4.08
0,4	0.5[2]	536[98]	3.3	27.6[26]	418[74]	3.3
1,0			3.09			-

3.2 Transient luminescence of Ce^{3+} -ions in $K_3RE(PO_4)_2$

The decay time of Ce^{3+} -ions in the systems $K_3La_{1-x}Ce_x(PO_4)_2$, $K_3La_{1-x-y}Ce_xTb_y(PO_4)_2$, and $K_3Ce_{1-y}Tb_y(PO_4)_2$ was investigated at room temperature and at about 10 K using synchrotron radiation for an excitation in the fundamental absorption range of the orthophosphate system³ at 160 nm for the cerium emission at 336 nm.

Table II contains some results of lifetime measurements of different orthophosphate compounds in dependence on the temperature.

The decay times were determined by the program ZFIT⁸ supposing an exponential behaviour; the measured curve was fitted with up to three exponential curves.

In general it could be observed:

- cerium doped phosphors have short decay times in the ns-range, the corresponding transitions 5d - 4f are parity and spin allowed
- the decay time of the cerium ions in the system $K_3La_{1-x}Ce_x(PO_4)_2$ is in all compounds about 20 ns and nearly independent on the Ce^{3+} concentration
- a temperature dependence on the cerium lifetimes (at about 10 K the decay times of all compounds are a little increased)
- in cerium, terbium compounds the decay time of the Ce^{3+} -emission is essentially faster than in $K_3La_{0.9}Ce_{0.1}(PO_4)_2$ or $K_3Ce(PO_4)_2$ at RT as well as at about 10 K, a fact caused by cerium—terbium energy transfer (see Table II, Figure 2)

Table II
Cerium decay time of some orthophosphates $K_3RE(PO_4)_2$ (RE=La, Ce, Tb) measured at 300 K and about 10 K; exc. 160 nm, em. 336 nm; MCA-measuring range 200 ns; in [] information on yield in %

compound	300 K			≈ 10 K		
	τ_1	τ_2 ns [%]	τ_3	τ_1	τ_2 ns [%]	τ_3
$K_3La_{0.9}Ce_{0.1}(PO_4)_2$ -powd.	5.1[5]	21.6[88]	101[7]	1.2[1]	23.5[86]	168[13]
$K_3La_{0.65}Ce_{0.1}Tb_{0.25}(PO_4)_2$ cryst. powd.	1.5[18]	9.7[34]	57[48]	2.1[17]	26.1[30]	186[53]
	3.4[51]	8.5[37]	209[12]	3.9[38]	17.9[50]	200[12]
$K_3Ce(PO_4)_2$ -powd.	8.6[13]	21.4[84]	65[3]	2.7[2]	21.2[91]	176[6]
$K_3Ce_{0.7}Tb_{0.3}(PO_4)_2$ -powd.	2.5[93]	9.9[4]	126[3]	3.1[48]	14.7[43]	168[9]

In all cases shorter and longer decay times could be found; the longer times could only be determined relative inaccurately.

Further information could be received by time resolved measurements of Ce^{3+} -spectra using a time gate for shorter and longer times (see Ref. 3, 2). The short time excitation of the 336 nm emission of the cerium ion corresponds to the usually found Ce^{3+} excitation spectra. The time-delayed cerium excitation spectrum confirms the characteristic absorption edge at 160 nm of the orthophosphate host.

The influence of the orthophosphate host absorption on the decay time of Ce^{3+} - and Tb^{3+} - ions and the following energy transfer from the host to the Ce^{3+} - and Tb^{3+} - ions could be proved. Generally the decay times for an excitation in the host are slower than those measured for the Ce^{3+} - and Tb^{3+} - ion levels. The work will be continued.

ACKNOWLEDGEMENTS

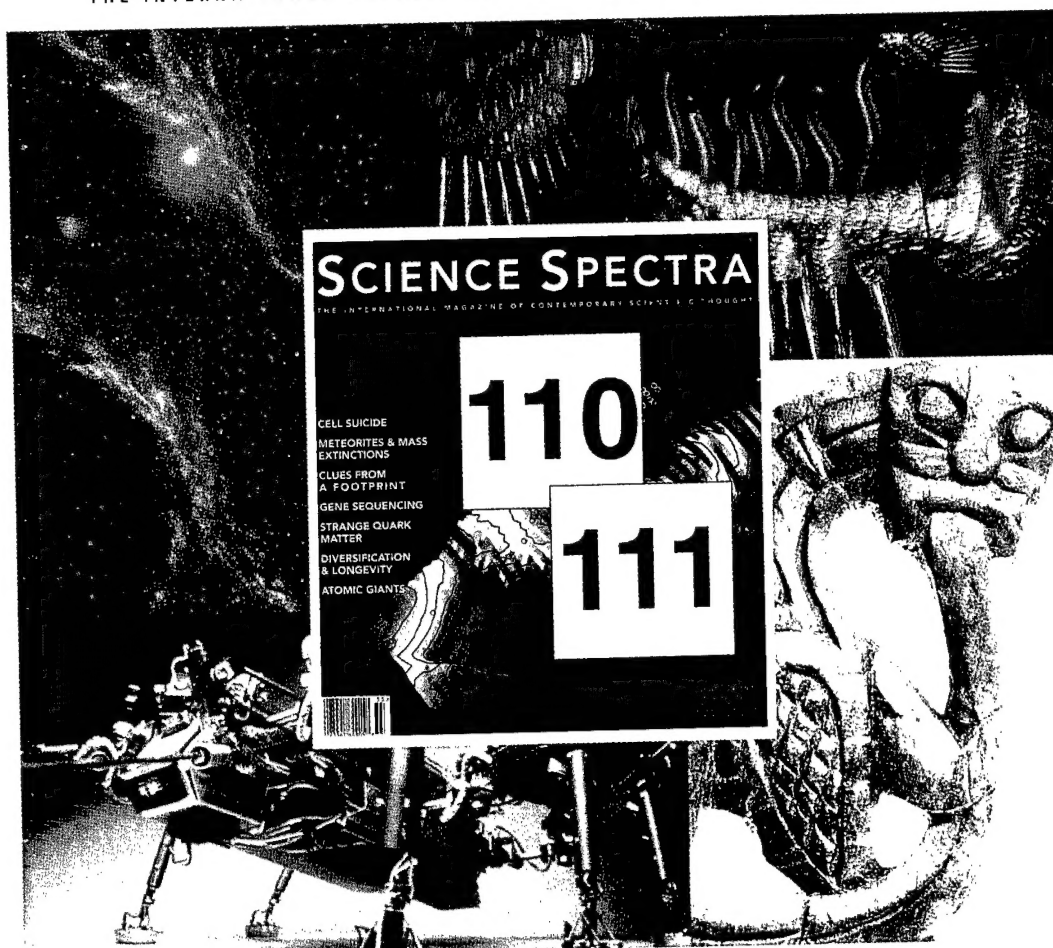
We thank Dr. P. Gürtler, Dr. M. Kraas, Dr. M. Joppien, J. Becker, I. Ast and A. Rohmann for their kind support. The work has been funded by the BMFT of Germany (contract 05 5HGGAB1).

REFERENCES

1. B. Finke, H. Wulff and L. Schwarz, *Z. physik. Chem. (Leipzig)* **262** (1981) 1152. B. Finke, PhD Thesis, Greifswald 1984.
2. H. Y. P. Hong and S. R. Chinn, *Mat. Res. Bull.* **11**, (1976) 421.
3. B. Finke, L. Schwarz, P. Gürtler and M. Kraas, *phys. stat. sol. A* **130**, (1992) K125. B. Finke, L. Schwarz, P. Gürtler, M. Kraas, M. Joppien and J. Becker, *J. Lumin.* **60&61** (1994) 975.
4. Dähne, W. Becker, M. Scholz, K. Teuchner, H. Lucht and H. Schneider, *Feingerätetechnik* **29**, (1980) 463.
5. P. Gürtler, E. Roick, G. Zimmerer and M. Pouey, *Nucl. Instr. & Meth.* **208**, (1983) 835.
6. U. Hahn, N. Schwentner and G. Zimmerer, *Nucl. Instr. & Meth.* **152**, (1978) 261.
7. L. Schwarz, B. Finke, B. Reimer and A. Krüger, *Exp. Techn. d. Physik* **39**, (1991) 431.
8. P. Gürtler, M. Joppien and S. Kampf, *Internal Report Desy F41*, Hasylab 88-02.

SCIENCE SPECTRA

THE INTERNATIONAL MAGAZINE OF CONTEMPORARY SCIENTIFIC THOUGHT



FROM CELLS TO SUPERNOVAS, FROM NUCLEAR CHEMISTRY TO ARTIFICIAL INTELLIGENCE,
FROM ANCIENT HISTORY TO FUTURE THOUGHT...

Science Spectra is a magazine for scientists, by scientists, that takes you on a journey to the frontiers of research and contemporary scientific thought. With a team of editors who are leading scientists in their fields, and backed by the international science publishing house Gordon and Breach, *Science Spectra* is a cross-disciplinary magazine that brings you the full spectrum of today's science.

Subscribe now at US\$32/£20/Sfr48/Aus.\$34 for four issues (15% off cover price), or at US\$49/£32/Sfr73/Aus.\$52 for eight issues (35% off cover price). Your check or money order should be directed and made payable to:

North/South America:

c/o International Publishers Distributor
PO Box 41010,
Newark NJ 07101-8007, USA
or call 1-800-545-8398

Europe:

c/o International Publishers Distributor
Postfach, CH-4004 Basel,
Switzerland
or call (+44)0-73-456-8316

Asia:

c/o International Publishers Distributor
Kent Ridge Rd., PO Box 1180,
Singapore 911106
or call +65 741 6933

Australia:

c/o Fine Arts Press
PO Box 480 Roseville,
NSW 2069 Australia
or call +61 2 417 1033

GIB

Gordon and Breach Publishers

Notes for Contributors

TYPESCRIPTS

Submissions: Papers should be typed on good quality paper with double spacing and wide (3 cm) margins, using one side only, and submitted in duplicate to the Editor in Chief or to the appropriate Regional Editor:

J. P. Biersack, Editor in Chief, Hahn-Meitner-Institut, Glienickestrasse 100, 14109 Berlin, Germany

N. Itoh, Department of Physics, Faculty Of Science, Nagoya University, Furo-cho, Chikusa-ku, Nagoya 464, Japan

H. Kronmüller, Max-Planck-Institut für Metallforschung, Institut für Physik, Heisenbergstrasse 1, 70569 Stuttgart 80, Germany

M. A. Kumakhov, Russian Research Center, Moscow 123182, Russia

N. Tolk, Department of Physics and Astronomy, Vanderbilt University, P.O.Box 1807-B, Nashville, Tennessee 37325, USA

The editors and publisher cannot be responsible for correcting English grammar, spelling, and idiom. Authors should ensure before submission that papers are correct in style and language.

Abstracts, key words, running heads: Each paper requires an abstract of 100-150 words summarizing the significant coverage and findings. Abstracts should be accompanied by up to six key words which between them characterize the contents of the paper. These will be used for indexing and data retrieval purposes. Please also provide an abbreviation of the paper's title (no more than 35 characters) for use as a running head.

Terms of Acceptance: Submission of a manuscript is taken to imply that the paper represents original work not previously published, is not being considered elsewhere for publication, and if accepted for publication will not be published elsewhere in the same form, in any language, without the consent of the publisher. It is also assured that the author has obtained all necessary permissions to include in the paper items such as quotations, reprinted figures, results of government-sponsored research, etc. It is a condition of acceptance for publication that the publisher acquires copyright of the paper throughout the world.

FIGURES

All figures should be numbered with consecutive arabic numbers, have descriptive captions, and be mentioned in the text. Keep figures separate from the text, but indicate an approximate position for each in the margin.

Preparation: Figures submitted must be of high enough standard for direct reproduction. Line drawings should be prepared in black (India) ink on white paper or tracing cloth, with all lettering and symbols included. Alternatively, good sharp photoprints ("glossies") are acceptable. Photographs intended for halftone reproduction must be good glossy original prints, of maximum contrast.

Clearly label each figure with the authors' names and figure number, indicating "top" where this is not obvious. Redrawing or retouching of unusable figures will be charged to authors.

Size: Figures should be planned so that they reduce to a 12.5 cm column width. The preferred width of submitted line drawings is 22 to 25 cm with capital lettering 4 mm high, for reduction by one-half. Photographs for halftone reproduction should be approximately twice the desired size.

Captions: A list of figure captions, with relevant figure numbers, should be typed on a separate sheet and included with the typescript.

COLOR PLATES

Whenever the use of color plates is an integral part of the research, the journal will publish color illustrations without charge to the authors.

EQUATIONS AND FORMULAE (MATHEMATICAL)

Whenever possible, mathematical equations should be typewritten, with subscripts and superscripts clearly shown. It is helpful to identify unusual or ambiguous symbols in the margin when they first occur. To simplify typesetting, please use: (1) the "exp" form of complex exponential functions; (2) fractional exponents instead of root signs; and (3) the solidus (/) to simplify fractions—e.g. $\exp x^a$

Marking: The printer will set mathematical symbols in italics, except for obvious groups like sin and log. Any symbols which are to be left in roman (upright) type should be encircled in pencil in the typescript; bold symbols should be underlined with a wavy line.

EQUATIONS AND FORMULAE (CHEMICAL)

Ring formulae, and other complex chemical matter, are extremely difficult to typeset. Please therefore, supply reproducible artwork for equations containing such chemistry. Long reaction sequences should be designated as "Schemes" and treated like figures: i.e. keep artwork separate from the text, indicate in the margin an appropriate position, and supply a separate list of scheme captions. Where necessary, individual chemical formulae can be identified with bold arabic numbers. Chemical equations referred to in the text should be indicated with arabic numbers set over to the right in parentheses.

Marking: Where chemistry is straightforward and can be set (e.g. single-line formulae), please help the typesetter by distinguishing between e.g., double bonds and equal signs, and single bonds and hyphens, where there is ambiguity. The printer finds it difficult to identify which symbols should be set in roman (upright), italic, or bold type, especially where the paper contains both mathematics and chemistry. Therefore, please help the printer as much as possible by adding marginal notes in pencil.

TABLES

Number tables consecutively with roman numerals, and give each a clear descriptive caption at the top. Avoid the use of vertical rules in tables.

UNITS

Metric units are preferred. Acceptable abbreviations of units are given in the *Style Manual* of the American Institute of Physics and similar publications.

REFERENCES AND NOTES

References and notes are indicated in the text by consecutive superior arabic numbers. The full list should be collected and typed at the end of the paper in numerical order. Listed references should be complete in all details but excluding article titles in journals. Authors' initials should precede their names: journal title abbreviations should conform to *Physical Abstracts*. Examples:

1. A. B. Smith and C. D. Jones, *J. Appl. Phys.* **34**, 296 (1965).
2. R. B. Brown, *Molecular Spectroscopy* (Gordon and Breach, New York, 1970), 3rd ed., Chap. 6, pp. 95, 106.

TEXT HEADINGS

Set first-level headings in the text over to the left, type all in capitals (upper-case); begin the text on the following line. Second-level headings should be typed in small (lower-case) letters with all main words capitalized. Underline the heading and start the text on the next line. For third-level headings, only the first letter should be a capital. Underline, then run on the text after three typewriter spaces.

FIRST LEVEL HEADING

Second-Level Text Headings

Third-level headings. With text run on.

PROOFS

Authors will receive proofs (including figures) by airmail for correction, which must be returned to the printer within 48 hours of receipt. Please ensure that a full postal address is given on the first page of the manuscript, so the proofs are not delayed in the post. Author's alterations in excess of 10% of the original composition will be charged to authors.

REPRINTS

The senior author of each paper will receive 25 complimentary reprints. Additional reprints may be ordered by completing the appropriate form sent with proofs.

PAGE CHARGES

There are no page charges to individuals or to institutions.

A FINAL NOTE

Typescripts which do not conform to the required standards of preparation for submission outlined here will be returned to authors for correction before review.

(Continued from inside front cover)

© 1995 by OPA (Overseas Publishers Association) Amsterdam BV. Published under license by Gordon and Breach Science Publishers SA, a member of The Gordon and Breach Publishing Group. All rights reserved.

Except as permitted under national laws or under the Photocopy License described below, no part of this publication may be reproduced or transmitted in any form or by any means, electronic, mechanical, photocopying or otherwise or stored in a retrieval system of any nature, without the advance written permission of the Publisher.

ORDERING INFORMATION

Four issues per volume. 1996 Volumes: 137-139

Orders may be placed with your usual supplier or with International Publishers Distributor at one of the addresses shown below. Journal subscriptions are sold on a per volume basis only; single issues of the current volume are not available separately. Claims for nonreceipt of issues will be honored free of charge if made within three months of publication of the issue. Subscriptions are available for microform editions; details will be furnished upon request.

All issues are dispatched by airmail throughout the world.

SUBSCRIPTION RATES

Base list subscription price per volume: ECU 283.00 (US\$368.00). * This price is available only to individuals whose library subscribes to the journal OR who warrant that the journal is for their own use and provide a home address for mailing. Orders must be sent directly to the Publisher and payment must be made by personal check or credit card.

Separate rates apply to academic and corporate/government institutions, and may also include photocopy license and postage and handling charges.

*ECU (European Currency Unit) is the worldwide base list currency rate; payment can be made by draft drawn on ECU currency in the amount shown or in local currency at the current conversion rate. The US Dollar rate is based upon the ECU rate and applies to North American subscribers only. Subscribers from other territories should contact their agents or the Publisher. All prices are subject to change without notice.

Publication Schedule Information: To ensure your collection is up-to-date, please call the following number for information about the latest issue published: USA (201) 643-7500 - Dial extension 290 - Enter the ISSN followed by # key. Note: If you have a rotary phone, please call our Customer Service at the numbers listed below.

Orders and enquiries should be placed through International Publishers Distributor at one of the addresses below:

Postfach, 4004 Basel
Switzerland
Telephone: (41-61) 261-01-38
Fax: (41-61) 261-01-73

820 Town Center Drive
Langhorne, PA 19047 USA
Telephone: (215) 750-2642
Fax: (215) 750-6343

Kent Ridge, PO Box 1180
Singapore 911106
Republic of Singapore
Telephone: 741-6933
Fax: 741-6922

Yohan Western Publications Distribution Agency
3-14-9, Okubo, Shinjuku-ku
Tokyo 169, Japan
Telephone: (03) 3208-0186
Fax: (03) 3208-5308

LICENSE TO PHOTOCOPY

This publication and each of the articles contained herein are protected by copyright. If the subscription price paid by the subscriber includes a fee for a photocopy license, then the subscriber is permitted to make multiple photocopies of single articles for the internal study or research purposes of the subscriber. The Photocopy License is not available to individuals or to certain other subscribers. The Photocopy License does not permit copying for any other purpose, such as copying for distribution to any third party (whether by sale, loan, gift or otherwise); as agent (express or implied) of any third party; for purposes of advertising or promotion; or to create collective or derivative works. All requests for permission to copy beyond the scope of the Photocopy License must be made to the Publisher. No copyright licensing organization in any territory has authority to grant such permission on the Publisher's behalf. Any unauthorized reproduction, transmission or storage may result in civil or criminal liability.

RIGHTS AND PERMISSIONS / REPRINTS OF INDIVIDUAL ARTICLES

Permission to reproduce and/or translate material contained in this journal must be obtained in writing from the Publisher. Copies of individual articles may be obtained from SCAN, the Publisher's own document delivery service. For either service, please write or fax to: International Publishers Distributor at one of the addresses listed above.

VOLUNTARY PAGE CHARGES

The United States National Science Foundation has extended the allowance of page charge funds for payments to journals regardless of the Publisher's commercial status. Previously this was reserved for only nonprofit society-sponsored journals. Voluntary page charge payments are now accepted for this journal, and authors may elect to pay any amount up to a maximum of \$25.00 per page. Payments will be refunded in the form of a voucher at 100% value of total payment. This voucher can be used by the author or the author's university library for any product or service offered by the Publisher, and thereby can be used to supplement library funding.

NEGATIVE PAGE CHARGES

The principal author of each article will receive a voucher for his contribution in the amount of ECU 15.00 (US \$20.00, Yen 3,000), which can also be used to purchase the Publisher's products directly or through university libraries, thereby reducing costs of publications to those authors supporting the journal.

Distributed by International Publishers Distributor.
Printed in Malaysia.

DECEMBER 1995